PB88-166707

REPORT NO.
UCB/EERC-87/02
JULY 1987

EARTHQUAKE ENGINEERING RESEARCH CENTER

# EARTHQUAKE SIMULATION TESTS AND ASSOCIATED STUDIES OF A 0.3-SCALE MODEL OF A SIX-STORY ECCENTRICALLY BRACED STEEL STRUCTURE

by

ANDREW S. WHITTAKER
CHIA-MING UANG
VITELMO V. BERTERO

Report to the National Science Foundation

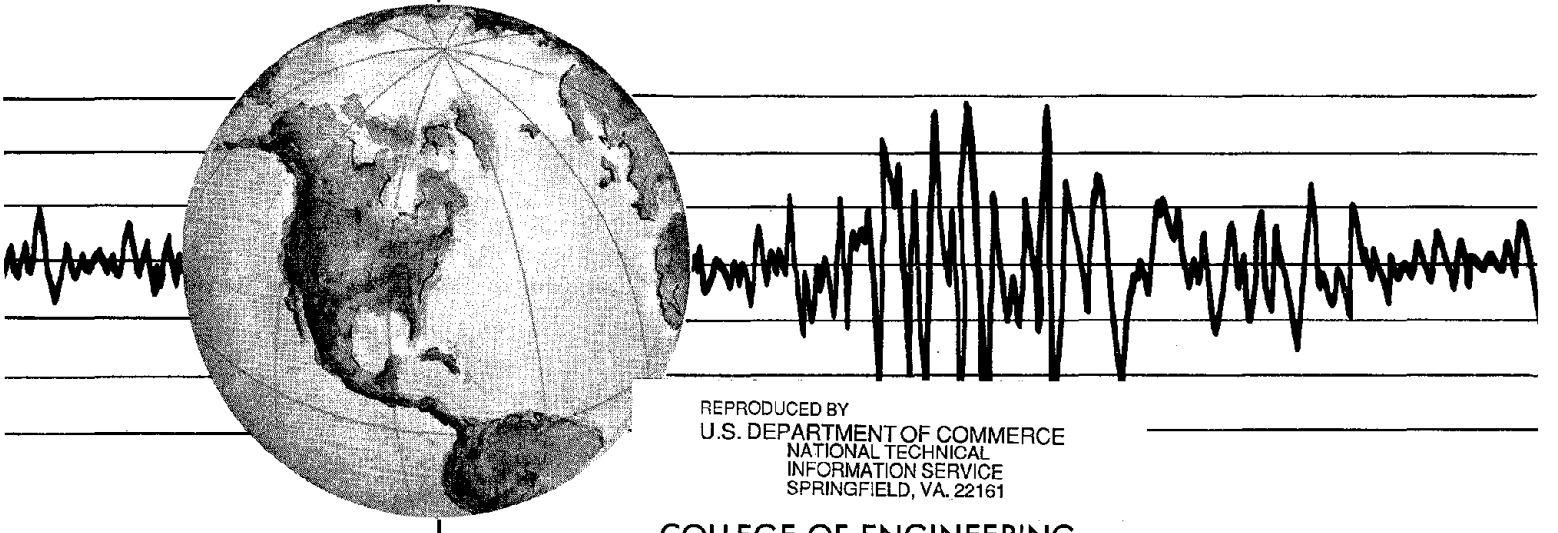

REPRODUCED BY
U.S. DEPARTMENT OF COMMERCE
NATIONAL TECHNICAL
INFORMATION SERVICE
SPRINGFIELD, VA. 22161

COLLEGE OF ENGINEERING

UNIVERSITY OF CALIFORNIA • Berkeley, California

For sale by the National Technical Information Service, U.S. Department of Commerce, Springfield, Virginia 22151

See back of report for up to date listing of EERC reports.

DISCLAIMER

Any opinions, findings, and conclusions or recommendations expressed in this publication are those of the authors and do not necessarily reflect the views of the National Science Foundation or the Earthquake Engineering Research Center, University of California, Berkeley

50272-101

| REPORT DOCUMENTATION PAGE | 1. REPORT NO. NSF/ENG-87030 | 2. | 3. Recipient's Accession No. PB88 166707/AS |
|---|---|---|---|

**4. Title and Subtitle**
Earthquake Simulation Tests and Associated Studies of a 0.3-scale Model of a Six-Story Eccentrically Braced Steel Structure

**5. Report Date**
July 1987

**6.**

**7. Author(s)**
Andrew S. Whittaker, Chia-Ming Uang and Vitelmo V. Bertero

**8. Performing Organization Rept. No.**
UCB/EERC-87/02

**9. Performing Organization Name and Address**
Earthquake Engineering Research Center
University of California
1301 South 46th Street
Richmond, California 94804

**10. Project/Task/Work Unit No.**

**11. Contract(C) or Grant(G) No.**
(C)
(G) ECE 82-08141
ECE 84-19739

**12. Sponsoring Organization Name and Address**
National Science Foundation
1800 G. Street, N.W.
Washington, D.C. 20550

**13. Type of Report & Period Covered**

**14.**

**15. Supplementary Notes**

**16. Abstract (Limit: 200 words)**

This report summarizes the research conducted in the Six-Story Eccentrically Chevron Braced Steel Building Structures Phase of the U.S.-Japan Cooperative Earthquake Research Program.

The selection, design and testing of the prototype are discussed and a review of the design of the eccentrically chevron braced prototype, in accordance with the 1985 UBC, 1984 ATC 3-06 and 1986 SEAOC, is presented. The results of the static and dynamic analyses of the prototype are discussed. The design, construction and instrumentation of the model are described and its mechanical characteristics are compared with those results predicted by DRAIN-2DX.

The experimental program, the earthquake simulator tests and the data acquisition and processing techniques, in addition to the predicted strength and response of the model, are discussed in detail. The results obtained from one serviceability limit state, one damageability limit state and three collapse limit state tests are described fully. An evaluation of these test results regarding the design and construction of eccentrically chevron braced dual systems is presented. Finally, a number of code-based recommendations are presented.

**17. Document Analysis a. Descriptors**

earthquake engineering
earthquake simulation
earthquake resistant design
limit state
serviceability limit state
damageability limit state
collapse limit state

**b. Identifiers/Open-Ended Terms**

**c. COSATI Field/Group**

| 18. Availability Statement: | 19. Security Class (This Report) | 21. No. of Pages |
|---|---|---|
| Release unlimited | unclassified | 425 |
| | 20. Security Class (This Page) unclassified | 22. Price |

-1-a

# U.S.-JAPAN COOPERATIVE EARTHQUAKE RESEARCH PROGRAM

# EARTHQUAKE SIMULATION TESTS AND ASSOCIATED STUDIES OF A 0.3-SCALE MODEL OF A SIX STORY ECCENTRICALLY BRACED STEEL STRUCTURE

by

**Andrew S. Whittaker**
*Graduate Student*

**Chia-Ming Uang**
*Research Engineer*

and

**Vitelmo V. Bertero**
*Professor*

**A Report to Sponsor:**
**National Science Foundation**

**Report No. UCB/EERC-87/02**
**Earthquake Engineering Research Center**
**College of Engineering**
**University of California**
**Berkeley, California**
**July 1987**

# ABSTRACT

This report summarizes the research conducted in the Six-Story Eccentrically K-braced Steel Building Structures Phase of the U.S.-Japan Cooperative Earthquake Research Program.

The University of California, Berkeley portion of the research program has the following objectives: (i) to review the design of the prototype and to predict its behavior; (ii) to design, fabricate and instrument the largest scale model of the prototype that could be tested on the Earthquake Simulator at the Earthquake Engineering Research Center; (iii) to conduct earthquake simulator testing of the reduced-scale model; (iv) to evaluate the reliability of testing reduced-scale models; (v) to evaluate the experimental results and their implications regarding earthquake resistant design and construction of eccentrically K-braced steel structures; (vi) to evaluate the reliability of computer programs to predict the seismic response of eccentrically K-braced steel structures; and (vii) to formulate recommendations for improving the design and construction of eccentrically K-braced steel frames and dual systems.

The selection, design and testing of the prototype are discussed and a review of the design of the eccentrically K-braced prototype, in accordance with the 1985 UBC, 1984 ATC 3-06 and 1986 SEAOC, is presented. The results of the static and dynamic analyses of the prototype are presented and discussed. The design, construction and instrumentation of the model are described and its mechanical characteristics are compared with those results predicted by DRAIN-2DX.

The experimental program, the earthquake simulator tests and the data acquisition and processing techniques, in addition to the predicted strength and response of the model, are discussed in detail. The results obtained from one serviceability limit state, one damageability limit state and three collapse limit state tests are described fully. An evaluation of these test results regarding the design and construction of eccentrically K-

braced dual systems is presented.

The measured response of the model is compared with its analytically predicted response as well as the prototype's measured response.

Finally, a summary of the results of the research program, pertinent conclusions and a number of code-based recommendations are presented in addition to suggestions for future research in the field of braced steel structures.

# ACKNOWLEDGMENTS

The research reported here was supported by the National Science Foundation Grant Numbers ECE 82-08141 and 84-19739. The ongoing encouragement from Drs. S.C. Liu, J.B. Scalzi and M.P. Gaus of the NSF is greatly appreciated. Any opinions, discussions, findings, conclusions and recommendations are those of the authors and do not necessarily reflect the views of the sponsor.

The staff of the Earthquake Engineering Research Center, especially Messrs. Don Clyde and Carlos Llopez, Drs. Jerry Dimsdale, Beverley Bolt and Katsuya Igarashi and Mr. Wesley Neighbour have provided invaluable assistance and advice over the course of the experimental program; their contributions to this research program are gratefully acknowledged.

The authors also wish to acknowledge the contributions to this project of Professors Ray Clough, Stephen Mahin and Graham Powell, Dr. Rakesh Allahabadi and of their research colleagues at the Earthquake Engineering Research Center.

## Table of Contents

## List of Tables

## List of Figures

# I. INTRODUCTION

## 1.1 Introductory Remarks

### 1.1.1 Earthquake Resistant Design

There are two major differences between the design of earthquake resistant structures and those structures designed to resist standard excitations. These two differences are the uncertainties associated with the seismic disturbance and the consequent response of the structure to that disturbance. These circumstances make it apparent that a deterministic approach to earthquake resistant design (EQRD) is inappropriate. A probabilistic approach to both the estimation of the disturbance and the bounding of the mechanical behavior of the structure is far more realistic.

A probabilistic approach to EQRD is consistent with the philosophy of comprehensive design. A comprehensive design procedure necessitates a clear understanding of

- the sources of possible excitation and their subsequent interaction with the structure;
- the mechanical behavior of materials, structural elements and non-structural elements at both local and global levels;
- (i) functional requirements of the structure,
  (ii) serviceability requirements (*serviceability limit state*),
  (iii) levels of acceptable damage (*damageability limit state*),
  (iv) safety against collapse (*collapse limit state*);
- the construction process and aesthetic, maintenance and economic requirements.

The large uncertainties associated with estimating the demand on the structure (in terms of its strength, stiffness, stability, energy dissipation capacity and stable hysteretic behavior) and estimating the capacity of the structure, can be ameliorated through the use of conceptual design. Conceptual design, by definition, demands the correct selection of structural materials, structural configuration, vertical and lateral load resisting

systems and proper proportioning and detailing of members, connections and supports. The primary objective of a sound conceptual design is to control or decrease the seismic forces and to increase or maximize the ability of the structure to supply strength, stiffness and stable hysteretic behavior.

The problems associated with satisfying the principles of earthquake resistant design are obvious. Current research at the University of California at Berkeley has centered upon developing efficient earthquake resistant structural systems which satisfy the pertinent requirements of conceptual design - the **eccentrically braced frame** is one of these systems.

### 1.1.2 Structural Steel Framing Systems

The serviceability limit state dictates that, for minor frequent earthquake ground motions, the bare structure and the associated non-structural components should suffer no damage and that discomfort to the occupants should be minimal. Structural damage is typically avoided by providing the structure with sufficient strength to remain elastic. Non-structural damage and occupant discomfort is precluded by ensuring that the structure has sufficient stiffness to prevent significant deformation.

The damageability limit state dictates that for less frequent, moderate earthquakes the structure should suffer no damage but that minor non-structural damage is acceptable. This limit state is compatible with minor inelastic behavior in certain critical structural locations; the deformations therein produced are large enough to cause limited non-structural damage.

The collapse limit state guards against structural collapse under very infrequent, severe earthquakes; structural and non-structural damage is expected during these rare events. Furthermore, the collapse limit state guards against that non-structural damage that may jeopardize the safety of the occupants and the occupants of adjacent structures. To prevent structural collapse, the structure must be able to absorb and dissipate large amounts of energy. In general, those structural systems which exhibit large

ductility, stable hysteretic behavior and a significant degree of redundancy in the number of framing systems will perform satisfactorily in major seismic events. A dual system, that is, one comprised of at least two different, yet compatible structural systems, satisfies these requirements if the redundancy in the individual structural systems is sufficiently high.

The damageability and collapse limit states are justified on economic grounds; the costs associated with providing the structure with sufficient strength and stiffness to preclude any damage in either moderate or severe earthquakes is prohibitive and may be significantly larger than that required to rectify the resulting damage.

Guided by the requirements of these three limit states, the correct choice of structural materials and structural system can be made. Structural steel has been used extensively in regions of high seismic risk because of its excellent strength and ductility. Traditionally, two fundamentally different steel framing systems have been used for the design and construction of low, medium and high-rise buildings. For low-rise buildings (1 to 5 stories), ductile-moment resisting space frames have been used extensively. For medium and high-rise buildings (6 to 40 stories), ductile-moment resisting space frames have been used in conjunction with concentrically braced frames that supply the elastic stiffness required to prevent excessive elastic deformations under the action of low level earthquake shaking or wind loading.

The first type of framing system, the **ductile moment-resisting space frame** (DMRSF), is depicted in Figure 1.1. The DMRSF provides unobstructed space between columns which is advantageous from the architectural standpoint and it has desirable energy absorption and dissipation characteristics from the structural engineers' standpoint. The DMRSF does however have a number of shortcomings for buildings of six or more stories; to comply with serviceability requirements, that is to limit deformations, member sizes significantly larger than those required for a comparable concentrically braced system are necessary. In addition, the large shear forces in the panel zones give

rise to shearing deformations that increase the inter-story displacements and result in increased second-order (P-$\Delta$) effects. As such, the DMRSF is generally a more expensive structural system than the concentrically braced system for a structure of a given height.

The second of these systems, the **concentrically braced frame** (CBF), is shown in Figure 1.2. In this system, diagonal bracing elements with coincident centerlines form a vertically cantilevered truss; as a result the lateral story forces are resisted primarily via axial forces in the bracing members. Its large stiffness makes it an efficient framing system in the elastic range; the performance of the CBF in the inelastic range, however, is not as impressive. The inelastic cyclic performance of such a system has shown that repeated buckling of the bracing elements causes a marked reduction in brace capacity and results in pinched hysteresis loops. This result manifests itself in a significant decrease in the ability of the structure to absorb and dissipate energy; brace failure leads to unacceptably large inter-story drifts and non-structural damage. Present and proposed codes of practice recognize the shortcomings of the concentrically braced framing system by requiring a larger seismic coefficient than that required for DMRSFs. Furthermore, in regions of high seismic risk, supplementary DMRSFs are required to act as a secondary line of defense against structural collapse.

It is apparent that neither of these two traditional framing systems meets all three principal requirements of a sound earthquake resistant design. An alternative system that encompasses the attributes of both the CBF and the DMRSF is the **eccentrically braced frame** (EBF).

### 1.1.3 The Eccentrically Braced Frame - An Alternative

The eccentrically braced frame is a hybrid framing system, the parent systems being the CBF and the DMRSF. In the eccentrically braced frame, axial forces in the bracing elements are transferred to either the columns or other braces via beam flexure and shear in an element known as an **active link** [1]. Figure 1.3 illustrates four possible types of eccentrically braced frame, the D-braced, the split K-braced (also known as

chevron braced), the V-braced and the inverted V-braced frames [2]. If an EBF is correctly designed, proportioned and constructed, it possesses similar lateral stiffness to a CBF but greater ductility and energy absorption and dissipation capacity. Moreover, for a level of energy absorption and dissipation capacity similar to that of the DMRSF, it offers significant advantages in terms of drift control and overall material cost.

The active link is designed and detailed as the primary energy dissipator for the structural system. The length of the active link determines the principal mode by which it will dissipate energy. The shorter links (shear links) dissipate energy principally through inelastic shear deformation in the web of the link while the longer links (moment links) dissipate energy through inelastic normal strains in the flanges. Extensive experimental studies at Berkeley [1-7] on the cyclic inelastic behavior of isolated links have shown that those active links designed to yield primarily in shear have excellent energy dissipation capacity under severe cyclic loading. Furthermore, it has been shown that shear links are better energy dissipators than moment links.

Capacity design is used to proportion the bracing elements that frame into the shear link; the braces are designed to remain elastic at a load level associated with the ultimate shear strength of the shear link; thereby overcoming one of the major shortcomings of the CBF (deterioration of brace post-buckling strength and stiffness under cyclic loading). The elastic stiffness of the EBF for short link lengths approaches that of the CBF. The variation in elastic lateral stiffness for two eccentrically braced frames [1] is presented in Figure 1.4. For short link lengths of the order of 10% of the bay width, the stiffness of the EBF approaches that of the CBF whereas for long link lengths of the order of 30% of the bay width, the EBF stiffness approaches that of the DMRSF. Clearly, it is possible to tune the lateral stiffness of the eccentrically braced frame to a predetermined value through the judicious choice of the link length.

The eccentrically braced frame meets the requirements of all three limit states; it possesses excellent strength and stiffness characteristics in the elastic range, yet, it is able

to dissipate large amounts of energy in the inelastic range. Furthermore, the geometry of the EBF facilitates planning freedom yet minimizes structural cost. It is an attractive structural system from the standpoint of the building owner, the architect and the structural engineer for buildings whose height varies between 6 and 40 stories.

## 1.2 U.S.-Japan Cooperative Earthquake Research Program

The overall objective of the U.S.-Japan Cooperative Research Program [8] is to improve seismic safety practices through studies to determine the relationship between full-scale tests, small-scale tests, component tests and analytical studies for reinforced concrete (Phase 1) and steel (Phase 2) structures. The research program has been tailored to :

- analyzing and testing building systems as realistically as possible,
- reviewing the effectiveness of current earthquake resistant design procedures and structural systems in light of the experimental results,
- research that is of practical interest and value to the engineering profession.

In order to meet the Phase 2 objectives of the research program, the Joint Technical Coordinating Committee (JTCC) decided to test a full-scale, six story, steel building (hereafter referred to as the **prototype**) designed to the then current U.S. and Japanese codes of practice. The prototype was constructed and pseudo-dynamically tested in the Large-Size Structures Laboratory of the Building Research Institute (B.R.I.) in Tsukuba, Japan.

In addition, a series of tests on reduced-scale models of the prototype, connections, structure sub-assemblages and composite floor systems were undertaken. A medium-scale model (hereafter referred to as the **model**) was tested on the earthquake simulator at the University of California, Berkeley (UCB).

## 1.3 Objectives of the Studies at the University of California.

### 1.3.1 General

As part of the Steel Structures Phase of the research program, two models, one concentrically K-braced and the other eccentrically K-braced, were tested on the earthquake simulator at the University of California. Uang and Bertero [9] have reported on the behavior of the concentrically K-braced model. The principal objective of the studies presented in this report was to investigate the experimental and analytical response of the eccentrically K-braced model to realistic earthquake ground motions.

### 1.3.2 First Stage : Preliminary Analytical Studies

**Review of the Prototype Design** : A thorough review of the prototype was undertaken to check whether it represented the best possible design and construction practice in the U.S.A.. The design review gave the authors the opportunity to both identify and rectify any weaknesses prior to the construction of the model. The prototype was originally designed in accordance with the 1979 edition of the Uniform Building Code and the 1981 Japanese Aseismic Code [10]. In Chapter 3 of this report, the prototype is reanalyzed and its design evaluated in accordance with :

- the Uniform Building Code (UBC), 1985 Edition [11],
- the Applied Technology Council Recommendations (ATC 3-06), 1984 Edition [12],
- the SEAOC "Recommended Lateral Force Requirements", 1986 Edition [13].

**Analysis of the Seismic Performance of the Prototype :** The dynamic characteristics and seismic performance of the prototype [14,15,16,17] were reviewed prior to the installation of the eccentric braces in the model. The results of these experimental and analytical studies as well as the physical limitations of the earthquake simulator were used to select the length scale of the model. These studies are described in Chapters 4 and 5.

### 1.3.3 Second Stage : Experimental Earthquake Simulator Studies

The objective of the testing program was to subject the model to earthquake simulator (shaking table) motions to elicit structural response that could be broadly categorized into the following :

- Serviceability Limit State Response,
- Damageability Limit State Response,
- Collapse Limit State Response.

Prior to the earthquake simulator tests, a series of diagnostic tests was undertaken to evaluate the dynamic characteristics of the eccentrically K-braced model and to verify the instrumentation and data reduction procedures. Details of the testing program are presented in Chapter 7.

### 1.3.4 Third Stage : Data Evaluation and Correlation Studies

The techniques used to process the raw test data are briefly discussed in Chapters 5 and 7. Five earthquake simulator tests are discussed in detail in Chapter 8; the implications of these test results with respect to current practice in the design of eccentrically K-braced dual systems are discussed in Chapter 9. Correlation of the earthquake simulator test results with the analytically predicted behavior and the prototype test results is presented in Chapter 10. Conversion factors for the United States System and the International System of Units (S.I.) are listed in Table 1.1.

## 1.4 Literature Review

Roeder and Popov [3] published a report in 1978 that discussed the experimental performance and associated analytical studies of diagonally braced frames incorporating active (shear) links. This report showed that an eccentrically braced system, such as that shown in Figure 1.3, has significant advantages over the more traditional concentrically braced and moment-resisting space frames. Roeder demonstrated that in order to

maximize the outstanding cyclic shear yielding properties of shear links, web stiffeners have to be provided to control and delay the onset of web buckling.

Manheim [5] extended Roeder's research to include split K-braced frames (Figure 1.3b) and developed an analysis and design procedure for eccentrically braced frames.

Yang [18] studied the experimental response of a five story, one-third scale model of an eccentrically X-braced structure on the earthquake simulator at the University of California. A simplified mathematical model was formulated and correlated with the experimentally measured response; shear yielding behavior was modeled by vertical truss elements.

Hjelmstad [1] investigated the behavior of links which yielded in both shear and flexure; that research showed that active links yielding in shear were more efficient than those yielding in flexure from the standpoint of energy dissipation. Furthermore, he concluded that the onset of web buckling could and should be delayed by the provision of web stiffeners; that the energy dissipation capacity of a shear link is greatly diminished by web buckling and that the post-buckling behavior of a shear link depends on the spacing of the transverse web stiffeners.

Malley [4,6] demonstrated the excellent energy dissipation capacity of shear links as well as suggesting guidelines for their design, detailing and construction.

Kasai [2,7,19,20,21] studied experimental and analytical responses of shear links. A plastic design method for eccentrically braced frames was proposed and the accuracy of the method was demonstrated by a direct comparison with the results of elasto-plastic finite element analyses. Kasai discussed inelastic shear link deformation at both the local and global level; the effects of material strain-hardening, moment-shear-axial force interaction and loading history were combined to formulate a simple criterion for web stiffener spacing.

Ricles [22] investigated the effect of composite action on the behavior of shear links; effective slab widths at different load levels were reported upon and eccentric brace

design forces were suggested.

Engelhardt [23,24] showed that depending upon the geometry and member sizes of the eccentrically braced frame, plastic hinges may develop in the beam and brace outside the link and that a significant loss of frame strength and inelastic deformation capacity may result. Engelhardt is currently testing links that yield predominantly in flexure (moment links); the effects of web stiffener spacing, connection detailing, link rotation capacity and yielding of the beam and brace outside of the link are under investigation.

# II. SELECTION, DESIGN AND TESTING OF THE PROTOTYPE

## 2.1 Selection of the Prototype Test Structure

A full-scale, six story, two bay by two bay office building utilizing composite construction was chosen as the subject for intensive investigation. The test structure was chosen to be representative of a medium-rise office building.

The plan view and frame elevations of the six story test building are shown in Figure 2.1. The structure, 49.21 ft square in plan and 73.43 ft high, consists of three frames parallel to the loading direction; two ductile moment-resisting space frames on Grid Lines A and C and an eccentrically braced frame on Grid Line B. Transverse to the loading direction there are three frames; two cross-braced frames on Grid Lines 1 and 3 and an unbraced frame on Grid Line 2. All column-to-girder connections in the transverse frames were bolted, shear type connections. The cross-bracing provided lateral stiffness in the transverse direction as well as enhancing the torsional stiffness of the structure.

The composite floor system, shown in Figure 2.2, was constructed using lightweight reinforced concrete cast on 1.6 mm thick, standard steel floor decking supported by steel W girders. To develop full composite action, shear studs were provided to transfer the shear forces developed on the slab-to-girder interface. The lightweight concrete had a specified strength of 3.0 ksi and the slab's wire mesh reinforcement consisted of 0.24 inch (6mm) diameter deformed bars on a 4 inch square grid.

## 2.2 Design of the Prototype Test Structure

The design criteria, loads and procedure were reported in detail by Foutch et al. [15] for the concentrically K-braced prototype. The design criteria adopted for the concentrically K-braced prototype were :

(i) The design gravity and earthquake loads should be representative of those specified in both the U.S.A. and Japan.

(ii) Allowable stresses under earthquake loading can be increased by one-third above those values specified for gravity or permanent loading.

(iii) Girders and columns should be W sections of ASTM-A36 steel.

(iv) Bracing members should be ASTM A500 Grade B square steel tubing and should be designed to resist both tension and compression.

(v) Girders in the braced bay should be designed for gravity loads without consideration of the supporting effect provided by the braces.

(vi) Girder-to-column connections should be designed as moment connections in the loading direction and shear connections in the transverse direction. The strength of the connections should satisfy the requirements of the Japanese Aseismic Design Code [10].

The design gravity loads are listed in Table 2.1; although the individual loads did not reflect the minimum quantities specified in the U.S.A. or Japan (due to inherent differences in the codes of practice), the total gravity load was appropriate for both countries.

The design earthquake forces were evaluated using the 1981 Japanese Aseismic Design Code and the 1979 Uniform Building Code (UBC). Generally the base shear coefficient calculated using the Japanese Aseismic Code is significantly larger than the corresponding UBC coefficient. However, by making different assumptions regarding site conditions and apportioning twice the UBC designated level of lateral force to the moment-resisting space frames (50% of the design lateral force), a final base shear coefficient of **0.197** was chosen.

The total reactive weight selected by the design group did not include the floor live load or the weight of the perimeter walls; if these loads had been included, the resultant

lateral load resisting system would have been too strong to be suitably damaged given the physical limitations of the B.R.I. facility. The design reactive weight was chosen to be 1400 kips. The reactive weight of the structure excluding the external walls was 1356 kips (Table 2.3), that is, 97% of the design reactive weight.

The design procedure, connection details and construction notes for the concentrically K-braced prototype was presented by Foutch et al. [15] and Uang and Bertero [9].

Table 2.2 lists the W section sizes used for the column, girder and brace members in the prototype; the mark numbers are shown in Figure 2.1. The prototype floor weights are presented in Table 2.3; the second column contains those dead loads noted in Table 2.1 multiplied by the corresponding contributing areas; the third column lists the loads in the second column excluding the weight of the external wall and the fourth column lists the as-tested weights of the individual floors. The measured material properties of the prototype's structural steel and lightweight concrete are presented in Table 2.4.

The eccentrically K-braced prototype was a modified version of the concentrically K-braced prototype. The design of the shear links and the eccentric braces was undertaken by Kasai and Popov [25]. The design of the shear links and the eccentric braces was constrained by :

(i) the geometry of the existing concentrically K-braced prototype,

(ii) the existing steel W sections, especially those in the concentrically braced frame (Frame B).

The length of the active link was chosen to ensure web shear yielding and was based on the equation of statics that incorporates interaction in the moment-shear space, namely :

$$b \leq b^* = \frac{2M_p^*}{V_p} \tag{2.1}$$

where $b$ = shear link length

$b^*$ = maximum shear link length

$$M_p^* = \sigma_y(d-t_f)(b_f-t_w)t_f$$

$$V_p = \frac{\sigma_y(d-t_f)t_w}{\sqrt{3}}$$

where $\sigma_y$, d, $t_f$, $b_f$ and $t_w$ are the yield stress, overall depth, flange thickness, flange width and web thickness of the beam section, respectively. For a W18×40 structural section rolled from A36 steel, the maximum shear link length, $b^*_{max}$, is 33 inches; for W18×35, $b^*_{max}$ is 28 inches and for W16×31, $b^*_{max}$ is 29 inches. If moment-shear interaction is ignored, the maximum shear link lengths are 48 inches, 43 inches and 43 inches, respectively. A shear link length of 28 inches (711 mm) was chosen for all six levels of the prototype; web stiffener thickness and spacing were based upon the research findings of Manheim [5]. The eccentric braces were designed to remain elastic at a load level consistent with the ultimate shear strength of the corresponding links.

## 2.3 Program of Study

### 2.3.1 Experimental Research

The pseudo-dynamic earthquake simulation testing of the prototype was conducted in three stages :

(1) **Stage 1 Testing - Concentrically K-Braced Frame**

The 1978 Miyagi-Ken-Oki (MO) N00E earthquake record was used as the input signal. The three tests had different levels of peak acceleration and were classed as follows :

(a) **Minor Test** - Serviceability Limit State

MO - Peak acceleration of 65 gals or 6.6%g

(b) **Moderate Test** - Damageability Limit State

MO - Peak acceleration of 250 gals or 25.5%g

(c) **Final Test** - Collapse Limit State

MO - Peak acceleration of 500 gals or 51.0%g

Free and forced vibration tests were also undertaken to evaluate the natural frequencies, mode shapes and modal damping ratios of the prototype.

(2) **Stage 2 Testing - Eccentrically K-Braced Frame :**

Five earthquake simulation tests were conducted in Stage 2; two tests utilized the 1952 Kern County Taft N21E earthquake record and the remaining three used sinusoidal input whose period approximated the fundamental period of the prototype. The three tests using sinusoidal input were all part of the one test conducted after the Taft 500 gals Test. The five tests can be classed as follows :

(a) **Minor Tests** - Serviceability Limit State

Taft - Peak acceleration of 65 gals or 6.6%g

Sine - Peak acceleration of 97 gals or 9.9%g

(b) **Moderate Test** - Damageability Limit State

Sine - Peak acceleration of 270 gals or 27.5%g

(c) **Final Tests** - Collapse Limit State

Taft - Peak acceleration of 500 gals or 51.0%g

Sine - Peak acceleration of 320 gals or 32.6%g

The procedure used to install the eccentric bracing and repair the structural slab prior to the commencement of Stage 2 is described in detail in Reference 17. The results of these five tests and the associated vibration tests are presented by Kawakami et al. [17], Yamanouchi et al. [26] and the B.R.I. Steel Group [27].

(3) **Stage 3 Testing - Unbraced Frame**

The testing of the unbraced structure used the NS component of the 1940 El Centro earthquake record with a peak acceleration of 350 gals (35.6%g) as the input signal. The results of this test and the associated free vibration tests are presented in Reference 28.

### 2.3.2 Analytical Research

Analytical studies have been undertaken by a number of researchers, both in the U.S.A. and Japan, in an attempt to predict the local and global responses of both the concentrically and eccentrically K-braced prototypes; the results of two of these studies are discussed briefly below.

Uang and Bertero [9] studied the analytical response of the concentrically K-braced prototype; their mathematical model incorporated the AISC formulation for composite slab contributions and the measured mechanical properties of the prototype. The correlation between the predicted and measured response of the prototype to the 65 gals, 250 gals and 500 gals Miyagi-Ken-Oki N00E earthquake records was extremely good. Collapse analyses of the prototype were undertaken using both a triangular load distribution and a uniform load distribution; these results gave a good estimate of its maximum strength.

Boutros and Goel [29] developed a mathematical model for the eccentrically K-braced prototype; the global displacement response of their analytical model was in reasonable agreement with the experimental response (for the limited number of displacements presented in Reference 29). The correlation of the measured and analytical story shear and shear link response time histories was not presented.

# III. DESIGN REVIEW OF THE PROTOTYPE

## 3.1 General

The design of the eccentrically K-braced prototype is reviewed in accordance with the 1985 UBC [11], 1984 ATC 3-06 [12] and 1986 SEAOC [13] in this chapter. The three dimensional analyses of the prototype were performed using the substructuring option in the SAP-80 [30] computer program. In Section 3.5, the provisions of the UBC, ATC and SEAOC are discussed in terms of the design and construction of eccentrically K-braced frames.

## 3.2 Prototype Design Review - UBC 1985

### 3.2.1 General

The prototype would be classified by the UBC as a dual system consisting of ductile moment-resisting space frames and braced frames. The UBC stipulates the following design criteria for dual systems :

- The moment-resisting space frames and braced frames shall resist the design lateral force in accordance with their relative rigidities.
- The ductile moment-resisting space frames shall resist not less than 25% of the design lateral force.
- The braced frame acting independently of the ductile moment-resisting space frame shall resist the design lateral forces.

If these three criteria are satisfied, the UBC assigns a horizontal force factor (K) of 0.8 to the structure; structures designed using such a factor must incorporate ductile moment-resisting space frames. Furthermore, in regions of high seismic risk (Seismic Zones 3, 4 and part of Zone 2), all members in the braced frames must be designed for 125% of the design lateral force (Section 2312 (j) 1G). The factor of 1.25 is intended to compensate

for the limited ductility in axially loaded compression members and relates primarily to concentrically braced frames.

### 3.2.2 Design Loading

The analysis of the prototype was based on gravity (dead and live) loads and earthquake loads. Wind loads are negligible with respect to earthquake loads in Seismic Zone 4 and were ignored in the analyses.

**Gravity Loading :** The dead and live loads listed in Table 2.1 were used as the gravity loads for the analysis and design of the prototype. The weight of the external wall was included as a design dead load but not as a reactive weight for the reasons cited in Section 2.2. Live load reductions as and when permitted by the UBC were considered in formulating the gravity loads.

**Earthquake Loading :** In accordance with UBC Clause 2312, the equivalent lateral force procedure was used to calculate the design lateral loads. The UBC design base shear ($V_b$) is determined as follows :

$$V_b = C_s W = Z\ I\ K\ C\ S\ W \tag{3.1}$$

where Z, I, K, C, S and W, respectively, are the coefficients that depend on the seismic zone, building importance, type of building frame, period of the building, soil properties and the reactive weight of the building (=1356 kips). The following values, consistent with the original design [15], were used to calculate the design lateral loads :

$Z = 1.0$ for a building in Seismic Zone 4

$I = 1.0$ for non-essential buildings

$K = 0.8$ for a dual braced system

$S = 1.5$ if $T_s$ is not evaluated

$$T = \frac{0.05 h_n}{\sqrt{D}} = 0.05 \frac{70.5'}{\sqrt{49.2'}} = 0.50 \text{ second}$$

$$C = \frac{1.0}{15\sqrt{T}} = 0.094 \ .$$

The design base shear given by Equation 3.1 is

$$V_b = 0.113\ W = 0.113 \times 1356 = 153.4 \text{ kips} \ . \tag{3.2}$$

The lateral force distribution corresponding to Equation 3.2 and Clause 2312 of the UBC is given by the following equation :

$$F_x = V_b \frac{W_x h_x}{\sum_{i=1}^{n} W_i h_i} \tag{3.3}$$

where $F_x$ , $W_x$ , $W_i$ , $h_x$ and $h_i$ are the lateral force at level 'x', the reactive weights at levels 'x' and 'i', respectively, and the heights above the base to levels 'x' and 'i', respectively. The resulting lateral force distribution is presented in Table 3.1. Torsional moments, equivalent to the story shear acting at an eccentricity of 5% of the maximum building dimension, were included in the analyses.

### 3.2.3 Discussion of the UBC Analyses

The following loading combinations were considered :

(i) 1.0 DL + 1.0 LL (Dual System)

(ii) 1.0 DL + 1.0 LL ± 1.0 EQ (Dual System)

(iii) 1.0 DL + 1.0 LL ± 1.25 EQ (Braced Frame Alone)

(iv) 1.0 DL + 1.0 LL ± 0.25 EQ (DMRSF Alone)

The critical load case for the eccentrically braced frame was 1.0 DL + 1.0 LL ± 1.25EQ and for the ductile moment-resisting space frames, the critical load case was 1.0 DL + 1.0 LL ± 0.25 EQ. The stress ratios in the columns, beams, bracing elements and shear links in the braced frame were satisfactory provided that the beams outside the shear links were assumed to be restrained over their entire lengths. The horizontal components of the eccentric brace forces were included as axial forces in the beams outside

the shear links. The stress ratios in the column and beam elements of the ductile moment-resisting space frames were less than unity.

The peak lateral displacements and inter-story drift ratios are shown in Table 3.2; the inter-story drift ratios were calculated using the inter-story drifts multiplied by 1.0/K in accordance with UBC Clause 2312. All of the inter-story drift indices were significantly less than the specified limit of 0.5%. As braced frames are generally not required for structures of this height and considering that the base shear coefficient was significantly less than the 0.197 used to design the structure, the drift results obtained above are reasonable.

## 3.3 Prototype Design Review - ATC 3-06 1984

### 3.3.1 General

The test structure would be classified by the ATC as a dual system and to be consistent with Section 3.2, it was assigned to Seismic Performance Category C. The ATC stipulates the following design criteria for a dual system :

- The special moment frames and the braced frames shall resist the total seismic force in proportion to their relative rigidities.
- The special moment frames shall be capable of resisting at least 25% of the prescribed seismic force.

The ATC, in a manner similar to the UBC, does not differentiate between concentrically and eccentrically braced frames; the dual braced system is assigned a Response Modification Factor (R) equal to six. This factor is used to reduce the linear elastic response spectra (LERS) to an inelastic derived response spectra (IDRS).

### 3.3.2 Design Loading

The ATC analysis was based upon the gravity loads noted in Section 3.2.2 and the earthquake loads presented below.

**Earthquake Loading :** The ATC lateral force procedure was used to calculate the design lateral loads; the prototype would be classified as a *regular* building in both plan and elevation. The ATC seismic base shear ($V_b$) is determined as follows :

$$V_b = C_s W \tag{3.4}$$

where $C_s$ and W are the seismic design coefficient and the reactive weight (=1356 kips), respectively. The seismic design coefficient is calculated as follows :

$$C_s = \frac{1.2 A_v S}{R T^{2/3}} \tag{3.5}$$

where $A_v$, S, R and T, respectively, are coefficients depending upon the seismic zone, soil properties, the type of structure and the period of the building. To be consistent with the UBC analysis, the following values of the ATC parameters were chosen :

$A_a = A_v = 0.4$

$S = 1.5$ for soft soil deposits

$R = 6.0$ the response modification factor for dual systems

$$T = \frac{0.05 h_n}{\sqrt{L}} = 0.05 \frac{70.5'}{\sqrt{49.2'}} = 0.50 \text{ second} .$$

On the basis of Equations 3.4 and 3.5, the seismic design coefficient is equal to 0.190. However, the ATC states that for Soil Type 3 (S=1.5) and $A_a \geq 0.3$ the value of $C_s$ can be calculated as follows :

$$C_s = \frac{2.0 A_a}{R} \tag{3.6}$$

and the resulting design seismic base shear at first significant yielding is

$$V_b = 0.133 \times W = 0.133 \times 1356 = 180.7 \text{ kips} . \tag{3.7}$$

The lateral seismic shear force distribution corresponding to Equation 3.7 and Section 4.3 of ATC 3-06 is determined as follows :

$$F_x = C_{vx} V_b \tag{3.8}$$

$$C_{vx} = \frac{W_x h_x^k}{\sum_{i=1}^{n} W_i h_i} \tag{3.9}$$

where k (=1 in this instance) is a factor relating to the period of the building and the remaining terms are defined in Section 3.2.2. The resulting lateral force profile is presented in Table 3.3. Torsional moments, equivalent to the story shear acting at an eccentricity of 5% of the building dimension, perpendicular to the loading direction, were included in the analyses.

### 3.3.3 Discussion of the ATC Analyses

The following loading combinations were considered :

(i) $1.2Q_D + 1.0Q_L \pm 1.0Q_E$ (Dual System)

(ii) $0.8Q_D \pm 1.0Q_E$ (Dual System)

(iii) $1.2Q_D + 1.0Q_L \pm 0.25Q_E$ (MRSF Alone)

(iv) $0.8Q_D \pm 0.25Q_E$ (MRSF Alone)

The influence of non-orthogonal loading was included in the analyses using the simplified approach noted in ATC Section 3.7.2, that is, 100% of the seismic forces in one direction and 30% of the seismic forces in the perpendicular direction were assumed to act concurrently.

The critical load case for the eccentrically K-braced frame was 1.2 $Q_D$ + 1.0 $Q_L$ ± 1.0 $Q_E$ and the critical load case for the special moment frames was 1.2 $Q_D$ + 1.0 $Q_L$ ± 0.25 $Q_E$. The stress ratios in all the structural elements in both the braced and unbraced frames were less than unity. The inclusion of the bi-directional ground motion had only a minor influence on the computed stress levels.

The peak lateral displacements and inter-story drift ratios are shown in Table 3.4. The design story drifts were calculated using the calculated elastic drifts factored by the deflection amplification factor ($C_d$ = 5.0 for a dual system) given in Table 3-B of ATC 3-06. As an office building, the prototype would be classified into Seismic Hazard Exposure Group 2; the calculated inter-story drifts were significantly less than the limiting value of 1.5%.

## 3.4 Prototype Design Review - SEAOC 1988

### 3.4.1 General

In accordance with SEAOC, the design of a dual braced system must satisfy the following requirements :

- The moment-resisting space frames and the braced frame shall resist the lateral loads in proportion to their relative rigidities.
- The specially detailed moment-resisting space frames shall be capable of resisting at least 25% of the base shear.

SEAOC differentiates between concentrically and eccentrically braced dual systems by assigning different coefficients and regulations to the two framing systems. To obtain an inelastic derived response spectrum, SEAOC reduces the smoothed linear elastic response spectrum by a factor denoted by $R_w$. This factor serves a similar function to the Response Modification Factor (R) used in the ATC. For eccentrically K-braced dual systems, SEAOC assigns a value of 12 to $R_w$.

### 3.4.2 Design Loading

The SEAOC analysis was based upon the gravity loads noted in Section 3.2.2 and the earthquake loads presented below.

**Earthquake Loading :** A static force procedure was used to calculate the design lateral loads. The SEAOC design base shear is determined using the following formula :

$$V_b = \frac{ZIC}{R_w} W \tag{3.10}$$

where Z, I, C and $R_w$, respectively, are coefficients depending on the seismic zone, the building occupancy, the soil type, the building period and the type of building frame. To be consistent with the UBC analysis, the following values of these parameters were chosen :

$Z = 0.4$ for Seismic Zone 4

$I = 1.0$ for a non-essential structure

$R_w = 12$ for a dual system with an eccentrically braced frame

$S = 1.5$ for soft soil deposits (Type $S_3$)

$T = C_t(h_n)^{3/4} = 0.030(70.5')^{3/4} = 0.73$ second

$$C = \frac{1.25S}{T^{2/3}} = 2.37 \ .$$

For a structure in Seismic Zone 4 founded on Soil Type $S_3$, $C_{max}$ can be taken as 2.25. On the basis of Equation 3.10, the design base shear ($V_b$) is

$$V_b = 0.075\ W = 0.075 \times 1356 = 101.8 \text{ kips} \ . \tag{3.11}$$

The lateral force distribution corresponding to Equation 3.11 and Section 1E4 is determined through the use of an equation similar to that used by the UBC (Equation 3.3). The SEAOC lateral force distribution is shown in Table 3.5. Torsional moments, equivalent to the story shear acting at an eccentricity of 5% of the building dimension, perpendicular to the loading direction, were included in the analyses.

### 3.4.3 Discussion of the SEAOC Analyses

The following loading combinations were considered :

(i) $1.0P_{DL} + 1.0P_{LL} \pm 1.0P_{EQ}$ (Dual System)

(ii) $1.0P_{DL} + 1.0P_{LL} \pm 0.25P_{EQ}$ (DMRSF Alone)

The influence of non-orthogonal loading was included in the analyses using the simplified approach noted in SEAOC Section 1H(c)2 and outlined in Section 3.3.3.

The critical load case for the eccentrically K-braced frame was 1.0 $P_{DL}$ + 1.0 $P_{LL}$ ± 1.0 $P_{EQ}$ and the critical load case for the ductile moment resisting space frames was 1.0 $P_{DL}$ + 1.0 $P_{LL}$ ± 0.25 $P_{EQ}$. The stress ratios in all structural elements in both the braced and unbraced frames were significantly smaller than unity. Similarly, the column compressive stresses did not exceed 1.7 $F_a$ under the application of 1.0 $P_{DL}$ + 1.0 $P_{LL}$ ± 4.5 $P_{EQ}$, nor $F_y$ under the application of 1.0 $P_{DL}$ ± 4.5 $P_{EQ}$ (4.5 = 3 $R_w$/8).

The lateral displacements and inter-story drift ratios are shown in Table 3.6; all of the inter-story drift ratios were substantially less than the code specified limit of 0.03/$R_w$ (=0.0025) or 0.25%.

Section 4H of the SEAOC guidelines deals with the design and proportioning of eccentrically braced frames; a number of these clauses (noted in the parentheses) are discussed below. The detailing of the prototype shear link at Level L2 is shown in Figure 3.1.

**(1) Link Beam :** The flange width-thickness ratios ($b_f/2t_f$) for W18×40, W18×35 and W16×31 are 5.73, 7.05 and 6.28, respectively, and do not exceed the SEAOC limit of $52/\sqrt{F_y}$ = 8.67. This clause guards against local buckling of the flanges of the shear link in the presence of high axial compressive stresses and promotes the use of compact sections.

**(3) Link Beam Rotation :** The geometry of an eccentrically K-braced frame is shown in Figure 3.2a and the assumed inelastic displacement field is shown in Figure 3.2b. The equation of kinematics relating $\theta_p$, $\gamma_p$ and L is

$$\gamma_p \, e = \theta_p \, L \qquad (3.12)$$

where $\gamma_p$ = plastic shear strain

$\theta_p$ = factored elastic rotation (=3 $\theta_{el} R_w/8$)

$\theta_{el}$ = elastic inter-story drift index or rotation

e = clear length of the active link

L = centerline dimension of the braced bay

The elastic inter-story drift index ($\theta_{el}$) was calculated using the inter-story drifts that resulted from the application of the equivalent lateral forces. The maximum plastic shear strain calculated from Equation 3.12 was 0.03 radian and significantly less than the maximum specified value of 0.06 radian for these six shear links.

**(4) Link Beam Web :** The shear stresses in all six shear links resulting from the equivalent lateral forces were substantially less than the maximum specified values. As doubler plates do not proportionally reduce shear stresses and as they can give rise to undesirable stress concentrations, their use in shear links is precluded.

**(6) Link Beam Stiffeners :** The thickness of the full depth stiffeners exceeds the minimum requirements in Clause 6. The minimum requirements specified in this clause were based upon the results obtained from shear link specimens tested at Berkeley [2].

**(7-9) Intermediate Web Stiffeners Requirements :** Intermediate web stiffeners in the shear link were required as per Clause 7; the web stiffener spacing for all six shear links complied with Clause 8.

**(12) Brace Strength :** The nominal shear yielding strength of the shear links ($V_p$), the nominal shear link strength resolved into the plane of the eccentric braces ($P_r = V_p/\cos\alpha$), the eccentric brace design axial forces ($1.5P_r$) and the eccentric brace stress ratios are listed in Table 3.7. The strength of the shear links and the braces were based upon the nominal yield stresses of their respective steels. All twelve eccentric braces satisfied the requirements of this clause. In order to ensure that the eccentric braces remain elastic at the ultimate strength of the associated shear link, SEAOC assumes that the maximum shear strength of a bare steel shear link is 150% of its nominal shear yielding strength. The effect of composite action on the strength of shear links has been

ignored in this clause.

**(13) Column Strength :** The column elements in both the eccentrically braced frame and in the ductile moment-resisting space frames remain elastic at a load level equal to 125% of the strength of the eccentrically braced frame. The strength of the eccentrically braced frame was calculated in accordance with Clause 12. This clause is designed to ensure that plastic hinges are excluded from the column elements and therefore, that the integrity of the vertical load support system is not compromised.

**(16) Axial Forces :** Axial forces equal to the horizontal component of the eccentric brace forces were included in the design of those beams immediately outside the shear links. A common design assumption is to transfer the horizontal component of the brace axial forces through the concrete slab. At load levels consistent with severe earthquake shaking, the concrete slab adjacent to the shear link is severely damaged and the corresponding slab-to-stud-to-steel beam interface is highly degraded. A conservative assumption is to transfer the entire component of the eccentric brace force through the steel beam. The importance of maintaining elastic beam and brace elements outside the shear (or moment) link has been discussed by Engelhardt [24].

**(17) Beam Flanges :** The prototype was detailed such that transverse W beams framed into both ends of all six shear links. This provided the restraint against lateral-torsional buckling required by this clause. Intermediate stiffeners were not required since the shear link length was less than $76b_f/\sqrt{F_y}$. The strength of the lateral end bracing significantly exceeded the requirement of 1.5% of the beam flange strength.

## 3.5 Summary and Conclusions

### 3.5.1 Design Base Shear

The prototype design base shear coefficients for the UBC, ATC and SEAOC are listed in Table 3.8. These coefficients are based upon the previously noted assumptions; that the structure is sited in a region of high seismic risk and is founded on soft soil

deposits. The UBC requires that the braced frames resist 125% of the design base shear (Section 3.2.1) whereas ATC and SEAOC require that the braced frames resist that percentage of the design base shear that is distributed to them in accordance with their relative rigidities (assumed equal to 90% in this instance). Extrapolating the UBC and SEAOC coefficients to yielding levels (by assuming an average working stress ratio of 0.8 which includes the one-third increase in the allowable stress under earthquake loading) and assuming deformation compatibility between the braced and unbraced frames, the UBC coefficient exceeds that of the ATC by 38% and that of SEAOC by 94%. Although the UBC base shear coefficient is greater than that of the ATC and SEAOC, it is significantly smaller than that required by the 1981 Japanese Aseismic Code [10].

As the prototype was designed for a base shear coefficient of 0.197, the prototype cannot be considered as representative of a structure designed in accordance with either the UBC, ATC or SEAOC.

**3.5.2 Elastic and Inelastic Drift Levels**

The yielding level inter-story drift indices (IDI) specified by the UBC, ATC and SEAOC are as follows :

(i) UBC : $\text{IDI} = 0.005\ \text{K} \times \frac{0.75}{0.6} = 0.0050$

(ii) ATC : $\text{IDI} = 0.0030$

(iii) SEAOC : $\text{IDI} = \frac{0.03}{\text{R}_w} \times \frac{0.75}{0.6} = 0.0031$ .

On the basis of the base shear coefficients and inter-story drift indices presented above, the story stiffness required by SEAOC is significantly less than that required by either the UBC or SEAOC.

The maximum inelastic inter-story drift indices implicitly or explicitly specified by the UBC, ATC and SEAOC are as follows :

(i) UBC $\text{IDI} = \frac{3}{\text{K}} \times 0.005\ \text{K} = 0.0150$

(ii) ATC IDI = 0.0150

(iii) SEAOC IDI = $\frac{0.03}{R_w} \times \frac{3R_w}{8} = 0.0112$ .

The experimental results presented in Chapter 8 suggest that the SEAOC inter-story drift limit of 1.12% is too conservative for eccentrically K-braced dual systems. If current design practices are followed, the flexibility of the DMRSF in the dual system is such that its strength will not be developed at inter-story drift indices of approximately 1.1% to 1.2%. These drift limits would therefore preclude the DMRSF from dissipating energy and to a large degree, negate its role in the dual system. The issues of maximum possible inter-story drifts, the role of the DMRSF in the dual system and the compatibility of the braced and unbraced frames in the dual system are discussed in Chapters 9 and 11.

### 3.5.3 Comparison of Code Design Base Shear Spectra

The 1985 UBC, 1984 ATC and 1986 SEAOC design base shear spectra are presented in Figure 3.3 for eccentrically K-braced dual systems sited on rock or firm ground (Figure 3.3a) and soft soil (Figure 3.3b). The soft soil site was categorized as Type 3 in accordance with all three seismic regulations. In Figure 3.3, the design base shear forces have been extrapolated to yielding levels (as discussed above) and the increase in the effective yielding level base shear (due to the moment frames having to resist 25% of the design base shear and so on) has not been included. On the rock site, the ATC design base shear forces are significantly greater (40%) than either the UBC or SEAOC whereas on the soft soil site, both the UBC and ATC design base shear forces are significantly greater than those of SEAOC (50%).

Although the ATC and SEAOC linear elastic design response spectra are similar for both rock and soft soil sites, there is a significant difference between their respective response modification factors. The Response Modification Factor for eccentrically K-braced dual systems is six for the ATC whereas for SEAOC it is 9.6 (=12×0.8) if the

design base shear spectra are scaled to yielding levels. The unsuitability of these modification factors and the linear elastic design response spectra to which these factors are applied, is discussed in detail in Chapter 9.

### 3.5.4 Discussion of Code Guidelines

Conceptually, the ATC approach to earthquake resistant design is preferable to that of the UBC and SEAOC in that a strength design method instead of a working stress design method is used. The use of strength methods in conjunction with realistic elastic and inelastic design response spectra is a cornerstone of a rational earthquake resistant design. The use of a working stress design method for structures assumed to undergo significant inelastic deformation is highly questionable.

The requirement in the UBC that the braced frame resist 125% of the design base shear significantly increases the effective UBC base shear coefficient. The use of SEAOC (and to a lesser extent the ATC), supposedly the most advanced earthquake resistant design regulations in the U.S.A., will lead to eccentrically braced frames with a lower level of resistance to earthquake ground motion (Figure 3.3). Although SEAOC (and ATC) has upgraded the required capacity of certain elements, the net effect will be deleterious to the behavior of braced steel structures during severe earthquake shaking.

The ATC and SEAOC values for the Response Modification Factors (R and $R_w$, respectively) are highly questionable. Bertero [31] has reported on the shortcomings associated with using a constant response modification factor over the period range, the numerical value of the factors as well as the use of a constant factor irrespective of the redundancy of the structural system.

SEAOC acknowledges the superior properties of the eccentrically braced frame with respect to concentrically K-braced and X-braced frames. The EBF design guidelines (Section 4H) encapsulate the results of the recent research in this field and offer a simple, yet effective means to design eccentrically braced frames. Although these guidelines are a definite improvement for the design and construction of eccentrically braced frames,

the improvements are negated to a large degree by the significant decrease in their required lateral strength.

# IV. ANALYTICAL RESPONSE OF THE PROTOTYPE

## 4.1 General

The analyses reported in this chapter include the derivation of the analytical flexibility matrix, natural periods and mode shapes of the prototype in addition to the prediction of its strength using both simple plastic theory and a step-by-step static nonlinear procedure.

In Section 4.5, the seismic response of the prototype is predicted for the earthquake records used for the pseudo-dynamic testing in Tsukuba, Japan. The global response quantities from these analytical studies and the pseudo-dynamic testing are presented and compared. These analyses were performed with the computer programs DRAIN-2D [32] and DRAIN-2DX [33].

## 4.2 Analytical Assumptions and Mathematical Idealization

The analyses presented in this chapter were based on the following assumptions :

(i) Structure dimensions were based on centerline measurements and the flexible connection regions were modeled to account for the offsets of the columns and beams from the connection centerlines.

(ii) The in-plane floor diaphragms were assumed to be rigid, that is, the horizontal displacements of the floor joints at a given level were assumed to be equal.

(iii) The reactive floor weights were associated with the six horizontal translational degrees of freedom; these weights are listed in the last column of Table 2.3.

The mathematical idealization of the prototype is presented in Figure 4.1. The mathematical models used for the modeling of the prototype are discussed below.

**(1) Columns :** A two component model was used to simulate the moment-rotation relationship of the column elements (Figure 4.2). The model consists of an elastic and an elasto-plastic component in parallel; yielding is constrained to concentrated plastic hinges at the column ends. A strain-hardening ratio of 5% was used on the basis of the Japanese coupon test results. The column axial force and bending moment interaction yield surface is shown in Figure 4.2b; the coordinates of the transition points for major and minor axis flexure were selected as (1.0, 0.15) and (1.0, 0.40), respectively [34].

**(2) Beams :** A two component model was used to model the bilinear behavior of the beam elements; a strain-hardening ratio of 5% was assumed for the reasons cited above. Composite action was included in the analyses; in accordance with the AISC specification [35], one quarter of the beam span was used to calculate the effective slab width. The calculation of the positive moment capacity of the section was based upon composite action including the contribution of the associated slab reinforcement; the negative moment capacity was calculated by ignoring the concrete slab but including the contribution of the slab reinforcement within the effective width. Material properties were based upon the reported properties of the steel beams and the lightweight concrete rather than their nominal properties (Table 2.4).

**(3) Braces :** The brace elements were modeled as truss elements; the net lengths of the braces were used in lieu of their nominal centerline lengths. The choice of the strain-hardening ratio was not as critical as that for the column elements since the brace behavior was expected to be elastic in the range under consideration.

**(4) Panel Zones :** The flexibility and strength of beam-to-column panel zones can significantly influence the distribution and the sequence of formation of plastic hinges in a structure. The inclusion of composite action in calculating the positive flexural capacity of beam elements may increase the result two or threefold. Depending on the topography of the panel zone, the introduction of composite action can relocate the possible plastic hinge into the panel zone from the beam outside the column. A two component

model was used to simulate the behavior of the panel zone. The panel zone element permits the beams and columns intersecting at a joint to rotate by different amounts; the relative rotation between the beam and column is equal to the shearing deformation in the panel zone. Translational displacements of the beams and columns at the joint are assumed to be identical. The panel zone is idealized as a rotational spring and Figures 4.3, 4.4 and 4.5 illustrate the formulation of the element and the nomenclature used below.

Krawinkler et al. [36,37] developed a trilinear relationship for the behavior of panel zones :

**(a) Elastic range:**

$$\gamma_p^{av} < \bar{\gamma}_y \tag{4.1}$$

$$\bar{\gamma}_y = \frac{1}{G}\frac{\sigma_y}{\sqrt{3}}\sqrt{1-(P_c/P_{cy})^2} \tag{4.2}$$

$$K_e = \frac{\Delta M}{\gamma_p^{av}} = \frac{G(d_c-t_{cf})t_{cw}d_b}{1-\rho} \tag{4.3}$$

$$\rho = \frac{V_c d_b}{\Delta M} \tag{4.4}$$

where $\gamma_p^{av}$ and G are the average panel zone shear deformation and the shear modulus of steel, respectively; the remaining terms are explained in Figure 4.5. If the column axial load ($P_c$) is small with respect to the critical axial load and the beneficial influence of column shear is ignored, the panel zone yielding moment ($\Delta M_y$) can be approximated as follows :

$$\Delta M_y = \frac{\sigma_y}{\sqrt{3}}\sqrt{1-(P_c/P_{cy})^2}\left[\frac{(d_c-t_{cf})d_b t}{1-\rho}\right] \approx \frac{(d_c-t_{cf})d_b t}{\sqrt{3}}\sigma_y \tag{4.5}$$

**(b) Post-elastic range:**

$$\bar{\gamma}_y < \gamma_p^{av} \leq 4\bar{\gamma}_y \tag{4.6}$$

$$K_t = \frac{G}{1-\rho}\frac{62.4\ I_{cf}}{5\ t_{cf}} \tag{4.7}$$

where $I_{cf}$ is the inertia of one column flange about an axis through its midheight and $t_{cf}$ is the thickness of that flange.

**(c) Strain-hardening range:**

$$\gamma_p^{av} > 4\bar{\gamma}_y \tag{4.8}$$

$$K_s = K_e\frac{E_{sh}}{E} \tag{4.9}$$

where $E_{sh}$ is the tangent modulus of the steel at the onset of strain-hardening.

The suggested trilinear panel zone model was reduced to a bilinear model for input into DRAIN-2DX. The linear elastic behavior was evaluated in the manner suggested above; the equivalent strain hardening ratio was obtained by examining the range of expected response and choosing a value of $E_{sh}$ such that the appropriate strength level was achieved at the upper end of that range.

**(5) Shear Links** The moment-shear (M-V) interaction surface for a typical W section is shown in Figure 4.6; the interaction surface can be approximated by the lower bound expression of Neal [38]. The three regions noted in Figure 4.6 correspond to

**(a) Region 1 :** Plastic hinges developing the full plastic moment $M_p$ which are simultaneously subjected to relatively small shear forces (moment links),

**(b) Region 2 :** Plastic hinges developing a moment smaller than $M_p$ but larger than $M_p^*$ (Equation 2.1) which are associated with relatively large shear forces,

**(c) Region 3 :** Plastic hinges developing a moment smaller than $M_p^*$ and associated with web shear yielding ($V \approx V_p^*$).

The balance point in Figure 4.6 is associated with simultaneous yielding in shear of the beam web and axial yielding of the beam flanges. The free body of the shear link at the

balance point is shown in Figure 4.7. The maximum shear hinge length ($b^*$), based on ideal plastic theory, is given by Equation 2.1. The increase in shear capacity above $V_p^*$ in that region where the associated moment is small (Region 3) is related to the contribution of the flanges to the shear capacity of the cross-section. A number of researchers [1,2] have studied the interaction of flexure and shear and the results of these studies are presented in Figure 4.7 in addition to the lower bound solutions proposed by Neal [38,39] and Hodge [40]. The conclusion that can be drawn from Figure 4.8 is that there is negligible moment-shear interaction at the level of first yield. Horne [41] proposed that there is no apparent reduction in $M_p$ until V approaches $V_p$ because the regions subjected simultaneously to maximum shear and bending moment are surrounded by an elastic core which limits plastic flow. The relationship proposed by Horne assumes a parabolic reduction in $M_p$ for V greater than 0.5 $V_p$, where $V_p$ is based upon the total web area ($=d \times t_w$) and a shear stress equal to $0.6\sigma_y$. The $M_{pr}$ corresponding to $V_p$ is $M_p$ minus the plastic moment capacity of the web.

The shear link was modeled as a bilinear element in which the plastic shear capacity was converted to an equivalent value in flexure assuming no interaction in the moment-shear (M-V) stress space and ignoring the contribution of the composite slab :

$$M_p^v = \frac{V_p e}{2} \tag{4.10}$$

where $V_p = \dfrac{A_w \sigma_y}{\sqrt{3}}$

$A_w$ = beam web area ($d \times t_w$)

$\dfrac{\sigma_y}{\sqrt{3}}$ = Von-Mises yield stress in pure shear.

The equivalent plastic moment capacities ($M_p^v$) and the strain hardening ratio of 3% were calculated from the test results presented by Yamanouchi et al. [26].

The use of a beam element to model shear links is only an approximation; the accuracy of this assumption is a function of the geometry of the entire structure, the shape of the yield surface and the geometry of the shear link. This model is unable to account for concurrent axial yielding of the flanges (flexural behavior) and web shear yielding, nor is the element stiffness matrix strictly correct in the post-shear yielding range. The geometry of the entire structure affects the distribution of bending moments in the individual shear links. A shear link, with negligible vertical load over its length, will yield instantaneously in shear over its entire length (for no M-V interaction) whereas the mathematical model will yield in flexure at either end when the coexisting moment reaches the equivalent plastic moment capacity. If the structure is symmetric about the eccentrically braced bay, this effect is generally small. For unsymmetric split K-braced frames or D-braced frames [2], the bending moments at either ends of the shear link are generally unequal; simultaneous yielding will not occur and the assumption of instantaneous yielding over the length of the link cannot be justified. For the symmetric K-braced prototype, the geometry of both the shear links and the entire structure justifies the use of a beam element to model the six shear links.

## 4.3 Analytical Natural Periods of Vibration and Mode Shapes

In this section, the flexibility and stiffness matrices corresponding to the six lateral dynamic degrees of freedom are evaluated and compared with the experimental values. Then, on the basis of these matrices and an assumed diagonal mass matrix, the analytical natural periods and mode shapes are calculated.

**Flexibility :** The flexibility matrix ($6\times6$) was evaluated by sequentially applying unit horizontal loads at each floor level of the model (Figure 4.1); the corresponding stiffness matrix was obtained by inverting the flexibility matrix. The analytical flexibility and stiffness matrices are shown in Tables 4.1 and 4.2, respectively; the experimental stiffness matrix [29] is shown in Table 4.4. The general structure of the analytical and

experimental stiffness matrices are quite similar. The two matrices are strongly tridiagonal and the maximum difference in the terms on the leading diagonals ($K_{ii}$) is of the order of 15%. The terms in the tridiagonal band of the experimental stiffness matrix are generally greater than those in the analytical stiffness matrix. This result can be attributed to the assumptions made in the modeling of the eccentric braces, shear links and the composite floor system. The correlation between the experimental and analytical stiffness matrices was better than expected considering the inaccuracies associated with obtaining the experimental matrix [9].

**Natural Periods and Mode Shapes** : The natural periods and mode shapes were evaluated by solving the following eigenvalue problem :

$$\underline{K}\phi = \omega^2 \underline{M}\,\phi \tag{4.11}$$

where $\underline{K} = \underline{F}^{-1}$ = stiffness matrix (6×6)

$\underline{M}$ = diagonal mass matrix (6×6)

$\phi$ = mode shape vector (6×1)

$\omega$ = angular frequency (rad/sec) .

The reactive weights used for the pseudo-dynamic testing (last column of Table 2.3) were used to form the diagonal terms of $\underline{M}$.

The analytical natural periods and mass orthogonal mode shapes are listed in Table 4.3 and the corresponding experimental values are listed in Table 4.5. The difference between the analytical periods and the prototype test results is less than 5% in the first three modes. This observation is a reflection of the small differences in the corresponding stiffness matrices. The analytical and experimental mode shapes show excellent correlation in all three modes (Figure 4.9).

The currently available mathematical models in DRAIN-2D and DRAIN-2DX can be used with confidence to predict the natural periods of vibration and mode shapes of planar bare steel structures.

## 4.4 Prediction of the Strength of the Prototype

### 4.4.1 General

In this section, the global strength and deformation characteristics of the prototype are predicted using simple plastic theory and a series of static step-by-step nonlinear analyses. To conduct these analyses, inverted-triangular (triangular) and rectangular (uniform) load patterns were considered. The first load pattern is similar to the traditional UBC (first mode) load pattern while the second can be associated with the formation of a soft first story (rigid body displacement in the upper five stories).

### 4.4.2 Simple Plastic Theory

An upper bound to the strength of the structure can be obtained using the collapse mechanism approach [39,40,41]. Simple plastic theory assumes that the material is rigid-perfectly plastic (that is, no elastic deformation or strain-hardening), that deformations are infinitesimally small, that global and local member stability is assured, that flexure dictates the response of the structure and that axial, shear and flexural interaction can be ignored. In the two limit analyses presented below only a limited number of mechanisms were considered; the member properties noted in the previous section were used in conjunction with the material strengths reported by the Japanese researchers (Table 2.4). The plastic moment capacity of the panel zone elements was selected as $\Delta M_y$ (Equation 4.5). Recognizing the high shear strains that are developed in shear links, ultimate stresses ($\sigma_u$) in lieu of yield stresses ($\sigma_y$) were also used to calculate the internal work corresponding to each of the shear links. The calculation of the external work for the various mechanisms considered did not include a contribution from the loads that were uniformly distributed along the beams because there is no net vertical displacement of the resultant of these gravity loads.

In summary, the collapse load ($P_c$) as a function of the as-built reactive weight (W=1154 kips) for the prototype is as follows :

(i) **Stress level $\sigma_y$ for all members, ignoring the composite slab contribution**

Triangular Load Distribution $P_c = 0.55W$

Uniform Load Distribution $P_c = 0.60W$

(ii) **Stress level $\sigma_u$ for all shear links, $\sigma_y$ for all other members, ignoring the composite slab contribution**

Triangular Load Distribution $P_c = 0.65W$

Uniform Load Distribution $P_c = 0.72W$

(iii) **Stress level $\sigma_u$ for all shear links, $\sigma_y$ for all other members and including the composite slab contribution to the net internal work**

Triangular Load Distribution $P_c = 0.68W$

Uniform Load Distribution $P_c = 0.76W$

The collapse mechanisms for the three cases (of two load distributions) were identical. This mechanism is presented in Figure 4.10 for Frames A(C) and B in addition to the distribution of plastic and shear hinges. The peak strength of the prototype from the pseudo-dynamic testing was approximately 0.69W. The prototype failed prematurely due to the buckling of a gusset plate in the link to brace connection at Level L2. Therefore, a direct comparison between the analytical and the experimental results cannot be made. However, the limit analyses using the ultimate strength of the link and either of the two loading patterns gave a reasonable estimate of the strength of the prototype.

### 4.4.3 Step-by-Step Static Nonlinear Analysis

The computer program DRAIN-2DX was used to undertake collapse analyses of the prototype. Collapse analyses were undertaken for the cases in which the material strain-hardening was excluded and included.

The collapse analyses based upon the assumption of zero strain-hardening were undertaken to verify the results of the limit analyses discussed above. In this instance, axial-flexure interaction was excluded in accordance with the assumptions of simple

plastic theory. The analytical base shear versus first inter-story drift and roof drift relationships for both lateral load distributions are presented in Figures 4.11 and 4.12, respectively. The results of the limit analysis ($\sigma_y$ for all members) are shown in both of these figures in addition to a number of points from the prototype strength and deformation envelope (evaluated from the Japanese test data). At critical inter-story drift levels approaching 7%, the collapse loads predicted by DRAIN-2DX were within 1% of that predicted by simple plastic theory. The collapse mechanism predicted by DRAIN-2DX was similar to the kinematically admissible field assumed in the limit analysis for both load distributions. The hinge formation sequence in the collapse analysis for both load distributions is presented in Figure 4.13; since the shear links were modeled as beam elements, shear yielding is represented by plastic hinge formation at both ends of the shear links.

The collapse analyses that included strain-hardening (Section 4.2) were undertaken to predict the strength and deformation characteristics of the prototype. The analytical base shear versus first inter-story drift and roof drift relationships for both lateral load distributions are presented in Figures 4.14 and 4.15, respectively, together with the points at which the shear strains in the link at Level L2 exceeded 0.1 radian. The results of the limit analyses ($\sigma_u$ for the shear links, $\sigma_y$ for all other members) and a number of points from the experimental envelope are also shown in Figures 4.14 and 4.15. The analytical model overestimates the strength and stiffness of the prototype for both load distributions at drift indices in excess of 0.75%. For the uniform load distribution, the analytical base shear versus roof drift index relationship correlates reasonably well with the prototype relationship. The hinge formation sequence in the collapse analysis for both load distributions is presented in Figure 4.16; the hinges shown correspond to those that formed prior to the structure attaining a strength equal to its reactive weight (=1154 kips).

### 4.4.4 Conclusions and Code Implications

The analytical strength and deformation relationship (assuming a uniform load distribution), the prototype experimental strength envelope, the strength suggested by the limit analyses ($\sigma_u$ for the shear links, $\sigma_y$ for all other members) and the nominal yielding strength of the prototype (as a function of the as-tested reactive weight) are presented in Figure 4.17. The working stress design base shear for the prototype (Section 2.2) was

$$V_b = C_s W = 0.197\ (634.7\ \text{tons}) = 125\ \text{tons} = 276\ \text{kips}.$$

The yielding level design base shear ($V_{by}$) is approximately 345 kips (=276/0.8). Although the design reactive weight was 1400 kips, the as-tested reactive weight was only 1154 kips (523.6 tons) and therefore, the yielding level base shear coefficient ($C_y$), as a function of the as-tested reactive weight, is

$$C_y = \frac{V_{by}}{W_{(test)}} = \frac{345}{1154} = 0.30\ .$$

The minimum required strength and maximum deformation relationships for the UBC (Section 3.2) and ATC 3-06 (Section 3.3) are also shown in Figure 4.17.

The limit analyses, assuming that the ultimate strength of the links are developed, gave a good approximation to the strength of the prototype, subject to the limitations noted above. As such, this method provides a convenient means by which to bound the strength of a structure and negates to a large degree, the need to undertake step-by-step nonlinear collapse analyses at the preliminary design stage. The contribution of the composite slabs to the strength of the shear links can be significant (Section 9.7) but the extent of this contribution will depend upon the degree of its degradation. As the degree of slab degradation is difficult to quantify, the contribution of the composite slab to the internal work summation can conservatively be ignored.

The analytical strength and deformation relationship correlates reasonably well with the experimental relationship; in this instance the uniform load distribution yields a

better correlation than the triangular load distribution. This observation is consistent with the prototype deformation pattern at failure.

The measured strength of the prototype (=0.69W) was of the order of 220% of the design strength of 276 kips; that is, the overstrength of the prototype with respect to the 1981 Japanese Aseismic Code was approximately 120%.

As a result of overstrength, increased stiffness and enhanced energy dissipation capacity, structures designed in accordance with the current codes of practice have successfully withstood severe earthquake shaking [31].

## 4.5 Prediction of the Seismic Response of the Prototype

### 4.5.1 General

A computer-actuator on-line system, known as the the pseudo-dynamic method [42,43,44,45] was used to test the prototype at the Building Research Institute in Tsukuba, Japan. In this method, the equations of motion are numerically integrated in a step-by-step manner using the measured restoring forces and the displacements from the previous time step; the calculated displacements are then imposed on the structure.

The response of the prototype to the 1952 Kern County, Taft Lincoln School Tunnel (N21E component) earthquake record is predicted in this section; this earthquake record was used for the pseudo-dynamic testing of the prototype.

The California Institute of Technology [46] record of the Taft ground motion is 54.4 seconds in length and the peak acceleration (PA) is 0.156g (153 gals) at the 9.1 second mark of the record. The first twenty seconds of the acceleration time history are presented in Figure 4.18a; its normalized Fourier amplitude spectrum (FAS) is shown in Figure 4.18b. The linear elastic response spectra (LERS) of the first twenty seconds of the Taft record are shown in Figure 4.19. The FAS and LERS indicate that the dominant frequency content region of the Taft record encompasses the fundamental period of

the prototype.

The computer program DRAIN-2DX was used to evaluate the response of the mathematical model using a constant time step with an event-to-event solution strategy; the idealization of the structure was described in Section 4.2. Two analyses are presented in this section; the first corresponds to the PSD-Elastic Test (PA=6.6%g or 65 gals) and the second corresponds to the PSD-Inelastic Test (PA=51.0%g or 500 gals).

DRAIN-2DX allows the user to specify Raleigh damping and the damping matrix $\underline{C}$ is expressed as:

$$\underline{C} = \alpha\underline{M} + \beta\underline{K}_0 \tag{4.12}$$

where $\underline{K}_0$ and $\underline{M}$ are the initial stiffness and mass matrices, respectively. The first two modal damping coefficients calculated from the vibration tests performed prior to the PSD-Elastic Test, were 0.35% and 0.31% (Table 4.6), respectively. These damping coefficients were used in the pseudo-dynamic tests to evaluate the damping matrix explicitly [17,26].

The first mode damping ratio obtained from the Pseudo-Dynamic Free Vibration and Pulse Response Tests varied between 1.17% and 5.9%. The additional measured damping in the prototype was a function of its displacement response and the control system configuration [26]. A first modal damping ratio of 1.25% was measured during the PSD-Elastic Test [26]. This damping ratio was assumed to be representative of the equivalent viscous damping present in the prototype during pseudo-dynamic testing. Accordingly, the Raleigh damping coefficients were based upon 1.25% of critical damping in the first two modes.

### 4.5.2 Elastic Analysis - Taft 65 gals

The predicted lateral displacement time histories and selected story shear and inter-story drift relationships are presented in Figures 4.20 and 4.21, respectively. The prototype experimental lateral displacement time histories are shown as solid lines in

Figure 4.20. The correlation between the predicted and measured lateral displacement time histories is quite reasonable. The difference between the measured and analytical peak roof displacements is less than 1%. There is a slight phase difference between the responses after the 6.5 second mark; the phase lag remains constant after this point (if a time domain correction of 0.06 second is made at the 6.5 second mark, the correlation is excellent). The predicted and measured story shear and inter-story drift relationships for the first, third and fifth stories correlate extremely well in terms of both story stiffnesses and peak ordinates.

### 4.5.3 Inelastic Analysis - Taft 500 gals

The predicted lateral displacement time histories and selected story shear and inter-story drift relationships are presented in Figures 4.22 and 4.23, respectively. The prototype experimental lateral displacement time histories are shown as solid lines in Figure 4.22. The correlation between the predicted and measured lateral displacement time histories is quite reasonable; the displacements are in phase and the ordinates are generally in close agreement. The difference between the measured and analytical peak roof displacements is less than 10%. The predicted and measured story shear and inter-story drift relationships for the first, third and fifth stories correlate extremely well in terms of both story stiffnesses and peak ordinates.

The shear force and shear strain relationships ($V - \gamma$) for the shear link at Level L2 are presented in Figures 4.24a and 4.24b for the analytical and measured responses, respectively. The link shear force was assumed to be equal to the vertical component of the eccentric brace forces and the shear strains were calculated as the difference in the link end vertical displacements divided by the link length (=28 inches). The analytical model accurately estimates the shear forces but slightly underestimates the shear strains in this link. The contribution of the composite slab was ignored in the formulation of the shear link model.

### 4.5.4 Summary

One of the objectives of the research program (Section 1.3) is to verify the adequacy of the currently available computer programs to predict the dynamic characteristics, elastic response and inelastic response of steel structures. Categorical conclusions cannot be drawn from the results of the two analyses presented above, partly on account of the uncertainties associated with the pseudo-dynamic testing method. The correlation of any analytical and experimental results must be viewed in light of the assumptions made with regards to Young's modulus, composite slab contributions and degradation, variations in $\sigma_y$ and $\sigma_u$ and so on.

However, on the basis of the results presented above and those presented by Uang and Bertero [9], the computer programs DRAIN-2D [32], DRAIN-2DX [33] and ANSR-1 [47] can predict the elastic and inelastic response of planar bare steel braced frames provided that reasonable estimates of the mechanical characteristics of the constituent materials are made.

DRAIN-2DX and DRAIN-2D cannot treat the three dimensional response of building structures; that is, these programs cannot be used to predict the static response of unsymmetric structures nor can they accommodate the interaction of those elements framing perpendicular to the loading direction. For the prototype, the stiffness and mass were symmetrically distributed and the out-of-plane frames employed simple shear connections. As a result, the two dimensional mathematical model was able to predict the response of the three dimensional prototype accurately.

# V. CONSTRUCTION AND INSTRUMENTATION OF THE MODEL

## 5.1 General

In this chapter, the selection, design, construction and instrumentation of the reduced-scale model is discussed. In Section 5.2, the Earthquake Simulator test facilities of the University of California, Berkeley are briefly discussed. The rationale for the selection of the model's scaling factor and its dependence upon the geometric similitude laws are presented in Section 5.3. A summary of the model's fabrication and construction is presented in Sections 5.4 and 5.5, respectively. The instrumentation of the model is discussed in Section 5.6 and a brief introduction to the data reduction process is given in Section 5.7.

## 5.2 Earthquake Simulator Test Facilities

The model was tested in the Earthquake Simulator Laboratory (ESL) of the University of California, Berkeley.

The main feature of the ESL is a 20 ft by 20 ft earthquake simulator table. The table is 12 inches thick, heavily reinforced and post-tensioned; it weighs approximately 45 tons (100 kips). The 12 inch gap between the table and the foundation wall is sealed by a 24 inch wide strip of reinforced nylon fabric. The maximum allowable air pressure on the nylon fabric is 4 psi and the maximum weight on the table is therefore limited to 130 kips.

The earthquake simulator is driven by seven actuators, four 25 kip vertical actuators and three 50 kip horizontal actuators. During testing, the pit beneath the table is pressurized to counterbalance the weight of the table and the model; the vertical actuators do not support gravity loads during testing. A passive stabilizing system is present (with further assistance from the vertical actuators which act as active stabilizers) to

control the table pitching motion; the pitching motion is caused by the model's overturning moments. The nominal overturning capacity of the earthquake simulator is approximately 1700 ft-kips. A detailed discussion of the earthquake simulator characteristics is given by Rea and Penzien [48] and Rinawi [49]. Figure 5.1 depicts the earthquake simulator in plan and elevation and details the limitations on its dynamic performance [48]. The types of signals that can be input to the earthquake simulator include :

- Periodic Motion - the input waveform can be selected from those available in the function generator and input to the signal generator.
- Random Motion - white noise, filtered white noise, shot noise and other stochastic records can be input to the signal generator.
- Earthquake Ground Motion - time scaled or unscaled earthquake acceleration records can be selected from a library of such records and, after processing, input to the signal generator.

The digitized displacement time history is passed through a *Preston* D/A Converter, which converts the digitized signal to an analog signal. The analog signal is then passed to the *MTS* controller which generates the table displacement command signal.

## 5.3 Similitude Requirements and the Selection of the Scale Factor

A primary objective of the Berkeley studies was to design, construct and test the largest possible steel model of the prototype that could be accommodated on the earthquake simulator.

The model was designed to comply with the similitude requirements for a reduced scale model of the prototype shown in Figure 2.1. The most suitable model was determined to be an artificial mass simulation model [9] which satisfied similitude with regard to geometric and loading parameters. Furthermore, this model complied with all material requirements except mass density. To satisfy the latter requirement, lead ballast was

added to the roof and floor slabs in such a manner that it did not affect the stiffness of the structure.

As noted in the previous section, the maximum earthquake simulator payload is approximately 130 kips. Assuming that the model's foundation and reference frame weigh approximately 15 kips, the maximum possible structure weight is of the order of 115 kips. As the weight of the prototype was 1154 kips, the maximum length factor that could be used was $\sqrt{115/1154}$=0.316. A length scale factor of 0.3048 (hereafter denoted as 0.3) was adopted for the design and construction of the model. The scale factor of 0.3 not only complied with the weight, height and plan limitations of the earthquake simulator but it also facilitated unit correlation with the prototype results. The artificial mass similitude requirements for a length factor equal to 0.305 are listed in Table 5.1.

## 5.4 Design and Fabrication of the Model

### 5.4.1 General

In order to use reduced-scale models to predict the behavior of full-scale structures in all possible limit states, it is imperative to match the stress-strain relationships of their constituent materials. In order to achieve similitude with the prototype tested in Tsukuba, Japan, it was necessary to

(i) select the structural steels for the fabrication of the model that most closely matched those used in the prototype,

(ii) fabricate W steel sections using available plate sections as similitude scaled sections were commercially unavailable, and

(iii) design and construct a similitude scaled composite slab system.

The rationale behind the choice of the model's material characteristics is presented in the following section and by Uang and Bertero [9]. A summary of the mechanical

characteristics of the model's steel and concrete is presented below and in Table 5.2.

### 5.4.2 Mechanical Characteristics of the Model's Steelwork

*Girders and Columns* : Grade 50 X10 steel best matched (to a uniaxial strain level of 12%) the mechanical characteristics of the steel used in the prototype and was used to fabricate the model's W sections. Grade 50 X10 steel was unavailable in #14 gage (0.0747 inches) and Grade 50 Cor10 steel was used for this plate thickness. The stress-strain curves for these two steels are presented in Figure 5.2.

*Bracing Elements* : The bracing elements in Frame B were standard cold formed rectangular hollow sections produced from ASTM A500 Grade B Steel (Figure 5.2). The X-bracing in Frames 1 and 3 were double angle sections rolled from ASTM A500 Grade B steel.

### 5.4.3 Fabrication of Structural Sections

A detailed discussion of the design considerations and fabrication details of the column and girder elements is presented in Reference 9. The prototype's eccentric brace sizes and their nominal cross-sectional areas, the similitude scaled nominal cross-sectional areas and the model's eccentric brace sizes and their measured areas are presented in Table 5.3. The cross-sectional area of the model's eccentric braces were 22% greater than those of the similitude scaled prototype in the lower four stories. The model's eccentric braces were selected from commercially available stock and accurate scaling of the $8\times6\times0.375$ brace was not possible. As the plastic shear capacities of the model's shear links were appreciably greater than that of the similitude scaled prototype, larger braces than those required to satisfy similitude were chosen (Section 5.5). The $3\times2\times0.125$ brace was selected for the lower four stories to ensure that shear yielding of the links would preclude brace buckling in a manner similar to that assumed by Kasai [25] for the design of the prototype's eccentric bracing.

### 5.4.4 Design of the Composite Floor System

The composite floor system used in the model was a scaled version of the floor system used in the prototype [9]. As a precursor to the testing of the concentrically K-braced model, Uang [50] tested one steel and four composite girders. The primary objectives of this study were to study composite girder behavior in a beam-to-column subassemblage under cyclic loading and to provide the information required to select the metal decking, reinforcement, shear connectors and lightweight concrete mix design for the model. The composite floor system of the model was constructed as follows :

*Metal Decking* : The profile of the model's steel decking was chosen so as to approximate that of the similitude scaled prototype steel decking; these two profiles are superimposed in Figure 5.3. The 0.018 inch thick metal sheeting used for the model's steel decking was fabricated from ASTM A446 Grade A steel and was sandblasted to remove its galvanized coating.

*Shear Studs* : Shear studs with a diameter of 0.25 inch and a length of 1.56 inches were used in the model. The studs, designated as H-4L concrete anchors were fabricated from ASTM A108 Grade 1010 steel whose minimum yield and ultimate tensile stresses were 55 and 65 ksi, respectively. The connector spacing satisfied the AISC requirements for full composite action.

*Lightweight Concrete* : A graded lightweight coarse aggregate (maximum size of 0.25 inch) in conjunction with normal weight sands was used in the concrete mix design; the mix design is presented in Table 5.3. The net unit weight of the mix was 116 pcf; the dry unit weight, 28 days after casting was 112 pcf and the water/cement ratio was specified as 0.6. The nominal 28 day strength was 4.0 ksi and close to the target strength of 4.17 ksi. At the time of testing the eccentrically K-braced model, the compressive strength and modulus of elasticity of its concrete, measured using 3 inch by 6 inch cylinders, were 5.2 and 2,775 ksi, respectively. The strength and stiffness of the model's concrete were approximately 20% greater than that of the prototype. Tensile

splitting tests on 3 inch by 6 inch cylinders gave an average tensile strength of 600 psi or $8.3\sqrt{f'_c}$. The compressive stress-strain relationships for the 3 inch by 6 inch control specimens are presented in Figure 5.4a; the relationship between its compressive strength and age is presented in Figure 5.4b.

*Slab Reinforcement* : The wire mesh reinforcement was 0.0625 inch in diameter on a 1 inch pitch; the nominal cross-section area was within 10% of the similitude scaled value. The measured yield and ultimate tensile strengths of the mesh were 79 and 85 ksi, respectively.

## 5.5 Construction of the Model

The two significant differences between the prototype and the model were the design and construction of the foundation [9] and the detailing of a number of critical connections.

A number of the prototype's connection details were modified in the construction of the concentrically K-braced model. The prototype girder-to-column connection consisted of a welded flange connection and a bolted web connection. In the model, the web shear plate was welded to the girder web and the copes at the girder-to-column interface were eliminated. The tapered prototype column splice consisted of a bolted web shear plate connection and a welded flange connection whereas in the model, the untapered connection comprised full bearing butt plates with continuous perimeter welding.

The auxiliary reactive mass (in the form of lead ingots) was added to the concentrically K-braced model to attain the similitude scaled reactive mass of the prototype. To the model self-weight of 30.77 kips, nine hundred lead ingots weighing 76.31 kips were added and the total model weight was 107.1 kips compared with a similitude scaled weight of 107.3 kips. Table 5.4 lists the similitude scaled and measured reactive weight distribution of the model.

After the testing of the concentrically K-braced model had been completed, the concentric braces were removed from the 1-2 bay and the eccentric braces were installed in the 2-3 bay. No further modifications were made to the columns or girders prior to the testing of the eccentrically K-braced model.

Because the shear area of the columns and girders in a concentrically K-braced structure has negligible effect on its response, the shear areas were not as accurately scaled as either the cross-sectional area or the second moments of area. The geometric properties of the prototype's shear links, the similitude scaled shear links and the model's shear links are presented in Table 5.5. The prototype's yield stress ($\sigma_y$) in Table 5.5 is the sample mean yield stress and the model's yield stresses of 46 ksi and 53 ksi refer to the Grade 50 X10 and Cor10 steels used for the fabrication of its W sections (Section 5.4.4). The plastic shear capacities of the model's shear links were significantly larger than that required to satisfy the similitude laws : 14% for L2 and L3, 21% for L4 and L5 and 23% for L6 and LR, respectively. The gusset plate in the prototype's link to brace connection that failed during the PSD-Sine Test (at Level L2) was reinforced in the model with additional stiffening plates as shown in Figure 5.5.

## 5.6 Instrumentation of the Model

The instrumentation was designed to record global structural response, local element response and the response of certain critical regions. One hundred and seventy-six channels of data were collected for each test; the instrumentation incorporated accelerometers, linear potentiometers (LP), direct current linear voltage displacement transducers (DCDT), strain gages, strain rosettes and clip gages.

Linear potentiometers and DCDTs were used to monitor the global displacement response of the model. These instruments were mounted on a lightweight trussed steel portal frame that straddled the model in the transverse direction or on an instrumentation frame located off the earthquake simulator parallel to Grid Line 3; both

instrumentation frames, shown in Figure 5.6, were very stiff and had a very small period of vibration.

**Earthquake Simulator Table Response :** Ten channels of data recording the motion of the earthquake simulator table were collected for each test; these channels recorded the following information (refer Figure 2.1 for reference system) :

(i) Channels 1-2 : LVDT's mounted in the shaking table horizontal actuators measured the displacement time history at two locations (x-direction).

(ii) Channel 3 : The average of two accelerometers mounted beneath the table were used to measure its horizontal acceleration time history (x-direction).

(iii) Channel 4 : The average of four accelerometers mounted beneath the table were used to measure its vertical acceleration time history (z-direction).

(iv) Channels 5-7 : The pitch (x-z plane), roll (y-z plane) and twist (x-y plane) acceleration time histories (rad/sec$^2$) of the table were measured using the response of the four vertical and two horizontal accelerometers mounted beneath the table.

(v) Channels 8-10 : The vertical displacement time history of the table was measured using LVDTs mounted in the table's vertical actuators (z-direction).

**Model Global Response :** The parameters used to measure the global structural response include lateral displacement, inter-story drifts, accelerations, story shear forces and the overturning moments at each floor level. The following instrumentation was used to evaluate these time history responses :

(i) At each floor level on Frames A and B, total horizontal displacements and accelerations were measured using transducers (DCDTs, LPs and accelerometers).

(ii) The relative vertical displacements of the model were measured at its roof level using a trussed reference frame mounted on the model's foundation. A total of six transducers (DCDTs) was used to measure the vertical displacement of the model.

(iii) The relative transverse (parallel to Grid Line 1) displacements of the model were measured at the roof level by two transducers (DCDTs) mounted on the transverse reference frame.

**Model Local Response :**

**Braces**

*Brace Force*: In the lower three stories, four strain gages were installed at the quarter point of each brace adjacent to its upper end and combined into two data channels. Because of the limited number of data acquisition channels, two strain gages were installed at the quarter point of each brace in the remaining three stories. The strain gages were calibrated to measure axial force prior to the installation of the eccentric braces in the model.

*Brace Axial Deformation*: Transducers (DCDTs) were installed on the lower two stories to measure the axial deformation of the braces.

**Columns**

*Column Shear*: The columns were instrumented to determine the storywise shear distribution. One strain rosette was glued to each side of the column web (for the web parallel to Frame B) or to the column flange (for the flange parallel to Frame B) at the column mid-height; the output from these two rosettes were combined into a single channel to increase the accuracy of the channel data (Figure 5.7). All nine columns in the first story were instrumented; in the upper five stories, the columns in Frames A and B were instrumented and the shear forces in the Frame C columns were assumed to be identical to those in the corresponding columns in Frame A.

*Column Axial Force and Bending Moment*: In order to calculate the coexisting axial force and bending moments in the first story columns, two strain gages (combined into one channel) per column flange were installed at the column mid-height. The strain readings enabled the axial force and bending moment time histories to be evaluated.

*Column Axial Deformation*: Transducers (LVDTs) were installed adjacent to the Frame B columns in the lower two stories to evaluate the influence of column axial deformation on inter-story drift.

*Column Base Rotation*: The base of the first story columns in Frame B were instrumented (DCDTs) to measure the column end rotation.

**Shear Links**

*Shear Strain*: For the shear link at Level L2, equal end moments and applied shear forces up to 170% of its nominal plastic shear capacity, the flexural contribution to the total deformation was less than 2%. The diagonal DCDT displacements were therefore assumed to be kinematically related to shearing strains alone. The measured displacements were transformed into shear strains in a manner similar to that described by Yang [18]. In the lower three shear links, four transducers (DCDTs) at each level were used to measure the shear strains (Figure 5.8); the shear strains in the two half-panels were averaged in order to obtain the average shear strain in the link. In the upper three stories, two transducers (DCDTs) at each level were used to measure the shear strains.

*Shear Force*: The shear forces in the links were calculated in an indirect manner because it was not possible to evaluate the coexisting shear forces in the adjacent concrete slab. Strain rosettes were installed in the beam outside the Level 2 link (after Test 32 : see Table 7.1) in order to estimate the shear force distribution in and around the link. On the basis of these strain readings, the gravity load distribution and the average of the vertical components of the brace axial forces, the average shear forces in the shear links were estimated. A similar procedure was used to estimate the shear force in the remaining five shear links.

*Axial Strain*: In order to estimate the axial forces and bending moments in the shear links, the lower three links were appropriately instrumented (DCDT, strain gages : see Figure 5.8). Strain gages were installed on the link flanges to measure the axial flange strains; DCDTs were installed at the underside of the link flanges and at the centroid of

the link web to measure average axial deformations.

**Composite Floor**

*Slippage and Separation*: Two transducers (DCDTs) were installed (after Test 32 : see Table 7.1) immediately adjacent to the link at Level L2 to measure the degree of slippage (horizontal) of the metal decking from the steel beam and the separation (vertical) of the metal decking from the steel beam.

*Slab Cracking*: A clip gage was installed (after Test 24 : see Table 7.1) atop the concrete slab above the link at Level L2 to measure the extent of the slab cracking during the collapse level tests.

The model's steelwork was coated with a whitewash paint that distorted and peeled upon yielding of the steel; the whitewash facilitated the visual inspection of the structure. The instrumentation scheme is depicted in Figure 5.9 and listed in Appendix A.

## 5.7 Data Acquisition and Data Reduction

The data acquisition system functioned in the following manner :

(1) The transducer (load cells, strain gages, DCDTs, accelerometers etc) output was passed through *Pacific* Signal Conditioners which provided the excitation voltage for the transducers, amplified the transducer output and filtered that output to 100 Hz.

(2) The *Preston* Multiplexer scanned the signal conditioners and sequentially read each channel at a burst rate of 0.5MHz, that is, for two adjacent channels (#100 and #101 for example) and a given nominal time, the true read time difference was two microseconds. The scanning rate (ie, number of times per second each channel is sampled) was controlled by the computer software.

(3) The analog signal which was output from the Multiplexer was then passed through a *Preston* A/D Converter which converted the signal to a digital form. The

digitized record was then stored on hard disk on the in-house VAX 11-750.

Of the 176 channels of data, the first 128 channels were passed through the signal conditioners noted above and lowpass filtered to 100 Hz. The signals from the remaining 48 channels were passed through non-filtering amplifiers and this output contained a significant amount of high frequency noise. A time domain Ormsby filter was then used to filter the disturbed signals.

An interactive data analysis and graphics package [51] was used to process the acquired data; the package was expanded (by Uang et al.) to include bandpass filters, numerical intergration and differentiation, response spectra evaluation and so on.

A block diagram of the earthquake simulator control and data acquisition system is presented in Figure 5.10.

# VI. DYNAMIC CHARACTERISTICS OF THE MODEL

## 6.1 General

Uang and Bertero [9] have discussed the characteristics of the model during the construction phase and the testing period of the concentrically K-braced frame. The static and dynamic characteristics of the eccentrically K-braced model were monitored in a similar manner at various stages in its testing program. The objectives of these tests were threefold; first, to assess the variation in the model's dynamic characteristics as a function of earthquake simulator input; secondly, to facilitate the correlation of the model's performance with both the prototype and the concentrically K-braced model [9] and finally, to evaluate the reliability of currently available analytical techniques to predict the dynamic response of braced steel structures.

## 6.2 Analytical Dynamic Characteristics of the Model

The analytical prediction of the model's dynamic characteristics was undertaken in a similar manner to that described in Section 4.3 for the prototype. The DRAIN-2DX analyses were based upon the assumptions noted in Section 4.2 and the measured mechanical characteristics of the model's materials.

**Flexibility :** The analytical flexibility matrix and its corresponding stiffness matrix are presented in Tables 6.1a and 6.1b, respectively.

**Natural Periods and Mode Shapes :** The natural periods and mode shapes were evaluated using a standard eigenvalue routine; the diagonal mass matrix was based upon the measured reactive weights of each level of the model (Table 5.4). The analytical natural periods and mode shapes are listed in Table 6.1c.

If the model is assumed to be a shear-type building, the fundamental frequency increases from 3.24 Hz to 4.77 Hz. The shift in the fundamental frequency implies that the lateral stiffness of the model, assuming shear-type behavior, is 116% higher than its true lateral stiffness. The corresponding analytical flexibility matrix, stiffness matrix, natural periods and mode shapes are presented in Table 6.2. The assumption of a pure shear building for this eccentrically K-braced dual system is clearly inappropriate.

## 6.3 Evaluation of the Dynamic Characteristics of the Model

The three techniques that were used to evaluate the dynamic characteristics of the eccentrically K-braced model were the static flexibility method, free vibration testing and forced vibration testing.

**Static Flexibility Method (Unit Loading Test) :** The static flexibility test facilitated the determination of the dynamic characteristics of the model assuming a lumped mass system.

The model was laterally loaded at each floor level by a very stiff beam; the lateral force was applied to the loading beam by two cables that extended to the laboratory floor. The load was applied by tightening the turnbuckles in both cables simultaneously; the load levels in both cables were monitored by load cells. The vertical component of the cable force and the weight of the loading beam was carried by tubular steel columns anchored to the laboratory floor. Lateral loads were sequentially applied at each level of the model. The measured displacements of each story at each stage of the loading process yielded the flexibility matrix of the model corresponding to its six lateral degrees of freedom. A schematic representation of the static flexibility test set-up is presented in Figure 6.1.

**Free Vibration Tests :** Two methods were used to evaluate the free vibration response of the model :

**Method 1 :** The model was given a small lateral displacement by loading it at the roof level via two cables attached to Frames A and C; turnbuckles were inserted in both cables to adjust the frame displacements. The two cables were attached to a single cable (a Y configuration) and anchored to the laboratory floor. A 3/8 inch threaded rod was inserted into the cable close to the floor and when the appropriate displacement was induced at the roof level, the rod was cut and the model then responded in free vibration.

**Method 2 :** A small impulse was used as input to the earthquake simulator; the structure then responded in free vibration.

The free vibration response (displacements, accelerations) of the model was recorded by the data acquisition system. The following procedure was then used to estimate the natural periods of vibration and modal damping ratios of the model :

(i) The time histories noted above were transformed into the frequency domain using the Fast Fourier Transform (FFT). The dominant peaks in the Fourier amplitude spectra of the response are associated with the periods of vibration of the model.

(ii) Appropriate cut-off frequencies were selected and the band-passed response was transformed into the time domain using the Inverse Fast Fourier Transform (IFFT).

(iii) The band-passed time domain response of step (ii) was then treated as the free vibration decay response of a single degree-of-freedom system (SDOFS). The period of vibration was calculated by either the zero response crossing method or by determining the frequency associated with the peak of the FFT noted in step (i). The modal damping ratios were evaluated using the conventional logarithmic decrement approach [52].

(iv) Steps (ii) and (iii) were repeated with different cut-off frequencies to ascertain the sensitivity of the damping ratios.

The mode shapes of the model were evaluated using the amplitude and phase angle of the peaks of the Fourier amplitude spectra noted in step (i) for the recorded response at all six floor levels. The procedure noted above for obtaining the natural periods and modal damping ratios is depicted in Figure 6.2.

**Forced Vibration Tests :** The forced vibration response of the model was evaluated using a force generator mounted on its roof. The force generator was a small shaking table; it provided a constant acceleration of up to 0.6g in the frequency range of 2 to 20 Hz and it could generate a maximum force amplitude of 30 lbs with 50 lb of weight atop it [9]. The frequency of the input was varied from test to test, at and around the expected periods of vibration of the model. The normalized response to the input was evaluated as a function of the exciting frequency; the frequency associated with the peak normalized response and the half-power bandwidth method [52] were used to evaluate the natural periods of vibration and modal damping ratios, respectively.

## 6.4 Dynamic Characteristics of the Model

The dynamic characteristics of the model were evaluated prior to the earthquake simulator testing and are presented below.

**Static Flexibility Tests :** The static flexibility method described in Section 6.2 was used to evaluate the flexibility matrix (Table 6.3a) of the model. The corresponding stiffness matrix, presented in Table 6.3b, was evaluated using a symmetric flexibility matrix calculated as $f_{ij}^{*} = (f_{ij} + f_{ji})/2$. The eigensolver described in Section 4.3 was used to evaluate the natural periods of vibration and the mode shapes of the model. The mass matrix used in the eigen analysis was derived from the last column of Table 5.4. The first three natural frequencies of the model were 3.11 Hz, 9.71 Hz and 17.54 Hz ($T_1$ = 0.322 second, $T_2$ = 0.103 second, $T_3$ = 0.057 second). The natural periods and mode shapes are listed in Table 6.3c and the mode shapes are shown in Figure 6.3 in addition to the analytically derived mode shapes.

**Free Vibration Tests :** The first three natural frequencies of the model were 3.16 Hz, 9.52 Hz and 17.54 Hz ($T_1$ = 0.316 second, $T_2$ = 0.105 second, $T_3$ = 0.057 second) and the first two modal damping ratios were 0.7% and 0.5%. The natural periods and mode shapes are listed in Table 6.4 and the mode shapes are shown in Figure 6.3.

**Forced Vibration Tests :** The frequency response curves for the first two modes, based upon roof acceleration time histories, yielded natural frequencies of 3.13 Hz and 9.43 Hz ($T_1$ = 0.320 second, $T_2$ = 0.106 second); the corresponding modal damping ratios were 0.7% and 0.9%.

## 6.5 Comparison of the Analytical and Experimental Results

The natural periods predicted analytically using DRAIN-2DX, predicted in a semi-analytical manner using the measured flexibility matrix and those measured experimentally from free vibration tests are summarized in Table 6.5. The mode shapes calculated using these three methods are presented in Figure 6.3.

The degree of correlation between the analytical, semi-analytical and test results is very good in terms of both the natural periods of vibration and the mode shapes. The correlation between the semi-analytical and free vibration test results is generally good, especially considering the sources of error in the former technique [9].

The assumptions made in Section 4.2 overestimate the flexural stiffness of the model's composite floor system on account of the damage that it suffered during the testing of the concentrically K-braced model and because the model's foundation was not rigid as assumed in the mathematical model. The greater stiffness of the analytical model can be attributed in part to these two factors.

A comparison of the analytical and experimental results indicate that the mathematical model can be considered to be a good analytical representation of the eccentrically K-braced model.

## 6.6 Dynamic Characteristics of the Prototype and the Model

The model was designed and constructed to be a reduced-scale model of the prototype tested in Tsukuba, Japan. The accuracy to which the prototype was modeled was evaluated by comparing the dynamic characteristics of the prototype and the model. For the purposes of this comparison, the model's characteristics have been scaled to the prototype units in accordance with the similitude laws (Table 5.1).

**Flexibility** : The prototype and the model flexibility profiles are shown in Figure 6.4. The flexibility matrix determined from static flexibility tests is generally not symmetric because of experimental errors. On the basis of the flexibility profiles shown in Figure 6.4, the model flexibility is less than 4% higher than that of the prototype in the first three stories. The model flexibility is between 8% and 13% higher than that of the prototype in the upper three stories. The differences between the model and prototype flexibility profiles is borne out in the differences in their respective natural periods. The fundamental period of the model was 0.583 second as opposed to 0.545 second for the prototype.

**Natural Periods and Mode Shapes** : The natural periods of the prototype and the model obtained from free and forced vibration tests are shown in Table 6.6. The difference in fundamental periods was 1% from the free vibration tests and 2% from the forced vibration tests. The mode shapes of the prototype and the model, shown in Figure 6.5, were calculated using the semi-analytical technique and the static flexibility test results.

**Modal Damping Ratios** : Damping ratios are non-dimensional parameters and should therefore be the same in both the model and the prototype. The modal damping ratios ($\xi_i$) reported by the Japanese researchers [26,27] from the free and forced vibration tests conducted prior to the PSD-Elastic Test were 0.35% and 0.31% in the first two modes. The modal damping ratios of the model, calculated from the free vibration tests, were 0.7% and 0.5% in the first two modes (measured with the earthquake simulator locked

to the vertical and horizontal actuators). The cracks in the prototype's composite floor system were epoxy grouted prior to the installation of the eccentric braces [26] whereas those in the model were not repaired prior to the installation of its eccentric braces. The additional damping in the eccentrically K-braced model can be attributed to the lack of repair to its composite floor system.

## 6.7 Summary

A series of vibration tests were undertaken to evaluate the dynamic characteristics of the model. The model was carefully designed and constructed and its similitude scaled flexibility, natural periods and mode shapes correlated extremely well with those of the prototype. The major difference between the model and the prototype was in modal damping and this was a reflection of the repairs undertaken to the prototype's composite floor system. These studies have shown that it is feasible to design and construct medium-scale models of full-scale structures that can accurately reproduce natural periods, mode shapes and modal damping characteristics.

The DRAIN-2DX mathematical representation of the model was able to predict reliably its dynamic characteristics in the first three modes.

# VII. EARTHQUAKE SIMULATOR TESTING PROGRAM AND PROCEDURES

## 7.1 General

The model was subjected to a series of simulated ground motions after its initial mechanical characteristics had been determined (Chapter 6). Limit analyses using simple plastic theory and step-by-step static nonlinear analysis of the model were undertaken prior to the earthquake simulator testing to determine the strength of the model. The results of these studies are presented in Section 7.2. In order to select the earthquake records for the testing of the model, the response of the model to two ground motions was also evaluated prior to commencing the testing program; the response of the model to these ground motions is also presented in Section 7.2. The preliminary analytical studies were undertaken in order to plan the testing program and to determine the level of response expected from the model.

The earthquake simulator input motions and test program are described in Section 7.3 and 7.4, respectively; the data reduction process is discussed in Section 7.5. The methods used to analyze the test data from the energy standpoint are discussed in Section 7.6.

## 7.2 Analytical Response of the Model

### 7.2.1 Analytical Assumptions and Mathematical Idealization

The same mathematical idealizations and assumptions described in Section 4.2 (column, beam, panel zone, brace and shear link elements) for the prototype were used to predict the static and dynamic behavior of the model. The section properties of the model's elements were based upon the measured geometry of the W sections [9] and the material characteristics described in Section 5.4.

### 7.2.2 Prediction of the Strength of the Model

**General :** In this section, the global strength and deformation characteristics are predicted using simple plastic theory and a series of step-by-step static nonlinear analyses. To conduct these analyses, inverted-triangular (triangular) and rectangular (uniform) loading patterns were considered.

**Simple Plastic Theory :** An upper bound to the strength of the model can be obtained using the collapse mechanism approach [39,40,41]. The plastic moment capacity of the panel zone elements was selected as $\Delta M_y$ (Equation 4.5). Recognizing the high shear strains that are developed in shear links, ultimate stresses ($\sigma_u$) in lieu of the yield stresses ($\sigma_y$) were also used to calculate the internal work corresponding to each of the shear links. The calculation of the external work for the each of the various mechanisms considered did not include a contribution from the loads that were uniformly distributed along the beams since there is no net vertical displacement of the resultant of these gravity loads.

In summary, the collapse load ($P_c$) as a function of the as-built reactive weight (107.1 kips) for the model, is as follows :

(i) **Stress level $\sigma_y$ for all members, ignoring the composite slab contribution**

Triangular Load Distribution $P_c = 0.60W$

Uniform Load Distribution $P_c = 0.65W$

(ii) **Stress level $\sigma_u$ for all shear links, $\sigma_y$ for all other members, ignoring the composite slab contribution**

Triangular Load Distribution $P_c = 0.72W$

Uniform Load Distribution $P_c = 0.77W$

(iii) **Stress level $\sigma_u$ for all shear links, $\sigma_y$ for all other members and including the composite slab contribution to the net internal work**

Triangular Load Distribution $P_c = 0.76W$

Uniform Load Distribution $P_c = 0.81W$

The collapse mechanism for the triangular load distribution (all three cases) is presented in Figure 4.10. The collapse mechanism for the uniform load distribution was similar to that shown in Figure 4.10 except that the rigid body displacement field encompassed the upper four stories (as opposed to the upper three in Figure 4.10).

**Step-by-Step Static Nonlinear Analysis :** The computer program DRAIN-2DX was used to conduct the collapse analyses of the model for the two load distributions noted above and in a similar manner to that described in Section 4.4 for the prototype.

The model and prototype analytical base shear versus first inter-story drift index and roof drift index for the triangular and uniform load distributions are presented in Figures 7.1 and 7.2, respectively. The point at which the shear strain in the L2 shear link reached 0.1 radian is shown in these two figures for both loading patterns. The results of the limit analyses ($\sigma_u$ for all shear links, $\sigma_y$ for all other members) are also shown in these figures. The hinge formation sequence in the collapse analysis for both load distributions is presented in Figure 7.3; the hinges shown correspond to those that formed prior to the model attaining a strength equal to its reactive weight. As a result of the differences in the two load distributions, the hinge formation sequences and damage distributions in the model vary significantly although the lower three links undergo plastification in the same sequence (L2-L3-L4). The yielding and buckling of the eccentric braces indicated in Figure 7.3 is a result of the unbounded hardening of the corresponding shear links. At shear strain levels in the links of the order of 0.1 radian, the axial forces in all of the eccentric braces were less than their corresponding buckling loads. To maintain the vertical load integrity of the model, the desirable collapse mechanism should concentrate the inelastic deformation in all six shear links and would exclude plastic hinge formation in the columns (except at the column bases). The energy dissipation capacity of the model would be maximized if the six links deformed at the same

rate, if the plastic hinges in the panel zones were relocated to the adjacent composite beam and if the beams and braces outside the shear links remained elastic up to the ultimate strength of the composite shear links.

The collapse analyses indicate that the elastic stiffnesses of the prototype and the model (in dimensionless terms) are essentially identical and that the model strength is greater than that of the prototype (as a function of their respective reactive weights) at drift levels exceeding approximately 0.2%.

### 7.2.3 Prediction of the Seismic Response of the Model

The computer program DRAIN-2DX was used to predict the seismic response of the model. Two of the earthquake ground motions used to test the prototype were used as input to DRAIN-2DX. To comply with the similitude laws, the time scale of the earthquake record was factored by $\sqrt{0.3048}$ (=1/1.811). The time-scaled acceleration time history of the Taft N21E earthquake record, the corresponding Fourier amplitude spectrum and the linear elastic response spectra are shown in Figure 7.4. The first two modal damping ratios ($\xi_1$= 2.2%, $\xi_2$= 1.3%) were used to calculate the Rayleigh damping constants (Equation 4.12) and these were estimated from the results of the concentrically K-braced model testing [9]. The analytical roof displacement and base shear time histories corresponding to the two ground motions are shown in Figures 7.5 and 7.6, respectively.

### 7.2.4 Summary

The analytical envelopes of roof drift index versus base shear ratio are shown in Figure 7.7 for both the prototype and model. A strength and deformation envelope generated from the results of the dynamic analyses is also shown in Figure 7.7 in addition to a number of points from the prototype strength and deformation envelope (Chapter 4). This figure indicates that the similitude scaled strength of the model is approximately 20% higher than that of the prototype at a roof drift index exceeding 1%; in Section 5.5, the higher strength of the model was attributed to the greater strength of its shear links.

## 7.3 Earthquake Simulator Input Motion

The eccentrically K-braced model was subjected to four earthquake records : 1952 Kern County Taft N21E component; 1978 Miyagi-Ken-Oki N00E component; 1971 Pacoima Dam S14W component and an artificial sinusoidal motion.

TAFT N21E, July 21, 1952.

The real-time Taft earthquake acceleration record has a long duration of strong motion shaking, a peak acceleration of 15.6%g, a Richter Magnitude of 7.2 ($M_s$ = 7.7) and a broad frequency content. The time-scaled acceleration record was derived from earthquake records processed by the California Institute of Technology [46]. The frequency content of the time-scaled Taft record, although broad, is strongest in and around the fundamental frequency of the model. The energy content of the Taft signal is concentrated in two major bursts around the 3 and 7 second marks of the time-scaled signal. A truncated time-scaled input record was used for Test No 14, 16, 19, 21, 23, 25 and 26; the truncated signal was 16.7 seconds in length and captured all the major features of the complete earthquake record.

MIYAGI-KEN-OKI N00E, June 12, 1978.

The real-time Miyagi-Ken-Oki earthquake acceleration record (recorded at Tohoku University) has a long duration of strong motion shaking, a peak acceleration of 26%g, a Richter Magnitude of 7.4 and a reasonably broad frequency content. The frequency content of the time-scaled Miyagi-Ken-Oki record is strongest at and around the fundamental frequency of the model. The energy content of the Miyagi-Ken-Oki signal is concentrated in three distinct bursts around the 4, 6 and 8.5 second marks of the time-scaled signal.

PACOIMA DAM S14W, February 9, 1971.

The real-time Pacoima Dam earthquake acceleration record [46] has a moderate duration of strong motion shaking, a peak acceleration of 117%g and a Richter Magnitude of 6.4

($M_s$ = 6.6). A truncated version of the time-scaled acceleration record was used for Test Nos 29 and 30; for Test Nos 27 and 28, a truncated version of the real-time acceleration record was used.

SINE INPUT

The sinusoidal input consisted of over 4 seconds of sinusoidal acceleration followed by two rectangular acceleration pulses. The motion was designed to initially excite the structure in its fundamental mode and then to subject it to two severe acceleration pulses.

The acceleration time histories noted above were numerically integrated and base-line corrected to obtain the displacement command signal for the earthquake simulator. The nominal input intensity (acceleration) was selected prior to each test; the span setting on the earthquake simulator was chosen to reproduce the required intensity.

## 7.4 Earthquake Simulator Test Program

The program for testing the model was devised in order to subject it to a variety of earthquake records whose peak accelerations were varied to elicit response in both the elastic and inelastic range. To obtain a given level of response, the analytical studies described in Section 7.2 were used to select the required span setting of the earthquake simulator. Table 7.1 lists the test schedule for the eccentrically K-braced model, noting where appropriate, the maximum table acceleration, the peak base shear, the maximum roof displacement and the associated roof drift index. As indicated in Table 7.1, the earthquake simulator tests were categorized into four groups. The first group of tests were of a diagnostic nature; as such, they were low amplitude tests undertaken to verify the performance of the earthquake simulator, the instrumentation and the data acquisition system in addition to obtaining **serviceability** limit state response of the model. In these tests, the peak table accelerations varied between 3%g and 14%g.

The second group of tests simulated the **damageability** limit state of the model response. This series of tests was designed to produce minor structural damage in the form of shear link yielding as well as yielding in the critical regions in the moment-resisting space frames. In these tests, the peak table accelerations varied between 17%g and 32%g.

The third group of tests simulated the **collapse** limit state of the model response. This series of tests was designed to produce major structural damage in the shear links, panel zones, girders and columns in the braced frame as well as significant yielding in the critical regions in the moment-resisting space frames. In these tests, the peak table accelerations varied between 40%g and 66%g.

The fourth group of tests simulated the effects of **after-shocks** on the model. This series of tests was conducted after the web of the shear link at Level L2 had severely buckled. These tests were undertaken to study the global and local post-web buckling response of an eccentrically K-braced structure.

The variation of the model's mechanical characteristics with the degree of structural damage was investigated by undertaking free vibration tests prior to and after a number of the earthquake simulator tests.

## 7.5 Data Reduction

### 7.5.1 Data Noise

Electronically recorded data inevitably contains deleterious information in the form of both high and low frequency noise. One hundred and seventy-six channels of data were collected during each test. The transducer output from first 128 channels was passed through signal conditioners that removed that component of the output above 100 Hz. For the remaining 48 channels, the output contained a significant amount of noise. The problems associated with identifying and removing high and low frequency noise are discussed below.

**High Frequency Noise :** High frequency noise is easily identified; an example of a transducer signal, with and without high frequency noise is presented in Figure 7.8. The Ormsby time domain lowpass filter was used to remove high frequency noise. A cut-off frequency of 20 Hz was selected for the following three reasons. First, the residual data contained the response in the first three modes of vibration (Table 6.4); secondly, the Fourier amplitude spectra of the time-scaled earthquake records noted above were negligible above 20 Hz and finally, oil column resonance in the earthquake simulator's hydraulic actuators significantly distorts the frequency content of the input signal higher than 16 Hz (Figure 5.1).

**Low Frequency Noise :** Low frequency noise arises in the form of a permanent set in the channel data or in the form of an harmonically varying baseline. An example of the latter form of low frequency noise is shown in Figure 7.9a; the time history shown in Figure 7.9a is the lowpass filtered (removing all frequency content above 20 Hz) fifth story inter-story drift for the Taft-08 Test. The corrected response was obtained by removing that frequency content below 0.5 Hz from the time history. The cut-off frequency was chosen on the basis of the Fourier amplitude spectrum of the Taft-08 time scaled acceleration time history; this time history has negligible frequency content below 0.5 Hz. Accordingly, the removal of the frequency content below 0.5 Hz should not alter the true inter-story drift time domain response. The error function is shown in Figure 7.9a and the subsequent highpass filtered response is shown in Figure 7.9b.

Permanent offsets were observed in lateral displacement and axial strain gage time histories for the damageability and collapse limit state tests; these offsets reflect permanent deformation and in these instances, the channel data was not filtered. In those transducers whose readings at the termination of the test must decay to zero (accelerometers and column web shear rosettes for example), the permanent offsets were unacceptable. It was assumed that the drift in the channel reading increased uniformly over the duration of the test. The signal was corrected by rotating the abscissa to remove the

permanent offset. In these tests, the acceleration data rarely required correction; the column shear rosettes were corrected as necessary.

### 7.5.2 Sign Convention

The following sign convention, shown in Figure 7.10, was used for this report :

(i) Lateral displacement, inter-story drift, acceleration : positive to the right (west) side and upward in the vertical direction.

(ii) Brace axial strain, axial deformation and force : positive for elongation and tension.

(iii) Column shear force, story shear force : positive shear force induced by positive inter-story drift.

(iv) Link shear strain and shear force : positive shear strain up and to the right, positive shear force generates positive shear strain.

### 7.5.3 Element and Story Force Calculation

**Brace Force :** Each brace was calibrated prior to its installation in the model so that the gage readings produced axial force directly.

**Story Shear :** For these experiments, two methods were used to calculate the story shear force :

*Inertia Force* : The story shear force was calculated by summing the floor inertia forces at each level above that story. These inertia forces were calculated by multiplying the measured floor absolute accelerations by the corresponding floor masses (from Table 5.4). The advantage of this technique is that the calculation is straightforward if the accelerometers are accurately calibrated and the floor weights have been accurately evaluated. The disadvantage of this technique is that the effect of the damping force is ignored. The equilibrium equation of motion in vector form is :

$$\underline{f}_I = -(\underline{f}_S + \underline{f}_D) \tag{7.1}$$

where $\underline{f}_I$, $\underline{f}_S$ and $\underline{f}_D$ are the inertia force, the restoring force and the damping force vec-

tors, respectively. The story shear is related to the restoring force vector alone and therefore, this method is reliable when the damping is small.

*Storywise Force Summation* : The story shear force was calculated by adding the column shears from the strain rosette measurements (Figure 5.6) to the horizontal component of the eccentric brace forces; this is the rigorous method of calculating story shear forces.

The two methods were compared for the low intensity test of 7.8%g peak acceleration (Test No 7 in Table 7.1). The results of the two methods are presented in Figure 7.11; the difference between them is negligible and their correlation coefficient is approximately equal to 1. For the testing of the concentrically K-braced model, the inertia force method was used to evaluate the story shear force upon brace buckling [9]. For the testing of the eccentrically K-braced model, the second method was used to evaluate the story shear force because the eccentric braces remained elastic and the brace axial force was reliably measured.

The total story shear force at level '$i$' ($V_i^{TOTAL}$) can be divided as follows :

$$V_i^{TOTAL} = V_i^{BRACE} + V_i^{MRSF} \tag{7.2}$$

where $V_i^{TOTAL}$ = total shear in story $i$

$V_i^{MRSF}$ = shear resisted by the moment-resisting space frame in story $i$

= summation of column shears in story $i$

$V_i^{BRACE}$ = shear resisted by braces in story $i$

= sum of horizontal components of brace forces in story $i$ .

Note that the column shear forces in Frame B are included in the latter term in Equation 7.2.

**Column Axial Force and Bending Moment :** As noted in Section 5.6, all first story columns were instrumented at their mid-heights with strain rosettes and uniaxial strain gages (Figure 5.6). The computer program UNCOLA [53] was used to calculate the

coexisting axial force and bending moments. The bending moments at both ends of the first story columns were calculated using the UNCOLA output and column shear forces (Figure 7.12).

**Link Shear Force :** As the shear force in the composite link could not be directly measured, the average vertical component of the eccentric brace force minus that portion of shear force in the adjacent beam was deemed to be the link shear force. On the basis of strain rosette readings taken after Test 23 (Table 7.1), the shear force in the adjacent beam was estimated to be 7% of the vertical component of the eccentric brace force. The assumed shear force distribution (due to lateral forces alone) in the braced bay of Frame B is shown in Figure 7.13.

### 7.5.4 Member Designation

The member mark designation used in the remainder of this report is shown in Figure 7.14.

## 7.6 Energy Input, Distribution and Dissipation

Although earthquake resistant design based upon energy methods is not envisaged at this stage, use of energy methods to design, detail and categorize connections and critical regions are an attractive means to account for inelastic activity. The energy equations have been developed by a number of researchers [9,54] for SDOFS and MDOFS. To be consistent with the studies conducted by Uang and Bertero [9], the energy equations developed in Appendix B are used in the remainder of this report.

The input energy ($E_I$) is the input power integrated over the duration of the test. The kinetic energy ($E_K$) is proportional to the absolute velocity squared; the strain energy ($E_S$) is recoverable and is stored in the structure by elastic deformation; the viscous damped energy ($E_\mu$) is dissipated by a variety of mechanisms and is assumed to be proportional to relative velocity and the inelastic hysteretic energy ($E_H$) is dissipated by the inelastic activity in the structure.

The energy balance in the model can be expressed as follows :

$$E_K + E_A + E_\mu = E_I \tag{7.3}$$

where $E_A$ ($= E_S + E_H$) is the absorbed energy and the remaining terms are described above. For the model, a six degree-of-freedom lumped mass system was assumed and the terms derived in Appendix B can be quantified as follows :

**Input Energy ($E_I$) :**

$$E_I = \int (\sum_{i=1}^{6} m_i \ddot{v}_i^t)\, dv_g = \int (\sum_{i=1}^{6} m_i \ddot{v}_i^t)\, \dot{v}_g dt = \int P_I\, dt \tag{7.4}$$

where $P_I$ is the input power (kip-inch/sec) and the remaining terms are described in Appendix B. The input power is approximately equal to the base shear ($V_b$) multiplied by the ground velocity ($\dot{v}_g$); the difference between the sum of the inertia forces ($\sum m_i \ddot{v}_i^t$) and the base shear is the internal damping force in the first story. The assumption that the input energy can be estimated as

$$E_I = \int (V_b \dot{v}_g dt)$$

is therefore conceptually incorrect although, as shown in Figure 7.11, the differences are negligible.

**Kinetic Energy ($E_K$) :**

$$E_K = \frac{1}{2} \dot{\underline{v}}^{tT} \underline{m} \dot{\underline{v}}^t = \frac{1}{2} \sum_{i=1}^{6} m_i (\dot{v}_i^t)^2 \tag{7.5}$$

where $m_i$ = *ith* floor lumped mass (fromTable 5.4)

$\dot{v}_i^t$ = absolute lateral velocity at the *ith* floor level .

The absolute velocity ($\dot{v}_i^t$) at a given level was calculated by numerically differentiating the absolute horizontal displacements (Channels 23 - 26).

**Absorbed Energy ($E_A$) :**

$$E_A = \int \underline{f}_S^T d\underline{v} = \sum_{i=1}^{6} \int f_{Si} dv_i \tag{7.6}$$

$$= E_S + E_H$$

where $f_{Si}$ = the restoring force acting at level *i*

= the difference in the story shear above and below level *i*

$v_i$ = *ith* level relative lateral displacement .

A transformation can be used to express $E_A$ in terms of the story shear and the inter-story drift :

$$E_A = \int \underline{V}^T d\underline{\delta} = \sum_{i=1}^{6} \int V_i d\delta_i \tag{7.7}$$

where $V_i$= *ith* level story shear

$\delta_i$= *ith* level inter-story drift .

The absorbed energy is calculated by integrating the story shear with respect to the corresponding inter-story drift. The absorbed energy can be divided into recoverable elastic strain energy ($E_S$) and the non-recoverable inelastic hysteretic energy ($E_H$). The elastic strain energy is calculated as follows:

$$E_S = \sum_{i=1}^{6} \frac{V_i^2}{2K_i} \tag{7.8}$$

where $K_i$ is the unloading stiffness of the $\delta_i$ versus $V_i$ curve; for these studies, it was assumed to be equal to the initial tangent stiffness. The inelastic hysteretic energy is calculated as follows :

$$E_H = E_A - E_S = \sum_{i=1}^{6} \int V_i d\delta_i - \sum_{i=1}^{6} \frac{V_i^2}{2K_i} \tag{7.9}$$

**Viscous Damped Energy ($E_\mu$) :**

The viscous damped energy is calculated as follows :

$$E_\mu = \int \underline{f_D}^T d\underline{v} = \sum_{i=1}^{6} \int f_{Di} dv_i$$

$$= \int \underline{q}^T d\underline{\delta} = \sum_{i=1}^{6} \int q_i d\delta_i \qquad (7.10)$$

where $q_i$ is the damping force in the *ith* story. The viscous damped energy is difficult to evaluate explicitly and in this report was evaluated by reformulating Equation 7.3 as follows :

$$E_\mu = E_I - E_A - E_K \quad .$$

# VIII. EARTHQUAKE SIMULATOR TEST RESULTS

## 8.1 General

As noted in Table 7.1, the eccentrically K-braced model (Figure 8.1) was subjected to twenty-four simulated ground motions.

The testing of the eccentrically K-braced prototype at the B.R.I. used the 1952 Kern County Taft N21E earthquake record [46] with two levels of peak ground acceleration. The first test, designated by the Japanese as PSD-Elastic, had a peak ground acceleration of 65 gals ( 980 gals = 1g = 386.4 in/sec/sec ) and represented a serviceability limit state earthquake. The second test, designated by the Japanese as PSD-Inelastic, had a peak ground acceleration of 500 gals and represented a collapse limit state earthquake. The prototype was then subjected to a sinusoidal input motion whose amplitude was increased from cycle to cycle up to a peak ground acceleration of 320 gals.

The results of all twenty-four earthquake simulator tests are not presented in this report. In order to satisfy the objectives of the research program and to encapsulate the behavior of the eccentrically K-braced model at various intensities of loading, the results of the following tests are presented in Sections 8.3 through 8.7 :

(1) Test No. 7 : **Serviceability Limit State**

Test No. 7, with a peak acceleration of 7.8%g, was the most suitable test for comparison with the prototype PSD-Elastic Test.

(2) Test No. 16 : **Damageability Limit State**

Test No. 16, with a peak acceleration of 27.0%g, was suitable for evaluating the response of the model in this limit state.

(3) Test No. 23 : **Collapse Limit State**

Test No. 23, with a peak acceleration of 57.3%g, was the most suitable test for comparison with the prototype PSD-Inelastic Test.

(4) Test No. 26 : **Collapse Limit State**

The peak acceleration of 66.3%g was accompanied by the formation of alternate diagonal tension fields in the shear link at Level L2 and by significant yielding in the shear link at Level 3.

(5) Test No. 34 : **Aftershock Test**

This test was designed to ascertain the response of the eccentrically K-braced model to an earthquake aftershock; the peak acceleration of 69.6%g was accompanied by the failure of the shear link at Level L2.

These five tests will be designated as Taft-08, Taft-27, Taft-57, Taft-66 and Sine-70 in the remainder of this report.

The variations in the natural periods and damping ratios of the model throughout the test program as functions of base excitation intensities are summarized in Section 8.2. A summary of the structural damage incurred by the model is presented in Section 8.8.

The use of peak ground acceleration (PGA) to describe the intensity of a given ground motion is generally unsuitable, so the ATC [12] introduced the concept of effective peak acceleration (EPA). The EPA suggested by the ATC for regions of high seismic risk is 0.4g [12]. Bertero [31] has shown that although EPA is a better intensity index conceptually than PGA, it is difficult to determine qualitatively. EPA is used in this report as a damage potential index since it facilitates direct comparison of the input motions for the four Taft Tests noted above. It was evaluated from the 5% damped, linear elastic response spectrum for each motion as follows :

(i) The straight line (constant acceleration) of best fit to the spectral shape in the period range of 0.055 to 0.275 second was selected. In order to comply with the

similitude laws, the period range of 0.1 to 0.5 second (used by the ATC to evaluate the EPA) was time scaled by the same factor ($=1/\sqrt{1.811}$) used for the acceleration time histories.

(ii) The acceleration ordinate of the line was divided by a factor of 2.5 to obtain the EPA.

The reduction factor of 2.5 is consistent with the the spectrum amplification factor suggested by Newmark and Hall [55] for 5% damping and one sigma cumulative probability. The amplification factors suggested by Newmark and Hall were 2.71, 2.30 and 2.01 for the acceleration, velocity and displacement regions, respectively.

## 8.2 Global Response

### 8.2.1 Variation of Natural Periods and Damping Ratios

The natural period and damping ratio variations for the first three modes are summarized in Table 8.1. The first row of Table 8.1 corresponds to the model prior to the installation of the eccentric braces, that is, a DMRSF. Figure 8.2 depicts the variation of natural periods and damping ratios with the sequence of testing.

The fundamental periods noted in the first and second rows of Table 8.1 indicate that the ratio of the stiffness of the dual system to that of the DMRSF alone is

$$\frac{K_{DUAL}}{K_{MRSF}} = \left(\frac{0.672}{0.316}\right)^2 = 4.5 \qquad (8.1)$$

and that the eccentric braces significantly increased the stiffness of the model in the elastic range. The variations in the natural periods and equivalent viscous damping ratios over the duration of the testing program were relatively small. The free and forced vibration tests employed low levels of excitation and hence, the natural periods and damping ratios presented in Table 8.1 and Figure 8.2 are lower bounds to the values that existed during testing. Unless noted otherwise, the natural frequencies and

damping ratios listed in Table 8.1 relate to the complete air-supported earthquake simulator and model system. The damping in the complete system was appreciably higher than that in the fixed based model (2.2% versus 0.7%) because of the damping in the vertical and horizontal actuators and the passive stabilizers (Figure 5.1). The increase in the fundamental period of the complete system with respect to the fixed based model (0.316 second to 0.326 second) was due to the axial flexibility of the earthquake simulator's vertical actuators and passive stabilizers.

### 8.2.2 Response Envelopes

The envelopes of base shear versus first inter-story drift for the Taft-08, Taft-27, Taft-57, Taft-66 and Sine-70 Tests are shown in Figure 8.3; the envelopes correspond to the largest cycle of drift in each test. The cycle of the Taft-66 Test in Figure 8.3 indicates that the maximum strength of the model was reached during this test. At a lateral load level of approximately 0.5W, the tangent stiffness of the model in its first story decreased significantly and this was associated with shear yielding in Link L2.

## 8.3 Taft-08 Test

### 8.3.1 Response Time History

The measured table horizontal acceleration and displacement and the corresponding linear elastic response spectrum for 0%, 2%, 5%, 10% and 20% damping are shown in Figure 8.4; the EPA of the Taft-08 Test was 0.064g. The relative lateral displacement, inter-story drift, story shear force and lateral inertia force time histories at each level are shown in Figures 8.5 to 8.8, respectively. The lateral displacement time histories indicated that the response was primarily in the first mode and that there was little contribution from the higher modes. The story shear force time histories shown in Figure 8.7 were calculated by summing the column shears and the horizontal components of the eccentric brace forces; the story shear force resisted by the eccentric braces is also shown in Figure 8.7. The base overturning moment time history, calculated by summing the

product of the inertia force and floor height at each floor level, is shown in Figure 8.9; the overturning moment resisted by the eccentric braces is also shown in this figure.

The response time histories of the *change* in column $1C_{A1}$ axial force and end moments are shown in Figure 8.10. The bending moment at the base of the column was of the order of one-quarter to one-third of the moment at the second floor level. The design gravity load (dead load plus total live load) on column $1C_{A1}$ was 15.3 kips. Tension was not developed in column $1C_{A1}$ during this test despite the fact that the dead load axial force in the column was significantly less than that axial force given by the design gravity loads. The column axial force and bending moment interaction curves are presented in Section 8.3.4.

### 8.3.2 Inter-story Drift and Story Shear Relationship

The inter-story drift and total story shear relationships for each story are presented in Figure 8.11. The response was linear with only minor deviations in the six stories; the discrepancy is attributed to the lack of transducer sensitivity in this displacement range.

### 8.3.3 Maximum Response Envelopes

The envelopes of maximum response of relative displacements, inter-story drifts, story shear forces, inertia forces and overturning moments over the height of the model are shown in Figure 8.12 and summarized in Table 8.2.

The distribution and magnitude of the overturning moments over the height of the model are important as they are a reflection of both the lateral force distribution (important from the standpoint of capacity design) and the likelihood of developing tension in the perimeter columns.

It is clear from Figure 8.12a that in the elastic range, the eccentric braces in each story resisted most of the story shear. The maximum drift in the first story was greater than that in the remaining stories because the floor to floor height in the first story was approximately 30% greater than that in the second to sixth stories (Figure 2.1).

In dual systems, interaction between braced and unbraced frames can result in an elastic force distribution that is not in proportion to their individual stiffnesses because of the inherent differences in their displacement profiles under lateral loading The interaction can give rise to a situation whereby in the upper levels of a structure, the story shear force carried by the unbraced frame exceeds the total applied story shear. No evidence of this form of interaction was noted during the elastic level test (Figure 8.12a). This can be attributed to the moderate height of the model and the relative stiffnesses of the braced and unbraced frames.

The lateral displacement, inertia force, story shear, inter-story drift and overturning moment profiles over the height of the model at the times of maximum base shear and maximum roof displacement are shown in Figure 8.13. The lateral force profile was approximately triangular and consistent with that profile assumed by the UBC and ATC for masses evenly distributed over the height of a structure and in the period range under consideration ($T < 0.7/\sqrt{1.811}$).

The maximum inter-story drift index of 0.13% occurred in the first story. The maximum base shear coefficient ($V_b/W$) of 0.159 exceeded the UBC design base shear coefficient (=0.113) for this low amplitude, serviceability limit state earthquake . As the model was not designed in accordance with the UBC, this result is not a reflection of the overstrength inherent in UBC designed structures but rather a comparison between the ***design*** base shear in a region of high seismic risk (=0.113 W) and the base shear that was developed during ***minor*** earthquake shaking.

### 8.3.4 Column Axial Force and Bending Moment Interaction

Axial strains due to gravity load effects and residual strains were not included in the column axial strain time histories since all of the data channels were initialized prior to each test. The axial force in the columns due to gravity loads were calculated assuming a uniform distribution of gravity load over the plan area of each floor and using a tributary area approach. The end moment (M) and axial force (N) interaction curves for

the first story columns in Frames A and B are shown in Figure 8.14 and 8.15, respectively. The AISC [35] M-N yield surface, based upon linear elastic-perfectly plastic material properties, is also shown in these two figures. Although the axial forces and bending moments on all nine columns were negligible, the columns in the braced bay were subjected to a significantly higher axial force demand than those in the DMRSF. The M-N interaction curves for columns $1C_{A2}$ and $1C_{B2}$ were not presented because of transducer failures during the test.

### 8.3.5 Energy Distribution

The method described in Section 7.6 was used to calculate the input energy, the kinetic energy and the strain energy time histories. For the intensity of input motion in the Taft-08 Test, viscous damping is the only mechanism by which input energy is dissipated. The viscous damped energy ($E_\mu$) was calculated as follows :

$$E_\mu = E_I - E_K - E_S \quad . \tag{8.2}$$

Figure 8.16 shows the input energy, the kinetic energy, the viscous damped energy and the elastic strain energy time histories for the Taft-08 Test.

## 8.4 Taft-27 Test

### 8.4.1 Response Time History

The measured table horizontal acceleration and displacement and the corresponding linear elastic response spectrum for 0%, 2%, 5%, 10% and 20% damping are shown in Figure 8.17; the EPA of the Taft-27 Test was 0.19g. The relative lateral displacement, inter-story drift, story shear force and lateral inertia force time histories at each level are shown in Figures 8.18 to 8.21, respectively. The lateral displacement response was primarily in the first mode. The time histories of story shear force and the story shear force resisted by the eccentric braces are shown in Figure 8.20. The time histories of the base overturning moment and the overturning moment resisted by the eccentric braces

are shown in Figure 8.22.

### 8.4.2 Inter-story Drift and Story Shear Relationship

The inter-story drift and story shear relationships for each story are presented in Figure 8.23. Nonlinear behavior was evident in the first story only and the response in the upper five stories was essentially linear.

### 8.4.3 Maximum Response Envelopes

The envelopes of maximum response of relative displacements, inter-story drifts, story shear forces, inertia forces and overturning moments over the height of the model are shown in Figure 8.24 and summarized in Table 8.3. The lateral displacement, inertia force, story shear, inter-story drift and overturning moment profiles over the height of the model at the times of maximum base shear and maximum roof displacement are shown in Figure 8.25. As for the Taft-08 Test, the interaction between braced and unbraced frames that can result in story shear distributions that are not proportional to their individual stiffnesses, was not observed (Figure 8.25a). The lateral force profile was approximately triangular and therefore consistent with that assumed by the UBC and ATC.

The maximum inter-story drift index of 0.45% occurred in the first story. The maximum base shear coefficient of 0.491 exceeded the UBC design base shear coefficient (=0.113) by a factor of more than four for this damageability limit state earthquake and was 63% greater than the nominal yielding strength of the model (=0.3W : see Section 4.4.4).

### 8.4.4 Column Axial Force and Bending Moment Interaction

The end moment (M) and axial force (N) interaction curves for the first story columns in Frames A and B are shown in Figure 8.26 and 8.27, respectively. All the first story columns remained elastic during this test; the high axial force demand on the braced bay columns is clearly evident in Figure 8.27.

### 8.4.5 Shear Link Response

The relationships between link shear force (defined in Section 7.5.3) and shear strain for the Level 2 to Level 6 shear links are presented in Figure 8.28. The response of the shear link at the roof level (LR) is not presented (or for the Taft-57, Taft-66 and Sine-70 Tests) because of transducer failure. The Link L2 shear force versus shear strain relationship is presented in Figure 8.29; the nominal shear yielding strength ($V_p$) and the corresponding shear strain ($\gamma_y$) of the bare steel link (based upon the measured material characteristics for Grade 50 X10 steel) are also shown in this figure. The peak shear force in this composite shear link was 25.4 kips, that is, 161% of the nominal shear yielding strength of the bare steel link. It is clear from this figure that the elastic stiffness of the composite link was significantly higher than that of the bare steel link alone.

### 8.4.6 Energy Distribution

For the intensity of input motion in the Taft-27 Test, both inelastic behavior and viscous damping are involved in the dissipation of the input energy. Figure 8.30 presents the input energy, the kinetic energy and the elastic strain energy time histories and the time history of the energy dissipated by the six shear links. The energy dissipated in each shear link ($E_L$) was calculated as follows :

$$E_L = 8.54 \int V_L \, d\gamma \qquad \text{(kip-in)} \tag{8.3}$$

where 8.54 (inches) is the length of each shear link, $V_L$ is the link shear force, $d\gamma$ is the incremental shear strain and the integration is performed over the duration of the time history. Of the energy dissipated by the shear links, in excess of 70% is dissipated in Link L2. Figures 8.28 and 8.30 indicate that the storywise dissipation of energy in the shear links was nonuniform and that the potential energy dissipation capacity of the model was not mobilized. The hatched area in Figure 8.30 is that energy dissipated by viscous damping in the model and inelastic behavior in those elements other than the

shear links.

## 8.5 Taft-57 Test

### 8.5.1 Response Time History

The measured table horizontal acceleration and displacement and the corresponding linear elastic response spectrum for 0%, 2%, 5%, 10% and 20% damping are shown in Figure 8.31; the EPA of the Taft-57 Test was 0.44g. The relative lateral displacement, inter-story drift, story shear force and lateral inertia force time histories at each level are shown in Figures 8.32 to 8.35, respectively. The horizontal component of the eccentric brace forces as a function of the corresponding total story shear (≡ story shear ratio) is presented in Figure 8.36 for all six stories. In the elastic range, the eccentric braces in the first five stories resisted approximately 80% of the story shear and in the sixth story, the eccentric braces resisted approximately 70% of the story shear. The 10% decrease for the sixth story is a result of the decrease in the size of the eccentric braces in the sixth story from those in the fifth story; the columns and beams in these two stories were identical. The intermittent drop in the percentage of the first story shear force resisted by the eccentric braces corresponded to the times of significant yielding in Link L2 and the consequent decrease in the tangent stiffness of the the braced bay in the first story. The time histories of the base overturning moment and the overturning moment resisted by the eccentric braces are shown in Figure 8.37.

### 8.5.2 Inter-story Drift and Story Shear Relationship

The inter-story drift and total story shear relationships for each story are presented in Figure 8.38. The inter-story drift and brace story shear (the horizontal component of the eccentric brace force) and the inter-story drift and DMRSF story shear relationships for each story are presented in Figures 8.39 and 8.40, respectively. Nonlinear behavior was confined to the lower two stories and the response in the upper four stories was essentially linear. Figure 8.39 indicates that the input energy was dissipated primarily in

the braced bay of the first story and that the contribution of the DMRSF to the energy dissipation capacity of the model at these drift levels was minimal. Upon shear yielding in Link L2, the DMRSF contribution to the shear capacity of the first story increased such that the global shear strength of the model did not diminish. The strength demand on the first story DMRSF was approximately twice that in the second story in which shear yielding of Link L3 was not observed. The role of the DMRSF in a dual braced system is discussed in Section 9.6.

### 8.5.3 Maximum Response Envelopes

The envelopes of maximum response of relative displacements, inter-story drifts, story shear forces, inertia forces and overturning moments over the height of the model are shown in Figure 8.41 and summarized in Table 8.4. From Figure 8.41a, it is clear that the shear resistance of the braced bay was smaller in the first story than in the second story. Although the shear capacity of Links L2 and L3 were nominally identical, the floor to floor height in the first story was 30% greater than that in the second story. Accordingly, the horizontal component of the eccentric brace force was smaller in the first story than in the second story.

The ultimate lateral strength of the first story braced bay (defined as the maximum possible lateral load imparted to the eccentric braces) was reached during this test. In the model, Link L2 acted as a structural *fuse* and limited the axial forces that could be imparted to the eccentric braces and therefore prevented the buckling of the eccentric braces. The increase in the first story shear force beyond that level associated with the ultimate lateral strength of the braced bay was resisted by the DMRSF. The ductility of the eccentrically K-braced frame was mobilized to allow the more flexible DMRSF to resist additional lateral load and thus to perform one of its intended roles in the dual system.

The inertia force profiles were approximately uniform and consistent with the formation of a soft first story; the inter-story drift envelope confirmed this soft story

formation. The lateral displacement, inertia force, story shear, inter-story drift and overturning moment profiles over the height of the model at the times of maximum base shear and maximum roof displacement are shown in Figure 8.42.

The maximum inter-story drift index of 1.28% occurred in the first story. The maximum base shear coefficient of 0.845 exceeded the UBC design base shear coefficient (=0.113) by a factor of more than seven for this collapse limit state earthquake and exceeded the nominal yielding strength of the model (=0.3W : see Section 4.4.4) by a factor of 2.8.

### 8.5.4 Column Axial Force and Bending Moment Interaction

The end moment (M) and axial force (N) interaction curves for the first story columns in Frames A and B are shown in Figures 8.43 and 8.44, respectively. Lüders bands were noted at the bases of both braced bay columns ($1C_{B2}$ and $1C_{B3}$) on the completion of the test and this observation is consistent with the information presented in the interaction curves. Yielding lines were not observed at the bases of the columns in Frames A and C.

### 8.5.5 Eccentric Brace Response

The current philosophy for the design of bracing members in eccentrically braced frames is to base the brace capacity upon the ultimate strength of the associated shear link and thus to ensure that the bracing member remains elastic. The brace axial force versus axial deformation relationships for the eccentric braces in the first two stories are presented in Figure 8.45 in addition to their nominal buckling loads ($P_{cr}$) and tensile strengths ($T_y$). The brace response was linear in all four cases; the minor nonlinear displacement response can be attributed to the insensitivity of these DCDTs to the small deformations developed in the braces during the test.

### 8.5.6 Shear Link Response

The shear force and shear strain time histories for the Links L2 to L6 inclusive are shown in Figures 8.46 and 8.47, respectively. Permanent shearing deformations developed in Links L2 and L3 following the large burst of input energy around the 9 second mark in the test. The difference in the scales of the ordinates for the lower two and the upper level shear links should be noted; the shear strains in Links L4 to LR were significantly smaller than those that were developed in Links L2 and L3. The relationships between link shear force and shear strain for the Level 2 to Level 6 shear links are presented in Figure 8.48. Stable hysteretic behavior was typical of all the shear links that were cycled into the inelastic range. The maximum shear strains ranged from 8.0% (=0.08 radian) in Link L2 to 0.36% (=0.0036 radian) in Link L6. Web buckling commenced in the right-hand panel (adjacent to Grid Line 3) of Link L2 at the 9 second mark in this test. The Link L2 shear force versus shear strain relationship is presented in Figure 8.49; the shear yielding strength ($V_p$) and the corresponding shear strain ($\gamma_y$) of the bare steel link are also shown in this figure. The peak shear force in this composite shear link was 33.6 kips, that is, 213% of the nominal shear yielding strength of the bare steel link. The implications of composite link overstrength on the design of eccentric bracing are discussed in Section 9.7.

### 8.5.7 Energy Distribution

For the intensity of input motion in the Taft-57 Test, inelastic behavior is the primary source of energy dissipation. Figure 8.50 presents the input energy, the kinetic energy and the elastic strain energy time histories in addition to the time history of the energy dissipated by the six shear links; the shear links dissipated in excess of 94% of the input energy. Of the energy dissipated by the shear links, in excess of 78% was dissipated in Link L2. The hatched area in Figure 8.50 represents that energy dissipated by viscous damping in the model and inelastic behavior in those elements other than the shear links. Figures 8.39, 8.48 and 8.50 clearly indicate that the storywise dissipation of

the input energy was highly nonuniform and that with the as-tested configuration, the energy dissipation capacity of the model cannot be mobilized.

## 8.6 Taft-66 Test

### 8.6.1 Response Time History

The measured table horizontal acceleration and displacement and the corresponding linear elastic response spectrum for 0%, 2%, 5%, 10% and 20% damping are shown in Figure 8.51; the EPA of the Taft-08 Test was 0.53g. The relative lateral displacement, inter-story drift, story shear force and lateral inertia force time histories at each level are shown in Figures 8.52 to 8.55, respectively. The horizontal component of the eccentric brace forces as a function of the corresponding total story shear is presented in Figure 8.56 for all six stories. As for the Taft-57 Test, the only appreciable drop in the percentage of the story shear resisted by the eccentric braces occurred in the first story. The time histories of the base overturning moment and the overturning moment resisted by the eccentric braces are shown in Figure 8.57.

### 8.6.2 Inter-story Drift and Story Shear Relationship

The inter-story drift and total story shear relationships for each story are presented in Figure 8.58. The inter-story drift and brace story shear and the inter-story drift and DMRSF story shear relationships for each story are presented in Figures 8.59 and 8.60, respectively. Nonlinear behavior was confined to the lower three stories; the response in the upper three stories was essentially linear. Figure 8.59 indicates that the input energy was dissipated primarily in the braced bays of the first and second stories and that the contribution of the DMRSF to the energy dissipation capacity of the model at these drift levels was minimal.

### 8.6.3 Maximum Response Envelopes

The envelopes of maximum response of relative displacements, inter-story drifts, story shear forces, inertia forces and overturning moments over the height of the model are shown in Figure 8.61 and summarized in Table 8.5. The inertia force profiles were approximately uniform and consistent with the formation of a soft first story; the inter-story drift envelope confirmed this soft story formation. The lateral displacement, inertia force, story shear, inter-story drift and overturning moment profiles over the height of the model at the times of maximum base shear and maximum roof displacement are shown in Figure 8.62. It is clear from Figure 8.62 that the inelastic deformation was concentrated in the first story.

The maximum inter-story drift index of 1.29% occurred in the first story. The maximum base shear coefficient of 0.856 exceeded the UBC design base shear coefficient (=0.113) by a factor of more than seven for this collapse limit state earthquake and exceeded the nominal yielding strength of the model (=0.3W : see Section 4.4.4) by a factor of 2.9.

### 8.6.4 Column Axial Force and Bending Moment Interaction

The end moment (M) and axial force (N) interaction curves for the first story columns in Frames A and B are shown in Figures 8.63 and 8.64, respectively. The columns in the braced bay were subjected to a significantly higher axial force demand than those in the DMRSF. As for the Taft-57 Test, the braced bay columns ($1C_{B2}$ and $1C_{B3}$) yielded and additional Lüders lines were observed at the bases of these two columns upon the completion of this test. Although the M-N interaction curves of Figure 8.63 suggest that the bases of the columns in Frame A (and C) yielded during this test, yielding lines were not observed in the predicted locations.

### 8.6.5 Eccentric Brace Response

The brace axial force versus axial deformation relationships for the braces in the first two stories are presented in Figure 8.65 in addition to their nominal buckling loads

($P_{cr}$) and tensile strengths ($T_y$). The brace response was linear in all four cases.

### 8.6.6 Shear Link Response

The shear force and shear strain time histories for the Links L2 to L6 inclusive are shown in Figures 8.66 and 8.67, respectively. Permanent shearing deformations developed in Links L2, L3 and L4 following the large burst of input energy around the 9 second mark in the test. The difference in the scales of the ordinates for the lower two and the upper level shear links should be noted. The relationships between link shear force and shear strain for the Level 2 to Level 6 shear links are presented in Figure 8.68. Stable hysteretic behavior was typical of all the shear links that were cycled into the inelastic range. The maximum shear strains ranged from 9.2% (=0.092 radian) in Link L2 to 0.45% (=0.0045 radian) in Link L6. Major web buckling and diagonal tension field formation was re-initiated in the right-hand panel of the Link L2 at the 4 second mark in the test corresponding to a burst of input energy (Figure 8.70). The Link L2 shear force versus shear strain relationship is presented in Figure 8.69; the nominal shear yielding strength ($V_p$) and its corresponding shear strain ($\gamma_y$) for the bare steel link are also shown in this figure. The peak shear force in this composite shear link was 33.1 kips, that is, 210% of its nominal shear yielding strength.

### 8.6.7 Energy Distribution

For the intensity of input motion in the Taft-66 Test, inelastic behavior is the primary source of energy dissipation. Figure 8.70 presents the input energy, the kinetic energy and the elastic strain energy time histories in addition to the time history of the energy dissipated by the six shear links; the shear links dissipated in excess of 93% of the input energy. Of the energy dissipated by the shear links, 72% was dissipated in Link L2 and 22% was dissipated in Link L3; the contribution of the remaining four shear links to the energy dissipation capacity of the model was minimal. The hatched area in Figure 8.70 represents that energy dissipated by viscous damping in the model and inelastic behavior in those elements other than the shear links.

### 8.6.8 Concrete Slab Performance

The contribution of the lightweight concrete floor slab to the response of the composite shear link is dependent upon the degree of its degradation and the integrity of the link-to-concrete slab interface. Following the Taft-57 Test, DCDTs were installed adjacent Link L2 to measure the vertical and horizontal separation of the steel beam and the concrete slab. Separation of the composite slab from the steel beam requires that the concrete slab, bearing on and/or bonded to the shear studs, must fail. Following the Taft-66 Test, it was observed that the beam to slab interface was heavily damaged and the degree of separation, both horizontal and vertical, shown in Figure 8.71 is consistent with these visual observations.

## 8.7 Sine-70 Test

### 8.7.1 Response Time History

The measured table horizontal acceleration and displacement and the corresponding linear elastic response spectrum for 0%, 2%, 5%, 10% and 20% damping are shown in Figure 8.72; the EPA of the Sine-70 Test was 0.55g. The target acceleration time history was generated from the following :

- a rectangular pulse of 0.25g amplitude and 0.4 second duration (0.0 - 0.4 second),
- sinusoidal input of 0.40g amplitude, period 0.4 second and 4.8 second duration (0.4 - 5.2 seconds),
- a rectangular pulse of 0.40g amplitude and 0.30 second duration (5.2 - 5.5 seconds),
- a rectangular pulse of 0.60g amplitude and 0.31 second duration (5.5 - 5.81 seconds).

The target acceleration time history was poorly reproduced in this test and this is clearly evident in Figure 8.72.

The relative lateral displacement, inter-story drift, story shear force and lateral inertia force time histories at each level are shown in Figures 8.73 to 8.76, respectively.

The response of the model in its second mode ($T_2 = 0.11$ second) to the harmonic excitation is clearly seen in Figures 8.74, 8.75 and 8.76. The horizontal component of the eccentric brace forces as a function of the corresponding total story shear is presented in Figure 8.77 for all six stories. The percentage of the story shear resisted by the eccentric braces in the upper five stories remained essentially constant over the duration of the test. The time histories of the base overturning moment and the overturning moment resisted by the eccentric braces are shown in Figure 8.78.

### 8.7.2 Inter-story Drift and Story Shear Relationship

The inter-story drift and total story shear relationships for each story are presented in Figure 8.79. The inter-story drift and brace story shear and the inter-story drift and DMRSF story shear relationships for each story are presented in Figures 8.80 and 8.81, respectively. Nonlinear behavior was confined to the lower two stories; the response in the upper four stories was essentially linear. Figure 8.80 indicates that the input energy was dissipated primarily in the braced bay of the first story and Figure 8.81 indicates that the contribution of the DMRSF to the energy dissipation capacity of the model at these drift levels was minimal.

### 8.7.3 Maximum Response Envelopes

The envelopes of maximum response of relative displacements, inter-story drifts, story shear forces, inertia forces and overturning moments over the height of the model are shown in Figure 8.82 and summarized in Table 8.6. The inertia force profiles were approximately uniform and consistent with the formation of a soft first story; the inter-story drift envelope confirmed the soft story formation. The lateral displacement, inertia force, story shear, inter-story drift and overturning moment profiles over the height of the model at the times of maximum base shear and maximum roof displacement are shown in Figure 8.83. The reduction in the shear strength of the braced bay ($\equiv$ eccentric braces) in the first story with respect to the Taft-66 Test was due to severe web buckling and flange fracture in Link L2. Despite severe web buckling, Link L2 was able

to resist significant shear forces because of diagonal tension field formation; the transverse stiffeners in Link L2 provided the anchorage required for the tension field formation. The maximum inter-story drifts, story shear forces and inertia forces were associated with the two acceleration pulse at the end of the input signal.

The maximum inter-story drift index of 1.23% occurred in the first story. The maximum base shear coefficient of 0.706 exceeded the UBC design base shear coefficient (=0.113) by a factor of more than 6 for this collapse limit state earthquake and exceeded the nominal yielding strength of the model (=0.3W : see Section 4.4.4) by a factor of 2.3.

### 8.7.4 Column Axial Force and Bending Moment Interaction

The end moment (M) and axial force (N) interaction curves for the first story columns in Frames A and B are shown in Figures 8.84 and 8.85, respectively. The interaction curves for column $1C_{A1}$ are not presented because of transducer failure. The columns in the braced bay were subjected to a significantly higher axial force demand than those in the DMRSF. No additional Lüders bands were noted at these column bases following this test although the interaction curves suggest that there was at least one yielding cycle at the bases of columns $1C_{B2}$ and $1C_{B3}$.

### 8.7.5 Eccentric Brace Response

The brace axial force versus axial deformation relationships for the braces in the first two stories are presented in Figure 8.86 in addition to their nominal buckling loads ($P_{cr}$) and tensile strengths ($T_y$). The brace response was linear in all four cases.

### 8.7.6 Shear Link Response

The shear force and shear strain time histories for the Links L2 to L6 inclusive are shown in Figures 8.87 and 8.88, respectively. Permanent shearing deformations were recorded in the bottom three shear links. The difference in the scales of the ordinates for the lower two and the upper level shear links should be noted. In Links L3 and L4,

the permanent shearing deformations resulted from the large acceleration pulse just prior to the 6 second mark in the test. For Link L2, the permanent deformations accumulated gradually from the 1 second mark in the test; the degradation in the stiffness of Link L2 can be considered as commencing at this time. The stiffness degradation in Link L2 was most probably due to a combination of crack propagation in both the flanges and in the web to transverse stiffener welds (with the subsequent reduction in the ability of the stiffeners to maintain the diagonal tension field). The relationships between link shear force and shear strain for the Level 2 to Level 6 shear links are presented in Figure 8.89. The maximum shear strains ranged from 4.3% (=0.043 radian) in Link L2 to 0.3% (=0.003 radian) in Link L6. The Link L2 shear force versus shear strain relationship is presented in Figure 8.90; the shear yielding strength ($V_p$) and its corresponding shear strain ($\gamma_y$) for the bare steel link are also shown in this figure. The peak shear force in this composite shear link was 28.0 kips, that is, 177% of its nominal shear yielding strength. The apparent paradox concerning the maximum first inter-story drift and the associated shear strain in Link L2 (for a similar maximum drift to the Taft-66 Test, the maximum shear strain was 4.3% compared with 9.2% in the Taft-66 Test) results from the fact that the flange fractured (Section 8.8.2) just outside the region bounded by the diagonal DCDTs. As a result, the link deformations associated with the maximum first inter-story drift were underestimated.

### 8.7.7 Energy Distribution

Figure 8.91 presents the input energy, the kinetic energy and the elastic strain energy time histories in addition to the time history of the energy dissipated by the six shear links; the shear links dissipated in excess of 77% of the input energy. Of the energy dissipated by the shear links, in excess of 62% was dissipated in Link L2; 62% is a lower bound to the energy dissipated by Link L2 because the Link L2 deformations were underestimated (Section 8.7.6). The influence of web buckling on the energy dissipated by Link L2 is clearly evident by comparing Figures 8.70 and 8.91. The percentage

of the input energy dissipated by Link L2 diminished upon its web buckling, this observation is consistent with the results obtained from tests on isolated shear links [1,2]. The degradation of Link L2 over the duration of the test is also clearly evident in this figure. The hatched area in Figure 8.91 is that energy dissipated by viscous damping in the model and inelastic behavior in those elements other than the shear links. Although the total energy input to the model during the Sine-70 Test was 15% less than that of the Taft-66 Test, the maximum kinetic energy in the model during the Sine-70 Test was significantly greater than that measured during the Taft-66 Test. This was a result of the choice of the earthquake simulator input for the Sine-70 Test that was designed to drive the damaged model to resonance.

### 8.7.8 Concrete Slab Performance

Following the Sine-70 Test, additional damage at the beam to slab interface was observed; the degree of separation, both horizontal and vertical, shown in Figure 8.92, is consistent with these observations. Although additional slab damage was noted upon the completion of this test, the magnitude of the vertical and horizontal separation was of the same order as that measured during the Taft-66 Test.

## 8.8 Summary of the Damage to the Model

### 8.8.1 Concrete Slab Crack Pattern

The pattern of the concrete slab cracking on each floor of the model is shown in Figure 8.93. These patterns were recorded upon the completion of the earthquake simulator testing program. Longitudinal cracks were observed atop the line of shear studs on the braced bay of Frame B and these patterns were consistent with those observed in the composite girder tests [50].

Major concrete slab damage was observed in the regions surrounding the shear links on the lower two floors. This damage was due to the large rotation demand associated with inelastic behavior of these two shear links. In these regions, significant slab

separation and slippage from the steel girder was noted. In these instances, the assumption of full composite action and/or the assumption that plane sections remain plane after deformation, are invalid. Minor slab damage was observed on Floors 4 and 5 adjacent to the shear links and cracks of negligible width were noted on the sixth floor and the roof. Minor slab cracking was also observed around the columns in Frames A and C in the lower four stories.

### 8.8.2 Permanent Structural Deformation and Damage

**Shear Links :** Web buckling and tension field formation were observed in Link L2; minor yielding was observed in Link L3 and no yielding was observed in the remaining four shear links. Initial web buckling in Link L2 was accompanied by extensive peeling of its whitewash painted surface (Figure 8.94). The web deformation field in Link L2 after the Sine-70 Test is shown in Figures 8.95. The failure of Link L2 can be attributed to flange and weld fracture in highly restrained regions adjacent to web stiffeners (Figure 8.95). The fracture of the lower flange dramatically reduced the flexural capacity of the section and by equilibrium, the coexisting shear force. Symmetric and anti-symmetric buckling patterns were observed in the central two panels of Link L2 but only minor web buckling was noted in the outer two panels. Separation of the intermediate stiffener welds from the shear link web was also observed in the two interior panels; out-of-plane deformation of the intermediate web stiffeners was not observed.

It was impossible to quantify the effect of residual stresses on the failure of Link L2. The fracture of the lower flange occurred in a zone susceptible to tri-axial stress concentrations due to the welding of the full depth stiffeners into the W section.

**Other :** Plastic hinges were observed at the bases of the columns in Frame B in the form of Lüders bands on the surface of the flanges, perpendicular to the column axis.

The use of the whitewash paint noted in Chapter 6 proved extremely useful in identifying the locations of yielding in the model.

# IX. EVALUATION OF THE EARTHQUAKE SIMULATOR TEST RESULTS

## 9.1 General

In Chapter 8, five tests of the model were described in detail; in this chapter, the pertinent results of these five tests are summarized and evaluated. The global behavior of the model is presented in Section 9.2 and the test results are compared with the requirements of the current seismic regulations in Section 9.3. The relationship between base shear force and the excitation intensity of the earthquake simulator is discussed in Section 9.4 and the relationships between input energy and a variety of parameters are discussed in Section 9.5. The behavior of the ductile moment-resisting space frame in the dual system is discussed in Section 9.6 and the response of the shear links at both the global and local levels is discussed in detail in Section 9.7.

## 9.2 Inter-story Drift and Story Shear Envelopes

The envelopes of inter-story drift index versus the corresponding total story shear ($V^{TOTAL}$), the story shear resisted by the eccentric braces ($V^{BRACE}$) and the story shear resisted by the DMRSF ($V^{DMRSF}$) for the Taft-08, Taft-27, Taft-57, and Taft-66 Tests are shown in Figure 9.1. The DMRSF story shear includes that shear force resisted by the three columns in Frame B. Nonlinear behavior was confined essentially to the lower three stories of the model and the upper three stories remained elastic. This figure clearly shows that the DMRSF was significantly more flexible than the eccentrically braced frame; the DMRSF remained elastic at drift levels approaching 1.3% in the first story. The total story shear and first inter-story drift relationship in Figure 9.1 indicates that because of the ductility of the eccentrically braced frame and the strength of the

DMRSF, the strength of the model in its first story was stable, that is, non-decreasing, following shear yielding of the web in Link L2.

## 9.3 Strength and Deformation Characteristics of the Model

### 9.3.1 General

In order to compare the test results with the minimum strength requirements of the current seismic regulations, the experimental envelopes of maximum base shear ratio ($V_B/W$) versus the roof drift index and critical (first) inter-story drift index are presented in Figures 9.2 and 9.3, respectively. The maximum first inter-story drift index in the prototype exceeded 2.0% and is not shown in Figure 9.3. The nominal yielding strength of the model (=0.3W : see Section 4.4.4) is also shown in these two figures.

### 9.3.2 1985 UBC, 1984 ATC and 1986 SEAOC Requirements

The UBC, ATC and SEAOC minimum strength and maximum deformation requirements are described in Sections 3.2 to 3.4, respectively, and are not restated here. These requirements are presented in Figure 9.2 for the roof drift index (assuming a uniform storywise inter-story drift over the height of the model) and in Figure 9.3 for the critical (first) inter-story drift index. The as-built weight of the model was 82% of its design reactive weight (=1154/1400 for the prototype) and this factor must be considered in analyzing the test results.

### 9.3.3 Comparison of the Test Results and the Code Requirements

Figure 9.3 indicates that the strength of the model is significantly higher than that required by either the UBC, ATC and SEAOC. Since the eccentrically K-braced model was designed for a base shear coefficient significantly higher than required by either the UBC, ATC or SEAOC (Section 3.5.1), the performance of the model cannot be viewed as representative of an eccentrically K-braced dual system designed and constructed in the U.S.A.. The maximum inter-story drift index of 1.28% for the Taft-66 Test did not

exceed the ultimate drift level specified by either the UBC or ATC (= 1.5%) but did exceed the SEAOC limit of 1.12%. Despite the fact that the eccentrically K-braced model was subjected to an earthquake record with a significantly higher effective peak acceleration than the concentrically K-braced model (0.53g for the EBF compared with 0.40g for the CBF), its peak inter-story drift index of 1.28% was significantly smaller than that of the concentrically K-braced model (=1.87%) [9].

The nominal elastic strength of a structure can be reduced if the structure exhibits stable ductile behavior. In the ATC [12], a so-called Response Modification Factor (R) is used to derive the minimum design base shear from the ATC linear elastic design response spectrum (LEDRS). The ATC states that "...the response modification factor, R, and ... have been established considering that structures generally have additional **overstrength** capacity above that whereby the design loads cause significant yield." Furthermore, the commentary states that R "... is an empirical response reduction factor intended to account for both **damping** and the **ductility** inherent in the structural system at displacements great enough to surpass initial yield and approach the ultimate load displacements of the structural system....". The equivalent viscous damping ratio selected by the ATC for constructing its LEDRS is 5%.

Figure 9.3 shows that the maximum strength of the model was 2.85 (=0.856/0.30) times its nominal yielding strength of 0.3W (Section 4.4.4) and that this was reached during the Taft-66 Test (Table 8.6). The linear elastic response spectrum (LERS) of the input horizontal acceleration time history for the Taft-57 Test, scaled by the similitude laws to the prototype units, is presented in Figure 9.4 for 2% damping (corresponding to $\xi_1$ for the model). The corresponding linear elastic response spectrum for the Taft earthquake record with a peak acceleration of 0.50g (the target peak acceleration for the Taft-57 Test) is also shown in this figure. The fundamental period of the model, scaled by the similitude laws to the prototype units, prior to the Taft-57 Test was approximately 0.60 second. The pseudo-acceleration spectra presented in Figure 9.4 emphasize

the fact that peak acceleration is a poor index by which to express the intensity of a given earthquake acceleration record because the spectral ordinates of the 0.57g earthquake simulator output signal are smaller than those of the 0.50g input signal over a significant period range.

If the term LERS($\xi$, $\overline{T}$) is defined as the elastic pseudo-acceleration spectral ordinate corresponding to a given earthquake ground motion, the required response modification factor ($R_{req'd}$) can be defined as follows :

$$R_{req'd} = \frac{LERS(\xi, \overline{T})_{max}}{C_y} \tag{9.1}$$

where $\xi$ and $\overline{T}$ represent the damping and bounds to the natural period for the structure under consideration and $C_y$ is its nominal yielding strength. Neglecting the increase in damping due to inelastic behavior, the response modification factor is the product of a reduction in the required elastic strength due to ductility ($R_\mu \equiv$ ductility factor) and a strength factor ($R_S$) that can be defined as follows :

$$R_S = \frac{\text{Maximum Strength Ratio}}{C_y} = \frac{(\text{Overstrength} + 1) \times C_y}{C_y} \quad . \tag{9.2}$$

The strength factor results from the non-optimization of structural sections, material overstrength, material strain-hardening and certain code-based minimum requirements. The strength factor associated with a structure designed using optimization techniques depends on the last three parameters. The actual response modification factor (R) is therefore

$$R = R_\mu \times R_S \quad . \tag{9.3}$$

Accordingly, if reasonable estimates of $R_S$, $R_\mu$ and $LERS(\xi, \overline{T})_{max}$ are known, the required yielding strength ($C_y$) can be estimated by equating Equations 9.1 and 9.3.

For the similitude scaled period range of the model (0.590 to 0.603 second), Figure 9.4 indicates that the total reduction from the Taft-57 LERS to the nominal yielding

strength (Figure 9.3) of 0.3W is by a factor of 4.2 (= R) with a strength factor ($R_S$) equal to 2.82 and a ductility factor ($R_\mu$) equal to 1.5. The total reduction from the Taft-66 LERS to the nominal yielding strength (Figure 9.3) of 0.3W is by a factor of 5.2 (≡ R) with a strength factor equal to 2.85 and a ductility factor equal to 1.85.

To evaluate the soundness of the current ATC and SEAOC LEDRS, the ATC LEDRS ($\xi$ =5%) is presented with the 5% damped LERS of the 1985 Chile (N10E - Llolleo), 1985 Mexico City (EW - SCT) and the 1986 San Salvador (EW - CIG) earthquake records in Figure 9.5. The following conclusions can be drawn from Figure 9.5 and the preceding figures in this chapter :

*Linear Elastic Design Response Spectrum* : The ATC LEDRS is significantly nonconservative compared with the LERS of the 1985 Chile (N10E - Llolleo), 1985 Mexico City (EW - SCT) and the 1986 San Salvador (EW - CIG) earthquake records. In the period range of 0.10 to 1.00 second, that is, for short period structures, the spectral ordinates of the Chile and San Salvador earthquake records are far greater than those of the ATC. In the period range of 1.50 to 3.25 seconds, that is, for long period structures, the spectral ordinates of the Mexico City earthquake record are far greater than those of the ATC. The choice of a damping ratio of 5% is questionable: for a highly cracked reinforced concrete structure, 5% damping would appear to be appropriate whereas for a steel structure with a properly isolated facade, a damping ratio of 2% to 3% is more appropriate.

Even if the response modification factor currently proposed in the ATC for eccentrically braced dual systems (=6) is assumed to be adequate, the nonconservative nature of the ATC LEDRS would suggest that structures sited in regions of high seismic risk run a significant chance of failure during severe earthquake shaking.

*Earthquake Simulator Input Motions* : The choice of the 1952 Taft earthquake record with peak accelerations of 0.57g and 0.66g to test the model for its collapse limit response was appropriate, especially in light of the 1985 Chile and 1986 San Salvador

earthquake records discussed above.

*Effective Peak Acceleration* : On the basis of the earthquake ground motions discussed above, the decision to anchor the ATC LEDRS to an effective peak acceleration (EPA) of 0.4g in regions of high seismic risk would appear to be nonconservative if ground motions such as those recorded in Chile and San Salvador can occur in the U.S.A.. If the ground motion amplification factor of 2.5 is to be retained in future editions of the ATC (and SEAOC), the LEDRS should be anchored to a significantly higher EPA (in the range between 0.6g and 0.8g, for example).

*Response Modification Factors* : The ATC response modification factor for eccentrically K-braced dual systems of 6 exceeds the experimentally measured value of 5.2. As the model was detailed more conservatively and constructed more stringently than a typical building, the maximum achievable reduction factors for full-scale eccentrically braced dual systems are most likely to be significantly less than five, assuming that current analysis and design procedures are used. If optimization procedures such as those suggested by Austin et al. [56] are used in the design process, the maximum achievable response modification factor for this framing system, based upon a ductility factor of approximately 1.5, is most likely to be of the order of 2 to 3.

The nominal yielding strength of a structure can be expressed as follows :

$$C_y = \frac{LERS(\xi, \overline{T})_{max}}{R_\mu \times R_S} \quad . \tag{9.4}$$

If the elastic spectral pseudo-acceleration is significantly underestimated and the maximum possible response modification factor is overestimated, the nominal yielding strength of a structure is likely to be too small for it to withstand severe earthquake shaking. The SEAOC reduction factor ($R_w$) of 12 for eccentrically braced frames in dual systems is 60% greater (at yielding levels) than that currently proposed by the ATC and completely unjustified on the basis of the results of this testing program.

*SEAOC IDRS - Eccentrically Braced Dual Systems* : As a result of the selected response modification factor, the SEAOC inelastic derived response spectrum (IDRS) for eccentrically braced frames is grossly nonconservative. The design base shear at yielding levels for an eccentrically braced dual system designed in accordance with 1986 SEAOC is approximately half that required by the UBC and less than 10% of the pseudo-acceleration ordinate for the 1985 Chile (N10E - Llolleo) and the 1986 San Salvador (EW-CIG) earthquake records for 5% damping and a fundamental period around 0.6 second.

*Lateral Force Distribution* : The design lateral force distributions for the UBC, ATC and SEAOC were presented in Sections 3.2 to 3.4, respectively. In all three instances, the design lateral force distributions were approximately triangular. The lateral force distribution on the model, the eccentric braces and the DMRSF are presented in Figure 9.6 at the times of maximum base shear force for the Taft-08 and Taft-66 Tests. For the Taft-08 Test, the inertia forces profiles were similar to the model's fundamental mode shape with a second mode effect being evident at the roof level. The distribution of these inertia forces between the braced bay ($\equiv$ eccentric braces) and the DMRSF corresponds to their relative elastic rigidities. The design lateral force distributions agree reasonably well with the inertia force distributions for the Taft-08 Test at the times of maximum base shear. For the Taft-66 Test, the inertia force profiles are closer to uniform than triangular and are a reflection of the formation of a soft first story in the model. The distribution of these inertia forces between the braced bay and the DMRSF at the times of maximum base shear do not correspond to their relative elastic stiffnesses and vary significantly from both the Taft-08 lateral force distributions and the design lateral force distributions suggested by the UBC, ATC and SEAOC.

The triangular load distribution will generally produce larger member forces in a structure than a uniform load pattern for a given base shear force. However, if capacity design procedures are used to predict the maximum possible base shear force given the

nominal overturning moment capacity of a structure, the uniform load distribution is more appropriate than the triangular load distribution. Therefore, although the code-based lateral force distributions are a reasonable basis on which to size the members in a structure, they are clearly inappropriate for certain capacity design procedures.

### 9.3.4 Comparison of the Model's Experimental and Analytical Strength

The analytically predicted strength versus deformation relationships for the model (Figures 7.1 and 7.2) and the envelope of the results of the Taft-08, Taft-27, Taft-57, Taft-66 and the Sine-70 Tests are presented in Figures 9.2 and 9.3.

**Critical Inter-Story Drift Index :** The relationship between the base shear ratio and the critical (first) inter-story drift index is presented in Figure 9.3. The elastic stiffness of the model is less than that predicted analytically; this fact can be attributed in part to the flexibility of the model's foundation (assumed to be rigid in the mathematical model) and the damage sustained by the composite floor system during the testing of the concentrically K-braced model [9]. This observation is confirmed by comparing the analytically predicted and the experimentally evaluated stiffness matrices of the model in Tables 6.1 and 6.2. The envelope of the test results is within 10% of the analytically predicted curve using a triangular lateral load pattern at drift levels exceeding 0.5%. For a given base shear force, the total lateral load for both the triangular and uniform load patterns are identical at Level L2 and the difference between the two analytical envelopes is due to variation in the distribution of the internal forces above Level L2. The influence of second order effects (P-$\Delta$ effect) was found to be insignificant for this eccentrically K-braced dual system. In the inelastic range, the difference between the analytical and experimental results can be attributed to the increased damage in the composite slab with increasing levels of excitation, the effect of which was to increase the flexibility of the model with respect to the analytically predicted result.

**Roof Drift Index :** As shown in Figure 9.2, at the lower levels of base excitation (Taft-08 and Taft-27), the test results are similar to the analytical prediction assuming a

triangular load pattern. At the higher levels of base excitation (Taft-57 and Taft-66), the test results are more closely represented by the analytical predictions based on a uniform load pattern. As noted in Chapter 4, the triangular load pattern corresponds to a first mode load pattern whereas the uniform load pattern represents a load pattern that is consistent with the formation of a soft first story. These observations are in complete agreement with the inertia force envelopes presented in Chapter 8 for the Taft-08, Taft-27, Taft-57, Taft-66 and Sine-70 Tests.

### 9.3.5 Comparison of the Model and Prototype Global Response

The analytical relationships between the base shear ratio and the roof and critical inter-story drift indices (Figures 4.14 and 4.15) for the eccentrically K-braced prototype are presented in Figures 9.2 and 9.3. For comparison, the model's results have been scaled to the prototype units. The maximum strength of the model (=0.856W) was 24% higher than that of the prototype (=0.687W). As the prototype did not attain its potential strength (Section 4.4.2), it was difficult to compare the strengths of the two structures. The limit analyses presented in Section 7.2 showed that the model's strength was approximately 20% higher than the prototype's strength and that this was due primarily to the higher plastic shear capacities of the model's shear links.

A number of researchers [57,58] have shown that strain rate can affect the strength of a structure. A significant increase in the strain rate will substantially increase the yield stress ($\sigma_y$) and marginally increase the ultimate stress ($\sigma_u$). The strength of the eccentrically K-braced bay is primarily a function of the ultimate strength rather than the yield strength of the shear links. For a strain rate of 0.1/sec (the strain rate in Link L2 to the level of first yield in that cycle in which the maximum strength of the model was reached was equal to 0.106/sec), the dynamic ultimate strength is of the order of 5% larger than the static ultimate strength [58]. Therefore, the strain rate effect on the strength of the eccentrically K-braced model was relatively small.

The higher strength of the model (=0.856W) with respect to the prototype (=0.687W) can be attributed to three factors, namely; the plastic shear capacities of the model's W shear links being 14% (L2 and L3), 21% (L4 and L5) and 23% (L6 and LR) higher than those of the prototype; the fact that the prototype did not attain its potential strength and the strain rate effect (albeit less than 5%).

The experimental strength and deformation relationships for the prototype and the model are presented in Figures 9.2 and 9.3. These figures clearly show that the prototype was stiffer than the model. This observation is in complete agreement with the flexibility profiles presented in Figure 6.4.

## 9.4 Base Shear, Excitation Intensity and Ductility

In Section 9.3, it was shown that peak acceleration is a very poor index by which to describe and categorize earthquake simulator excitation. Furthermore, peak acceleration has been shown to be a poor damage potential index for a given earthquake ground motion [59]. The linear elastic response spectral ordinates (PSA or PSV) of the measured earthquake simulator motion are used in the ensuing discussion to quantify the intensity of the base excitation. As the model responded primarily in its first mode, the fundamental period and the corresponding equivalent viscous damping ratio (measured prior to each test) are used below to define the appropriate spectral ordinates.

The pseudo-acceleration (PSA/g) versus base shear ratio ($V_B/W$) relationship for the model is shown in Figure 9.7 in addition to the base shear that would result from linear elastic response. The base shear did not increase linearly with the pseudo-acceleration of the base excitation because of nonlinear behavior in the model. The ordinates corresponding to the Taft-08 and Taft-27 Tests are greater than the linear elastic ordinates because of the contribution of the pitching motion of the earthquake simulator to the *effective* horizontal acceleration time history (Section 10.2.3).

The strength and deformation envelopes presented in Figures 9.2 and 9.3 are shown in Figures 9.8a and 9.8b. The maximum inter-story displacement ductility ($\mu_{CRIT}$) was approximately 2.0 and the roof displacement ductility ($\mu_{ROOF}$) was approximately 1.2 based on yield displacements calculated using the equal energy method [59]. The maximum inter-story displacement ductility of 2 is significantly less than that assumed by the UBC, ATC and SEAOC.

## 9.5 Energy Input and Dissipation

### 9.5.1 Test Results

The relationship of the base excitation intensity, expressed in terms of pseudo-acceleration ($PSA[\xi_1,T_1]/g$) to the maximum input energy ($E_I$) is shown in Figure 9.9. The input energy was calculated in accordance with Equation 7.4. Although the rate of increase in the maximum base shear decreased with increasing excitation intensity, the maximum input energy increased significantly with increasing excitation intensity. In Figure 9.10, the input energy per unit mass is replaced by equivalent velocity ($\equiv V_I = \sqrt{2E_I/(W/g)}$). For a linear elastic system, the input energy is proportional to the excitation intensity squared, that is, the equivalent velocity is linearly proportional to the excitation intensity.

The total input energy ($E_I$) is either dissipated as viscous damped energy ($E_\mu$) and inelastic hysteretic energy ($E_H$), or stored as kinetic energy ($E_K$) and elastic strain energy ($E_S$). The proportion of the total input energy that contributes to the *damage* of the structure ($E_D$) can be expressed as

$$E_D = E_H + E_S + E_K = E_A + E_K \,. \tag{9.5}$$

The maximum values of $E_S$ and $E_K$ occur alternately (at zero displacement and at maximum displacement), so the latter term can be ignored when estimating the maximum value of $E_D$ :

$$E_D \approx E_A \tag{9.6}$$

and the equivalent velocity corresponding to $E_D$ is

$$V_D = \sqrt{\frac{2E_D}{(W/g)}} . \tag{9.7}$$

Therefore, since $E_I$ is equal to $E_D$ plus $E_\mu$ and since $E_\mu$ is generally small for bare steel structures, $E_D$ is approximately equal to $E_I$.

A limit design method based on energy considerations was proposed by Housner [60] who suggested that the input energy contributing to structural damage was maximized by linear elastic response and that it could be estimated by

$$E_D = \frac{1}{2}kS_d^2 = \frac{1}{2}k\left(\frac{PSV}{\omega}\right)^2 = \frac{1}{2}m(PSV)^2 = \frac{1}{2}(\frac{W}{g})(PSV)^2 \tag{9.8}$$

or

$$V_D = \sqrt{\frac{2E_I}{(W/g)}} = PSV \tag{9.9}$$

where $S_d(\xi, T)$ is the spectral displacement for the earthquake ground motion under consideration. Housner stated that the hysteretic energy dissipation capacity ($E_H$) should exceed the quantity ($E_D$–$\overline{E}_S$), where $\overline{E}_S$ is the maximum strain energy that can be stored in the structure. For a linearly elastic, perfectly plastic, single degree-of-freedom system (SDOFS) with yield force $R_y$ and a yield displacement $\delta_y$, $\overline{E}_S$ is equal to $0.5\, R_y\, \delta_y$. Housner's relationship between $V_D$ and PSV is shown in Figure 9.10.

The use of the pseudo-velocity response spectrum to estimate the input energy significantly underestimated the earthquake simulator test results for the Taft-57, Taft-66 and Sine-70 Tests. Housner's assumption that an upper bound to the input energy spectrum could be obtained from the PSV spectrum for a given earthquake ground motion does not apply for the 1952 Kern County Taft N21E earthquake record for structures with small natural periods (0.0 - 0.5 second).

### 9.5.2 Relationship between Input Energy, Yielding Strength and Ductility

Using the computer program NONSPEC [61], the relationship between the non-dimensional parameter ($\eta$) defined as

$$\eta = \frac{C_y}{\ddot{v}_{g\,max}/g} = \frac{R_y}{m\,\ddot{v}_{g\,max}} \tag{9.10}$$

the ductility ($\mu$) and the fundamental period (T) are presented in Figure 9.11 for 2%, 5% and 10% damping for a SDOFS and the similitude scaled Taft-66 Test acceleration record. The parameters $C_y$, m and $\ddot{v}_{g\,max}$ in Equation 9.11 are the seismic yielding coefficient, the mass and the peak ground acceleration, respectively.

For the model and the Taft-66 Test, $\eta$ equals 1.3 (=0.856/0.663) and the required ductility ($\mu$), based upon a period of 0.6 second ($\approx 0.32\times1.811$) and a damping ratio of 2%, is 1.8. Assuming that a structure can be designed strictly in accordance with the minimum strength requirements of the UBC and that compatibility between the braced and unbraced frames is assured, the UBC yielding coefficient for such a structure on a rock site is approximately 0.21. For the Taft-66 Test, $\eta$ would therefore equal 0.31 (=0.21/0.663) and the required ductility, based upon the UBC derived period of 0.5 second (Section 3.2) and a damping ratio of 2%, would be in excess of 10; that is, twice the ductility implicitly assumed by the UBC and five times the maximum inter-story displacement ductility ($\mu_{CRIT} = 2$ : Section 9.4) that was measured in the testing program. For the 1985 Chile earthquake (N10E - Llolleo), $\eta$ would equal 0.31 (=0.21/0.67) and the required ductility, based upon a UBC derived period of 0.5 second (Section 3.2) and a damping ratio of 2%, would be in excess of 20; that is, four times the ductility implicitly assumed by the UBC and ten times the maximum inter-story ductility that was measured throughout the testing program. If a structure was designed to just satisfy the minimum strength requirements of the UBC, the displacement ductility demand on a SDOFS for the Chile earthquake record would be far greater than that which could be supplied by any eccentrically braced dual steel system.

The input energy spectra for the similitude scaled Taft-66 Test earthquake record are presented in Figure 9.12 for values of $C_y$ equal to 3.0, 0.8, 0.4 and 0.2. A value of $C_y$ equal to 3 corresponds to linear elastic response for the Taft-66 Test earthquake record. The strength of the model was equal to 0.856W, that is, $C_{max}$ is equal to 0.856. The similitude scaled input energy for the Taft-66 Test was 20,447 kip-in ($= 579/ 0.3048^3$) and this is indicated in Figure 9.12. For $C_y$ equal to 0.856, the interpolated energy input to a SDOFS with a mass of 2.986 kip/sec$^2$ (=1154/386.4) and a period of 0.60 second is 17,400 kip-in, that is, 86% of the scaled test result. As a result of the pitching motion of the earthquake simulator, the *effective* horizontal acceleration (Section 10.2.3) was greater than the measured horizontal acceleration (Channel 3 : see Appendix A). Therefore, the use of the horizontal acceleration time history as input to NONSPEC lead to the underestimation of the test result.

For the 1952 Taft N21E earthquake ground motion, the input energy is generally maximized by linear elastic response for natural periods exceeding 0.5 second. In the period range between 0.05 and 0.50 second, the assumption that the input energy is maximized by linear elastic response is significantly nonconservative; for the range of values of $C_y$ considered above, the input energy is maximized by a SDOFS with a yielding coefficient equal to 0.2. The relationship between $E_I$, $C_y$ and T is ***entirely*** dependent upon the earthquake ground motion under consideration and the results presented above for the Taft ground motion cannot be construed as being applicable for any other acceleration time history.

For a linear elastic structure, the input energy is proportional to the pseudo-velocity squared. If the input energy is anchored to the Taft-27 Test ($E_I$ = 46.7 kip–in), the predicted input energies to the Taft-57 and Taft-66 Tests are 454 kip-in and 695 kip-in, respectively, compared with the measured input energies of 427 kip-in and 579 kip-in, respectively. In this instance, the predicted energy input to the linear-elastic system is greater, albeit marginally, than the measured energy input to the model. This

should not be construed as a means by which to estimate the input energy given the input energy to a structure for an elastic level test.

The natural periods shown in Figure 8.2 were calculated either prior to, or following the earthquake simulator tests (Table 8.1) and not during the earthquake simulator tests. During the Taft-66 Test, the natural period varied between 0.33 second and 0.42 second; this variation was estimated from the relative displacement response time histories using the zero-crossing method. Although the period variation noted above can only be considered to be approximate, the trend of natural period elongation with increased response and thus increased damage is evident. The period of 0.42 second was measured during the time of maximum displacement response in the model. For a shift in the natural period from 0.60 second to 0.76 second (=0.42×1.811), the interpolated input energy for a seismic yielding coefficient equal to 0.856 (= maximum strength of the model) increases by approximately 50% and is 25% higher than linear elastic input energy for a natural period equal to 0.60 second.

A bounded approach to the evaluation of an energy spectral ordinate is essential given the probability of sharply varying energy spectral ordinates and the uncertainties associated with evaluating both $C_y$ and the fundamental period. The extent of the bound on the fundamental period should reflect the relationship between the degree of damage in the structure under consideration and the variation in its fundamental period resulting from that damage.

## 9.6 Ductile Moment-Resisting Space Frame Response

The UBC, ATC and SEAOC currently require that the DMRSF be designed to resist at least 25% of the minimum design base shear. This supposedly supplies a line of defense against the collapse of the dual system after the failure of the primary seismic load resisting elements.

The high strength demand on the DMRSF is clearly shown in Figure 8.60; it resulted from the formation of a soft first story during the Taft-57 and Taft-66 Tests and followed shear yielding and web buckling in Link L2. The envelope of the story shears resisted by the DMRSF is shown in Figure 9.13 in conjunction with the strength of each story of the DMRSF calculated assuming a storywise sway mechanism. The potential strength of the DMRSF was not developed in any of the six stories.

The current UBC requirements were drastically exceeded in the first story where the maximum story shear force resisted by the DMRSF was 38.2 kips or 119% of the nominal yielding strength of the *total* structure. However, the maximum story shear demand on the first and second stories of the DMRSF were only 63% and 23% of its first and second story strengths, respectively. The relatively high strength of the DMRSF can be attributed in part to the fact that it was designed for 34% of the design base shear (1981 Japanese Aseismic Code) in lieu of 25% of the UBC design base shear [14,15].

The envelopes of the story shear resisted by the DMRSF versus inter-story drift index for the five tests described in Chapter 8 are shown in Figure 9.1. The DMRSF supported the total gravity load of the model and resisted in excess of 40% of the first story shear following shear yielding and web buckling of Link L2.

The DMRSF achieved a strength of approximately 0.35W in the first story; however, its flexibility was such that at the maximum inter-story drift index of 1.28%, it did not dissipate energy.

A conceptually sound design of an eccentrically braced dual system would enable inter-story drifts of the order of 1.5% to 2.0% to be attained while the corresponding shear strains in the adequately stiffened shear links were limited to 0.06 to 0.10 radian. The DMRSF should therefore be designed to yield at drift levels of 1.2% to 1.5% and to dissipate significant energy in the inter-story drift range between 1.2% and 2.0%.

Since the design strength of the DMRSF was significantly larger than that required by the UBC, the inherent problems associated with lack of strength and stiffness compatibility of the braced frames and the DMRSF in a dual system would be significantly worse in a structure designed strictly in accordance with the current seismic regulations. It is clear therefore, that there is an urgent need to optimize the relative elastic stiffnesses, yielding strengths, deformability and ductility of the braced frames and the DMRSF.

## 9.7 Shear Link Response

### 9.7.1 General

In this section, emphasis is placed upon the response of Link L2 for two reasons. First, Link L2 was the only shear link to undergo appreciable web buckling and secondly, Link L2 and the adjacent structural members were extensively instrumented.

### 9.7.2 Effect of Composite Action

The lightweight reinforced concrete slab influenced the response of the shear links by increasing the stiffness and strength of the W shear link, by modifying the relative stiffnesses of the beams outside the shear link and by restraining the top flange of both the shear link and the beams outside the shear link against lateral-torsional buckling. Ricles [22] showed that the relative stiffness of the beam beyond the shear link influenced the behavior of the link and that the greater the relative restraint at either end of the shear link (maximized when the composite slab is in compression and minimized when the composite slab is in tension), the greater the degree of moment equalization at either end of the shear link. Furthermore, Ricles [22] indicated that the framing beams at both ends of the shear link (Figure 2.1) were necessary to prevent lateral-torsional buckling because the concrete slab was unable to restrain the bottom flange of the shear link.

Kasai [2] elaborated upon the redistribution of moments in the shear link with an emphasis on D-braced frames (Figure 1.3). For the symmetric eccentrically K-braced frame, the required degree of moment redistribution is significantly smaller than that required for the D-braced frame.

The link shear force ($V_L$) was defined in Section 7.5 as the vertical component of the eccentric brace force minus the coexisting shear force in the beam outside the shear link. The link shear force includes that force developed in the eccentric brace by the consistent deformation of the concrete slab spanning perpendicular to Frame B ($V_L^{SLAB}$). Figure 9.14 depicts the assumed displacement field in plan and elevation. The true shear force ($V_L^*$) in Link L2 is therefore

$$V_L^* = V_L - V_L^{SLAB} \quad .$$

The degree to which the three dimensional coupling affected the global response of the composite shear link is a function of the extent of the slab degradation which itself depended upon the deformation history of the shear link. An estimate of the strength of the concrete slab spanning between the beams parallel to Frame B (Figure 9.14) at Level L2 indicated that the maximum vertical force that could be attributed to the coupling effect was between 5 and 6 kips ($= V_L^{SLAB}$). This estimate was based on the measured vertical displacements in the concrete slab, the boundary conditions and the degree of slab damage. Accordingly, the true shear force ($V_L^*$) in Link L2 was estimated to be approximately 27 to 28 kips or 170% to 180% of the nominal shear yielding strength of Link L2 (=15.77 kips : Table 5.4).

SEAOC currently requires that the compressive strength of the eccentric braces be designed to resist 150% of the axial force generated by the yield strength of the corresponding link beam. On the basis of the test results, eccentric braces should be designed to resist : (i) at least 170% of the axial force generated by the shear yielding strength of the link ($V_p$) and (ii) the axial forces generated by the consistent deformation

of the concrete slab spanning perpendicular to the plane of the eccentrically braced frame. To calculate the required brace section, the AISC [35] formula for compression members can be adopted :

$$P_{cr} = \left[1 - \frac{(kl/r)^2}{2C_c^2}\right] \frac{F_y A}{FS} \tag{9.11}$$

where $C_c$ $(=\sqrt{2\pi^2 E_s/F_y})$ is the limiting effective slenderness ratio above which the brace will buckle elastically, k is an effective length factor and FS is a safety factor. As ultimate level forces are used to design the eccentric braces, the safety factor (FS) in Equation 9.11 should be set equal to 1.0.

### 9.7.3 Relationship between Shear Link Strength and Dual System Strength

The envelope of the total story shears resisted by the model during the Taft-66 Test (labeled as Taft-66 Demand) is shown in Figure 9.15 in conjunction with the strength of each story, including and excluding composite action. The *yielding* strength of each story of the eccentrically K-braced frame (Frame B) was calculated by assuming a point of contraflexure at the midpoint of each shear link and a yield stress in the web of each link of 46 ksi. The strength of the DMRSF in each story was estimated by assuming a storywise soft story formation. The *ultimate* strength of each story accounted for composite action and strain-hardening in the shear links by multiplying the *yielding* strength of the braced bay by a factor of 1.70 for the reasons noted in the previous section. The three dimensional coupling effect discussed in Section 9.7.2 was ignored for these analyses.

The UBC requirements were drastically exceeded in the first story where the story shear force resisted by the model was 91.6 kips or 285% of the nominal yielding strength of the model (=0.3W : see Section 4.4.4). The maximum story shear demand was 104% of its *yielding* strength and 83% of its *ultimate* strength in the first story. In the second story, the maximum story shear demand was 75% of its *yielding* strength and 58% of its *ultimate* strength.

Link L2 acted as a structural *fuse* to limit the axial forces in the first story eccentric braces. The maximum first story shear force resisted by the braced bay was 55.2 kips during the Taft-57 Test and the corresponding maximum shear force in Link L2 was 33.6 kips. For the Taft-66 Test, the maximum first story shear force resisted by the braced bay was 54.4 kips and the corresponding maximum shear force in Link L2 was 33.1 kips. The shear force in Link L2 was maximized in its pre-web buckling state during the Taft-57 Test; the post-web buckling strength of Link L2 was smaller than its pre-web buckling strength.

There are three prerequisites for the successful performance of a dual system incorporating eccentrically braced frames :

(i) **Yielding Strength :** A *minimum* yielding strength ($C_y$), irrespective of the prerequisites noted below, is required to avoid failure during severe earthquake shaking.

(ii) **Compatibility :** The compatibility of the stiffness and strength of the braced frames and the DMRSFs must permit the DMRSFs to participate in the primary lateral load resisting system and allow it to function successfully as the secondary lateral load resisting system, possessing adequate stiffness and strength at acceptable drift levels.

(iii) **Ductility and Strain Hardening :** The provision of adequate transverse web stiffening in the shear links facilitates internal force redistribution and the participation of the DMRSFs in the lateral load resisting system. The effect of strain-hardening is to prevent local buckling, increase plastic hinge lengths (thus reducing the curvature and strain ductility demands) in those members other than the shear links and also to increase the strength of a structure.

### 9.7.4 Kinematics of the Eccentrically Braced Frame

The relationship between the first inter-story drift and the shear strain in Link L2 for the Taft-66 Test is shown in Figure 9.16a; the envelope of the first story drift and the shear strain in Link L2 and the initial yielding cycle are shown in Figure 9.16b. The

inter-story drift ($\Delta$) is comprised of the elastic drift ($\Delta_e$) and the plastic drift ($\Delta_p$). The elastic drift includes axial, flexural and shear deformations of the columns, beams, eccentric braces, shear links and panel zones. The plastic drift is due primarily to the shearing deformations in the shear links and plastic rotation in columns. The inter-story drift ($\Delta$) and the shear strain ($\gamma$) can be separated into elastic and plastic components as follows :

$$\Delta = \Delta_e + \Delta_p \tag{9.12}$$

$$\gamma = \gamma_e + \gamma_p \ . \tag{9.13}$$

For Link L2, the maximum shear strain is of the order of 30 to 40 times the nominal yielding shear strain, that is, $\gamma_p$ is much larger than $\gamma_e$. The kinematic relationship between the link shear strain ($\approx\gamma_p$) and the plastic drift for the displacement field shown in Figure 3.2b is

$$\gamma_p = \frac{L}{e}\frac{\Delta_p}{h} \tag{9.14}$$

and from Equation 9.14 and Figure 9.16b, the peak shear strain ($\gamma$), is given by

$$\gamma \approx \gamma_p \approx \frac{L}{e}\frac{(\Delta - \Delta_e)}{h} \ . \tag{9.15}$$

The nominal elastic inter-story drift index ($\Delta_e/h \equiv \Theta_{yn}$), calculated from Figure 9.8b and using the equal energy approach [59], is approximately 0.65%, that is, 50% of the total inter-story drift, and consistent with the maximum inter-story displacement ductility ratio of 2.0. The theoretical peak shear strain in Link L2 is therefore

$$\gamma \approx \frac{90}{8.54} \times (1.30\% - 0.65\%) = 0.069 \text{ radian} \ .$$

This underestimates the measured peak shear strain (=0.092 radian) by approximately 25%. If the true elastic inter-story drift index ($\Theta_{yt}$) of 0.50% (Figure 9.8b) is used in lieu of the nominal value, the peak shear strain in Link L2 becomes

$$\gamma \approx \frac{90}{8.54} \times (1.30\% - 0.50\%) = 0.085 \text{ radian}$$

and this underestimates the measured peak shear strain by only 8%.

In order to extend the relationship between $\Delta$ and $\gamma$ to one that is design orientated, either the elastic and ultimate drifts must be known or there must be an explicit relationship between these two drift levels.

The UBC calculates ultimate drift levels by multiplying the drifts determined from the code-required lateral forces by a factor of 3/K (=3.75); the inelastic deformation factor is thus equal to (3/K) $\times$ 0.8 (=3.0) where 0.8 is the factor extrapolating the UBC working stress drift levels to yielding drift levels. The ATC calculates ultimate drift levels by multiplying the drifts determined from the code-required lateral forces by a deflection amplification factor ($C_d$) equal to 5 for a dual braced system. SEAOC calculates ultimate drift levels by multiplying the drifts determined from the code-required lateral forces by a factor of $3R_w/8$ (=4.50); the inelastic deformation factor is therefore equal to 3.6 (= 4.50$\times$0.80).

The measured inelastic deformation factor (= $\mu_{CRIT}$) for the model is approximately 2 and significantly less than that suggested by the current seismic regulations (3 to 5).

The relationship between the maximum elastic and inelastic inter-story drift indices is extremely complex. The use of a single coefficient (3/K, $C_d$, $3R_w/8$ for the UBC, ATC and SEAOC, respectively) to relate these two indices over the entire range of natural period is inappropriate.

A rigorous yet computationally efficient method for estimating shear strain in a link corresponding to a particular inter-story drift would be to perform a step-by-step nonlinear static collapse analysis using DRAIN-2DX.

### 9.7.5 Cyclic Web Buckling Control

As the lateral strength and ductility of the eccentrically braced frame are governed by the strength and ductility of its shear links, shear links and their connections to the eccentric braces must be detailed so as to preclude their premature failure. Cyclic loading of isolated shear links by Kasai et al. [2,21] has shown that the post-web buckling behavior and ultimate failure mode of a shear link is difficult to predict and that web buckling of a shear link leads to the degradation of its stable hysteretic behavior and therefore, its energy dissipation capacity. Accordingly, a realistic level of deformation in shear links for the collapse limit state is that deformation that can be accommodated just prior to web buckling. Web buckling can be controlled and delayed by the provision of transverse web stiffeners. Transverse stiffeners control the potentially sharp out-of-plane curvatures that can develop as the web buckles and serve to anchor, and therefore permit, the propagation of the diagonal tension fields that develop in conjunction with the buckling field. Diagonal tension field formation generates truss action in a shear link whereby the transverse stiffeners act as compression web elements and the flanges act as the tension and compression chords of the truss. The transverse stiffeners also anchor the tension field and provide lateral (vertical) restraint to the compression flange.

Kasai [2,21] defined the web buckling deformation angle ($\bar{\gamma}_B$) as the maximum deformation angle measured from the most distant point of zero shear for the entire preceding history to the point of failure (Figure 9.17). In the Taft-57 and Taft-66 Tests, the cycles of maximum deformation yielded values of $\bar{\gamma}_{max}$ equal to 0.153 and 0.160 radian, respectively; these cycles are presented in Figure 9.17. On the basis of the tests of thirty isolated shear links and assuming that the ultimate shear strain ($\gamma_u$) was approximately 50% of $\bar{\gamma}_B$, Kasai [2,21] developed an equation relating the topography of a shear link to a series of calibrated constants :

$$\frac{a}{t_w} + \frac{1}{5}\frac{d}{t_w} = C_B \tag{9.16}$$

where the constant $C_B$ equals 56, 38 and 29 for $\gamma_u$ equal to 0.03, 0.06 and 0.09 radian, respectively. In Equation 9.16, the parameters a, d and $t_w$ are the distance between the transverse stiffeners, the section depth and the web thickness, respectively. For Link L2, the calibrated constant $C_B$ equals

$$\frac{8.54}{4}\frac{1}{0.11} + \frac{1}{5}\frac{5.40}{0.11} = 29$$

and the theoretical ultimate deformation angle of 0.09 radian is extremely close to the experimental value of 0.092 radian (Figure 9.17). The experimental results confirm Kasai's relationship and Equation 9.16 can be used with confidence to select the spacing of transverse web stiffeners in shear links.

### 9.7.6 Inelastic Behavior and Energy Dissipation Capacity

The inelastic behavior of a shear link can be categorized into either its pre-web buckling state or its post-web buckling state. In the pre-web buckling state, the hysteretic behavior of shear links is reproducible, ductile and stable. In the post-web buckling range, the strength and stable deformation capacity of a shear link may degrade either gradually (over a small number of cycles) or suddenly, depending on its topography. Heavily stiffened shear links are prone to fail in a brittle or tearing manner along the perimeter of the link panel similar to failures observed in transversely stiffened plate girders [62]. The tearing failure of the shear link panel is generally caused by stress concentrations that develop at the anchorage points of the diagonal tension field. The post-web buckling behavior of a stiffened shear link is exceedingly complex and, for all purposes, impossible to predict. Since the stable response of an eccentrically braced frame to severe earthquake shaking depends primarily on the ductile, stable response of its shear links, the post-web buckling regime is not a desirable collapse limit state for shear link response.

The differences between the pre-web buckling and post-web buckling behavior of a shear link are clearly seen in Figure 9.18. Figure 9.18 presents the time history of the energy dissipation of Links L2 and L3 as a function of the total hysteretic and viscous damped energy for the Taft-57 (Link L2 pre-web buckling), Taft-66 (Link L2 post-web buckling) and Sine-70 (Link L2 post-web buckling) Tests. The energy dissipated by the shear links was calculated by integrating the link shear force as a function of the shear deformation over the duration of the time history and therefore includes that energy dissipated by the concrete slab spanning perpendicular to the braced frame in the proximity of the shear link. The input energy ($E_I$), the energy dissipated by the shear links ($E_L$), the percentage of the energy dissipated by Links L2 ($E_{L2}$) and L3 ($E_{L3}$) as a function of the energy dissipated by all six shear links for the Taft-08, Taft-27, Taft-57, Taft-66 and Sine-70 Tests are presented in Table 9.1.

The energy dissipated by Link L2 is maximized in its pre-web buckling state (74% of $E_I$ during the Taft-57 Test). The drop in the energy dissipated by Link L2 after web buckling as a percentage of $E_L$ is 7% for the Taft-66 Test and 17% for the Sine-70 Test. After web buckling of Link L2, the energy dissipated by Link L3 as a percentage of $E_L$ increased by 5% for the Taft-66 Test and 16% for the Sine-70 Test. The drop in energy dissipated by Link L2 was recovered in the remaining five shear links and in other yielding regions in the dual system such as the beam-to-column panel zones.

The hysteretic energy dissipated by the model was concentrated in its first and second stories and was in turn dominated by the hysteretic behavior of the shear links. The concentration of damage in the eccentrically K-braced dual system is undesirable although the energy dissipation capacity of the individual links was outstanding.

The ideal displacement field for an eccentrically braced frame should be based on rigid body displacements in the triangulated elements outside the shear links. This displacement field would maximize the strength and energy dissipation capacity of the eccentrically braced frame. A primary objective in the design of an eccentrically braced

frame should be to achieve such a displacement field in the inelastic range.

### 9.7.7 Low Cycle Fatigue and Incremental Collapse

**General :** Variable, repeated loading can give rise to structural collapse by either low cycle fatigue (alternating plasticity) or incremental collapse (crawling collapse). Low cycle fatigue is associated with a large number of alternate yielding cycles whereas incremental collapse results from the accumulation of plastic deformation in a sufficient number of plastic hinges, in a given cycle of loading, to permit rigid body motion in the structure. Although incremental collapse and low cycle fatigue are closely inter-related and may manifest themselves in a similar manner, they are in essence significantly different and thus deserve different degrees of attention.

As a result of the 1985 Mexico City and 1985 Chile earthquakes, attention has been focused upon the possibility of low cycle fatigue and incremental collapse becoming an important factor in earthquake resistant design. The 1985 Chile earthquake record (N10E at Llolleo) has an extremely long duration of strong motion shaking, a large effective peak acceleration and a strong frequency content in the range of natural period less than 0.7 second. For structures with small natural periods ($T_{model} = 0.32 \times 1.811$ : see Section 6.4), this earthquake record is possibly the most damaging, in terms of low cycle fatigue and incremental collapse, of any recorded to date. Consequently, the Llolleo earthquake record has been used in these studies to determine the likelihood of the model failing by either low cycle fatigue or incremental collapse.

**Test Results :** On the basis of these test results, it appears that low cycle fatigue and incremental collapse will not control the earthquake resistant design of eccentrically braced dual systems. The eccentrically K-braced model was subjected to a total of eleven damageability and collapse limit state earthquakes; even in regions of high seismic risk, a given structure would be unlikely to be subjected to more than one or two earthquake ground motions of these intensities.

The level of deformation in Link L2 is presented in Figures 9.19 to 9.22 for the Taft-27, Taft-57, Taft-66 and Sine-70 Tests, respectively. The number of cycles in which the shear strain ductility (anchored to the nominal yielding shear strain of the bare steel shear link, $\gamma_y$=0.0023) exceeds 1, 2, 5, 10, 20 and 30 is presented in the bar-charts. Figure 9.23 is a summary of Figures 9.19 to 9.22 and includes the results of the remaining damageability and collapse limit state tests (Table 7.1).

**Low Cycle Fatigue :** Cumulative deformation ductility is a better failure index than maximum deformation ductility for structures susceptible to low cycle fatigue because it is a measure of the total amount of inelastic deformation that the element has experienced. The cumulative inelastic deformation ductility is calculated by summing the absolute value of all of the inelastic deformation cycles and then normalizing the result to $\gamma_y$.

The computer program NONSPEC [61] was used to estimate the accumulative ductility ratio demand on a SDOFS subjected to the 1985 Chile (N10E - Llolleo) and the Taft-66 Test earthquake records. The strength of the model, expressed as a function of its design reactive weight (1400×0.093 : see Table 5.1) was 0.60W (=0.72×1154/1400), where the strength of the model (0.72W) was evaluated using the equal energy method (Figure 9.8b). The accumulative ductility ratio ($\mu_a$) for the Llolleo and Taft-66 earthquake records were 6.67 and 8.16, respectively. Since the model did not fail because of low cycle fatigue during the Taft-66 Test, it would not have failed by low cycle fatigue if it had been subjected to the long duration Llolleo earthquake record.

Up to the point of fracture, Link L2 demonstrated stable, well-rounded hysteretic behavior and resisted a significant number of large yielding cycles of shear strain ductility in excess of 10. The degradation in strength and stiffness immediately prior to failure that is consistent with the phenomenon of low cycle fatigue was not observed, despite the fact that the total accumulative ductility demand on Link L2 for all of the damageability and collapse level tests was of the order of four times that for the Taft-66 Test

alone.

**Incremental Collapse :** Incremental or crawling collapse can be initiated by earthquake ground motions that contain either numerous uni-directional acceleration pulses of moderate intensity or a small number of severe acceleration pulses. The Taft earthquake record contains a number of acceleration pulses but these pulses are offsetting and the permanent shear strains in Link L2 measured after the Taft-57 and Taft-66 Tests were small. In order to estimate the likelihood of incremental collapse of the model (and its full-scale equivalent), the maximum displacement ductility demand ($\mu$) and the maximum cyclic displacement ductility ($\mu_c$) were evaluated for the 1985 Chile and Taft-66 Test earthquake records. Using the same parameters as those noted above, the maximum displacement ductility and maximum cyclic displacement ductility were 2.95 and 3.16, respectively, for the Chile earthquake record and 2.73 and 2.84, respectively, for the Taft-66 Test earthquake record. The maximum displacement ductility and the maximum cyclic displacement ductility ratios for the 1985 Chile earthquake record were similar to those of the Taft-66 earthquake record. Since the model did not fail because of incremental collapse during the Taft-66 Test, it would not have failed if it had been subjected to the 1985 Chile earthquake record.

**Summary :** Categorical conclusions regarding the importance of incremental collapse and low cycle fatigue cannot be drawn on the basis of a limited number of earthquake ground motions and one test structure, especially a structure that was considerably stronger than required by the current seismic regulations. The research of Bertero and Popov [63] and Popov and Pinkney [64] demonstrated that properly designed and fabricated steel members and connections could sustain severe repeated and reversed loading.

Further studies regarding the influence of type and duration of earthquake ground motions on the likelihood of incremental collapse and low cycle fatigue are required. However, it would appear that low cycle fatigue is of minor concern for eccentrically braced frames unless the applied earthquake record is of extremely long duration and the

structure has a very short fundamental period and/or a very low yielding strength ($C_y \leq 0.20$) because the testing program has shown that a properly detailed and fabricated shear link can sustain a very large number of severe yielding reversals.

### 9.7.8 Summary and Conclusions

The shear links, when cycled into the inelastic range, exhibited two of the prerequisites for elements that control the inelastic response of structures under severe earthquake shaking, namely stable hysteretic behavior and large shear strain ductility. As a result of the testing program, a number of observations and recommendations can be made regarding the behavior of composite shear links and eccentrically braced frames.

*Composite Shear Links* : The interaction of the lightweight concrete slab with the bare steel shear link is extremely complex and is highly dependent on the degree of slab degradation (due to the severe inelastic deformation of the link) and the vertical and horizontal separation of the steel decking from the top flange of the shear link. Consequently, the maximum strength demand on a composite shear link should be supplied by the steel shear link alone.

*Link Shear Strains* : Rigid body kinematics can be used to relate the inelastic shear strains in the shear links and the corresponding inelastic inter-story drifts. However, the relationship between the ultimate and elastic inter-story drifts must be known to use the kinematic relationships. A step-by-step static nonlinear procedure such as that available in DRAIN-2DX, provides a simple yet rigorous method for determining the link shear strain corresponding to a particular inter-story frame drift.

*Detailing* : Transverse web stiffening of shear links is necessary to delay the onset of and then to control web buckling. To control web buckling in this instance is to avoid catastrophic failure of the link. Kasai's relationship relating the topography and deformation capacity of a shear link successfully predicted the web buckling deformation angle ($\bar{\gamma}_B$).

*Fabrication* : As the shear links dominate the response of eccentrically braced frames, stringent regulations regarding their fabrication should be implemented in order to minimize the deleterious effects of stress concentrations and residual stresses.

*Eccentric Brace Forces* : For eccentrically braced dual system similar to that tested on the earthquake simulator, the design axial forces in the eccentric braces should be based on at least 170% of the nominal shear yielding of the bare steel shear link ($V_p$) to account for the effects of strain hardening (150%) and composite action (20%+). The brace forces generated by the consistent deformation of the concrete slab spanning perpendicular to the plane of the eccentrically braced frame must be included in the design axial force.

*Eccentric Brace Connections* : The eccentric brace connections must be detailed and constructed to avoid yielding and/or local buckling and to maximize the ductility of the shear links by minimizing residual stresses and stress concentrations. In turn, this will maximize the strength of the eccentrically braced frame through increased internal force redistribution.

*Energy Dissipation Capacity* : The energy dissipation capacity of the model was controlled by the inelastic behavior of its shear links. Although the energy dissipation capacity of the shear links was outstanding, the model's storywise dissipation of the input energy was highly nonuniform and therefore, its potential energy dissipation capacity was not mobilized. An eccentrically braced frame should be designed such that the desirable rigid body displacement fields can be enforced upon either side of the shear links. This would significantly enhance the energy dissipation capacity of an eccentrically braced dual system and also distribute damage more uniformly over its height.

*Displacement Ductility* : Despite the high shear strain ductility measured in Link L2 during the Taft-66 Test ($\approx$ 40), the corresponding maximum inter-story displacement ductility was only 2. In order to achieve higher inter-story displacement ductility in the model, the length of Link L2 would have to be increased as the maximum shear strain in

this link cannot exceed the 0.09 radian achieved during the Taft-66 Test.

*Low Cycle Fatigue and Incremental Collapse* : Low cycle fatigue of eccentrically braced frames possessing reasonable strength ($C_y > 0.3$ for example) and adequately proportioned shear links (SEAOC Section 4H) is improbable, provided that the frames possess a reasonable degree of overstrength. On the basis of this testing program, it is difficult to make firm recommendations regarding the incremental collapse of eccentrically braced frames. For ductile eccentrically braced frames possessing fundamental periods in the middle to long period range (0.75 to 3.00 seconds) and significant overstrength with respect to the current seismic regulations, incremental collapse is improbable unless the structure is subjected to an earthquake of extremely long duration containing a large number of uni-directional acceleration pulses. For eccentrically braced frames possessing fundamental periods in the short period range, incremental collapse should be considered as a site-specific problem and dealt with accordingly. It should be noted however, that the use of short fundamental periods (0.0 to 0.5 second) in eccentrically braced dual systems is undesirable since it precludes the DMRSF from contributing to the primary lateral load resisting system because of its lack of stiffness compatibility with the far stiffer eccentrically braced frames.

# X. MODEL TEST RESULTS : ANALYTICAL CORRELATION AND PROTOTYPE COMPARISON

## 10.1 General

One objective of the U.S.-Japan research program is to determine the reliability of using currently available computer programs to predict the seismic response of structures. The analytical response of the model to the earthquake simulator motion and its correlation with the test results are described in Section 10.2. The computer program DRAIN-2DX was used to conduct these analytical studies.

Another objective of the research program is to evaluate the reliability of using scaled models and various testing techniques to study the seismic response of structures. The earthquake simulator testing of the model and the pseudo-dynamic testing of the prototype are compared and discussed in Section 10.3.

## 10.2 Analytical Correlation of the Seismic Response of the Model

### 10.2.1 Analytical Assumptions and Mathematical Idealizations

The same mathematical idealizations and assumptions as described in Section 4.2 (column, beam, panel zone and brace) for modeling the prototype were used to predict the seismic response of the model. The section properties of the model's elements noted above were based upon the measured geometry of the fabricated W sections [9] and the material characteristics described in Section 5.4. The geometric properties of the shear links were based upon the dimensions of the W sections but their plastic shear yielding strengths and strain hardening ratios were based upon the experimental shear force and shear strain envelopes (Chapter 8).

### 10.2.2 Mathematical Modeling

A number of researchers [9,18,49] have discussed the significance of earthquake simulator and model interaction. The four vertical actuators and the four vertical passive stabilizers were unable to constrain completely the pitching motion of the earthquake simulator table during testing. Accordingly, the earthquake simulator was included in the mathematical model used to predict the seismic response of the model (*Model 2* : see below).

Two analytical models [9,18] that have been used previously to predict the seismic response of structures are described below.

*Model 1* : For this mathematical model, the horizontal and the pitching motions of the earthquake simulator table are included as input in the analysis; the mathematical model is depicted in Figure 10.1a.

*Model 2* : For this mathematical model, the response of the entire earthquake simulator and model system to the measured horizontal acceleration is predicted. The earthquake simulator table is modeled as a rigid beam with a rotational mass of 1245 kip-in-sec$^2$. Two vertical springs are used beneath this rigid beam to simulate the axial flexibility of the vertical actuators; these springs introduce a pitching or rotational degree of freedom to the earthquake simulator and model system (Figure 10.1b). The springs are assumed to be linearly elastic and their stiffnesses are selected using a trial-and-error procedure. The period of the mathematical model is chosen to coincide with the fundamental period of the system measured during the test under consideration. In this study, the latter was calculated through the use of displacement and acceleration transfer functions. The Rayleigh damping constants were evaluated from the equivalent viscous damping ratios measured with the model atop the air-supported earthquake simulator.

### 10.2.3 Earthquake Simulator Response

The influence of the earthquake simulator pitching motion (Figure 10.1b) on the response of the model can be studied by means of a procedure developed by Uang [9].

The equation of motion for the model subjected to horizontal base excitation can be written in matrix form as follows :

$$\underline{m}\ddot{\underline{v}} + \underline{c}\dot{\underline{v}} + \underline{R} = -\underline{m}\underline{r}_x\ddot{v}_{gx} \tag{10.1}$$

where $\underline{R}$ = restoring force vector = $\underline{k}\underline{v}$ for a linear elastic system ;

$\underline{v}$ = relative lateral displacement vector ;

$\underline{r}_x^T = [1\ 1\ 1\ 1\ 1\ 1]$ = pseudo-static displacement vector ;

$v_{gx}$ = base horizontal displacement,

and $\underline{m}$, $\underline{c}$ and $\underline{k}$ are the mass, damping and stiffness matrices, respectively. To consider the pitching motion of the earthquake simulator, the equations of motion must be restructured. In accordance with the positive sign convention shown in Figure 10.1, the total lateral displacement vector can be written as follows :

$$\underline{v}^t = \underline{v} + \underline{r}_x v_{gx} - \underline{r}_\theta v_{g\theta} \tag{10.2}$$

where $\underline{r}_\theta^T = [h_6\ \ h_5\ \ h_4\ \ h_3\ \ h_2\ \ h_1]$ = pseudo-static rotation vector

and $v_{gx}$ and $v_{g\theta}$ are the horizontal and angular or pitching displacements of the base, respectively. For a linear elastic system, Equation 10.1 can be rewritten in the following form :

$$\underline{m}\ddot{\underline{v}} + \underline{c}\dot{\underline{v}} + \underline{k}\underline{v} = -\underline{m}\underline{r}_x\ddot{v}_{gx} + \underline{m}\underline{r}_\theta\ddot{v}_{g\theta} \tag{10.3}$$

where the right hand side of the equation represents the effective forcing function. For a linear elastic system with N lateral dynamic degrees of freedom, Equation 10.3 can be transformed into the modal coordinate system :

$$\underline{v} = \sum_{i=1}^{N} \underline{\phi}_i Y_i \tag{10.4}$$

where $\underline{\phi}_i$ and $Y_i$ are the corresponding mode shapes and generalized coordinates, respectively. Substituting Equation 10.4 into 10.3, premultiplying the resultant equation by

$\underline{\phi_i}^T$, dividing by the modal mass ($M_i$) and assuming an orthogonal damping matrix, Equation 10.3 can be rewritten as follows :

$$\ddot{Y}_i + 2\xi_i\omega_i\dot{Y}_i + \omega_i^2 Y_i = -\frac{\underline{\phi_i}^T \underline{mr_x}}{M_i}\ddot{v}_{gx} + \frac{\underline{\phi_i}^T \underline{mr_\theta}}{M_i}\ddot{v}_{g\theta} \qquad (10.5)$$

where $\dfrac{\underline{\phi_i}^T \underline{mr_x}}{M_i} \equiv L_{xi}$ = base horizontal acceleration participation factor for mode **i**

$\dfrac{\underline{\phi_i}^T \underline{mr_\theta}}{M_i} \equiv L_{\theta i}$ = base angular acceleration participation factor for mode **i** .

The horizontal and angular participation factors for the first three modes, assuming a diagonal mass matrix and using the mass orthonormalized mode shapes evaluated from the free vibration test results, are presented in Table 10.1. The dominance of the first mode pitching response with respect to the higher modes can be attributed to the similarity of the $\underline{r_\theta}$ and the $\underline{\phi_1}$ vectors. For a linear elastic system, Equation 10.3 can therefore be approximated as follows :

$$\underline{m}\ddot{v} + \underline{c}\dot{v} + \underline{k}v \approx -\underline{mr_x}\ddot{v}_{gx} + \underline{mr_x}(\alpha\ddot{v}_{g\theta}) = -\underline{mr_x}(\ddot{v}_{gx} - \alpha\ddot{v}_{g\theta}) \qquad (10.6)$$

$$\equiv -\underline{mr_x}\ddot{v}_{gx(eff)} \ .$$

The constant $\alpha$ is selected to equate the two first mode participation factors noted above ($L_{xi}$ and $L_{\theta i}$) :

$$\frac{\underline{\phi_1}^T \underline{mr_\theta}}{M_1} = \alpha\frac{\underline{\phi_1}^T \underline{mr_x}}{M_1} \qquad (10.7)$$

$$\alpha = \frac{\underline{\phi_1}^T \underline{mr_\theta}}{\underline{\phi_1}^T \underline{mr_x}}$$

and the effective base horizontal acceleration $\ddot{v}_{gx(eff)}$ is given by

$$\ddot{v}_{gx(eff)} = \ddot{v}_{gx} - \alpha\ddot{v}_{g\theta} = \ddot{v}_{gx} - \left(\frac{\underline{\phi_1}^T \underline{mr_\theta}}{\underline{\phi_1}^T \underline{mr_x}}\right)\ddot{v}_{g\theta} \ . \qquad (10.8)$$

The constant $\alpha$ was based upon first mode response only. This is a reasonable

assumption for most buildings subjected to earthquake ground motion. In order to include the contribution of the higher modes, a least-squares or similar technique should be used to determine the value of $\alpha$. The constant $\alpha$ is equal to 190 inches in the elastic range. In order to estimate a lower bound to the effective base horizontal acceleration, a mode shape corresponding to the formation of a soft first story can be assumed to be

$$\tilde{\phi} = [1\ 1\ 1\ 1\ 1\ 1]^T \ .$$

The corresponding value of $\alpha$ is 162 inches. The difference between the two values of $\alpha$ is less than 15%, so for these studies, $\alpha$ was assumed to be equal to 190 inches. The **effective base horizontal acceleration** ($\ddot{v}_{gx(eff)}$) was used by Uang [9] to predict the experimental response of the concentrically K-braced model (Model 1) and is used in Section 10.3 to compare the response of the prototype and the model.

### 10.2.4 Model 1 Analysis

The computer program DRAIN-2DX permits the user to input horizontal and/or vertical ground accelerations in terms of acceleration time histories; out-of-phase multiple support excitation cannot be considered. The use of the effective base horizontal acceleration has been shown to account satisfactorily for the earthquake simulator pitching motion and its effect on the response of the model [9].

### 10.2.5 Model 2 Analysis

The measured table horizontal acceleration time history (Channel 3 : see Appendix A) is used as the input to the DRAIN-2DX model of the earthquake simulator and model system. The use of a trial-and-error procedure to select the spring stiffnesses can only be justified if the mathematical representation of the 0.3 scale model can predict the dynamic characteristics of the fixed base 0.3 scale model accurately. In Chapter 6, the mathematical representation of the 0.3 scale model correlated extremely well with the results of the model's static flexibility and vibration tests. Therefore, the use of *Model 2* to predict the seismic response of the complete earthquake simulator and model system

is justified.

**Analytical Correlation of the Taft-08 Test Results**

A value of 900 kips/in was selected for the pitching spring constant ($k_p$) to reflect the model's fundamental period of 0.340 second during the test. The Rayleigh damping coefficients were based on the measured damping ratios : $\xi_1$=2.1% and $\xi_2$=1.1% (Table 8.1). The measured and analytically predicted lateral displacement and story shear time histories are shown in Figures 10.2 and 10.3, respectively. The correlation coefficients for the roof lateral displacement time history and the base shear time history are 0.93 and 0.92, respectively. DRAIN-2DX predicted the maximum roof lateral displacement to within 4% and overestimated the maximum base shear by approximately 3%.

Parametric studies showed that the displacement response of the model was extremely sensitive to the choice of the Rayleigh damping coefficients and the spring constants. In order to predict the response of the model accurately, it is of paramount importance to evaluate the fundamental period and modal damping ratio during the test since these properties depend heavily on the flexibility of the oil-columns in the vertical actuators and the passive stabilizers.

**Analytical Correlation of the Taft-27 Test Results**

A value of 660 kips/inch was selected for the pitching spring constant ($k_p$) to reflect the model's fundamental period of 0.350 second during the test. The Rayleigh damping coefficients were based on the measured damping ratios : $\xi_1$=2.2% and $\xi_2$=1.3% (Table 8.1). The measured and analytically predicted lateral displacement and story shear time histories are shown in Figures 10.4 and 10.5, respectively. The correlation coefficients for the roof lateral displacement time history and the base shear time history are 0.99 and 0.97, respectively. DRAIN-2DX overestimated the maximum roof lateral displacement by 6% and underestimated the maximum base shear by approximately 12%.

**Analytical Correlation of the Taft-57 Test Results**

A value of 400 kips/inch was selected for the pitching spring constant ($k_p$) to reflect the model's fundamental period of 0.375 second during the test. The Rayleigh damping coefficients were based on the measured damping ratios : $\xi_1$=2.3% and $\xi_2$=1.3% (Table 8.1). The measured and analytically predicted lateral displacement and story shear time histories are shown in Figures 10.6 and 10.7, respectively. The correlation coefficients for the roof lateral displacement time history, the base shear time history, the Link L2 shear force time history and the Link L2 shear strain time history are 0.97, 0.97, 0.96 and 0.90, respectively. DRAIN-2DX overestimated the maximum roof lateral displacement by 13% and the maximum base shear by approximately 5%. The measured and analytically predicted story shear versus inter-story drift relationships for the first, third and fifth stories are presented in Figure 10.8. The analytical model overestimated the elastic and post-elastic first story stiffnesses of the model and underestimated the maximum first inter-story drift. The measured and analytically predicted link shear force versus shear strain relationships for Links L2, L4 and L6 are presented in Figure 10.9; in this figure the link shear force is defined as the vertical component of the eccentric brace force.

### 10.2.6 Summary and Conclusions

Two mathematical models that are suitable for predicting the response of the eccentrically K-braced model have been considered. Only the model that included the earthquake simulator as part of the structural system (Model 2) was used to predict the response of the model.

In Model 2, the earthquake simulator pitching motion is treated as a *response* quantity and not as an *input excitation.* The difficulty with this method lies in the fact that the pitching spring stiffness is indeterminate. The spring stiffness varies from test to test with the fundamental period of the system and a trial-and-error procedure must be used to select it. Excellent correlation can be achieved if the pitching spring stiffness is

selected such that the fundamental period of the complete earthquake simulator and model system coincides with the measured fundamental period of the air-supported system during testing.

A number of conclusions can be drawn from these studies regarding the mathematical modeling of eccentrically K-braced dual steel systems :

*Shear Link Elements* : Shear links can be satisfactorily modeled with beam elements for the symmetric K-braced configuration. For the shear link model (Section 4.2), web shear yielding is replaced by equivalent plastic hinge formation at the link ends.

*Strength and Deformation Characteristics* : The increase in the strength of the shear links due to the composite action and the three dimensional coupling effect (Chapter 9) significantly altered the response of the eccentrically K-braced model. A series of parametric studies (not presented in this report) showed that if the mechanical characteristics of the W sections alone were used to model the bilinear response of the shear links, the displacement and story shear correlation with the Taft-27 and Taft-57 Test results was significantly poorer than when composite link properties were used.

These analytical studies have shown that currently available, inelastic dynamic computer programs, such as DRAIN-2DX, can accurately predict the seismic response of planar braced and unbraced steel frames provided that reasonable estimates are made of the mechanical properties of the structural members.

## 10.3 Correlation of the Model and Prototype Test Results

### 10.3.1 General

In this section the seismic response time histories of the prototype and the model are compared for similar excitations. The PSD-Elastic (65 gals) and PSD-Inelastic Tests (500 gals) were chosen to elicit response from the prototype that would be representative of the serviceability and collapse limit states. Two comparable earthquake simulator

tests, the Taft-08 and the Taft-57 Tests, were used to represent the corresponding limit states in the model. For comparison purposes, all of the model's response quantities have been scaled to the prototype level in accordance with the similitude laws (Table 5.1).

### 10.3.2 Serviceability Limit State: PSD-Elastic Test and Taft-08 Test

The base acceleration time history, its Fourier amplitude spectrum and the corresponding 2% damped linear elastic response spectrum for the PSD-Elastic Test, the Taft-08 Test based upon $\ddot{v}_{gx}$ and the Taft-08 Test based upon $\ddot{v}_{gx(eff)}$ (Equation 10.8) are presented in Figure 10.10. The relative lateral displacement and story shear time histories of the model and prototype are shown in Figures 10.11 and 10.12, respectively; rigid body displacements of the model due to the rotational base motion have been removed from the measured displacement time histories. The prototype PSD-Elastic Test stopped at 17.92 seconds whereas the Taft-08 Test duration exceeded 18 seconds. The PSD-Elastic Test had a peak base excitation level of 65 gals (0.066g) and the Taft-08 Test had a peak base excitation level of 76 gals (0.078g). The major difference between the response of the model and the prototype can be directly attributed to the effect of the rotational base motion (that is, table pitching motion) which is most clearly seen by comparing the three acceleration time histories in Figure 10.10a. The marked difference between the $\ddot{v}_{gx}$ and $\ddot{v}_{gx(eff)}$ acceleration time histories is most evident between the 12 and 18 second marks. The significant contribution of the pitching motion to the effective horizontal acceleration (Section 10.3.4) is also clearly shown in the Fourier amplitude spectrum (Figure 10.10b) and the linear elastic response spectrum (Figure 10.10c). The periods of the prototype ($T_p$) and the model ($T_m$) are based on their dynamic characteristics in their respective as-tested configurations. The distortion of the command signal (that is, between the command signal and $\ddot{v}_{gx(eff)}$) is clearly seen in Figure 10.10c and the elastic response of the model is of the order of twice that of the prototype. The lack of agreement between the story shear time histories of the prototype

and the model, shown in Figure 10.12, is similar to that obtained with the displacement time histories.

### 10.3.3 Collapse Limit State: PSD-Inelastic Test and Taft-57 Test

The acceleration time history, its Fourier amplitude spectrum and the corresponding 2% damped linear elastic response spectrum for the PSD-Inelastic Test, the Taft-57 Test based upon $\ddot{v}_{gx}$ and the Taft-57 Test based upon $\ddot{v}_{gx(eff)}$ are presented in Figure 10.13. The relative lateral displacement and story shear time histories of the model and prototype are shown in Figures 10.14 and 10.15, respectively. The story shear versus inter-story drift relationships in the first, third and fifth stories for the model and prototype are shown in Figure 10.16. The shear force versus shear strain relationships for the Link L2 of the model and the prototype are shown in Figure 10.17 where the link shear force is assumed to be equal to the vertical component of the eccentric brace forces. The prototype PSD-Inelastic Test stopped at 17.10 seconds and the Taft-57 Test was terminated after 16 seconds (= 16×1.811 in real time units). The PSD-Inelastic Test had a peak base excitation level of 500 gals (0.510g) and the Taft-57 Test had a peak base excitation level of 584 gals (0.573g). The major differences between the time history responses of the model and the prototype can be attributed to the effect of the pitching motion of the earthquake simulator (albeit relatively smaller than for the Taft-08 Test) and the greater strength of the model's shear links. The variations in the fundamental periods of the model and the prototype are indicated in Figure 10.13c. In the period ranges under consideration, the maximum elastic response of the model is approximately 25% greater than that of the prototype, and this is reflected in both the displacement and story shear time histories.

The story shear versus inter-story drift time histories for the prototype and the model presented in Figure 10.16 clearly show that the model was more flexible than the prototype in the first story. In addition, Figure 10.16 indicates that significantly more energy was dissipated in the first story of the model during the Taft-57 Test than in the

prototype during the PSD-Final Test. The maximum first inter-story drifts in the prototype (PSD-Inelastic) and the model (Taft-57 Test) are reflected in the maximum shear strains measured in their respective shear links at Level L2 (Figure 10.17). The greater strength of the model's Link L2 (Table 5.4) is also clearly evident in this figure.

### 10.3.4 Summary and Conclusions

*Model and Prototype Dynamic Characteristics* : The dynamic characteristics of both the prototype and the model were discussed in Section 6.6. The prototype was stiffer than the model (Figures 6.4, 9.1 and 9.2) and this was reflected in the model's slightly larger fundamental period. The correlation between the mode shapes of the prototype and the model was extremely good. The damping in the model was of the order of twice that in the prototype and this can be attributed to the repairs undertaken to the prototype's floor slabs. Despite the poor reproduction of the prototype's modal damping ratios, the eccentrically K-braced model can be considered to be an extremely good scale model of the prototype eccentrically K-braced dual system.

*Model and Prototype Strength and Deformation Response* : In Section 9.3.5, it was noted that the model (=0.856 W) was 24% stronger than the prototype (=0.687 W). This was attributed to the strength of the model's six shear links, the fact that the prototype did not attain its potential strength (Section 4.4.2) and the strain-rate effect (Section 9.3.5). The maximum first inter-story and roof drift indices, prior to softening in the case of the prototype, were approximately 1.3% and 0.7%, respectively, for both the prototype and the model. Since the prototype failed prematurely, it was not possible to compare the maximum available displacement ductilities of the prototype and the model. For the same reason, it was not possible to compare their strength and deformation characteristics apart from noting that, as a result of the greater strength of its shear links, the initial yielding strength of the model was approximately 25% greater than that of the prototype.

*Model and Prototype Dynamic Response* : The correlation between the time history responses of the model and the prototype in both the elastic and inelastic ranges was poor. In the elastic range, the effect of the pitching motion of the earthquake simulator (discussed below) and the differences in the modal damping ratios of the prototype and the model resulted in the poor correlation. In the inelastic range, the two principal reasons for the poor correlation were the pitching motion of the earthquake simulator and the greater strength of the model's six shear links.

*Testing of Medium-Scale Models* : This testing program has shown that it is viable to design, construct and test, medium-scale models of full-size buildings. The dynamic characteristics of the prototype and the model were extremely close; better agreement between their respective damping ratios would have been achieved if the model's floor slabs had been repaired upon completion of the testing of the concentrically K-braced model. These tests have also shown the importance of correctly scaling the physical and geometric properties of the critical components if the inelastic response of the model (and thus its full-size counterpart) is being investigated. The fact that the model's shear links were significantly stronger than the prototype's shear links led to the poor time history correlation in the inelastic range. The results of the model's testing program have also shown that for non-critical members such as the beams spanning parallel to Frames 1 to 3 and those parallel to and in between Frames A to C, the scaling requirements can be relaxed and standard member sizes and connections can be adopted.

*Dynamic Testing Techniques* : The testing of both full-scale structures using the pseudo-dynamic method and medium-scale structures using earthquake simulators has an on-going role in earthquake engineering research.

The principle advantages of the pseudo-dynamic method are that full-scale structures and subassemblages can be subjected to intensive testing and investigation and that the problems associated with design, detailing and construction of small or medium-scale models are avoided. Furthermore, the pseudo-dynamic testing method can be

conducted with conventional quasi-static testing facilities and the loading process can be halted to permit investigation of element behavior. The current limitations with the pseudo-dynamic testing method have been elaborated upon by a number of researchers [44,45]; these limitations include the inadequacy of certain step-by-step numerical integration algorithms, the propagation of experimental feedback errors in the integration procedure and the time lag between successive time steps and its consequent shortcomings. These limitations are the subject of investigation by Mahin, Shing and Thewalt [44,45,65].

The testing of medium-scale models on the earthquake simulator has a number of advantages over the pseudo-dynamic testing method; the major advantage is that general structures (either lumped or distributed mass systems) can be subjected to ***realistic***, time-scaled earthquake ground motions. However, this testing program has shown that, for the earthquake simulator testing of tall, heavy models, there is an urgent need to reduce the earthquake simulator pitching motion. The pitching motion of the earthquake simulator was shown to contribute significantly (up to 50% : Figure 10.10c) to the displacement response of the eccentrically K-braced model. This pitching motion must be reduced if either the earthquake simulator is to be used to reproduce the results of full-scale testing or the accurate reproduction of a given command signal is required. Schemes that should be investigated to reduce the pitching motion of the earthquake simulator include the replacement of the passive stabilizers by servo-controlled vertical actuators and the addition of two servo-controlled vertical actuators under the centerline edges of the earthquake simulator table, parallel to the direction of loading. The limitations of the earthquake simulator at the University of California are currently being investigated by Clough, Rinawi, and Blondet [49,66] and Dimsdale [67].

# XI. SUMMARY, CONCLUSIONS AND RECOMMENDATIONS

## 11.1 Summary

### 11.1.1 Pseudo-Dynamic Testing of the Prototype

*Test Structure* : The test structure was chosen to be representative of a medium-rise office building. The plan view of the two bay by two bay, six story building and the frame elevations are shown in Figure 2.1. The structure consisted of three frames parallel to the loading direction; two moment-resisting space frames on Grid Lines A and C and a symmetrically K-braced frame on Grid Line B. Transverse to the loading direction there were three frames; two cross-braced frames on Grid Lines 1 and 3 and an unbraced frame on Grid Line 2. Frames 1 and 3 were cross-braced in both bays at every story; all column to girder connections were bolted, shear type connections. The cross-bracing provided lateral stiffness in the transverse direction as well as enhancing the torsional stiffness of the structure. Frame 2 was unbraced and utilized simple, bolted connections. Upon completion of the testing of the concentrically K-braced prototype, the concentric bracing was removed from the 1-2 bay and the eccentric bracing was installed in the 2-3 bay. Because of the mass and stiffness symmetry of the test structure, it was not possible to study the inelastic torsional response of an eccentrically K-braced dual system.

*Design* : The design of the concentrically K-braced prototype was based upon the 1979 UBC and the 1981 Japanese Aseismic Code. The design gravity loads, listed in Table 2.1, were deemed appropriate for both the U.S.A. and Japan. The sum of the gravity dead loads was 1742 kips. The design earthquake forces were evaluated using the 1981 edition of the Japanese Aseismic Design Code. The base shear coefficient calculated using the Japanese Code was 17% larger than the UBC coefficient (Table 3.8). By making different assumptions regarding site conditions and apportioning twice the UBC

designated level of lateral force to the moment-resisting space frames, a final base shear coefficient of **0.197** was chosen. The design reactive weight of 1400 kips did not include the floor live load or the weight of the perimeter walls. The as-tested reactive weight was 1154 kips, that is, 82% of the design reactive weight and 66% of the design gravity dead load. The design of the eccentric braces and the shear links was based on the research conducted at Berkeley on isolated shear link behavior.

*Design Review* : The design of the eccentrically K-braced prototype, on the basis of the gravity loads and reactive weight (=1356 kips) noted in Section 3.2.2, was reviewed in accordance with the 1985 UBC, the 1984 ATC 3-06 and the 1986 SEAOC. The three dimensional analyses of the prototype were performed using the substructuring option in the SAP-80 computer program. The eccentrically K-braced dual system satisfied the 1985 UBC requirements provided that the beams outside the shear links were considered to be fully restrained over their entire lengths, whereas it satisfied the 1984 ATC 3-06 and the 1986 SEAOC requirements irrespective of the degree of lateral restraint. The specific design requirements for eccentrically braced frames in Section 4H of the 1986 SEAOC were satisfied by the prototype.

*Dynamic Characteristics* : The first two natural periods and modal damping ratios from the forced vibration testing were $T_1 = 0.568$ second, $T_2 = 0.193$ second, $\xi_1 = 0.35\%$ and $\xi_2 = 0.31\%$. The UBC and ATC simplified techniques for calculating $T_1$ underestimated the experimental result by 12%; the SEAOC technique overestimated the experimental result by 28%. Because of the absence of the external wall (22% of the gravity dead load) from the design reactive weight and in the construction of the prototype, these results were not expected to agree with code-based results. The modal damping ratios were significantly smaller than that assumed by the ATC (5%) and SEAOC (5%) for the construction of their respective linear elastic design response spectra. The absence of internal partions and an external facade in the prototype contributed to this significant discrepancy. Furthermore, the use of a constant damping ratio irrespective of

the structural system under consideration is highly questionable and warrants further investigation.

*Experimental Strength* : The nominal yielding strength of the prototype was 0.30W (= $C_y$ : see Section 4.4.4), where W is the as-tested reactive weight of the prototype (=1154 kips). The yielding strength was obtained by factoring the working stress base shear coefficient of 0.197 to yielding levels ($\times C_s/0.8$) and accounting for the difference between the design and as-tested reactive weights ($\times 1400/1154$). The maximum strength of the prototype during the PSD-Sine Test was 0.687 W. The prototype did not attain its potential strength because of the failure of a gusset plate in the eccentric brace connection at Level L2 during the PSD-Sine Test.

A lower bound to the prototype's response modification factor can be estimated from the PSD-Inelastic Test (Taft 500 gals) :

$$R = R_\mu \times R_S = \frac{1.18}{0.597} \times \frac{0.597}{0.30} = 1.97 \times 1.99 = 3.9$$

where 0.30 is the nominal yielding strength ($C_y$ : see Section 4.4); 1.18g is the elastic pseudo-acceleration spectral ordinate for the Taft 500 gals record corresponding to a period of 0.57 second and 2% damping and 0.597W was the peak shear resistance of the prototype during the PSD-Inelastic Test. The measured response modification factor was 65% of that assumed by ATC for dual braced systems (=6) and 40% of that assumed by SEAOC for eccentrically K-braced dual systems (extrapolated to yield $=12 \times 0.8 = 9.6$).

*Experimental Drift* : The maximum inter-story drift index of 2.12% occurred in the first story and resulted from the buckling of a gusset plate in the eccentric brace connection at Level L2. The first inter-story drift index corresponding to the maximum strength of the prototype was approximately 1.2%. The maximum inter-story drift indices were 1.89%, 1.03%, 0.54%, 0.42% and 0.32% in the second to sixth stories, respectively. The maximum inter-story drift indices in the first and second stories exceeded the UBC and

ATC limit of 1.50% for dual systems and the SEAOC limit of 1.12% for eccentrically braced dual steel systems.

*Analytical Correlation* : The computer program DRAIN-2DX was used to predict the natural periods and mode shapes, the static strength and deformation relationship and the seismic response of the prototype. The difference between the analytical and experimental natural periods was less than 5% in the first three modes (Section 4.3). The correlation between the first three analytical and experimental mode shapes was also extremely good (Figure 4.9). The analytical strength and deformation relationship correlated reasonably well with the experimental envelope up to the the maximum strength of the prototype. The uniform load pattern yielded better correlation with the experimental envelope than the triangular load pattern; this observation is consistent with the prototype's deformation pattern at failure. The seismic response of the pseudo-dynamically tested prototype was adequately predicted by DRAIN-2DX for both the elastic and inelastic level tests.

### 11.1.2 Earthquake Simulator Testing of the Model

#### Design, Fabrication and Construction

*W Sections* : The steel sections in the concentrically K-braced model were carefully detailed to satisfy the similitude laws for those parameters controlling its response. Attention was not focused on the precise similitude scaling of the web areas of the beam elements since they do not play a significant role in the response of a concentrically K-braced frame. As a result, the plastic shear capacities of the model's W shear links were between 14% and 23% higher than those of the prototype. This factor was reflected in the limit analyses which indicated that for a triangular load distribution, the model was approximately 12% stronger than the prototype (Sections 4.4.2 and 7.2.2).

*Eccentric Braces* : The cross-sectional area of the model's braces were 22% greater than that of the scaled prototype in the lower four stories because the scaled prototype brace size was unavailable as commercial stock. Since the model's shear links were stronger

than those required to satisfy the similitude laws, the eccentric brace sizes were selected so that they would not buckle at a load level corresponding to the ultimate strength of the links.

*Composite Floor System* : The model's lightweight concrete floor system was a scaled version of the prototype's floor system. At the time of testing the eccentrically K-braced model, the compressive strength and modulus of elasticity of the lightweight concrete were 5.2 ksi and 2,775 ksi, respectively. The model's square wire mesh reinforcement was 0.0625 inch in diameter on a 1 inch pitch. The studs on the model's W girders were designed to develop full composite action.

*Connections* : The proper scaling of connections in a small or medium-scale model, especially those connections that do not develop the strength of the W sections, is of paramount importance. Because of the small size of a number of the similitude scaled connections, it was not possible to construct them with standard welding equipment and techniques. As a result, the model's connections were generally stronger than those of the prototype. A number of the connection details used in the prototype were modified in the construction of the model. The beam copes and the bolted web connections in the prototype were eliminated and the webs of the beams were welded directly to the column cleat plates in the model. The eccentric brace to shear link connection used in the prototype (Figure 3.1) was modified in the model (Figure 5.5) by stiffening the gusset plate in the eccentric brace connection to increase its out-of-plane stiffness. Full depth intermediate transverse stiffeners were used in the model's shear links rather than the partial depth stiffeners used in the prototype's shear links. The objective of these modifications was an improvement in the stability and ductility of the critical connections and therefore, an improvement in the storywise displacement ductility of the model.

**Mechanical Characteristics**

*Concrete* : The 28-day compressive strength ($f_c'$) of the model's lightweight concrete closely matched that of the prototype but its Young's modulus ($E_c$) was approximately 20% higher than that of the prototype.

*Steel* : The stress-strain characteristics of the model's structural steel were similar to those of the prototype (Figure 5.2). The W sections were fabricated from Grade 50 X10 steel for all plate thicknesses except #14 gage; Grade 50 Cor10 was used for all #14 gage steel plate. ASTM A500 Grade B steel was used exclusively for the tubular eccentric braces.

**Earthquake Simulator Performance**

As a result of the interaction between the earthquake simulator and the model, the command acceleration signal was poorly reproduced. The pitching motion of the earthquake simulator was shown to increase the lateral displacement response of the model by up to 100%, depending on the intensity of the input signal.

*Excitation Intensity* : As a result of interaction between the earthquake simulator and the model as well as the inability of the earthquake simulator to reproduce the high frequency content of the command signal accurately, the use of peak horizontal acceleration to quantify the intensity of the earthquake simulator excitation with respect to the target acceleration was unreliable. The procedure used in these studies was to compute the linear elastic response spectrum (LERS) of the measured horizontal acceleration ($\xi = \xi_{1(\text{model})} = 2\%$) and then to compare the measured and target spectral ordinates in a bounded region adjacent the fundamental frequency of the model.

**Instrumentation and Data Acquisition System Performance**

*Instrumentation* : One hundred and seventy-six channels of data were collected for each test to record the global and local response of the model. The instrumentation incorporated accelerometers, linear potentiometers (LPs), direct current linear voltage

displacement transducers (DCDTs), strain gages, strain rosettes and clip gages. The lack of sufficient data acquisition channels made it impossible to monitor the behavior of a number of critical elements such as the concrete slabs in the vicinity of the shear links, the beams outside the links and the beam-to-column panel zones. The instrumentation used for the testing of the eccentrically K-braced model performed reasonably well; however, if the model was to be re-tested, a number of modifications in the emphasis and distribution of the instrumentation would be made.

*Data Acquisition System* : The data acquisition system performed extremely well for the duration of the testing program. The transducer output from the first 128 channels was passed through signal conditioners that removed that component of the output above 100 Hz. For the remaining 48 channels, the output contained a significant amount of high frequency noise that was removed using a numerical lowpass filter (Chapter 7). The rate of 100 samples per second proved adequate for the earthquake records used in the testing program and for the model under investigation.

**Earthquake Simulator Testing - Global Response**

*Dynamic Characteristics* : The model's first two natural periods and modal damping ratios calculated from the free vibration testing were $T_1 = 0.316$ second, $T_2 = 0.105$ second, $\xi_1 = 0.7\%$ and $\xi_2 = 0.5\%$. The model's first two natural periods and modal damping ratios calculated from the forced vibration testing were $T_1 = 0.320$ second, $T_2 = 0.106$ second, $\xi_1 = 0.7\%$ and $\xi_2 = 0.9\%$. The model's first two natural periods calculated from the flexibility tests were $T_1 = 0.322$ second and $T_2 = 0.104$ second. The variations in the natural periods and equivalent viscous damping ratios of the model, over the duration of the testing program, were relatively small (2.2% to 2.3% for $\xi_1$). As a result of the low excitation levels used in the vibration testing, the effective natural periods and modal damping ratios of the model during testing were greater than those values suggested by the free and forced vibration tests. The damping in the complete air-supported system was appreciably higher than that of the fixed base model (2.2%

versus 0.7%) because of the damping in the earthquake simulator's vertical and horizontal actuators and the passive stabilizers. The increase in the fundamental period of the complete air-supported system with respect to the fixed base model (0.316 second to 0.326 second) was due to the axial flexibility of the earthquake simulator's vertical actuators.

*Experimental Strength* : The maximum strength of the model of 0.856W (W = as-tested reactive weight of 107.1 kips) was reached during the Taft-66 Test. The response modification factor for the model (Section 9.3) was

$$R = R_{\mu} \times R_S = 1.85 \times 2.85 = 5.2 \ .$$

The measured response modification factor was 86% of that assumed by ATC for dual braced systems and 54% of that assumed by SEAOC (extrapolated to yield) for eccentrically K-braced dual systems.

*Experimental Drift* : The inter-story drift indices for the elastic level test (Taft-08) were 0.13%, 0.11%, 0.13%, 0.11%, 0.08% and 0.11% in the first to sixth stories, respectively. These inter-story drift indices were significantly less than that permitted by the UBC (0.50%), ATC (0.30%) and SEAOC (0.31%) although the corresponding maximum base shear force exceeded the design base shear force for all three seismic regulations. The maximum inter-story drift index of 1.28% occurred in the first story during the Taft-66 Test and was accompanied by severe shear yielding in Link L2. The maximum inter-story drift indices in the upper five stories, measured during the Taft-57 and Taft-66 Tests, were 0.84%, 0.66%, 0.54%, 0.61% and 0.50% in the second to sixth stories, respectively. The maximum inter-story drift index in the first story did not exceed the UBC and ATC limit of 1.50% for dual systems but did exceed the SEAOC limit of 1.12% for dual eccentrically braced systems.

*Lateral Force Distribution* : The inertia force profiles were approximately triangular for the elastic level tests and approximately uniform for the collapse level tests. The load distributions for the Taft-08 and Taft-27 Tests were similar to both those suggested by

the UBC, ATC and SEAOC as design lateral force distributions and the fundamental mode shape of the model. The contribution of the second mode to the inertia force profiles was evident at the roof level for both the Taft-08 and Taft-27 Tests. The distribution of the inertia forces between the braced bay and the DMRSF corresponded to their relative elastic stiffnesses for the Taft-08 and Taft-27 Tests; that is, the braced bay resisted approximately 80% of the inertia forces in the lower five stories and 70% of the inertia forces in the sixth story. The uniform load distribution was consistent with the formation of a soft first story during the Taft-57, Taft-66 and Sine-70 Tests and was significantly different from those assumed by the UBC, ATC and SEAOC as design lateral force distributions. For the Taft-57, Taft-66 and Sine-70 Tests, the distribution of the inertia forces between the braced bay and the DMRSF did not correspond to their relative elastic stiffnesses.

*Energy Input and Dissipation* : The total input energy ($E_I$) was dissipated as viscous damped energy and inelastic hysteretic energy or stored as kinetic energy and elastic strain energy. The proportion of the total input energy that contributed to the damage of the model was equal to the sum of the inelastic hysteretic energy and the elastic strain energy. For the elastic level test (Taft-08 Test), the inelastic hysteretic energy dissipation was negligible and the input energy was dissipated almost entirely by the viscous damping. For the damageability level test (Taft-27 Test), the input energy was dissipated by both the inelastic hysteretic and viscous damping mechanisms; the inelastic hysteretic energy dissipation was concentrated in the lower two shear links (L2 and L3). For the collapse level tests (Taft-57, Taft-66 and Sine-70 Tests), the input energy was dissipated principally by inelastic behavior and the contribution of the viscous damping was minor. The inelastic hysteretic energy dissipation capacity of the model was dominated by the energy dissipation capacity of its shear links. In the Taft-57 Test, the shear links dissipated in excess of 90% of the input energy; of the energy dissipated in the shear links, 79% was dissipated in Link L2.

Because the energy dissipation demand on a structure may determine whether it fails during severe earthquake shaking, the method suggested by Housner for estimating the energy that contributes to the damage of a structure ($E_D$) was reviewed (Section 9.5.1). Housner's use of the pseudo-velocity response spectrum to estimate an upper bound to the input energy, significantly underestimated the earthquake simulator test results for the Taft-57, Taft-66 and Sine-70 Tests. For the 1952 Taft N21E earthquake ground motion, the input energy was generally maximized by linear elastic response in the period range above 0.5 second. In the period range between 0.05 and 0.5 second, the assumption that the input energy is maximized by linear elastic response was significantly nonconservative; for the range of values of $C_y$ considered in Section 9.5.1, the input energy was maximized by a SDOFS with a yielding coefficient equal to 0.2. However, the relationship between $E_I$, $C_y$ and T depends entirely on the earthquake ground motion under consideration and the results presented in Section 9.5 for the Taft ground motion should not be construed as being applicable for any other acceleration time history.

*Ductile Moment-Resisting Space Frame* : The UBC, ATC and SEAOC currently require that the DMRSF be designed to resist at least 25% of the minimum design base shear. The high strength demand on the model's DMRSF is clearly shown in Figure 8.60 and it resulted from the formation of a soft first story during the Taft-57 and Taft-66 Tests and followed shear yielding and web buckling in Link L2. Although the UBC requirements were drastically exceeded in the first story where the story shear force resisted by the DMRSF was 38.2 kips (119% of the nominal yielding strength of the model), it did not yield and therefore did not contribute significantly to the hysteretic energy dissipation capacity of the model. The high strength of the DMRSF can be attributed in part to the fact that it was designed for 34% of the design base shear (1981 Japanese Aseismic Code) in lieu of 25% of the UBC design base shear [14,15]. The DMRSF was far more flexible than the braced frame; even at the maximum inter-story drift index of

1.28% (corresponding to $V_{DMRSF}$ = 38.2 kips in the first story), the DMRSF did not yield.

*Column Axial Forces* : The columns in the eccentrically K-braced bay were subjected to large axial force variations and relatively small bending moment variations. In the Taft-57 and Taft-66 Tests, the columns in the braced bay ($1C_{B2}$ and $1C_{B3}$) exceeded their nominal yielding strength (Figures 8.44 and 8.64) for a significant number of cycles.

*Frame Interaction* : In dual systems, interaction between braced frames and DMRSFs can result in an elastic force distribution that is not in proportion to their individual stiffnesses. This interaction can give rise to a situation whereby in the upper levels of a structure, the story shear force carried by the DMRSF exceeds the total applied story shear. However, no evidence of this form of interaction was noted during the elastic level test (Figure 8.12a). This can be attributed to the moderate height of the model, the negligible axial deformations in the braced bay columns and the relative stiffnesses of the braced frame and the DMRSF.

*Displacement Ductility* : Despite the high shear strain ductility measured in Link L2 during the Taft-66 Test ($\approx$ 40), the maximum inter-story displacement ductility was only 2. In order to achieve higher inter-story displacement ductility in the model, the length of Link L2 would have to be increased as the maximum shear strain in this link cannot exceed the 0.09 radian achieved during the Taft-66 Test.

*Low Cycle Fatigue and Incremental Collapse* : On the basis of the earthquake simulator tests described in this report, it appears that low cycle fatigue and incremental collapse will not control the earthquake resistant design of eccentrically braced structures. The eccentrically K-braced model was subjected to a total of eleven damageability and collapse limit state earthquakes; even in regions of high seismic risk, a building would be unlikely to be subjected to an earthquake ground motion that would produce more damage than one or two earthquake ground motions of these intensities. The ability of an eccentrically K-braced frame to avoid low-cycle fatigue depends on its shear links being

able to resist a large number of alternate yielding cycles of high shear strain ductility; the model's Link L2 demonstrated stable, well-rounded hysteretic behavior and resisted a large number of cycles of shear strain ductility in excess of 20.

**Earthquake Simulator Testing - Shear Link Response**

*Link Shear Force* : The link shear force ($V_L$) as defined in Section 7.5 is an upper bound on the true shear force ($V_L^*$) in the composite shear link. The latter is the link shear force minus that shear force resisted by flexural action in the composite slab ($V_L^{SLAB}$) spanning perpendicular to Frame B. The peak link shear force was 33.6 kips, that is, 213% of the nominal shear yielding strength ($V_p$) of the W steel link. An estimate of the strength of the concrete slab spanning perpendicular to Frame B at Level L2 indicated that the maximum vertical force that could be attributed to the coupling effect was between 5 and 6 kips, or approximately 20% of the link shear force. The maximum shear force in Link L2 was therefore equal to 27 to 28 kips, or, 170% to 180% of the nominal shear yielding strength of Link L2 (=15.77 kips : Table 5.4).

*Link Shear Strain* : The shear strains in all six shear links (L2 to LR) were maximized during the Taft-66 Test. Permanent shearing deformations developed in Links L2, L3 and L4 following the large burst of input energy around the 9 second mark in the Taft-66 Test. These deformations were accompanied by severe web buckling in the right-hand panel of Link L2 (adjacent to Grid Line 3). The maximum shear strains ranged from 0.092 radian in Link L2 to 0.0045 radian in Link L6. The distribution of the shear strains was highly nonuniform and the peak shear strains in the links varied by a factor of twenty.

*Link Strength and Stiffness* : Upon repeated web buckling in Link L2, the strength and stiffness of the eccentrically K-braced bay decreased. This was evident in Figures 8.77 and 8.82 where the maximum base shear and the percentage of the total base shear resisted by the braced bay in the Sine-70 Test dropped significantly with respect to the Taft-57 and Taft-66 Tests. The point at which Link L2 fractured was considered to

constitute failure for the model.

*Energy Dissipation Capacity* : The inelastic behavior of a shear link can be categorized into either its pre-web buckling state or its post-web buckling state; a discussion of the link behavior in these two states is presented in Section 9.7.6. The differences between the pre-web buckling and post-web buckling behavior of a shear link are clearly shown in Figure 9.17 and Table 9.1. The energy dissipated by Link L2 was maximized in its pre-web buckling state (74% of $E_I$). The decrease in the energy dissipated by Link L2 because of web buckling and composite slab degradation as a percentage of the energy dissipated by the links ($E_L$) was 7% for the Taft-66 Test and 17% for the Sine-70 Test. After web buckling of Link L2 (Taft-57 Test), the energy dissipated by Link L3 as a percentage of $E_L$ increased by 5% for the Taft-66 Test and 16% for the Sine-70 Test. The decrease in the energy dissipated by Link L2 was recovered in the remaining five shear links and in other yielding regions in the dual system such as the beam-column panel zones. This qualitative relationship between the energy dissipation capacity of pre-web buckled and post-web buckled shear links is in total agreement with results obtained from tests on isolated, bare steel shear links.

*Kinematics of the Eccentrically Braced Frame* : The relationship between the first inter-story drift ($\Delta$) and the shear strain ($\gamma$) in Link L2 for the Taft-66 Test is shown in Figure 9.15a; the envelope of the first inter-story drift and the shear strain in Link L2 and the initial yielding cycle is shown in Figure 9.15b. It was shown in Section 9.7.4 that the link shear strains are kinematically related to the plastic inter-story drift ($\Delta_p$) by the displacement field shown in Figure 3.2b. As discussed in that section, the experimental elastic story drift (0.5% or 0.65% depending upon the method used to calculate $\Delta_e$) and the experimental inelastic deformation factor ($=\mu_{CRIT} \approx 2$) do not agree with the values suggested by either the UBC, ATC or SEAOC.

*SEAOC Design Shear Strains* : To calculate the design shear strains in shear links, SEAOC uses an inelastic displacement field similar to that shown in Figure 3.2b, the

elastic level inter-story drift index and an amplification factor equal to $3R_w/8$ (Equation 3.12). The $3R_w/8$ factor, which is a direct carryover of the 3/K factor used in the UBC, is the assumed SEAOC relationship between the strength of the structure and the specified design force level. SEAOC assumes that the maximum structural deformations are also equal to $3R_w/8$ times the design level deformations although this incorrectly assumes that there will be no loss of stiffness in the inelastic range. The model achieved a strength of 0.856W, or 3.58 ($=2.4R_w/8$) times the working stress base shear coefficient of 0.238 ($=0.197\times1400/1154$). Corresponding to the maximum strength of 0.856W, the maximum inter-story drift index was 1.28% or 6.33 ($=4.2R_w/8$) times the first inter-story drift index corresponding to the working stress base shear coefficient of 0.238. The SEAOC Commentary [69] states that the maximum deformations could approach $R_w$ times the design deformations and that critical elements should have sufficient ductility to control these deformations. In order to develop a first inter-story drift equal to $3R_w/8$ times the design first inter-story drift, the ductility demand on Link L2 was extremely high. Link L2 would have been unable to develop the shear strains associated with a first inter-story drift equal to $R_w$ times the design first inter-story drift, irrespective of its transverse stiffening.

*Shear Link Length* : The strength, deformability, ductility and energy dissipation capacity of a dual eccentrically braced frame depends on the ability of its shear links to undergo significant, yet stable, inelastic deformation. To facilitate the involvement of the DMRSF in the lateral load resisting system, the eccentrically braced frame must be sufficiently ductile to develop inter-story drift indices of between 1.5% and 2.0%, which in turn places an extremely high shear strain ductility demand on the shear links. An indication of the shear link ductility demand can be obtained from Equation 3.12 where if it is assumed that the shear link and the braced bay yield simultaneously, the shear strain ductility demand on the link is approximately 30 for a inter-story displacement ductility demand of 2 and link length of one-fifteenth of the length of the braced bay.

The ductility demand on a shear link can be minimized through manipulation of the geometry of the eccentrically braced bay.

*Cyclic Web Buckling* : Since the lateral strength of an eccentrically braced bay is governed by the shear strength of its links, the links and their connections to the eccentric braces must be detailed so as to preclude their premature failure. Cyclic loading of isolated shear links by Kasai et al. [2,21] has shown that the post-web buckling behavior and the failure mode of a shear link are difficult to predict and that web buckling leads to the degradation of the link's stable hysteretic behavior. Accordingly, a realistic level of deformation in a shear link for the collapse limit state is that deformation which is associated with the onset of web buckling. Kasai defined the web buckling deformation angle ($\bar{\gamma}_B$) as the maximum deformation angle measured from the most distant point of zero shear for the entire preceding history to the point of failure (Figure 9.15). In the Taft-57 and Taft-66 Tests, the cycles of maximum deformation yielded values of $\bar{\gamma}_{max}$ equal to 0.153 and 0.160 radian, respectively. Assuming that the ultimate shear strain ($\gamma_u$) was approximately 50% of $\bar{\gamma}_B$, Kasai developed an equation (Equation 9.16) relating the topography of a shear link to a series of calibrated constants that included the distance between the transverse stiffeners, the section depth and the web thickness. The theoretical ultimate deformation angle in Link L2 equaled 0.09 radian and was extremely close to the maximum experimentally measured value of 0.092 radian. The results of this testing program confirmed Kasai's expression for transverse stiffener spacing in shear links.

**Analytical Prediction of Dynamic Characteristics and Seismic Response**

*Dynamic Characteristics* : The correlation of the analytically predicted flexibility matrices, natural periods and mode shapes of the model with the experimental results was extremely good. The difference between the predicted and the measured fundamental periods was approximately 4%. The analytical mode shapes were in complete agreement with the mode shapes measured experimentally using static flexibility and free

vibration test methods.

*Static Strength Analysis* : Limit analyses using triangular and uniform lateral load patterns successfully predicted the strength of the eccentrically K-braced model. For these analyses, the strengths of the shear links were based upon the ultimate yielding strength of the W sections. Step-by-step static nonlinear analyses were performed using the DRAIN-2DX; the triangular and uniform lateral load patterns provided an upper bound to the strength and deformation response of this model. In the elastic range, the model strength and deformation envelope was most closely predicted by the analysis that assumed a triangular lateral load pattern. In the inelastic range, the experimental envelope was most closely predicted by the analysis that assumed a uniform load pattern.

*Seismic Response* : The dynamic analyses that were performed using the DRAIN-2DX, predicted the seismic response of the complete earthquake simulator and model system in all limit states with an excellent degree of accuracy. The use of beam elements to model the shear links proved successful for this symmetric, eccentrically K-braced dual system.

### 11.1.3 Comparison of the Model and Prototype Responses

In the following discussion, the model's dynamic characteristics and responses have been scaled to the prototype units in accordance with the similitude laws (Table 5.1).

*Dynamic Characteristics* : The correlation of the prototype and model flexibility profiles was reasonable with the largest discrepancies occurring in the lower two stories. The measured fundamental periods (Table 6.5) and mode shapes (Figure 6.5) of the model and the prototype correlated extremely well : $T_{model} = 0.572$ second, $T_{prototype} = 0.565$ second, but the first modal damping ratios varied significantly : $\xi_{model} = 0.70\%$, $\xi_{prototype} = 0.35\%$. The discrepancy in these damping ratios can be attributed to the lack of repair to the model's floor slabs prior to the testing of the eccentrically K-braced model.

*Experimental Strength* : The correlation of the global displacement and story shear responses of the prototype and the model, up to the maximum strength of the prototype, was reasonable. The model was 24% stronger than the prototype (Section 9.3.5) and this was attributed to the greater shear strength of the model's shear links and the fact that the prototype did not develop its potential strength because of the failure of a gusset plate at Level L2.

*Experimental Drift* : The maximum inter-story drift in the first story of the prototype (2.12%) was significantly greater than that measured in the model (1.28%). The inter-story drift corresponding to the maximum strength of the prototype was approximately 1.2% and similar to the model's maximum inter-story drift index of 1.28%.

*Time History Response Correlation* : The time history correlation between the model and the prototype was poor for both the elastic and inelastic tests. In the elastic range, the poor correlation was attributed to the pitching motion of the earthquake simulator and the differences between their modal damping ratios. In the inelastic range, the poor correlation was attributed to the pitching of the earthquake simulator and the differences between their strengths.

## 11.2 Conclusions

### 11.2.1 General

Conclusions have been drawn and presented in the previous chapters on the results of the research conducted at Berkeley. A summary of the main conclusions in relation to the original objectives of the U.S.-Japan Cooperative Research Program are presented in this section. These conclusions are strictly speaking, only valid for the test structure (model or prototype) and for the type of excitation to which it was subjected.

The eccentrically K-braced dual system appears to have all the necessary characteristics for a building to survive severe earthquake shaking. These characteristics, namely sufficient elastic strength and stiffness to avoid structural and non-structural

damage during minor earthquake shaking and ductile, stable hysteretic behavior during severe earthquake shaking, satisfy the limit state requirements noted in Section 1.1. The results of this testing program have clearly shown that by using an appropriate level of design base shear (in excess of that specified by the U.S. seismic regulations) and careful design, detailing (SEAOC Section 4H) and fabrication, eccentrically braced dual systems can withstand the most severe earthquake ground motions that can be expected in the U.S.A..

The six major limitations noted below must be carefully considered prior to extrapolating these conclusions to other eccentrically braced steel structures :

*(1) Test Structure* : The model was a bare steel structure and the interacting effects of non-structural components were not considered. Non-structural components such as internal masonry partitions and external cladding play an important role in the response of buildings to earthquake shaking. The partitions can have a profound effect on the stiffness and strength of a building. The influence of the partitions on the strength and deformation characteristics of a building depends on the degree to which they are isolated from the structural frame. A detailed discussion of the effects of partitions on seismic response of structures is given by Brokken and Bertero [69].

*(2) Reactive Weight* : The prototype's as-tested weight of 1154 kips was significantly less than the design gravity dead weight of 1742 kips and the design reactive weight of 1400 kips. For the design of the prototype, the critical load cases involved dead loads (1742 kips), live loads and earthquake loads (based upon a reactive weight of 1400 kips) in combination. The earthquake loads dominated the design forces in the prototype. As all of the conclusions presented below are generally related to the nominal yielding strength of the structure (=0.3W : see Section 4.4.4), the lack of consistency between the gravity dead loads (=1742 kips) and the the reactive weight (=1400 kips) should not be construed as a major drawback to the testing program.

*(3) Seismic Regulations* : Since the test structure was designed for a working stress base shear coefficient of 0.197 that was significantly higher than that required by current U.S. seismic regulations (UBC, ATC, and SEAOC), the elastic stiffness, elastic strength and maximum strength of the test structure cannot be considered as representative of structures designed in accordance with these regulations. The distribution of the columns and beams over the height of the prototype (Figure 2.1 and Table 2.2) should also be considered prior to any evaluation of the response modification factors presented below.

*(4) Torsional Excitation and Stiffness* : The model (prototype) was symmetrically located with respect to the earthquake simulator (pseudo-dynamic) excitation for all of the tests. Their respective centers of mass coincided with their respective centers of stiffness in the loading direction (parallel to Frame B) in each story; therefore, storywise torsional loading was not introduced during testing. In addition, X-bracing was installed in Frames 1 and 3 to increase the torsional stiffness of the model (prototype) and to reduce the torsional response.

*(5) Foundation* : The foundations for both the model and the prototype were restrained against sliding, rocking and uplift; this foundation condition is rarely achieved in real buildings.

*(6) Earthquake Ground Motions* : Although the acceleration-scaled (peak acceleration>0.5g) 1952 Kern County Taft N21E earthquake record (time-scaled for the model) was a severe ground motion for the test structure, it cannot be considered as the maximum credible earthquake for either the test structure or eccentrically braced structures in general.

The profound influence of the first and fourth limitations on the inelastic response of structures has recently been acknowledged by the engineering profession. The eccentricity of the center of mass and stiffness contributed to the failure of a large number of buildings during the 1985 Mexico City earthquake. However, since the objective of this research program was to study the behavior of symmetrically braced steel structures, it

was not possible to study the torsional response of these systems at the same time.

### 11.2.2 Earthquake Simulator Testing of Reduced-Scale Models

One of the principal objectives of this research program was to verify the reliability of testing reduced-scale models as a means by which to predict the seismic behavior of full-scale buildings. The reliability of this procedure is a function of the accuracy to which the model can be constructed and the ability of the earthquake simulator to subject this model to realistic earthquake ground motions.

*Reduced-Scale Models* : A number of researchers have shown that the dynamic response of structural systems can be accurately simulated with reduced-scale models provided that : (i) the material characteristics can be successfully reproduced at the reduced-scale level; (ii) the fabrication techniques are appropriate to the scale of the model; (iii) the critical elements are accurately scaled in accordance with the laws of geometric similitude; (iv) the structural details at the critical regions and connections are correctly reproduced and (v) the failure of the reduced scale model is not initiated by unexpected localized phenomena such as weld fracture or local buckling.

These criteria were carefully considered prior to the construction of the concentrically K-braced model. A comparison of the dynamic characteristics of the prototype and the model showed that reduced-scale models can be used to predict the dynamic characteristics of full-size buildings.

*Earthquake Simulator Testing* : The earthquake simulator at the University of California, Berkeley, can subject reduced scale models to realistic earthquake ground motions although it is currently unable to reproduce high frequency input reliably [49] nor is it able to constrain the pitching motion of the earthquake simulator completely. However, unless accurate reproduction of the command signal is required, the earthquake simulator output motion is just as reasonable a ground motion as that given by the input signal. Therefore, these two shortcomings should not be considered as major drawbacks of earthquake simulator testing.

The results presented earlier in this report confirm that both the dynamic characteristics and the response of full-size buildings can be reliably predicted by earthquake simulator testing of medium-scale models.

### 11.2.3 Reliability of Current Analytical Techniques

On the basis of the analytical studies discussed in this report and the studies performed by Uang and Bertero [9] on a concentrically K-braced dual system, a number of conclusions can be drawn :

*Limit Analysis* : Limit analysis provides a simple means by which to calculate the strength of unbraced, braced and dual steel structures provided that reasonable estimates are made of the strength of the critical or controlling elements at the expected ultimate deformation levels. In order to apply limit analysis to dual steel structures the stiffer braced frames must possess sufficient ductility to permit the collapse mechanism of the entire structure to form.

*Static Strength Analysis* : Step-by-step static nonlinear analysis [33] can estimate the strength of planar, unbraced, braced and dual steel structures; this strength can be bounded through the use of triangular and uniform lateral loading patterns. Mathematical models currently available in computer programs such as DRAIN-2DX [33] can describe the experimental behavior of steel elements with a high degree of accuracy.

*Time History Analysis* : Computer programs, such as DRAIN-2DX, are capable of predicting the elastic and inelastic, two-dimensional response of braced steel structures.

### 11.2.4 Eccentrically Braced Dual Systems

A number of conclusions have been made in the preceding chapters regarding the analysis and design of eccentrically braced dual systems. The principal conclusions presented below are grouped under the headings of *General* and *Eccentrically Braced Frames.* In the general group, issues relating to the design and performance of the dual system, the code-based design lateral forces, the code-based linear elastic design response

spectrum, the response modification factors and dual system compatibility are discussed. The implications of the results of this testing program on design, detailing, fabrication and construction of eccentrically braced frames are discussed in the latter group.

**General :**

*Design and Construction* : Although the design base shear coefficient of 0.197 was significantly higher than that required by current seismic regulations in the U.S.A., the distribution of the W member sizes over the height of the prototype, that is, the degree of optimization of the W sections, can be considered to be representative of current design practice in the U.S.A..

*Overall Performance* : The performance of the model at both the global and local levels was extremely good from the standpoint of elastic stiffness, maximum strength and energy absorption and dissipation capacities. The drift levels at which the maximum strengths of both the prototype and the model were reached was between 1.2% and 1.3% and therefore larger than that permitted by the 1986 SEAOC but smaller than that permitted by the 1985 UBC and the 1984 ATC.

*Linear Elastic Design Response Spectra* : The ATC and SEAOC LEDRS are significantly nonconservative with respect to the LERS of the 1985 Chile (N10E - Llolleo), 1985 Mexico City (EW - SCT) and the 1986 San Salvador (EW - CIG) earthquake records (Figure 9.5). If earthquake ground motions such as these can occur in the United States, the ATC and SEAOC LEDRS for regions of high seismic risk should be amended to reflect the resultant spectral accelerations. If the ground motion amplification factor of 2.5 is to be retained in future editions of the ATC and SEAOC, the LEDRS should be anchored to a significantly higher effective peak acceleration (in the range between 0.6g and 0.8g, for example) to reflect spectral accelerations between 1.5g and 2.0g (Section 9.3). Furthermore, a family of linear elastic design response spectra should be specified instead of a single spectrum in order to reflect the variation in the equivalent viscous damping of the different structural systems (for example, 2% for an steel frame with a properly isolated

facade to 10% for a structure isolated on natural rubber bearings).

*Response Modification Factor* : The ATC and SEAOC Response Modification Factors (R and $R_w$, respectively) overestimated the measured reductions in the required elastic strengths of the eccentrically K-braced model and prototype. For both the prototype and the model, the maximum reduction due to ductility ($R_\mu$) was of the order of 1.90 (1.97 for the prototype and 1.85 for the model). It would appear that a ductility factor of between 1.5 and 2.0 is appropriate for eccentrically braced dual systems with fundamental periods of up to 0.75 to 1.00 second. The strength factors ($R_s$) for the model and the prototype were equal to 2.85 and 2.29 (=0.687/0.30 for the PSD-Sine Test), respectively. For properly designed and detailed eccentrically K-braced dual steel structures, a strength factor of between 2 and 3 would appear to be consistent with current design practices in the U.S.A.. The use of optimization procedures [56] will drastically reduce the strength factor. Response modification factors of the order of 2.0 to 2.5 would appear to be appropriate if optimization procedures are incorporated into the design process.

Since the model was constructed under more stringent conditions and supervision than those practiced in the construction industry, the model's response modification factor of 5.2 must be seen as an upper bound to that which could be achieved in full-scale buildings.

There is an urgent need to study response modification factors further, both experimentally and analytically. For each type of framing system, the response modification factor should reflect a number of parameters, such as natural period, the redundancy in the primary lateral load resisting system, the torsional redundancy of the entire system and the increase (if any) in the equivalent viscous damping due to inelastic behavior.

*Inelastic Derived Response Spectra* : If the SEAOC inelastic spectral ordinate for the eccentrically braced structure ($C_y = 0.109$ : see Section 3.5) is used in conjunction with the model's measured response modification factor of 5.2 and a ground motion amplification factor of 2.5, the maximum effective peak acceleration is 0.23g. This is

57% of that assumed by SEAOC (=0.40g) as appropriate for a region of high seismic risk. Therefore, the use of $C_y$ equal to 0.109 for an eccentrically braced dual system would appear to be appropriate only for regions of low to moderate seismic risk. For regions of high seismic risk, where effective peak accelerations of 0.6g to 0.8g might be expected (see above), the SEAOC base shear coefficients are nonconservative by a factor of approximately 3 to 4. Therefore, if an eccentrically K-braced dual system is designed using current methods for the base shear coefficients suggested by SEAOC (and to a lesser extent by ATC 3-06 and the UBC), there is a significant possibility of its failure during severe earthquake shaking.

*Code Lateral Forces* : The 1984 ATC and 1986 SEAOC seismic regulations are based on lateral seismic forces that are derived by reducing the linear elastic response spectrum by a response modification factor. These lateral seismic forces cannot be justified in terms of either the linear elastic response spectra or the response modification factors, for the reasons cited above. The 1985 UBC does not use a LERS or response modification factors but its choice of inelastic design response spectra are also inappropriate for regions of high seismic risk.

*Dual System Compatibility* : The strength and deformation compatibility of the braced frame and the DMRSF has received insufficient attention in the past despite the important contribution that the DMRSF makes to the inelastic response of the dual system. To take full advantage of the individual structural systems, their strength and deformation characteristics must be compatible. The initial stiffness of the DMRSF should be sufficiently large and the braced frame should possess sufficient ductility without strength deterioration, so as to allow the yielding strength of the DMRSF to be mobilized at acceptable levels of inter-story drift. Current seismic regulations do not address this important issue.

The design strength of the model's DMRSF was significantly higher than that required by any of the U.S. seismic regulations. The lack of stiffness and strength

compatibility between the braced frames and the DMRSF in a dual system will be significantly worse if these systems are designed strictly in accordance with the minimum requirements of the U.S. seismic regulations.

*Energy Absorption and Dissipation* : The energy absorption and dissipation capacity of the eccentrically K-braced model was excellent; this result suggests that properly designed, detailed and fabricated eccentrically braced dual steel systems can survive severe earthquake shaking.

*Low Cycle Fatigue and Incremental Collapse* : Categorical conclusions regarding the importance of incremental collapse and low cycle fatigue cannot be drawn on the basis of these studies of a limited number of earthquake ground motions and one test structure, especially a structure that was considerably stronger than that required by the current seismic regulations. It would appear, however, that low cycle fatigue or alternating plasticity will not control the design of eccentrically braced dual systems unless the applied earthquake record is of extremely long duration and the structure has a very short fundamental period and/or a very low yielding strength ($C_y \leq 0.15W$). Further studies regarding the influence of : (i) the type and duration of earthquake ground motion and (ii) the type of structural system and its dynamic and strength characteristics, on the likelihood of incremental collapse and low cycle fatigue are needed.

**Eccentrically Braced Frames**

*Composite Shear Links* : The interaction of the lightweight concrete slab and the W shear links is extremely complex and is highly dependent on the degree of slab damage. Therefore, the maximum strength demand on the composite shear link should be supplied by the steel W section alone.

*SEAOC Link Design Shear Strains* : The SEAOC inelastic deformation factor of $3R_w/8$ underestimated the relationship between the design inter-story drifts and the maximum inter-story drifts in Level 2 of the model and therefore, was unable to predict the maximum shear strain in Link L2. A rigorous yet simple method for estimating the link

shear strain for a particular inter-story drift index is through the use of step-by-step static nonlinear analyses [33].

*Shear Link Length* : It is of paramount importance to minimize the shear strain demand on a link for a given inter-story drift index. This is especially important in dual systems where the strength of the DMRSF may be developed only at drift levels of the order of 1% to 1.5%. To reduce the ductility demand on the shear link for a required displacement ductility and link shear strength ($V_p$), the W section with the largest $M_p$ should be chosen; this will maximize the link length (Equation 2.1) and minimize the shear strain ductility demand.

*Shear Link Transverse Web Stiffening* : Kasai's expression (Equation 9.16) relating transverse stiffener spacing, the section depth and the web thickness in a shear link accurately predicted the web buckling deformation angle ($\bar{\gamma}_B$). This result suggests that Kasai's expression can be used with confidence to select the transverse stiffener spacing in shear links.

*Shear Link Detailing and Fabrication* : Shear links must be detailed to maximize their ductility and thus to both maximize the strength of the dual system through internal force redistribution and to maximize the displacement ductility of the eccentrically braced frame. Stringent regulations regarding the fabrication of shear links are needed to minimize the deleterious effects of stress concentrations and residual stresses and to permit the shear links to develop shear strains of up to 0.1 radian.

*Eccentric Brace Axial Forces* : For shear links constructed as part of a composite floor system and of similar configuration to those of the test structure, the design axial forces in the eccentric braces should be based upon at least 170% of the nominal shear yielding strength ($V_p$) of the W shear link to account for the strain hardening of the link (150%) and the effect of composite action (20%+). The brace forces developed by the consistent deformation of the concrete slab spanning perpendicular to the plane of the eccentrically braced frame must also be included in the design axial forces. The AISC formula

(Equation 9.11 with the safety factor FS set equal to 1.0) can be used to to determine the required eccentric brace sizes.

*Eccentrically Braced Frame Column Forces* : The design of the columns in the eccentrically braced bay should be based upon the maximum expected strength of the corresponding eccentrically braced bay and the axial forces from the column above. The strength of the eccentrically braced bay should account for the effects of link strain hardening, composite action and the three-dimensional coupling effect noted above. This requirement is necessary to maintain the integrity of the vertical load carrying capacity of the eccentrically braced bay.

*Energy Dissipation Capacity* : The energy dissipation capacity of the model was outstanding but it was concentrated in the lower two shear links (Links L2 and L3). The latter feature is undesirable since the model's potential energy dissipation capacity is not mobilized. Enforcing a rigid body displacement field (Figure 3.2b) on both sides of the shear link will optimize the strength and energy dissipation capacity of the eccentrically braced frame, ensure a more even distribution of damage in the frame and reduce the likelihood of low cycle fatigue and incremental collapse for a similar level of input energy.

## 11.3 Recommendations for Future Research

Further experimental and analytical research must be undertaken to better understand the behavior of eccentrically braced steel structures; this research should focus upon the issues noted below. This research, however, should not be limited to eccentrically braced steel structures but extended to structural systems in general.

*Eccentrically and Concentrically Braced Frames* : The results of the testing of both the eccentrically K-braced model and the concentrically K-braced model [9] should be carefully reviewed in order to ascertain the relative merits of the two framing systems. These studies should focus upon their respective elastic stiffnesses, yielding strengths,

overstrengths, ultimate strengths, response modification factors, available ductilities, energy dissipation capacity and failure modes.

*Linear Elastic Design Response Spectra* : On the basis of the 1971 San Fernando Valley, 1985 Mexico City, 1985 Chile, 1986 San Salvador earthquake ground motions, it is clear that the current ATC and SEAOC linear elastic design response spectra are nonconservative for regions of high seismic risk, especially if the characteristics of the latter three earthquakes are reproducible in the U.S.A.. Additional studies into the effective peak accelerations to which the LEDRS are anchored, the site dependency of the spectra, the shape of the spectra and the influence of soil type on the spectra, are required. The need for accurate microzonation of the urban areas in regions of high seismic risk has been discussed previously [31]; the additional studies noted above should be extended to satisfy this need.

*Response Modification Factor* : The ATC and SEAOC Response Modification Factors (R and $R_w$) overestimate the maximum possible reduction in the required elastic strength of the eccentrically K-braced and concentrically K-braced dual steel structures [9] tested on the earthquake simulator. There is a need to calibrate, both analytically and experimentally, the strength of braced steel buildings that have been designed and constructed in accordance with the current seismic regulations. Furthermore, the influence of optimum design procedures on the strength factor ($R_S$) and therefore the response modification factor requires further attention. Additional research into the influence of natural period, ductility and redundancy of the structural system on the response modification factor is required.

*Code Seismic Forces* : The minimum seismic forces specified by the 1985 UBC, 1984 ATC and the 1986 SEAOC are nonconservative with respect to those forces developed during severe earthquake shaking. The minimum seismic forces must be upgraded to a level whereby a structure designed in accordance with these minimum seismic forces and the other code-based minimum requirements will survive severe earthquake shaking.

*Dual System Compatibility* : The interaction of braced and ductile moment-resisting frames in the dual system requires further study. Emphasis should be focused upon evaluating the demand on the ductile moment-resisting space frames upon the yielding of the braced frame such that the strength and deformation envelope of the entire system remains stable up to drift levels exceeding 1.5%. The relationships between the relative lateral stiffness, deformability, ductility and yielding strengths of the braced frame and the DMRSF should be investigated.

*Energy Dissipation Capacity* : The distribution of energy dissipation over the height of the model was highly nonuniform and was concentrated in the lower two stories of the model. Enforcing a rigid body displacement field (as assumed in the kinematic relationship described in Chapter 3) would enhance the strength and energy dissipation capacity of an eccentrically braced frame and ensure a more uniform distribution of damage over its height. Methods and techniques by which this displacement field can be economically achieved should be investigated to determine the possible increases in strength, stiffness and energy dissipation capacity of the eccentrically braced dual system.

*Energy Methods* : The unique ability of an eccentrically braced frame to concentrate inelastic activity in a number of predetermined locations make it possible to evaluate a lower bound to its energy dissipation capacity. To develop a rational design procedure [70] incorporating energy methods, energy spectra for SDOFS must be developed in a manner that reflects a number of parameters that include the local and global geological conditions, distance from the active fault and the characteristics of previously recorded earthquake ground motions.

*Low Cycle Fatigue and Incremental Collapse* : Although the experimental results presented in this report do not support the inclusion of low cycle fatigue and incremental collapse provisions in the current earthquake resistant regulations for eccentrically braced frames, additional studies are required to ascertain the influence of strong motion duration, the type and frequency content of the earthquake ground motion, the

structural system and its strength and dynamic characteristics on the likelihood of either low cycle fatigue or incremental collapse.

*Torsional Redundancy* : The issue of torsional redundancy and its effect on the inelastic response of unbraced, braced and dual steel systems requires urgent attention as the current seismic regulations do not address this poorly understood subject. The end result of this research should be guidelines that dictate the minimum number of lines of framing in mutually orthogonal directions and additional eccentricities that reflect the degree of torsional redundancy in the structure.

## REFERENCES

[1] Hjelmstad, K.D. and Popov, E.P., "Seismic Behaviour of Active Beam Links in Eccentrically Braced Frames," *Report No. UCB/EERC-83/15,* Earthquake Engineering Research Center, University of California, Berkeley, CA, July 1983.

[2] Kasai, K. and Popov, E.P., "A Study of Seismically Resistant Eccentrically Braced Steel Frame Systems," *Report No. UCB/EERC-86/01,* Earthquake Engineering Research Center, University of California, Berkeley, CA, January 1986.

[3] Roeder, C.W. and Popov, E.P., "Inelastic Behaviour of Eccentric Braced Steel Frames Under Cyclic Loading," *Report No. UCB/EERC-77/18,* Earthquake Engineering Research Center, University of California, Berkeley, CA, August 1977.

[4] Malley, J.O. and Popov, E.P., "Design Considerations for Shear Links in Eccentric Braced Frames," *Report No. UCB/EERC-83/24,* Earthquake Engineering Research Center, University of California, Berkeley, CA, November 1983.

[5] Manheim, D., "On the Design of Eccentric Braced Frames," *Thesis presented to the University of California, Berkeley, in partial fulfillment of the degree of Doctor of Engineering,* Berkeley, CA, 1982.

[6] Malley, J.O. and Popov, E.P., "Design of Links and Beam-Column Connections for Eccentric Braced Steel Frames" *Report No. UCB/EERC-83/03,* Earthquake Engineering Research Center, University of California, Berkeley, CA, January 1983.

[7] Kasai, K. and Popov, E.P., "General Behaviour of WF Steel Shear Links," *Journal of Structural Engineering,* ASCE, Volume 112, No. 2, February 1986.

[8] U.S.-Japan Planning Group, Cooperative Research Program Utilizing Large-Scale Testing Facilities, "Recommendations for a U.S.-Japan Cooperative Research Program Utilizing Large Scale Facilities," *Report No. UCB/EERC-79/26,*, Earthquake Engineering Research Center, University of California, Berkeley, CA, September 1979.

[9] Uang, C.M. and Bertero, V.V., "Earthquake Simulation Tests and Associated Studies of a 0.3-Scale Model of a Six-Story Concentrically Braced Steel Structure," *Report No. UCB/EERC-86/10,* Earthquake Engineering Research Center, University of California, Berkeley, CA, December 1986.

[10] International Association for Earthquake Engineering, *Earthquake Resistant Regulations - A World List,* July 1984.

[11] International Conference of Building Officials., *Uniform Building Code,* 1985 Edition, Whittier, California.

[12] Applied Technology Council, "*Tentative Provisions for the Development of Seismic Regulations for Buildings,*" ATC 3-06, National Bureau of Standards, U.S. Department of Commerce, Washington, D.C., 1984.

[13] Structural Engineers Association of California, *Recommended Lateral Force Requirements,* San Francisco, CA, 1986.

[14] Yamanouchi, H., and Midorikawa, M., "Design of the Full-Scale Six-Story Steel Building," *The Third Joint Technical Coordinating Committee,* U.S.-Japan Cooperative Research Program Utilizing Large Scale Test Facilities, Tsukuba, Japan, July 1982.

[15] Foutch, D.A., Yamanouchi, H., Midorikawa, M., and Nishiyama, I., "Construction of Full-Scale Six-Story Steel Test Structure," *The Fourth Joint Technical Coordinating Committee,* U.S.-Japan Cooperative Research Program Utilizing Large Scale Test Facilities, June 1983, Tsukuba, Japan.

[16] Foutch, D.A. et al., "Summary of the Design and Construction of the Full-Scale Specimen and Results of the Phase 1 Tests," *Structures Congress 3,* ASCE Annual Convention, San Francisco, CA, October 1984.

[17] Kawakami, Y., Midorikawa, M., and Nishiyama, I., "U.S.-Japan Cooperative Large Scale Earthquake Research Program : Earthquake Simulation Tests of a Full-Scale

Model of a Six-Story Test Structure," *Building Research Institute,* Tsukuba, Japan, May 1985.

[18] Yang, M., "Seismic Behavior of an Eccentrically X-Braced Steel Structure," *Report No. UCB/EERC-82/14,* Earthquake Engineering Research Center, University of California, Berkeley, CA, September 1982.

[19] Kasai, K., "A Plastic Design Method of Eccentrically Braced Frames," *CE299 Report,* Department of Civil Engineering, University of California, Berkeley, CA.

[20] Kasai, K. and Popov, E.P., "On Seismic Design of Eccentrically Braced Steel Frames," *Proceedings of the Eighth World Conference on Earthquake Engineering,* San Francisco, CA, 1984.

[21] Kasai, K. and Popov, E.P., "Cyclic Web Buckling Control for Shear Link Beams," *Journal of Structural Engineering,* ASCE, Volume 112, No. 3, March 1986.

[22] Ricles, J.M., "Cyclic Behaviour of Composite Shear Links," *CE299 Report,* Department of Civil Engineering, University of California, Berkeley, CA, 1985.

[23] Engelhardt, M.D., "Brace to Beam Connections in Earthquake Resistant Eccentrically Braced Frames," *Progress Report to AISC,* University of California, Berkeley, CA, January 1986.

[24] Engelhardt, M.D., "Long Links in Eccentrically Braced Frames - A Preliminary Assessment," *CE299 Report,* Department of Civil Engineering, University of California, Berkeley, CA, 1987.

[25] Kasai, K., *Private Communication.*

[26] Yamanouchi, H., Midorikawa, M. et al., "Inelastic Seismic Tests on a Full-Scale Six Story Eccentric K-Braced Steel Building," *Proceedings of the 17th Joint Panel Meeting of the U.S.-Japan Cooperative Program in Wind and Seismic Effects,* Tsukuba, Japan, May 1985.

[27] B.R.I. Steel Group, "Phase II Test Results," *The Sixth Joint Technical Coordinating Committee*, US-Japan Cooperative Research Program Utilizing Large Scale Testing Facilities, June 1985.

[28] B.R.I. Steel Group, "Phase III Test Results," *The Sixth Joint Technical Coordinating Committee*, US-Japan Cooperative Research Program Utilizing Large Scale Testing Facilities, June 1985.

[29] Boutros, M.K. and Goel, S.C., "Analytical Modelling of Braced Steel Structures," *Report No. UMCE 85-7,* The University of Michigan, Ann Arbor, Michigan, August 1985.

[30] Wilson, E.L., *The SAP-80 Series of Structural Analysis Programs for CP/M-80 Microcomputer Systems,* February 1984.

[31] Bertero, V.V., "Implications of Recent Earthquakes and Research on Earthquake-Resistant Design and Construction of Buildings," *Report No. UCB/EERC-86/03,* Earthquake Engineering Research Center, University of California, Berkeley, CA, March 1986.

[32] Kannan, A.E. and Powell, G.H., "DRAIN-2D, A General Purpose Computer Program for Dynamic Analysis of Inelastic Plane Structures," *Report No. UCB/EERC-73/6,* Earthquake Engineering Research Center, University of California, Berkeley, CA, April, 1973.

[33] Allahabadi, R. and Powell, G.H., "DRAIN-2DX, A General Purpose Computer Program for Dynamic Analysis of Inelastic Plane Structures," *UCB/EERC Report in Preparation,* Earthquake Engineering Research Center, University of California, Berkeley, CA.

[34] Chen, W.F and Atsuta, T., *Theory of Beam-Columns, Volumes 1 and 2,* McGraw-Hill, New York, 1976.

[35] American Institute of Steel Construction, *Specification for the Design, Fabrication and Erection of Structural Steel for Buildings,* New York, N.Y., 1980.

[36] Krawinkler, H., Bertero, V.V. and Popov, E.P., "Inelastic Behavior of Steel Beam to Column Subassemblages," *Report No. UCB/EERC-71/07,* Earthquake Engineering Research Center, University of California, Berkeley, CA, 1971.

[37] Bertero, V.V., Krawinkler, H. and Popov, E.P., "Further Studies on the Seismic Behavior of Steel Beam - Column Subassemblages," *Report No. UCB/EERC-73/27,* Earthquake Engineering Research Center, University of California, Berkeley, CA, 1973.

[38] Neal, B.G., "Effect of Shear Force on the Fully Plastic Moment of an I Beam," *Journal of Mechanical Engineering Science,* Volume 3(3), 1961.

[39] Neal, B.G., *The Plastic Methods of Structural Analysis,* Science Paperbacks, 1977.

[40] Hodge, P.G., *Plastic Analysis of Structures,* McGraw-Hill, New York, 1959.

[41] Horne, M.R. and Morris, L.J., *Plastic Design of Low-Rise Frames,* The MIT Press, 1982.

[42] Takanashi, H. et al., "Nonlinear Earthquake Response Analysis of Structures by a Computer-Actuator On-Line System," *Bulletin of Earthquake Resistant Structure Research Center,* The Institute of Industrial Science, University of Tokyo, No. 8, December 1974.

[43] Takanashi, H. et al., "Earthquake Response Analysis of a 1 Bay - 2 Story Steel Frame by Computer-Actuator On-Line System," *Bulletin of Earthquake Resistant Structure Research Center,* The Institute of Industrial Science, University of Tokyo, No. 11, December 1977.

[44] Shing, P.S. and Mahin, S.A., "Experimental Error Propagation in Pseudodynamic Testing," *Report No. UCB/EERC-83/12,* Earthquake Engineering Research Center, University of California, Berkeley, CA, June 1983.

[45] Shing, P.S. and Mahin, S.A., "Pseudodynamic Test Method for Seismic Performance Evaluation: Theory and Implementation," *Report No. UCB/EERC-84/01,* Earthquake Engineering Research Center, University of California, Berkeley, CA, July 1983.

[46] California Institute of Technology, "Strong Motion Accelerograms : Volumes 1-4"; *EERL Reports,* Earthquake Engineering Research Laboratory, California Institute of Technology, Pasadena, CA, July 1969 - present.

[47] Mondkar, D.P. and Powell, G.H., "ANSR-1, General Purpose Computer Program for Analysis of Non-linear Structure Response," *Report No. UCB/EERC-75/17,* Earthquake Engineering Research Center, University of California, Berkeley, CA, 1975.

[48] Rea, D. and Penzien, J., "Dynamic Response of a 20 ft x 20 ft Shaking Table, " *Proceedings of the Fifth World Conference on Earthquake Engineering,* Vol. 2, Rome, Italy, 1974.

[49] Rinawi, A., "Pitching Effects in the Earthquake Engineering Research Center Shaking Table," *CE299 Report,* Department of Civil Engineering, University of California, Berkeley, April 1987.

[50] Uang, C.M., "Experimental and Analytical Study of the Hysteretic Behavior of Steel Composite Girders," *CE299 Report,* University of California, Berkeley, May 1985.

[51] Becker, R.A. and Chambers, J.M., *S - An Interactive Environment for Data Analysis and Graphics,* The Wadsworth Statistics/Probability Series, 1984.

[52] Clough, R.W. and Penzien, J., *Dynamics of Structures,* McGraw-Hill, New York, 1975.

[53] Kaba, S.A. and Mahin, S.A., "Interactive Computer Analysis Methods for Predicting the Inelastic Cyclic Behavior of Structural Sections," *Report No. UCB/EERC-*

*83/18,* Earthquake Engineering Research Center, University of California, Berkeley, CA, July 1983.

[54] Zahrah, T.H. and Hall, W.J., "Seismic Energy Absorption in Simple Structures," *Report No. UILU-ENG-82-2011,* University of Illinois at Urbana-Champaign, 1982.

[55] Newmark, N.M. and Hall, W.J., *Earthquake Spectra and Design,* Earthquake Engineering Research Institute, 1982

[56] Austin, M.A., Pister, K.S. and Mahin, S.A., "A Methodology for Computer-Aided Design of Earthquake-Resistant Steel Structures," *Report No. UCB/EERC-85/13,* Earthquake Engineering Research Center, University of California, Berkeley, CA, July 1983.

[57] Monkarz, P.D. and Krawinkler, H., "Theory and Application of Experimental Model Analysis in Earthquake Engineering," *Report No 50,* The John A. Blume Earthquake Engineering Center, Department of Civil Engineering, Stanford University, Stanford, CA, June 1981.

[58] Soroushian, P. and Choi, K., "Steel Mechanical Properties at Different Strain Rates," *Journal of Structural Engineering,* ASCE, Volume 113, No. 4, April 1987.

[59] Mahin, S.A. and Bertero, V.V., " An Evaluation of Inelastic Seismic Design Spectra," *Journal of Structural Engineering,* ASCE, Volume 107, No. ST1, September 1981.

[60] Housner, G.W., "Limit Design of Structures to Resist Earthquakes," *Proceedings of the World Conference on Earthquake Engineering,* Berkeley, California, 1956.

[61] Mahin, S.A. and Lin, J., "Construction of Inelastic Response Spectra for Single Degree of Freedom System," *Report No. UCB/EERC-83/17,* Earthquake Engineering Research Center, University of California, Berkeley, CA, March 1983.

[62] Evans, H.R., "An Appraisal, by Full-Scale Testing, of New Design Procedures for Steel Girders Subjected to Shear and Bending," *Proceedings of the Institution of*

*Civil Engineers,* No. 81, June 1986.

[63] Bertero, V.V. and Popov, E.P., "Effects of Large Alternating Strains on Steel Beams," *Journal of Structural Engineering,* ASCE, Volume 91, No. ST1, February 1961.

[64] Popov, E.P. and Pinkey, R.B., "Cyclic Yield Reversal in Steel Building Connections," *Journal of Structural Engineering,* ASCE, Volume 95, No. ST3, March 1969.

[65] Thewalt, C. and Mahin, S.A., "Hybrid Solution Techniques for Generalized Pseudo-Dynamic Testing," *Report No. UCB/EERC-87/09,* Earthquake Engineering Research Center, University of California, Berkeley, July 1987.

[66] Rinawi, A., Blondet, J.M. and Clough, R.W., "Analytical and Experimental Studies of Table-Structure Interaction," *Paper submitted to the Ninth World Conference on Earthquake Engineering,* Tokyo, Japan, August 1988.

[67] Dimsdale, J.S., "Redesign of an Earthquake Simulator," *Paper submitted to the Ninth World Conference on Earthquake Engineering,* Tokyo, Japan, August 1988.

[68] Structural Engineers Association of California, *Recommended Lateral Force Requirements of the SEAOC Seismology Committee : Commentary,* Final Draft, April 1987.

[69] Brokken, S. and Bertero, V.V., "Studies on the Effects of Infills in Seismic Resistant R/C Construction," *Report No. UCB/EERC-81/12,* Earthquake Engineering Research Center, University of California, Berkeley, CA, September 1981.

[70] Bertero, V.V., Uang, C.M. and Whittaker, A.S., "Test Structures : Experimental Response and Code Compliance," *ASCE Specialty Conference,* Orlando, Florida, August 1987.

# Appendix A1

## List of Instrumentation

## Tests 1 - 24

| Channel : Explanation | | | |
|---|---|---|---|
| 1 | Table h1 Displacement | 33 | Horizontal Displacement R-A |
| 2 | Table h2 Displacement | 34 | Horizontal Displacement 6-A |
| 3 | Table Horizontal Acceleration | 35 | Horizontal Displacement 5-A |
| 4 | Table Vertical Acceleration | 36 | Horizontal Displacement 4-A |
| 5 | Table Pitch Acceleration | 37 | Horizontal Displacement 3-A |
| 6 | Table Roll Acceleration | 38 | Horizontal Displacement 2-A |
| 7 | Table Twist Acceleration | 39 | Column Axial Strain 1-B1L |
| 8 | Table v2 Displacement | 40 | Column Axial Strain 1-B1R |
| 9 | Table v3 Displacement | 41 | Column Axial Strain 1-B2L |
| 10 | Table v4 Displacement | 42 | Column Axial Strain 1-B2R |
| 11 | Horizontal Acceleration R-B | 43 | Column Axial Strain 1-B3L |
| 12 | Horizontal Acceleration 6-B | 44 | Column Axial Strain 1-B3R |
| 13 | Horizontal Acceleration 5-B | 45 | Column Axial Strain 1-A1L |
| 14 | Horizontal Acceleration 4-B | 46 | Column Axial Strain 1-A1R |
| 15 | Horizontal Acceleration 3-B | 47 | Column Axial Strain 1-A2L |
| 16 | Horizontal Acceleration 2-B | 48 | Column Axial Strain 1-A2R |
| 17 | Horizontal Acceleration R-A | 49 | Column Axial Strain 1-A3L |
| 18 | Horizontal Acceleration 6-A | 50 | Column Axial Strain 1-A3R |
| 19 | Horizontal Acceleration 5-A | 51 | L4 Link Shear Strain LD1 |
| 20 | Horizontal Acceleration 4-A | 52 | L4 Link Shear Strain LD2 |
| 21 | Horizontal Acceleration 3-A | 53 | L2 Link Flange Deformation TFR |
| 22 | Horizontal Acceleration 2-A | 54 | L2 Link Flange Deformation BFR |
| 23 | Horizontal Displacement R-B | 55 | L5 Link Shear Strain D1 |
| 24 | Horizontal Displacement 6-B | 56 | L5 Link Shear Strain D2 |
| 25 | Horizontal Displacement 5-B | 57 | L6 Link Shear Strain D1 |
| 26 | Horizontal Displacement 4-B | 58 | L6 Link Shear Strain D2 |
| 27 | Horizontal Displacement 3-B | 59 | L4 Link Flange Deformation TFL |
| 28 | Horizontal Displacement 2-B | 60 | L4 Link Flange Deformation TFR |
| 29 | Column Shear 6-A1 | 61 | Column Shear 1-B3 |
| 30 | L2 Link Flange Axial Strain TFL | 62 | Column Shear 1-B2 |
| 31 | L2 Link Flange Deformation TFL | 63 | Column Shear 1-B1 |
| 32 | L2 Link Flange Deformation BFL | 64 | Column Shear 1-A3 |
| | | 65 | Column Shear 1-A2 |
| | | 66 | Column Shear 1-A1 |

67 Column Shear 1-C3
68 Column Shear 1-C2
69 Column Shear 1-C1
70 Column Shear 2-B3
71 Column Shear 2-B2
72 Column Shear 2-B1
73 Column Shear 2-A3
74 Column Shear 2-A2
75 Column Shear 2-A1
76 Column Shear 3-B3
77 Column Shear 3-B2
78 Column Shear 3-B1
79 Column Shear 3-A3
80 Column Shear 3-A2
81 Column Shear 3-A1
82 Column Shear 4-B3
83 Column Shear 4-B2
84 Column Shear 4-B1
85 Column Shear 4-A3
86 Column Shear 4-A2
87 Column Shear 4-A1
88 Column Shear 5-B3
89 Column Shear 5-B2
90 Column Shear 5-B1
91 Column Shear 5-A3
92 Column Shear 5-A2
93 Column Shear 5-A1
94 Column Shear 6-B3
95 Column Shear 6-B2
96 Column Shear 6-B1
97 Column Shear 6-A3
98 Column Shear 6-A2
99 Brace 1 Axial Force T
100 Brace 1 Axial Force S
101 Brace 2 Axial Force T
102 Brace 2 Axial Force S
103 Brace 3 Axial Force T
104 Brace 3 Axial Force S
105 Brace 4 Axial Force T
106 Brace 4 Axial Force S
107 Brace 5 Axial Force T
108 Brace 5 Axial Force S
109 Brace 6 Axial Force
110 L3 Link Flange Axial Strain BFL
111 Brace 7 Axial Force T
112 Brace 7 Axial Force S
113 Brace 8 Axial Force
114 L2 Link Flange Axial Strain BFL
115 Brace 10 Axial Force T
116 Brace 10 Axial Force S
117 Brace 11 Axial Force
118 Brace 12 Axial Force
119 L2 Shear Strain LD1
120 L2 Shear Strain LD2
121 L2 Shear Strain RD1
122 L2 Shear Strain RD2
123 L3 Shear Strain LD1
124 L3 Shear Strain LD2
125 L3 Shear Strain RD2
126 L3 Shear Strain RD1
127 L4 Shear Strain RD2
128 L4 Shear Strain RD1
129 L7 Shear Strain D1
130 L4 Link Flange Deformation BFR
131 Brace 1 Axial Deformation
132 Brace 2 Axial Deformation
133 Brace 3 Axial Deformation
134 Brace 4 Axial Deformation
135 L7 Link Shear Strain D2
136 L4 Link Flange Deformation BFL
137 Column 1-B1 Axial Deformation
138 Column 1-B2 Axial Deformation
139 Column 1-B3 Axial Deformation
140 Column 2-B1 Axial Deformation
141 Column 2-B2 Axial Deformation
142 Column 2-B3 Axial Deformation
143 Vertical Displacement R-B1
144 Vertical Displacement R-B23
145 Vertical Displacement R-B2
146 Vertical Displacement R-B3
147 Vertical Displacement R-A1
148 L3 Link Flange Deformation BFR

149 Transverse Displacement R-A1
150 Transverse Displacement R-A3
151 Vertical Acceleration R-B1
152 Vertical Acceleration R-B2
153 Vertical Acceleration R-B3
154 Transverse Acceleration R-1A
155 Transverse Acceleration R-3A
156 L3 Link Web Axial Deformation
157 L2 Link Vertical Displacement L
158 L2 Link Vertical Displacement R
159 L2-L3 Link Relative Displacement BL
160 L2-L3 Link Relative Displacement BR
161 L2-L3 Link Relative Displacement TL
162 L2-L3 Link Relative Displacement TR
163 L2 Link Web Axial Deformation
164 L3 Link Flange Deformation TFL
165 L3 Link Flange Deformation BFL
166 L3 Link Flange Deformation TFR
167 L3 Link Flange Axial Strain TFL
168 Brace 9 Axial Force
169 Rotational Deformation 1-B2
170 Brace 3 Axial Root Strain
171 Column Axial Strain 1-B1
172 Column Axial Strain 1-B2
173 Column Axial Strain 1-A1
174 Column Axial Strain 1-A2
175 Flange Axial Strain 2-B3R-BF
176 Flange Axial Strain 2-B3R-TF

# Appendix A2

## List of Instrumentation

## Tests 25 - 31

| Channel | Explanation |
|---|---|
| 1 | Table h1 Displacement |
| 2 | Table h2 Displacement |
| 1 | Table h1 Displacement |
| 2 | Table h2 Displacement |
| 3 | Table Horizontal Acceleration |
| 4 | Table Vertical Acceleration |
| 5 | Table Pitch Acceleration |
| 6 | Table Roll Acceleration |
| 7 | Table Twist Acceleration |
| 8 | Table v2 Displacement |
| 9 | Table v3 Displacement |
| 10 | Table v4 Displacement |
| 11 | Horizontal Acceleration R-B |
| 12 | Horizontal Acceleration 6-B |
| 13 | Horizontal Acceleration 5-B |
| 14 | Horizontal Acceleration 4-B |
| 15 | Horizontal Acceleration 3-B |
| 16 | Horizontal Acceleration 2-B |
| 17 | Horizontal Acceleration R-A |
| 18 | Horizontal Acceleration 6-A |
| 19 | Horizontal Acceleration 5-A |
| 20 | Horizontal Acceleration 4-A |
| 21 | Horizontal Acceleration 3-A |
| 22 | Horizontal Acceleration 2-A |
| 23 | Horizontal Displacement R-B |
| 24 | Horizontal Displacement 6-B |
| 25 | Horizontal Displacement 5-B |
| 26 | Horizontal Displacement 4-B |
| 27 | Horizontal Displacement 3-B |
| 28 | Horizontal Displacement 2-B |
| 29 | Column Shear 6-A1 |
| 30 | L2 Link Flange Axial Strain TFL |
| 31 | L2 Link Flange Deformation TFL |
| 32 | L2 Link Flange Deformation BFL |
| 33 | Horizontal Displacement R-A |
| 34 | Horizontal Displacement 6-A |
| 35 | Horizontal Displacement 5-A |
| 36 | Horizontal Displacement 4-A |
| 37 | Horizontal Displacement 3-A |
| 38 | Horizontal Displacement 2-A |
| 39 | Column Axial Strain 1-B1L |
| 40 | Column Axial Strain 1-B1R |
| 41 | Column Axial Strain 1-B2L |
| 42 | Column Axial Strain 1-B2R |
| 43 | Column Axial Strain 1-B3L |
| 44 | Column Axial Strain 1-B3R |
| 45 | Column Axial Strain 1-A1L |
| 46 | Column Axial Strain 1-A1R |
| 47 | Column Axial Strain 1-A2L |
| 48 | Column Axial Strain 1-A2R |
| 49 | Column Axial Strain 1-A3L |
| 50 | Column Axial Strain 1-A3R |
| 51 | L4 Link Shear Strain LD1 |
| 52 | L4 Link Shear Strain LD2 |
| 53 | L2 Link Flange Deformation TFR |
| 54 | L2 Link Flange Deformation BFR |
| 55 | L5 Link Shear Strain D1 |
| 56 | L5 Link Shear Strain D2 |
| 57 | L6 Link Shear Strain D1 |
| 58 | L6 Link Shear Strain D2 |
| 59 | L4 Link Flange Deformation TFL |
| 60 | L4 Link Flange Deformation TFR |
| 61 | Column Shear 1-B3 |
| 62 | Column Shear 1-B2 |
| 63 | Column Shear 1-B1 |
| 64 | Column Shear 1-A3 |

65 Column Shear 1-A2
66 Column Shear 1-A1
67 Column Shear 1-C3
68 Column Shear 1-C2
69 Column Shear 1-C1
70 Column Shear 2-B3
71 Column Shear 2-B2
72 Column Shear 2-B1
73 Column Shear 2-A3
74 Column Shear 2-A2
75 Column Shear 2-A1
76 Column Shear 3-B3
77 Column Shear 3-B2
78 Column Shear 3-B1
79 Column Shear 3-A3
80 Column Shear 3-A2
81 Column Shear 3-A1
82 Column Shear 4-B3
83 Column Shear 4-B2
84 Column Shear 4-B1
85 Column Shear 4-A3
86 Column Shear 4-A2
87 Column Shear 4-A1
88 Column Shear 5-B3
89 Column Shear 5-B2
90 Column Shear 5-B1
91 Column Shear 5-A3
92 Column Shear 5-A2
93 Column Shear 5-A1
94 Column Shear 6-B3
95 Column Shear 6-B2
96 Column Shear 6-B1
97 Column Shear 6-A3
98 Column Shear 6-A2
99 Brace 1 Axial Force T
100 Brace 1 Axial Force S
101 Brace 2 Axial Force T
102 Brace 2 Axial Force S
103 Brace 3 Axial Force T
104 Brace 3 Axial Force S
105 Brace 4 Axial Force T
106 Brace 4 Axial Force S
107 Brace 5 Axial Force T
108 Brace 5 Axial Force S
109 Brace 6 Axial Force
110 L3 Link Flange Axial Strain BFL
111 Brace 7 Axial Force T
112 Brace 7 Axial Force S
113 Brace 8 Axial Force
114 L2 Link Flange Axial Strain BFL
115 Brace 9 Axial Force
116 Brace 10 Axial Force
117 Brace 11 Axial Force
118 Brace 12 Axial Force
119 L2 Shear Strain LD1
120 L2 Shear Strain LD2
121 L2 Shear Strain RD1
122 L2 Shear Strain RD2
123 L3 Shear Strain LD1
124 L3 Shear Strain LD2
125 L3 Shear Strain RD2
126 L3 Shear Strain RD1
127 L4 Shear Strain RD2
128 L4 Shear Strain RD1
129 L7 Shear Strain D1
130 L4 Link Flange Deformation BFR
131 Brace 1 Axial Deformation
132 Brace 2 Axial Deformation
133 Brace 3 Axial Deformation
134 Brace 4 Axial Deformation
135 L7 Link Shear Strain D2
136 L4 Link Flange Deformation BFL
137 Column 1-B1 Axial Deformation
138 Column 1-B2 Axial Deformation
139 Column 1-B3 Axial Deformation
140 Column 2-B1 Axial Deformation
141 Column 2-B2 Axial Deformation
142 Column 2-B3 Axial Deformation
143 Vertical Displacement R-B1
144 Vertical Displacement R-B23
145 Vertical Displacement R-B2
146 Vertical Displacement R-B3

147 Vertical Displacement R-A1
148 L3 Link Flange Deformation BFR
149 L2 Link Vertical Separation
150 Transverse Displacement R-A3
151 Vertical Acceleration R-B1
152 Vertical Acceleration R-B2
153 Vertical Acceleration R-B3
154 Transverse Acceleration R-1A
155 Transverse Acceleration R-3A
156 L2 Link Horizontal Slippage
157 L2 Link Vertical Displacement L
158 L2 Link Vertical Displacement R
159 L2-L3 Link Relative Displacement BL
160 L2-L3 Link Relative Displacement BR
161 L2-L3 Link Relative Displacement TL
162 L2-L3 Link Relative Displacement TR
163 L2 Link Crack Width on Grid B
164 L3 Link Flange Deformation TFL
165 L3 Link Flange Deformation BFL
166 L3 Link Flange Deformation TFR
167 L3 Link Flange Axial Strain TFL
168 -
169 Rotational Deformation 1-B2
170 Brace 3 Axial Root Strain
171 Column Axial Strain 1-B1
172 Column Axial Strain 1-B2
173 Column Axial Strain 1-A1
174 Column Axial Strain 1-A2
175 Flange Axial Strain 2-B3R-BF
176 Flange Axial Strain 2-B3R-TF

# Appendix A3

## List of Instrumentation

## Tests 32 - 36

| Channel : Explanation | | | |
|---|---|---|---|
| 1 | Table h1 Displacement | 31 | L2 Link Flange Deformation TFL |
| 2 | Table h2 Displacement | 32 | L2 Link Flange Deformation BFL |
| 1 | Table h1 Displacement | 33 | Horizontal Displacement R-A |
| 2 | Table h2 Displacement | 34 | Horizontal Displacement 6-A |
| 3 | Table Horizontal Acceleration | 35 | Horizontal Displacement 5-A |
| 4 | Table Vertical Acceleration | 36 | Horizontal Displacement 4-A |
| 5 | Table Pitch Acceleration | 37 | Horizontal Displacement 3-A |
| 6 | Table Roll Acceleration | 38 | Horizontal Displacement 2-A |
| 7 | Table Twist Acceleration | 39 | Column Axial Strain 1-B1L |
| 8 | Table v2 Displacement | 40 | Column Axial Strain 1-B1R |
| 9 | Table v3 Displacement | 41 | Column Axial Strain 1-B2L |
| 10 | Table v4 Displacement | 42 | Column Axial Strain 1-B2R |
| 11 | Horizontal Acceleration R-B | 43 | Column Axial Strain 1-B3L |
| 12 | Horizontal Acceleration 6-B | 44 | Column Axial Strain 1-B3R |
| 13 | Horizontal Acceleration 5-B | 45 | Column Axial Strain 1-A1L |
| 14 | Horizontal Acceleration 4-B | 46 | Column Axial Strain 1-A1R |
| 15 | Horizontal Acceleration 3-B | 47 | Column Axial Strain 1-A2L |
| 16 | Horizontal Acceleration 2-B | 48 | Column Axial Strain 1-A2R |
| 17 | Horizontal Acceleration R-A | 49 | Column Axial Strain 1-A3L |
| 18 | Horizontal Acceleration 6-A | 50 | Column Axial Strain 1-A3R |
| 19 | Horizontal Acceleration 5-A | 51 | L4 Link Shear Strain LD1 |
| 20 | Horizontal Acceleration 4-A | 52 | L4 Link Shear Strain LD2 |
| 21 | Horizontal Acceleration 3-A | 53 | L2 Link Flange Deformation TFR |
| 22 | Horizontal Acceleration 2-A | 54 | L2 Link Flange Deformation BFR |
| 23 | Horizontal Displacement R-B | 55 | L5 Link Shear Strain D1 |
| 24 | Horizontal Displacement 6-B | 56 | L5 Link Shear Strain D2 |
| 25 | Horizontal Displacement 5-B | 57 | L6 Link Shear Strain D1 |
| 26 | Horizontal Displacement 4-B | 58 | L6 Link Shear Strain D2 |
| 27 | Horizontal Displacement 3-B | 59 | L4 Link Flange Deformation TFL |
| 28 | Horizontal Displacement 2-B | 60 | L4 Link Flange Deformation TFR |
| 29 | Column Shear 6-A1 | 61 | Column Shear 1-B3 |
| 30 | L2 Link Flange Axial Strain TFL | 62 | Column Shear 1-B2 |
| | | 63 | Column Shear 1-B1 |
| | | 64 | Column Shear 1-A3 |

65 Column Shear 1-A2
66 Column Shear 1-A1
67 Column Shear 1-C3
68 Column Shear 1-C2
69 Column Shear 1-C1
70 Column Shear 2-B3
71 Column Shear 2-B2
72 Column Shear 2-B1
73 Column Shear 2-A3
74 Column Shear 2-A2
75 Column Shear 2-A1
76 Column Shear 3-B3
77 Column Shear 3-B2
78 Column Shear 3-B1
79 Column Shear 3-A3
80 Column Shear 3-A2
81 Column Shear 3-A1
82 Column Shear 4-B3
83 Column Shear 4-B2
84 Column Shear 4-B1
85 Column Shear 4-A3
86 Column Shear 4-A2
87 Column Shear 4-A1
88 Column Shear 5-B3
89 Column Shear 5-B2
90 Column Shear 5-B1
91 Column Shear 5-A3
92 Column Shear 5-A2
93 Column Shear 5-A1
94 Column Shear 6-B3
95 Column Shear 6-B2
96 Column Shear 6-B1
97 Column Shear 6-A3
98 Column Shear 6-A2
99 Brace 1 Axial Force T
100 Brace 1 Axial Force S
101 Brace 2 Axial Force T
102 Brace 2 Axial Force S
103 Brace 3 Axial Force T
104 Brace 3 Axial Force S
105 Brace 4 Axial Force T
106 Brace 4 Axial Force S
107 Brace 5 Axial Force T
108 Brace 5 Axial Force S
109 Brace 6 Axial Force
110 Beam B4 Shear Strain R
111 Brace 7 Axial Force T
112 Brace 7 Axial Force S
113 Brace 8 Axial Force
114 Beam B4 Shear Strain L
115 Brace 9 Axial Force
116 Brace 10 Axial Force
117 Brace 11 Axial Force
118 Brace 12 Axial Force
119 L2 Shear Strain LD1
120 L2 Shear Strain LD2
121 L2 Shear Strain RD1
122 L2 Shear Strain RD2
123 L3 Shear Strain LD1
124 L3 Shear Strain LD2
125 L3 Shear Strain RD2
126 L3 Shear Strain RD1
127 L4 Shear Strain RD2
128 L4 Shear Strain RD1
129 L7 Shear Strain D1
130 L4 Link Flange Deformation BFR
131 Brace 1 Axial Deformation
132 Brace 2 Axial Deformation
133 Brace 3 Axial Deformation
134 Brace 4 Axial Deformation
135 L7 Link Shear Strain D2
136 L4 Link Flange Deformation BFL
137 Column 1-B1 Axial Deformation
138 Column 1-B2 Axial Deformation
139 Column 1-B3 Axial Deformation
140 Column 2-B1 Axial Deformation
141 Column 2-B2 Axial Deformation
142 Column 2-B3 Axial Deformation
143 Vertical Displacement R-B1
144 Vertical Displacement R-B23
145 Vertical Displacement R-B2
146 Vertical Displacement R-B3

147 Vertical Displacement R-A1
148 L3 Link Flange Deformation BFR
149 L2 Link Vertical Separation
150 Transverse Displacement R-3A
151 Vertical Acceleration R-B1
152 Vertical Acceleration R-B2
153 Vertical Acceleration R-B3
154 Transverse Acceleration R-1A
155 Transverse Acceleration R-3A
156 L2 Link Horizontal Slippage
157 L2 Link Vertical Displacement L
158 L2 Link Vertical Displacement R
159 L2-L3 Link Relative Displacement BL
160 L2-L3 Link Relative Displacement BR
161 L2-L3 Link Relative Displacement TL
162 L2-L3 Link Relative Displacement TR
163 L2 Link Crack Width on Grid B
164 L3 Link Flange Deformation TFL
165 L3 Link Flange Deformation BFL
166 -
167 L2 Link Flange Axial Strain BFL
168 -
169 Rotational Deformation 1-B2
170 Brace 3 Axial Root Strain
171 Column Axial Strain 1-B1
172 Column Axial Strain 1-B2
173 Column Axial Strain 1-A1
174 Column Axial Strain 1-A2
175 Flange Axial Strain 2-B3R-BF
176 Flange Axial Strain 2-B3R-TF

# Appendix A4 - Nomenclature

| | |
|---|---|
| Ln | Level n |
| A-n | Line A Level n |
| n-Am | Grid A-m Story n |
| n-AmL | Grid A-m Story n Left |
| n-AmR | Grid A-m Story n Right |
| B-n | Grid Line B Level n |
| n-Bm | Grid B-m Story n |
| n-BmL | Grid B-m Story n Left |
| n-BmR | Grid B-m Story n Right |
| C-n | Grid Line C Level n |
| n-Cm | Grid C-m Story n |
| n-CmL | Grid C-m Story n Left |
| n-CmR | Grid C-m Story n Right |
| Dn | Diagonal n |
| LDn | Left Diagonal n |
| RDn | Right Diagonal n |
| TL | Top Left |
| TR | Top Right |
| BL | Bottom Left |
| BR | Bottom Right |
| TFL | Top Flange Left |
| TFR | Top Flange Right |
| BFL | Bottom Flange Left |
| BFR | Bottom Flange Right |
| T | Top |
| S | Side |
| B | Bottom |
| L | Left |
| R | Right |
| n-BmR-BF | Level n Beam m Right Bottom Flange |
| n-BmL-BF | Level n Beam m Left Bottom Flange |
| n-BmR-TF | Level n Beam m Right Top Flange |
| n-BmL-TF | Level n Beam m Left Top Flange |

# Appendix B - Derivation of Energy Equation

For a typical N story building with the story weights lumped at each floor level; the equation of motion is :

$$\underline{f}_I + \underline{f}_D + \underline{f}_S = 0 = \underline{m}\ddot{\underline{v}}^t + \underline{f}_D + \underline{f}_S \,. \tag{B.1}$$

where $\underline{f}_I = \underline{m}\ddot{\underline{v}}^t$ = inertia force vector;

$\underline{f}_D$ = damping force vector;

$\underline{f}_S$ = restoring force vector;

$\underline{m}$ = diagonal mass matrix;

$\underline{v}^t$ = absolute lateral displacement vector = $\underline{v} + \underline{r}v_g$;

$\underline{v}$ = relative lateral displacement;

$v_g$ = base motion displacement;

$\underline{r}$ = Nx1 unity column vector.

If Equation B.1 is transposed and integrated with respect to $\underline{v}$, the following equation is obtained :

$$\int \ddot{\underline{v}}^{tT}\underline{m}d\underline{v} + \int \underline{f}_D{}^T dv + \int \underline{f}_S{}^T dv = 0 \,. \tag{B.2}$$

The first term in Equation B.2 can be expressed as follows :

$$\begin{aligned}
\int \ddot{\underline{v}}^{tT}\underline{m}d\underline{v} &= \int \ddot{\underline{v}}^{tT}\underline{m}(d\underline{v}^t - \underline{r}dv_g) = \int \frac{d\dot{\underline{v}}^{tT}}{dt}\underline{m}d\underline{v}^t - \int \ddot{\underline{v}}^{tT}\underline{m}\underline{r}dv_g \\
&= \int d\dot{\underline{v}}^{tT}\underline{m}\dot{\underline{v}}^t - \int \ddot{\underline{v}}^{tT}\underline{m}\underline{r}dv_g = \int \sum_{i=1}^{N} m_i \dot{v}_i^t d\dot{v}_i^t - \int (\sum_{i=1}^{N} m_i \ddot{v}_i^t)dv_g \\
&= \sum_{i=1}^{N} \frac{1}{2} m_i (\dot{v}_i^t)^2 - \int (\sum_{i=1}^{N} m_i \ddot{v}_i^t)dv_g \\
&= \frac{1}{2}\dot{\underline{v}}^{tT}\underline{m}\dot{\underline{v}}^t - \int (\sum_{i=1}^{N} m_i \ddot{v}_i^t)dv_g \,.
\end{aligned} \tag{B.3}$$

Noting that integration is a linear operator, substituting Equation B.3 into Equation B.2 gives :

$$\frac{1}{2}\dot{\underline{v}}^{t^T}\underline{m}\dot{\underline{v}}^{t} + \int \underline{f}_D^T d\underline{v} + \int \underline{f}_S^T d\underline{v} = \int (\sum_{i=1}^{N} m_i \ddot{v}_i^{t}) dv_g \tag{B.4}$$

where $$\frac{1}{2}\dot{\underline{v}}^{t^T}\underline{m}\dot{\underline{v}}^{t} = \frac{1}{2}\sum_{i=1}^{N} m_i (\dot{v}_i^{t})^2 = \text{the kinetic energy } ( E_K ) \tag{B.5}$$

$$\int \underline{f}_D^T d\underline{v} = \text{the viscous damped energy } ( E_\mu ) \tag{B.6}$$

$$\int \underline{f}_S^T d\underline{v} = \int \sum_{i=1}^{N} f_{Si} dv_i = \sum_{i=1}^{N} \int f_{Si} dv_i \tag{B.7}$$

$$= \text{the absorbed energy } ( E_A )$$

$$\int (\sum_{i=1}^{N} m_i \ddot{v}_i^{t}) dv_g = \text{the input energy } ( E_I ) , \tag{B.8}$$

or, the energy balance in the N story building can be expressed as :

$$E_K + E_\mu + E_A = E_I \tag{B.9}$$

The relative displacements ($\underline{v}$) can be related to the inter-story drifts ($\underline{\delta}$) by the following displacement transformation :

$$\underline{\delta} = \underline{a}\,\underline{v} \tag{B.10}$$

where $\underline{\delta}$ = the inter-story drift vector

$\underline{a}$ = displacement transformation matrix = $\begin{bmatrix} 1 & -1 & & & \\ & 1 & -1 & & \\ & & \ddots & & \\ & & & -1 & \\ & & & 1 & -1 \\ & & & & 1 \end{bmatrix}$.

The story shear and damping force vectors can be expressed in terms of $\underline{f}_S$ and $\underline{f}_D$, respectively, using the displacement transformation matrix noted above :

$$\underline{f}_S = \underline{a}^T \underline{V} \tag{B.11}$$

$$\underline{f}_D = \underline{a}^T \underline{q} \tag{B.12}$$

where $\underline{V}$ = the story shear vector (Nx1)

$\underline{q}$ = the story damping force vector (Nx1) .

Generally, the story shear force is calculated in preference to the story restoring force and Equation B.7 can be expressed as :

$$E_A = \int \underline{f}_S^T d\underline{v} = \int \underline{V}^T \underline{a}(\underline{a}^{-1} d\underline{\delta}) = \int \underline{V}^T d\underline{\delta} . \tag{B.13}$$

In a similar manner, Equation B.6 can be expressed as :

$$E_\mu = \int \underline{f}_D^T d\underline{v} = \int \underline{q}^T \underline{a}(\underline{a}^{-1} d\underline{\delta}) = \int \underline{q}^T d\underline{\delta} . \tag{B.14}$$

As noted in Section 7.6, $E_\mu$ is extremely difficult to evaluate. For lightly damped structure undergoing severe inelastic deformation, $E_\mu$ is small compared with $E_H$ and the former term can be ignored without compromising the derivation. For structures remaining in the elastic range, $E_\mu$ is the only energy dissipation mechanism.

The energy absorbed by the structure (Equation B.13) can be divided into recoverable elastic strain energy ($E_S$) and non-recoverable inelastic hysteretic energy ($E_H$), that is :

$$E_A = \int \underline{f}_S^T d\underline{v} = E_S + E_H \tag{B.15}$$

where $$E_S = \sum_{i=1}^{N} \frac{V_i^2}{2K_i} \tag{B.16}$$

$$E_H = E_A - E_S = \sum_{i=1}^{N} \int V_i d\delta_i - \sum_{i=1}^{N} \frac{V_i^2}{2K_i} \tag{B.17}$$

The $K_i$ in Eq. (B.16) is the unloading stiffness of $\delta_i$ versus $V_i$ curve. In the elastic range, $K_i$ is merely the story stiffness; in the inelastic range, the latter term is significantly less than the former term and $K_i$ can be taken as the story stiffness with minimal loss of accuracy. The latter assumption is reasonable if the $V_i$ and $\delta_i$ hysteresis loops are well-rounded.

# TABLES

| Quantity | Multiply | by | to obtain |
|---|---|---|---|
| Length | inch | 25.400 | millimeter |
| | foot | 0.3048 | meter |
| Area | square inch | $0.64516 \times 10^{-3}$ | square millimeter |
| | square foot | $0.92903 \times 10^{-1}$ | square meter |
| Mass | pound | 0.45359 | kilogram |
| Stress | pound-force per square inch | 6.894757 | kilopascal |
| Force | pound-force | 4.448222 | newton |
| | kip | 4.448222 | kilonewton |
| Bending Moment | pound-force-inch | 0.11298 | newton-meter |
| | kip-in | 0.11298 | kilonewton-meter |
| | pound-force-foot | 1.255818 | newton-meter |

**TABLE 1.1 S.I. CONVERSION FACTORS**

| | Floor (psf) | Roof (psf) |
|---|---|---|
| Metal Deck | 6 | 6 |
| 3.5" Lightweight Concrete | 39 | 39 |
| Ceiling & Floor Finishes | 10 | |
| Ceiling & Roofing | | 20 |
| Partitions | 20 | |
| Structural Steel & Fireproofing | 15 | 10 |
| Total | 90 | 75 |

Exterior Wall Weight = 30 psf

**(a) DEAD LOAD**

| | Typical Floor (psf) | Roof (psf) |
|---|---|---|
| Live Load | 60 | 20 |

**(b) LIVE LOAD**

**TABLE 2.1 PROTOTYPE DESIGN LOADS**

| Story | Column Designation Mark No's | | | | |
|---|---|---|---|---|---|
| | C1 | C2 | C3 | C4 | C5 |
| 5-6 | 10W49 | 10W33 | 10W33 | 12W49 | 12W49 |
| 3-4 | 12W65 | 12W53 | 10W89 | 10W60 | 12W72 |
| 2 | 12W79 | 12W65 | 12W50 | 12W79 | 12W106 |
| 1 | 12W87 | 12W87 | 12W65 | 12W106 | 12W136 |

**(a) COLUMNS**

| Level | Girder Designation Mark No's | | | |
|---|---|---|---|---|
| | G1 | G2 | G3 | G4 |
| Roof,6 | 16W31 | 16W31 | 18W35 | 21W50 |
| 5 | 16W31 | 18W35 | | |
| 4 | 18W35 | 18W35 | | |
| 3 | 18W35 | 18W40 | | |
| 2 | 18W40 | 18W40 | | |

**(b) GIRDERS**

| Story | Brace Designation Mark No's |
|---|---|
| | B1 |
| 5-6 | 8×6×0.313 |
| 1-4 | 8×6×0.375 |

**(c) ECCENTRIC BRACES**

**TABLE 2.2 PROTOTYPE SECTION SIZES**

| Floor | Design Weight (kips) incl. External Wall | Design Weight (kips) excl. External Wall | As Built Weight (kips) |
|---|---|---|---|
| Roof | 227.7 | 193.7 | 166.9 |
| 6th | 300.6 | 232.5 | 195.5 |
| 5th | 300.6 | 232.5 | 195.5 |
| 4th | 300.6 | 232.5 | 195.5 |
| 3rd | 300.6 | 232.5 | 195.5 |
| 2nd | 311.7 | 232.5 | 205.2 |
| Total | 1742 | 1356 | 1154 |

**TABLE 2.3 PROTOTYPE FLOOR WEIGHTS**

| Member Type | | Nominal Stress | Sample Min Stress | Sample Max Stress | Sample Mean Stress | No. of Samples |
|---|---|---|---|---|---|---|
| Column | $\sigma_y$ | 36 | 37 | 54 | 43 | |
| | $\sigma_u$ | 58 | 63 | 71 | 66 | 26 |
| Girder | $\sigma_y$ | 36 | 40 | 53 | 46 | |
| | $\sigma_u$ | 58 | 63 | 71 | 67 | 8 |
| Brace | $\sigma_y$ | 46 | 56 | 63 | 59 | |
| | $\sigma_u$ | 58 | 66 | 72 | 68 | 8 |

$\sigma_y$ = yield stress (ksi) $\sigma_u$ = ultimate tensile stress (ksi)

**(a) STRUCTURAL STEEL**

| | Specified Compressive Strength (ksi) | Measured Compressive Strength (ksi) |
|---|---|---|
| Concrete | 3.00 | 4.17 |

**(b) REINFORCED CONCRETE**

**TABLE 2.4 PROTOTYPE MATERIAL PROPERTIES**

| Level | $W_x$ (kips) | $H_x$ (ft) | $F_x$ (kips) |
|---|---|---|---|
| Level Roof | 193.7 | 70.5 | 36.9 |
| Level 6 | 232.5 | 59.4 | 37.3 |
| Level 5 | 232.5 | 48.2 | 30.3 |
| Level 4 | 232.5 | 37.1 | 23.3 |
| Level 3 | 232.5 | 25.9 | 16.3 |
| Level 2 | 232.5 | 14.8 | 9.3 |
| TOTAL | | | 153.4 |

**TABLE 3.1 UBC LATERAL FORCE DISTRIBUTION**

| Level | Peak Displacement (in) | Inter-story Drift Index (%) |
|---|---|---|
| Level Roof | 0.76 | 0.08 |
| Level 6 | 0.67 | 0.11 |
| Level 5 | 0.55 | 0.12 |
| Level 4 | 0.42 | 0.12 |
| Level 3 | 0.29 | 0.12 |
| Level 2 | 0.16 | 0.11 |

**TABLE 3.2 UBC INTER-STORY DRIFT INDICES**

| Level | $W_x$ (kips) | $H_x$ (ft) | $F_x$ (kips) |
|---|---|---|---|
| Level Roof | 193.7 | 70.5 | 43.5 |
| Level 6 | 232.5 | 59.4 | 44.0 |
| Level 5 | 232.5 | 48.2 | 35.7 |
| Level 4 | 232.5 | 37.1 | 27.4 |
| Level 3 | 232.5 | 25.9 | 19.2 |
| Level 2 | 232.5 | 14.8 | 10.9 |
| Total | | | 180.7 |

**TABLE 3.3 ATC LATERAL FORCE DISTRIBUTION**

| Level | Peak Displacement (in) | Peak Inter-Story Drift Index (%) |
|---|---|---|
| Level Roof | 0.90 | 0.38 |
| Level 6 | 0.80 | 0.56 |
| Level 5 | 0.65 | 0.56 |
| Level 4 | 0.50 | 0.56 |
| Level 3 | 0.35 | 0.60 |
| Level 2 | 0.19 | 0.54 |

**TABLE 3.4 ATC INTER-STORY DRIFT INDICES**

| Level | $W_x$ (kips) | $H_x$ (ft) | $F_x$ (kips) |
|---|---|---|---|
| Level Roof | 193.7 | 70.5 | 24.5 |
| Level 6 | 232.5 | 59.4 | 24.8 |
| Level 5 | 232.5 | 48.2 | 20.1 |
| Level 4 | 232.5 | 37.1 | 15.4 |
| Level 3 | 232.5 | 25.9 | 10.8 |
| Level 2 | 232.5 | 14.8 | 6.2 |
| Total | | | 101.8 |

**TABLE 3.5 SEAOC LATERAL FORCE DISTRIBUTION**

| Level | Peak Displacement (in) | Inter-Story Drift Index (%) |
|---|---|---|
| Level Roof | 0.51 | 0.05 |
| Level 6 | 0.45 | 0.06 |
| Level 5 | 0.37 | 0.07 |
| Level 4 | 0.28 | 0.07 |
| Level 3 | 0.19 | 0.06 |
| Level 2 | 0.11 | 0.06 |

**TABLE 3.6 SEAOC INTER-STORY DRIFT INDICES**

| Level | Shear Link | Brace | $V_p$ (kips) | $1.5P_r$ (kips) | $\frac{f_a}{F_a}$ |
|---|---|---|---|---|---|
| 2 | W18×40 | 8×6×0.375 | 114 | 216 | 0.86 |
| 4 | W18×35 | 8×6×0.375 | 108 | 233 | 0.60 |
| 6 | W16×31 | 8×6×0.313 | 88 | 189 | 0.60 |

$V_p$ = web shear yielding capacity of the link

$$P_r = \frac{V_p}{\cos\alpha} \quad ; \quad \frac{f_a}{F_a} = \frac{\text{actual stress}}{\text{allowable stress}}$$

**TABLE 3.7 SEAOC ECCENTRIC BRACE DESIGN FORCES**

| | UBC | ATC | SEAOC |
|---|---|---|---|
| Nominal Base Shear Coefficient ($C_s$) | 0.113 | 0.133 | 0.075 |
| Braced Frame Base Shear Coefficient | 1.25*0.113 = 0.141 | 0.9*0.133 = 0.120 | 0.9*0.075 = 0.068 |
| Moment Frames Base Shear Coefficient | 0.25*0.113 = 0.028 | 0.25*0.133 = 0.033 | 0.25*0.075 = 0.019 |
| Total Base Shear Coefficient ($C_t$) | 0.169 | 0.153 | 0.087 |
| $C_t$ Extrapolated to Yield Level ($C_{ty}$) | 0.211 | 0.153 | 0.109 |

**TABLE 3.8 YIELD LEVEL BASE SHEAR COEFFICIENTS**

| | Roof | 6th | 5th | 4th | 3rd | 2nd |
|---|---|---|---|---|---|---|
| Roof | 6.79 | 5.29 | 3.88 | 2.70 | 1.70 | 0.89 |
| 6th | 5.29 | 4.86 | 3.65 | 2.60 | 1.67 | 0.89 |
| 5th | 3.88 | 3.65 | 3.38 | 2.49 | 1.64 | 0.89 |
| 4th | 2.70 | 2.60 | 2.49 | 2.35 | 1.61 | 0.89 |
| 3rd | 1.70 | 1.67 | 1.64 | 1.61 | 1.53 | 0.90 |
| 2nd | 0.89 | 0.89 | 0.89 | 0.89 | 0.90 | 0.85 |

**TABLE 4.1 PROTOTYPE ANALYTICAL FLEXIBILITY MATRIX ($\times 10^{-3}$ inch/kip)**

| | Roof | 6th | 5th | 4th | 3rd | 2nd |
|---|---|---|---|---|---|---|
| Roof | 988.4 | -1171.9 | 61.1 | 63.9 | 32.3 | 27.1 |
| 6th | -1171.9 | 2500.2 | -1405.0 | 52.8 | 23.5 | 0.1 |
| 5th | 61.1 | -1405.0 | 2970.1 | -1740.9 | 114.8 | -1.5 |
| 4th | 63.9 | 52.8 | -1740.9 | 3417.7 | -2000.1 | 239.8 |
| 3rd | 32.3 | 23.5 | 114.8 | -2000.1 | 3836.2 | -2146.2 |
| 2nd | 27.1 | 0.1 | -1.5 | 239.8 | -2146.2 | 3170.9 |

**TABLE 4.2 PROTOTYPE ANALYTICAL STIFFNESS MATRIX (kip/inch)**

| Mode | 1st | 2nd | 3rd | 4th | 5th | 6th |
|---|---|---|---|---|---|---|
| Period (sec) | 0.556 | 0.201 | 0.111 | 0.080 | 0.065 | 0.054 |
| Mode Shapes | | | | | | |
| Roof | 1.00 | 1.00 | 0.93 | 0.72 | 0.33 | -0.03 |
| 6th | 0.88 | 0.38 | -0.35 | -1.00 | -0.82 | -0.17 |
| 5th | 0.72 | -0.34 | -1.00 | -0.12 | 1.00 | -0.48 |
| 4th | 0.54 | -0.82 | -0.41 | 0.85 | -0.37 | 0.86 |
| 3rd | 0.37 | -0.94 | 0.65 | 0.14 | -0.56 | -1.00 |
| 2nd | 0.20 | -0.70 | 1.00 | -0.75 | 0.63 | 0.58 |

**TABLE 4.3 PROTOTYPE ANALYTICAL NATURAL PERIODS AND MODE SHAPES**

| | Roof | 6th | 5th | 4th | 3rd | 2nd |
|---|---|---|---|---|---|---|
| Roof | 1095.0 | -1324.9 | 67.1 | 128.7 | 2.1 | 47.4 |
| 6th | -1324.9 | 2869.8 | -1648.1 | 47.4 | 68.8 | -62.0 |
| 5th | 67.1 | -1648.1 | 3523.5 | -2099.6 | 107.1 | 110.8 |
| 4th | 128.7 | 47.4 | -2099.6 | 3853.1 | -2112.6 | 155.6 |
| 3rd | 2.1 | 68.8 | 107.1 | -2112.6 | 4100.3 | -2311.6 |
| 2nd | 47.4 | -62.0 | 110.8 | 155.6 | -2311.6 | 3462.4 |

**TABLE 4.4 PROTOTYPE EXPERIMENTAL STIFFNESS MATRIX (kip/inch) [29]**

| Mode | 1st | 2nd | 3rd | 4th | 5th | 6th |
|---|---|---|---|---|---|---|
| Period (sec) | 0.548 | 0.193 | 0.106 | 0.075 | 0.060 | 0.052 |
| Mode Shapes | | | | | | |
| Roof | 1.00 | 1.00 | 0.90 | 0.71 | 0.32 | -0.04 |
| 6th | 0.88 | 0.36 | -0.33 | -1.00 | -0.81 | 0.22 |
| 5th | 0.72 | -0.33 | -0.97 | -0.10 | 1.00 | -0.62 |
| 4th | 0.55 | -0.80 | -0.43 | 0.79 | -0.31 | 0.97 |
| 3rd | 0.38 | -0.91 | 0.65 | 0.17 | -0.69 | -1.00 |
| 2nd | 0.21 | -0.68 | 1.00 | -0.71 | 0.73 | 0.55 |

**TABLE 4.5 PROTOTYPE EXPERIMENTAL NATURAL PERIODS AND MODE SHAPES**

| | NATURAL PERIODS (secs) | | | DAMPING RATIO (%) | |
|---|---|---|---|---|---|
| Method | $T_1$ | $T_2$ | $T_3$ | $\xi_1$ | $\xi_2$ |
| Free Vibration | 0.565 | | | 0.36 | |
| Forced Vibration | 0.568 | 0.201 | | 0.35 | 0.31 |
| Unit Loading | 0.548 | 0.193 | 0.106 | | |
| PSD Pulse #1 | 0.550 | | | 1.25 | |

**TABLE 4.6 PROTOTYPE NATURAL PERIODS AND DAMPING RATIOS [17]**

| PARAMETER | MODEL/PROTOTYPE | |
|---|---|---|
| LENGTH | L | 0.305 |
| TIME | $\sqrt{L}$ | 0.552 |
| MASS | $L^2$ | 0.093 |
| DISPLACEMENT | L | 0.305 |
| VELOCITY | $\sqrt{L}$ | 0.552 |
| ACCELERATION | 1 | |
| STRESS | 1 | |
| STRAIN | 1 | |
| FORCE | $L^2$ | 0.093 |
| MOMENT | $L^3$ | 0.028 |
| ENERGY | $L^3$ | 0.028 |
| AREA | $L^2$ | 0.093 |
| MOMENT OF INERTIA | $L^4$ | 0.0087 |

**TABLE 5.1 SIMILITUDE RELATIONSHIPS**

| Material | SSD*1 ($lb/y^3$) | Fraction*2 Weight |
|---|---|---|
| Cement | 592 | 1.00 |
| Water | 355 | 0.60 |
| Coarse Aggregate *3 | 891 | 1.51 |
| Fine Aggregate *4 | 1306 | 2.21 |

*1 Saturated Surface Dry Condition
*2 Fraction weight with respect to Cement
*3 Lightweight Coarse Aggregate
*4 Normalweight Fine Aggregate (sand)

**(a) MODEL CONCRETE MIX DESIGN**

| Material | Stress Level | | Prototype (ksi) | Model (ksi) |
|---|---|---|---|---|
| Concrete | $f_c'$ | Nominal | 3.00 | 3.00 |
| | | Measured | 4.17 | 4.00 |
| Steel WF Sections | $\sigma_y$ | Nominal | 36.0 | 50.0 |
| | | Measured | 43.0*1 | 46.0*2 |

*1 Column Sample Mean [9]
*2 Grade 50 X10

**(b) MECHANICAL CHARACTERISTICS OF THE PROTOTYPE AND THE MODEL**

**TABLE 5.2 MECHANICAL CHARACTERISTICS OF THE MODEL**

| Story | Prototype Brace | Nominal Area ($in^2$) | Similitude Area ($in^2$) | Model Brace | Measured Area ($in^2$) |
|---|---|---|---|---|---|
| 1st | 8×6×0.375 | 9.58 | 0.890 | 3×2×0.125 | 1.090 |
| 2nd | 8×6×0.375 | 9.58 | 0.890 | 3×2×0.125 | 1.090 |
| 3rd | 8×6×0.375 | 9.58 | 0.890 | 3×2×0.125 | 1.090 |
| 4th | 8×6×0.375 | 9.58 | 0.890 | 3×2×0.125 | 1.090 |
| 5th | 8×6×0.313 | 8.11 | 0.753 | 3×2×0.083 | 0.776 |
| 6th | 8×6×0.313 | 8.11 | 0.753 | 3×2×0.075 | 0.749 |

**TABLE 5.3 ECCENTRIC BRACE SIZES**

| Floor | Prototype Weight As-Built (kips) | Similitude Scaled Weight (kips) | Model Weight As Built (kips) |
|---|---|---|---|
| Roof | 166.9 | 15.52 | 15.52 |
| 6th | 195.5 | 18.18 | 18.16 |
| 5th | 195.5 | 18.18 | 18.14 |
| 4th | 195.5 | 18.18 | 18.08 |
| 3rd | 195.5 | 18.18 | 18.10 |
| 2nd | 205.2 | 19.09 | 19.08 |
| Total | 1154 | 107.3 | 107.1 |

**TABLE 5.4 MODEL FLOOR WEIGHT DISTRIBUTION**

| SECTION | | W18×40 | W18×35 | W16×31 |
|---|---|---|---|---|
| PROTOTYPE | D | 17.90 | 17.70 | 15.88 |
| | $B_f$ | 6.02 | 6.00 | 5.53 |
| | $T_f$ | 0.53 | 0.43 | 0.44 |
| | $T_w$ | 0.32 | 0.30 | 0.28 |
| | $D_w$ | 16.85 | 16.85 | 15.00 |
| | $I_{xx}$ | 612 | 510 | 375 |
| | A | 11.8 | 10.3 | 9.12 |
| | $A_w$ | 5.64 | 5.31 | 4.37 |
| | $Z_{xx}$ | 78.4 | 66.5 | 54.0 |
| | $\sigma_y$ | 46 | 46 | 46 |
| | $V_p$ | 150 | 141 | 116 |
| SCALED PROTOTYPE | D | 5.46 | 5.40 | 4.84 |
| | $B_f$ | 1.83 | 1.83 | 1.69 |
| | $T_f$ | 0.16 | 0.13 | 0.13 |
| | $T_w$ | 0.10 | 0.09 | 0.08 |
| | $D_w$ | 5.14 | 5.14 | 4.57 |
| | $I_{xx}$ | 5.28 | 4.40 | 3.24 |
| | A | 1.10 | 0.96 | 0.85 |
| | $A_w$ | 0.52 | 0.49 | 0.41 |
| | $Z_{xx}$ | 2.22 | 1.89 | 1.53 |
| | $V_p$ | 13.9 | 13.1 | 10.8 |
| MODEL | D | 5.40 | 5.40 | 4.84 |
| | $B_f$ | 1.66 | 1.77 | 1.77 |
| | $T_f$ | 0.19 | 0.14 | 0.14 |
| | $T_w$ | 0.11 | 0.11 | 0.09 |
| | $D_w$ | 5.03 | 5.13 | 4.57 |
| | $I_{xx}$ | 5.29 | 4.49 | 3.34 |
| | A | 1.14 | 1.01 | 0.88 |
| | $A_w$ | 0.59 | 0.59 | 0.44 |
| | $Z_{xx}$ | 2.27 | 1.95 | 1.58 |
| | $\sigma_{yw}$ | 46 | 46 | 53 |
| | $V_p$ | 15.8 | 15.8 | 13.3 |

All units : in, $in^2$, $in^3$, $in^4$, kips and ksi

**TABLE 5.5 SHEAR LINK SECTION PROPERTIES**

| | Roof | 6th | 5th | 4th | 3rd | 2nd |
|---|---|---|---|---|---|---|
| Roof | 22.8 | 17.6 | 12.7 | 8.8 | 5.6 | 2.8 |
| 6th | 17.6 | 16.2 | 12.0 | 8.5 | 5.5 | 2.8 |
| 5th | 12.7 | 12.0 | 11.0 | 8.2 | 5.4 | 2.8 |
| 4th | 8.8 | 8.5 | 8.2 | 7.7 | 5.3 | 2.8 |
| 3rd | 5.6 | 5.5 | 5.4 | 5.3 | 5.0 | 2.9 |
| 2nd | 2.8 | 2.8 | 2.8 | 2.8 | 2.9 | 2.6 |

**(a) ANALYTICAL FLEXIBILITY MATRIX ($\times 10^{-3}$ inch/kip)**

| | Roof | 6th | 5th | 4th | 3rd | 2nd |
|---|---|---|---|---|---|---|
| Roof | 276.9 | -330.0 | 23.9 | 14.9 | 6.6 | 8.0 |
| 6th | -330.0 | 728.6 | -463.5 | 71.0 | -7.8 | 2.0 |
| 5th | 23.9 | -463.5 | 1016.2 | -648.5 | 79.5 | -11.3 |
| 4th | 14.9 | 71.0 | -648.5 | 1159.4 | -710.0 | 149.0 |
| 3rd | 6.6 | -7.8 | 79.5 | -710.0 | 1340.7 | -815.1 |
| 2nd | 8.0 | 2.0 | -11.3 | 149.0 | -815.1 | 1134.5 |

**(b) ANALYTICAL STIFFNESS MATRIX (kip/inch)**

| Mode | 1st | 2nd | 3rd | 4th | 5th | 6th |
|---|---|---|---|---|---|---|
| Period (sec) | 0.308 | 0.111 | 0.062 | 0.045 | 0.034 | 0.027 |
| Mode Shapes | | | | | | |
| Roof | 1.00 | 1.00 | 1.00 | 1.00 | 1.00 | 1.00 |
| 6th | 0.95 | 0.38 | -0.50 | -1.62 | -3.17 | -6.07 |
| 5th | 0.76 | -0.40 | -1.11 | 0.07 | 4.95 | 17.1 |
| 4th | 0.57 | -0.89 | -0.43 | 1.22 | 2.36 | -30.1 |
| 3rd | 0.40 | -0.98 | 0.81 | 0.01 | -2.71 | 35.7 |
| 2nd | 0.22 | -0.72 | 1.17 | -1.05 | 3.47 | -23.1 |

**(c) ANALYTICAL NATURAL PERIODS AND MODE SHAPES**

**TABLE 6.1 ANALYTICAL DYNAMIC CHARACTERISTICS OF THE MODEL**

| | Roof | 6th | 5th | 4th | 3rd | 2nd |
|---|---|---|---|---|---|---|
| Roof | 9.05 | 6.95 | 5.45 | 4.10 | 3.15 | 1.95 |
| 6th | 6.95 | 6.95 | 5.45 | 4.10 | 3.15 | 1.95 |
| 5th | 5.45 | 5.45 | 4.10 | 3.15 | 3.15 | 1.95 |
| 4th | 4.10 | 4.10 | 4.10 | 4.10 | 3.15 | 1.95 |
| 3rd | 3.15 | 3.15 | 3.15 | 3.15 | 3.15 | 1.95 |
| 2nd | 1.95 | 1.95 | 1.95 | 1.95 | 1.95 | 1.95 |

**(a) ANALYTICAL FLEXIBILITY MATRIX ($\times 10^{-3}$ inch/kip)**

| | Roof | 6th | 5th | 4th | 3rd | 2nd |
|---|---|---|---|---|---|---|
| Roof | 476.2 | -476.2 | 0.0 | 0.0 | 0.0 | 0.0 |
| 6th | -476.2 | 1142.9 | -666.7 | 0.0 | 0.0 | 0.0 |
| 5th | 0.0 | -666.7 | 1407.4 | -740.7 | 0.0 | 0.0 |
| 4th | 0.0 | 0.0 | -740.7 | 1793.4 | -1052.7 | 0.0 |
| 3rd | 0.0 | 0.0 | 0.0 | -1052.7 | 1886.0 | -833.3 |
| 2nd | 0.0 | 0.0 | 0.0 | 0.0 | -833.3 | 1346.1 |

**(b) ANALYTICAL STIFFNESS MATRIX (kip/inch)**

| Mode | 1st | 2nd | 3rd | 4th | 5th | 6th |
|---|---|---|---|---|---|---|
| Period (sec) | 0.210 | 0.076 | 0.047 | 0.036 | 0.029 | 0.024 |
| Mode Shapes | | | | | | |
| Roof | 1.00 | 1.00 | 1.00 | 1.00 | 1.00 | 1.00 |
| 6th | 0.99 | 0.46 | -0.58 | -1.72 | -3.09 | -5.17 |
| 5th | 0.87 | -0.20 | -1.02 | 0.10 | 3.90 | 15.7 |
| 4th | 0.71 | -0.71 | -0.24 | 1.58 | -1.13 | -34.0 |
| 3rd | 0.58 | -0.86 | 0.50 | 0.43 | -2.37 | 35.4 |
| 2nd | 0.38 | -0.72 | 0.95 | -1.83 | 2.22 | -14.7 |

**(c) ANALYTICAL NATURAL PERIODS AND MODE SHAPES**

**TABLE 6.2 ANALYTICAL DYNAMIC CHARACTERISTICS OF THE PURE SHEAR BUILDING**

| | Roof | 6th | 5th | 4th | 3rd | 2nd |
|---|---|---|---|---|---|---|
| Roof | 24.196 | 18.706 | 13.922 | 9.421 | 6.804 | 3.440 |
| 6th | 19.852 | 17.165 | 13.059 | 9.223 | 6.516 | 3.419 |
| 5th | 14.345 | 13.029 | 11.548 | 8.463 | 6.079 | 3.203 |
| 4th | 9.882 | 8.946 | 8.264 | 7.224 | 5.375 | 3.020 |
| 3rd | 6.782 | 6.200 | 5.597 | 5.382 | 5.052 | 2.916 |
| 2nd | 3.838 | 3.648 | 3.140 | 3.147 | 2.975 | 2.690 |

**(a) EXPERIMENTAL FLEXIBILITY MATRIX ($x10^{-3}$ inch/kip)**

| | Roof | 6th | 5th | 4th | 3rd | 2nd |
|---|---|---|---|---|---|---|
| Roof | 404.6 | -542.7 | 92.1 | 41.5 | -46.2 | 69.1 |
| 6th | -542.7 | 1144.5 | -680.8 | 84.9 | 58.8 | -143.3 |
| 5th | 92.1 | -680.8 | 1316.6 | -939.3 | 117.5 | 172.0 |
| 4th | 41.5 | 84.9 | -939.3 | 1743.7 | -881.6 | -89.1 |
| 3rd | -46.2 | -58.8 | 117.4 | -881.6 | 1355.8 | -636.3 |
| 2nd | 69.1 | -143.3 | 172.0 | -89.1 | -636.3 | 1064.1 |

**(b) EXPERIMENTAL STIFFNESS MATRIX (kip/inch)**

| Mode | 1st | 2nd | 3rd | 4th | 5th | 6th |
|---|---|---|---|---|---|---|
| Period (sec) | 0.322 | 0.103 | 0.057 | 0.039 | 0.030 | 0.025 |
| Mode Shapes | | | | | | |
| Roof | 1.00 | 1.00 | 1.00 | 1.00 | 1.00 | 1.00 |
| 6th | 0.94 | 0.37 | -0.34 | -1.50 | -2.06 | -4.43 |
| 5th | 0.75 | -0.37 | -1.39 | -0.16 | 1.48 | 10.4 |
| 4th | 0.55 | -0.88 | -0.44 | 1.01 | 0.45 | -14.17 |
| 3rd | 0.40 | -1.01 | 0.78 | 0.81 | -2.06 | 8.55 |
| 2nd | 0.23 | -0.79 | 1.26 | -1.52 | 1.74 | -0.83 |

**(c) EXPERIMENTAL NATURAL PERIODS AND MODE SHAPES**

**TABLE 6.3 EXPERIMENTAL DYNAMIC CHARACTERISTICS OF THE MODEL FROM STATIC FLEXIBILITY TESTS**

| Mode | 1st | 2nd | 3rd |
|---|---|---|---|
| Period (sec) | 0.316 | 0.105 | 0.057 |
| Mode Shapes | | | |
| Roof | 1.00 | 1.00 | 1.00 |
| 6th | 0.88 | 0.39 | -0.42 |
| 5th | 0.71 | -0.30 | -1.07 |
| 4th | 0.55 | -0.74 | -0.40 |
| 3rd | 0.41 | -0.89 | 0.66 |
| 2nd | 0.26 | -0.71 | 1.00 |

**TABLE 6.4 EXPERIMENTAL DYNAMIC CHARACTERISTICS OF THE MODEL FROM FREE VIBRATION TESTS**

| | $T_1$ (secs) | $T_2$ (secs) | $T_3$ (secs) | $\xi_1$ (%) | $\xi_2$ (%) |
|---|---|---|---|---|---|
| Free Vibration | 0.316 | 0.105 | 0.057 | 0.7 | 0.5 |
| Forced Vibration | 0.320 | 0.106 | | 0.7 | 0.9 |
| Flexibility Test | 0.322 | 0.103 | 0.057 | | |
| Analytical DRAIN-2DX | 0.308 | 0.111 | 0.061 | | |

**TABLE 6.5 SUMMARY OF THE DYNAMIC CHARACTERISTICS OF THE MODEL**

| | | Free Vibration | | | Forced Vibration | | |
|---|---|---|---|---|---|---|---|
| Mode | | 1st | 2nd | 3rd | 1st | 2nd | 3rd |
| **Prototype** | $T_i$ (sec) | 0.565 | - | - | 0.568 | 0.201 | - |
| | $\xi_i$ (%) | 0.35 | - | - | 0.35 | 0.31 | - |
| **Model** | $T_i$ (sec) | 0.572 | 0.190 | 0.103 | 0.580 | 0.192 | - |
| | $\xi_i$ (%) | 0.7 | 0.5 | - | 0.7 | 0.9 | - |

**TABLE 6.6 COMPARISON OF THE DYNAMIC CHARACTERISTICS OF THE PROTOTYPE AND THE MODEL**

| TEST NO. | FILENAME | TABLE MOTION | PA*1 (%G) | $V_b^{max}$ (kips) | IDI*2 (%) | RDI*3 (%) | REMARKS |
|---|---|---|---|---|---|---|---|
| 1 | 850415.01 | MO | 16.2 | 30.7 | 0.44 | 0.23 | Preliminary |
| 2 | 850419.01 | FR.V*4 | | | | | Dynamic |
| 3 | 850419.02 | FLEX*5 | | | | | Testing |
| 4 | 850424.02 | FO.V*6 | | | | | |
| 5 | 850514.01 | MO | 9.51 | 17.2 | 0.13 | 0.10 | Elastic Limit |
| 6 | 850514.02 | TAFT | 3.0 | 7.9 | 0.07 | 0.11 | State Testing |
| 7 | 850514.03 | TAFT | 7.8 | 16.9 | 0.12 | 0.11 | |
| 8 | 850514.04 | TAFT | 9.9 | 31.2 | 0.22 | 0.19 | |
| 9 | 850514.05 | FR.V | | | | | |
| 10 | 850514.06 | MO | 7.8 | 15.1 | 0.11 | 0.09 | |
| 11 | 850514.07 | MO | 7.0 | 11.9 | 0.09 | 0.07 | |
| 12 | 850516.01 | MO | 14.3 | 25.1 | 0.20 | 0.17 | |
| 13 | 850517.01 | MO | 17.6 | 37.2 | 0.28 | 0.24 | Damageability |
| 14 | 850517.02 | TAFT | 21.4 | 50.7 | 0.42 | 0.36 | Limit State |
| 15 | 850517.03 | FR.V | | | | | Testing |
| 16 | 850518.01 | TAFT | 27.0 | 52.5 | 0.48 | 0.35 | |
| 17 | 850518.02 | MO | 27.5 | 57.0 | 0.58 | 0.40 | |
| 18 | 850518.03 | FR.V | | | | | |
| 19 | 850520.01 | TAFT | 33.8 | 64.1 | 0.67 | 0.45 | |
| 20 | 850520.02 | FR.V | | | | | |
| 21 | 850520.03 | TAFT | 40.3 | 82.7 | 1.04 | 0.62 | Collapse Limit |
| 22 | 850520.04 | FR.V | | | | | State Testing |
| 23 | 850520.05 | TAFT | 57.3 | 90.6 | 1.25 | 0.66 | |
| 24 | 850520.06 | FR.V | | | | | |
| 25 | 850522.01 | TAFT | 9.4 | 20.9 | 0.18 | 0.16 | |
| 26 | 850522.02 | TAFT | 66.3 | 91.6 | 1.28 | 0.72 | |
| 27 | 850522.03 | PACO*7 | 7.7 | 10.8 | 0.11 | 0.08 | Post-Buckling |
| 28 | 850522.04 | PACO*7 | 21.8 | 48.4 | 0.54 | 0.38 | Testing |
| 29 | 850522.06 | PACO | 12.8 | 17.1 | 0.17 | 0.10 | |
| 30 | 850522.07 | PACO | 96.0 | 70.9 | 0.98 | 0.63 | |
| 31 | 850522.08 | FR.V | | | | | |
| 32 | 850523.01 | SINE | 24.2 | 46.1 | 0.47 | 0.31 | |
| 33 | 850523.02 | SINE | 54.7 | 62.6 | 0.79 | 0.43 | |
| 34 | 850523.03 | SINE | 69.5 | 75.6 | 1.14 | 0.65 | |
| 35 | 850523.04 | FR.V | | | | | |
| 36 | 850524.02 | FR.V | | | | | |

*1 PA = Peak Table Acceleration

*2 IDI = Maximum Inter-story Drift Index

*3 RDI = Maximum Roof Drift Index

*4 Free Vibration Test

*5 Flexibility Test

*6 Forced Vibration Test

*7 Real-Time Pacoima Record

**TABLE 7.1 MODEL TEST SCHEDULE**

| | Natural Period (sec) | | | Damping Factor (%) *1 | | |
|---|---|---|---|---|---|---|
| | 1 st | 2 nd | 3 rd | 1 st | 2 nd | 3 rd |
| DMRSF *2 | 0.672 | 0.240 | 0.139 | 0.7 | 0.4 | 0.3 |
| Before MO 9.5%g *2 | 0.316 | 0.105 | 0.057 | 0.7 | 0.5 | ---- |
| After Taft 21.4%g | 0.326 | 0.106 | 0.058 | 2.2 | 1.1 | ---- |
| After MO 27.5%g | 0.326 | 0.107 | 0.058 | 2.2 | 1.3 | ---- |
| After Taft 33.8%g | 0.326 | 0.107 | 0.058 | 2.3 | 1.3 | ---- |
| After Taft 57.3%g | 0.333 | 0.108 | 0.060 | 2.3 | 1.3 | ---- |
| Before Sine 24.2%g | 0.333 | 0.108 | 0.060 | 2.3 | 1.3 | ---- |
| After Sine 69.5%g | 0.333 | 0.111 | 0.060 | 2.3 | 1.3 | ---- |
| After Sine 69.5%g *2 | 0.333 | 0.111 | 0.060 | 2.3 | 1.3 | ---- |

*1 Free Vibration Tests

*2 Earthquake Simulator Locked in Position

**TABLE 8.1 VARIATION IN THE DYNAMIC CHARACTERISTICS OF THE MODEL**

| Floor/Story | 6 | 5 | 4 | 3 | 2 | 1 |
|---|---|---|---|---|---|---|
| Lateral Displ (in.) | 0.28 | 0.24 | 0.21 | 0.17 | 0.11 | 0.07 |
| Time (sec) | 8.67 | 8.67 | 8.67 | 8.67 | 8.67 | 8.67 |
| Inter-story Drift (in.) | 0.043 | 0.033 | 0.044 | 0.052 | 0.043 | 0.072 |
| Inter-story Drift Index (%) | 0.11 | 0.08 | 0.11 | 0.13 | 0.11 | 0.13 |
| Time (sec) | 8.66 | 8.68 | 8.66 | 8.66 | 8.66 | 8.67 |
| Story Shear (k) | -4.7 | 7.9 | 11.3 | 14.8 | 16.2 | 17.0 |
| Story Shear/Total Wt.(%) | 4.4 | 7.4 | 10.6 | 13.8 | 15.1 | 15.9 |
| Time (sec) | 8.48 | 8.65 | 8.65 | 8.66 | 8.66 | 8.67 |
| Inertia Force (k) | 4.4 | -4.1 | -3.3 | -2.5 | 2.1 | -1.8 |
| Time (sec) | 8.65 | 8.65 | 8.66 | 8.67 | 8.44 | 2.94 |
| Overturn. Moment (k-in) | 173 | 499 | -965 | -1525 | -2154 | -3021 |
| Time (sec) | 8.48 | 8.48 | 8.65 | 8.65 | 8.66 | 8.66 |

**TABLE 8.2 TAFT-08 TEST RESPONSE ENVELOPES**

| Floor/Story | 6 | 5 | 4 | 3 | 2 | 1 |
|---|---|---|---|---|---|---|
| Lateral Displ (in.) | 0.89 | 0.77 | 0.65 | 0.48 | 0.37 | 0.24 |
| Time (sec) | 8.85 | 8.85 | 8.86 | 8.86 | 8.86 | 8.86 |
| Inter-story Drift (in.) | 0.121 | -0.145 | 0.164 | -0.126 | -0.128 | 0.245 |
| Inter-story Drift Index (%) | 0.30 | 0.36 | 0.40 | 0.31 | 0.32 | 0.45 |
| Time (sec) | 8.85 | 8.66 | 8.86 | 8.67 | 8.68 | 8.86 |
| Story Shear (k) | -13.5 | -23.2 | -35.1 | -42.8 | 47.9 | 52.5 |
| Story Shear/Total Wt.(%) | 12.6 | 21.6 | 32.7 | 40.0 | 44.7 | 49.1 |
| Time (sec) | 8.65 | 8.65 | 8.66 | 8.66 | 8.85 | 8.85 |
| Inertia Force (k) | 12.2 | 11.7 | 9.5 | -7.4 | -7.3 | -7.2 |
| Time (sec) | 8.65 | 8.66 | 8.67 | 8.87 | 5.63 | 5.62 |
| Overturn. Moment (k-in) | 497 | 1458 | 2792 | -4400 | -6212 | -8813 |
| Time (sec) | 8.65 | 8.65 | 8.66 | 8.84 | 8.84 | 8.85 |

**TABLE 8.3 TAFT-27 TEST RESPONSE ENVELOPES**

| Floor/Story | 6 | 5 | 4 | 3 | 2 | 1 |
|---|---|---|---|---|---|---|
| Lateral Displ (in.) | 1.73 | 1.58 | 1.37 | 1.17 | 0.98 | 0.69 |
| Time (sec) | 8.54 | 8.54 | 8.54 | 8.55 | 8.55 | 8.55 |
| Inter-story Drift (in.) | -0.203 | 0.249 | 0.222 | 0.213 | 0.290 | 0.691 |
| Inter-story Drift Index (%) | 0.50 | 0.61 | 0.54 | 0.52 | 0.71 | 1.28 |
| Time (sec) | 8.30 | 4.53 | 8.51 | 4.54 | 8.55 | 8.55 |
| Story Shear (k) | -22.2 | -36.4 | 54.2 | -66.1 | 80.6 | 90.6 |
| Story Shear/Total Wt.(%) | 20.7 | 34.0 | 50.6 | 61.7 | 75.2 | 84.5 |
| Time (sec) | 8.68 | 8.29 | 4.53 | 8.31 | 8.54 | 8.54 |
| Inertia Force (k) | 19.9 | -18.0 | -15.7 | -17.0 | -17.6 | -15.3 |
| Time (sec) | 8.68 | 4.53 | 8.54 | 8.55 | 6.16 | 6.16 |
| Overturn. Moment (k-in) | 812 | 2311 | -4322 | -6722 | -9422 | -13280 |
| Time (sec) | 8.68 | 8.68 | 4.52 | 4.53 | 4.53 | 4.53 |

**TABLE 8.4 TAFT-57 TEST RESPONSE ENVELOPES**

| Floor/Story | 6 | 5 | 4 | 3 | 2 | 1 |
|---|---|---|---|---|---|---|
| Lateral Displ (in.) | 1.80 | 1.63 | 1.43 | 1.28 | 1.03 | 0.69 |
| Time (sec) | 4.55 | 4.55 | 8.56 | 8.56 | 8.56 | 8.56 |
| Inter-story Drift (in.) | 0.192 | -0.230 | 0.206 | 0.271 | 0.341 | 0.695 |
| Inter-story Drift Index (%) | 0.47 | 0.57 | 0.51 | 0.66 | 0.84 | 1.29 |
| Time (sec) | 5.71 | 8.31 | 4.53 | 4.55 | 8.55 | 8.56 |
| Story Shear (k) | 25.4 | 41.5 | 58.3 | 72.6 | 81.7 | -91.7 |
| Story Shear/Total Wt.(%) | 23.7 | 38.7 | 54.4 | 67.7 | 76.2 | 85.6 |
| Time (sec) | 5.71 | 5.71 | 4.53 | 4.54 | 4.55 | 8.35 |
| Inertia Force (k) | -22.5 | -19.2 | -16.1 | -17.7 | -18.5 | 15.5 |
| Time (sec) | 5.71 | 4.53 | 4.55 | 8.56 | 6.17 | 8.74 |
| Overturn. Moment (k-in) | -920 | -2566 | 4609 | -7171 | -10086 | -14217 |
| Time (sec) | 5.71 | 5.71 | 8.30 | 4.53 | 4.53 | 4.54 |

**TABLE 8.5 TAFT-66 TEST RESPONSE ENVELOPES**

| Floor/Story | 6 | 5 | 4 | 3 | 2 | 1 |
|---|---|---|---|---|---|---|
| Lateral Displ (in.) | 1.63 | 1.47 | 1.29 | 1.10 | 0.88 | 0.61 |
| Time (sec) | 5.73 | 5.73 | 5.73 | 5.74 | 5.74 | 5.74 |
| Inter-story Drift (in.) | 0.172 | -0.221 | -0.197 | 0.264 | -0.314 | 0.614 |
| Inter-story Drift Index (%) | 0.42 | 0.54 | 0.48 | 0.65 | 0.77 | 1.23 |
| Time (sec) | 5.73 | 5.97 | 5.97 | 5.77 | 5.96 | 5.74 |
| Story Shear (k) | -20.9 | -36.6 | -51.9 | -63.2 | 68.6 | 75.6 |
| Story Shear/Total Wt.(%) | 19.5 | 34.2 | 48.5 | 59.1 | 64.1 | 70.6 |
| Time (sec) | 5.97 | 5.97 | 5.96 | 5.96 | 5.71 | 5.73 |
| Inertia Force (k) | 18.7 | 17.3 | 14.4 | 14.1 | 14.7 | 13.0 |
| Time (sec) | 5.97 | 5.96 | 5.95 | 5.46 | 5.46 | 5.45 |
| Overturn. Moment (k-in) | 761 | 2194 | 4108 | 6372 | 8887 | 12464 |
| Time (sec) | 5.97 | 5.97 | 5.97 | 5.97 | 5.97 | 5.97 |

**TABLE 8.6 SINE-70 TEST RESPONSE ENVELOPES**

| TEST | $E_I$ *1 | $E_L$ *2 | $\frac{E_{L2}}{E_L}$ *3 | $\frac{E_{L3}}{E_L}$ *4 | Link L2 Behavior |
|---|---|---|---|---|---|
| TAFT-08 | 5 | 0 | 0.00 | 0.00 | Elastic |
| TAFT-27 | 47 | 13 | 0.70 | 0.15 | Inelastic Pre-Web Buckling |
| TAFT-57 | 426 | 403 | 0.79 | 0.17 | Inelastic Pre-Web Buckling |
| TAFT-66 | 579 | 549 | 0.72 | 0.22 | Inelastic Post-Web Buckling |
| SINE-70 | 497 | 385 | 0.62 | 0.33 | Inelastic Post-Web Buckling |

*1 $E_I$ = Input Energy (kip-in)

*2 $E_L$ = Energy Dissipated by Shear Links

*3 $E_{L2}$ = Energy Dissipated by Link L2

*4 $E_{L3}$ = Energy Dissipated by Link L3

**TABLE 9.1 SHEAR LINK ENERGY DISSIPATION**

| Participation Factor | Horizontal $\mathbf{L_{xi}}$ | Pitching $\mathbf{L_{\theta i}}$ |
|---|---|---|
| First Mode | 0.487 | 92.74 |
| Second Mode | -0.180 | 1.899 |
| Third Mode | 0.075 | 1.324 |

**TABLE 10.1 MODAL PARTICIPATION FACTORS**

# FIGURES

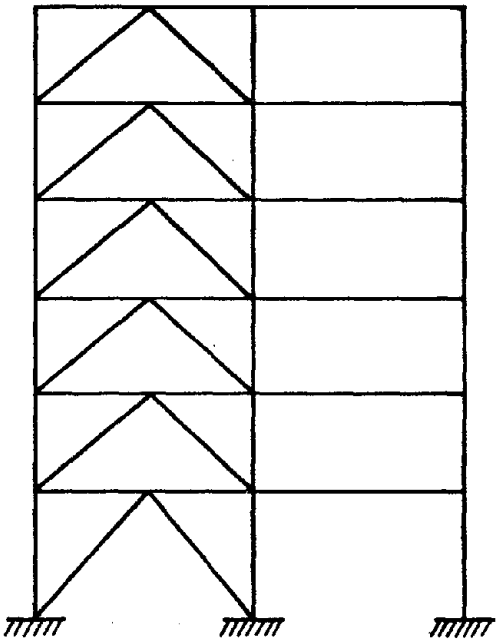

FIGURE 1.1 CONCENTRICALLY BRACED FRAME

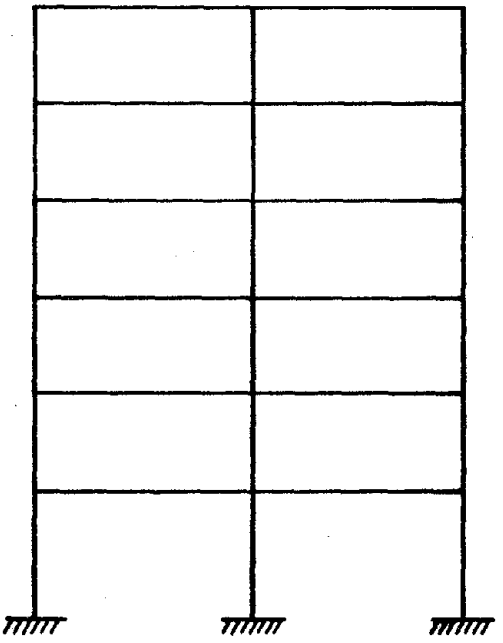

FIGURE 1.2 DUCTILE MOMENT-RESISTING SPACE FRAME

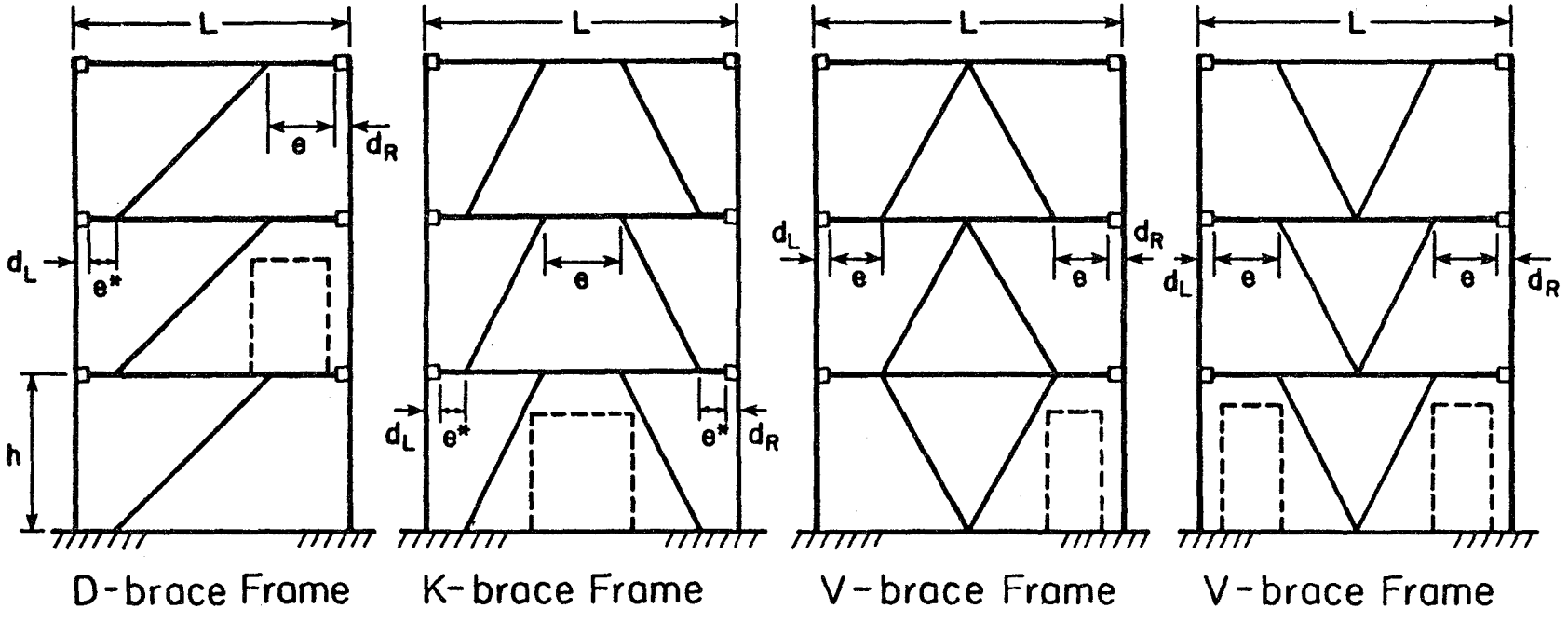


FIGURE 1.3 ECCENTRICALLY BRACED FRAMES [2]

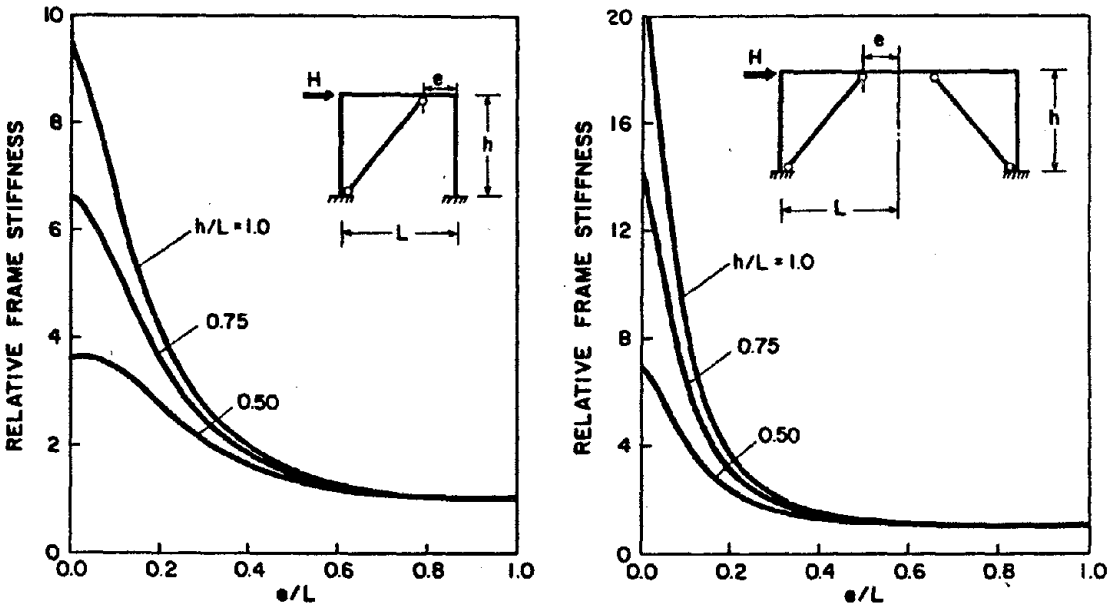


(a) D-Brace

(b) Split K-Brace

**FIGURE 1.4 VARIATION IN THE ELASTIC STIFFNESS OF TWO ECCENTRICALLY BRACED FRAMES [1]**

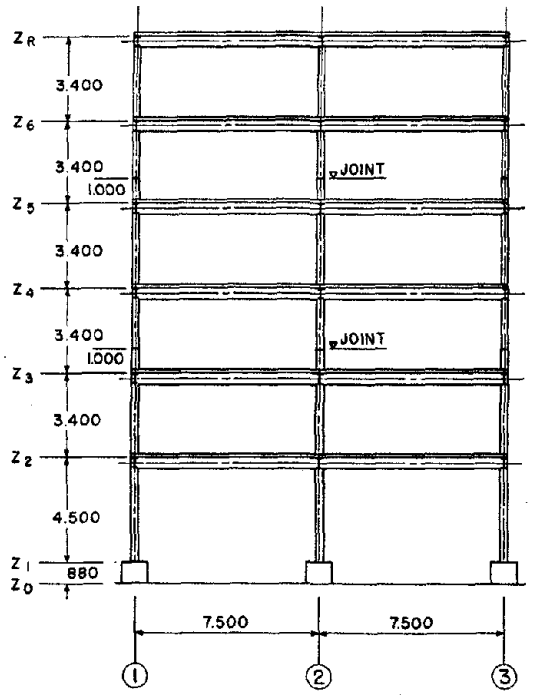


(a) Frames A and C

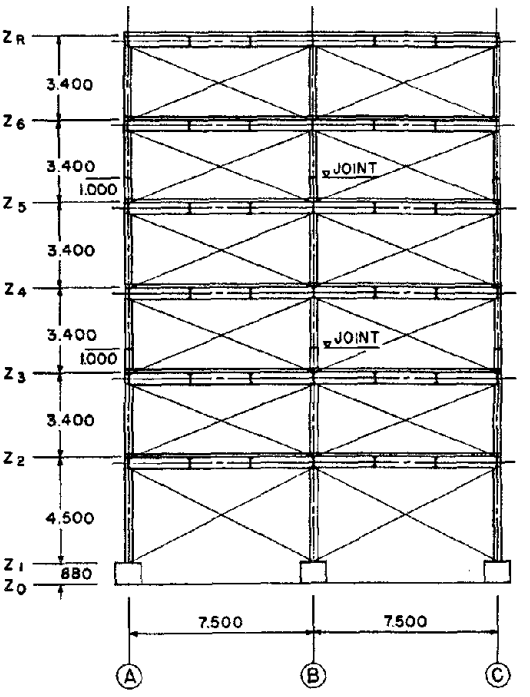


(b) Frame 1 and 3

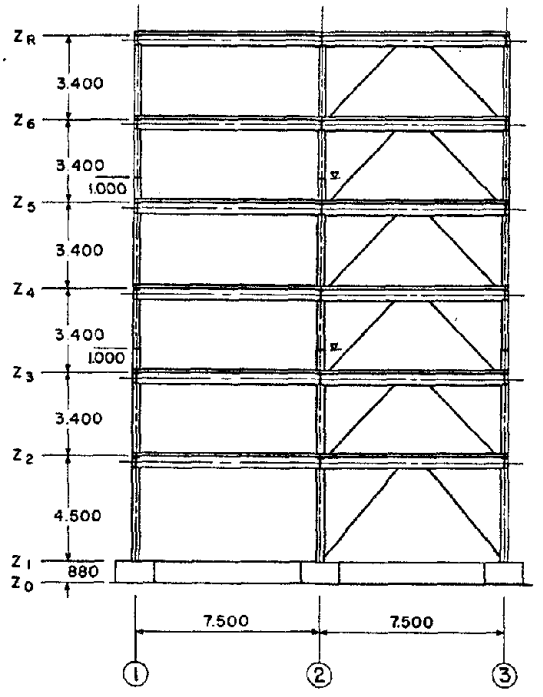


(c) Frame B

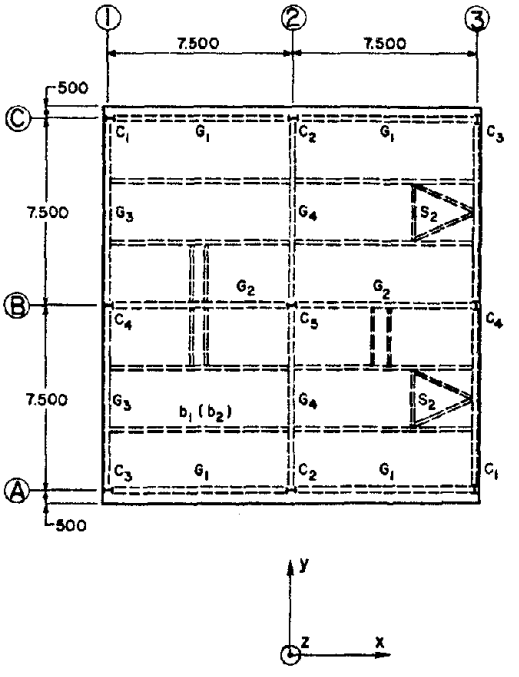


(d) Plan

FIGURE 2.1 PROTOTYPE PLAN AND ELEVATIONS

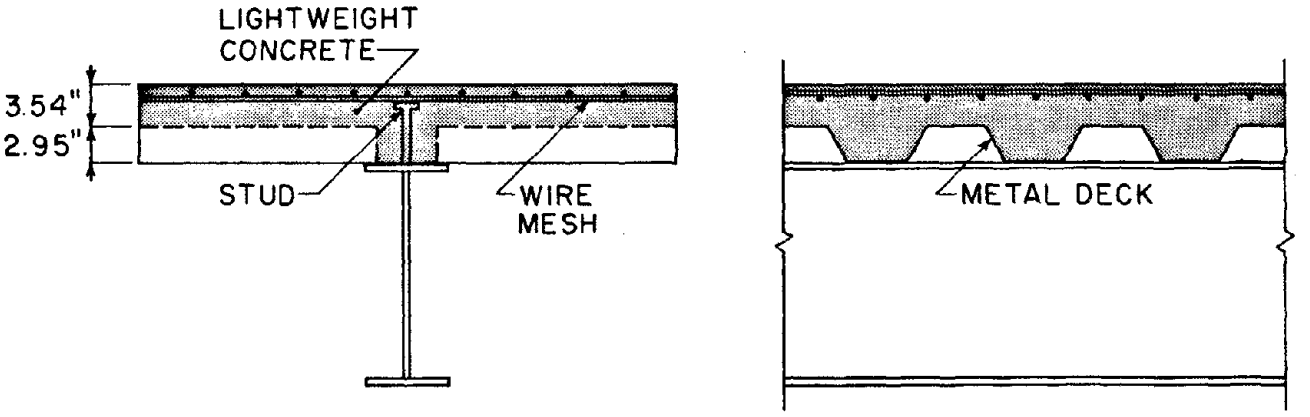


**FIGURE 2.2 COMPOSITE GIRDER CROSS SECTIONS (FRAME B)**

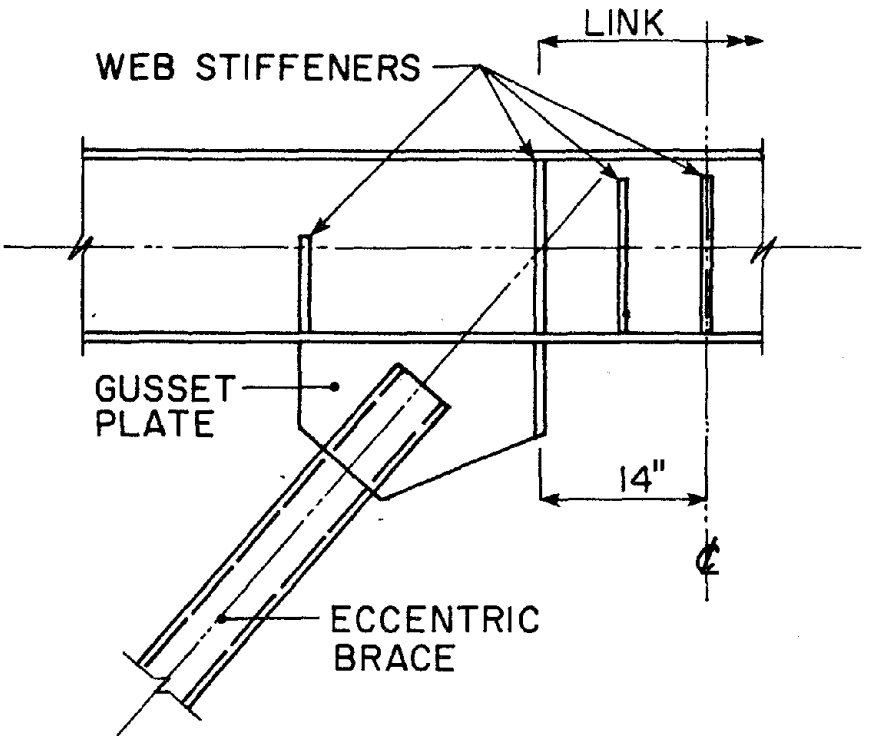


FIGURE 3.1 PROTOTYPE SHEAR LINK

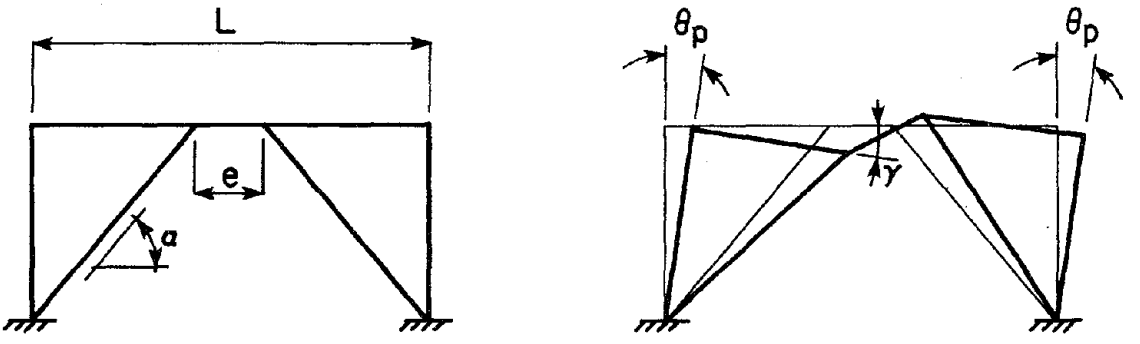


FIGURE 3.2 KINEMATICS OF THE ECCENTRICALLY K-BRACED FRAME

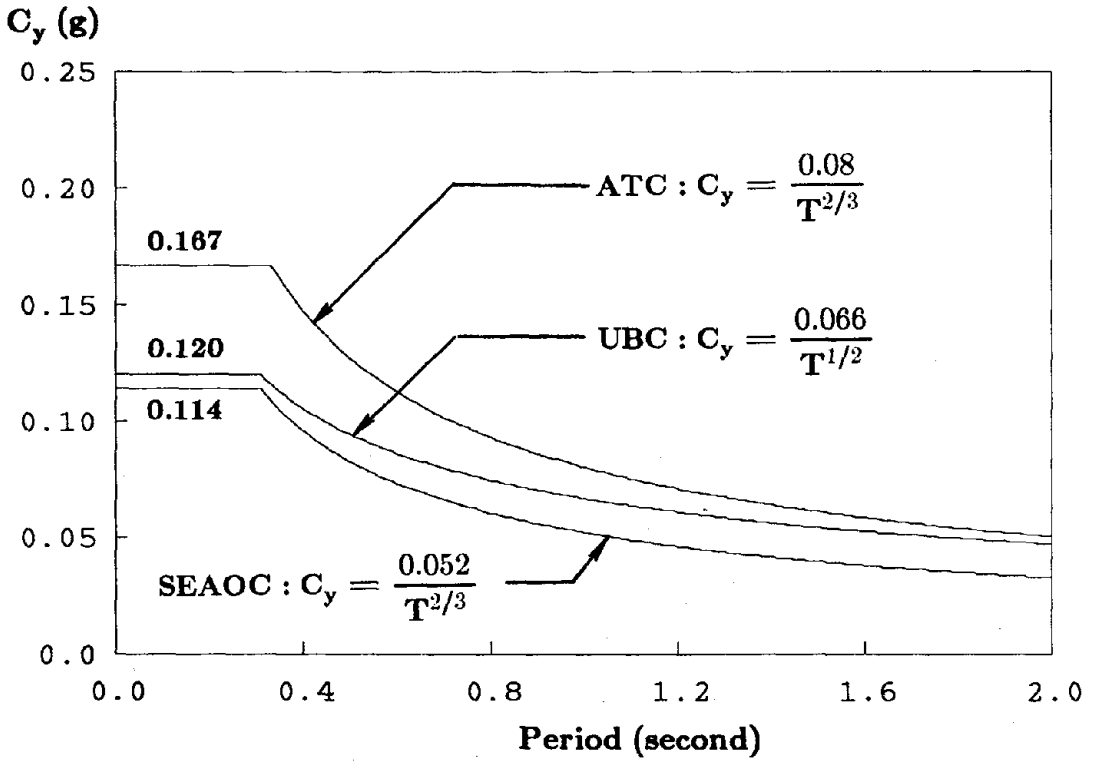


(a) Rock or Firm Soil Site

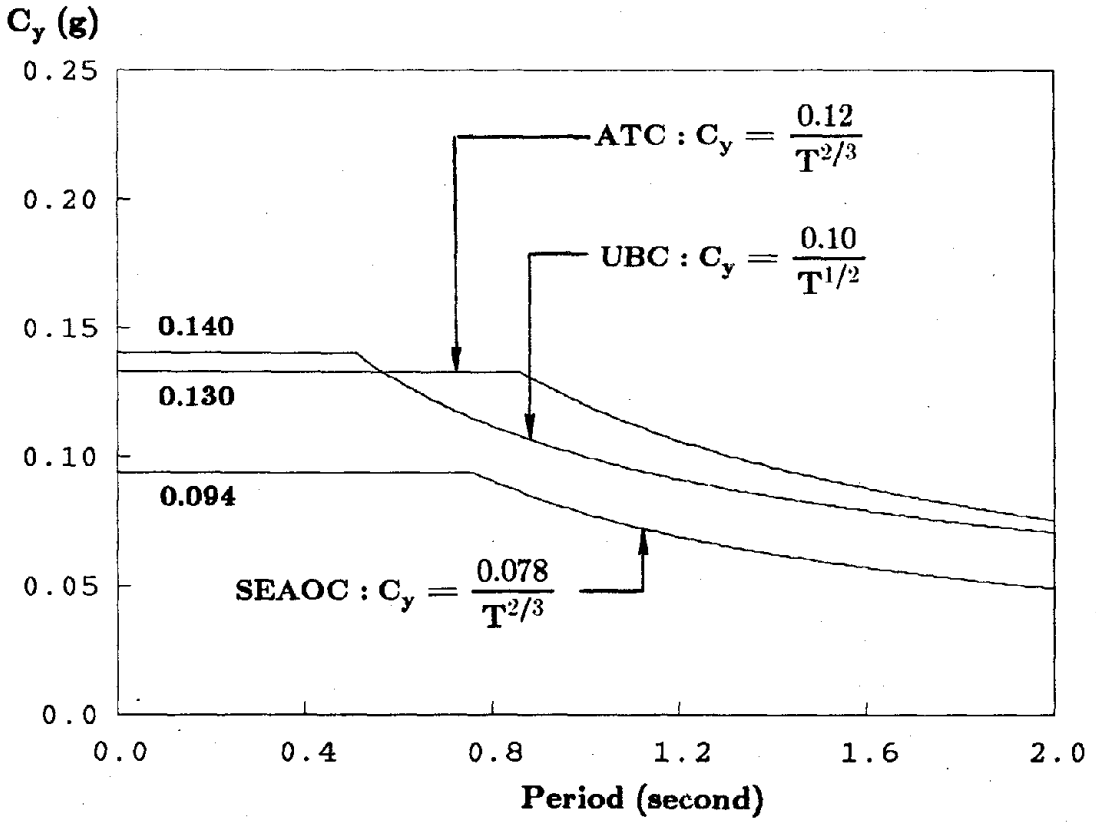


(b) Soft Soil Site

**FIGURE 3.3 UBC, ATC AND SEAOC SPECTRA**

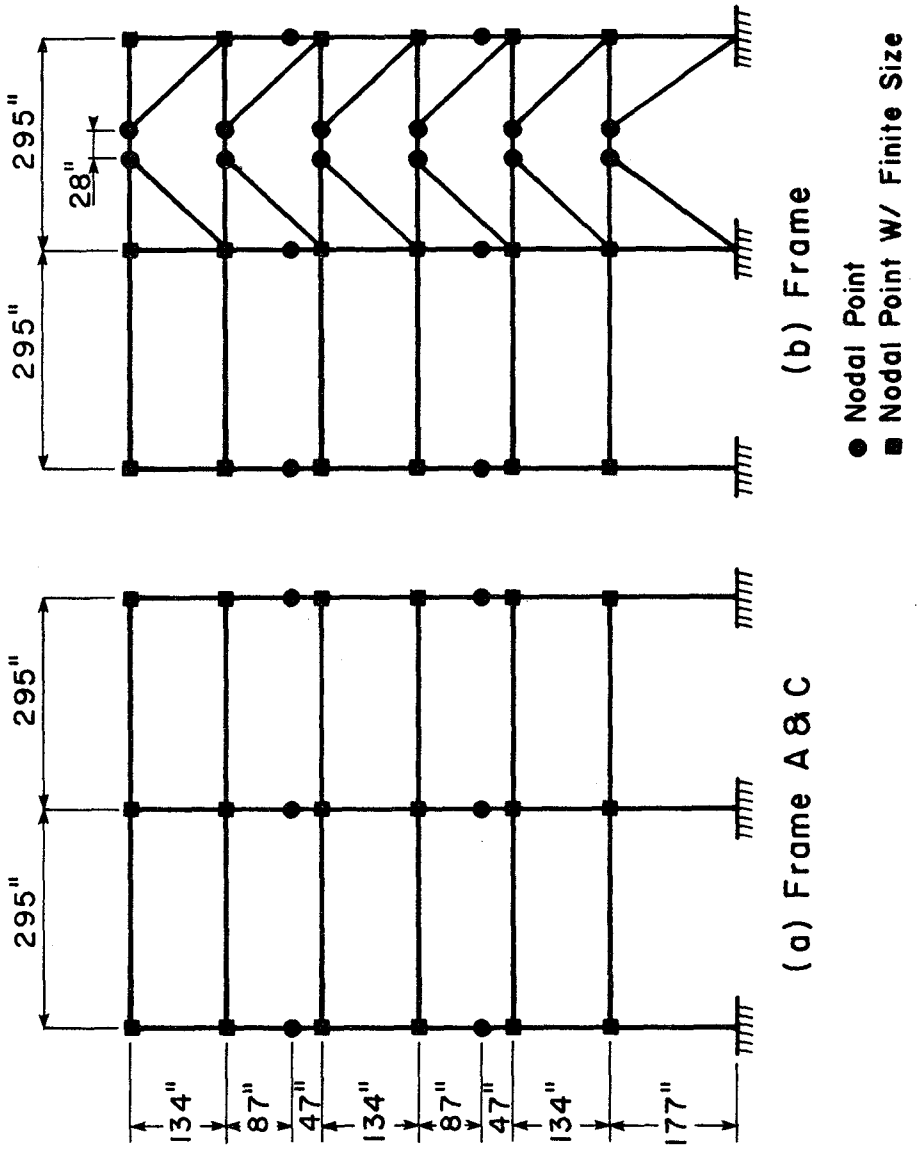


FIGURE 4.1 MATHEMATICAL MODEL OF THE PROTOTYPE

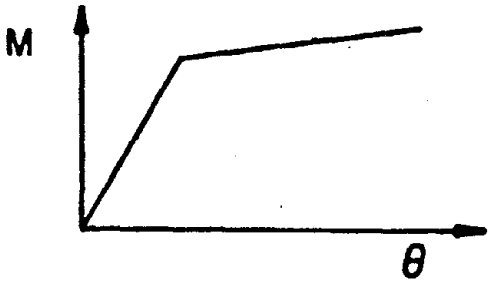


(a) Bilinear Moment-Rotation Relationship

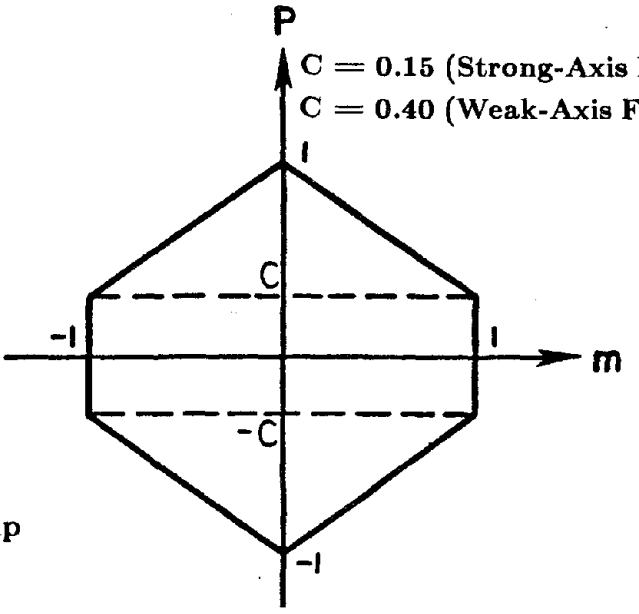


(b) Yield Surface

FIGURE 4.2 MATHEMATICAL MODEL OF THE COLUMN

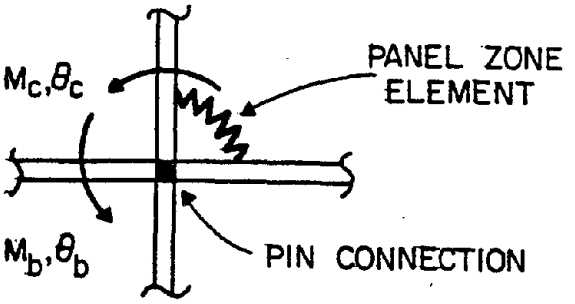


FIGURE 4.3 PANEL ZONE IDEALIZATION

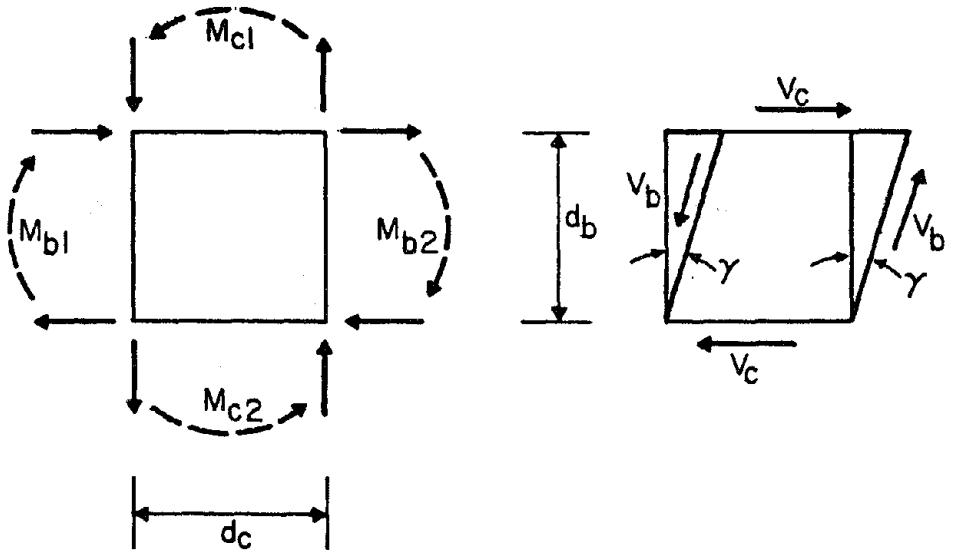


FIGURE 4.4 PANEL ZONE ACTIONS AND DEFORMATIONS

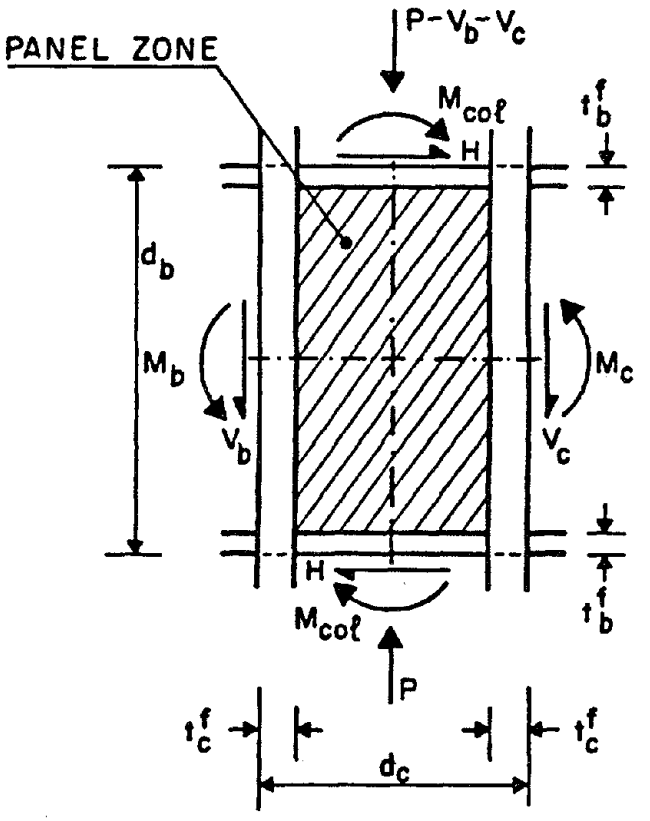


FIGURE 4.5 PANEL ZONE NOMENCLATURE

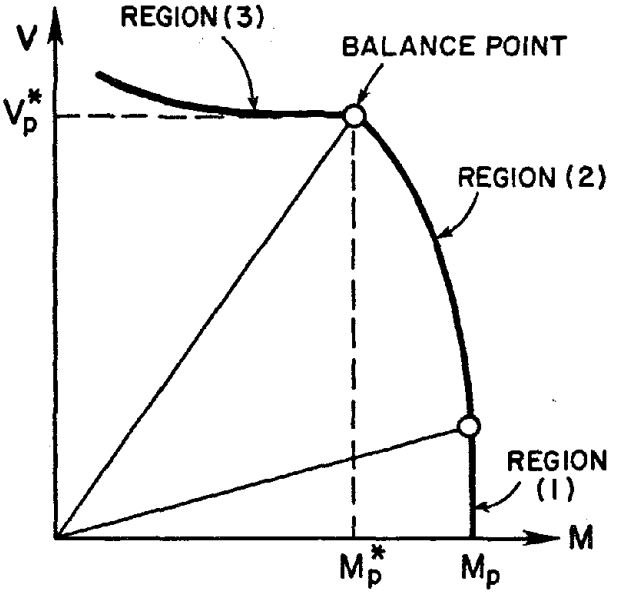


FIGURE 4.6 IDEAL M-V INTERACTION FOR W SECTIONS [2]

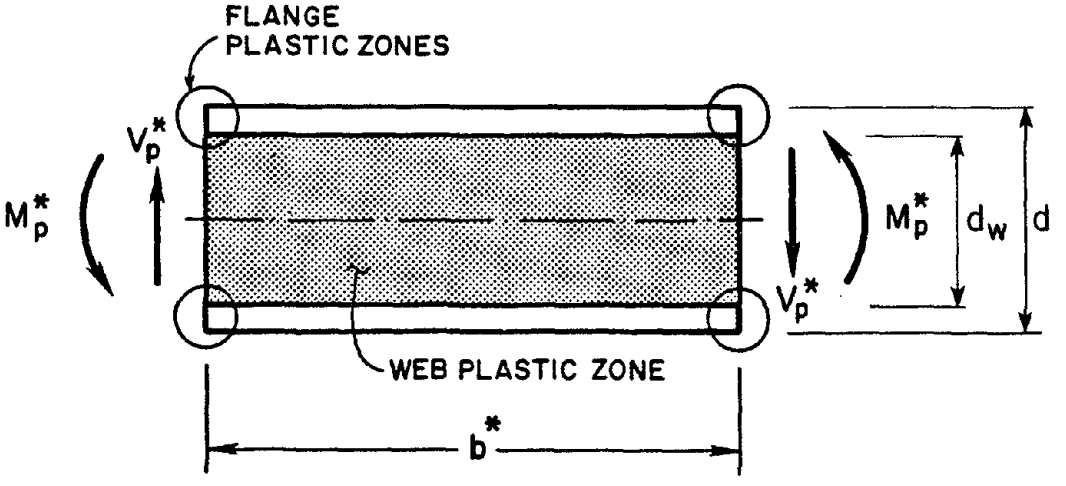


FIGURE 4.7 MAXIMUM SHEAR LINK LENGTH OF AN IDEAL PLASTIC LINK [2]

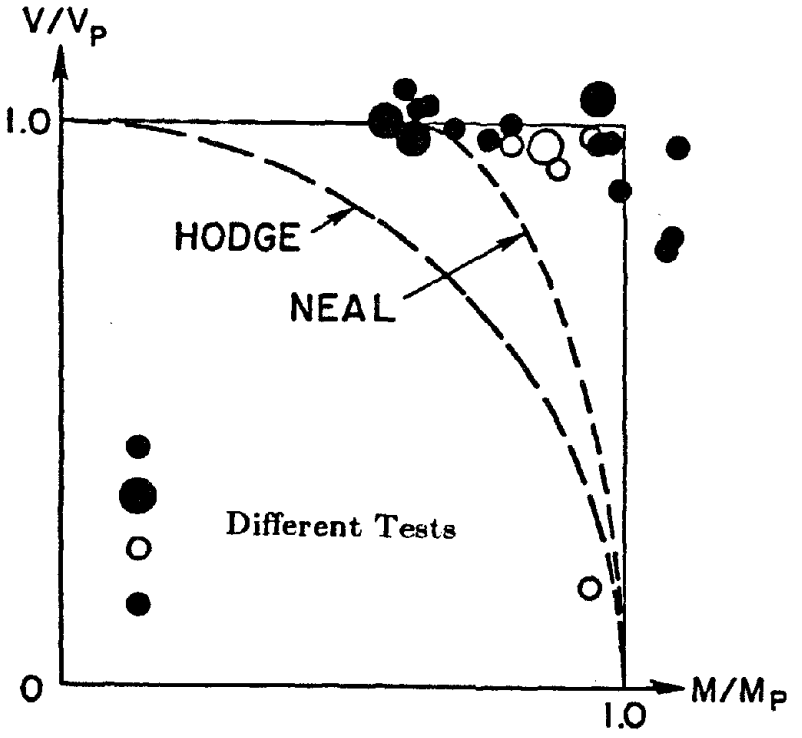


**FIGURE 4.8 ANALYTICAL AND EXPERIMENTAL M-V INTERACTION FOR W SECTIONS [22]**

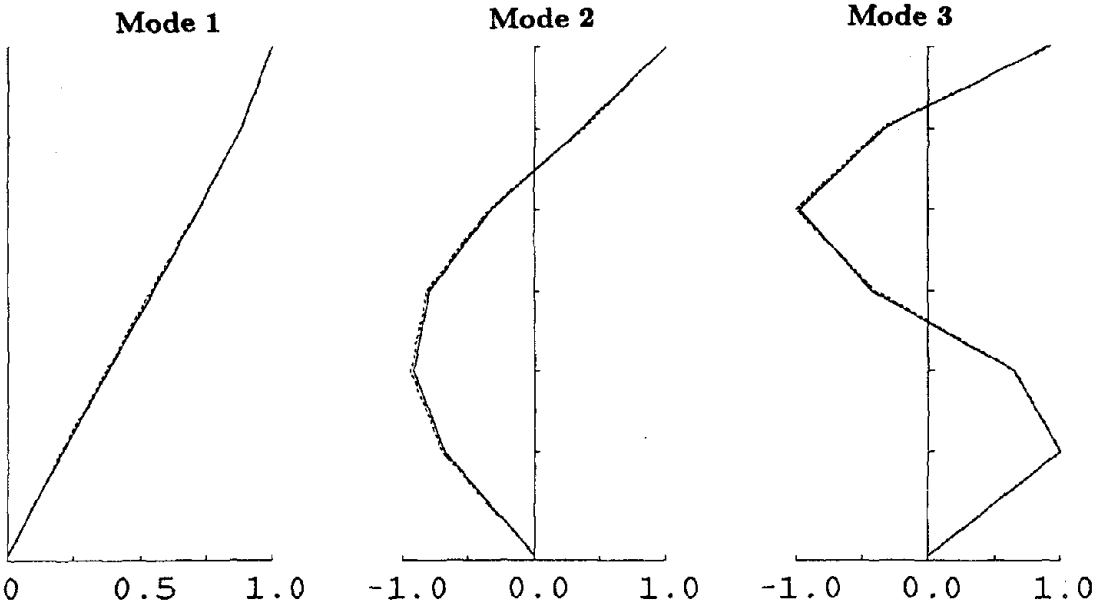


**(Solid Line: *Experimental*; Dotted Line: *Analytical*)**

**FIGURE 4.9 PROTOTYPE MODE SHAPES**

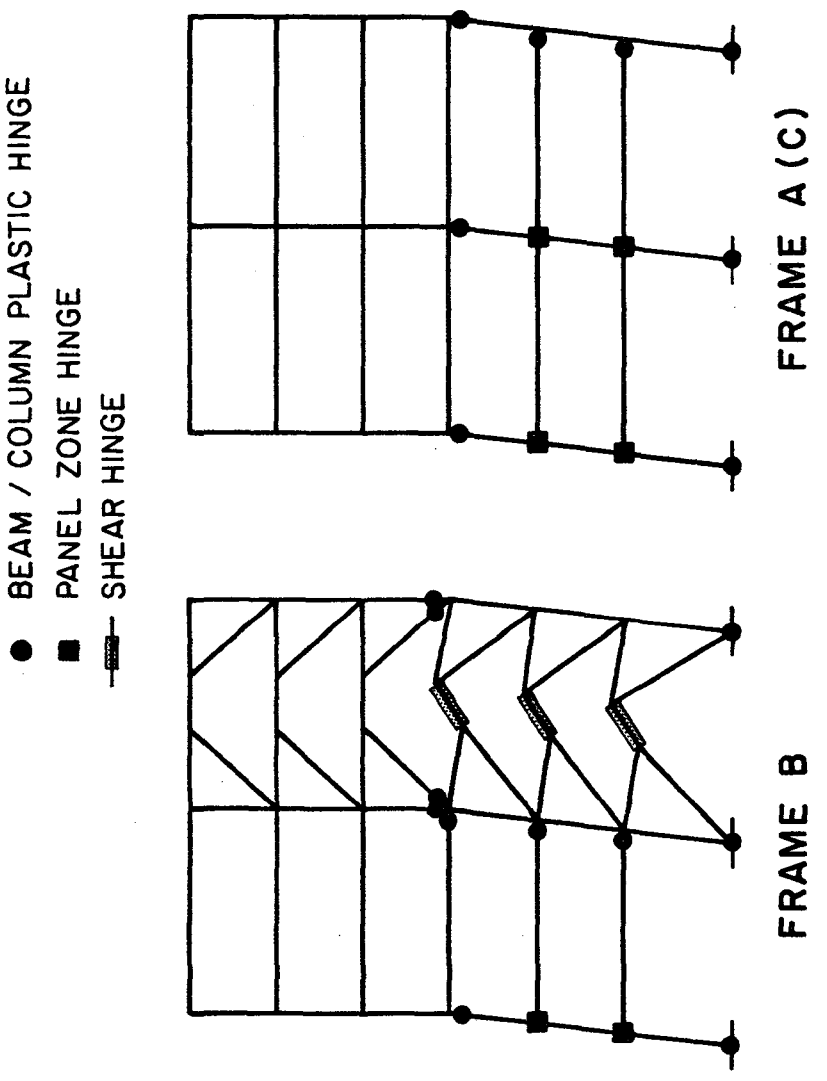


FIGURE 4.10 COLLAPSE MECHANISM

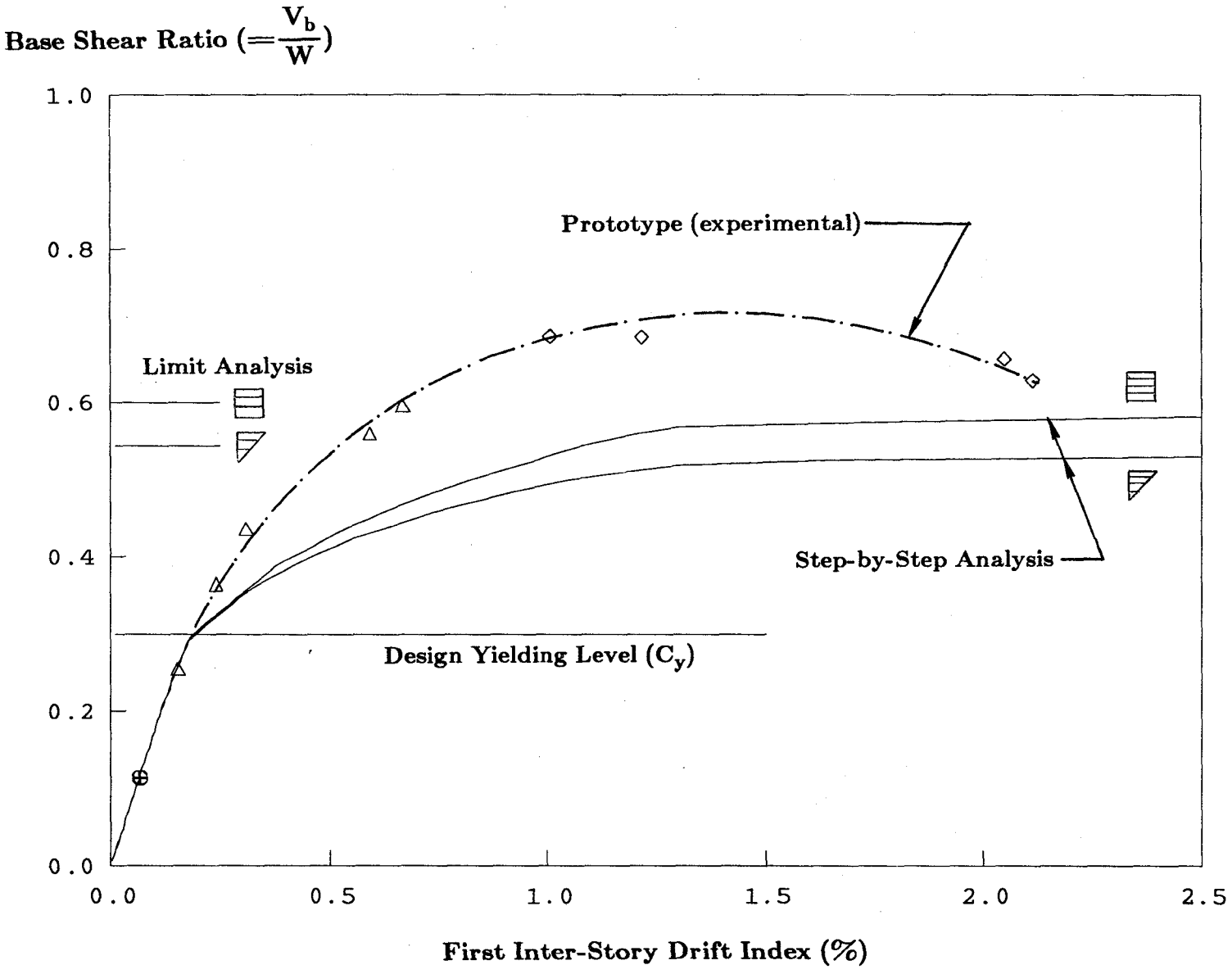


**FIGURE 4.11 PROTOTYPE STRENGTH AND FIRST IDI RELATIONSHIPS ($E_{SH}$=0)**

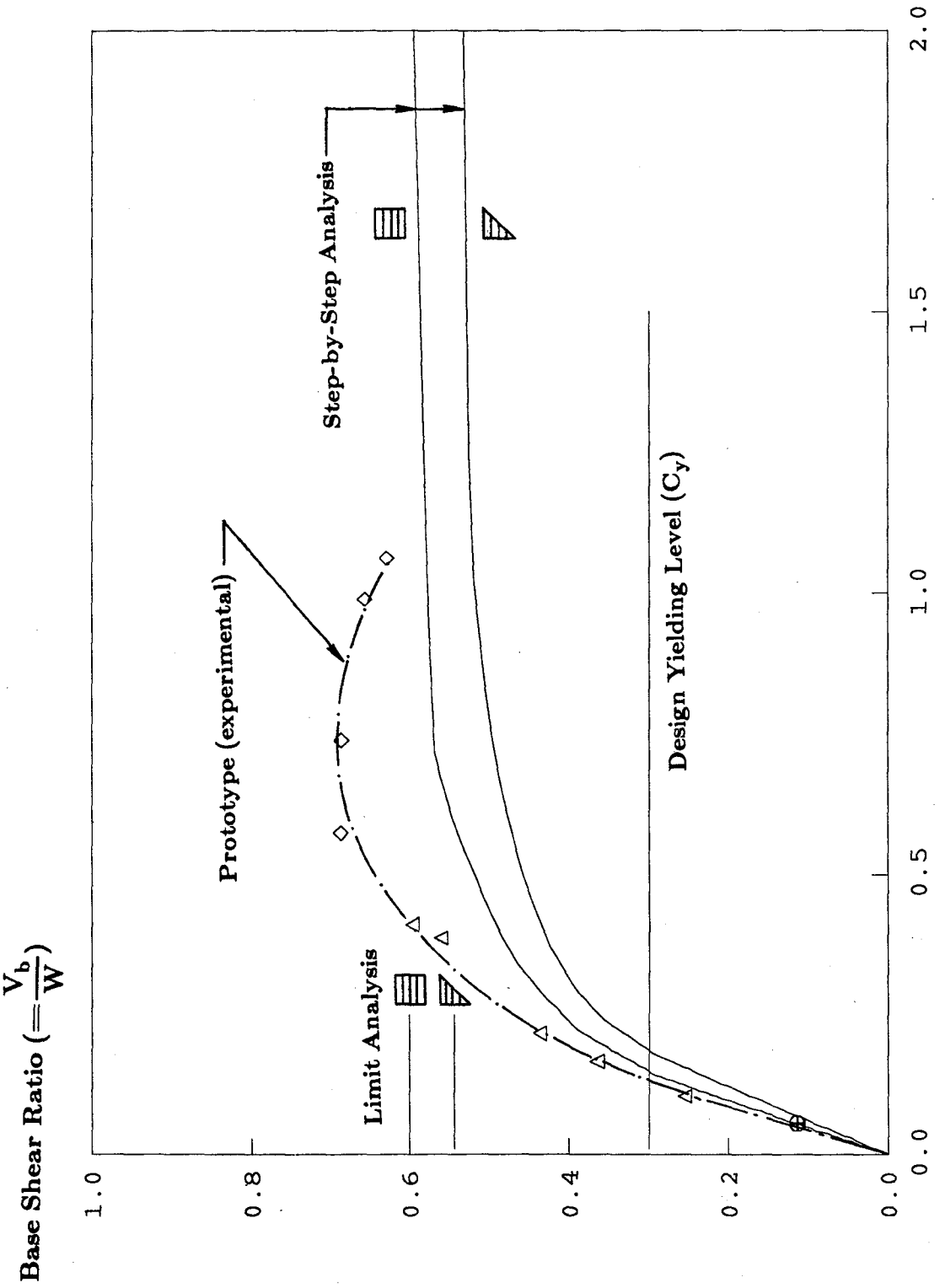


FIGURE 4.12 PROTOTYPE STRENGTH AND RDI RELATIONSHIPS ($E_{SH}$=0)

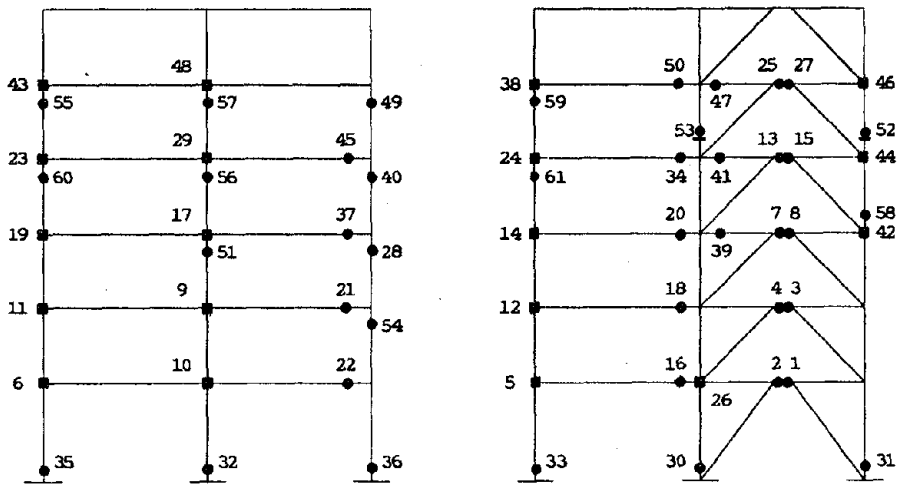


Frame A or C Frame B

(a) Triangular Load Pattern

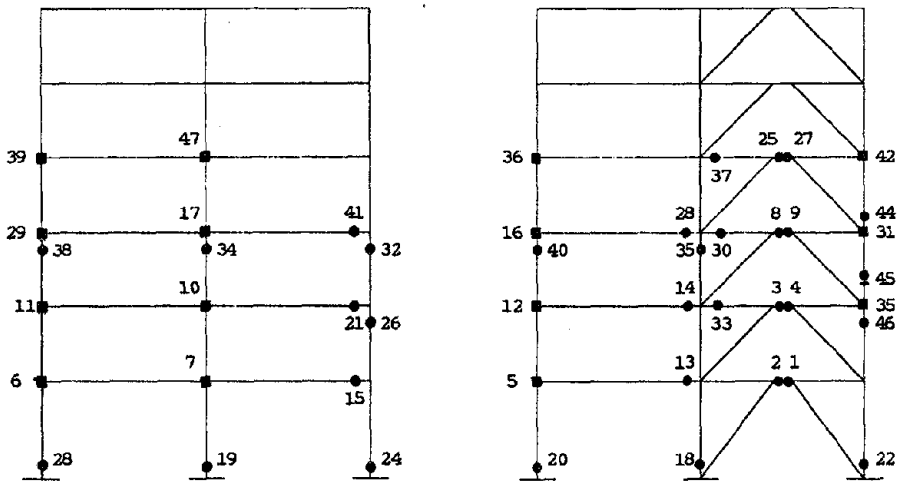


Frame A or C Frame B

(b) Rectangular Load Pattern

- ● Flexural Member Plastic Hinge
- ■ Panel Zone Plastic Hinge
- ○ Brace Yielding
- ◐ Brace Buckling

FIGURE 4.13 PLASTIC HINGE FORMATION SEQUENCE ($E_{SH}$=0)

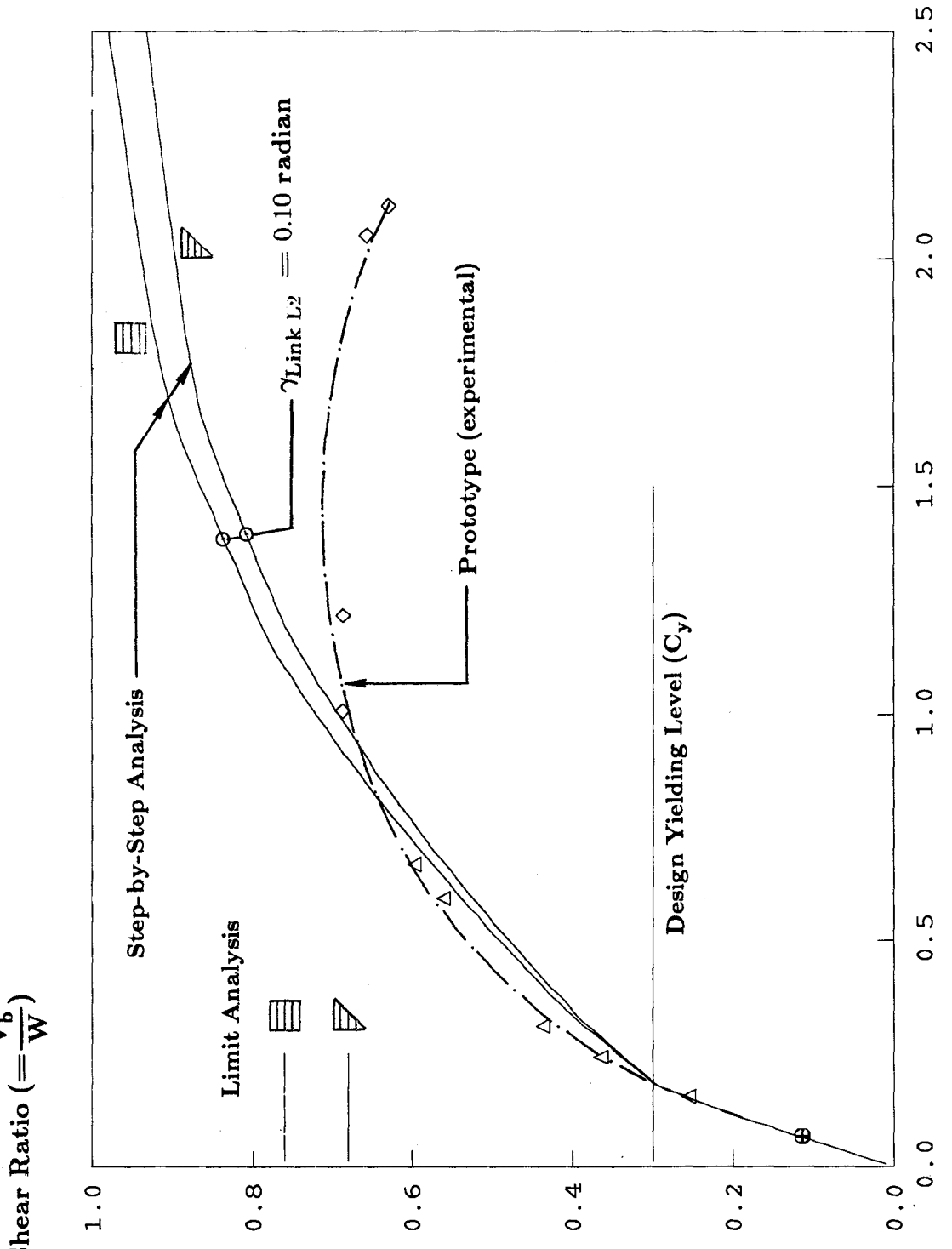


FIGURE 4.14 PROTOTYPE STRENGTH AND FIRST IDI RELATIONSHIPS

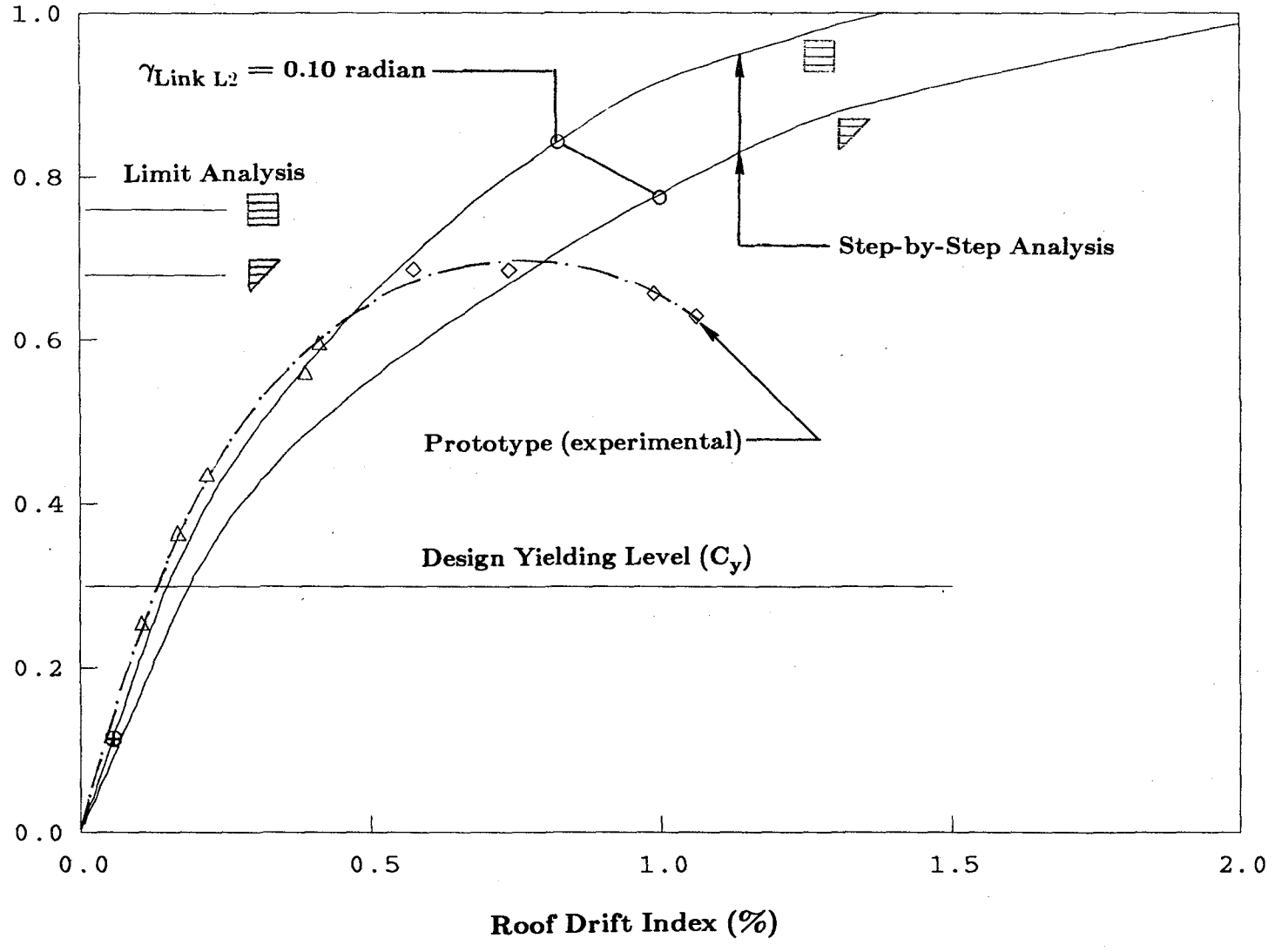


FIGURE 4.15 PROTOTYPE STRENGTH AND RDI RELATIONSHIPS

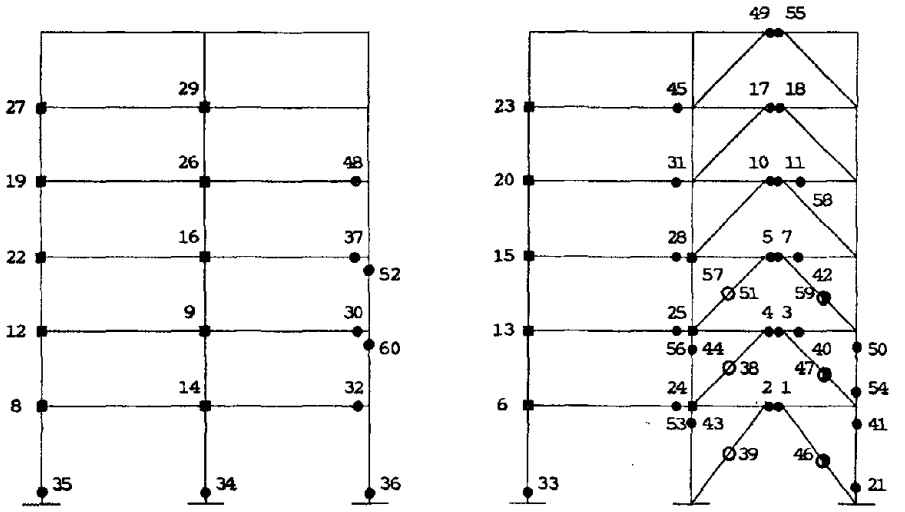


Frame A or C Frame B

(a) Triangular Load Pattern

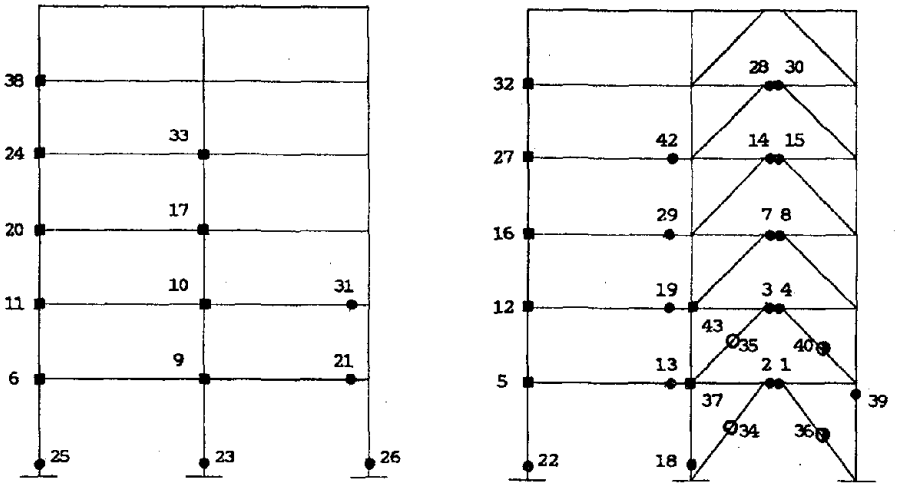


Frame A or C Frame B

(b) Rectangular Load Pattern

- ● Flexural Member Plastic Hinge
- ■ Panel Zone Plastic Hinge
- ○ Brace Yielding
- ◐ Brace Buckling

FIGURE 4.16 PLASTIC HINGE FORMATION SEQUENCE

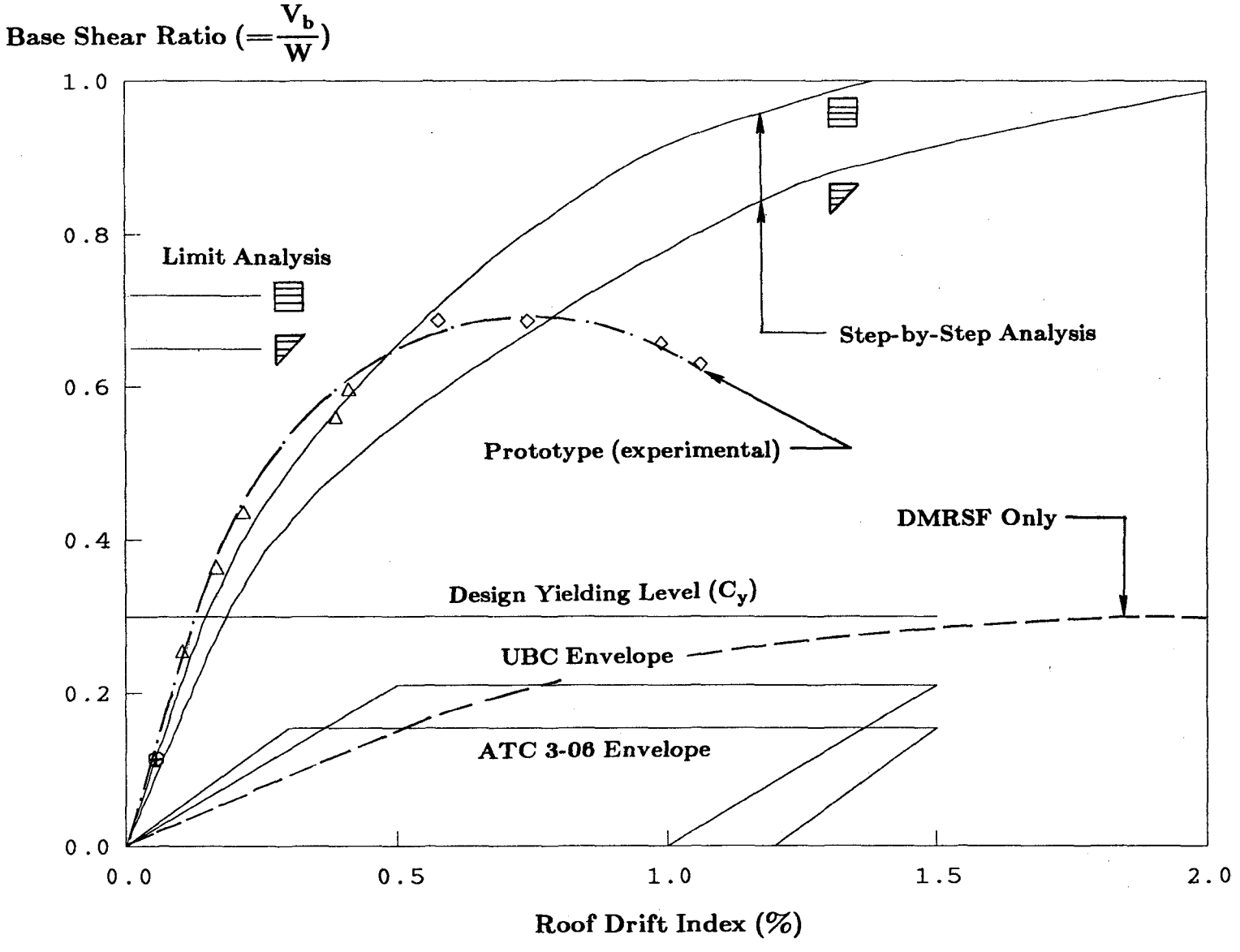


FIGURE 4.17 PROTOTYPE BASE SHEAR RATIO AND RDI RELATIONSHIPS

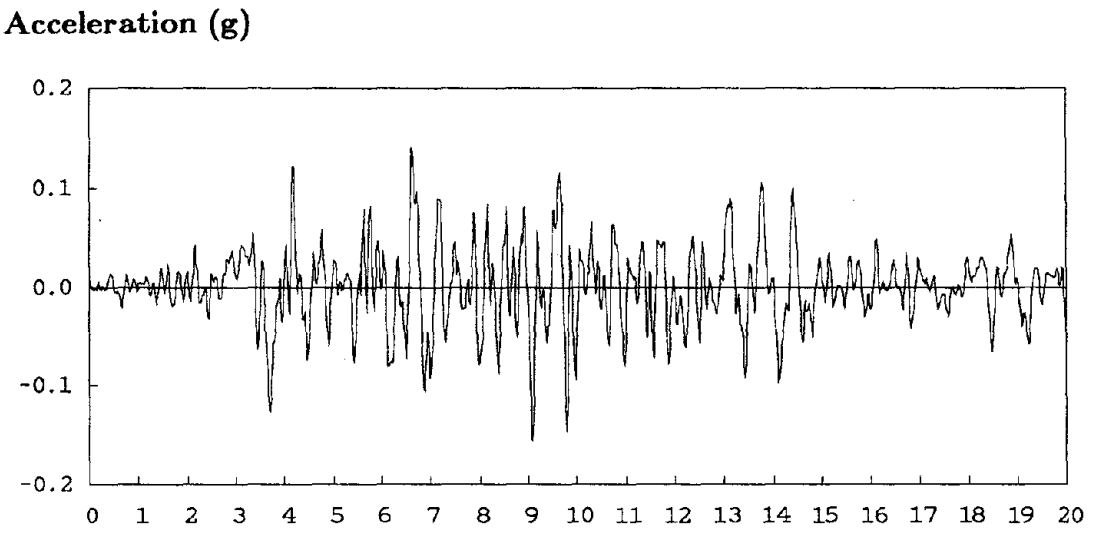


(a) Acceleration Time History

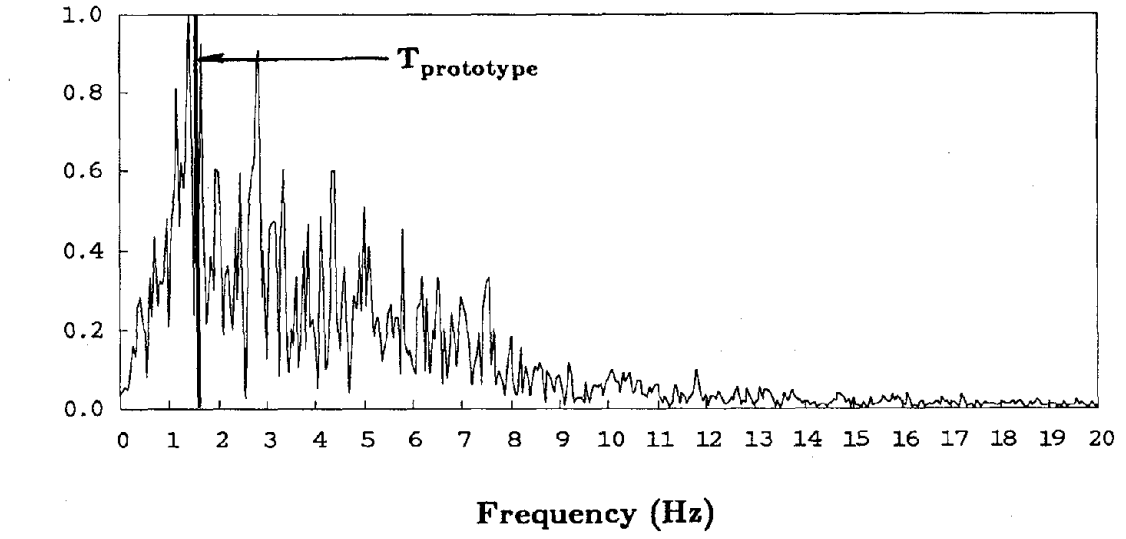


(b) Normalized Fourier Spectrum

**FIGURE 4.18 1952 KERN COUNTY TAFT N21E EARTHQUAKE RECORD**

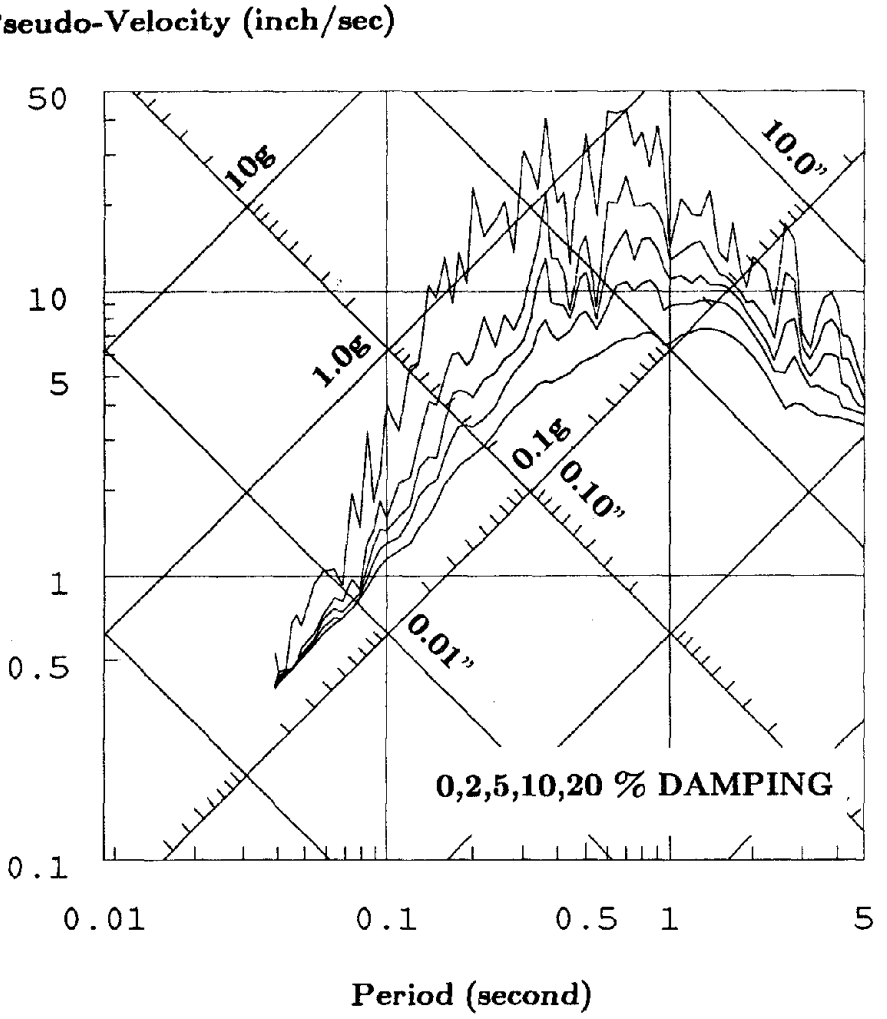


**FIGURE 4.19 1952 KERN COUNTY TAFT N21E RESPONSE SPECTRA**

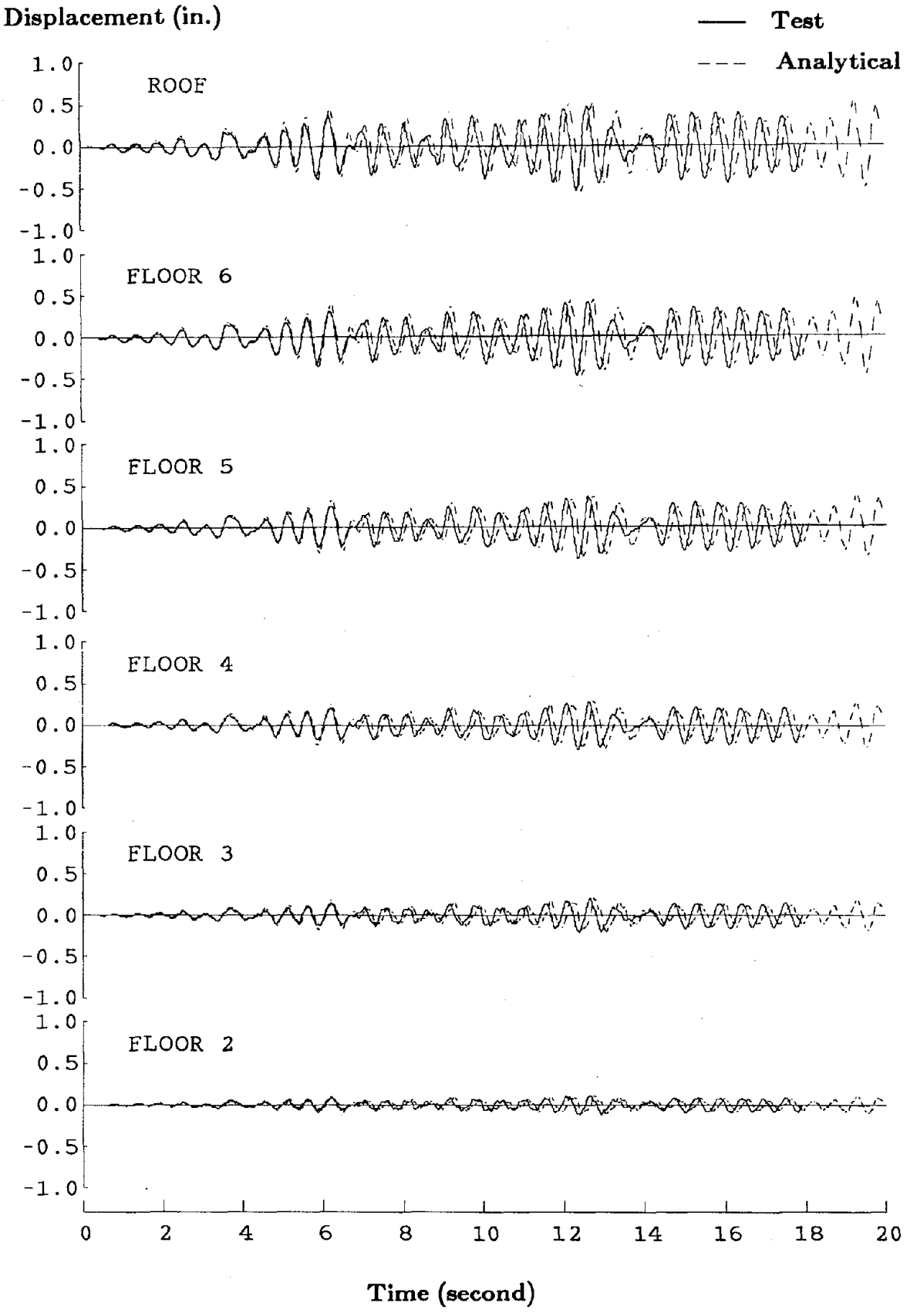


**FIGURE 4.20 PROTOTYPE DISPLACEMENT RESPONSE TAFT 65 GALS**

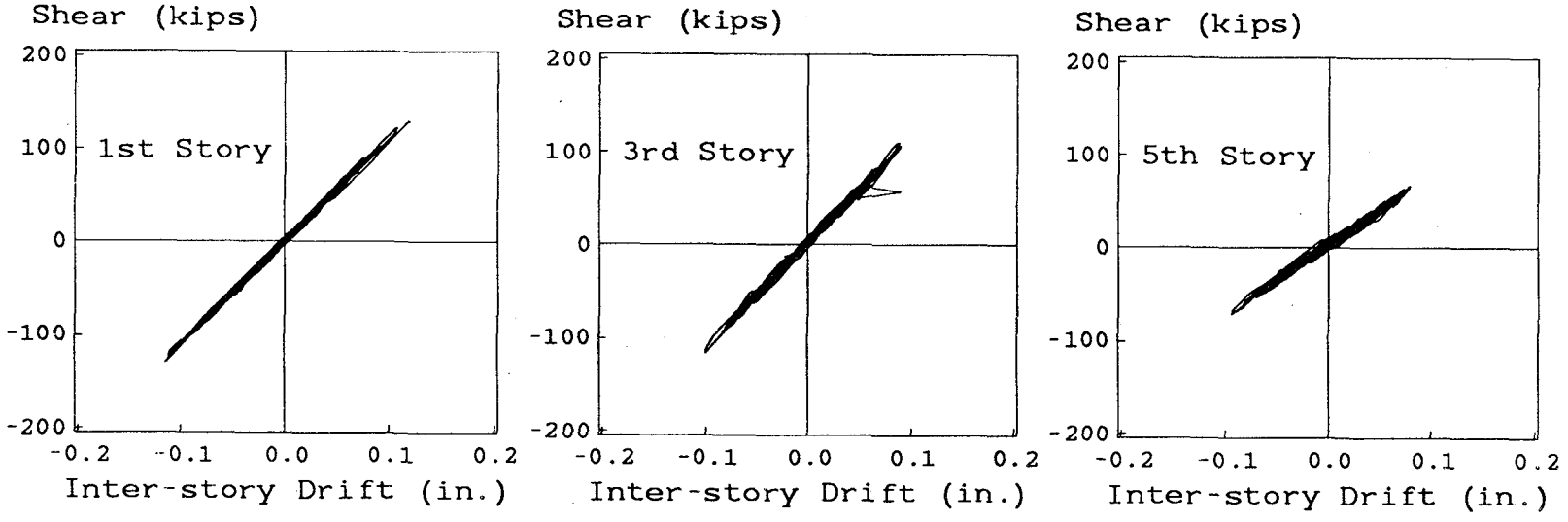


**(a) Experimental**



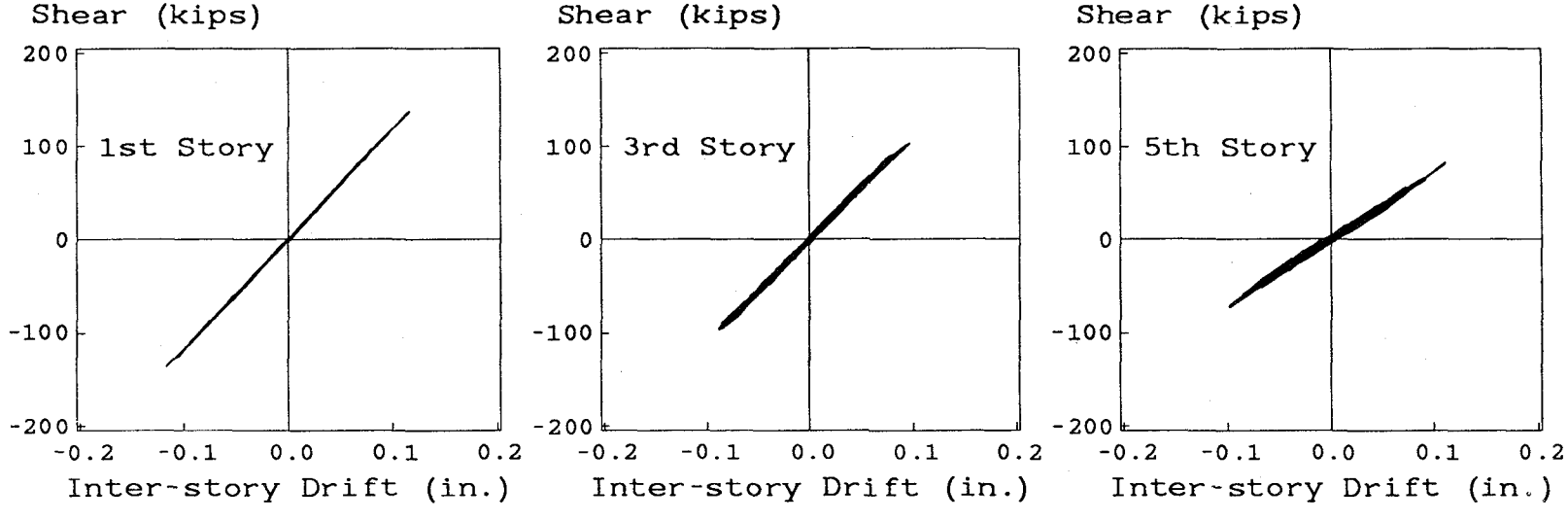


**(b) Analytical**

**FIGURE 4.21 PROTOTYPE STORY SHEAR RESPONSE TAFT 65 GALS**

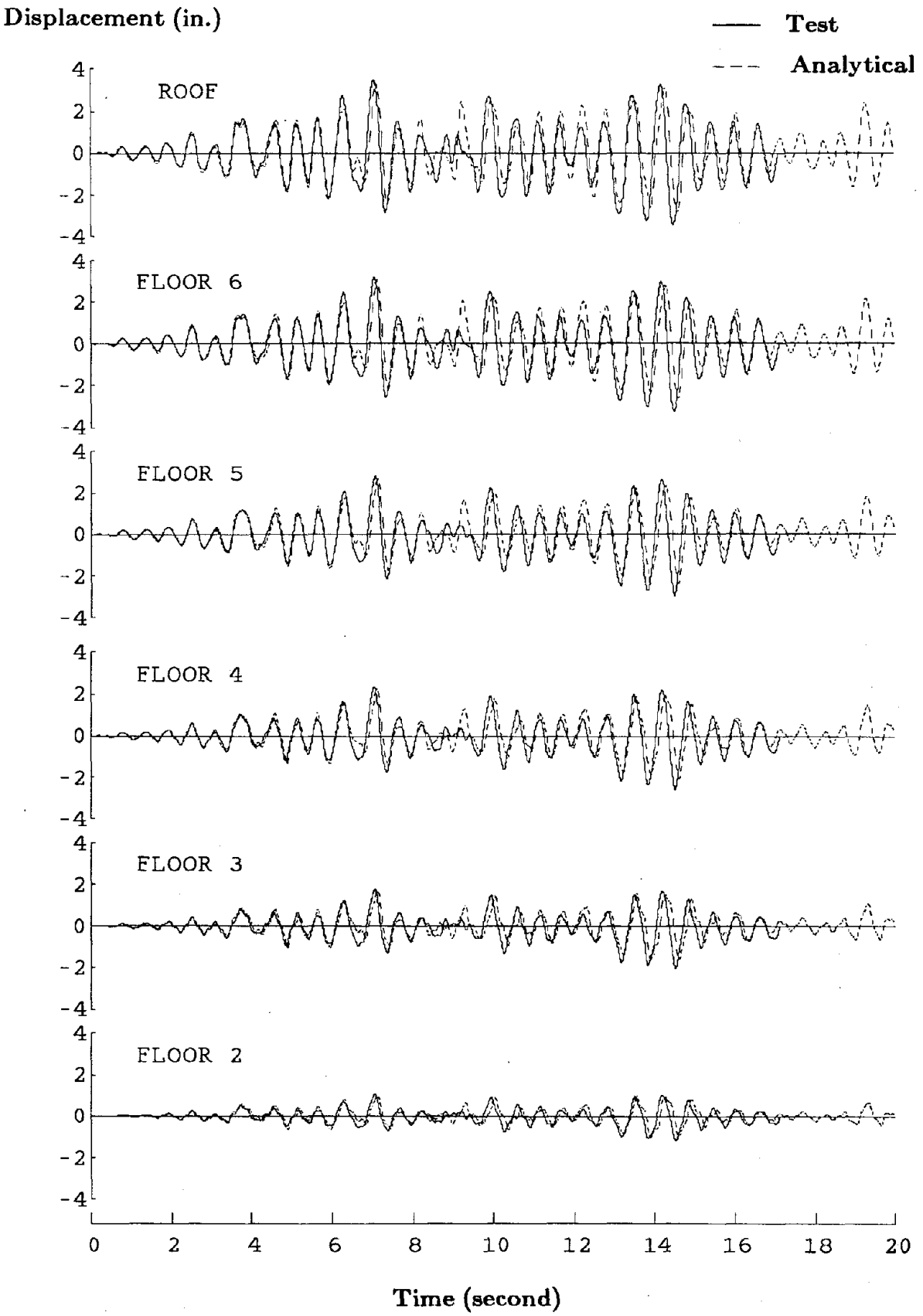


**FIGURE 4.22 PROTOTYPE DISPLACEMENT RESPONSE TAFT 500 GALS**

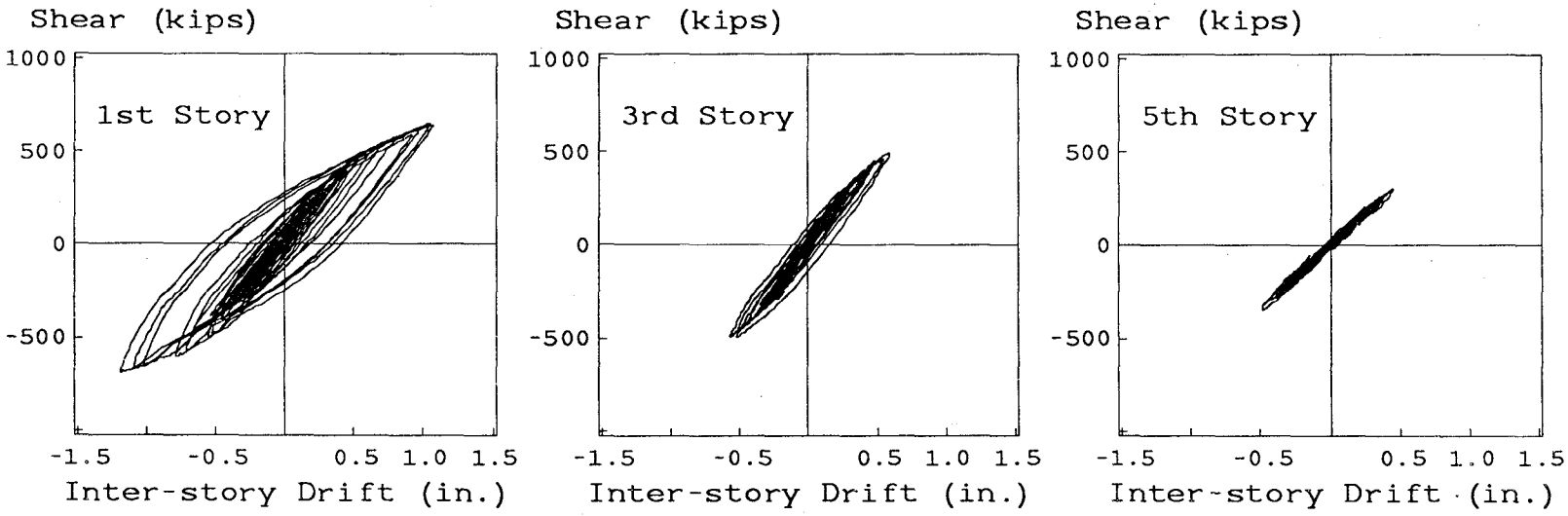


**(a) Experimental**

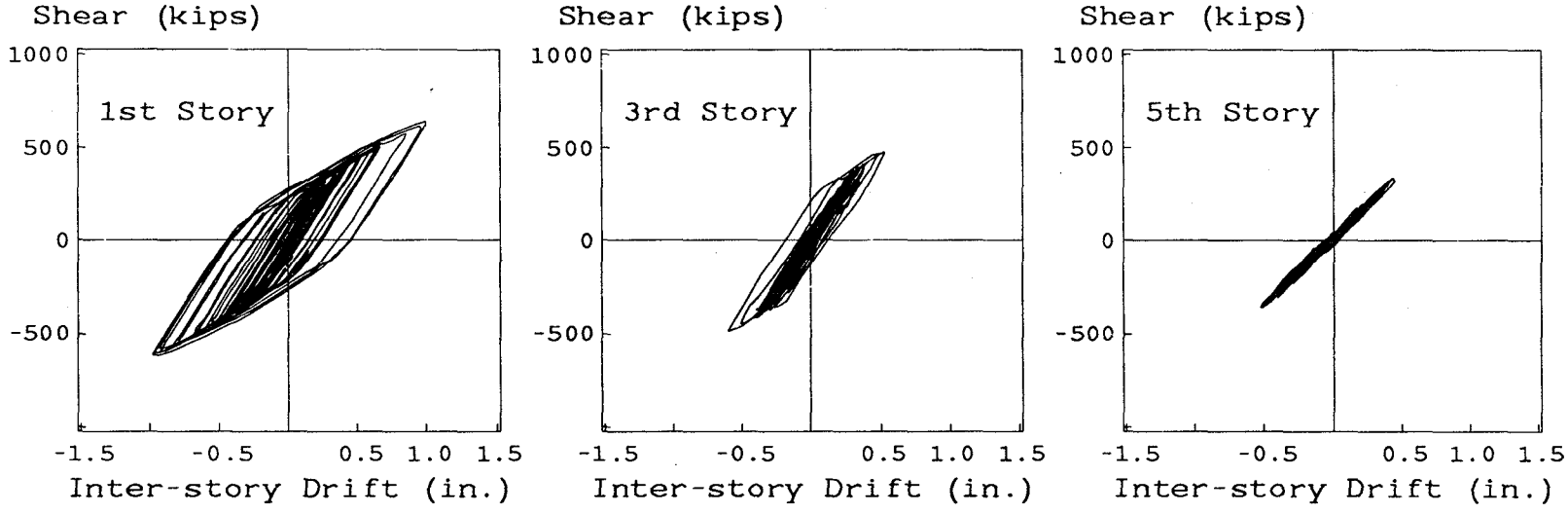


**(b) Analytical**

**FIGURE 4.23 PROTOTYPE STORY SHEAR RESPONSE TAFT 500 GALS**

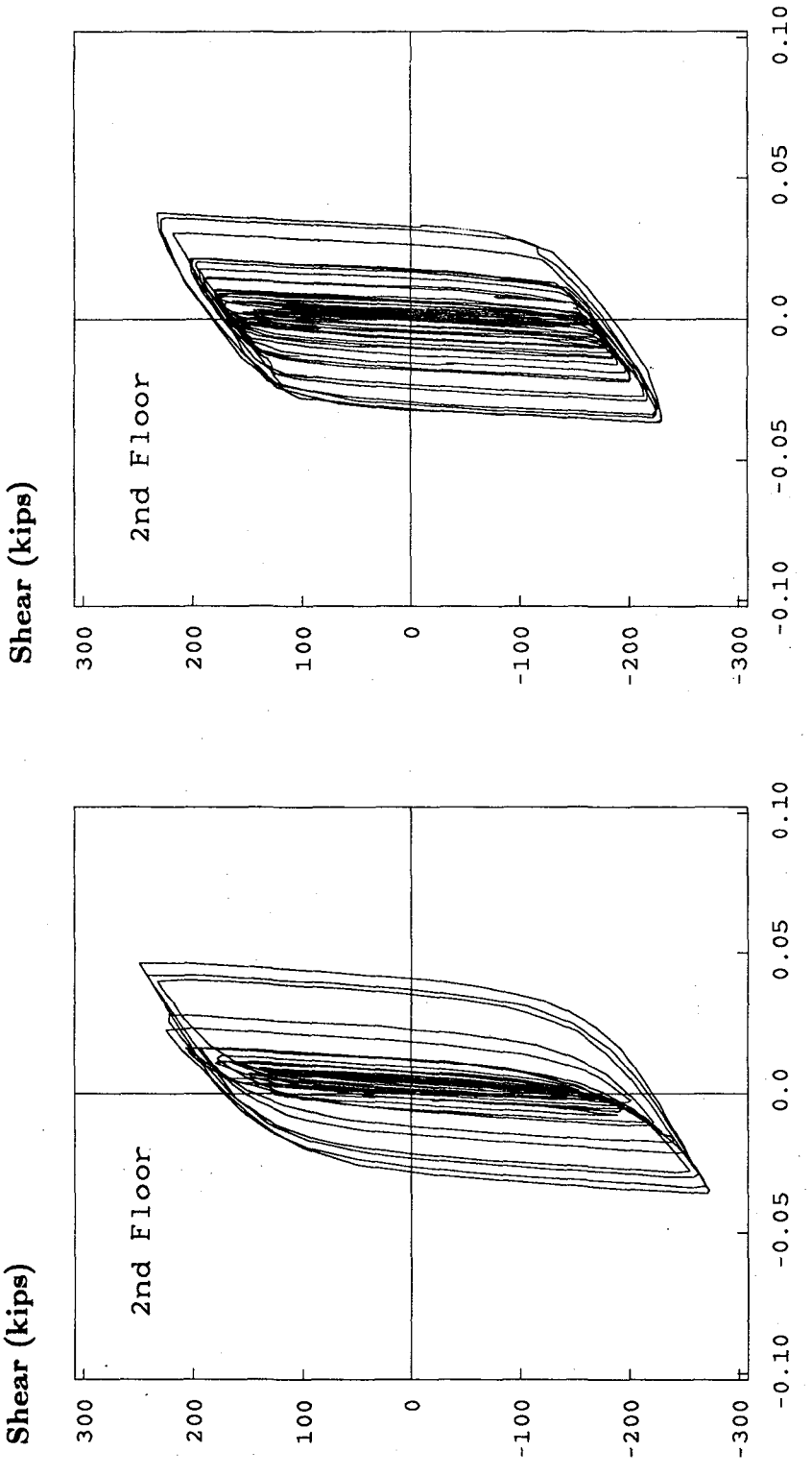


(a) Experimental (b) Analytical

**FIGURE 4.24 PROTOTYPE SHEAR LINK RESPONSE TAFT 500 GALS**

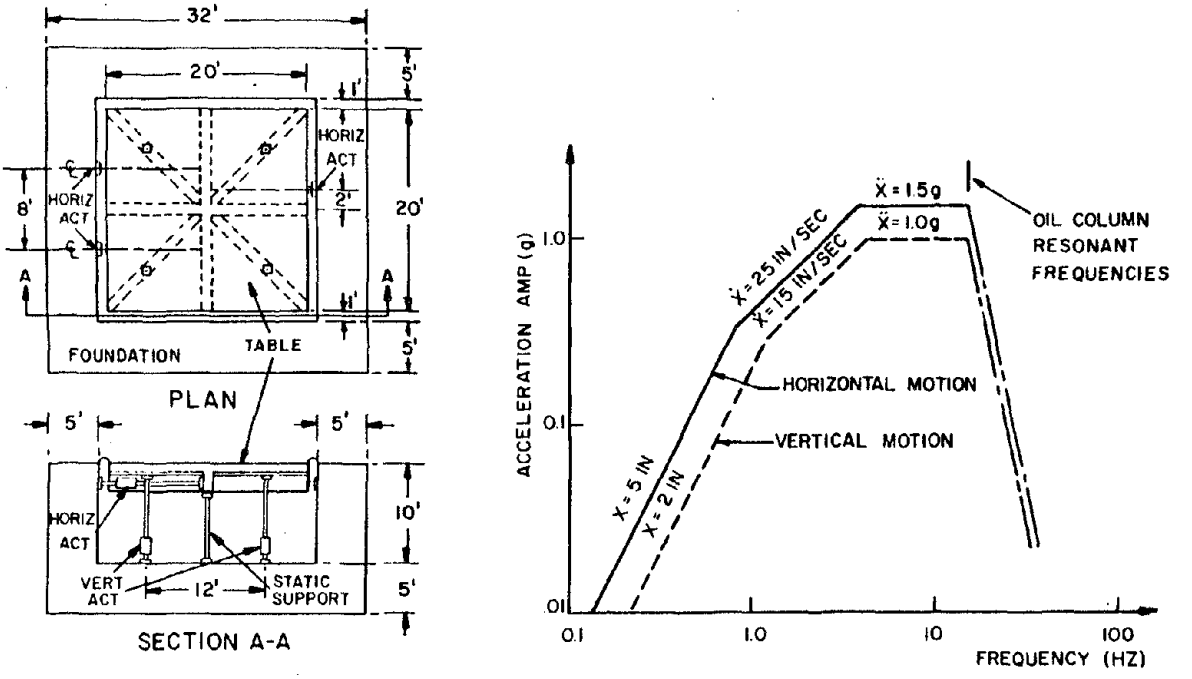


**FIGURE 5.1 DYNAMIC PERFORMANCE OF THE EARTHQUAKE SIMULATOR**

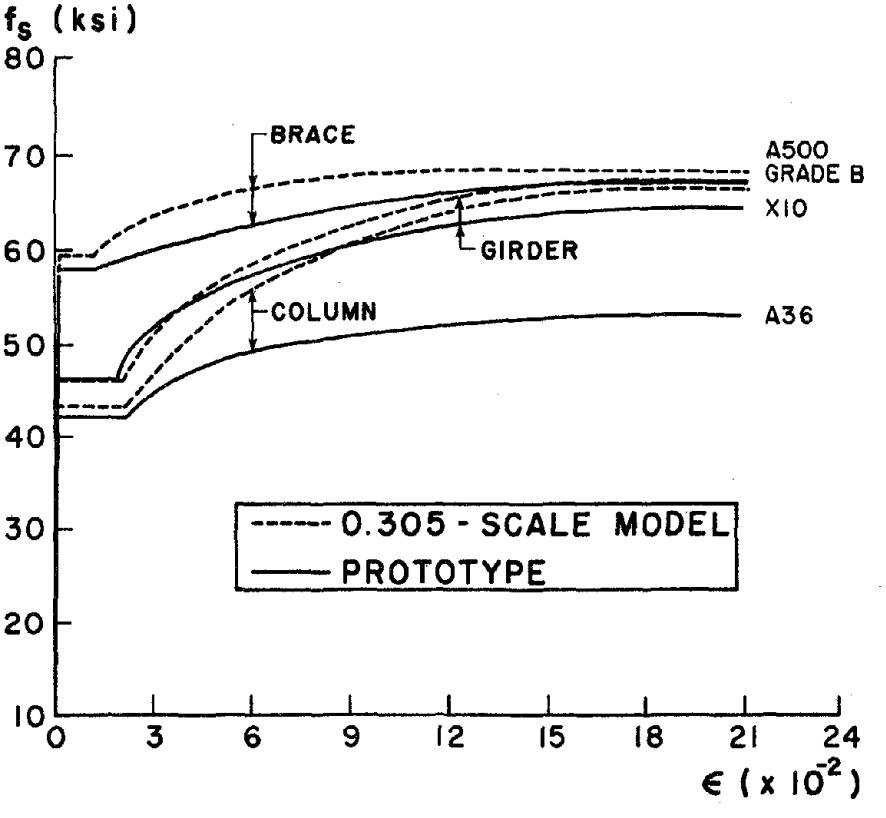


**FIGURE 5.2 MEAN STEEL STRESS-STRAIN RELATIONSHIPS**

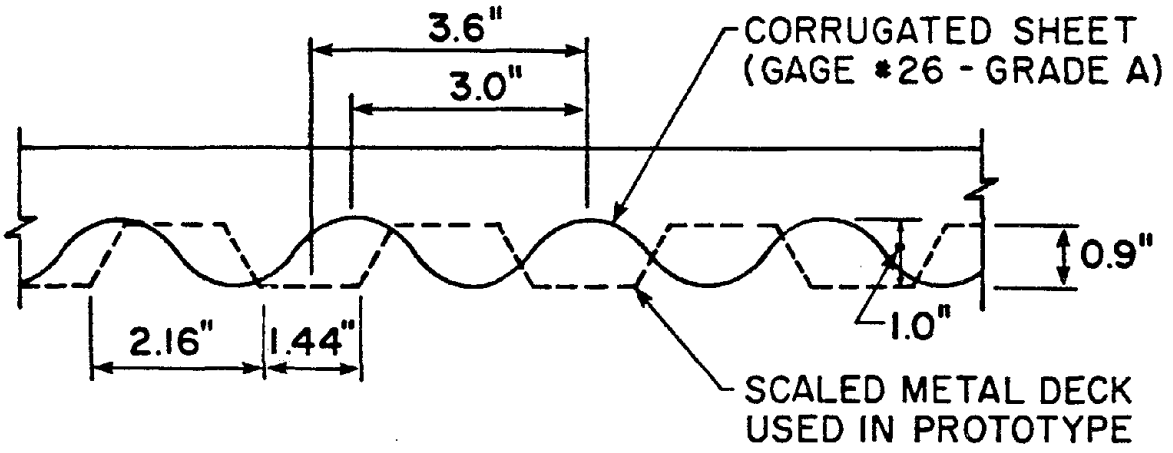


FIGURE 5.3 MODEL AND SCALED PROTOTYPE METAL DECK PROFILES

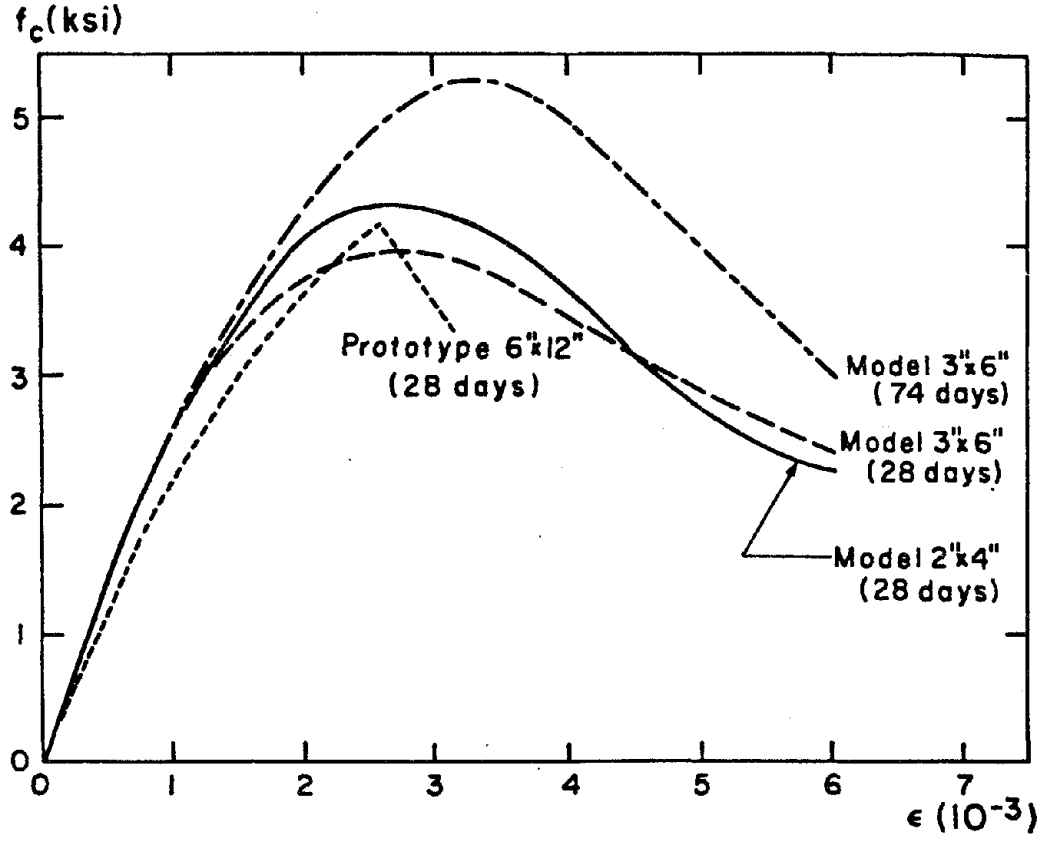


(a) Typical Stress Versus Strain Curves

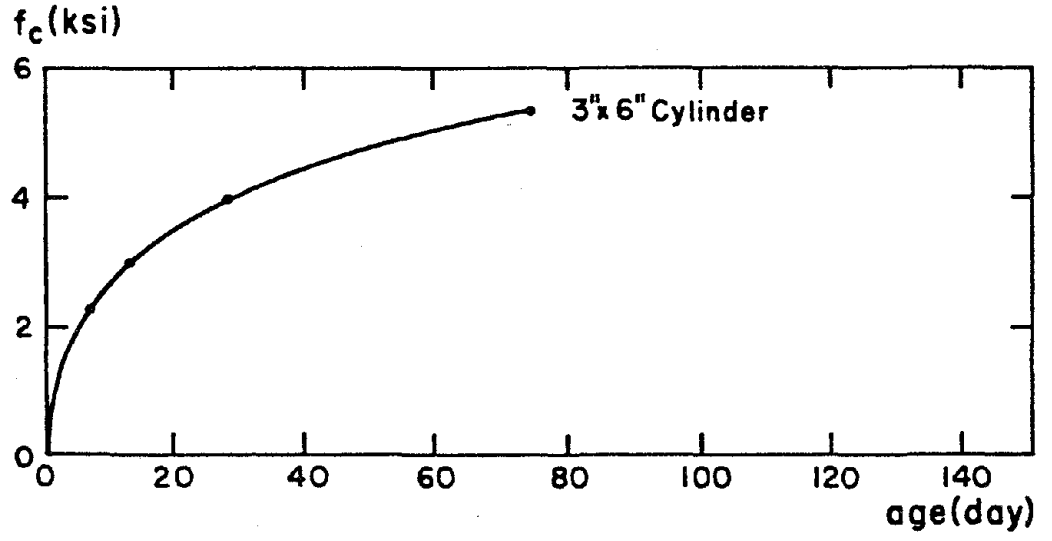


FIGURE 5.4 MODEL CONCRETE MECHANICAL CHARACTERISTICS

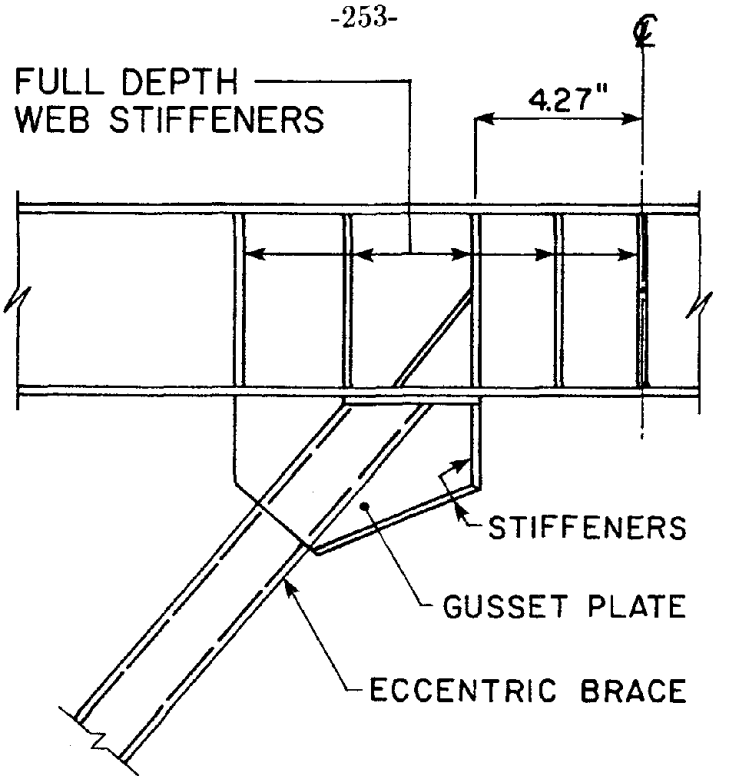


**FIGURE 5.5 MODEL SHEAR LINK**

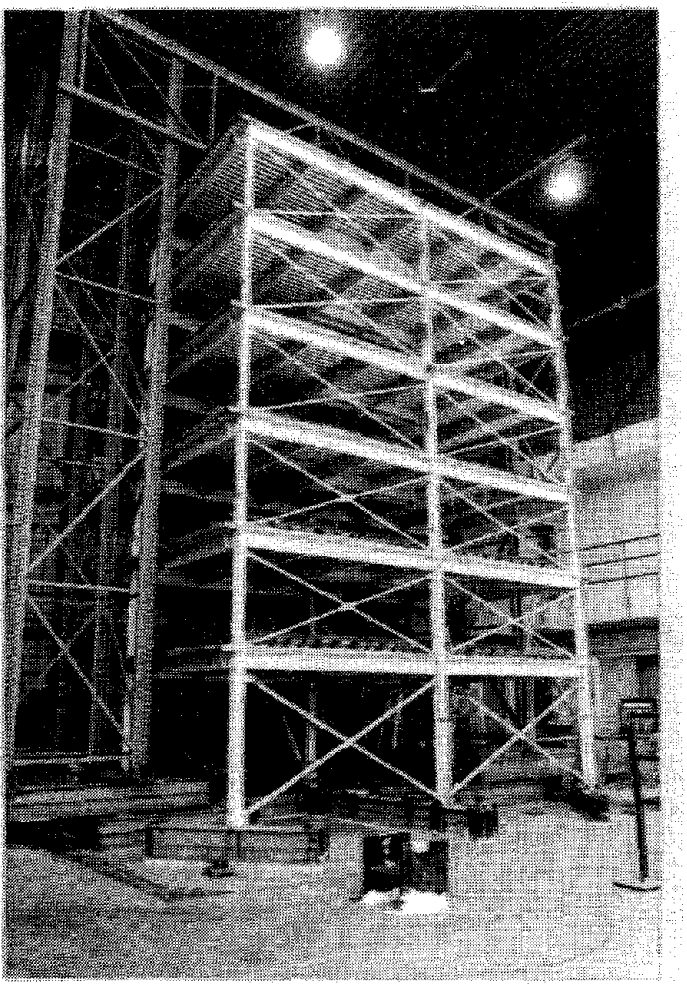

**FIGURE 5.6 INSTRUMENTATION REFERENCE FRAMES**

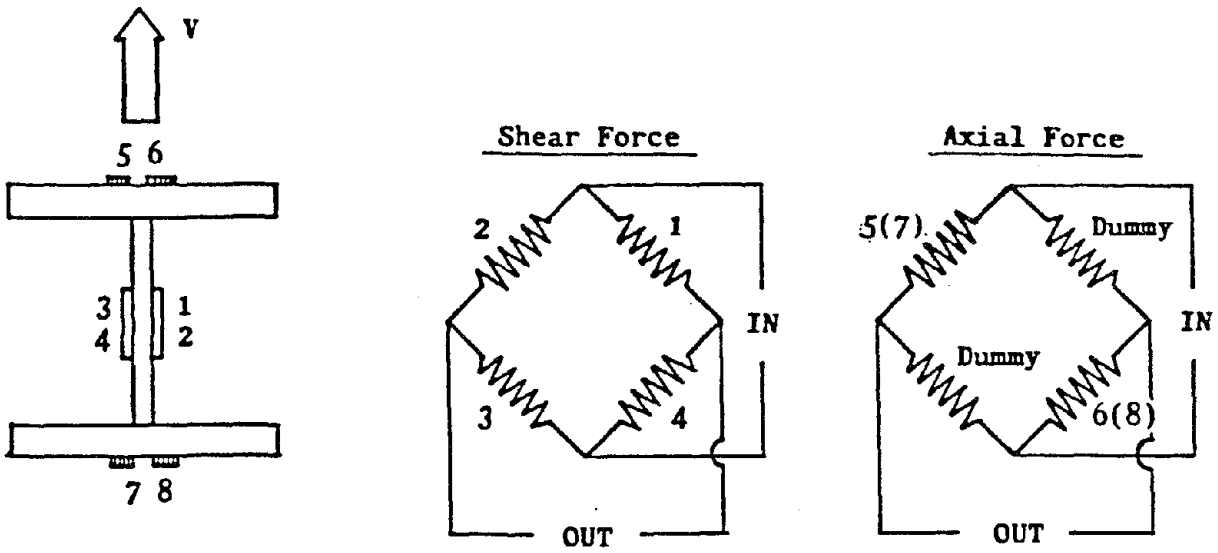


(a) Strong Axis bending

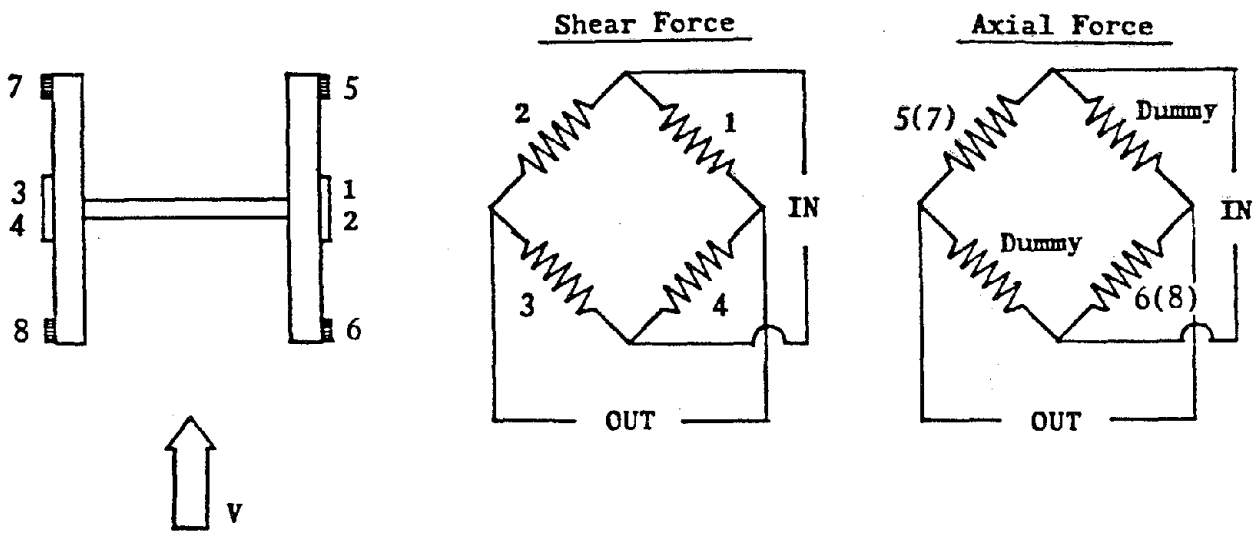


(b) Weak Axis bending

FIGURE 5.7 COLUMN STRAIN GAGE INSTRUMENTATION

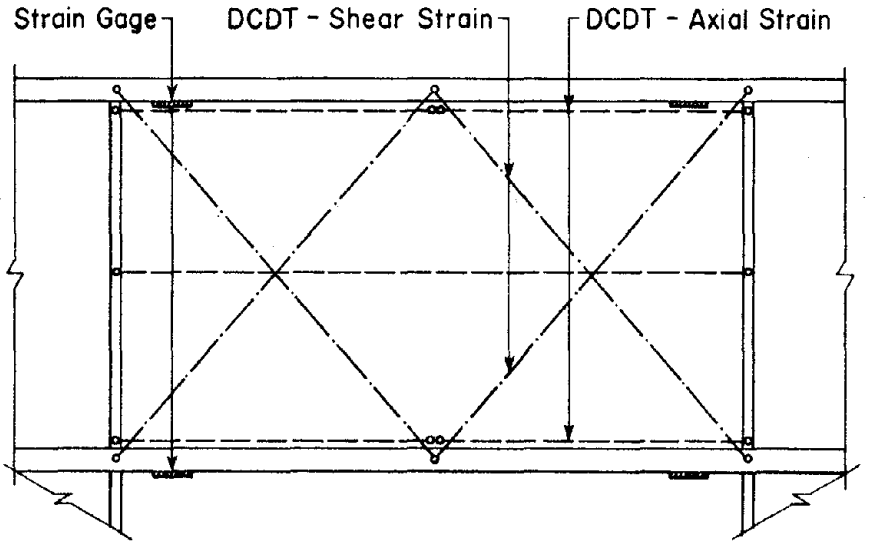


**(a) Schematic Representation**

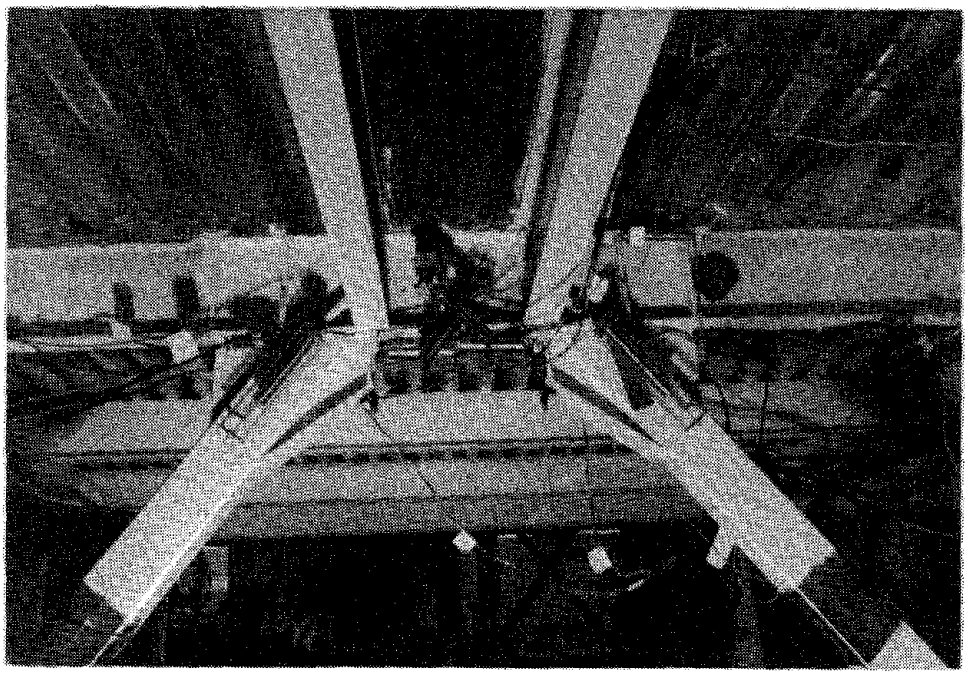

**(b) Experimental Layout**

**FIGURE 5.8 SHEAR LINK INSTRUMENTATION**

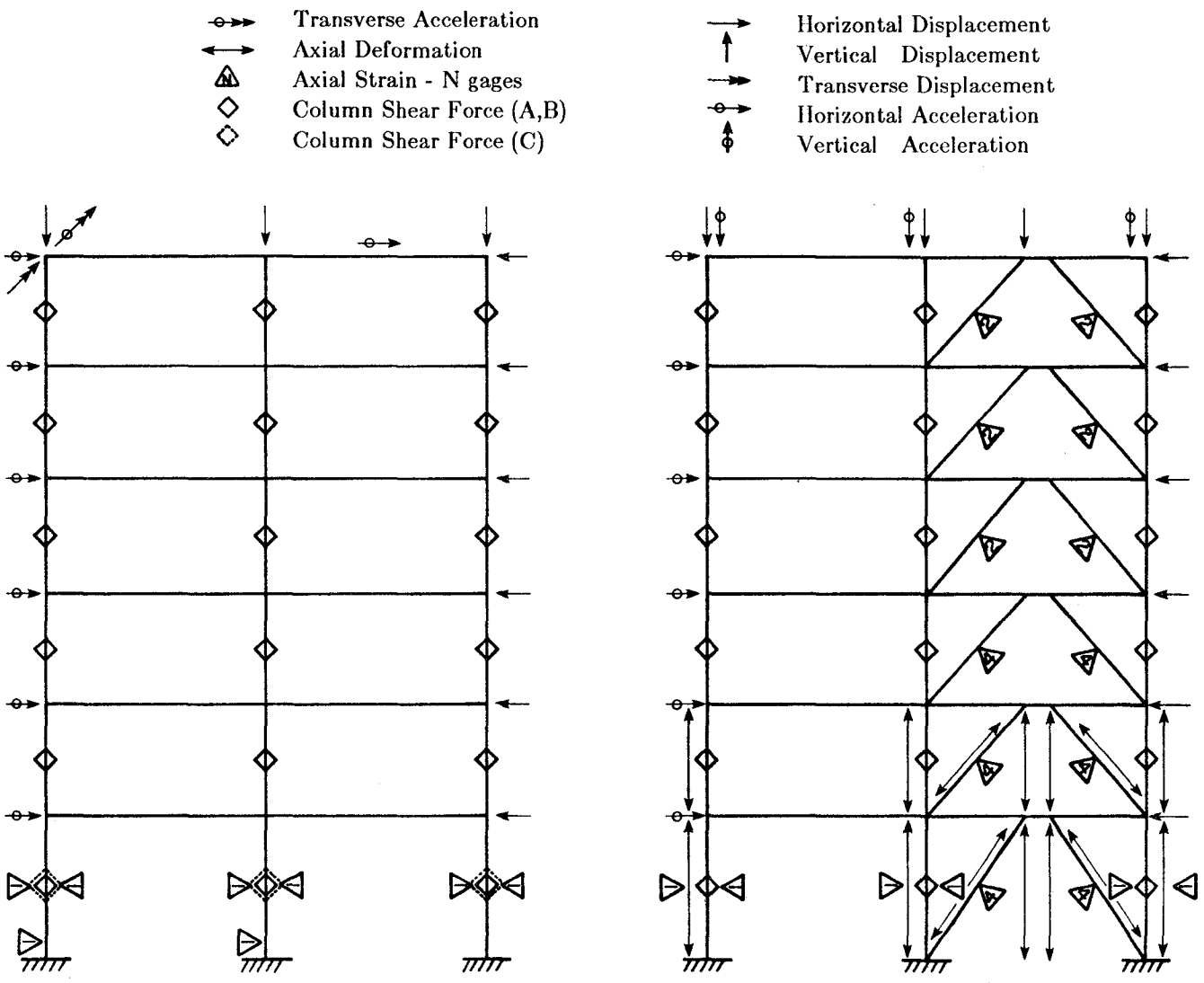


**FIGURE 5.9 INSTRUMENTATION OF THE MODEL**

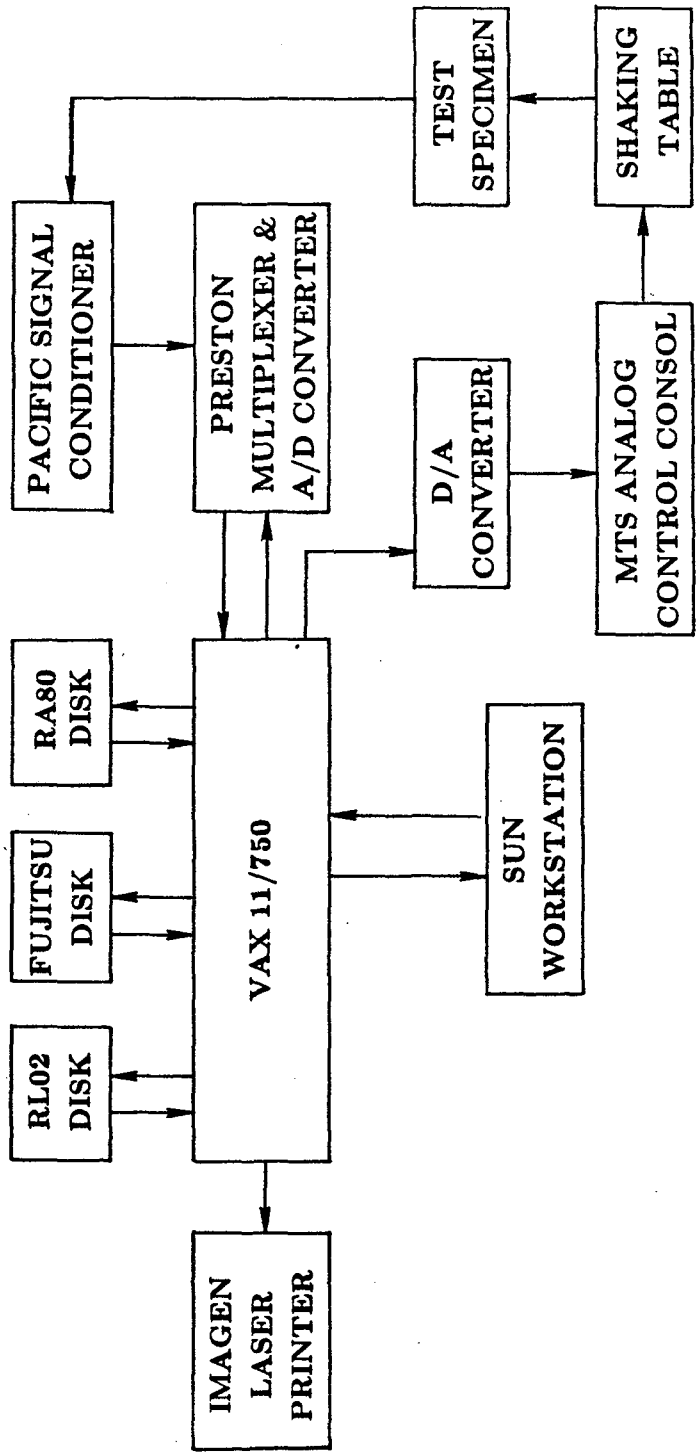


FIGURE 5.10 EARTHQUAKE SIMULATOR SYSTEM BLOCK DIAGRAM

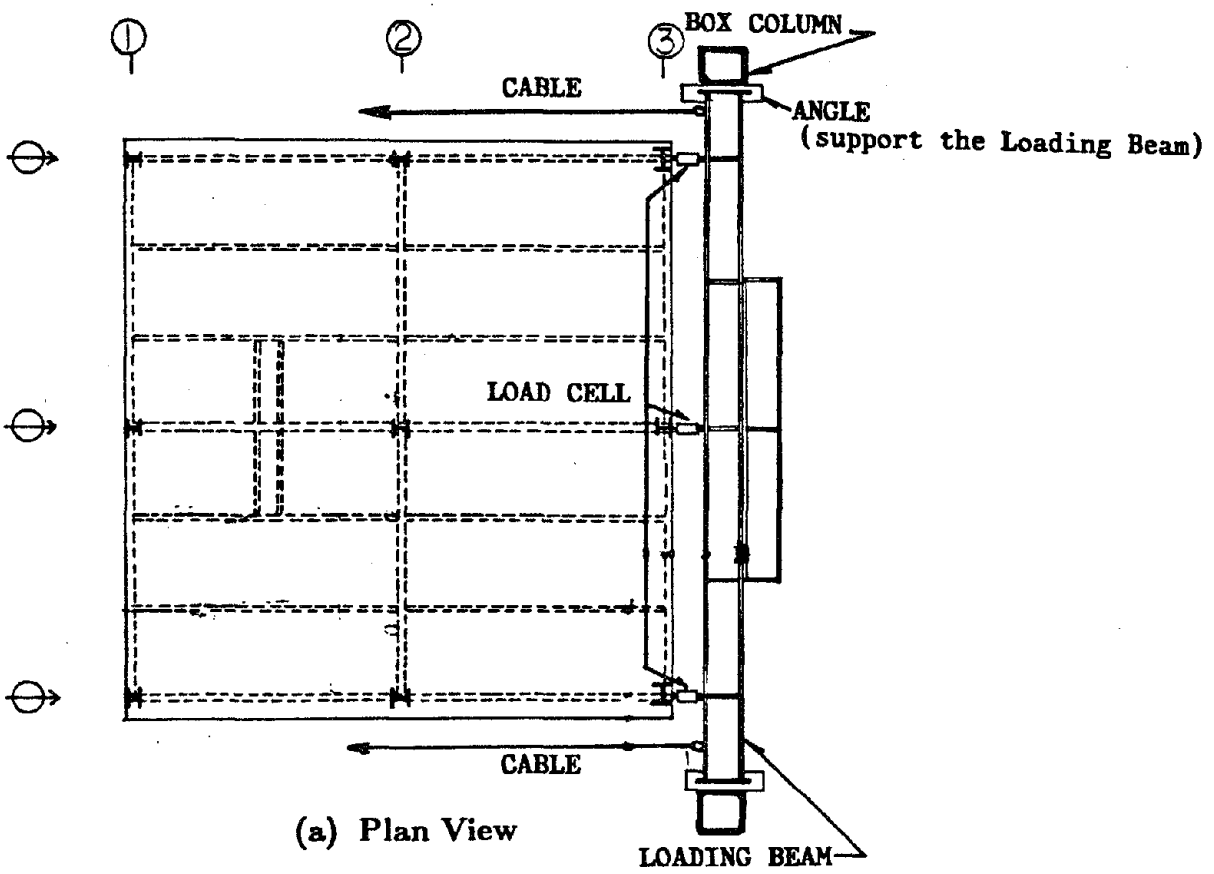


(a) Plan View

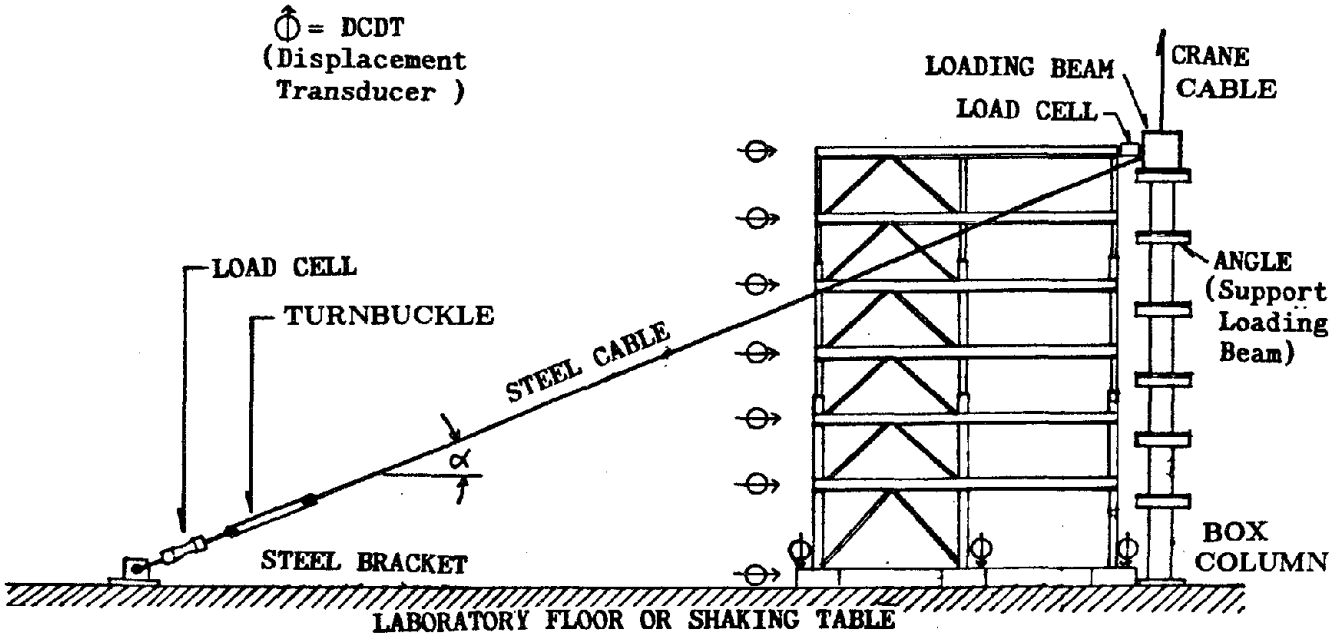


(b) Elevation

FIGURE 6.1 STATIC FLEXIBILITY TEST SET-UP

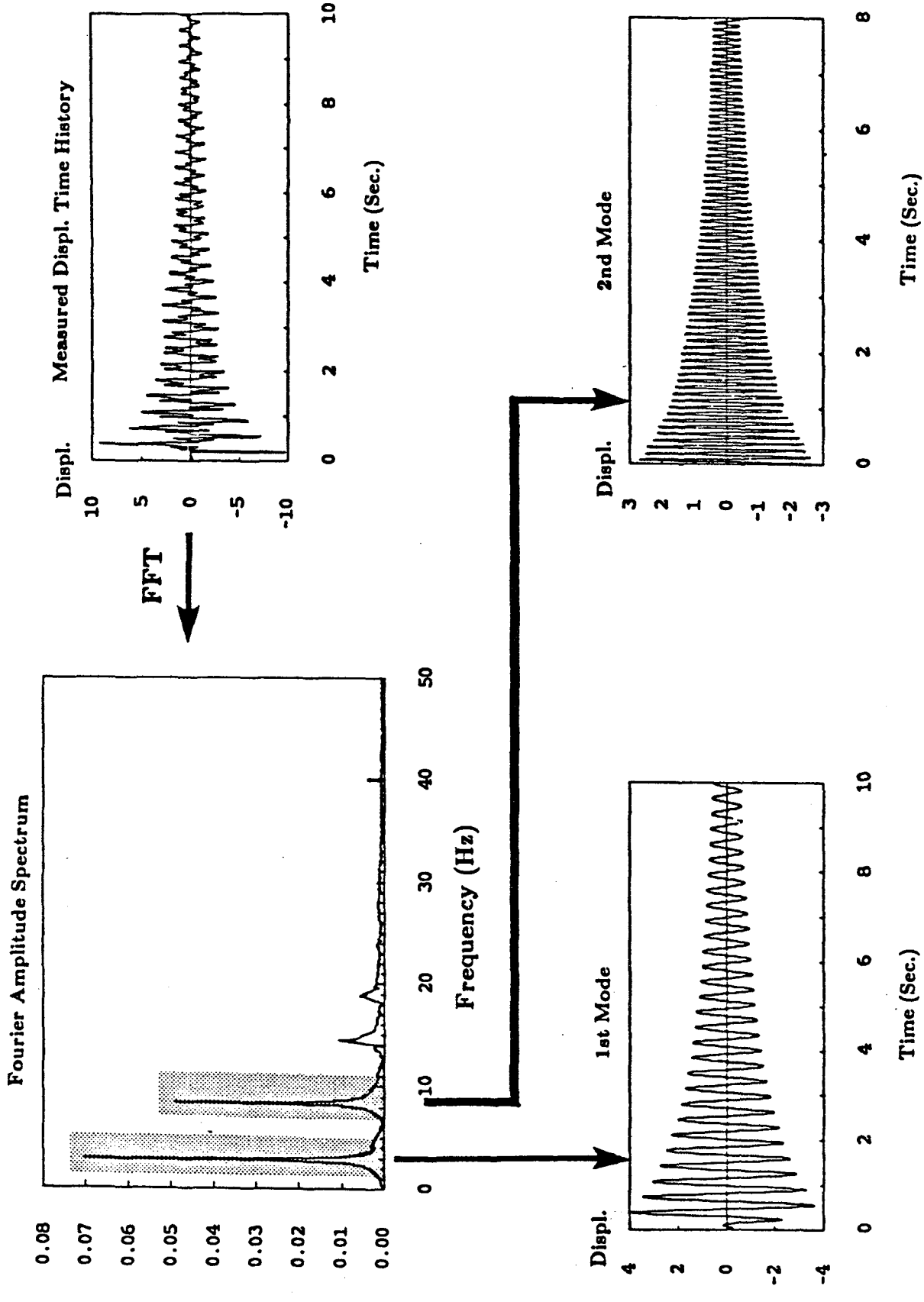


FIGURE 6.2 FREE VIBRATION TESTS AND FREQUENCY DOMAIN PROCEDURES

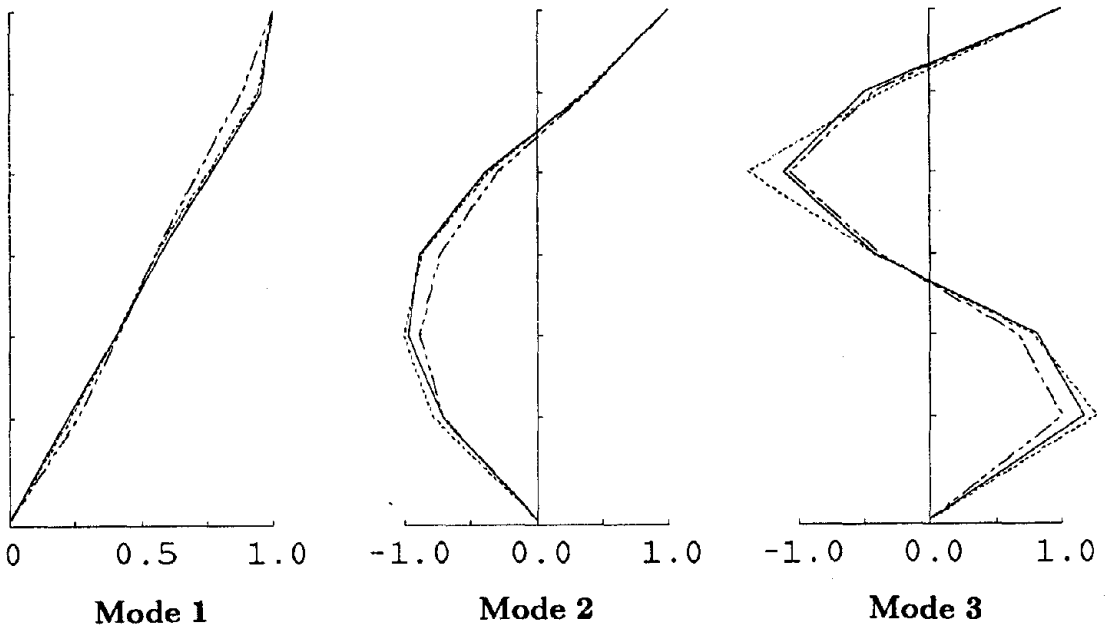


(**Solid:** *Analytical* ; **Dash-Dot:** *Free Vibration* ; **Dot:** *Flexibility Test*)

**FIGURE 6.3 MODEL MODE SHAPES**

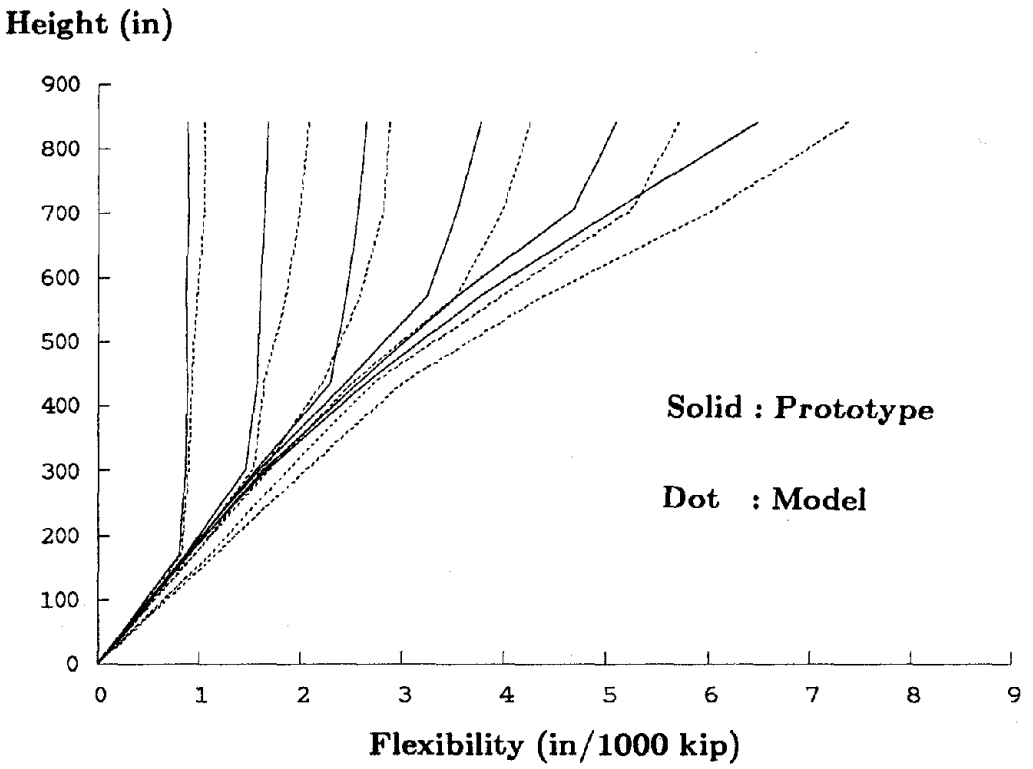


**FIGURE 6.4 PROTOTYPE AND MODEL FLEXIBILITY PROFILES**

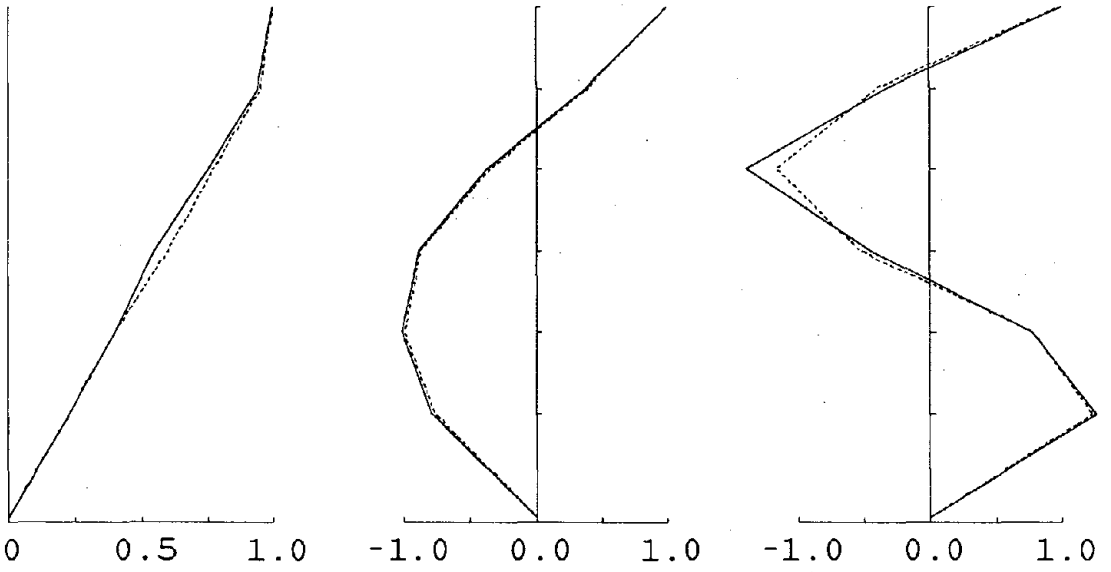


**(Solid:** *Prototype* **; Dash-Dot:** *Model***)**

**FIGURE 6.5 PROTOTYPE AND MODEL MODE SHAPES**

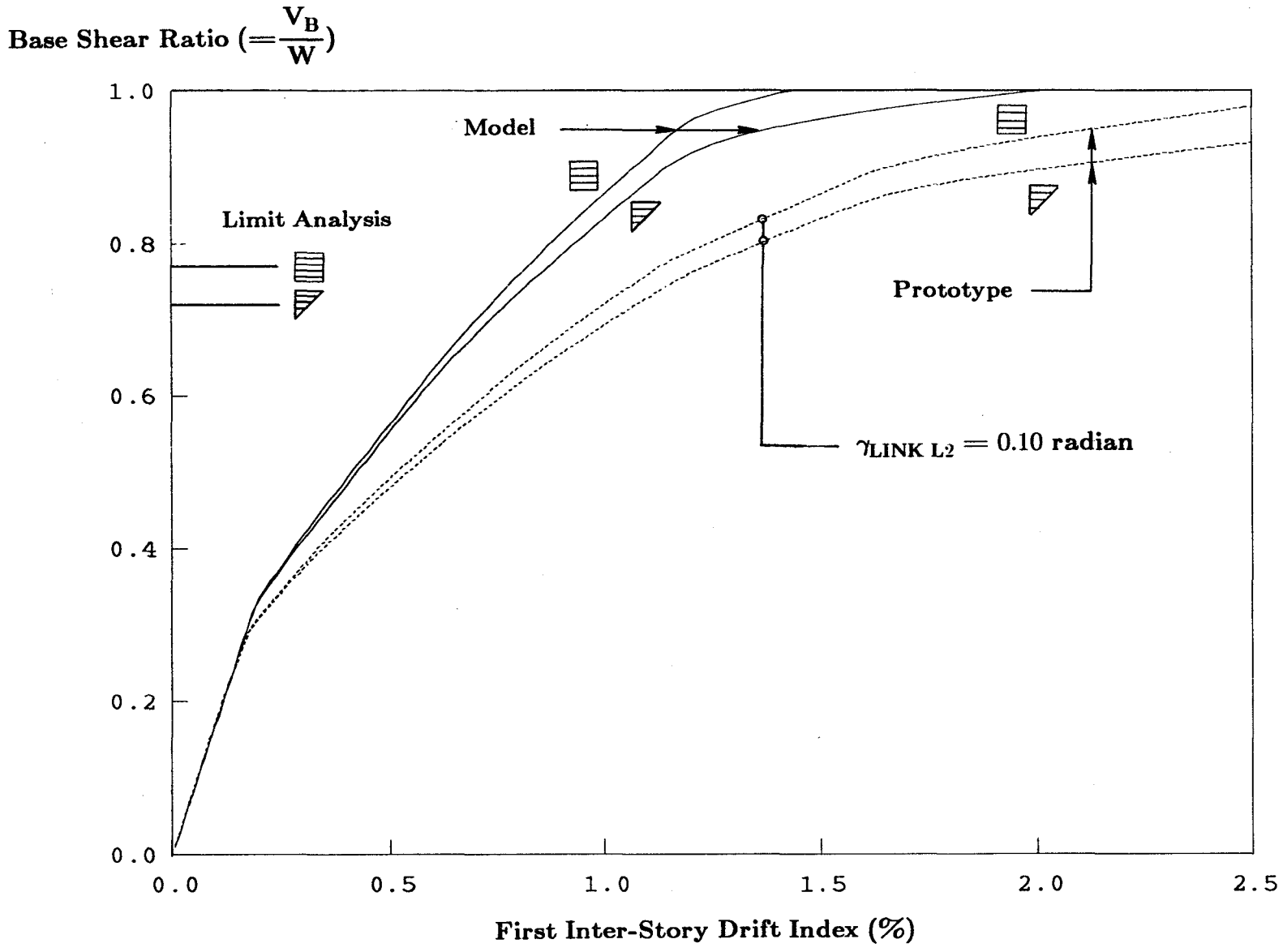


**FIGURE 7.1 ANALYTICAL PROTOTYPE AND MODEL STRENGTH AND CRITICAL IDI RELATIONSHIPS**

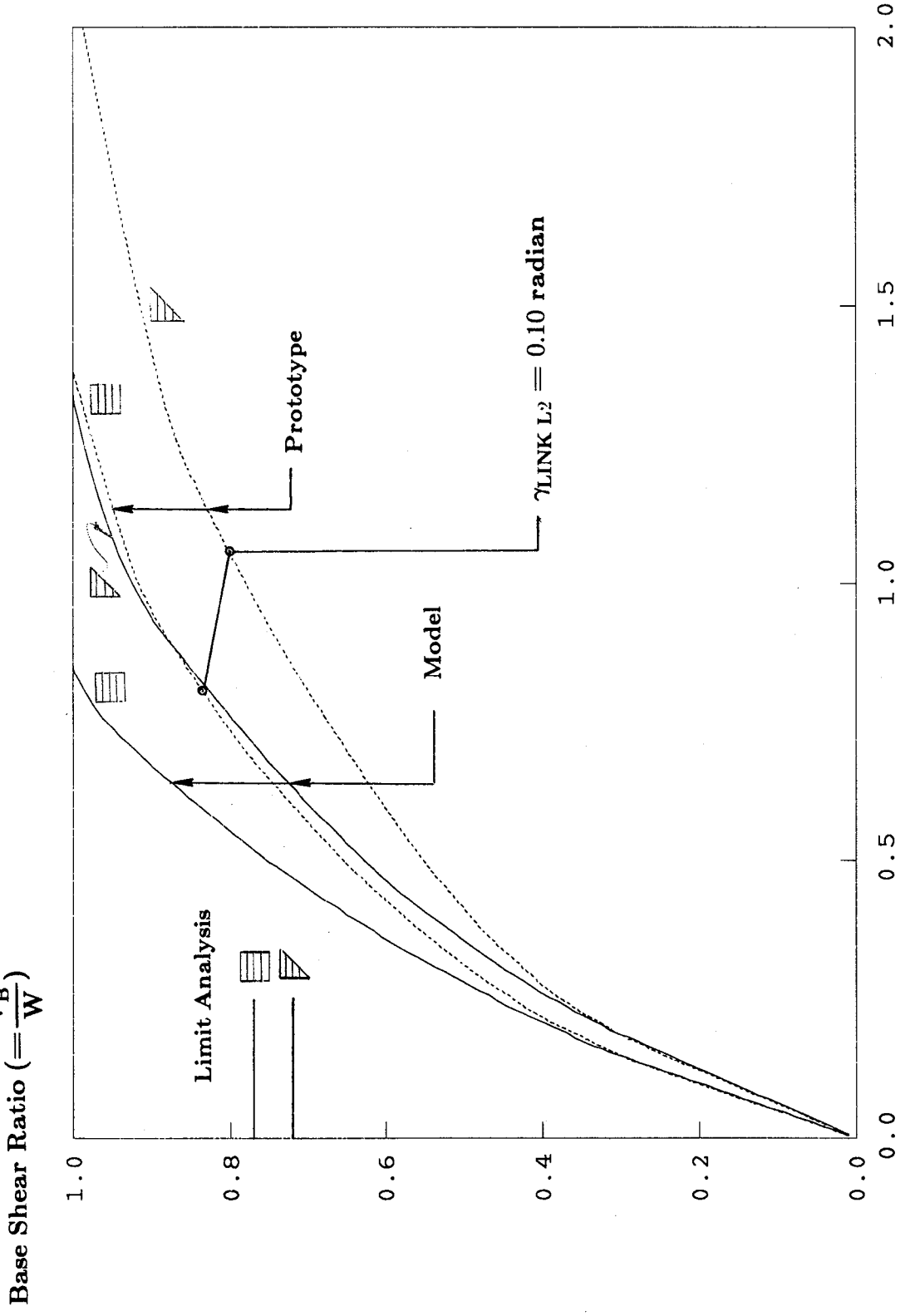


**FIGURE 7.2 ANALYTICAL PROTOTYPE AND MODEL STRENGTH AND RDI RELATIONSHIPS**

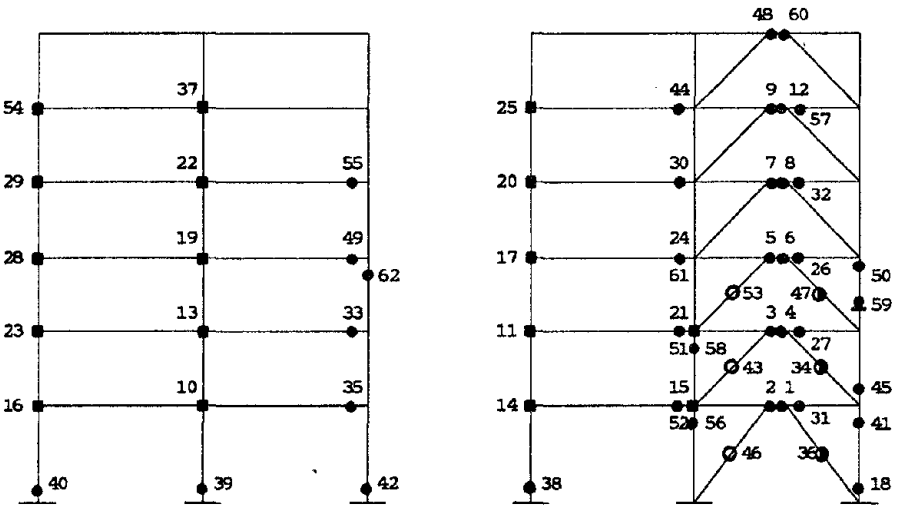


Frame A or C Frame B

(a) Triangular Load Pattern

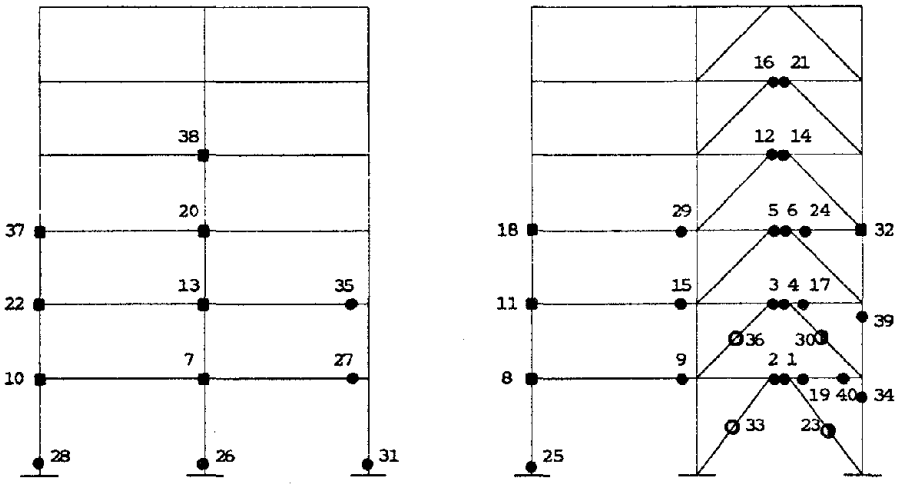


Frame A or C Frame B

(b) Rectangular Load Pattern

● Flexural Member Plastic Hinge
■ Panel Zone Plastic Hinge
○ Brace Yielding
◑ Brace Buckling

FIGURE 7.3 PLASTIC HINGE FORMATION SEQUENCE

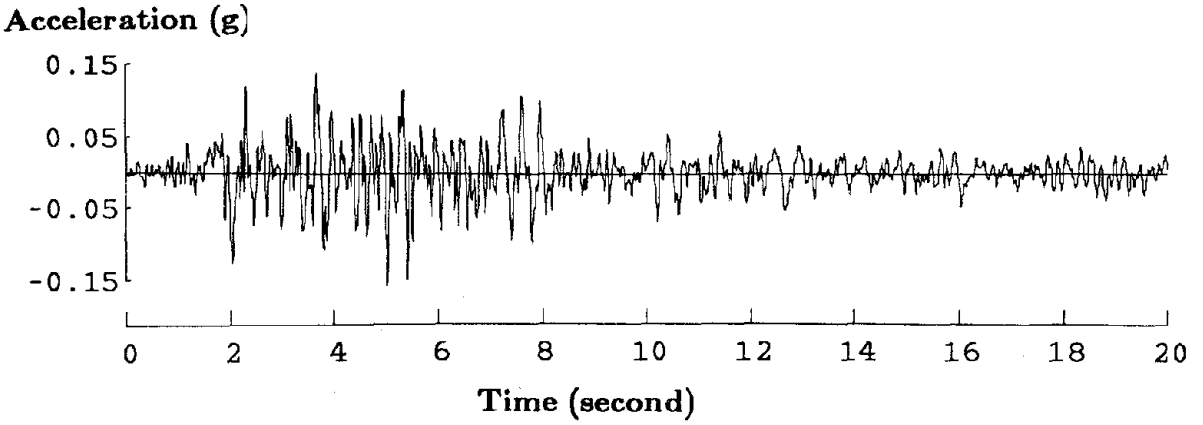


(a) Acceleration Time History

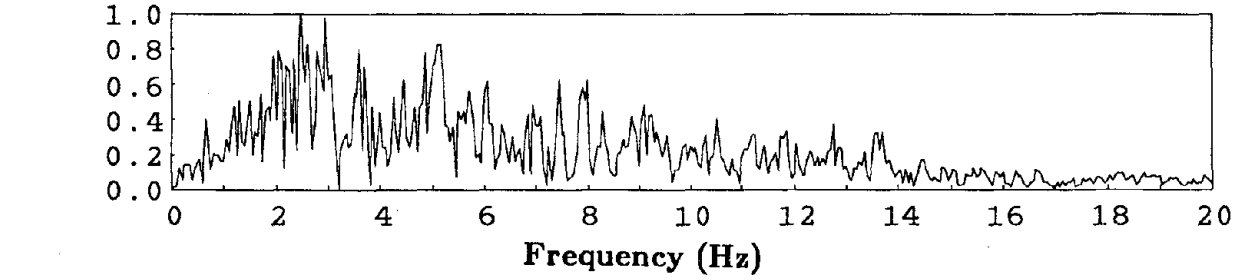


(b) Normalized Fourier Amplitude Spectrum

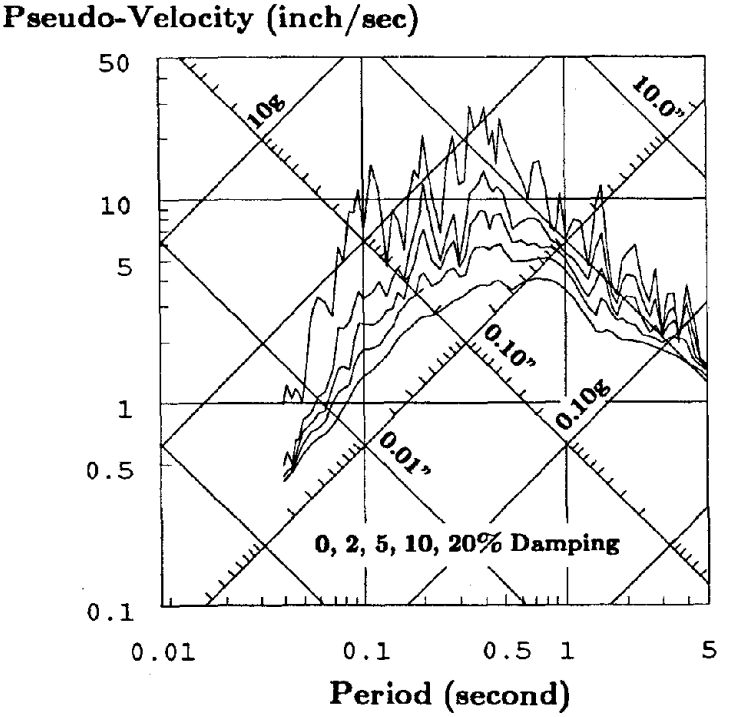


(c) Linear Elastic Response Spectra

**FIGURE 7.4 TIME SCALED TAFT N21E EARTHQUAKE RECORD**

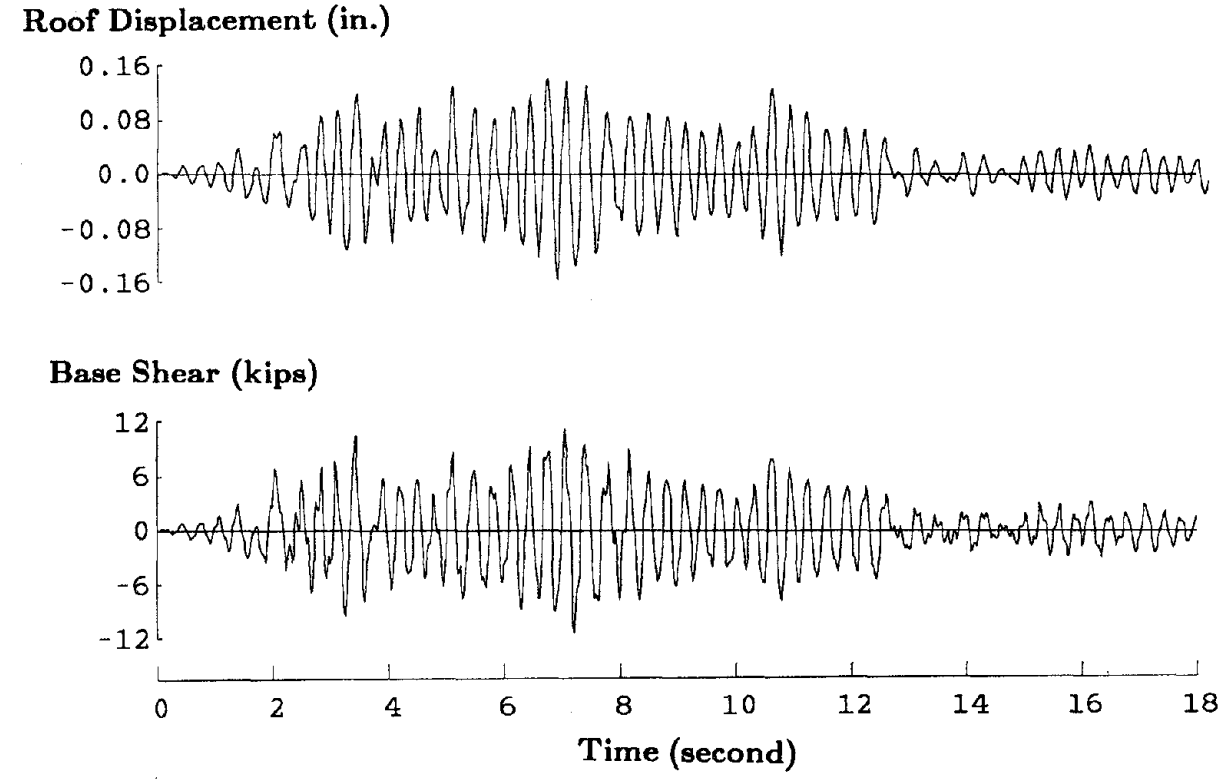


FIGURE 7.5 PREDICTED MODEL SEISMIC RESPONSE (TAFT 65 GALS)

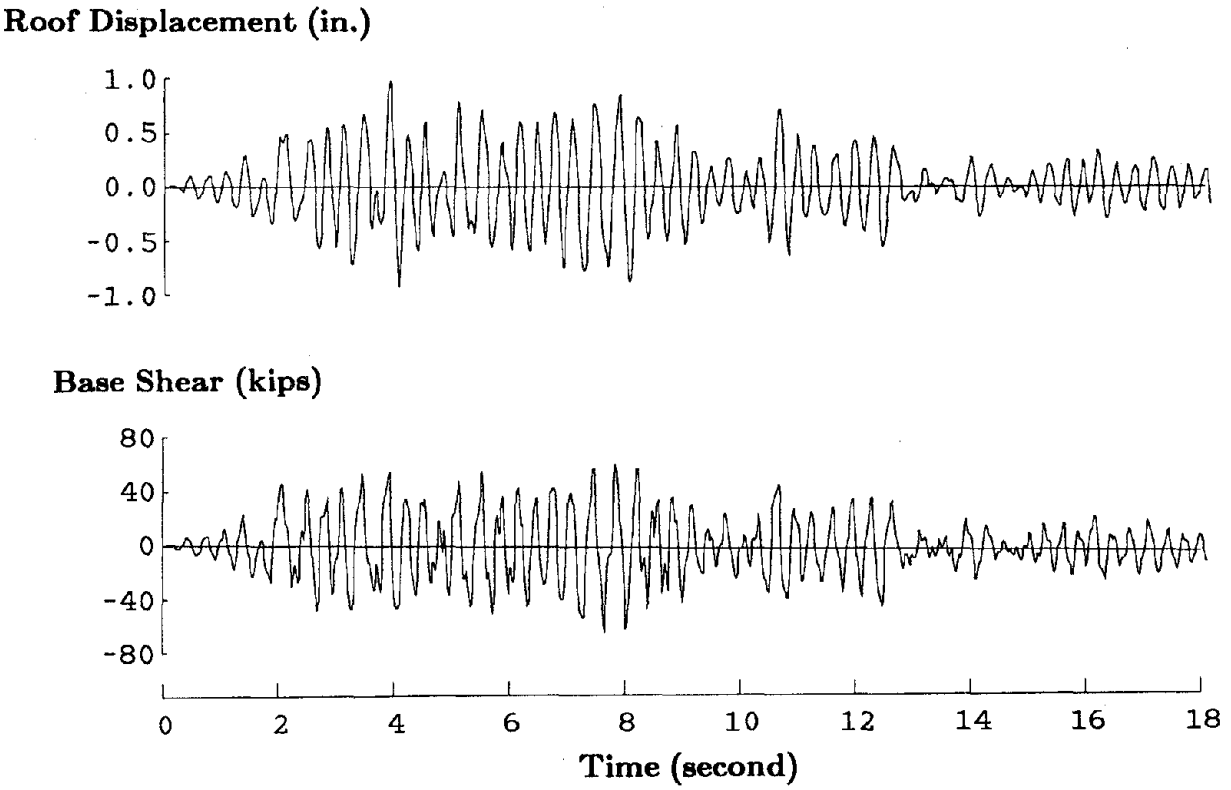


FIGURE 7.6 PREDICTED MODEL SEISMIC RESPONSE (TAFT 500 GALS)

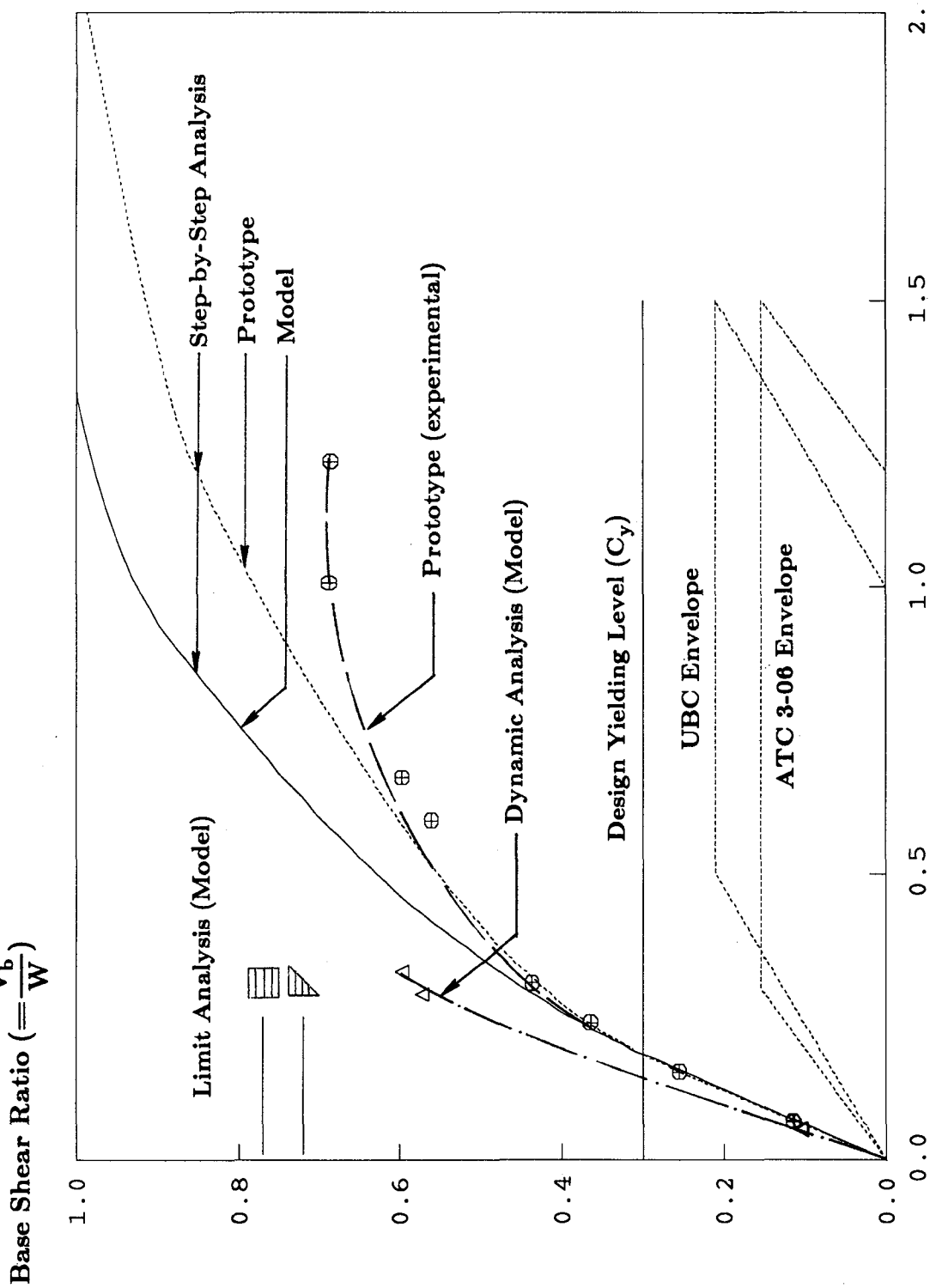


**FIGURE 7.7 STRENGTH AND DEFORMATION CHARACTERISTICS OF THE PROTOTYPE AND THE MODEL**

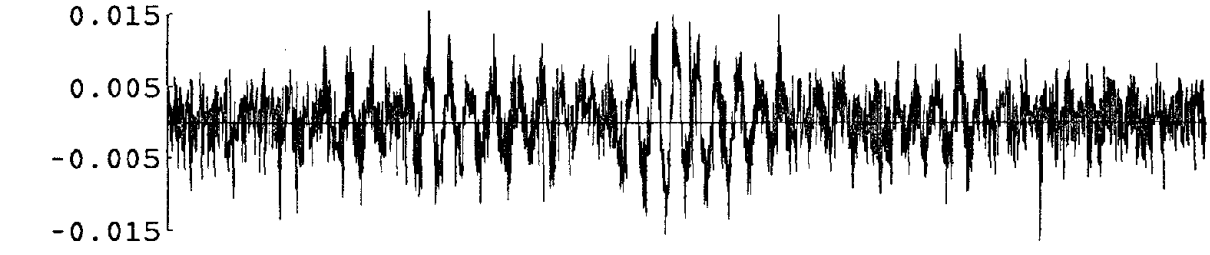


(a) Uncorrected $Br_4$ Deformation

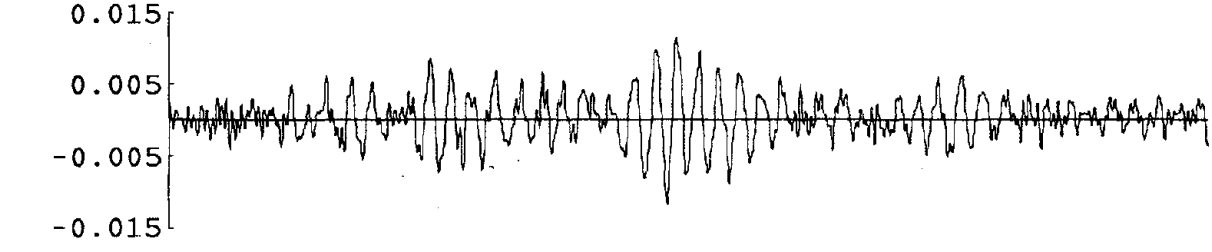


(b) Filtered $Br_4$ Deformation

**FIGURE 7.8 HIGH FREQUENCY NOISE FILTER**

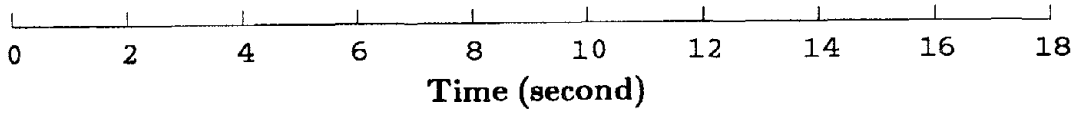


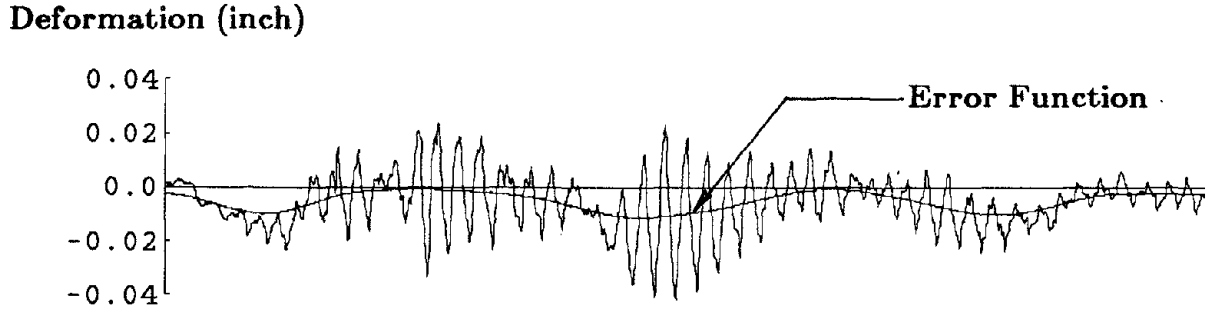


(a) Uncorrected Fifth Inter-story Drift

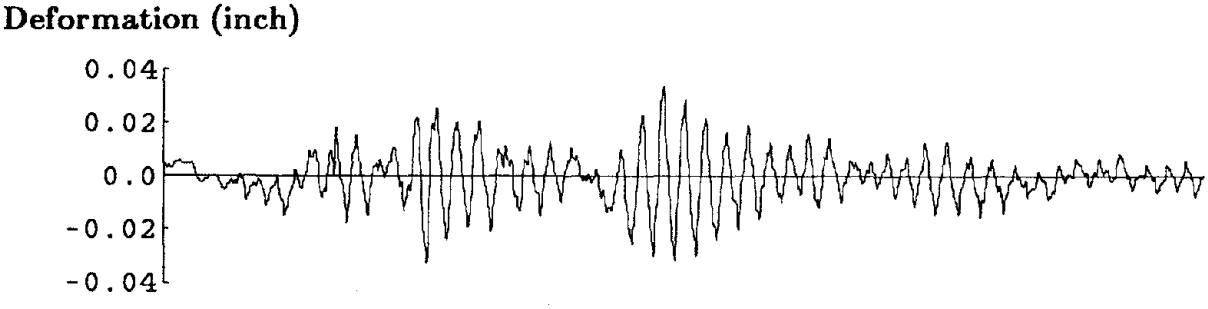


(b) Filtered Fifth Inter-story Drift

**FIGURE 7.9 LOW FREQUENCY NOISE FILTER**

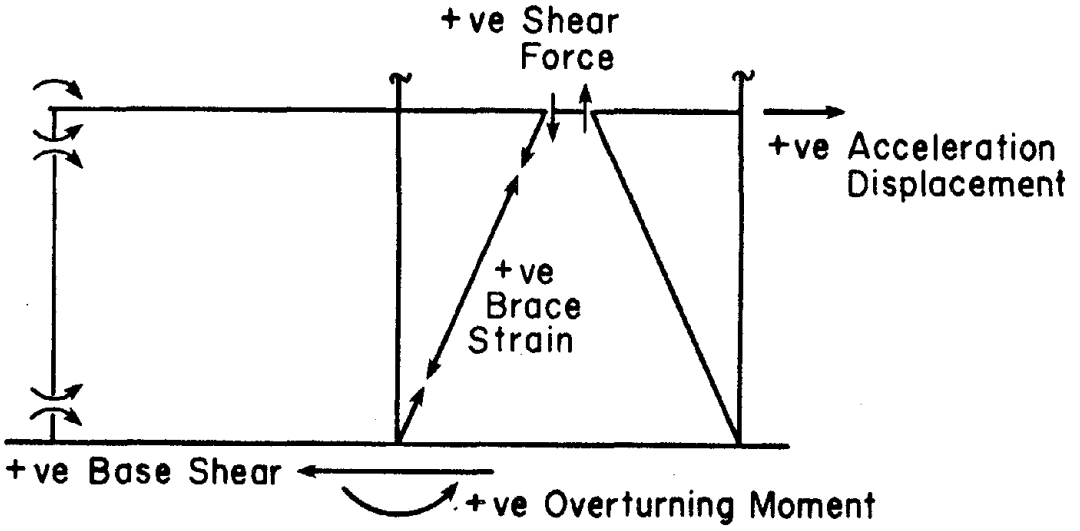


FIGURE 7.10 MODEL SIGN CONVENTION

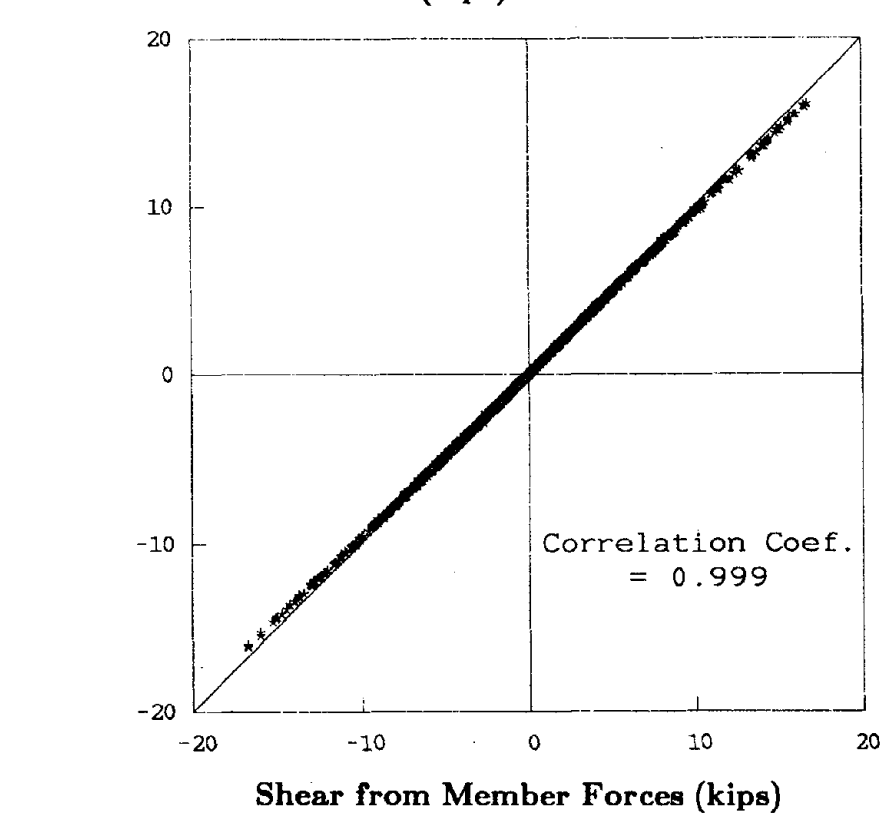


FIGURE 7.11 BASE SHEAR COMPARISON

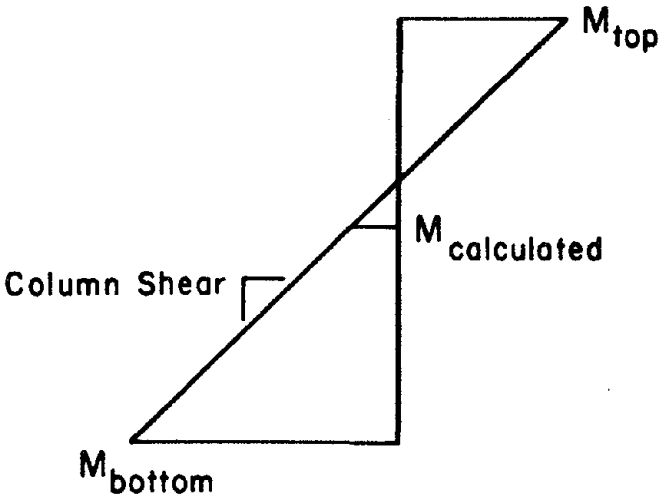


FIGURE 7.12 FIRST STORY COLUMN END MOMENT EVALUATION

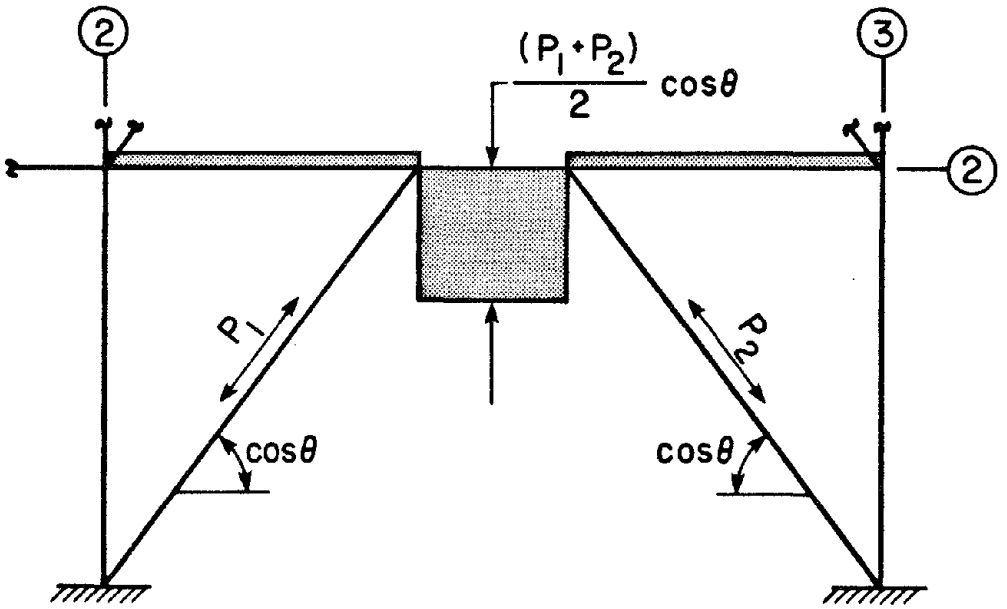


FIGURE 7.13 LEVEL L2 SHEAR FORCE DISTRIBUTION UNDER LATERAL LOADING

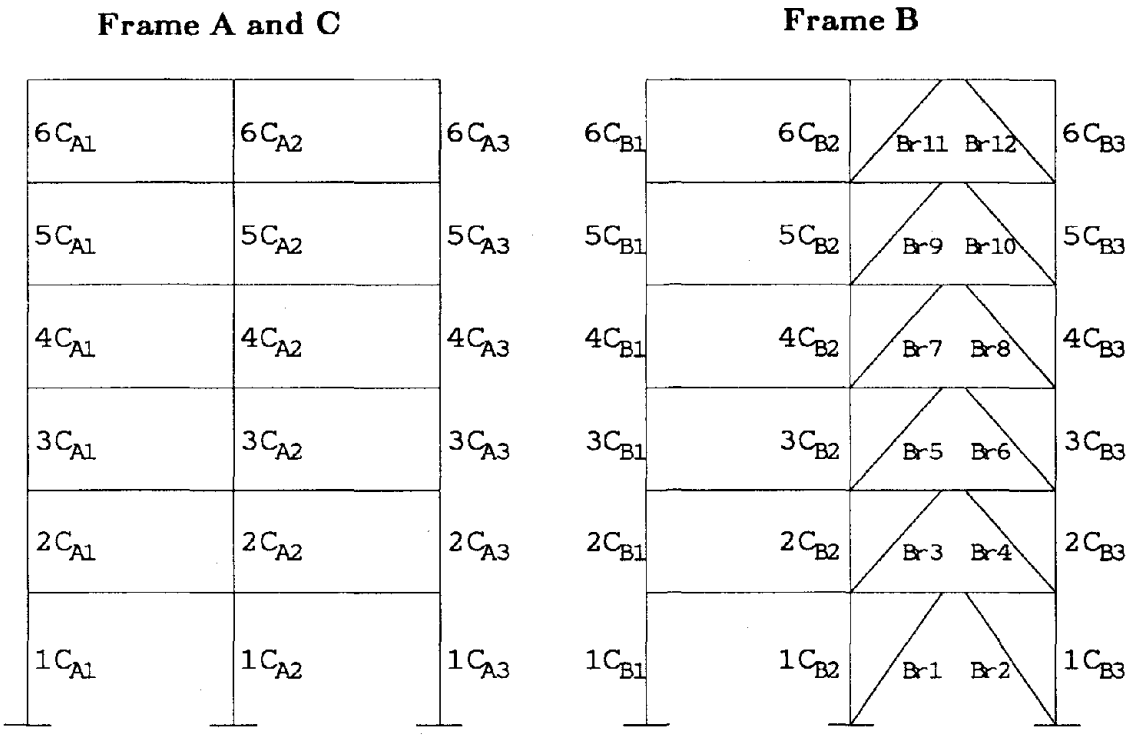


**(a) Column and Brace Designation**

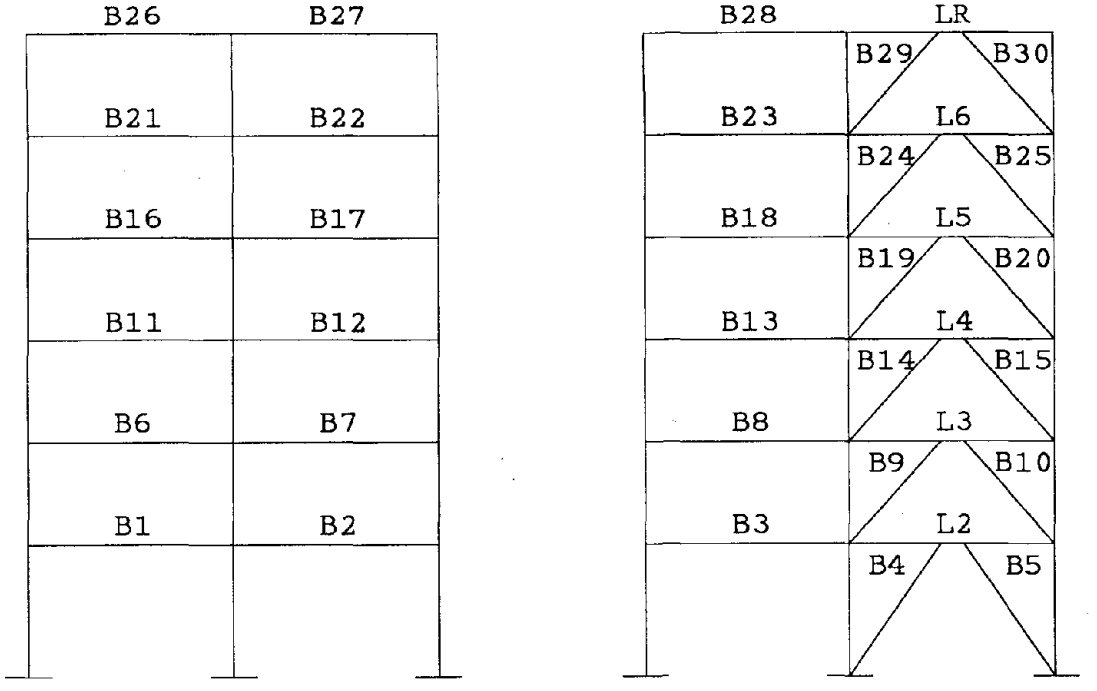


**(b) Beam and Shear Link Designation**

**FIGURE 7.14 MODEL MEMBER DESIGNATION**

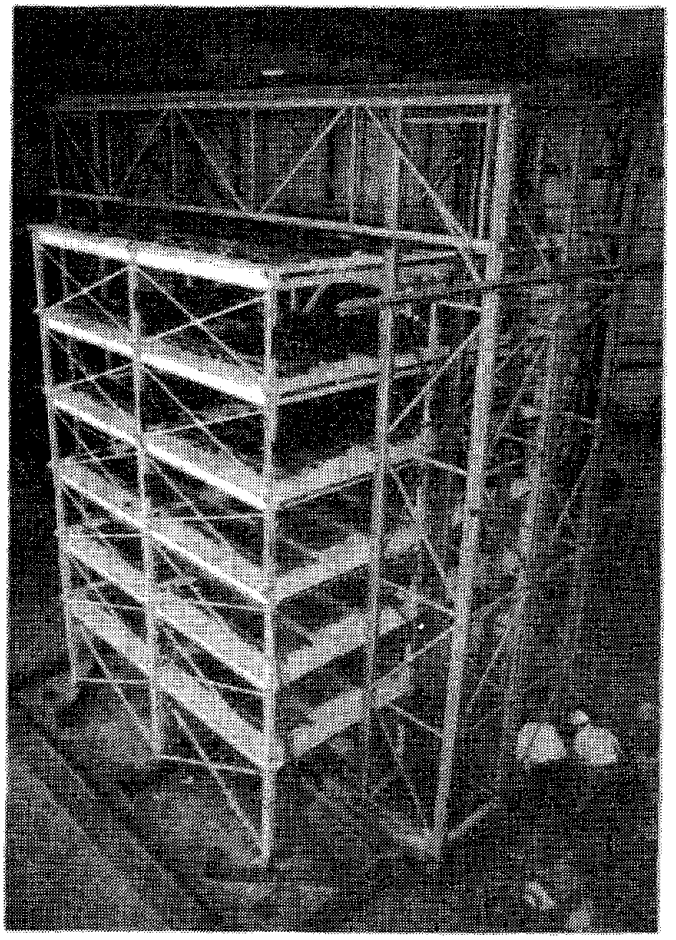

**FIGURE 8.1 ECCENTRICALLY K-BRACED MODEL**

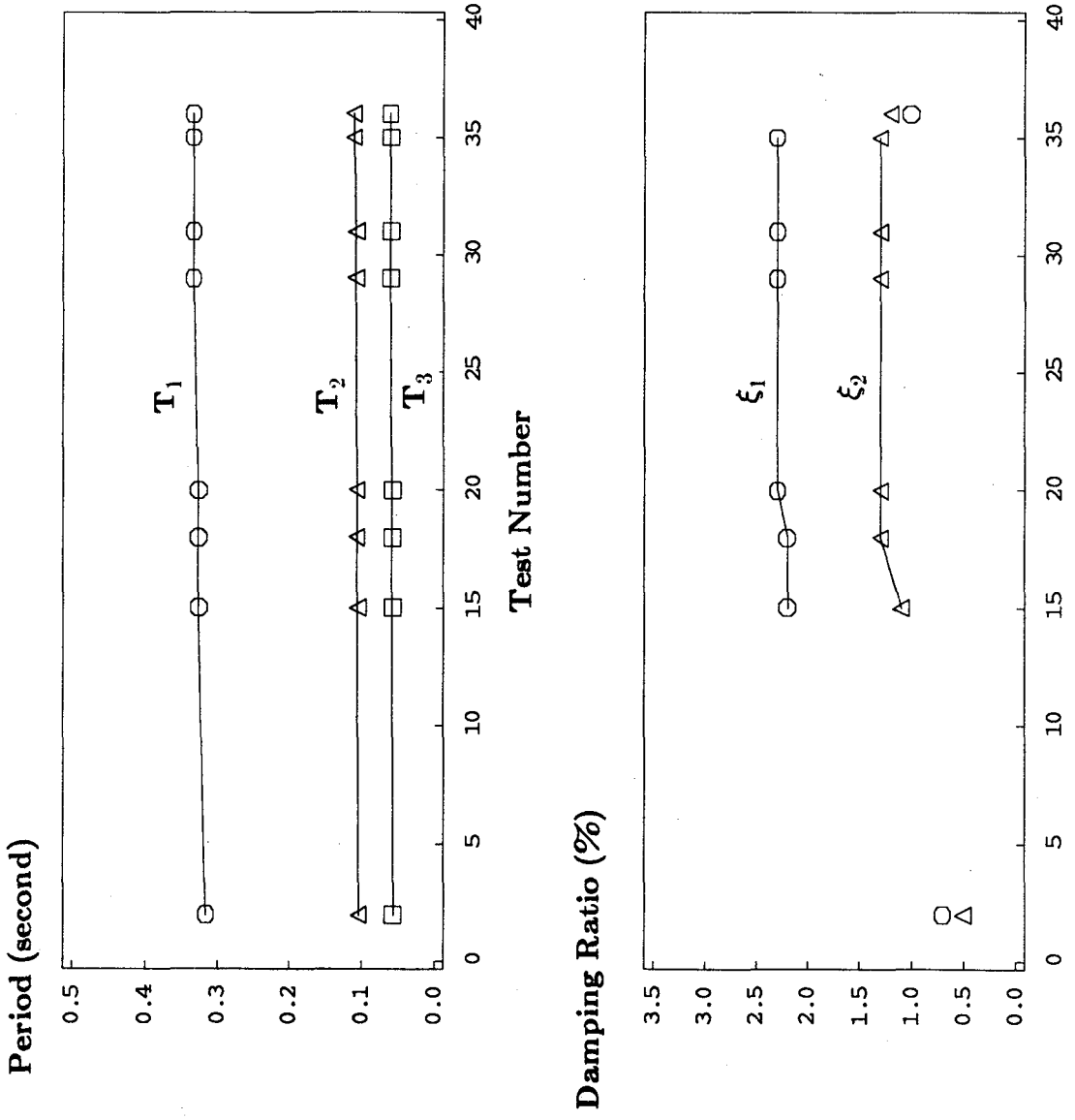


FIGURE 8.2 VARIATIONS IN THE DYNAMIC CHARACTERISTICS OF THE MODEL

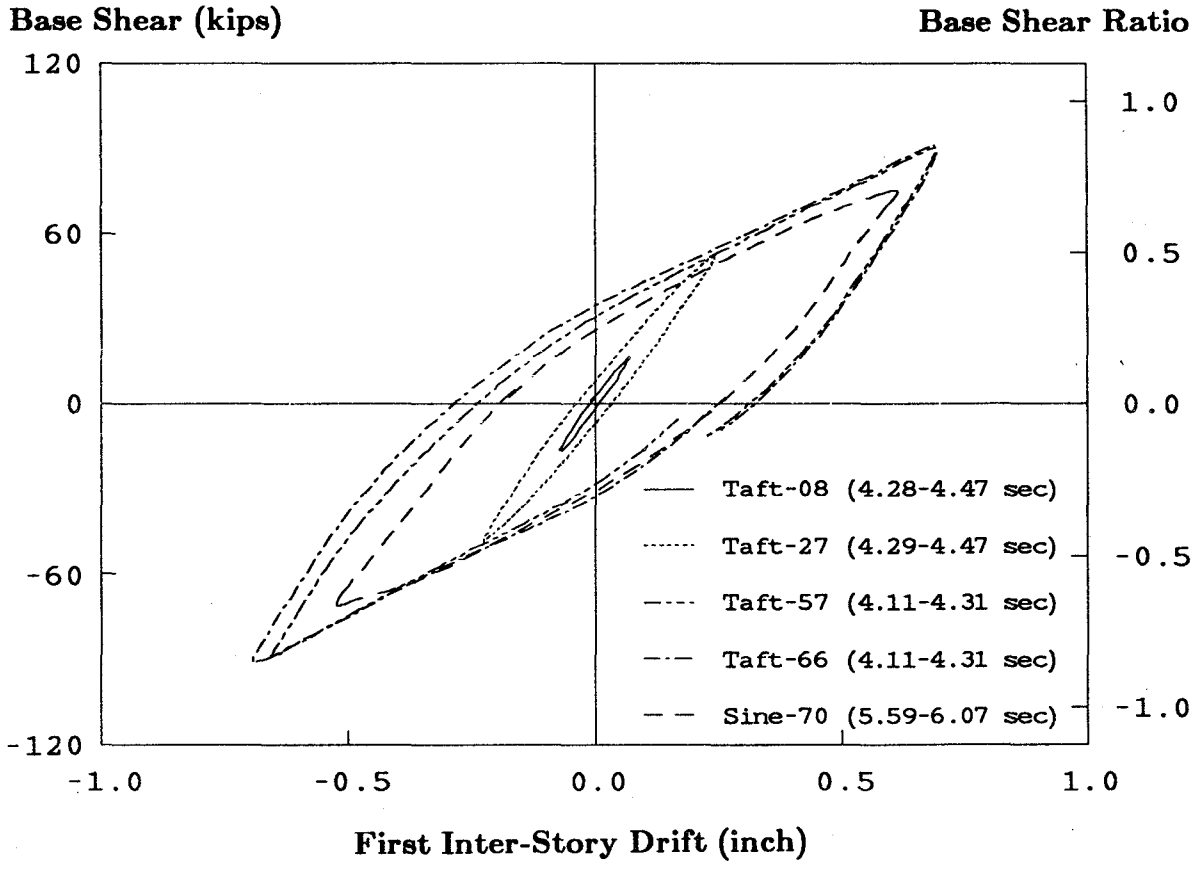


**FIGURE 8.3 MAJOR CYCLES OF BASE SHEAR AND FIRST INTER-STORY DRIFT INDEX**

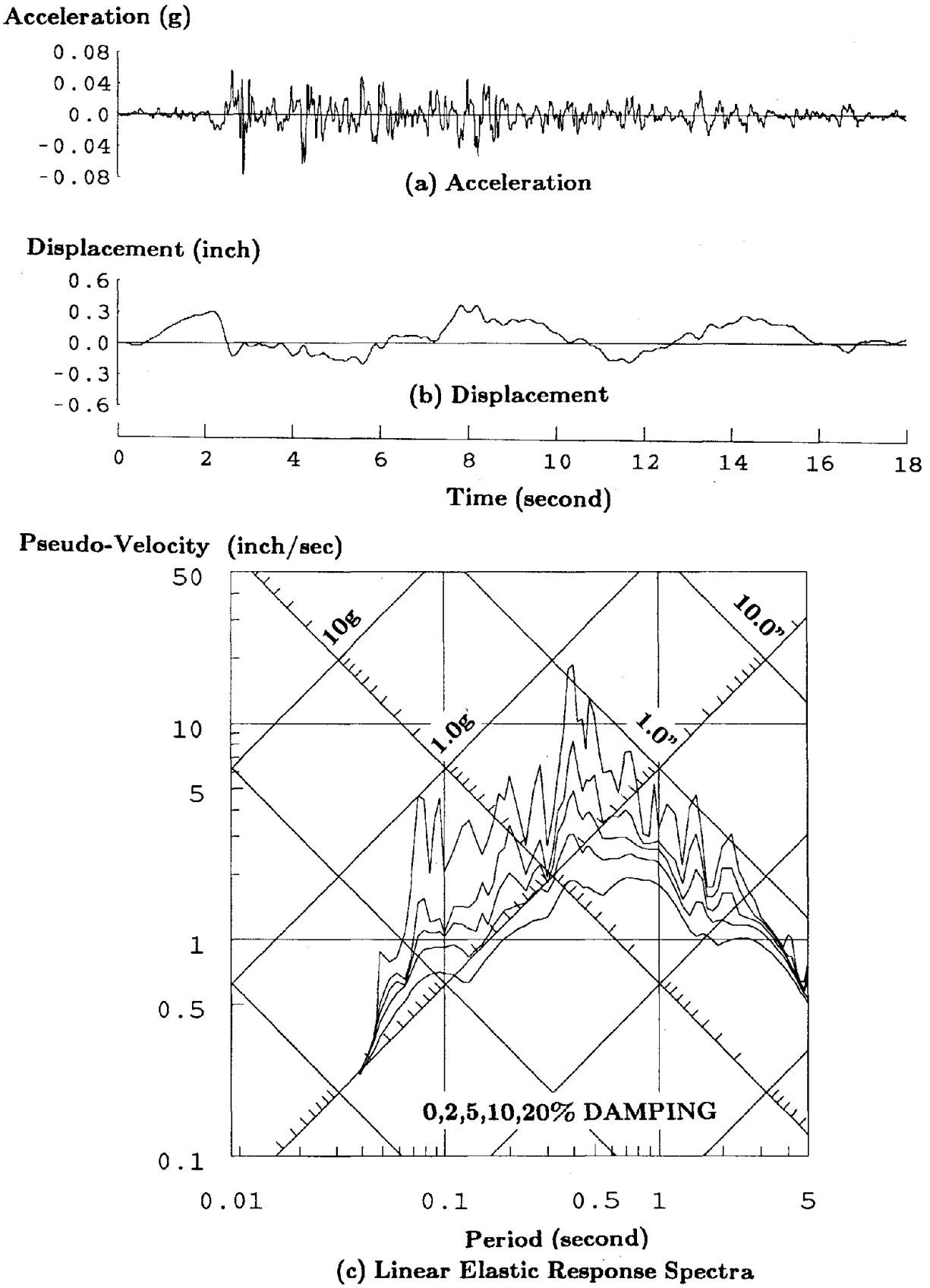


**FIGURE 8.4 TAFT-08 MEASURED TABLE MOTION**

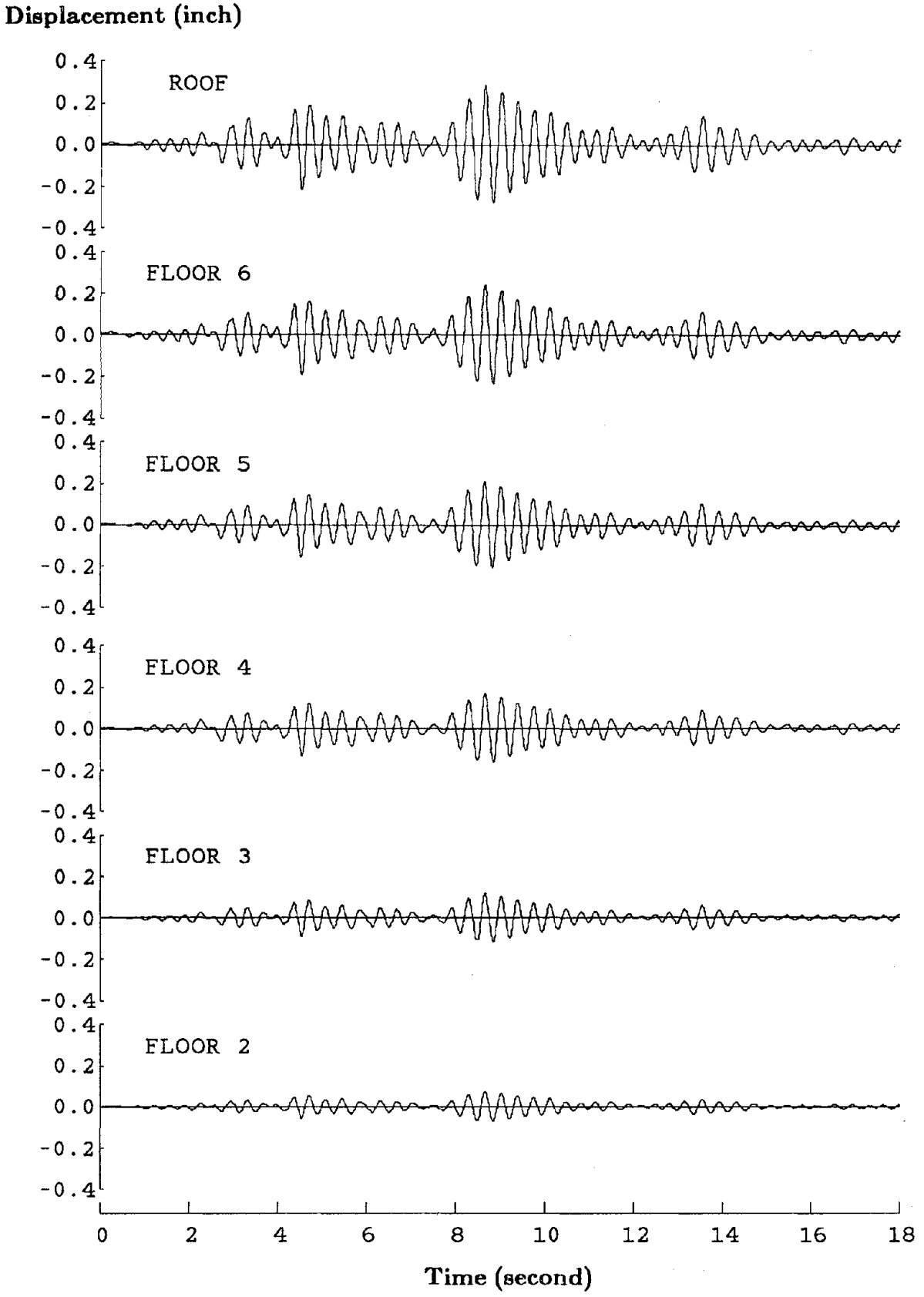


**FIGURE 8.5 TAFT-08 LATERAL DISPLACEMENT TIME HISTORY**

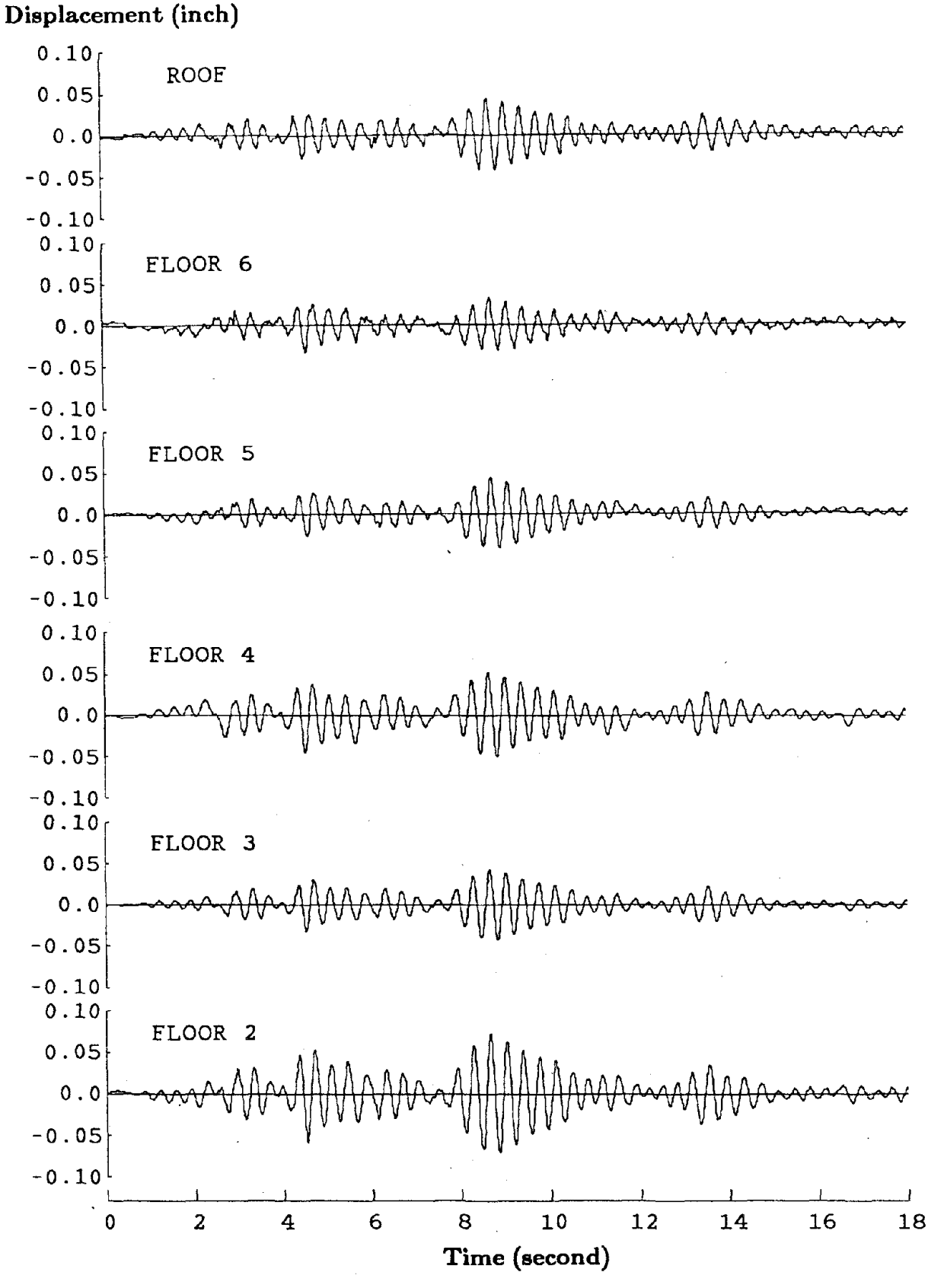


**FIGURE 8.6 TAFT-08 INTER-STORY DRIFT TIME HISTORY**

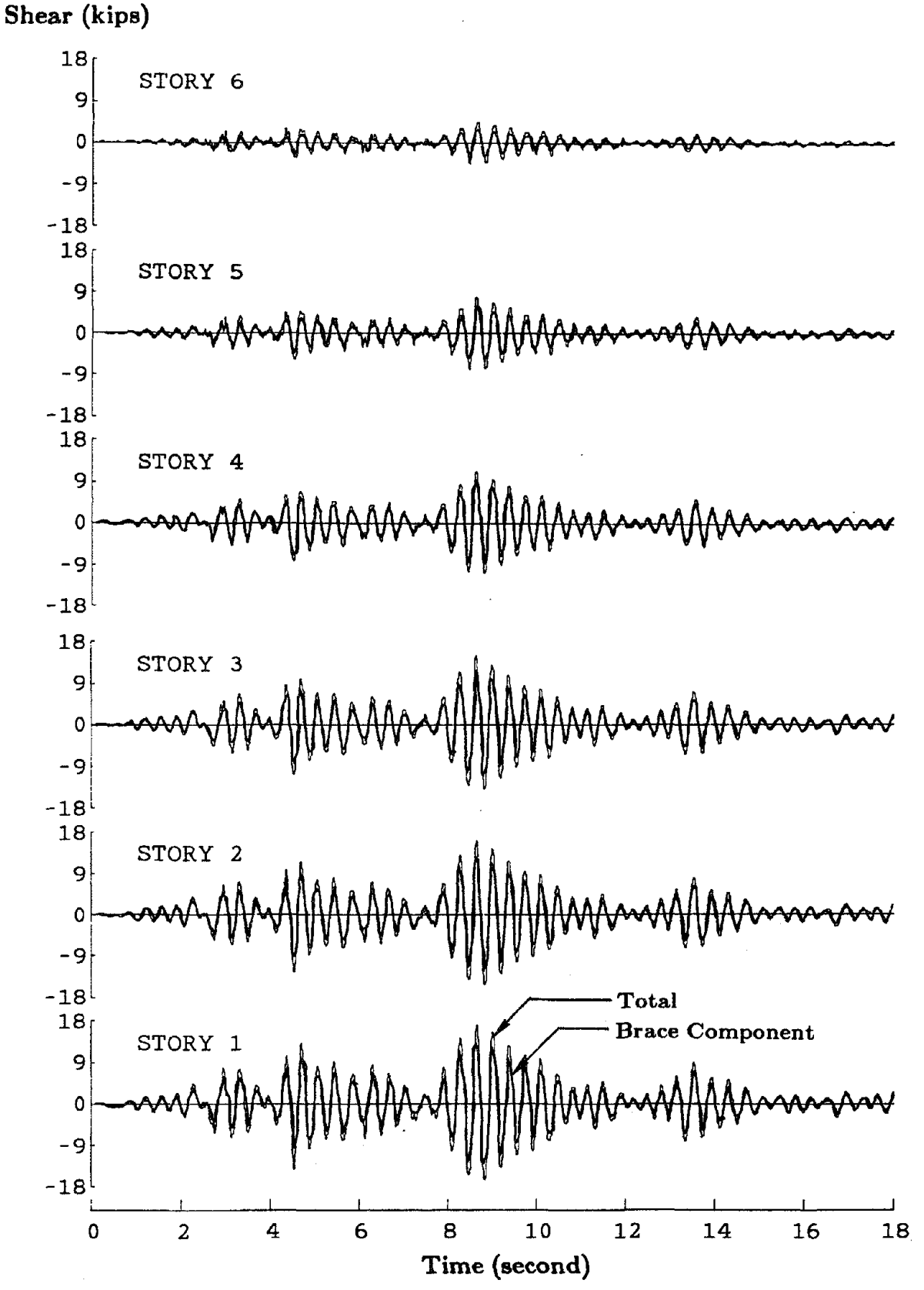


**FIGURE 8.7 TAFT-08 STORY SHEAR TIME HISTORY**

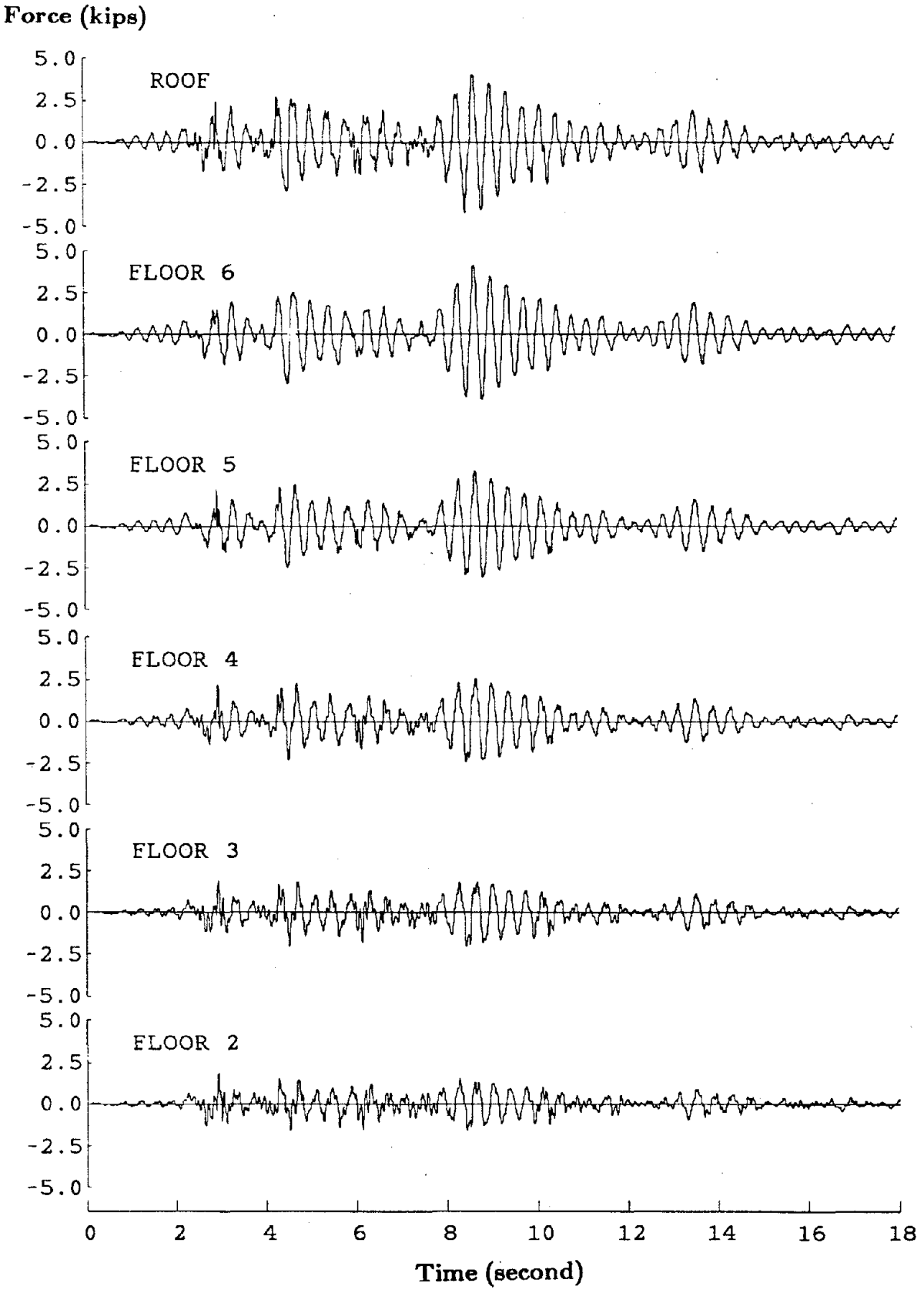


**FIGURE 8.8 TAFT-08 INERTIA FORCE TIME HISTORY**

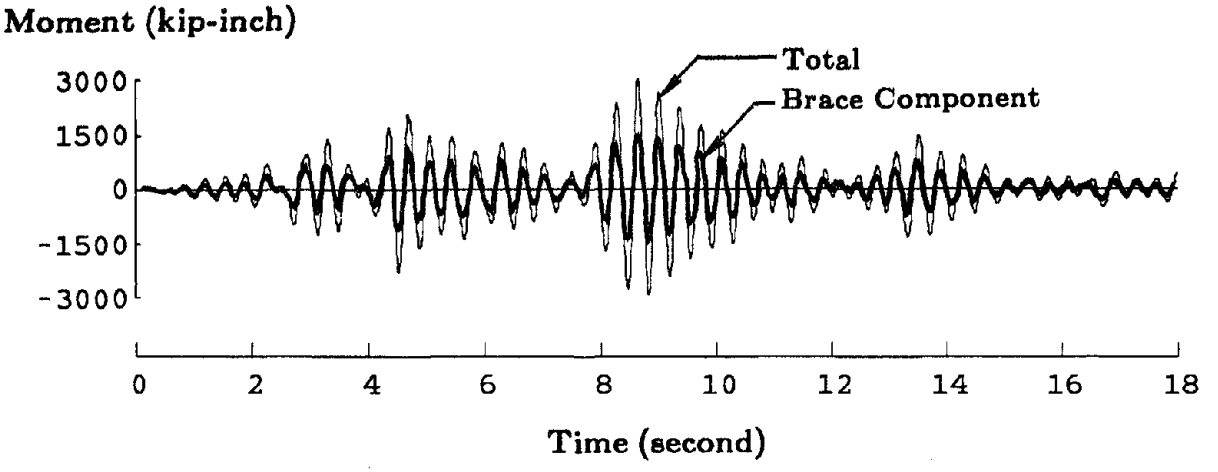


FIGURE 8.9 TAFT-08 BASE OVERTURNING MOMENT TIME HISTORY

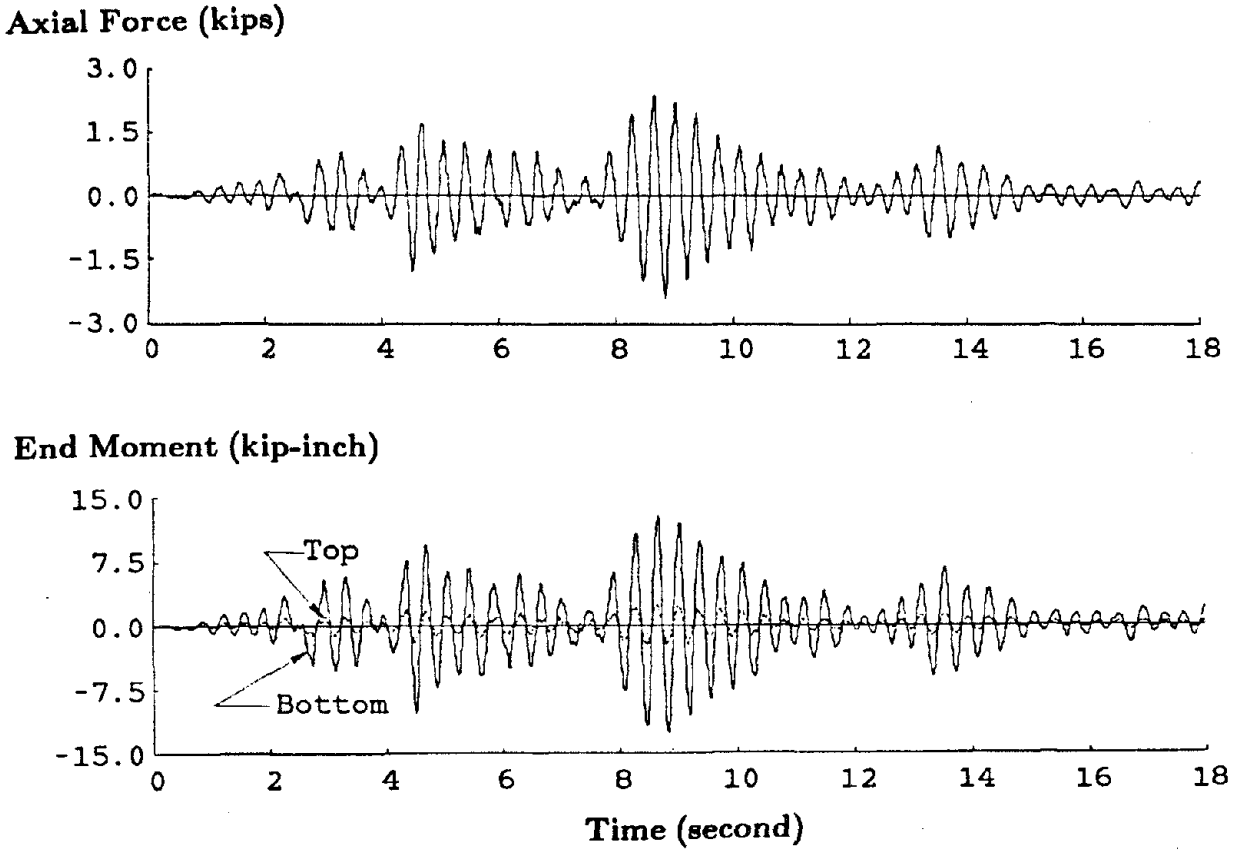


FIGURE 8.10 TAFT-08 COLUMN $1C_{A1}$ AXIAL FORCE AND END MOMENT TIME HISTORY

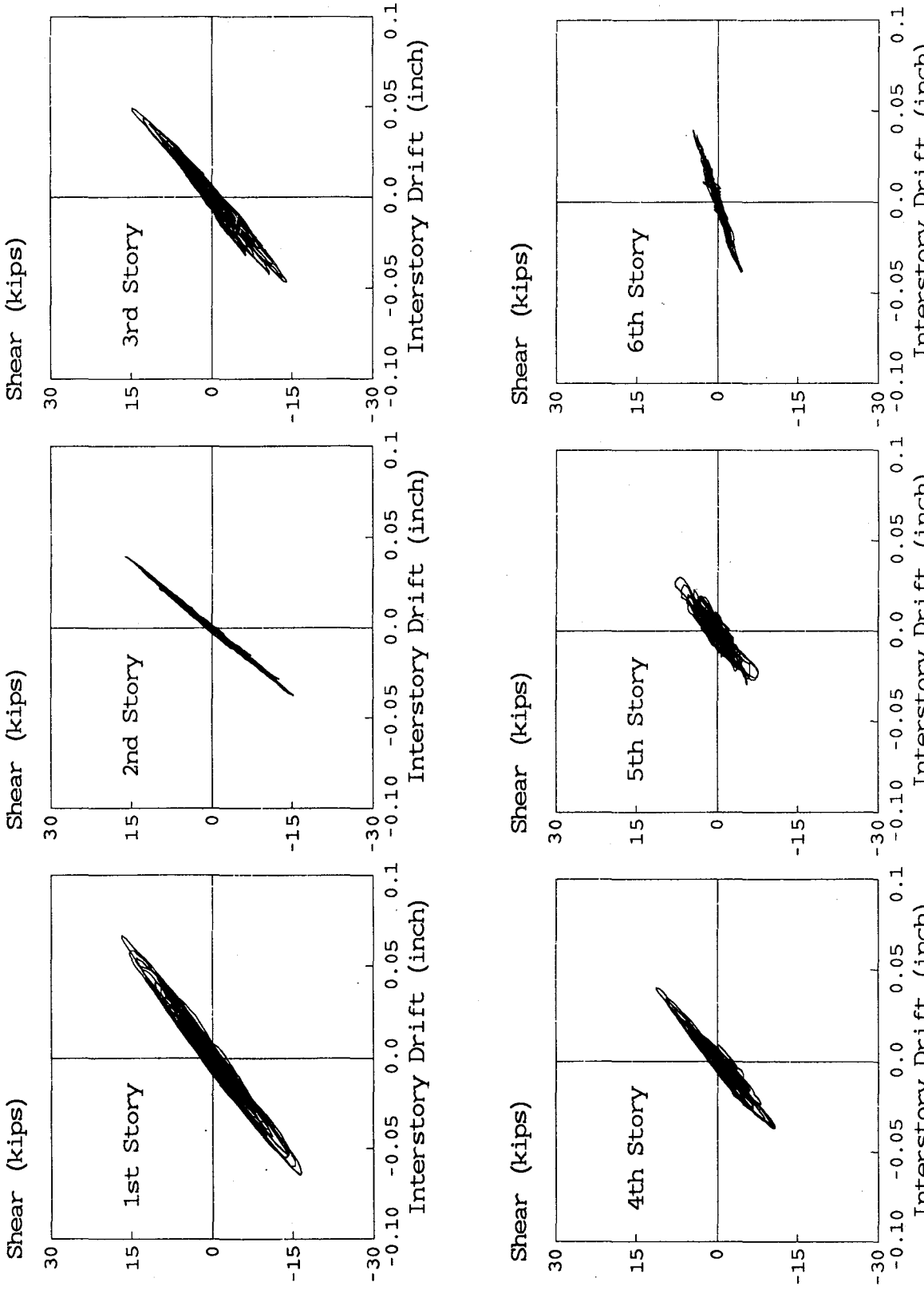


**FIGURE 8.11 TAFT-08 TOTAL STORY SHEAR AND INTER-STORY DRIFT**

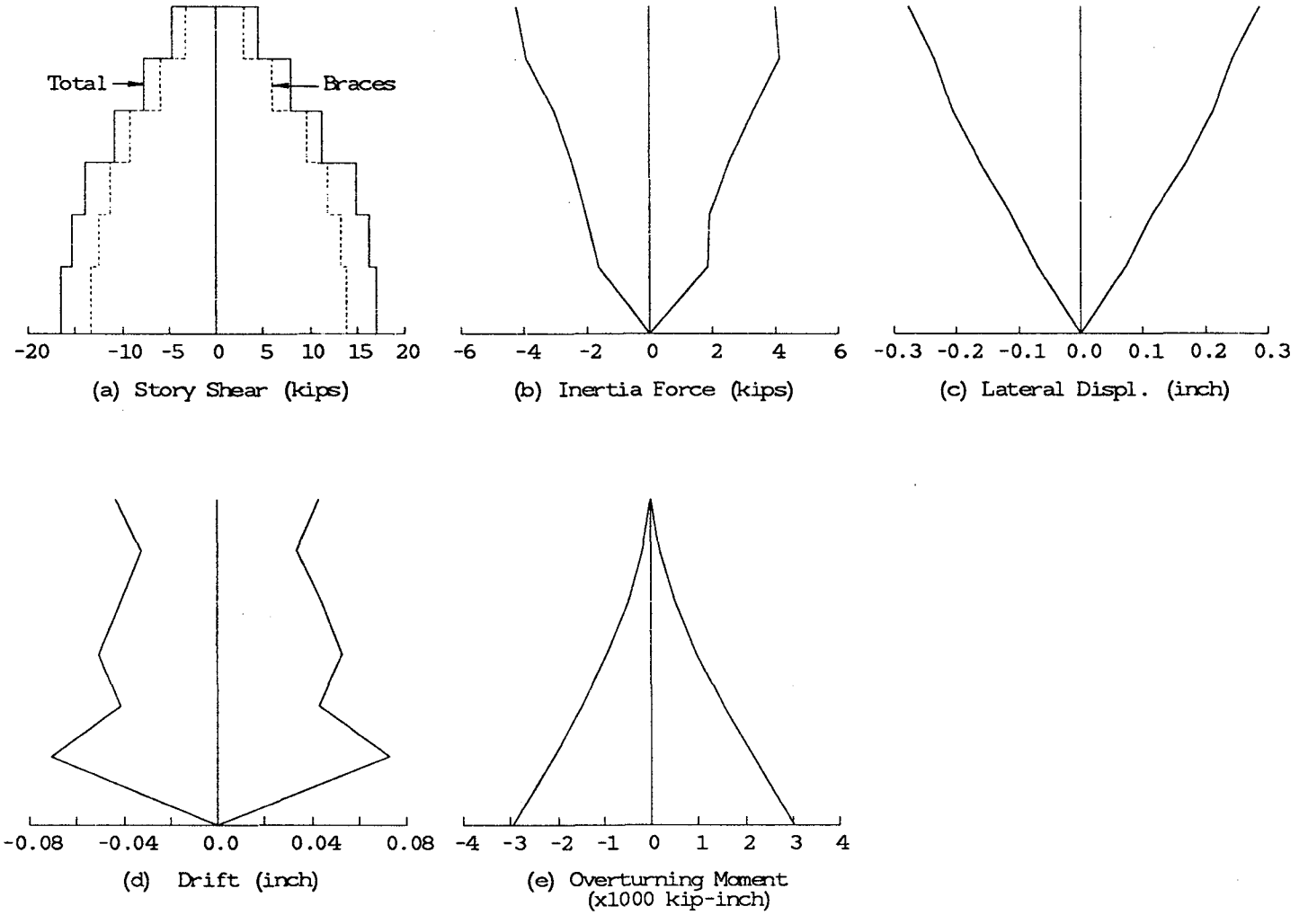


**FIGURE 8.12 TAFT-08 RESPONSE ENVELOPES**

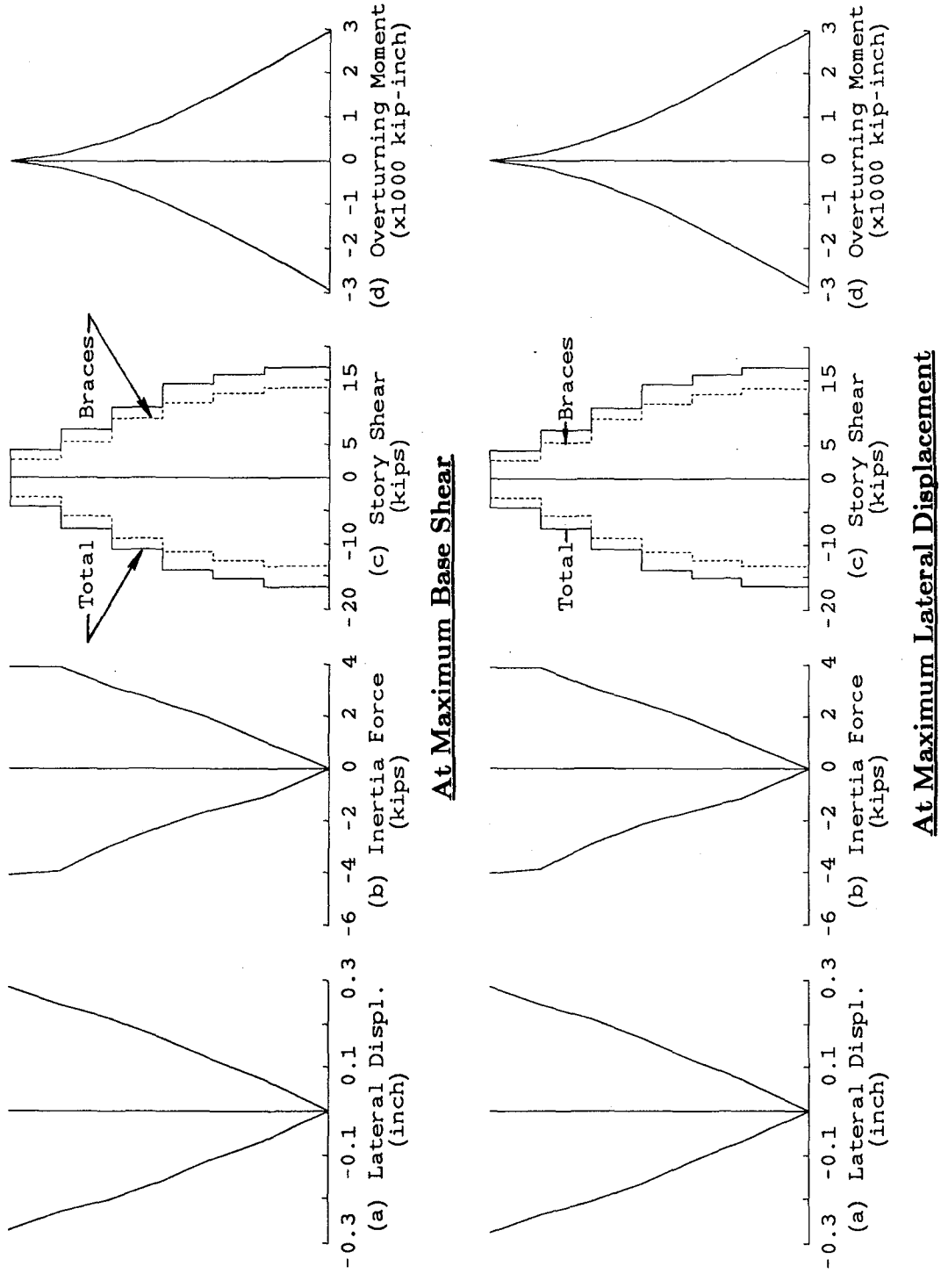


FIGURE 8.13 TAFT-08 RESPONSE PROFILES AT MAXIMUM RESPONSE

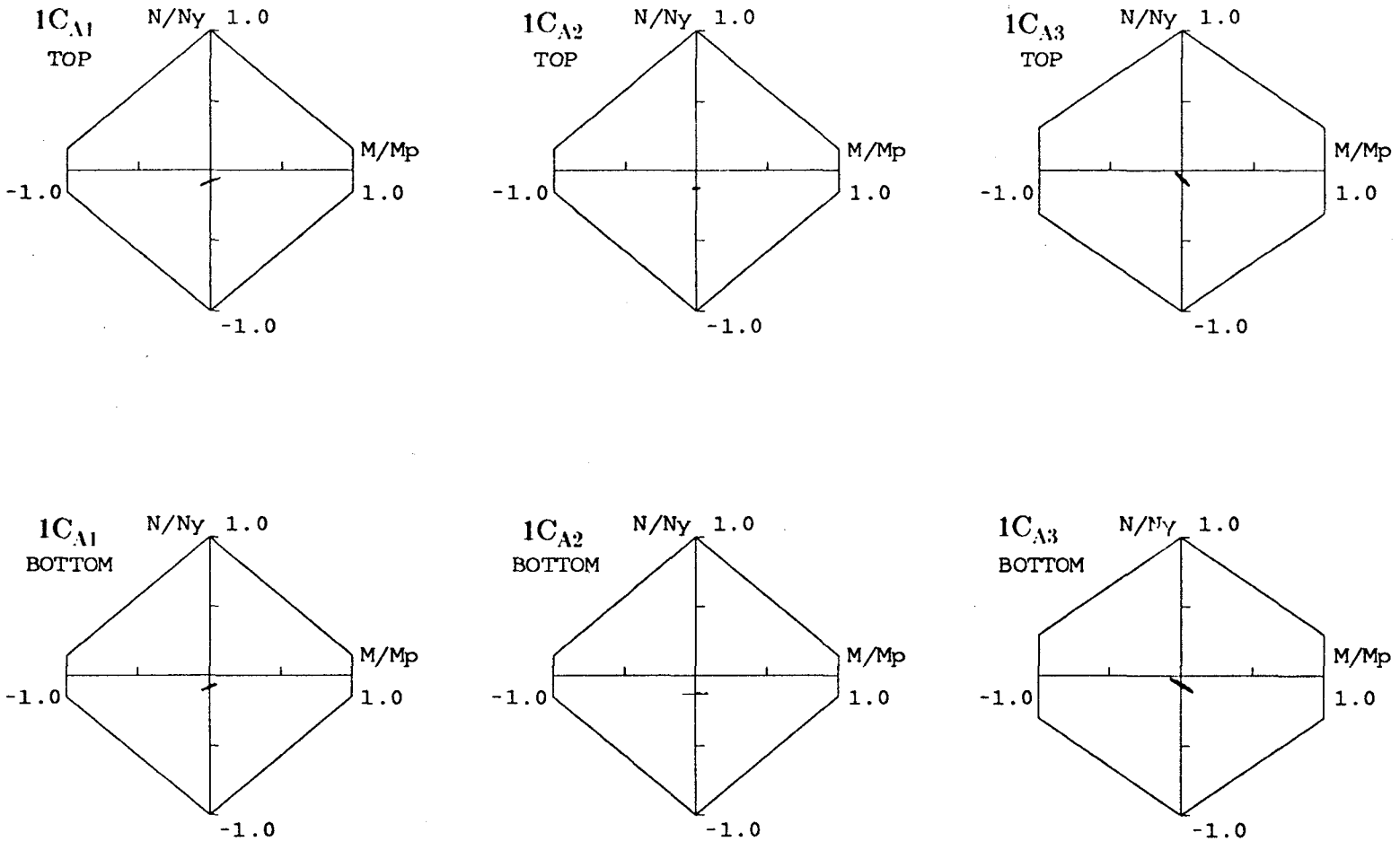


**FIGURE 8.14 TAFT-08 FIRST STORY COLUMN AXIAL FORCE AND END MOMENT INTERACTION CURVES (FRAME A)**

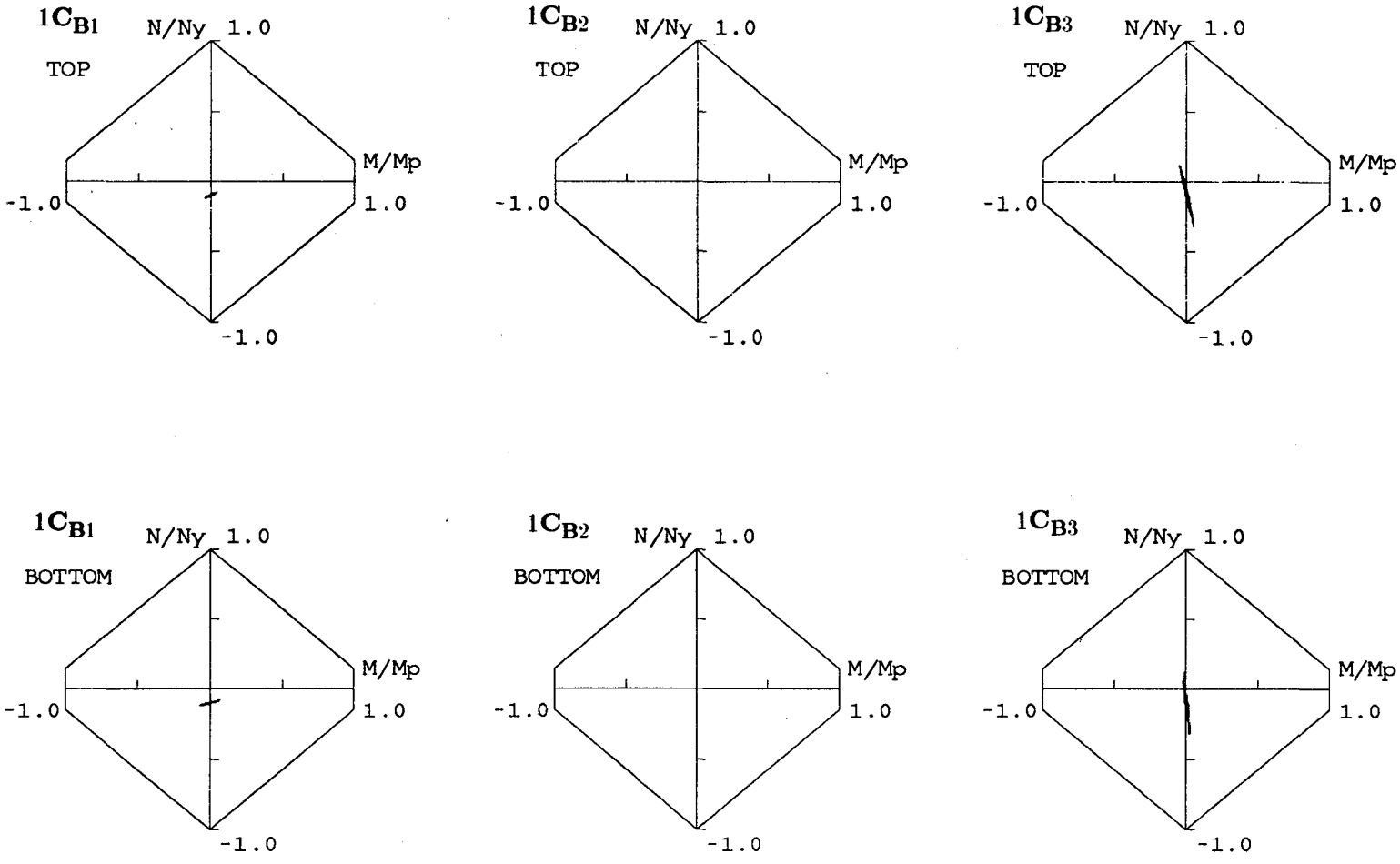


**FIGURE 8.15 TAFT-08 FIRST STORY COLUMN AXIAL FORCE AND END MOMENT INTERACTION CURVES (FRAME B)**

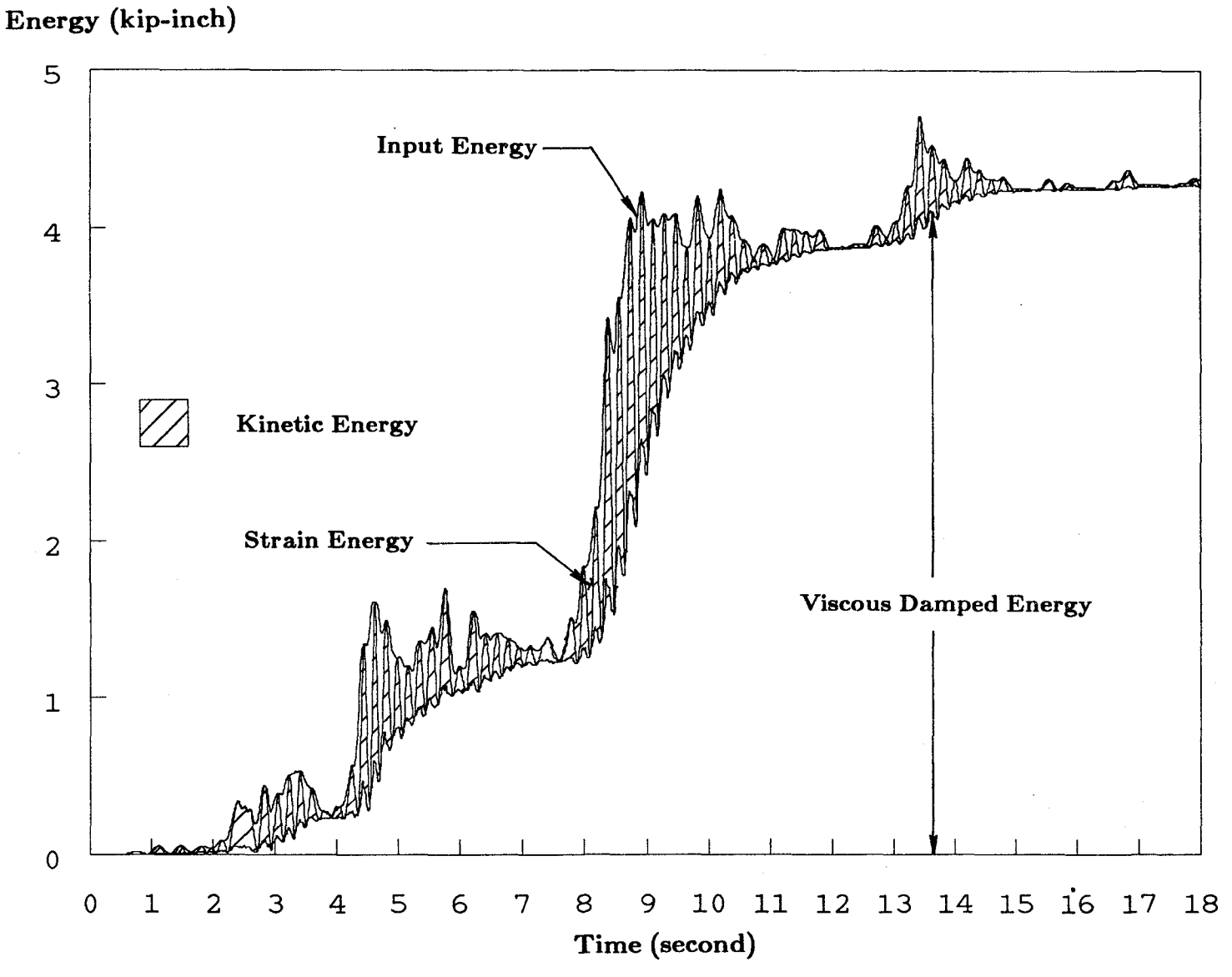


**FIGURE 8.16 TAFT-08 ENERGY TIME HISTORY**

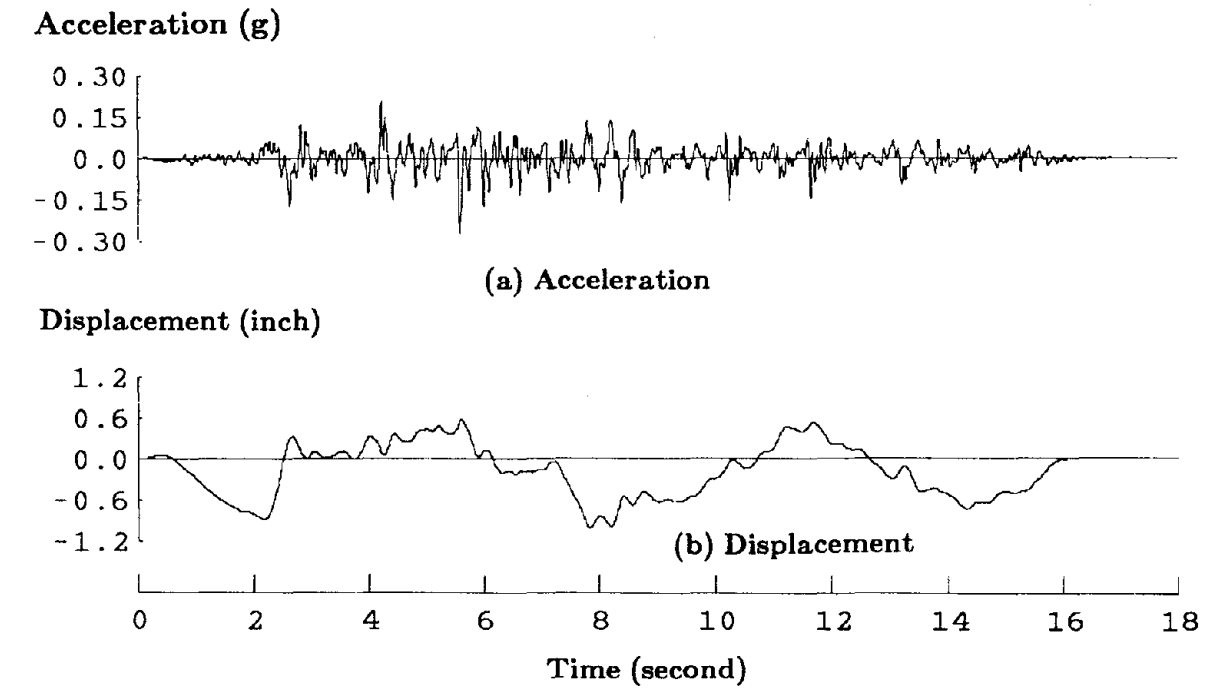


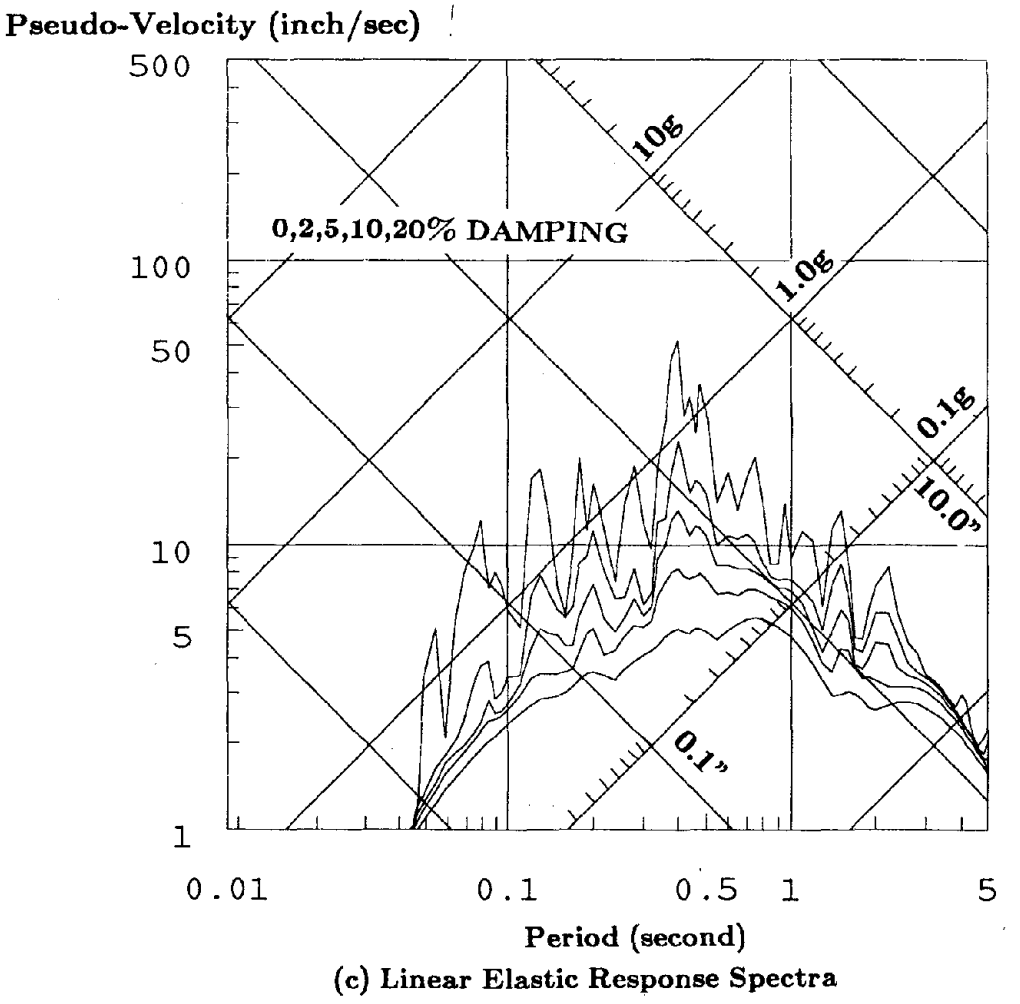


**FIGURE 8.17 TAFT-27 MEASURED TABLE MOTION**

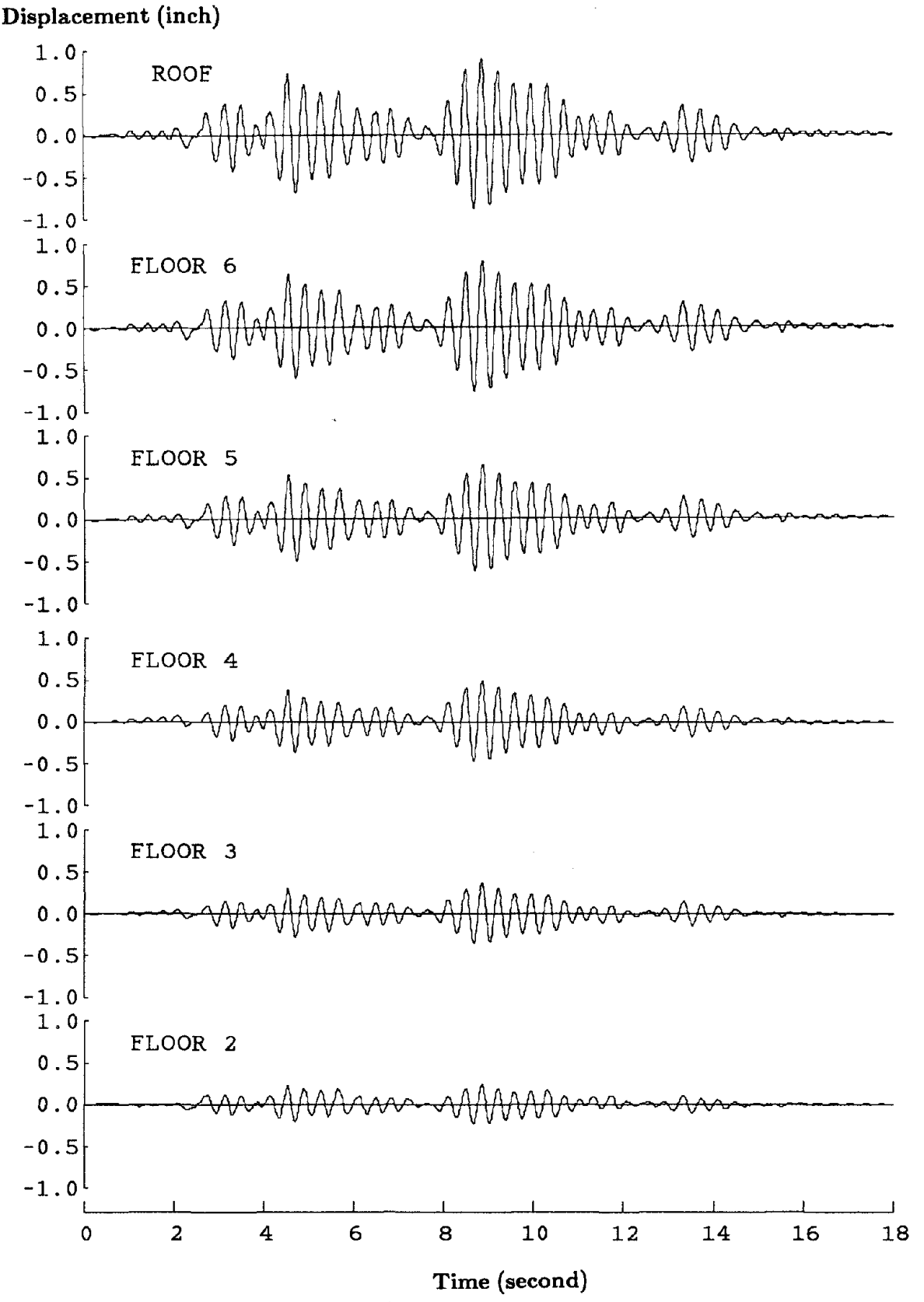


**FIGURE 8.18 TAFT-27 LATERAL DISPLACEMENT TIME HISTORY**

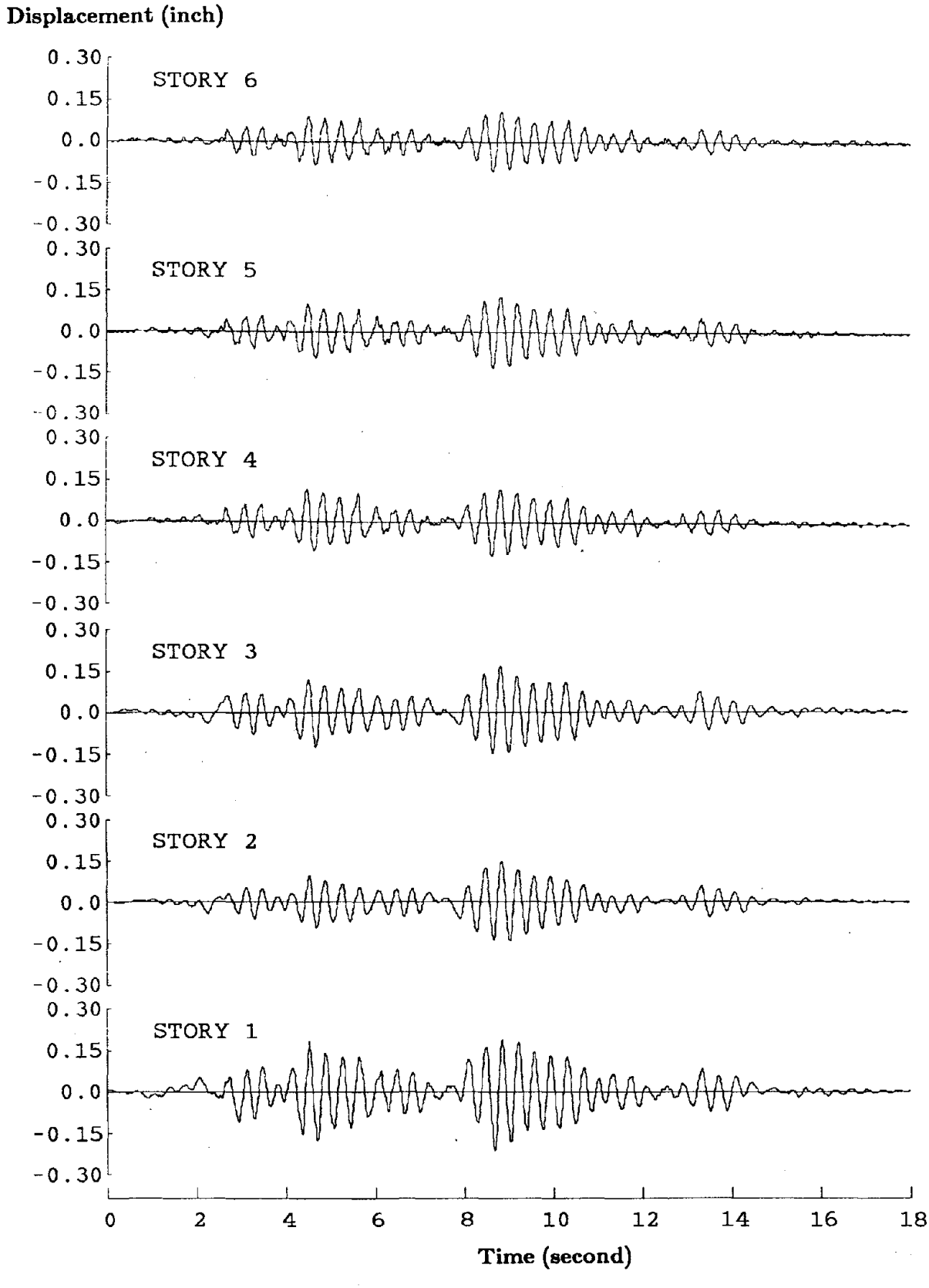


**FIGURE 8.19 TAFT-27 INTER-STORY DRIFT TIME HISTORY**

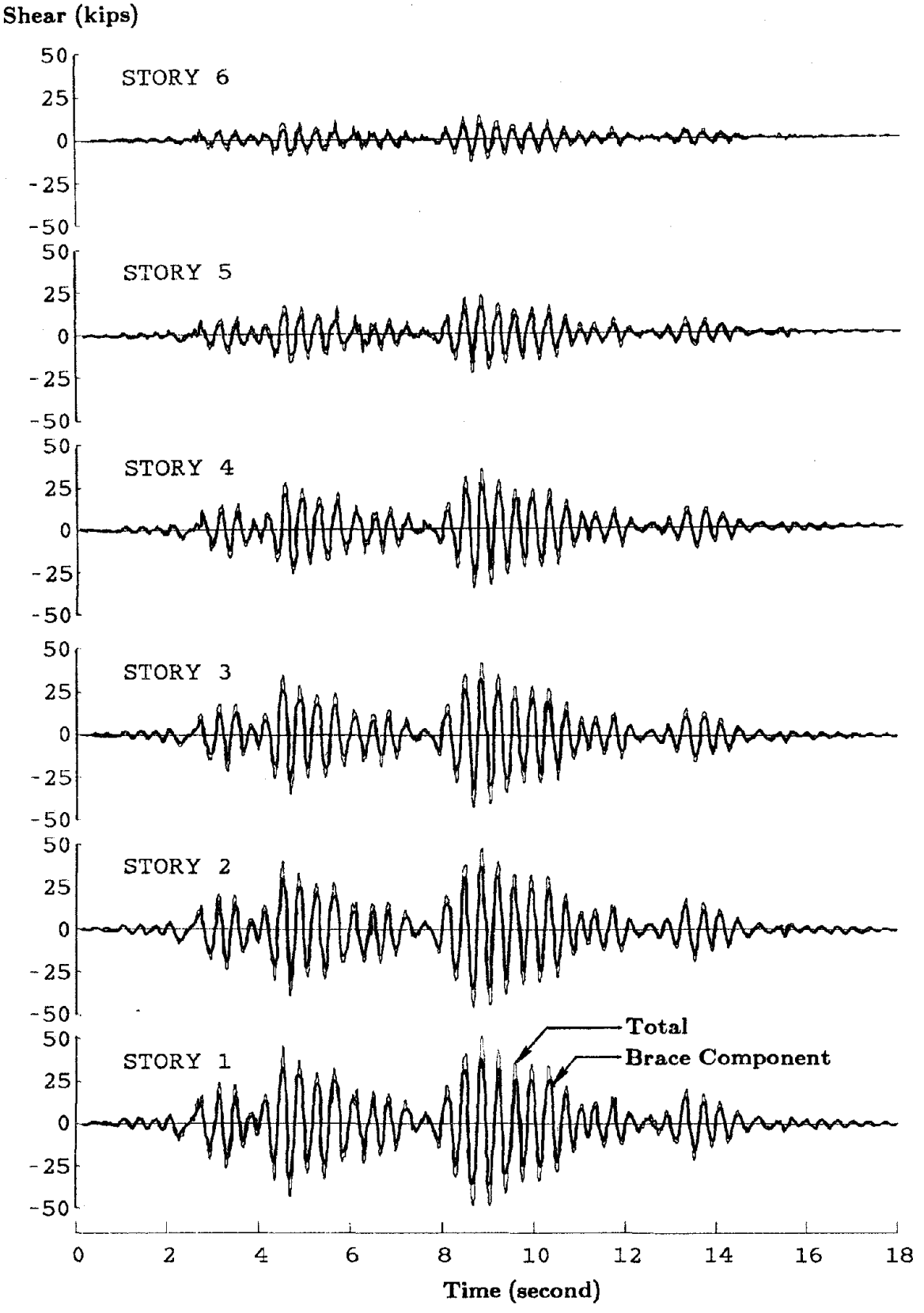


**FIGURE 8.20 TAFT-27 STORY SHEAR TIME HISTORY**

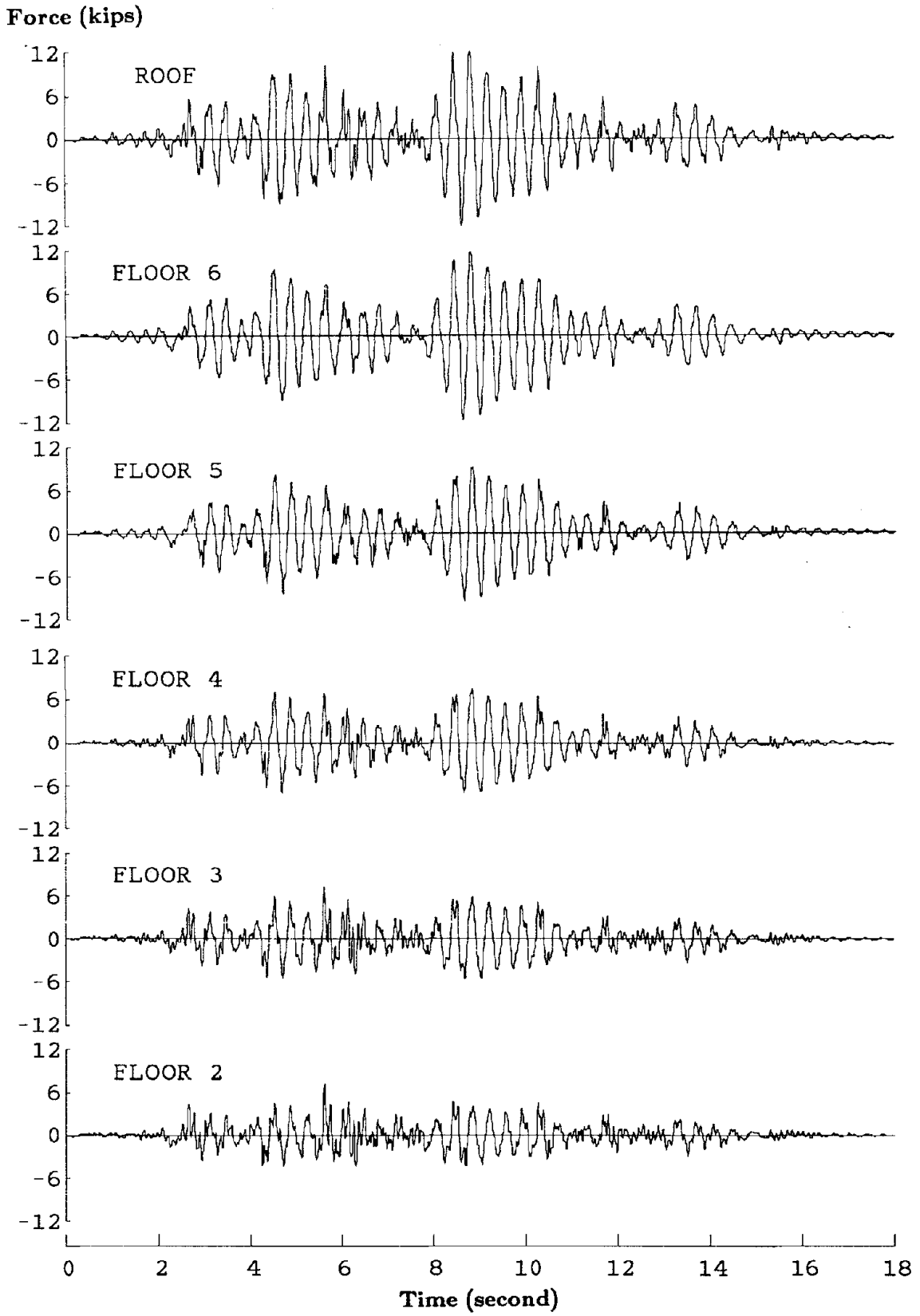


**FIGURE 8.21 TAFT-27 INERTIA FORCE TIME HISTORY**

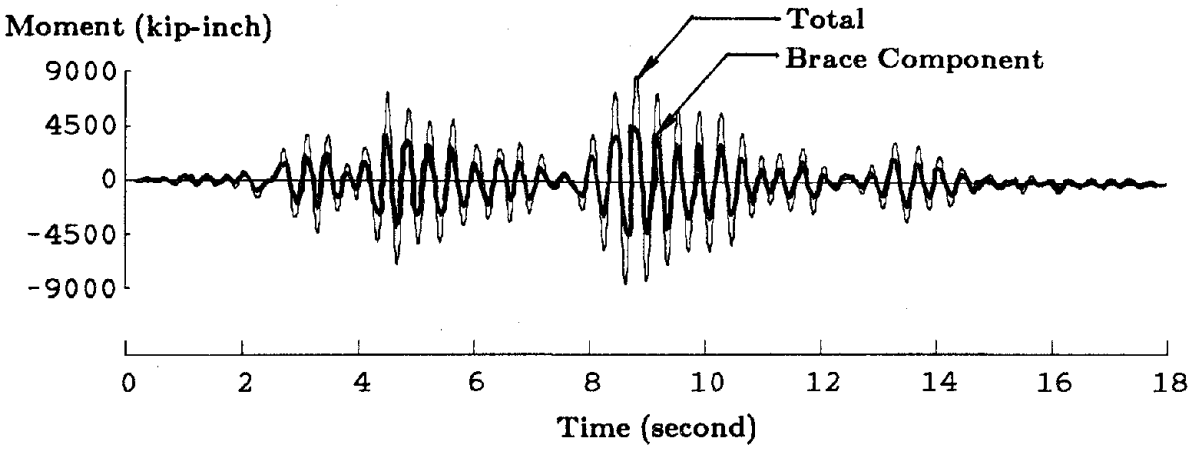


FIGURE 8.22 TAFT-27 BASE OVERTURNING MOMENT TIME HISTORY

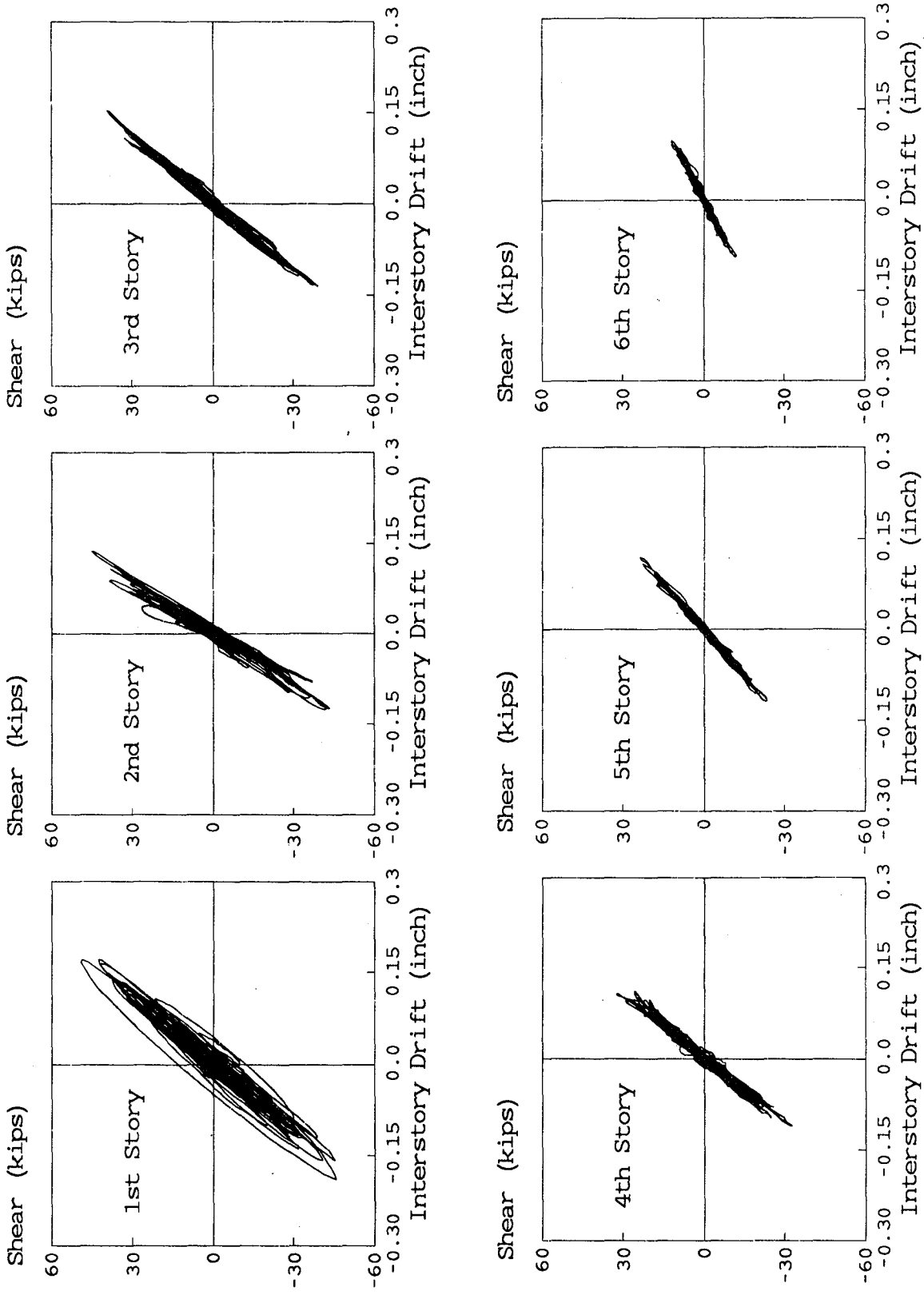


**FIGURE 8.23 TAFT-27 TOTAL STORY SHEAR AND INTER-STORY DRIFT**

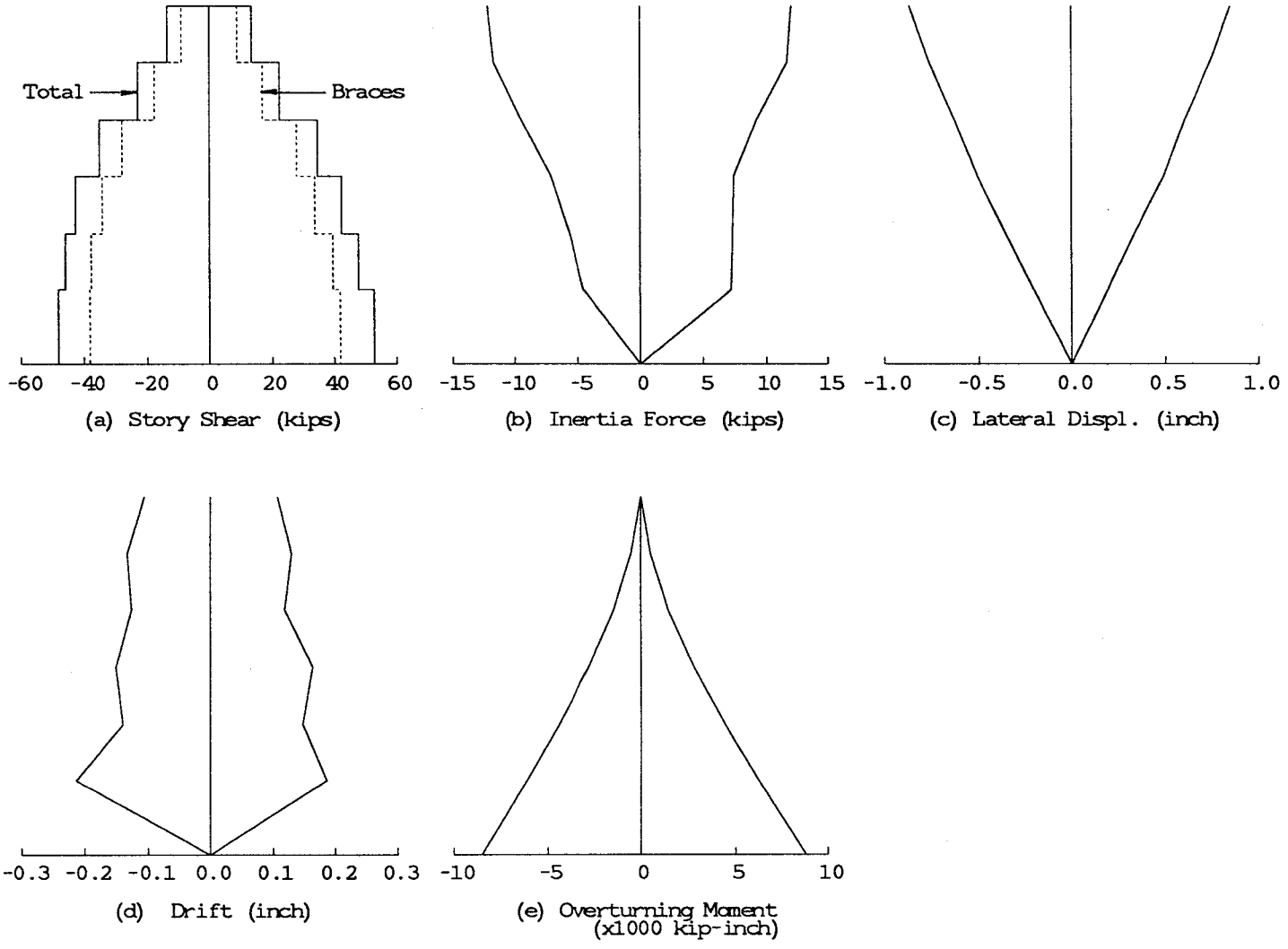


**FIGURE 8.24 TAFT-27 RESPONSE ENVELOPES**

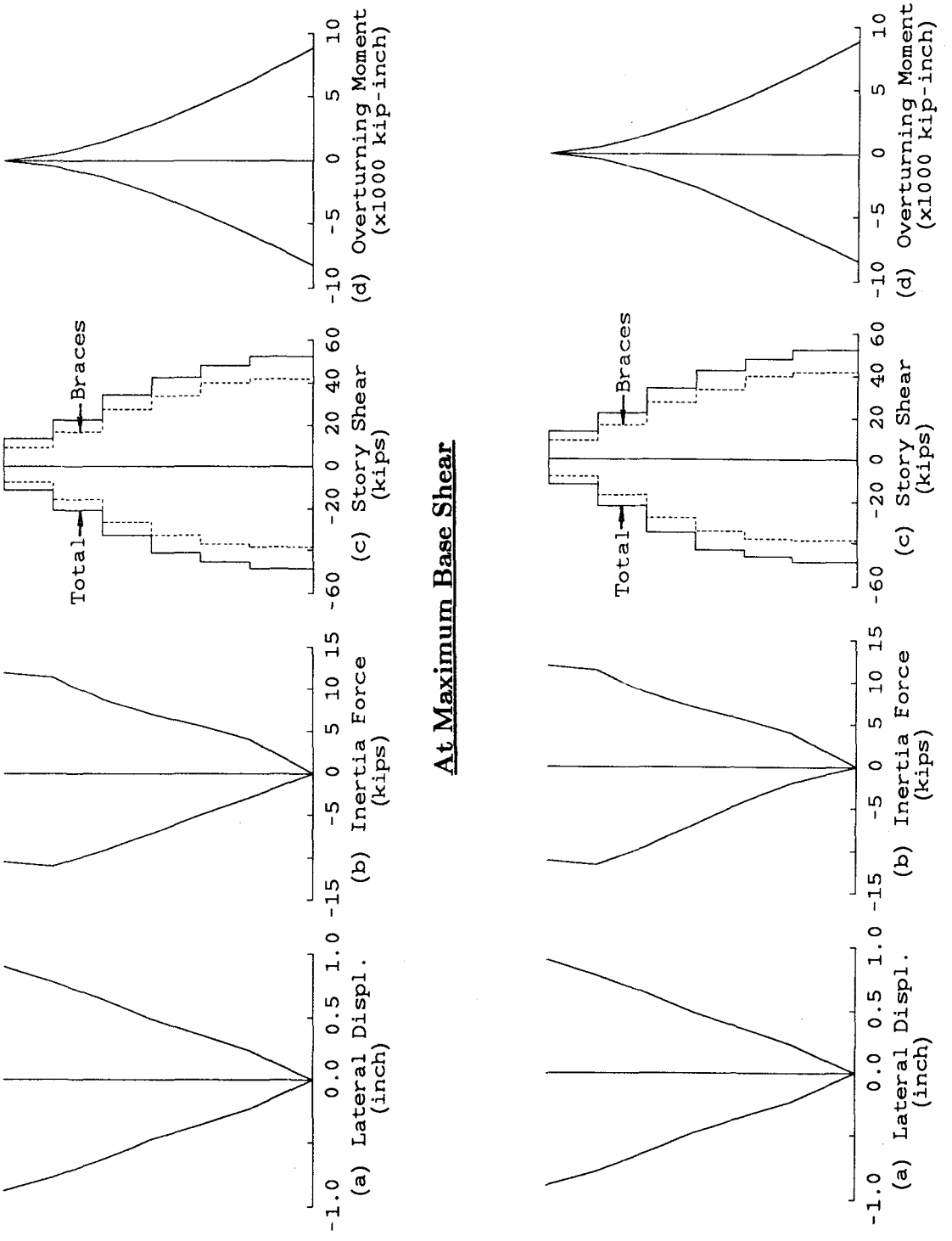


**FIGURE 8.25 TAFT-27 RESPONSE PROFILES AT MAXIMUM RESPONSE**

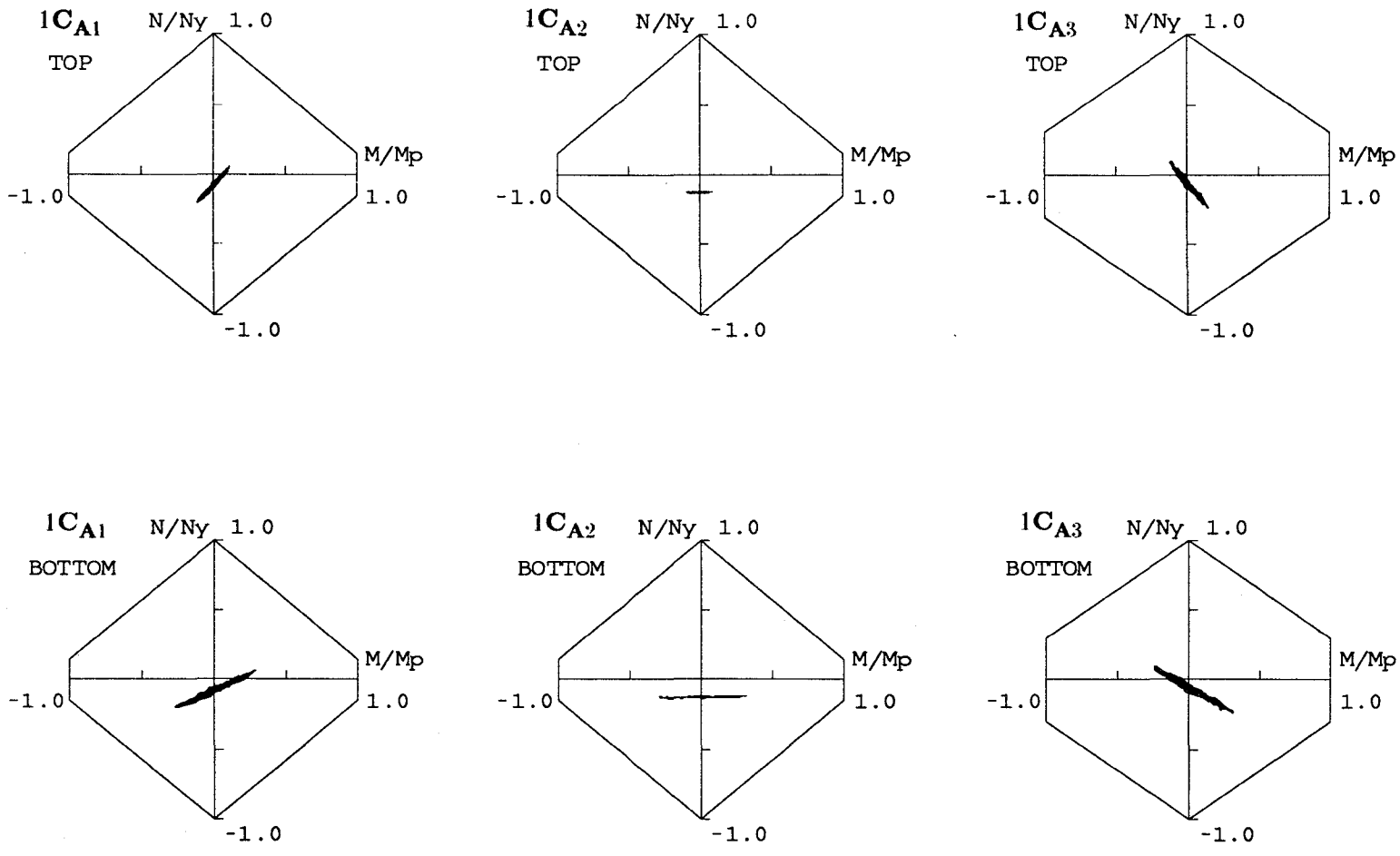


**FIGURE 8.26 TAFT-27 FIRST STORY COLUMN AXIAL FORCE AND END MOMENT INTERACTION CURVES (FRAME A)**

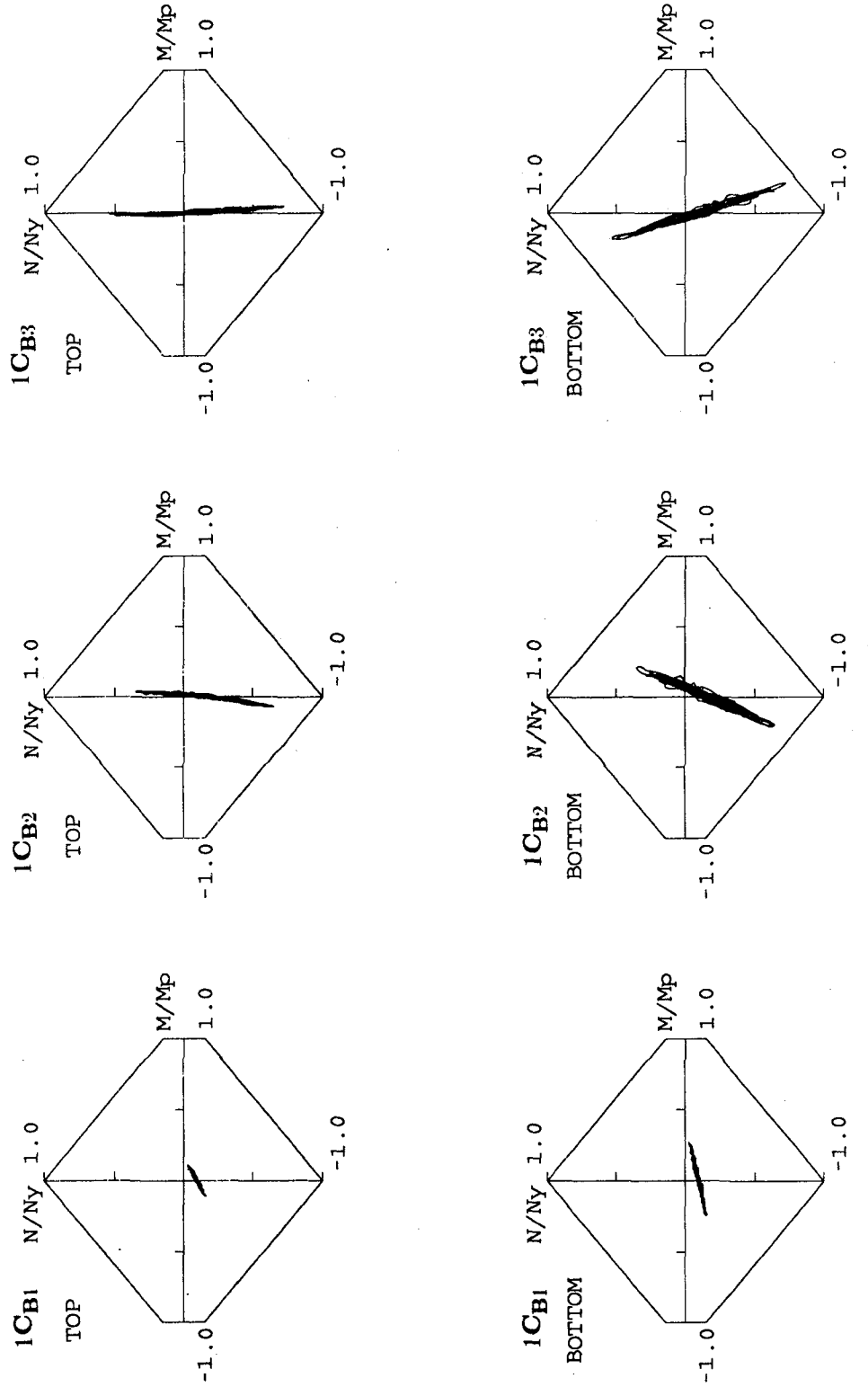


**FIGURE 8.27 TAFT-27 FIRST STORY COLUMN AXIAL FORCE AND END MOMENT INTERACTION CURVES (FRAME B)**

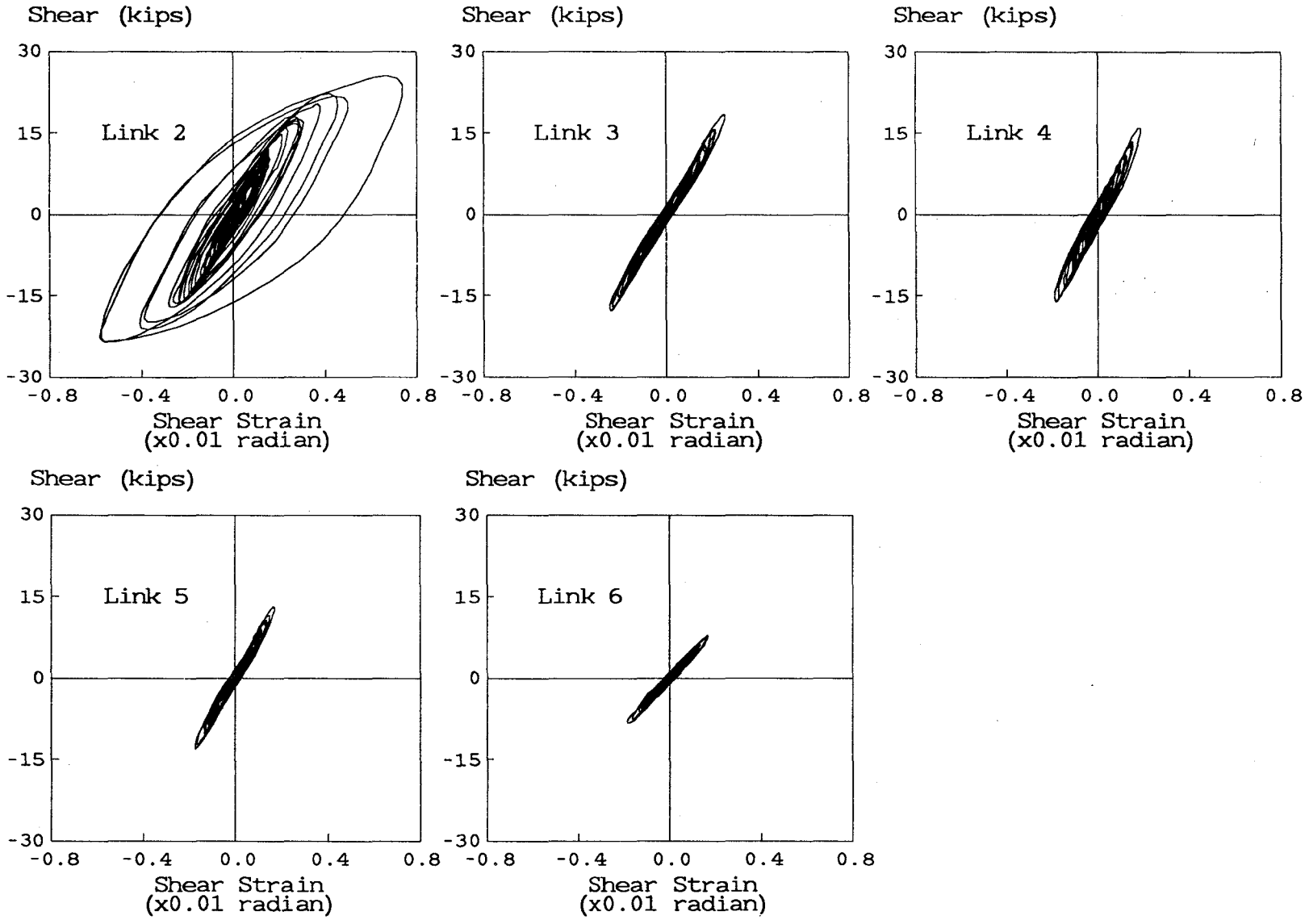


**FIGURE 8.28 TAFT-27 LINK SHEAR FORCE AND SHEAR STRAIN RELATIONSHIP**

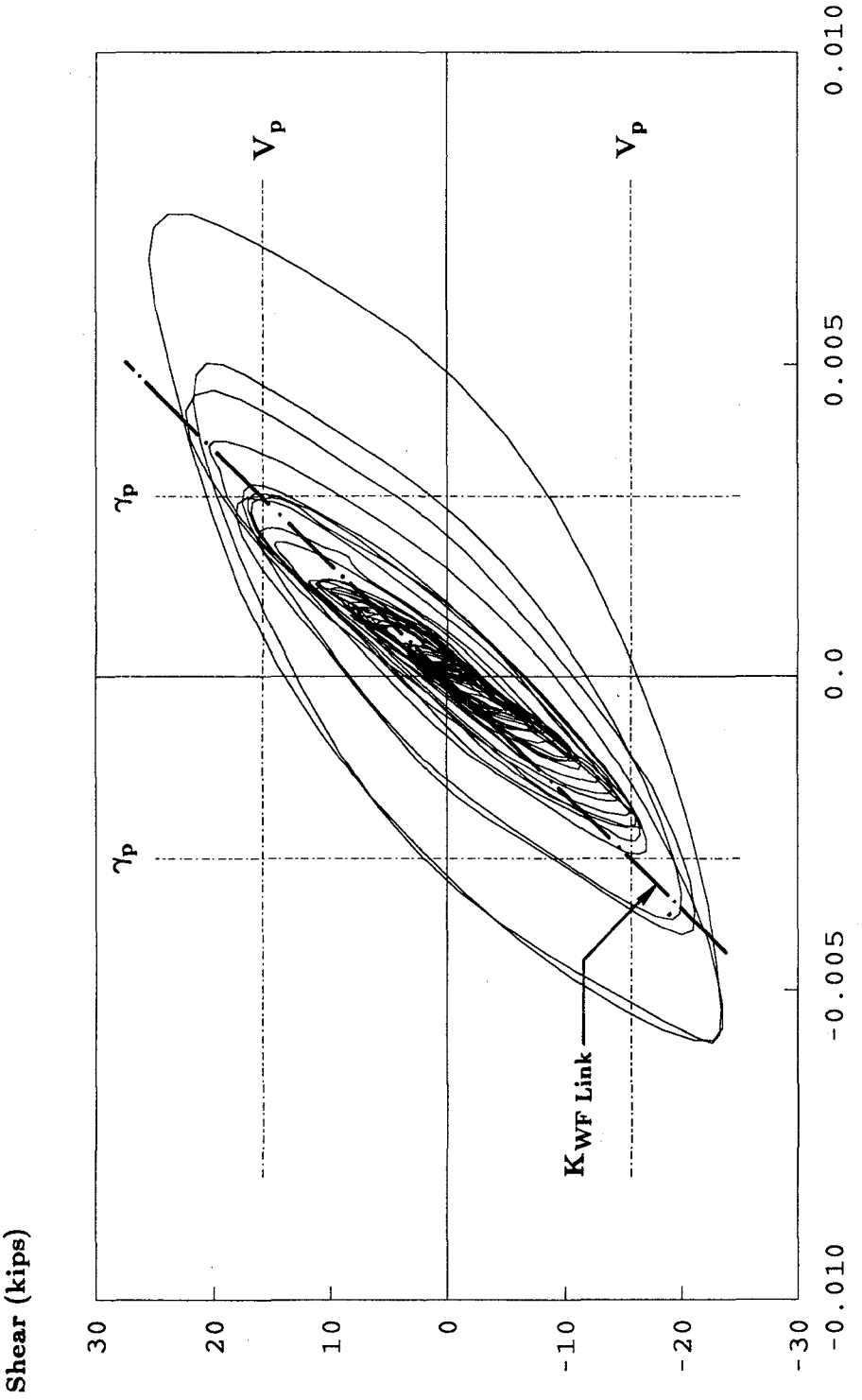


FIGURE 8.29 TAFT-27 LINK L2 SHEAR FORCE AND SHEAR STRAIN RELATIONSHIP

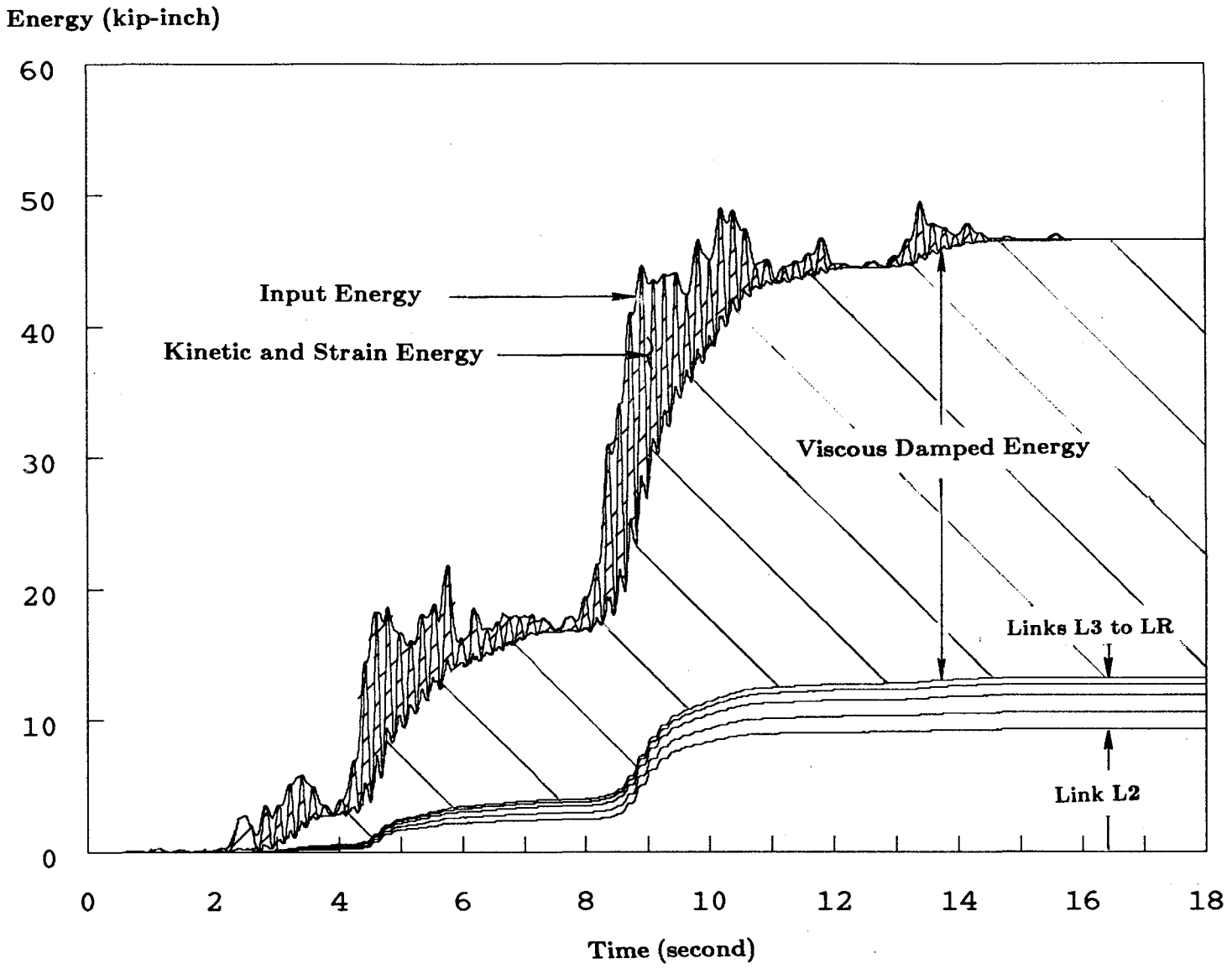


**FIGURE 8.30 TAFT-27 ENERGY TIME HISTORY**

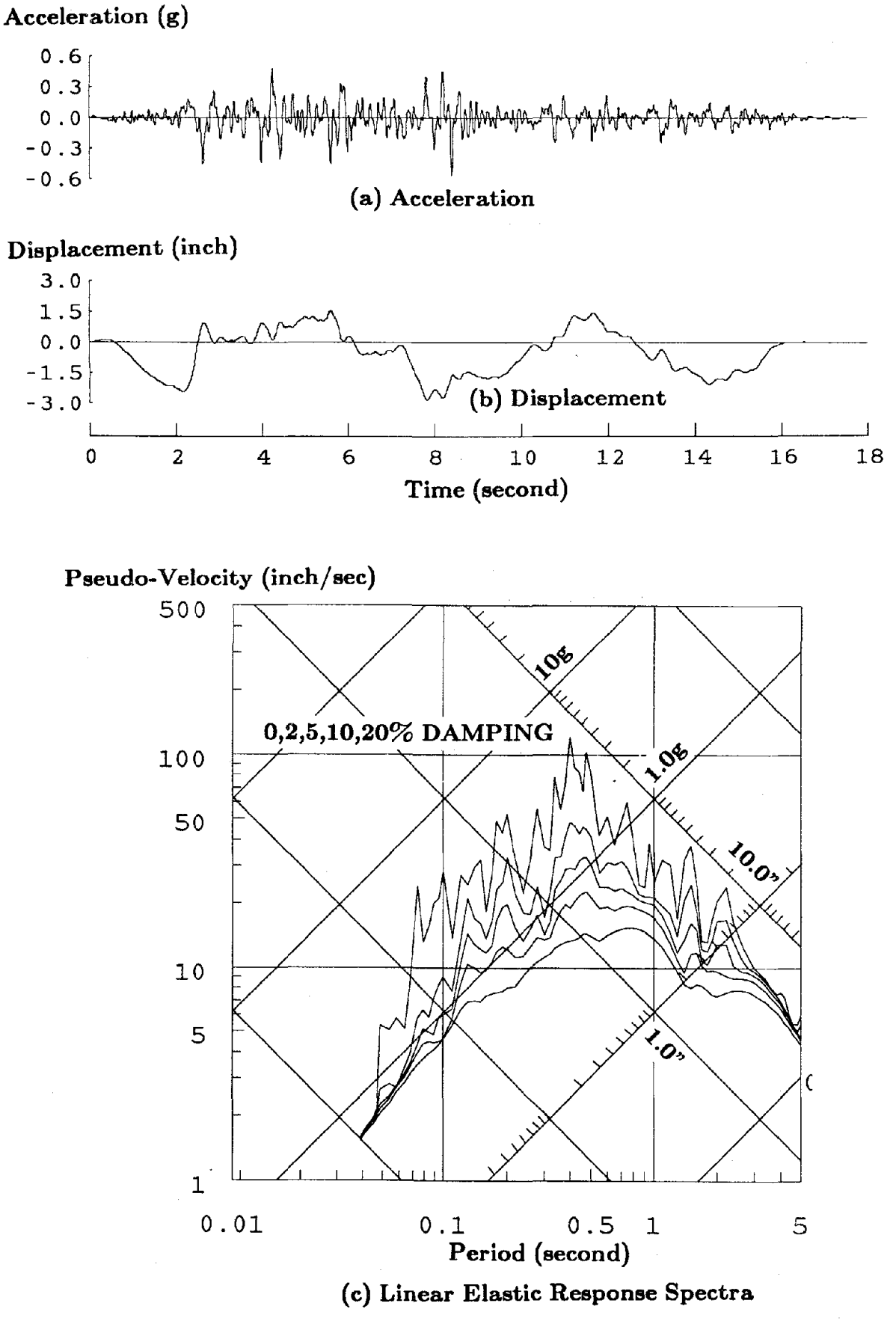


**FIGURE 8.31 TAFT-57 MEASURED TABLE MOTION**

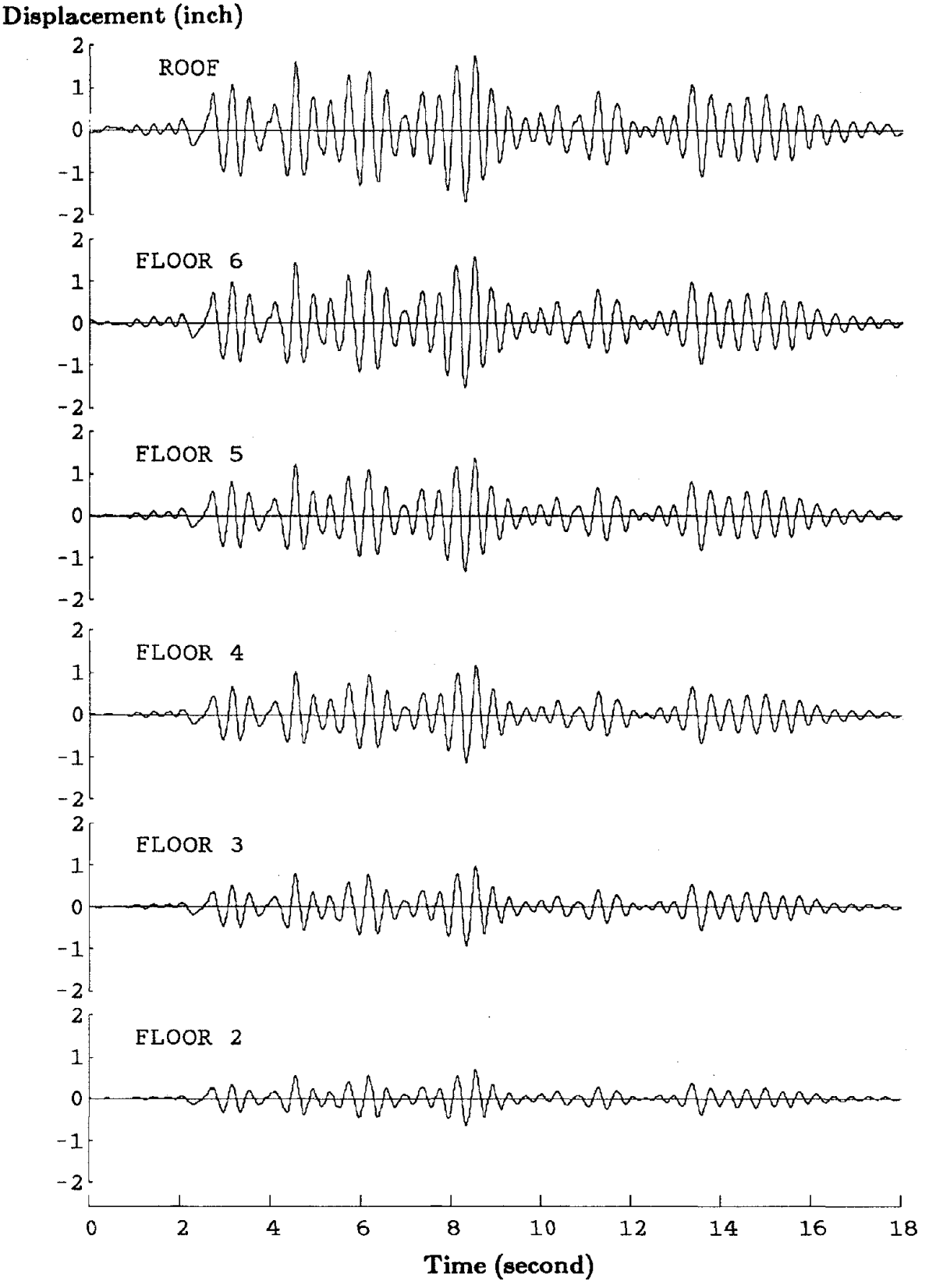


**FIGURE 8.32 TAFT-57 LATERAL DISPLACEMENT TIME HISTORY**

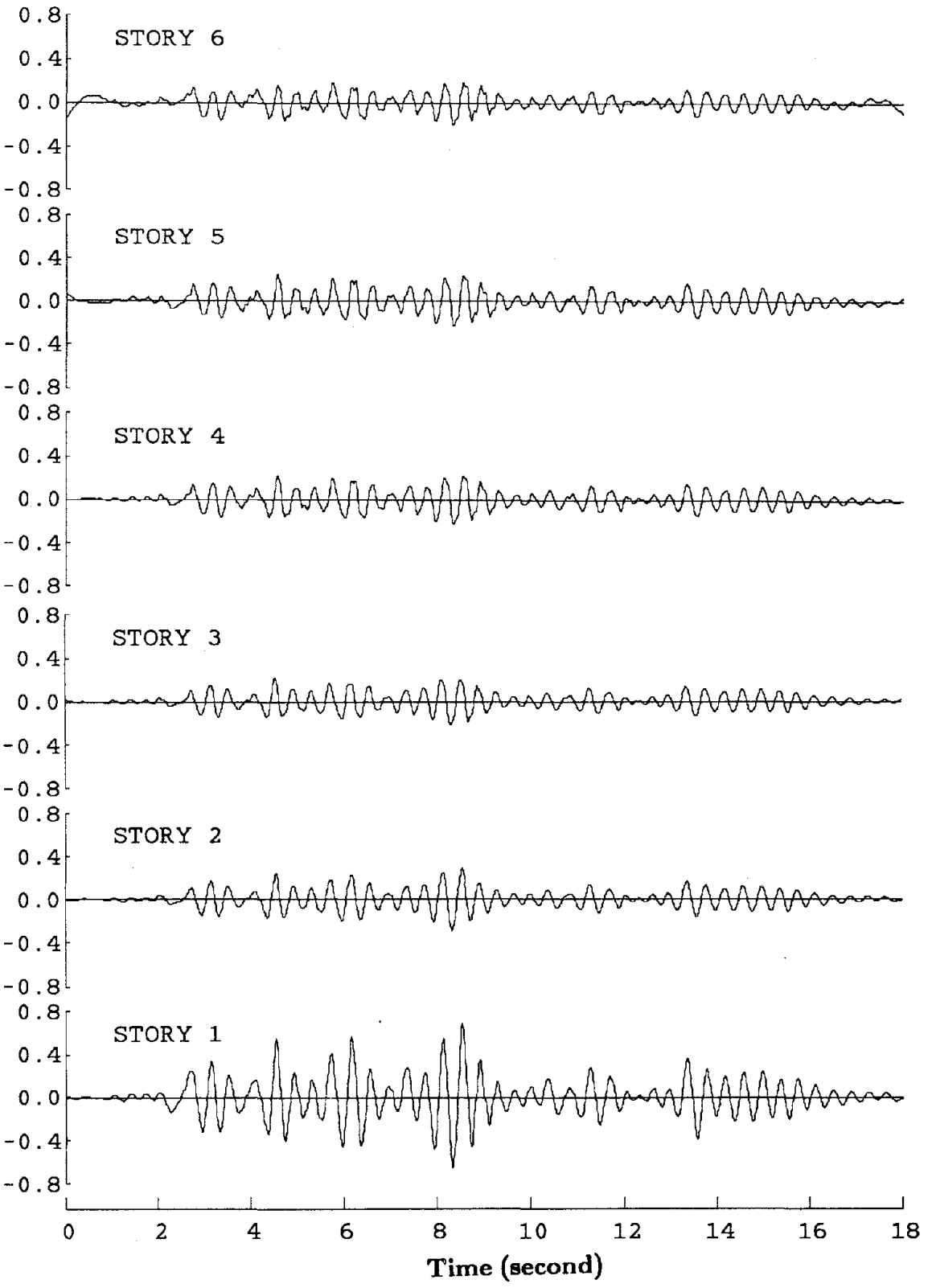


**FIGURE 8.33 TAFT-57 INTER-STORY DRIFT TIME HISTORY**

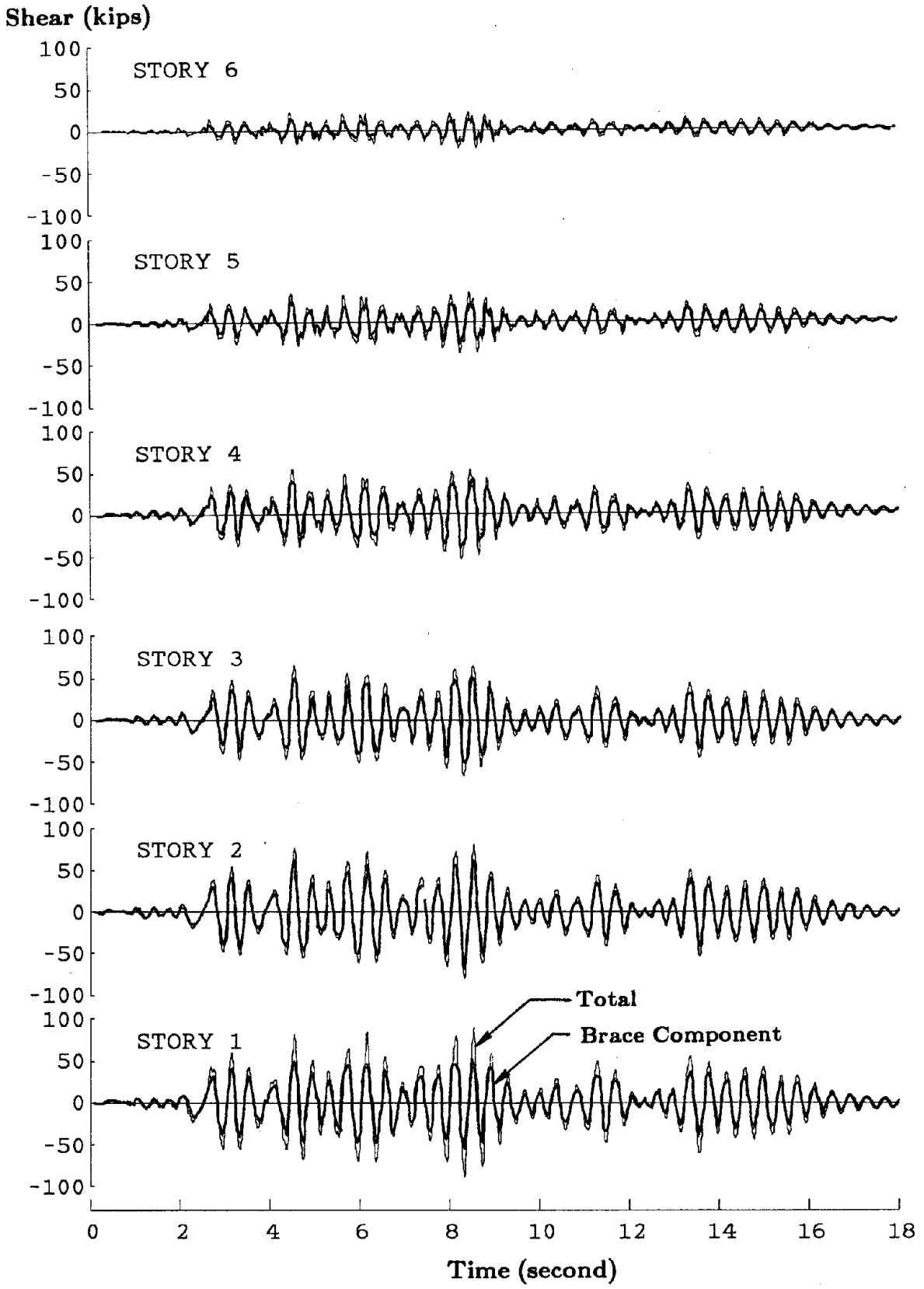


FIGURE 8.34 TAFT-57 STORY SHEAR TIME HISTORY

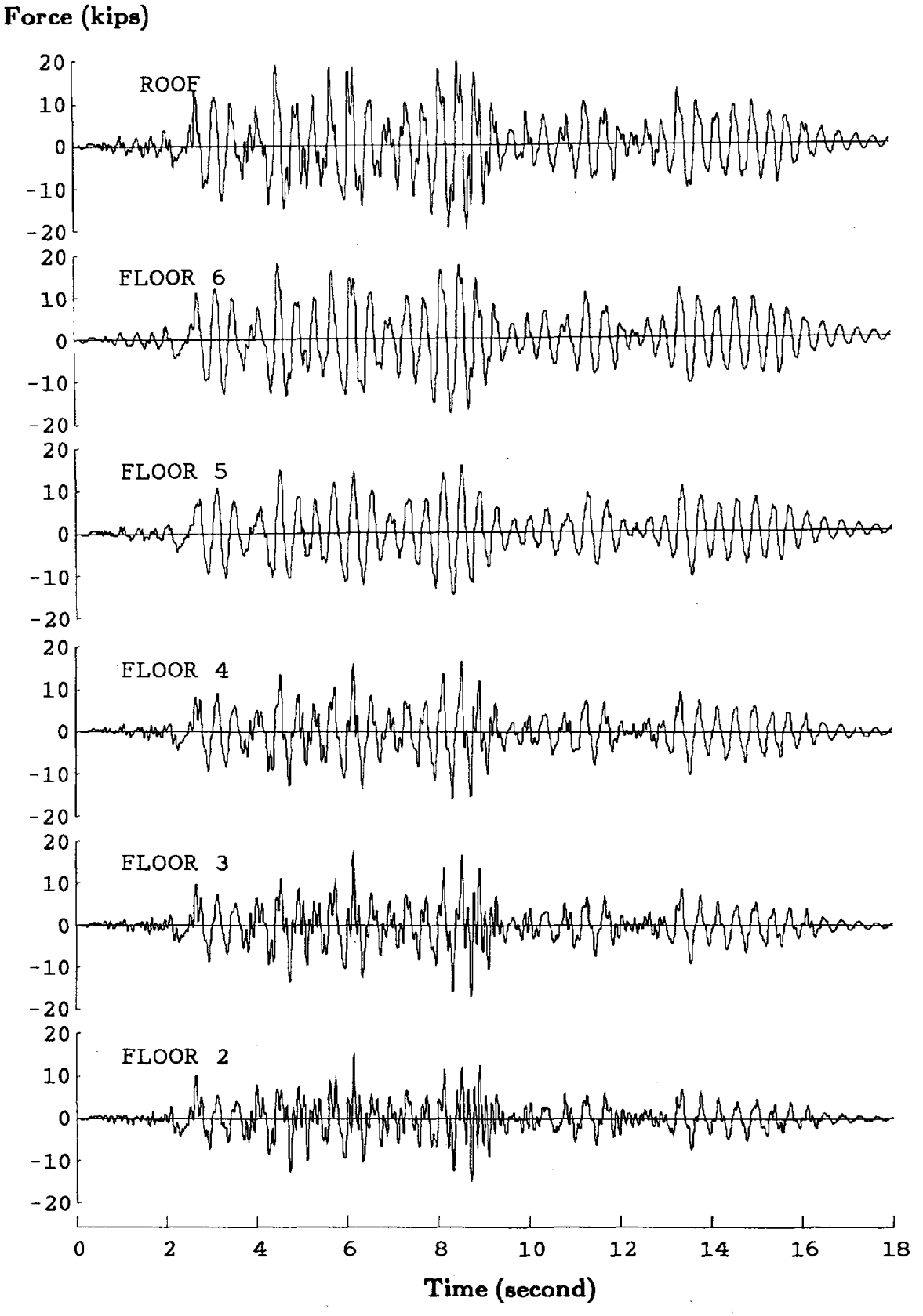


**FIGURE 8.35 TAFT-57 INERTIA FORCE TIME HISTORY**

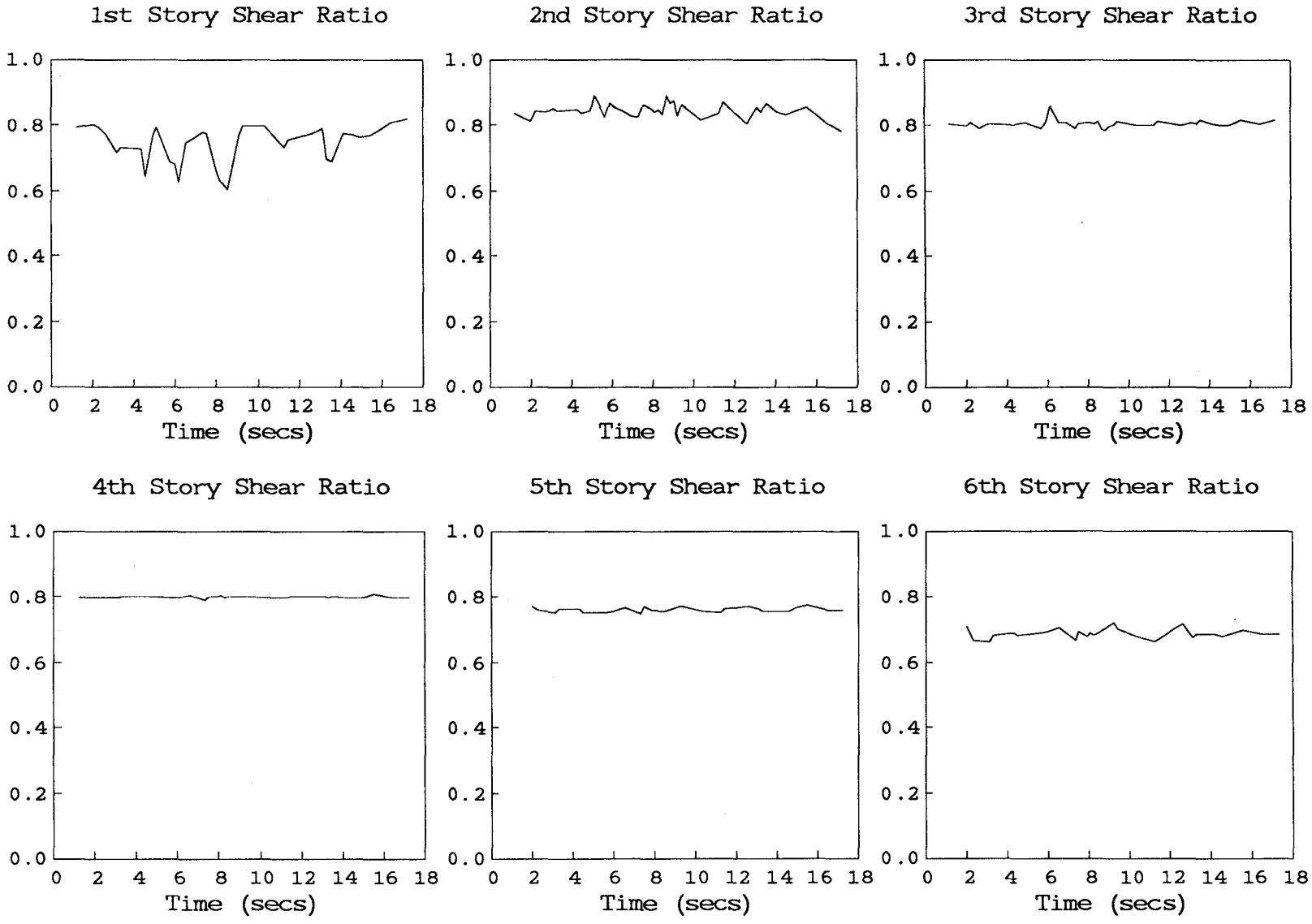


**FIGURE 8.36 TAFT-57 STORY SHEAR RATIO**

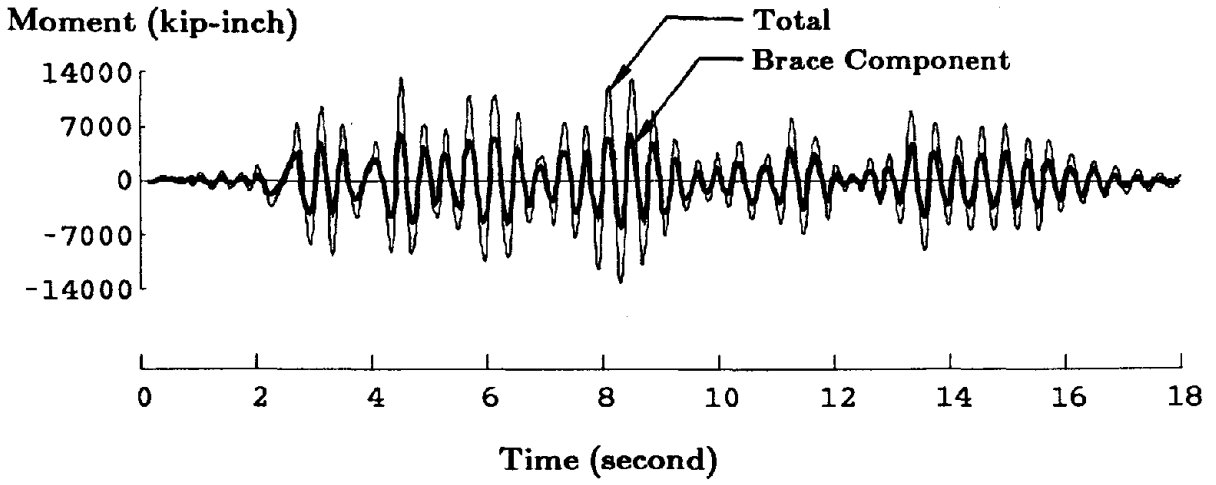


FIGURE 8.37 TAFT-57 BASE OVERTURNING MOMENT TIME HISTORY

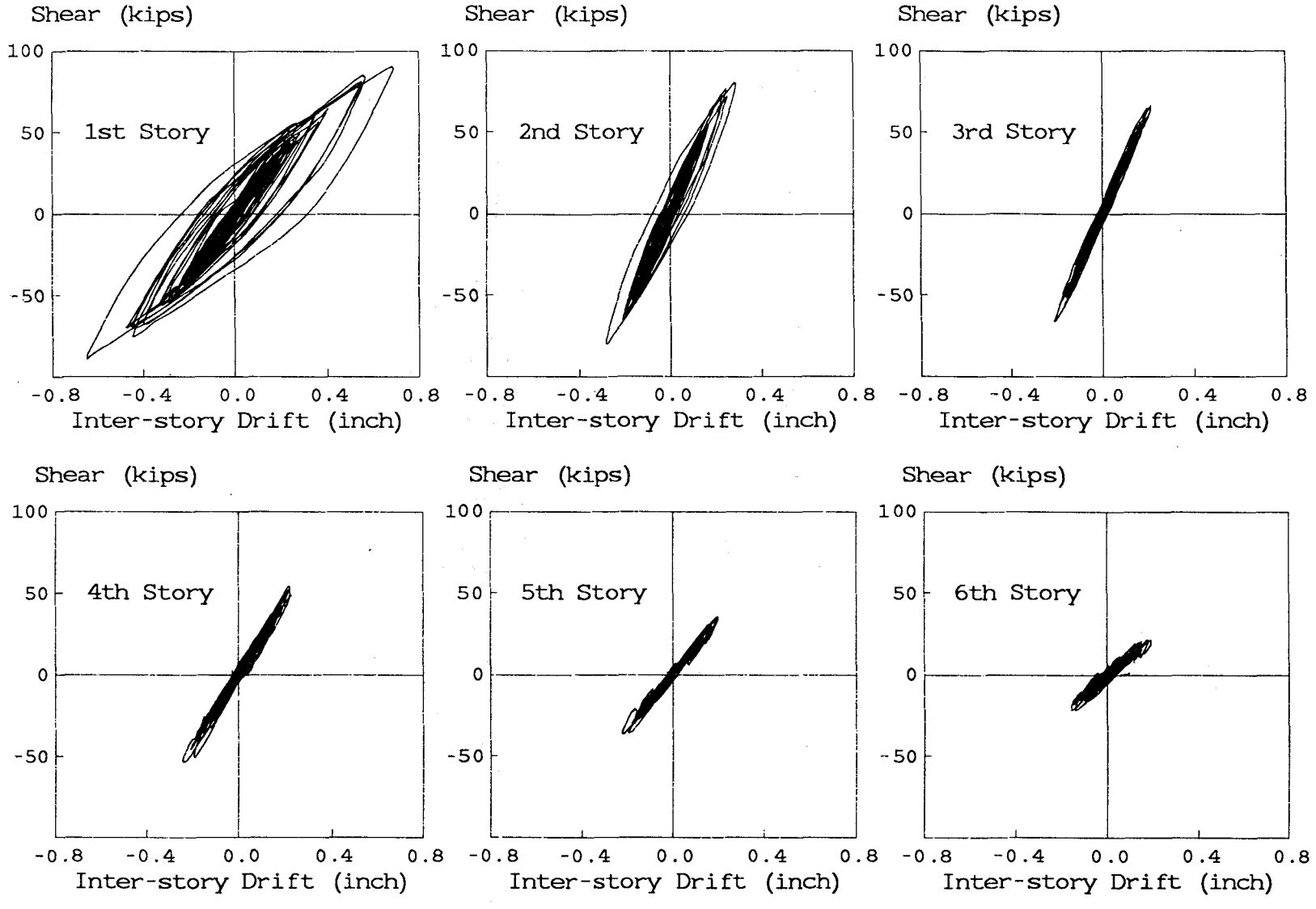


**FIGURE 8.38 TAFT-57 TOTAL STORY SHEAR AND INTER-STORY DRIFT**

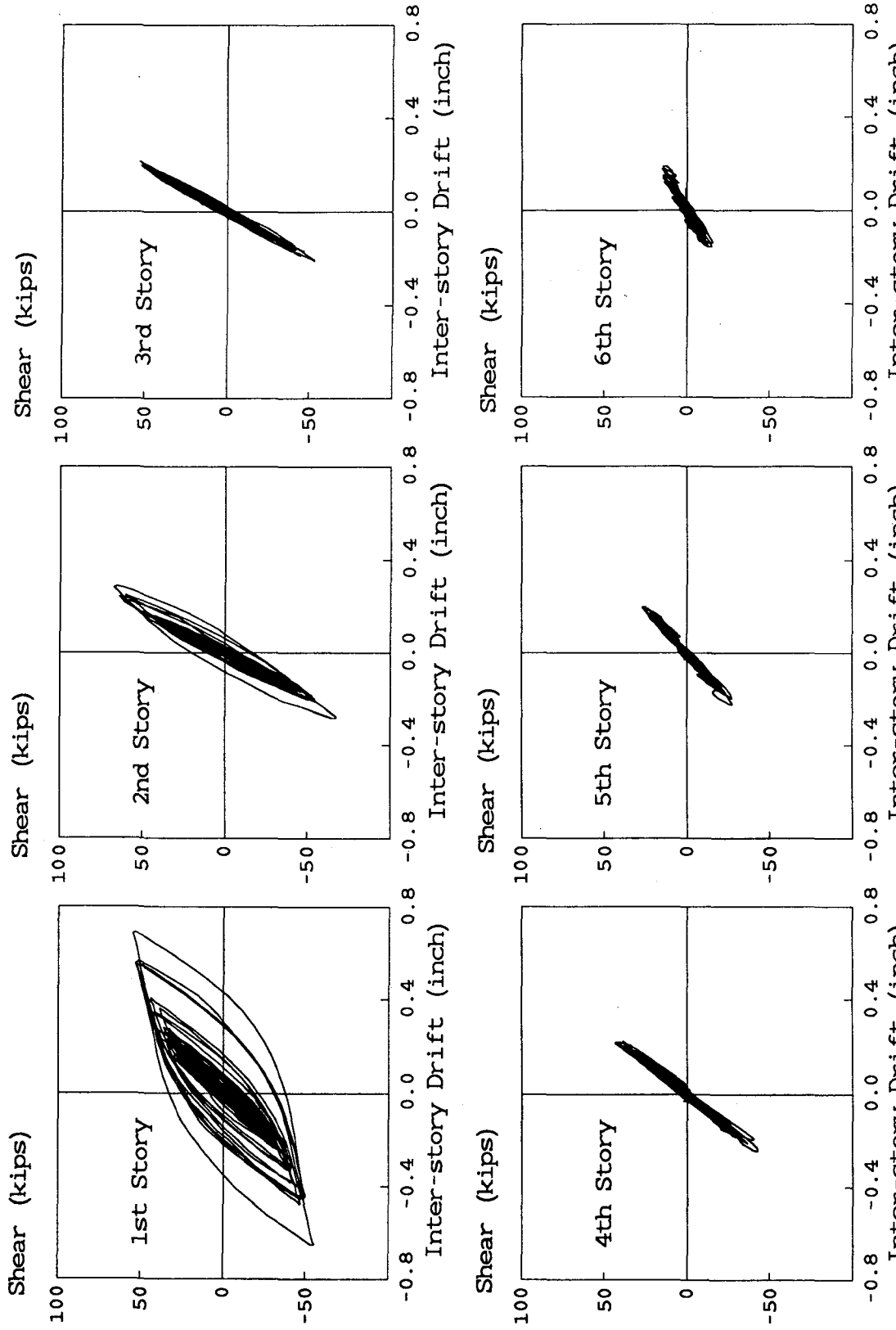


**FIGURE 8.39 TAFT-57 BRACE STORY SHEAR AND INTER-STORY DRIFT**

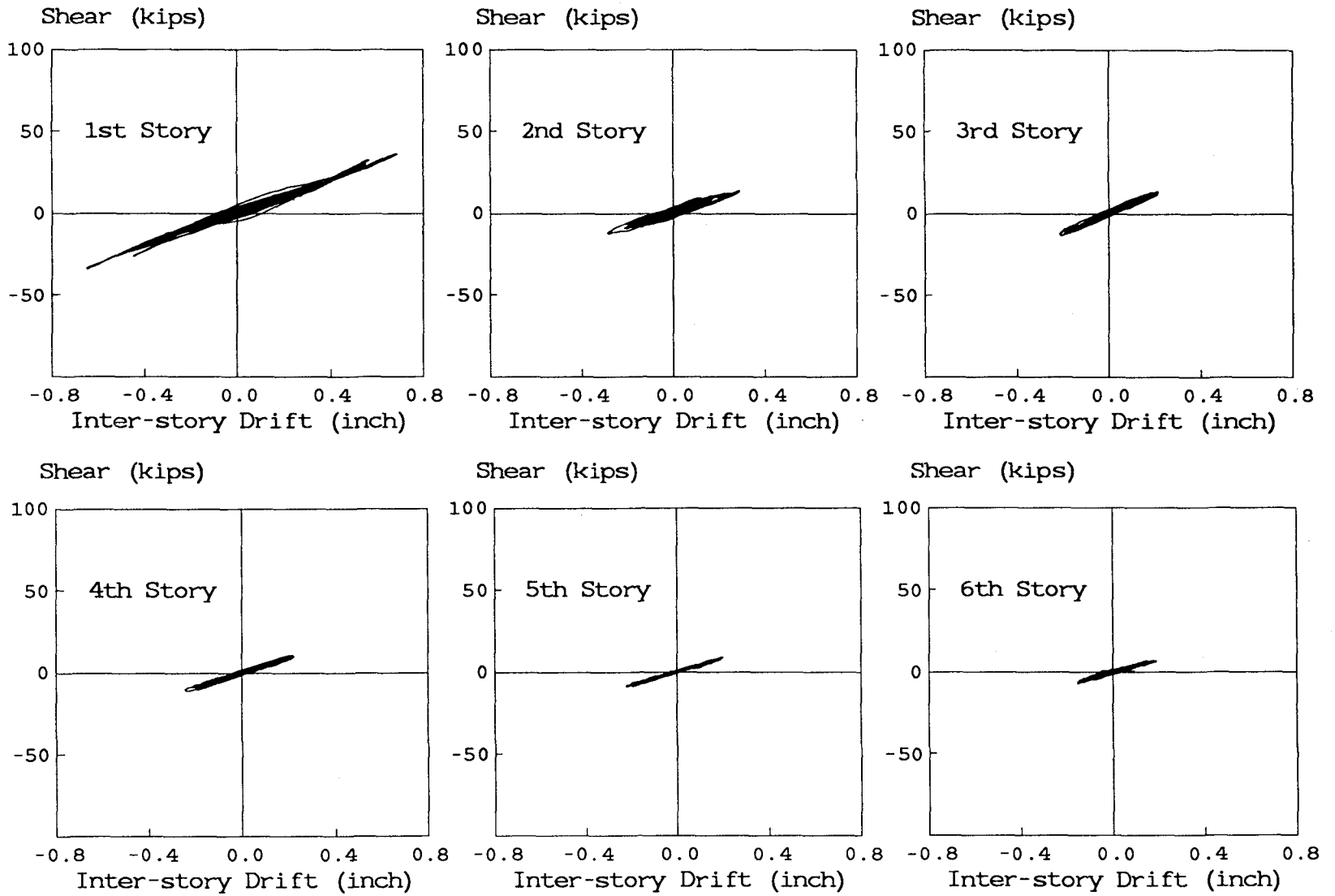


**FIGURE 8.40 TAFT-57 DMRSF STORY SHEAR AND INTER-STORY DRIFT**

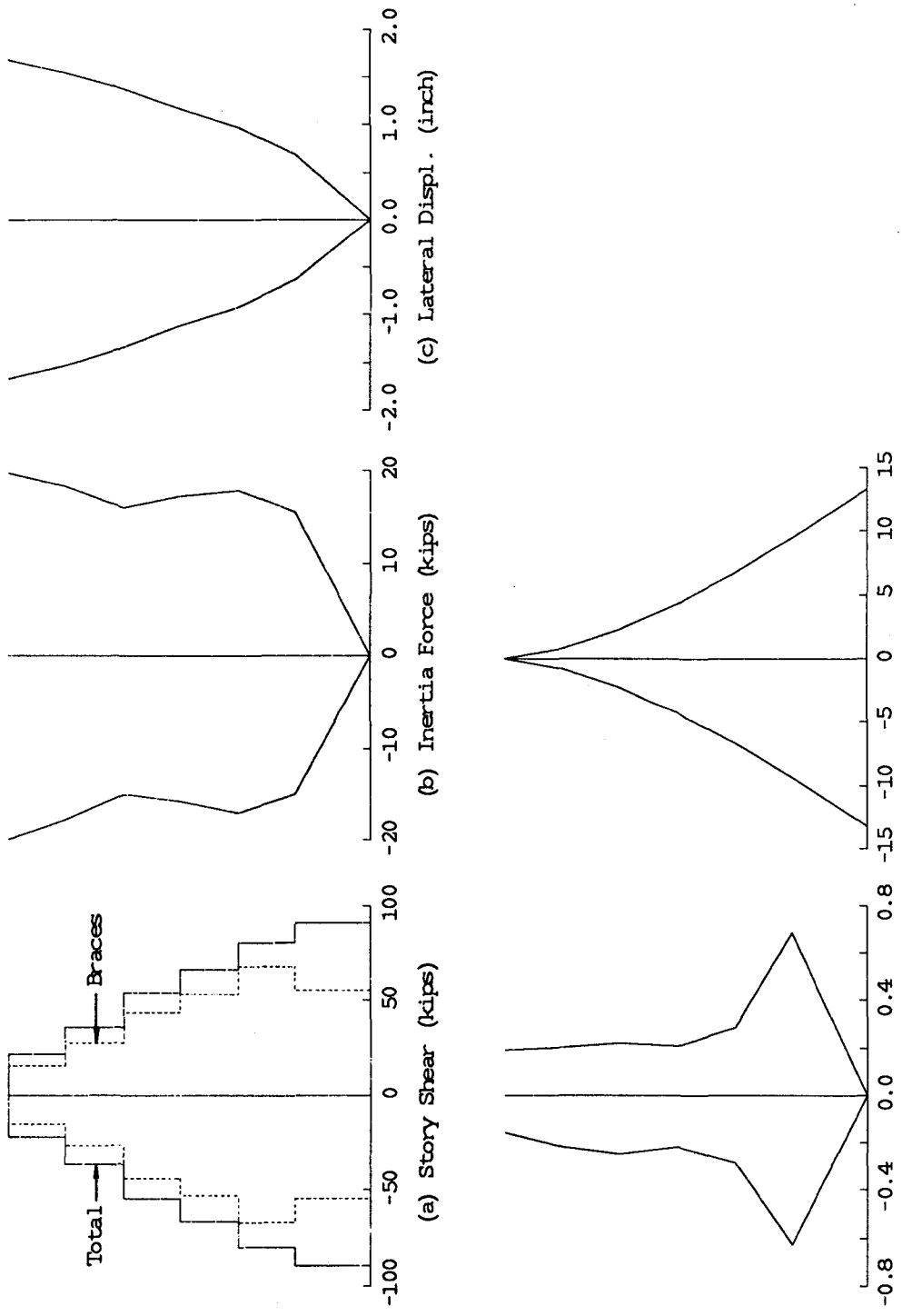


**FIGURE 8.41 TAFT-57 RESPONSE ENVELOPES**

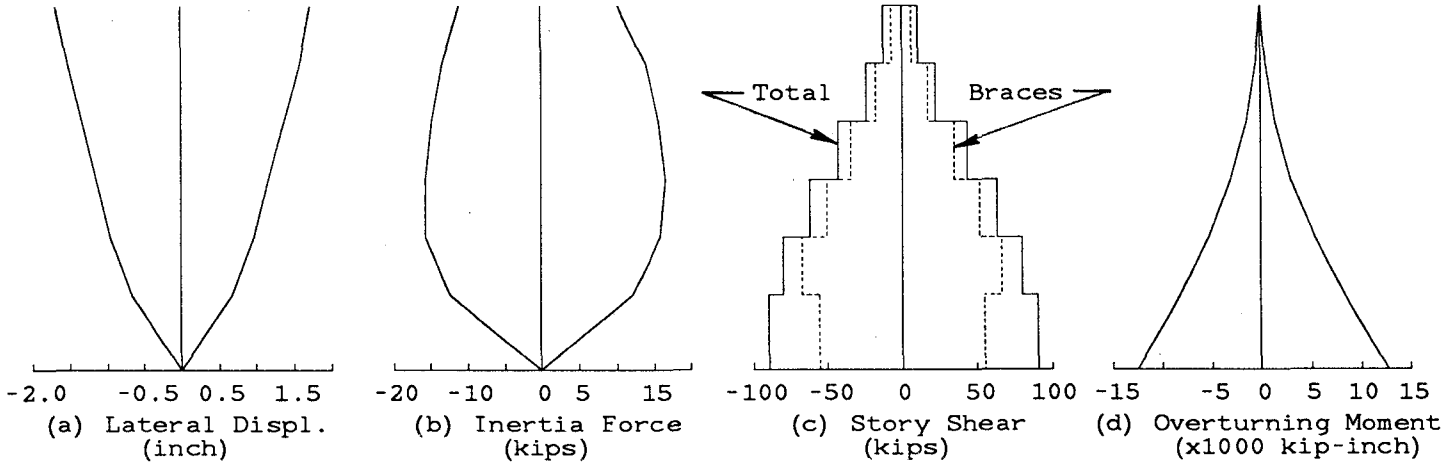


**At Maximum Base Shear**

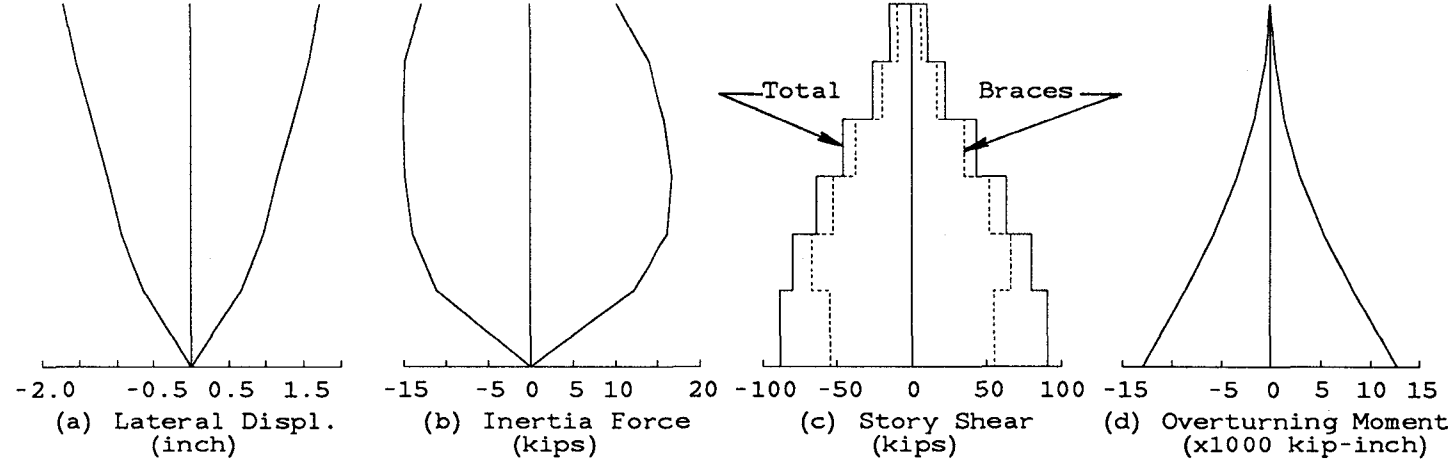


**At Maximum Lateral Displacement**

**FIGURE 8.42 TAFT-57 RESPONSE PROFILES AT MAXIMUM RESPONSE**

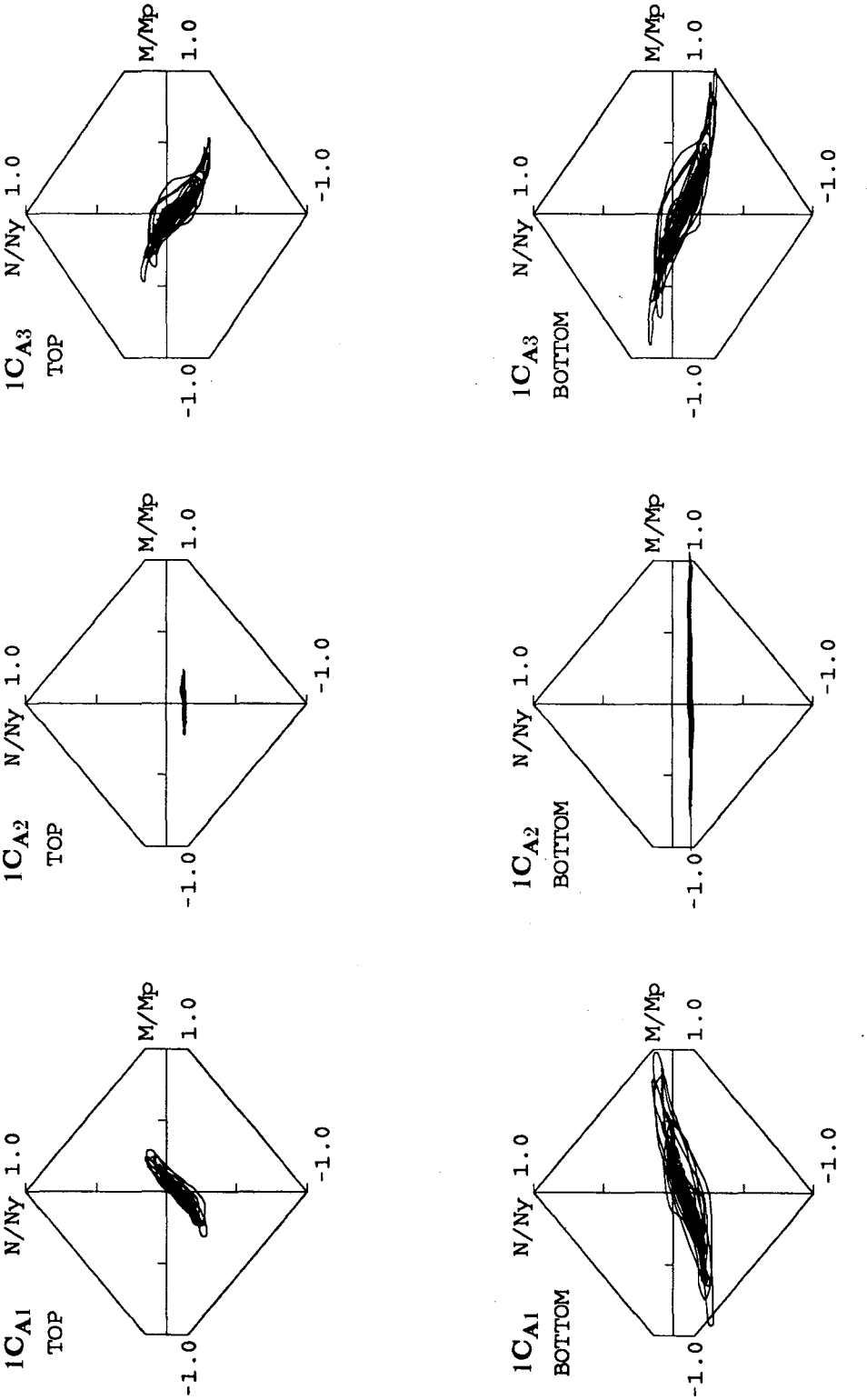


FIGURE 8.43 TAFT-57 FIRST STORY COLUMN AXIAL FORCE AND END MOMENT INTERACTION CURVES (FRAME A)

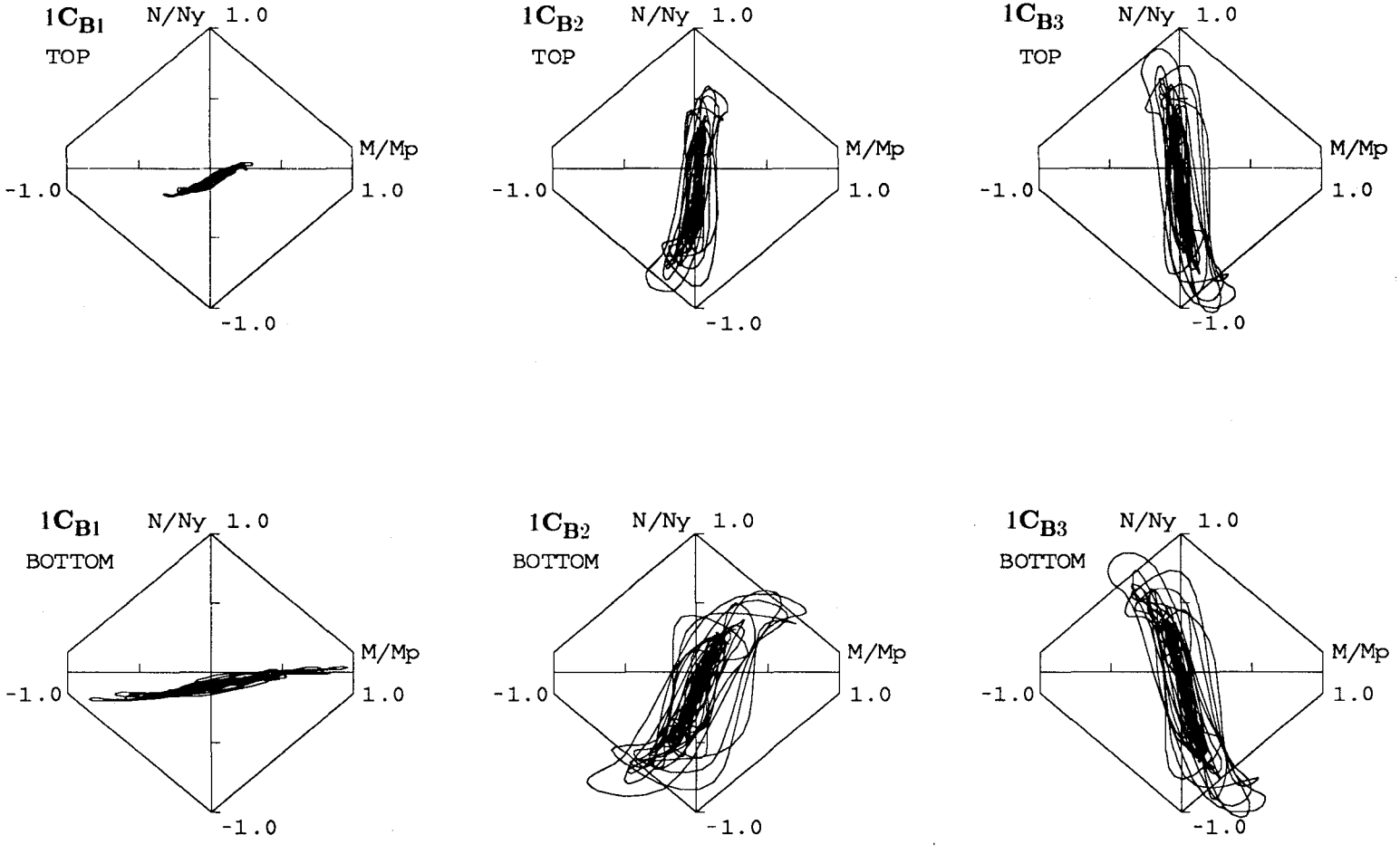


**FIGURE 8.44 TAFT-57 FIRST STORY COLUMN AXIAL FORCE AND END MOMENT INTERACTION CURVES (FRAME B)**

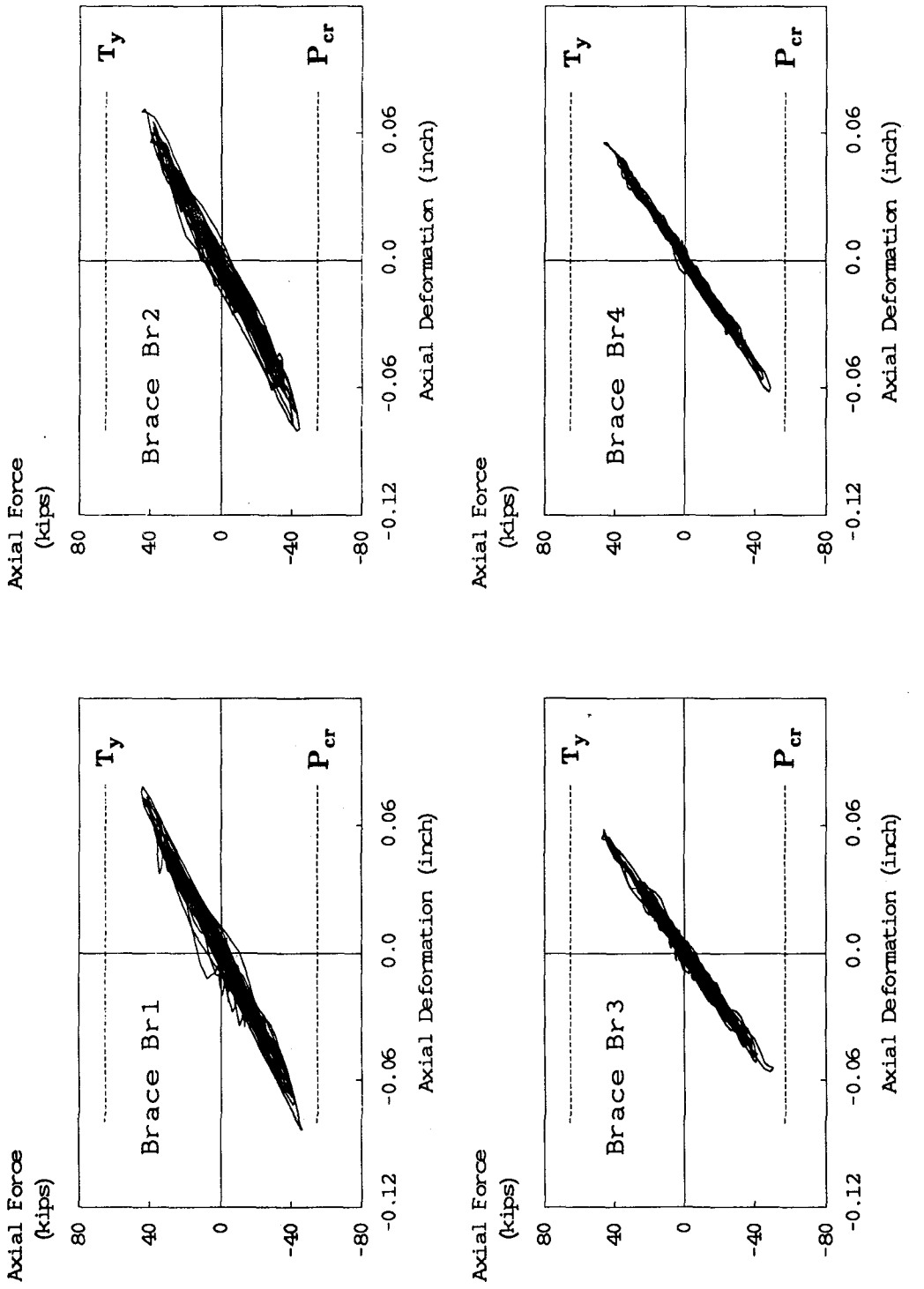


**FIGURE 8.45 TAFT-57 BRACE AXIAL FORCE AND DEFORMATION RELATIONSHIP**

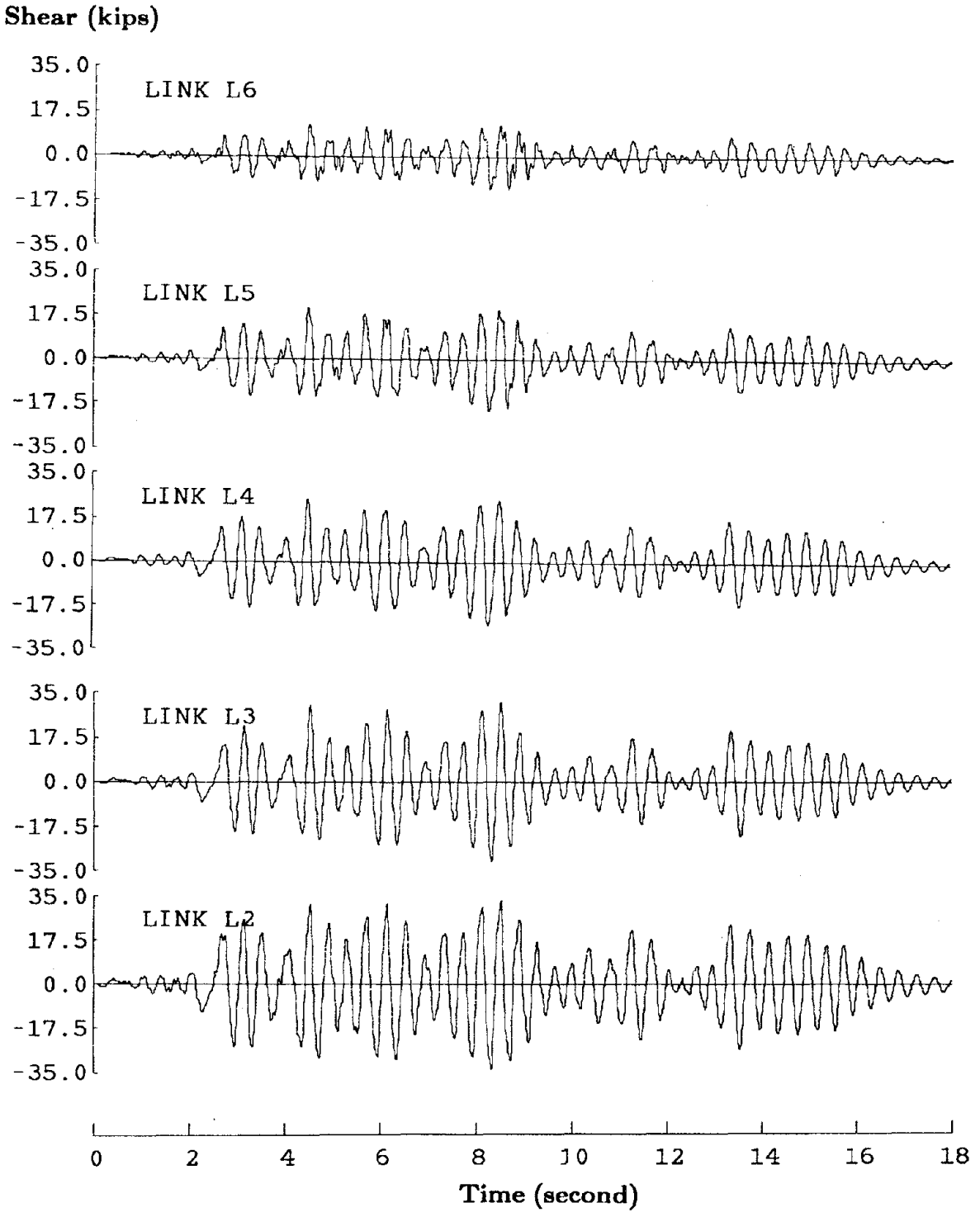


**FIGURE 8.46 TAFT-57 LINK SHEAR FORCE TIME HISTORY**

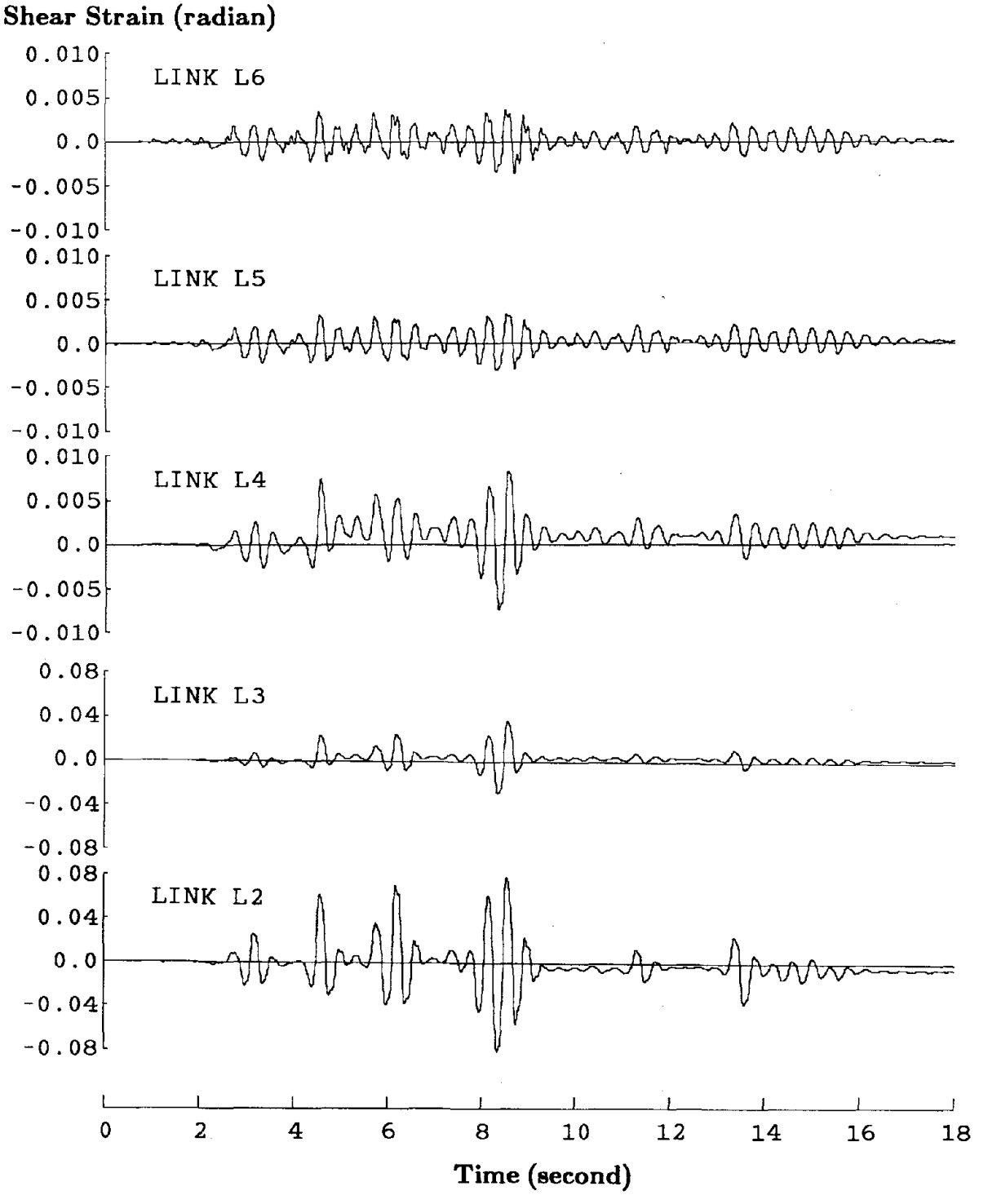


**FIGURE 8.47 TAFT-57 LINK SHEAR STRAIN TIME HISTORY**

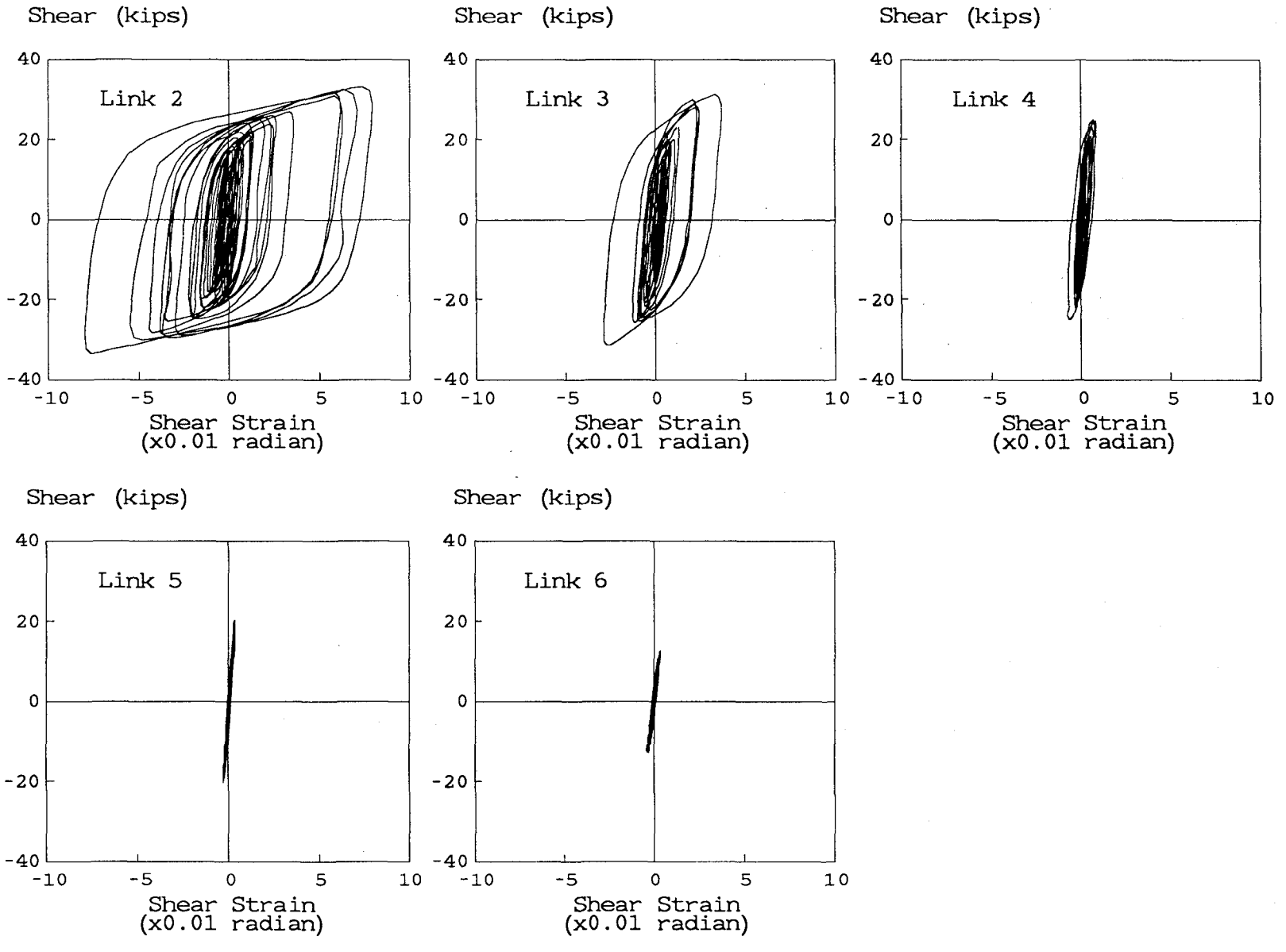


**FIGURE 8.48 TAFT-57 LINK SHEAR FORCE AND SHEAR STRAIN RELATIONSHIPS**

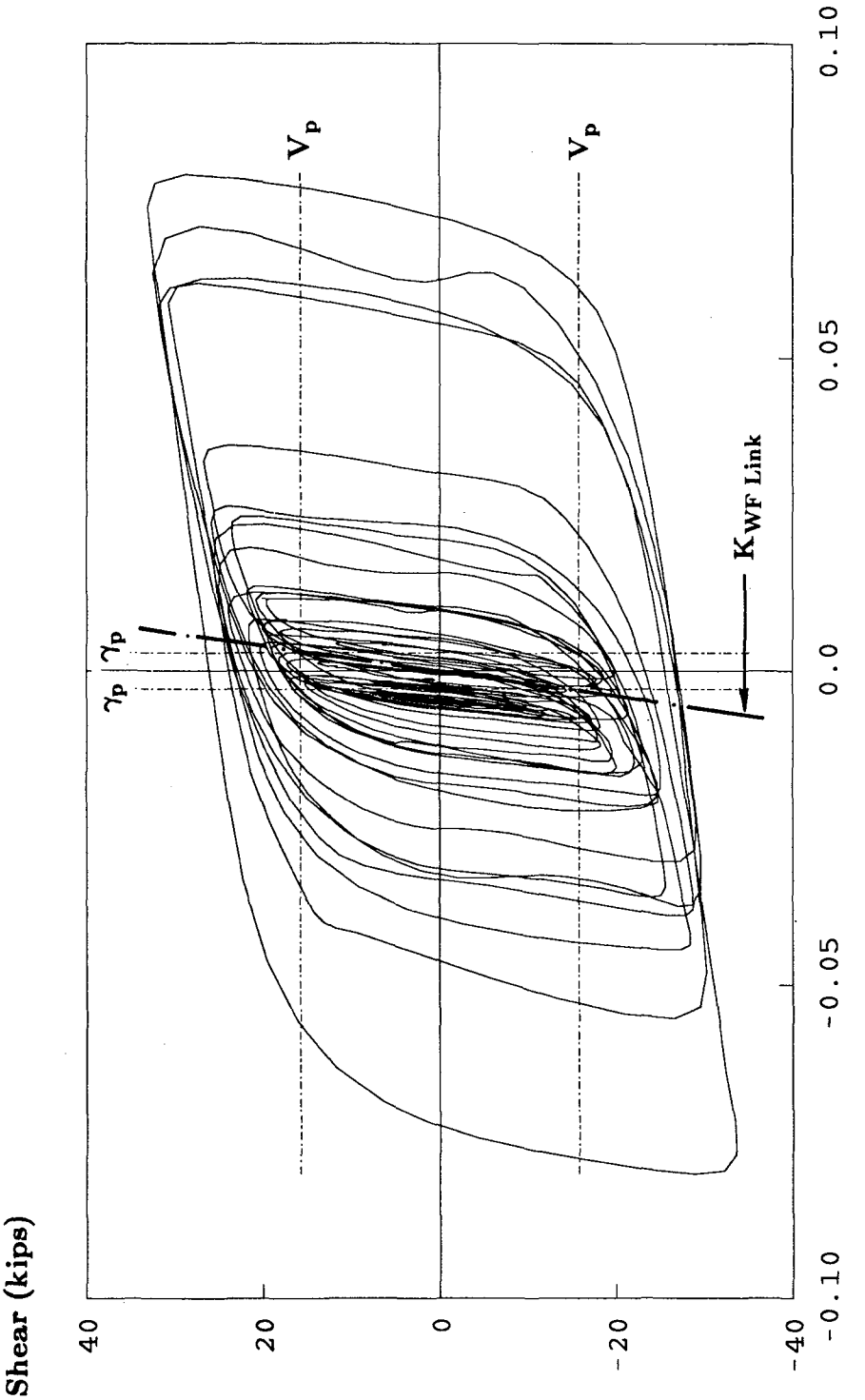


**FIGURE 8.49 TAFT-57 LINK L2 SHEAR FORCE AND SHEAR STRAIN RELATIONSHIP**

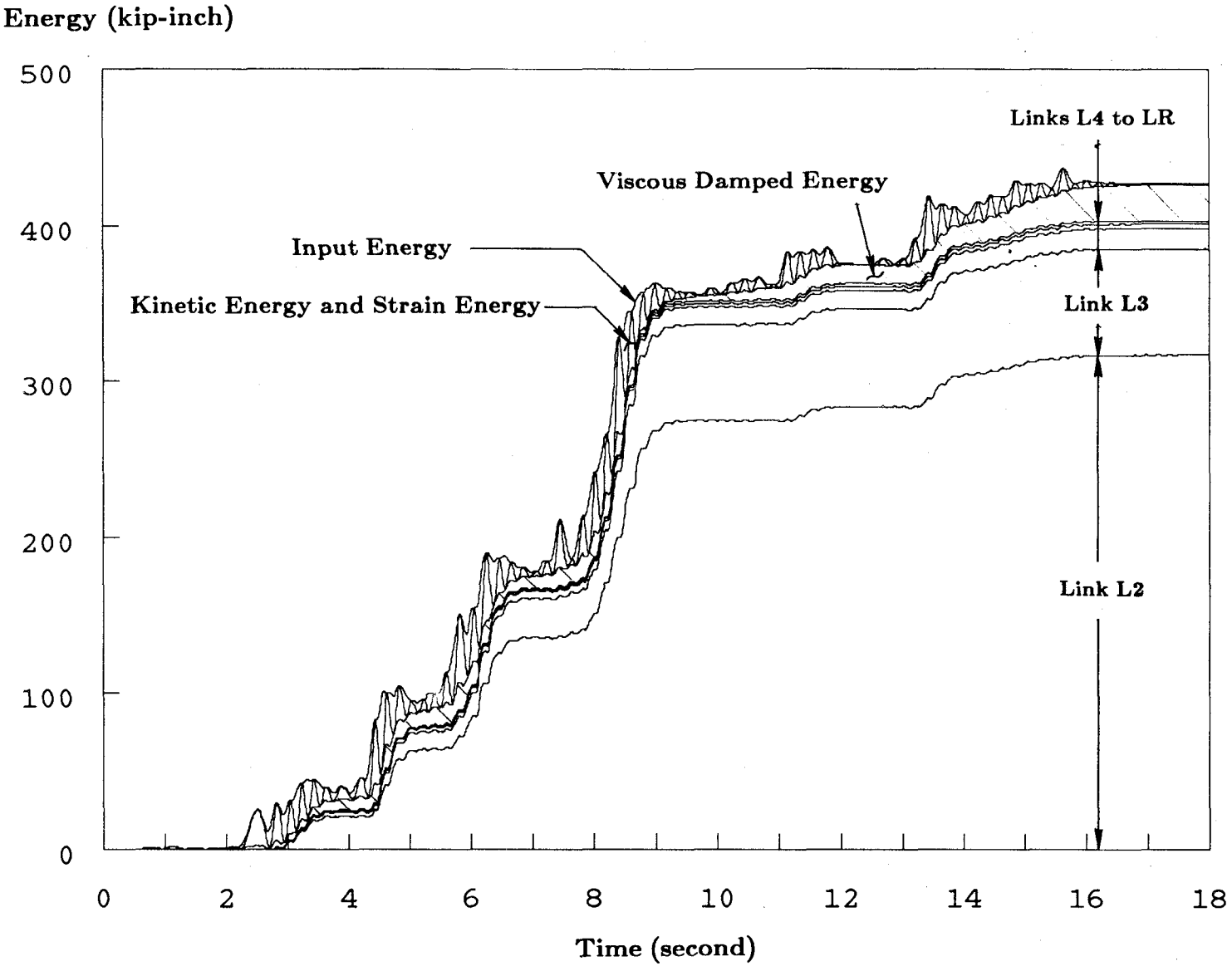


**FIGURE 8.50 TAFT-57 ENERGY TIME HISTORY**

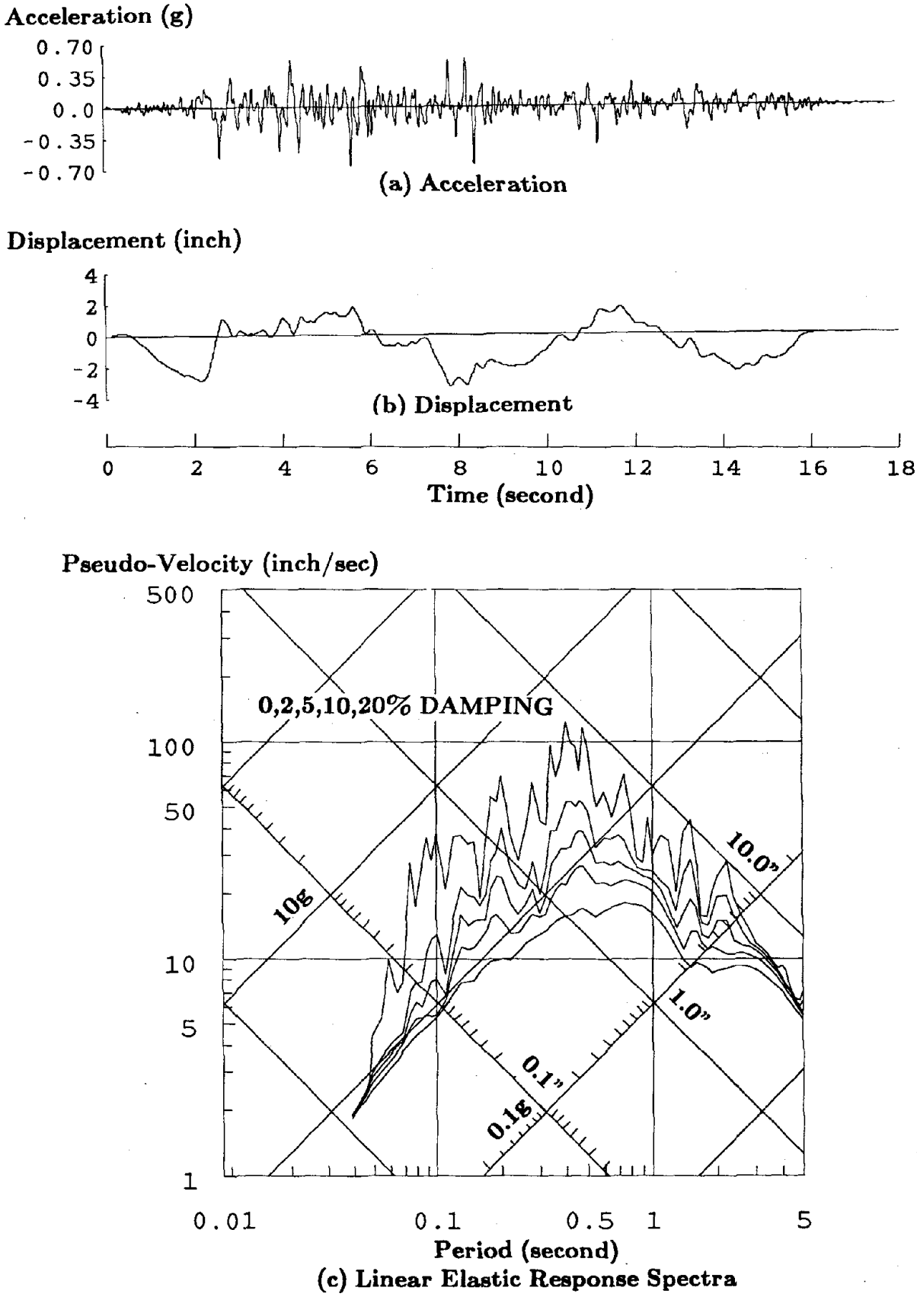


**FIGURE 8.51 TAFT-66 MEASURED TABLE MOTION**

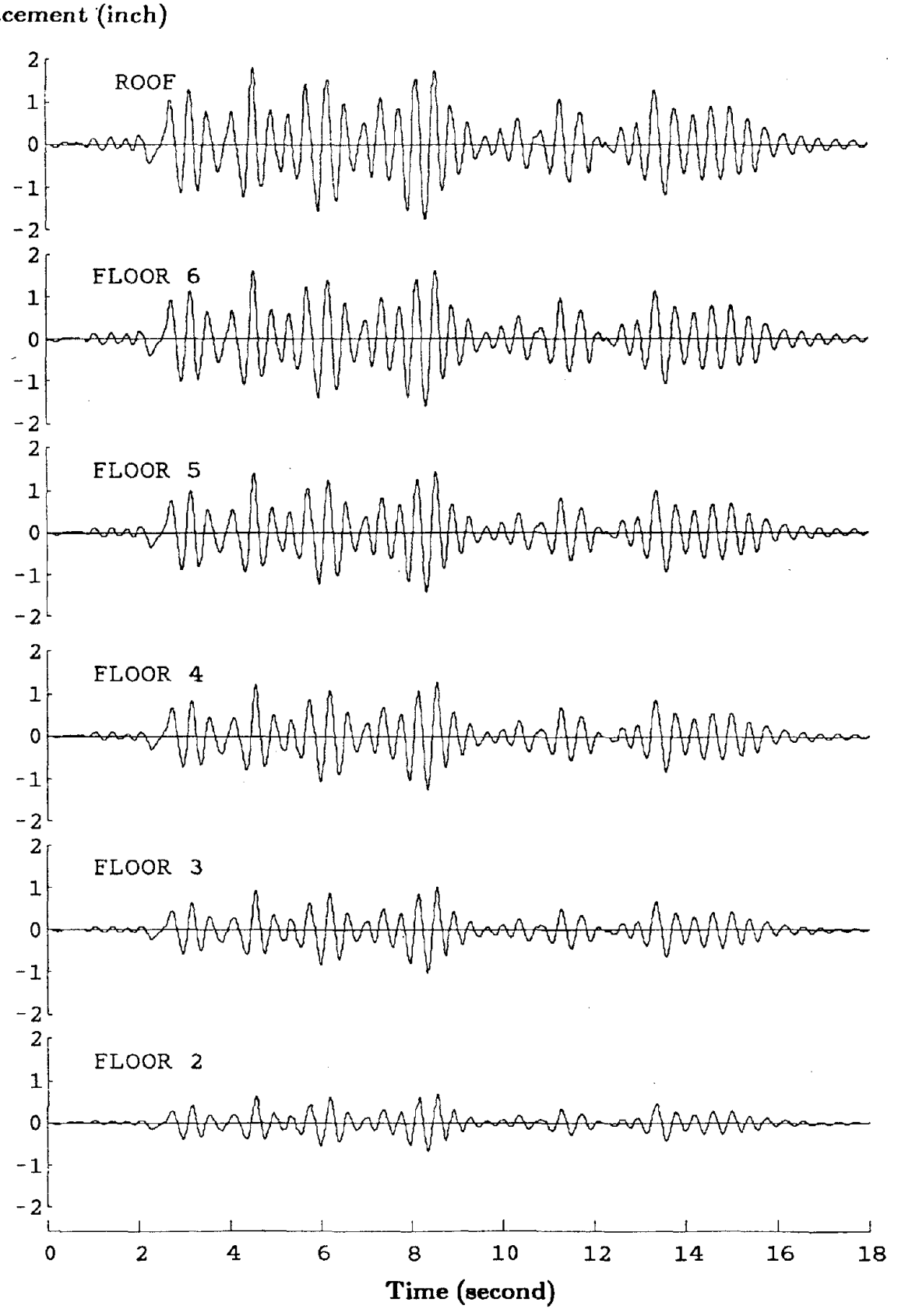


**FIGURE 8.52 TAFT-66 LATERAL DISPLACEMENT TIME HISTORY**

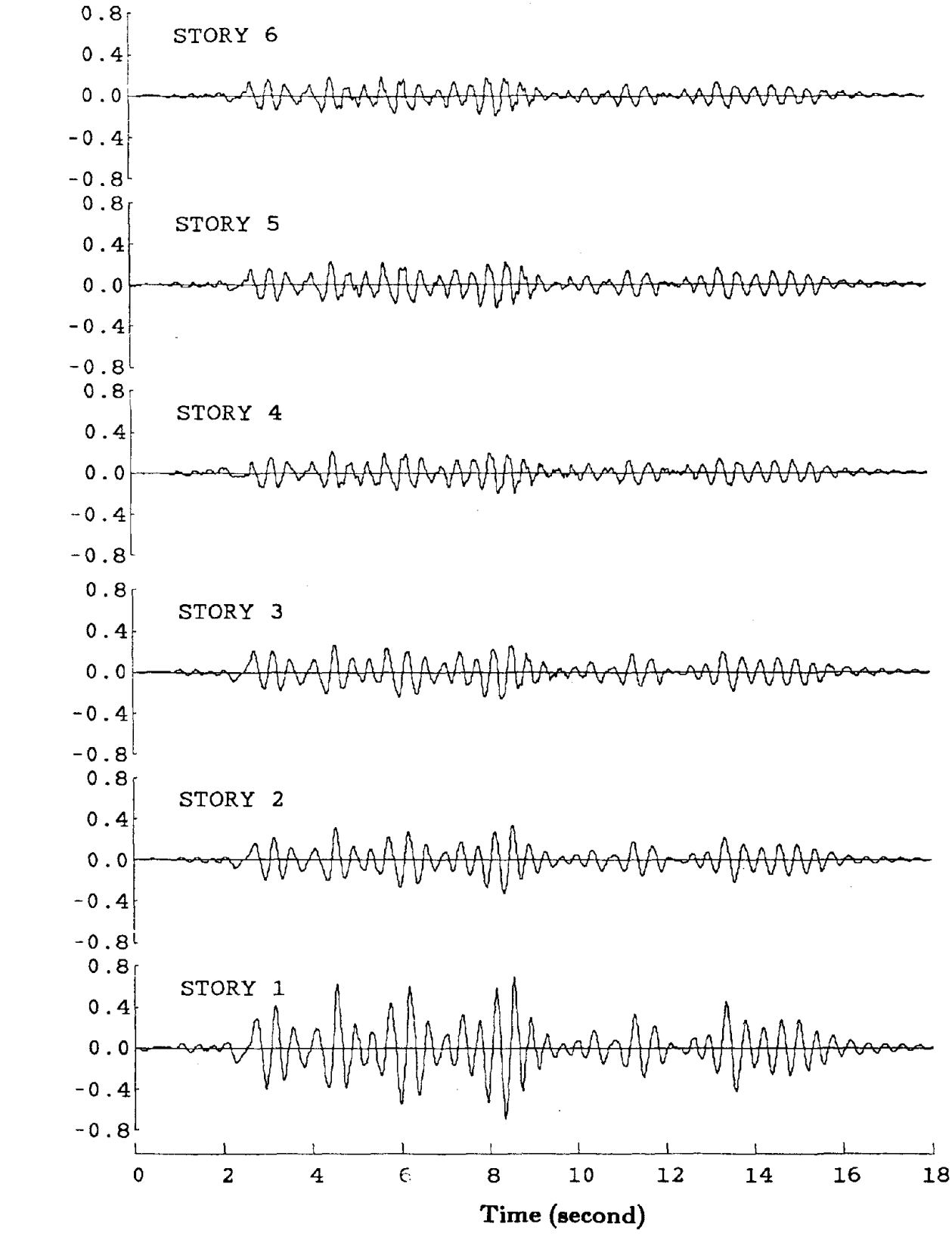


**FIGURE 8.53 TAFT-66 INTER-STORY DRIFT TIME HISTORY**

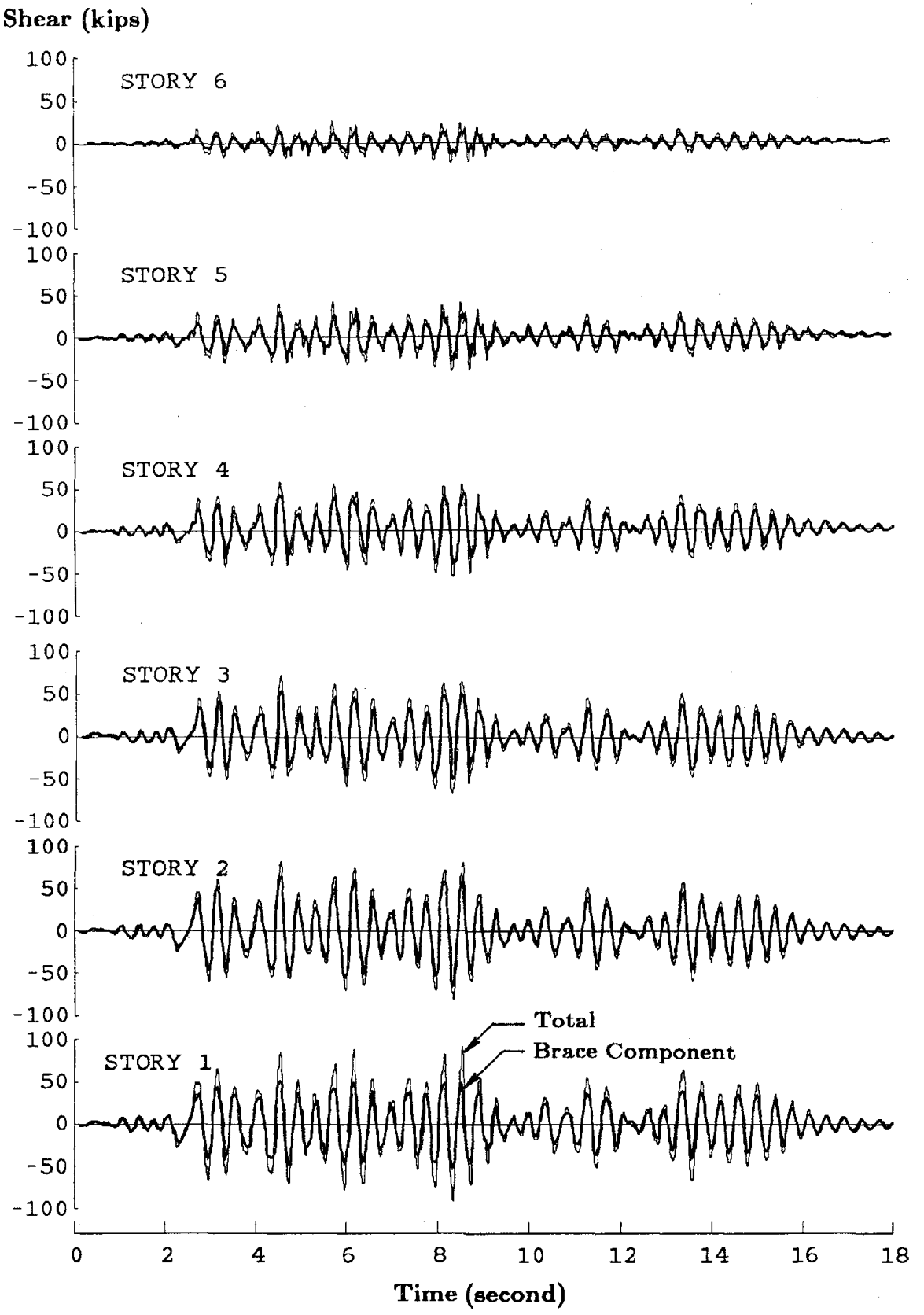


**FIGURE 8.54 TAFT-66 STORY SHEAR TIME HISTORY**

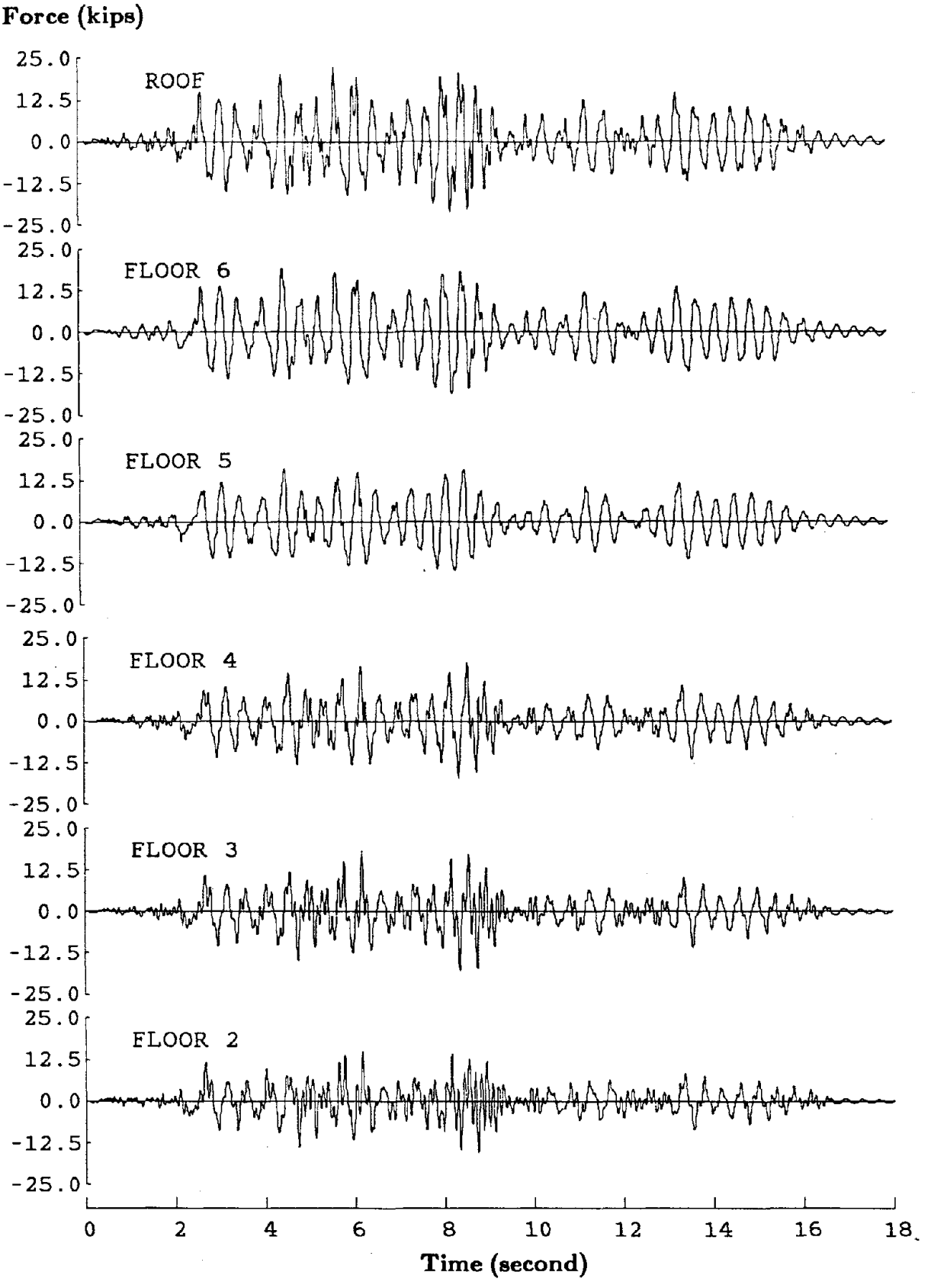


**FIGURE 8.55 TAFT-66 INERTIA FORCE TIME HISTORY**

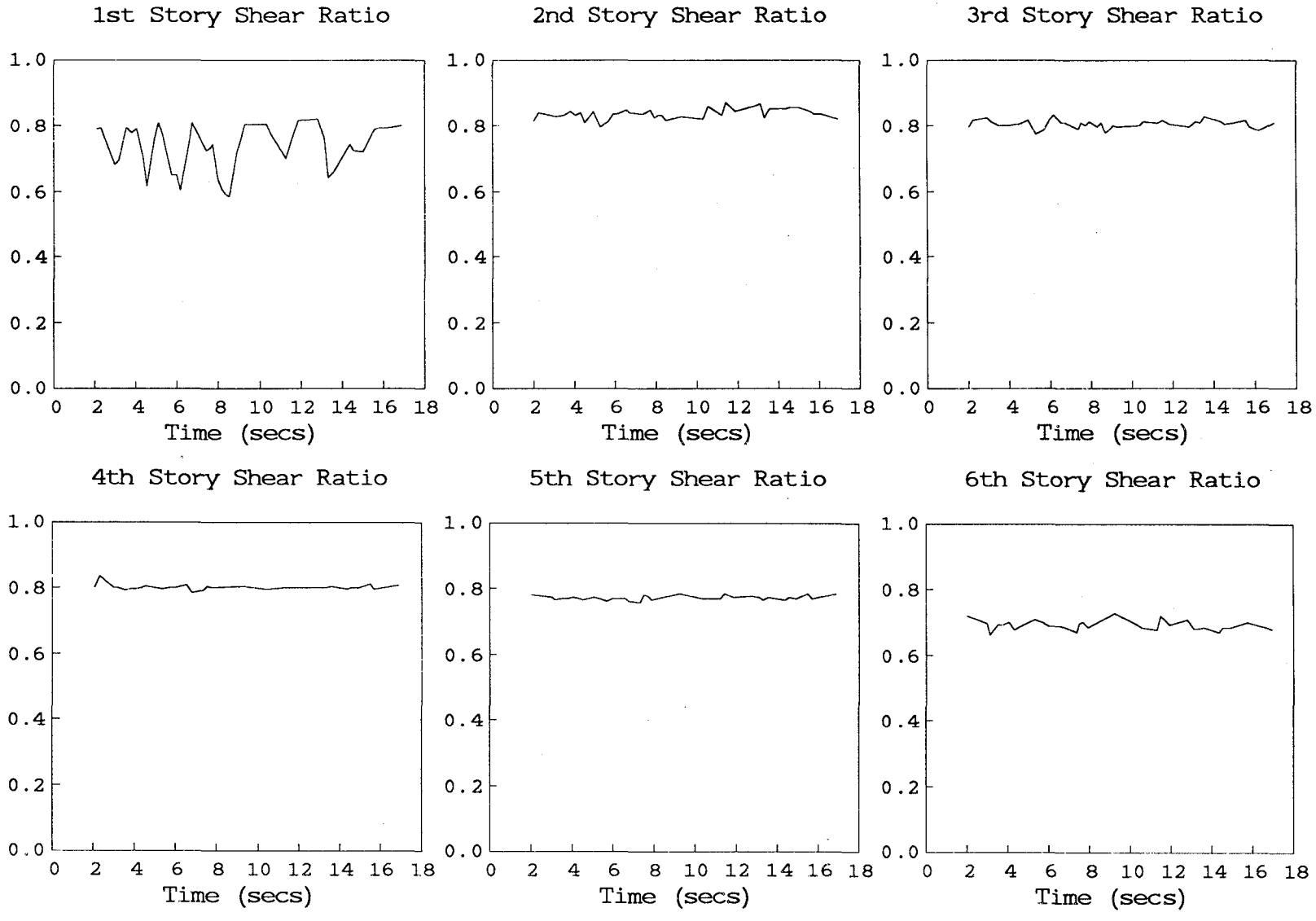


**FIGURE 8.56 TAFT-66 STORY SHEAR RATIO**

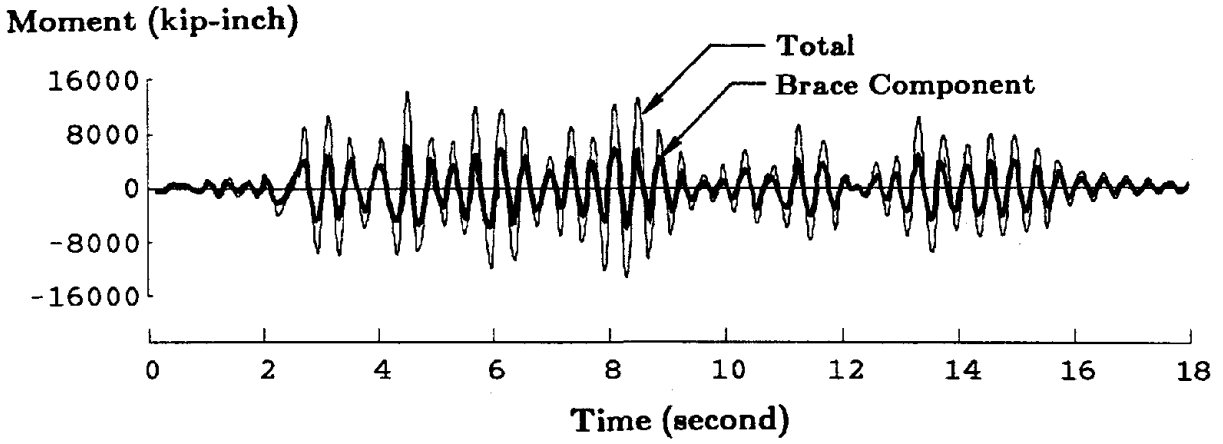


FIGURE 8.57 TAFT-66 BASE OVERTURNING MOMENT TIME HISTORY

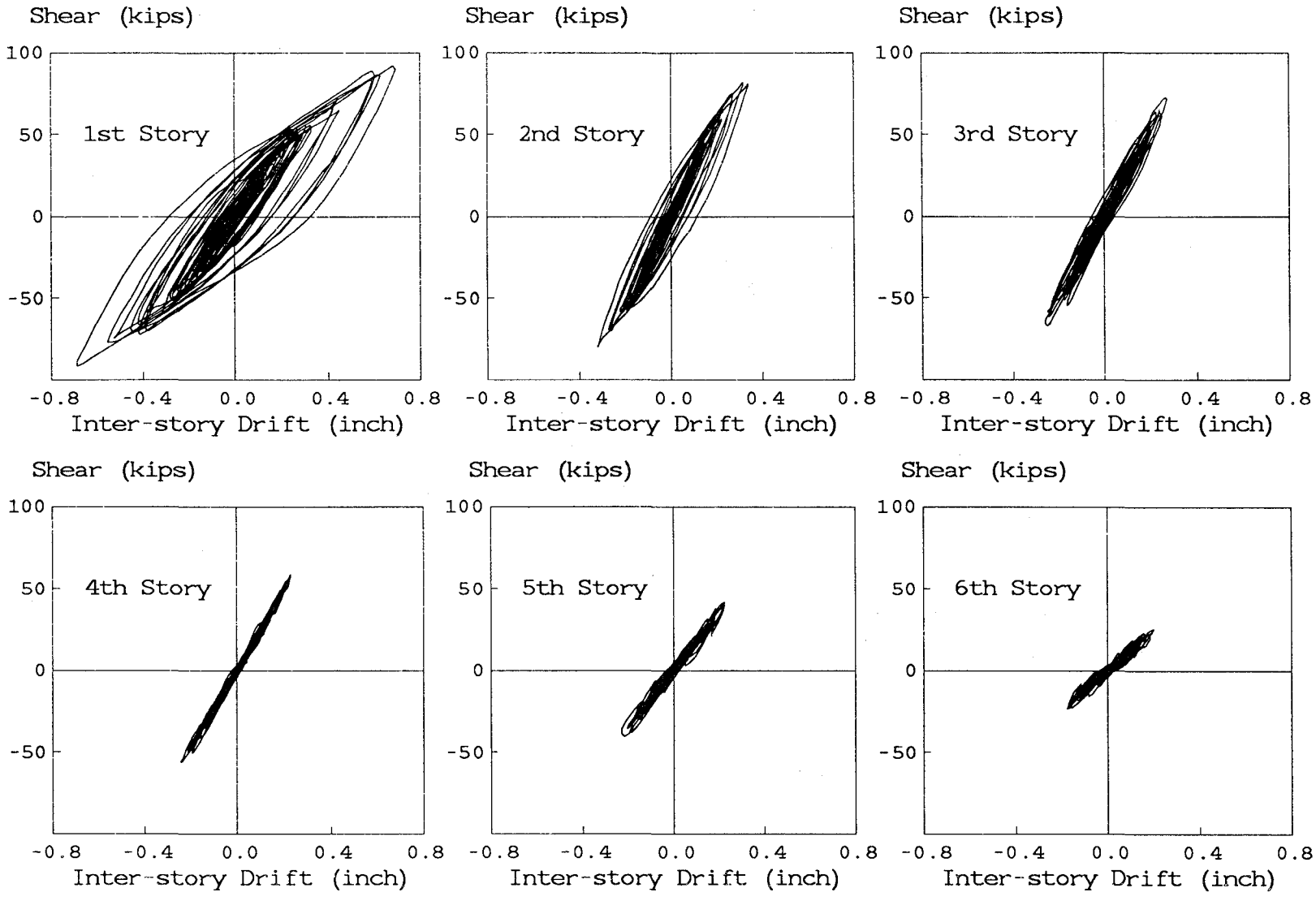


**FIGURE 8.58 TAFT-66 TOTAL STORY SHEAR AND INTER-STORY DRIFT**

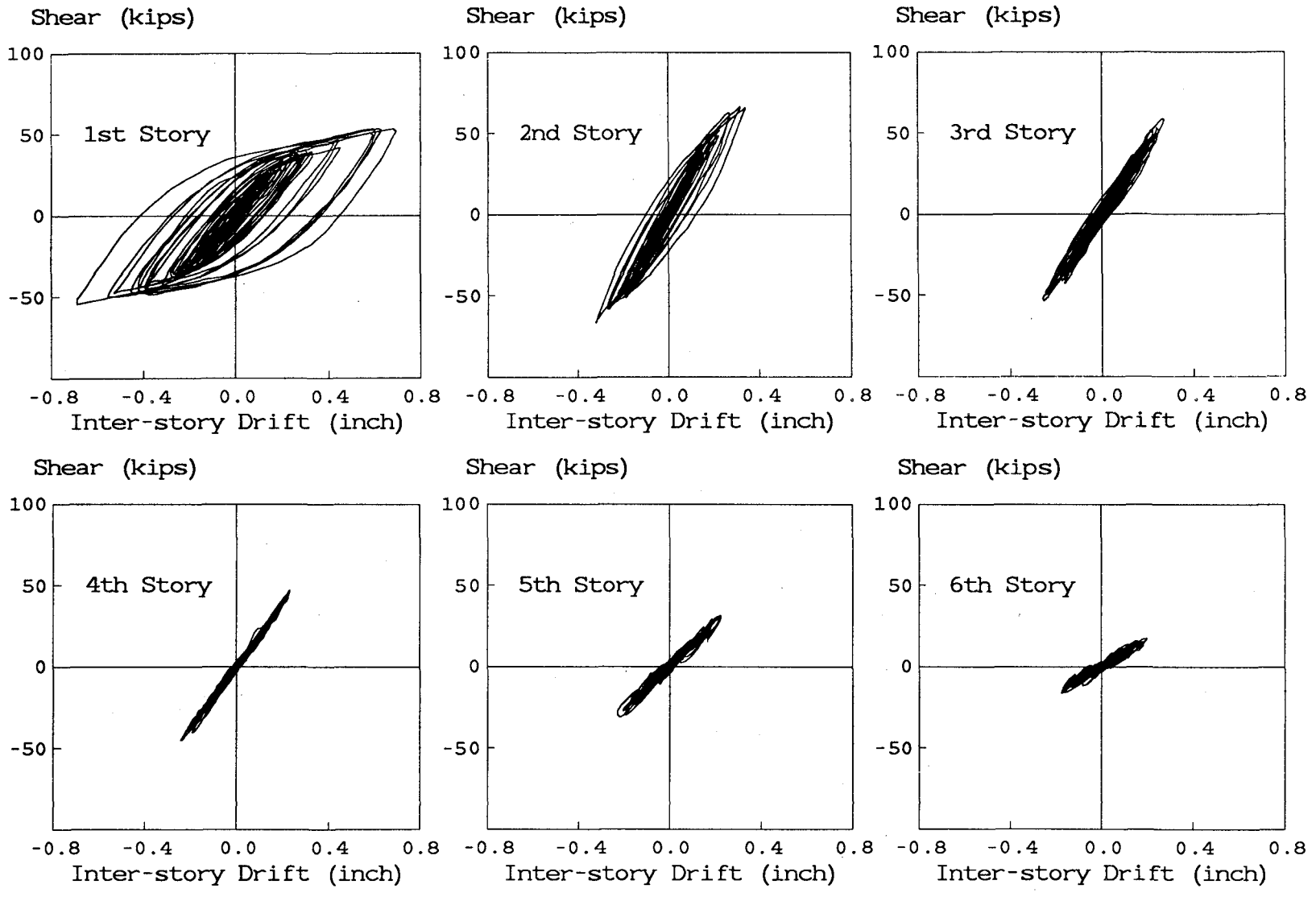


**FIGURE 8.59 TAFT-66 BRACE STORY SHEAR AND INTER-STORY DRIFT**

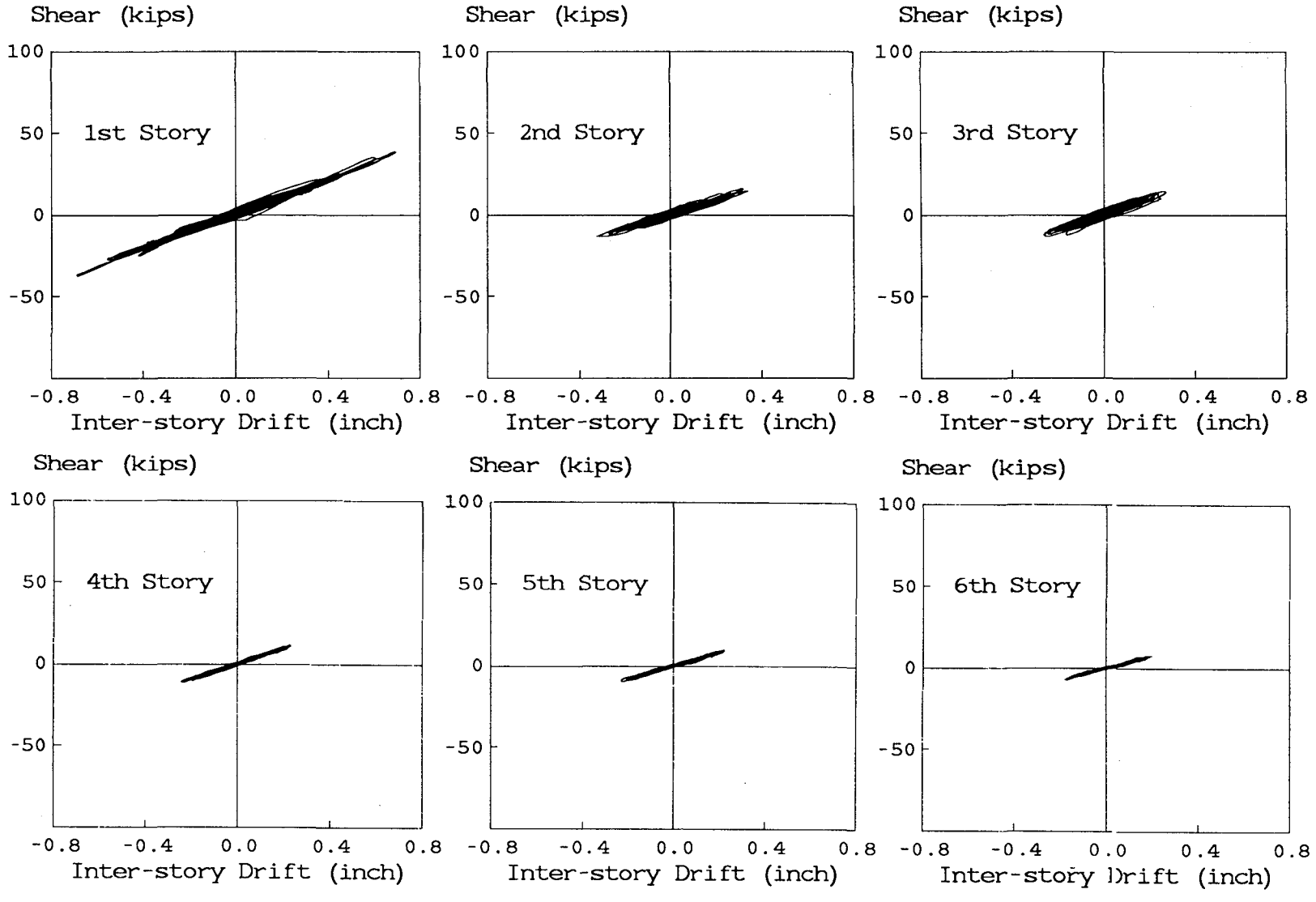


**FIGURE 8.60 TAFT-66 DMRSF STORY SHEAR AND INTER-STORY DRIFT**

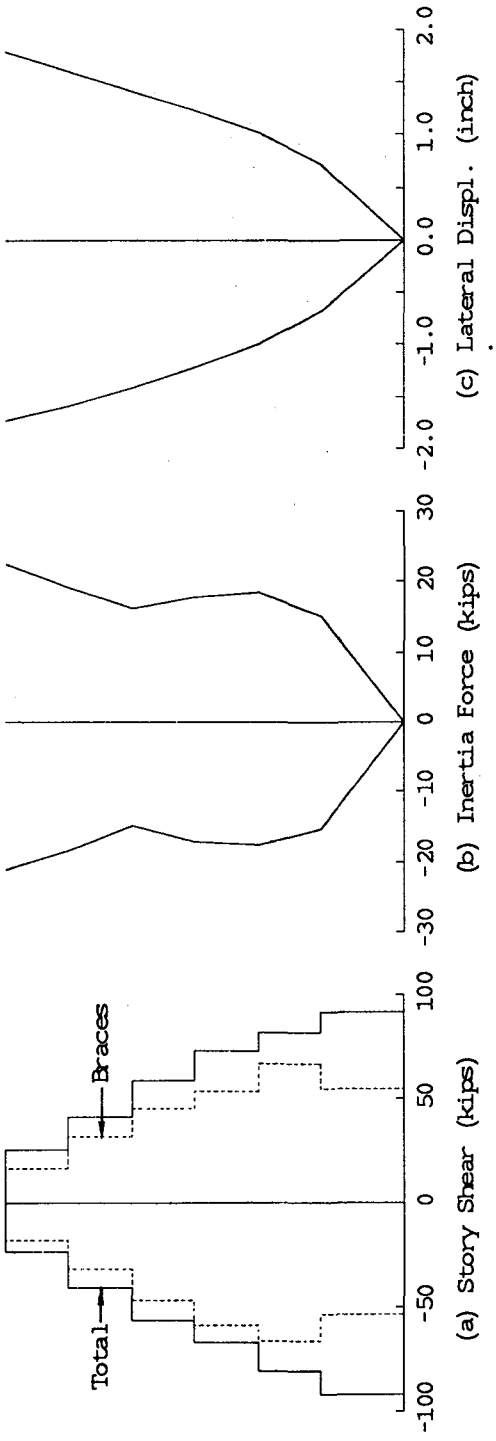


**FIGURE 8.61 TAFT-66 RESPONSE ENVELOPES**

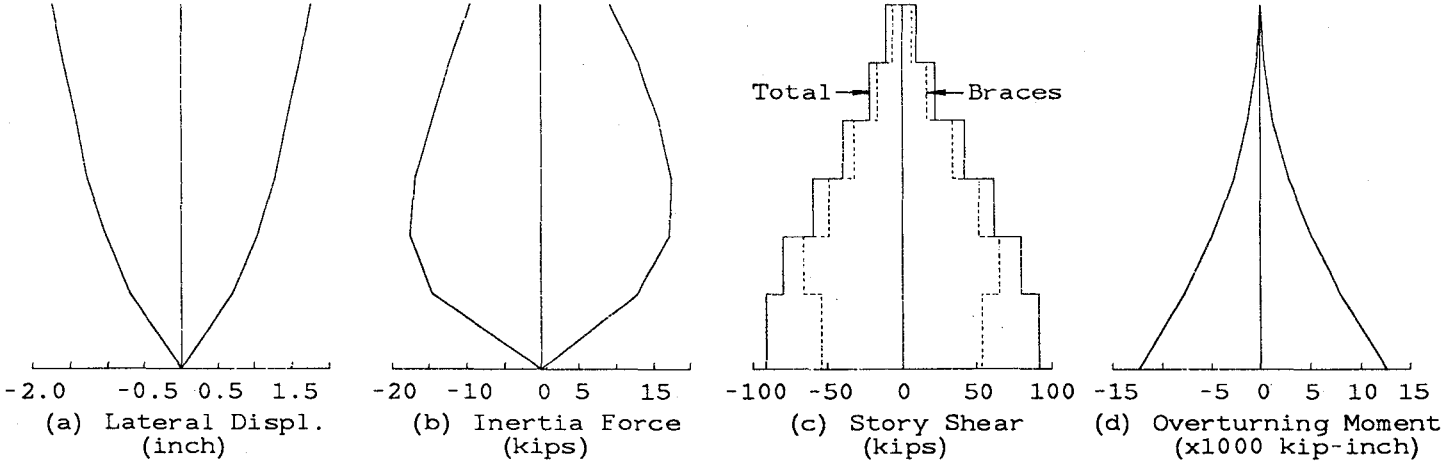


**At Maximum Base Shear**

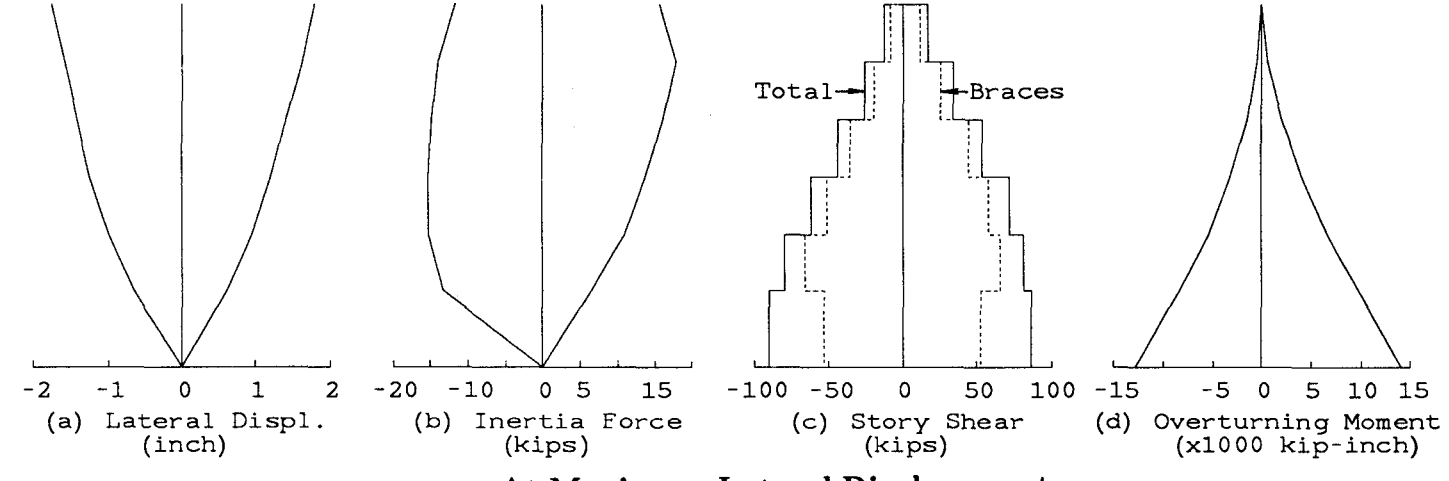


**At Maximum Lateral Displacement**

**FIGURE 8.62 TAFT-66 RESPONSE PROFILES AT MAXIMUM RESPONSE**

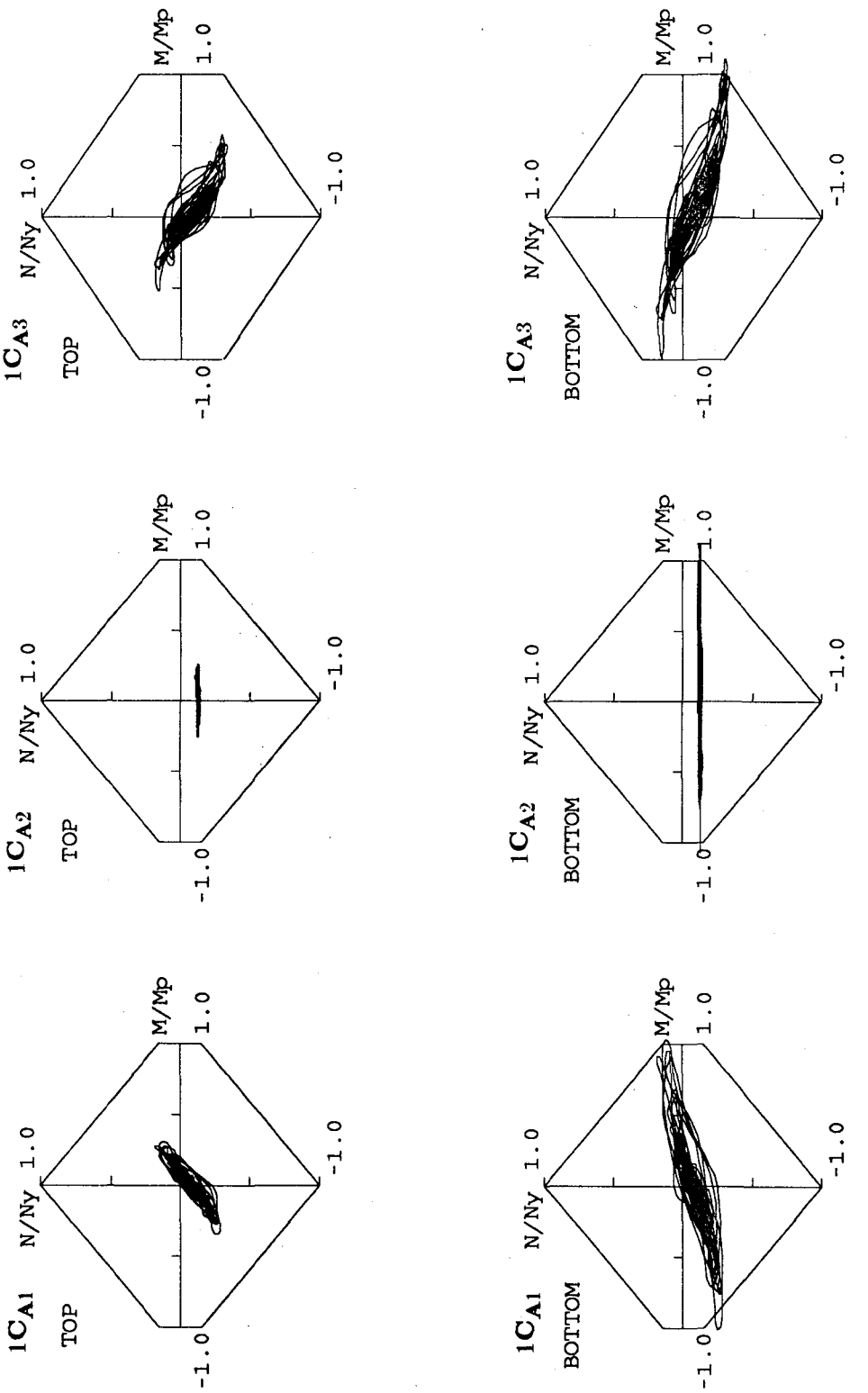


**FIGURE 8.63 TAFT-66 FIRST STORY COLUMN AXIAL FORCE AND END MOMENT INTERACTION CURVES (FRAME A)**

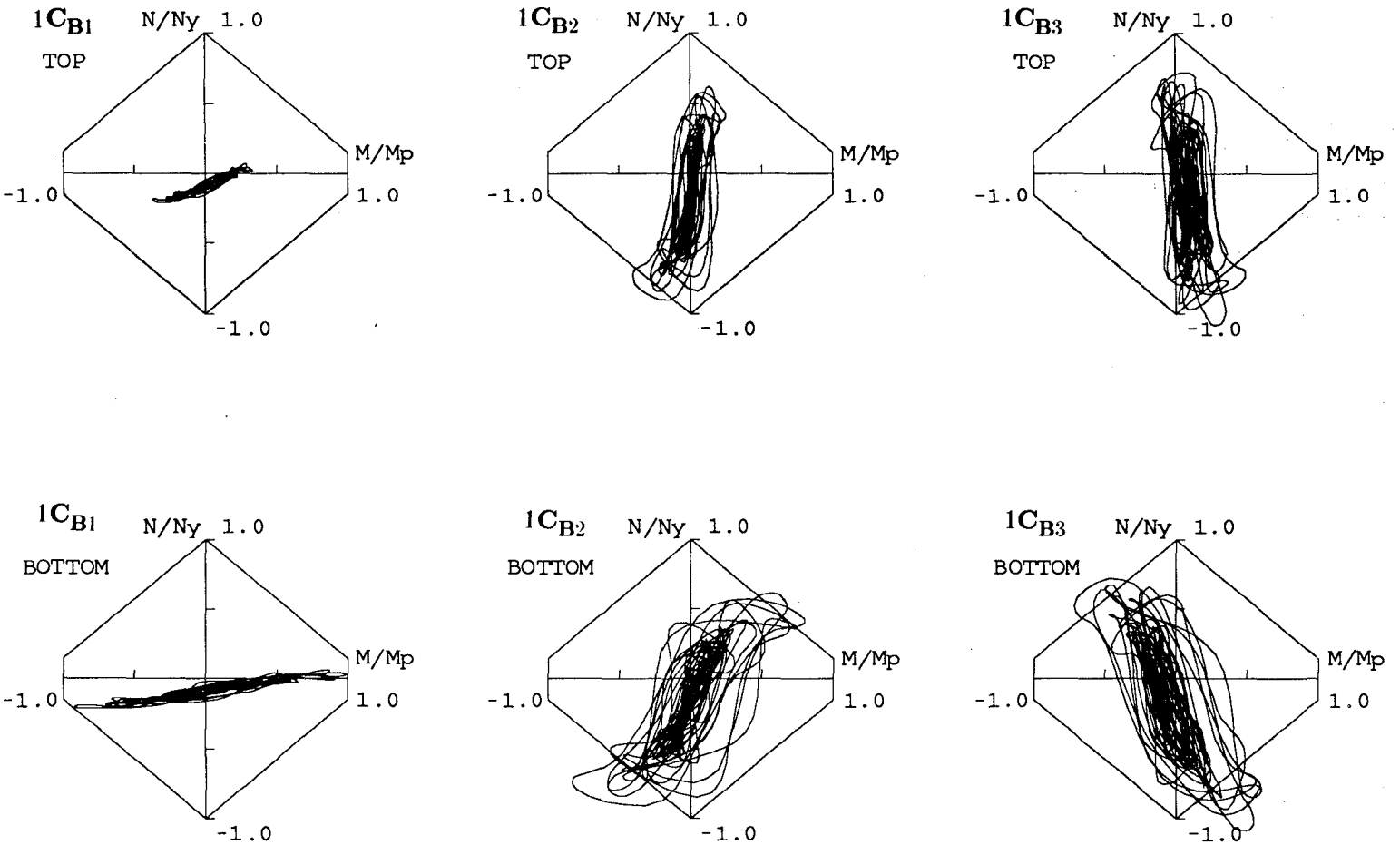


**FIGURE 8.64 TAFT-66 FIRST STORY COLUMN AXIAL FORCE AND END MOMENT INTERACTION CURVES (FRAME B)**

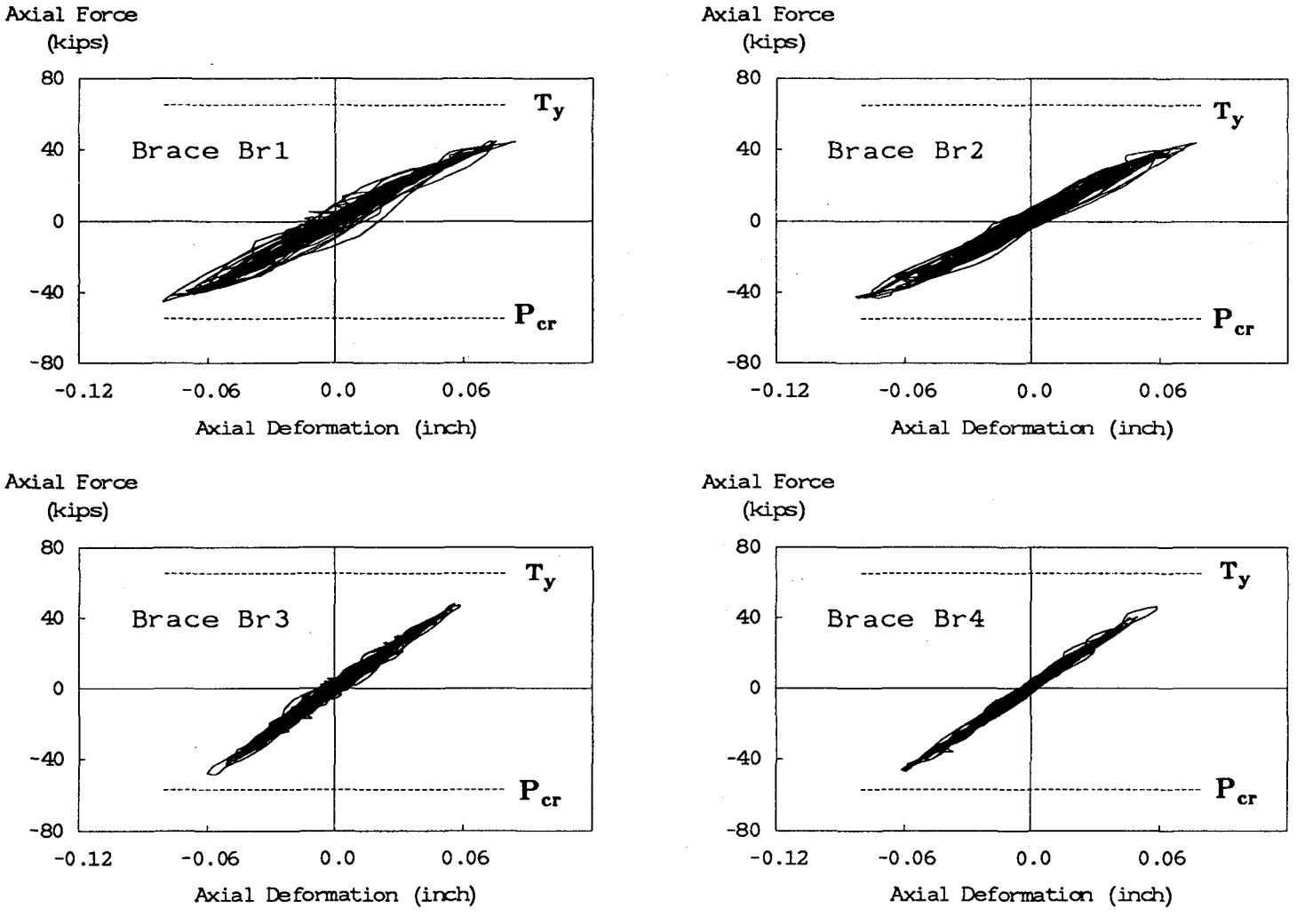


**FIGURE 8.65 TAFT-66 BRACE AXIAL FORCE AND DEFORMATION RELATIONSHIP**

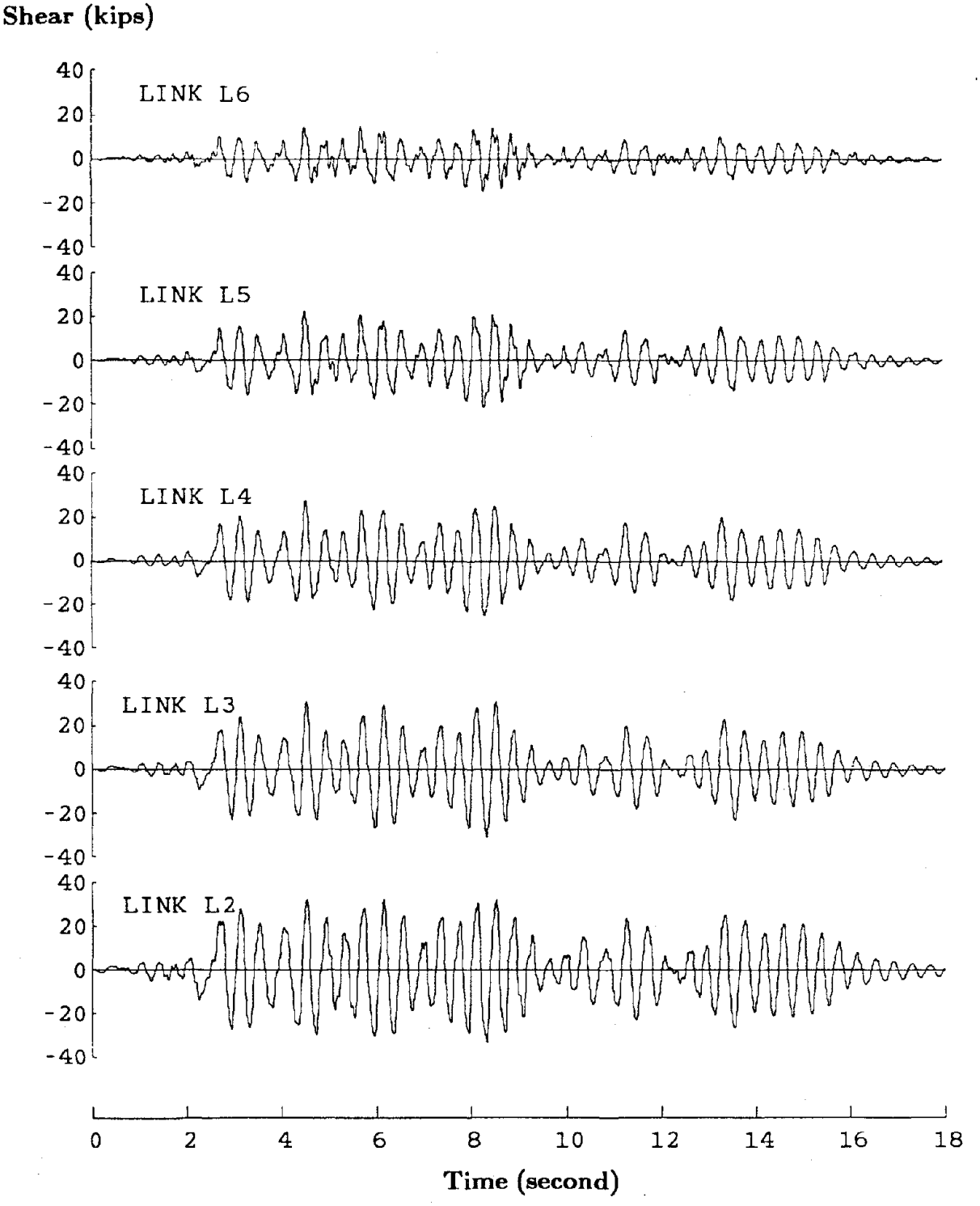


**FIGURE 8.66 TAFT-66 LINK SHEAR FORCE TIME HISTORY**

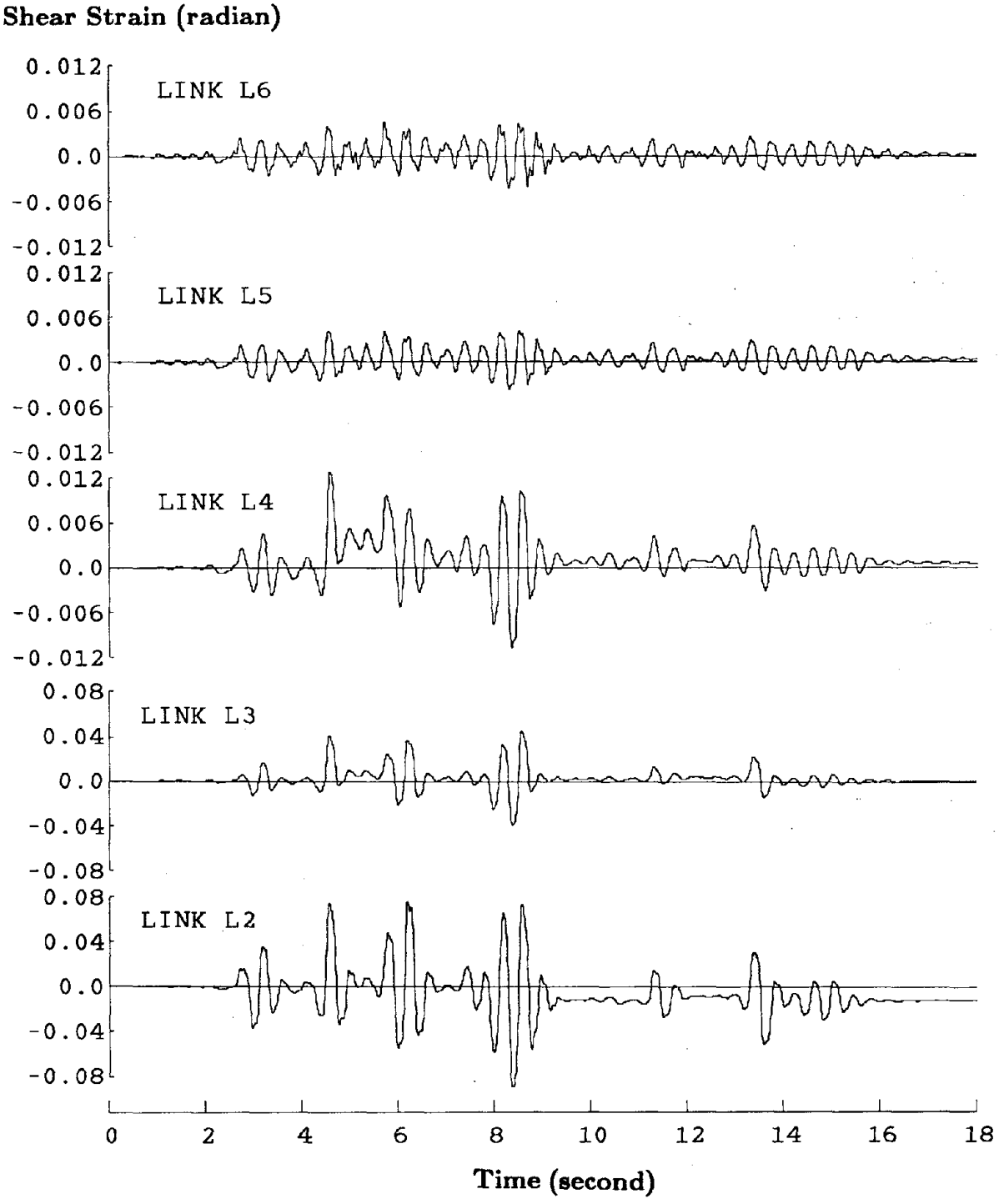


**FIGURE 8.67 TAFT-66 LINK SHEAR STRAIN TIME HISTORY**

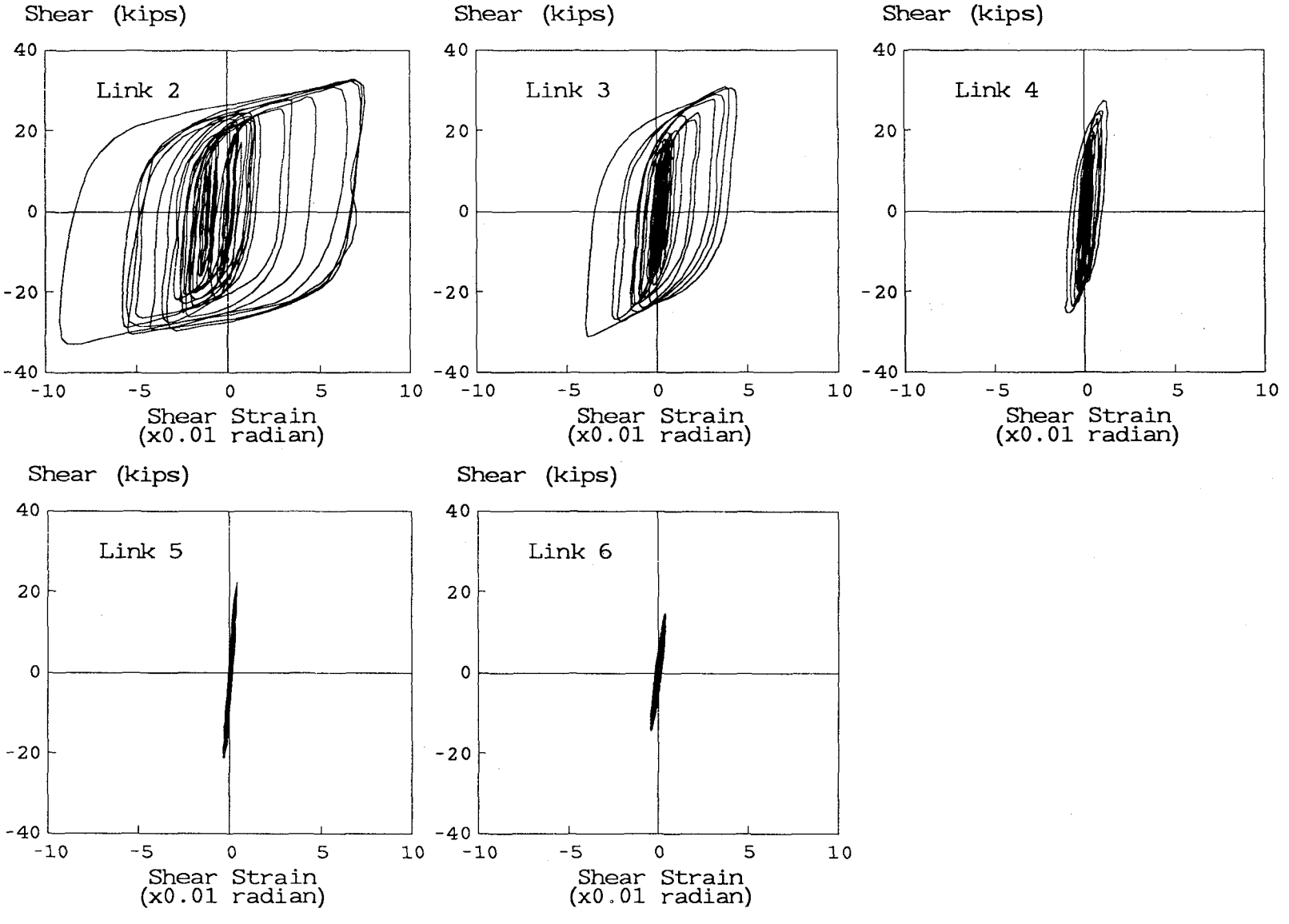


**FIGURE 8.68 TAFT-66 LINK SHEAR FORCE AND SHEAR STRAIN RELATIONSHIPS**

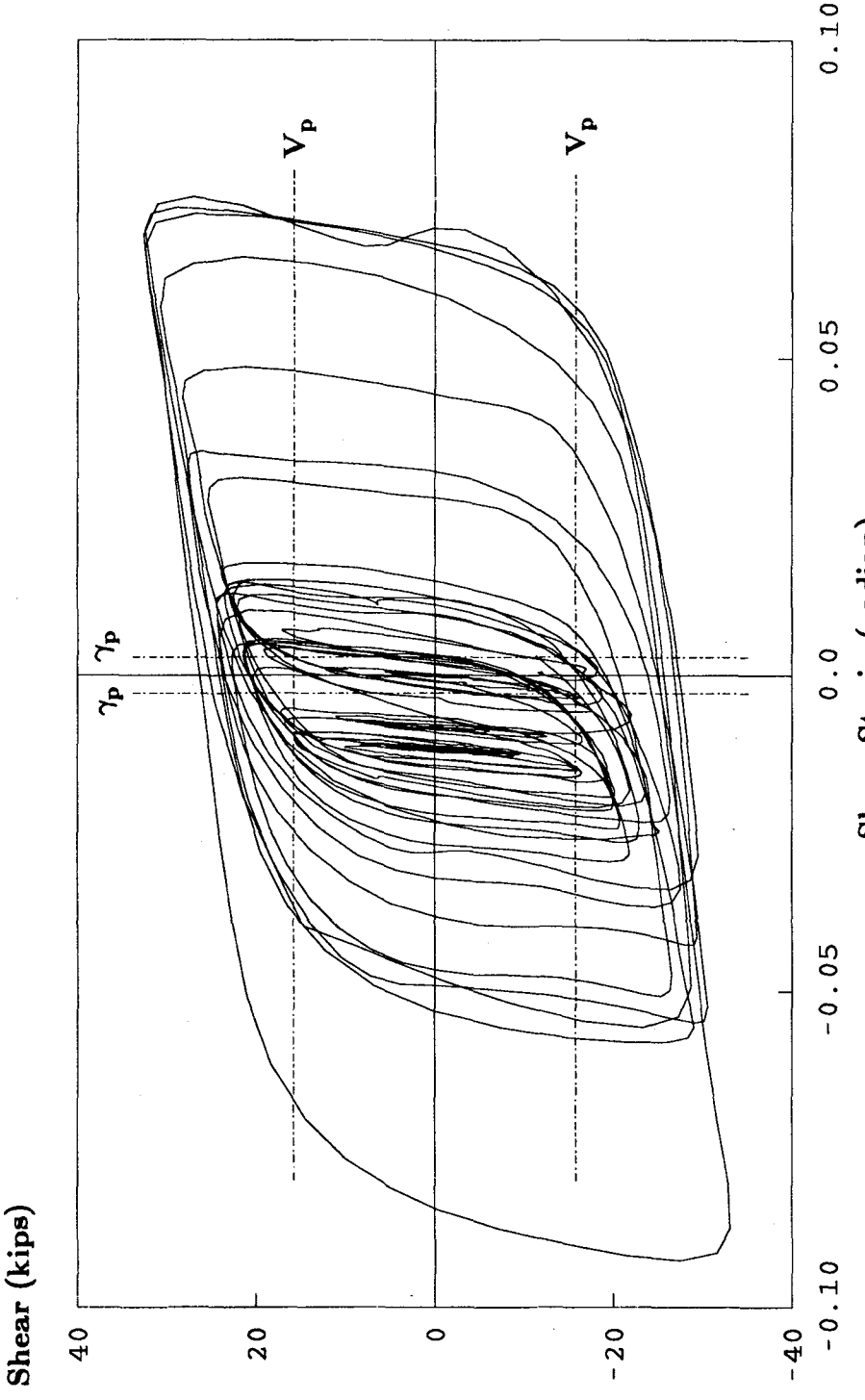


**FIGURE 8.69 TAFT-66 LINK L2 SHEAR FORCE AND SHEAR STRAIN RELATIONSHIP**

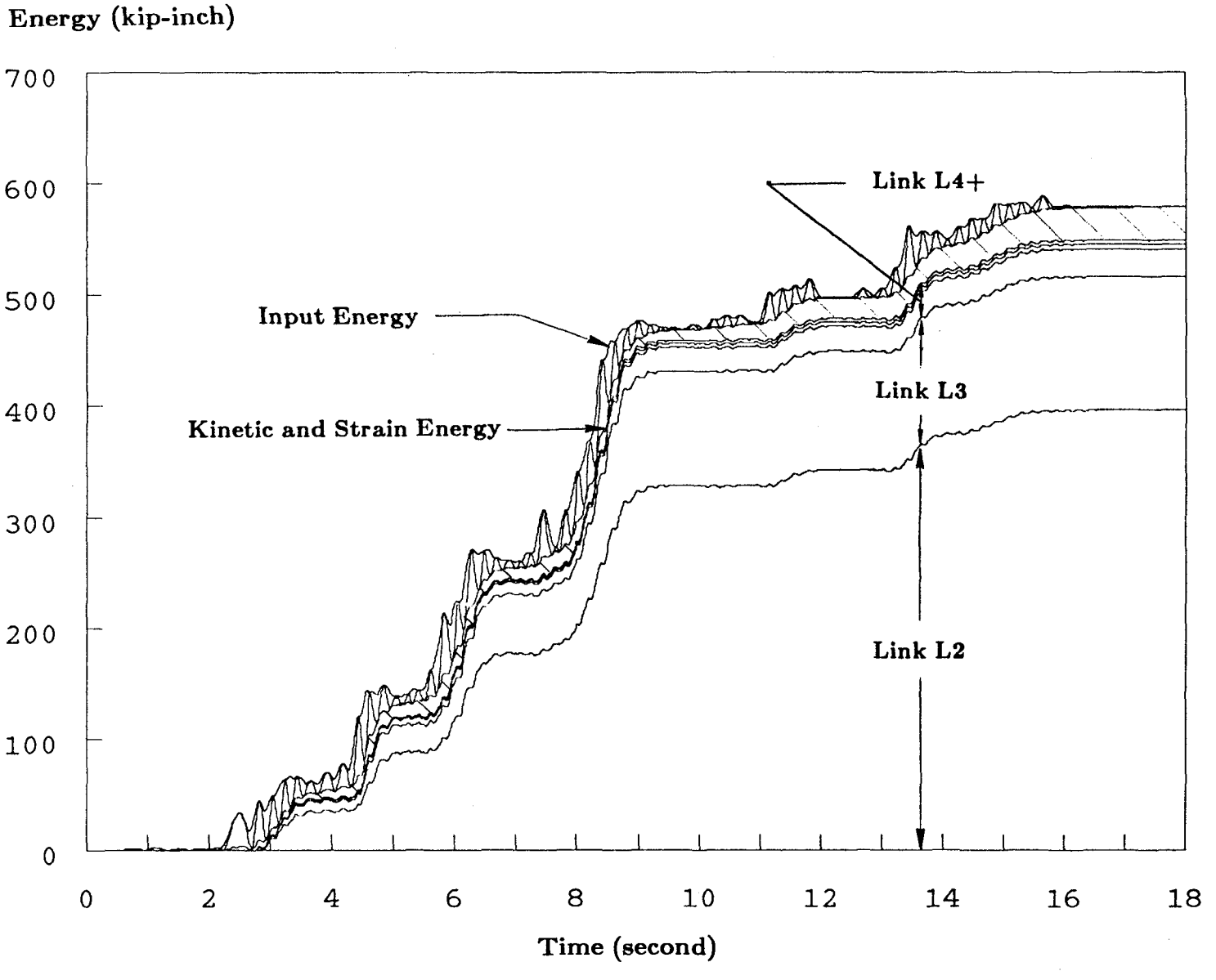


**FIGURE 8.70 TAFT-66 ENERGY TIME HISTORY**

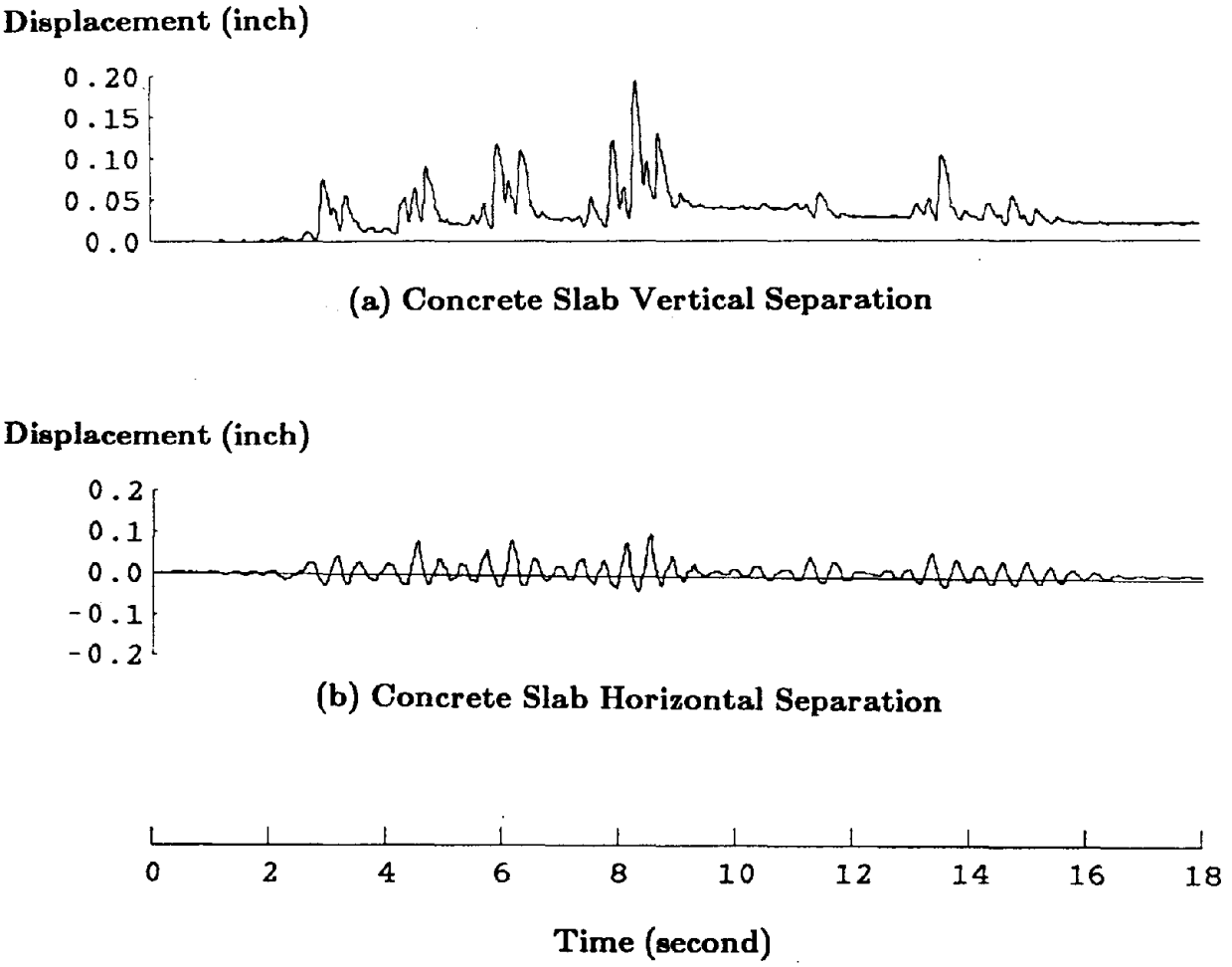


**FIGURE 8.71 TAFT-66 L2 COMPOSITE SLAB SEPARATION TIME HISTORY**

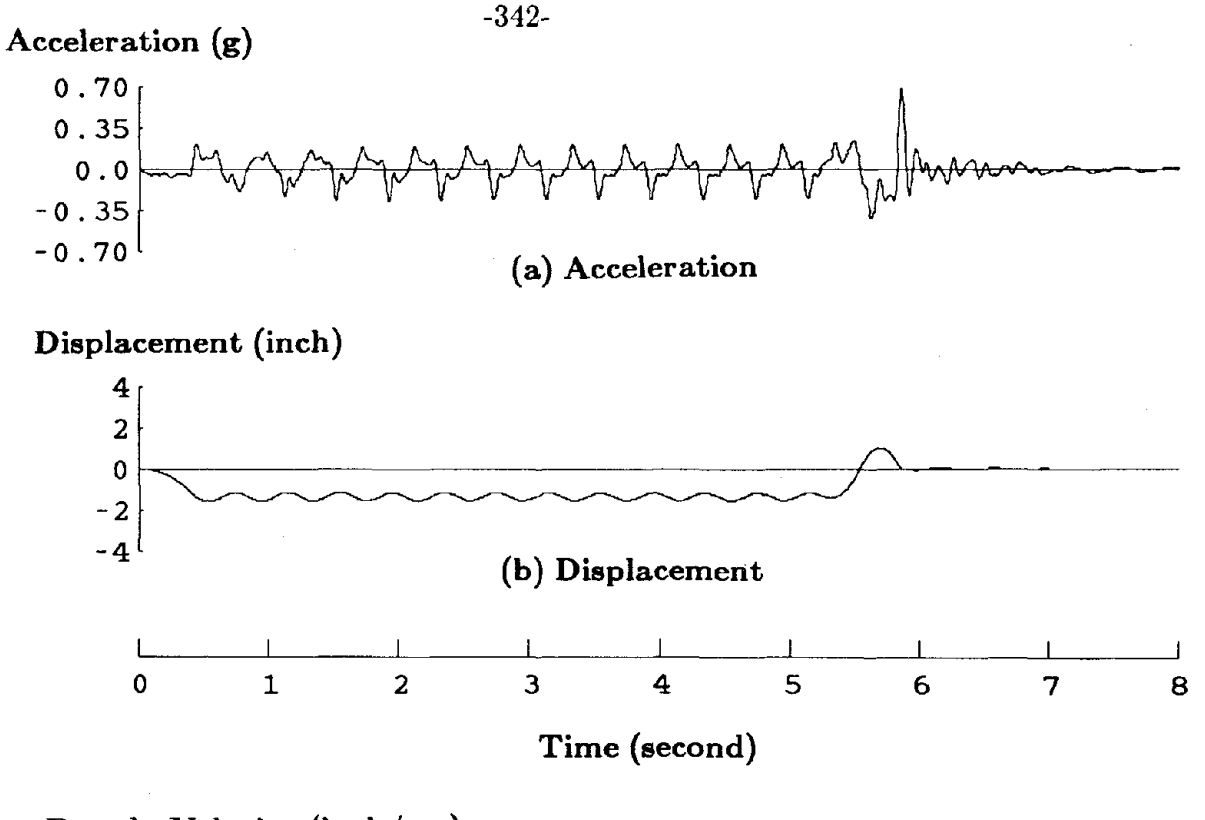


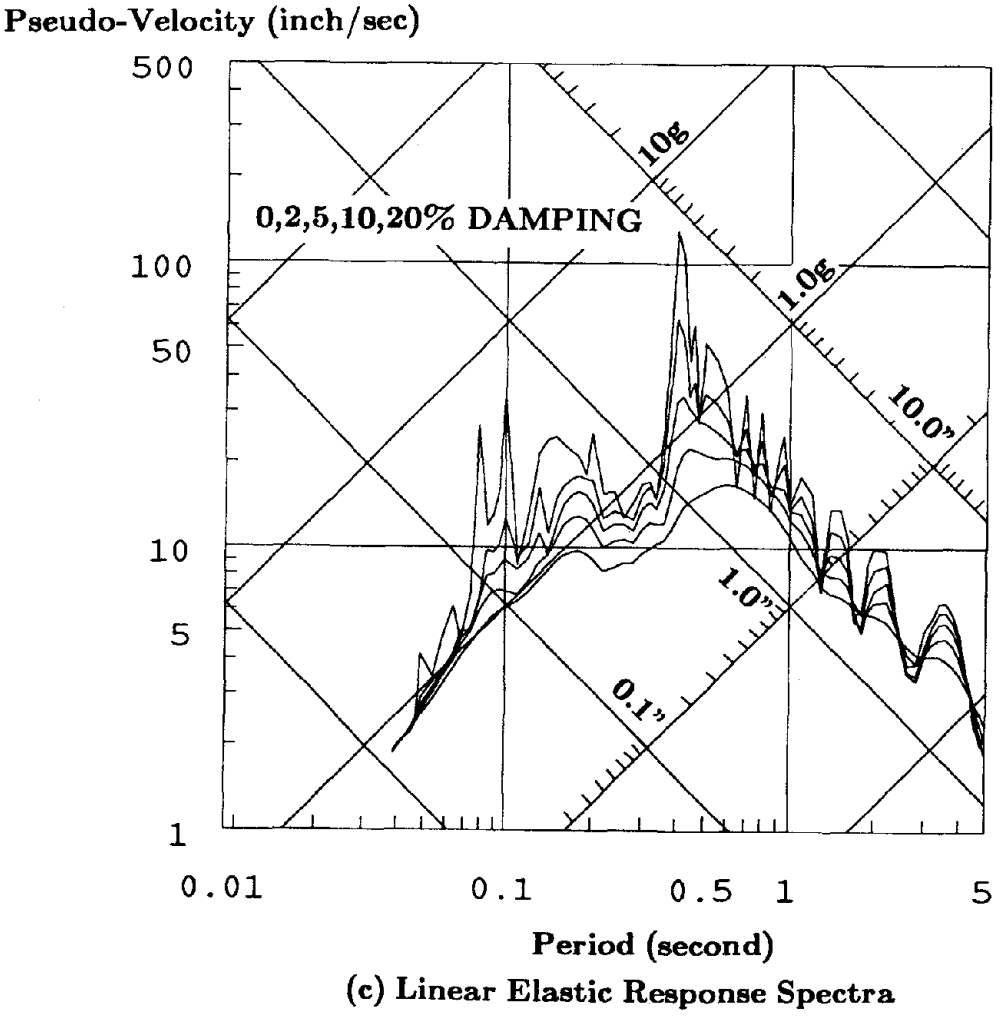


**FIGURE 8.72 SINE-70 MEASURED TABLE MOTION**

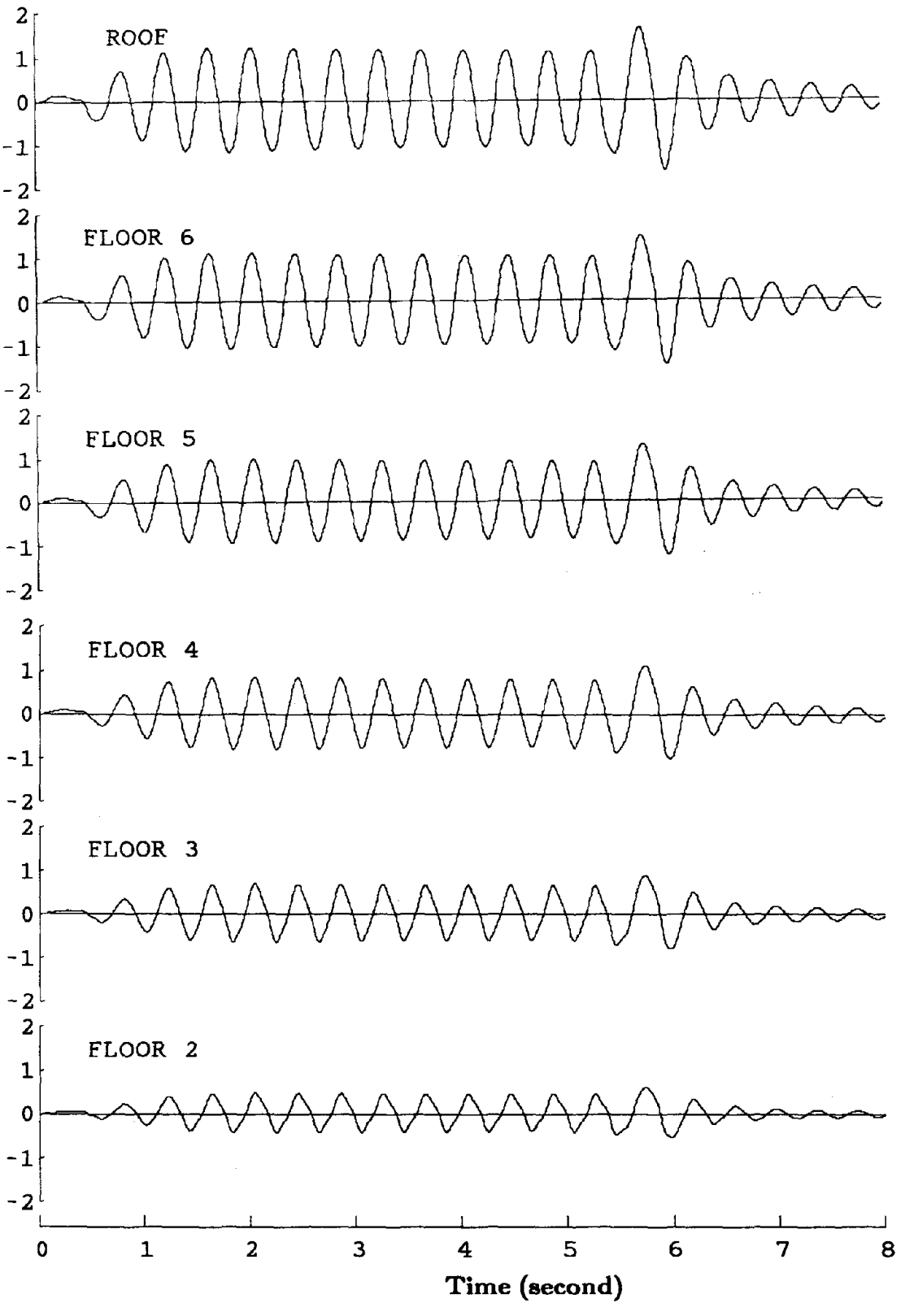


**FIGURE 8.73 SINE-70 LATERAL DISPLACEMENT TIME HISTORY**

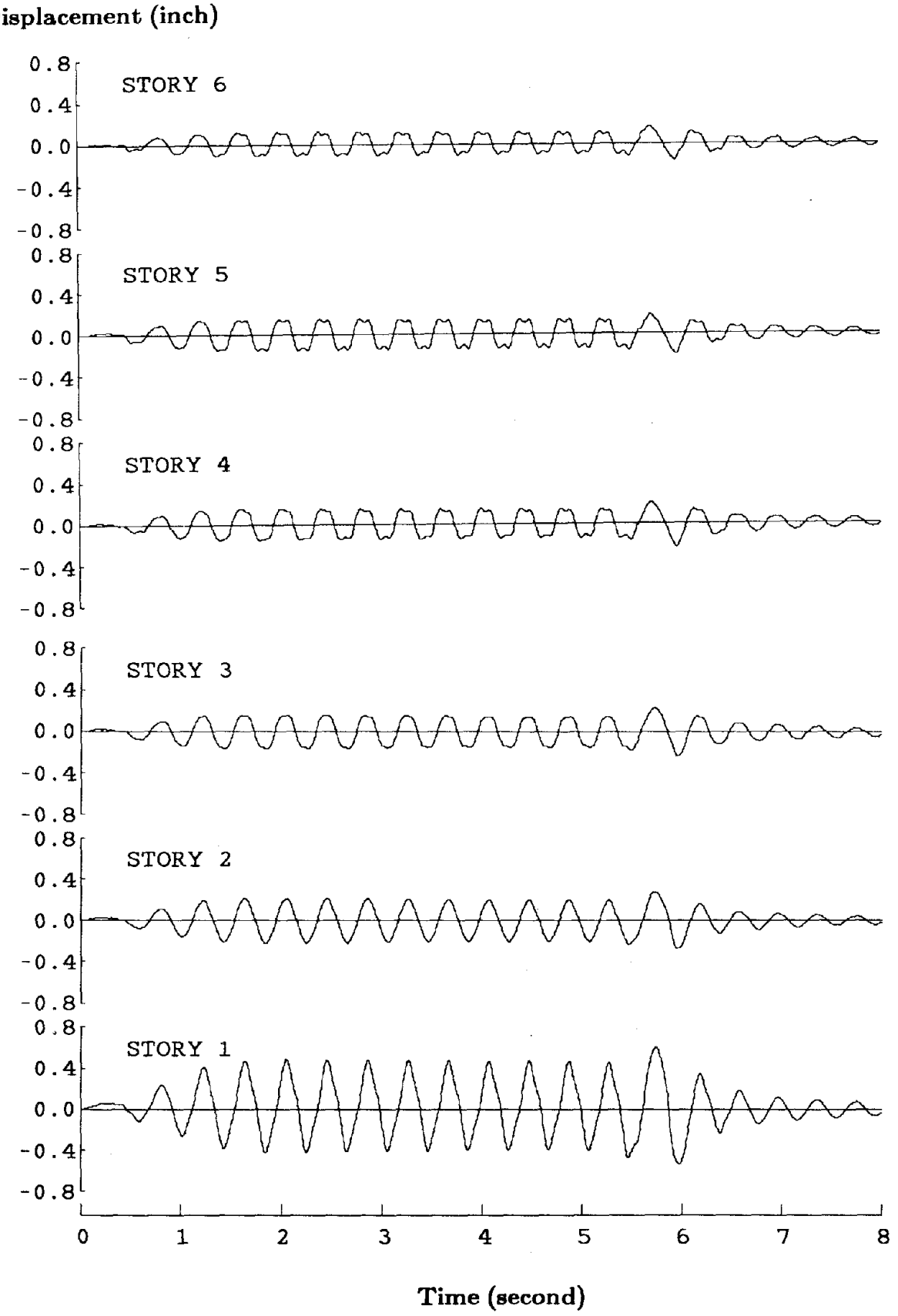


**FIGURE 8.74 SINE-70 INTER-STORY DRIFT TIME HISTORY**

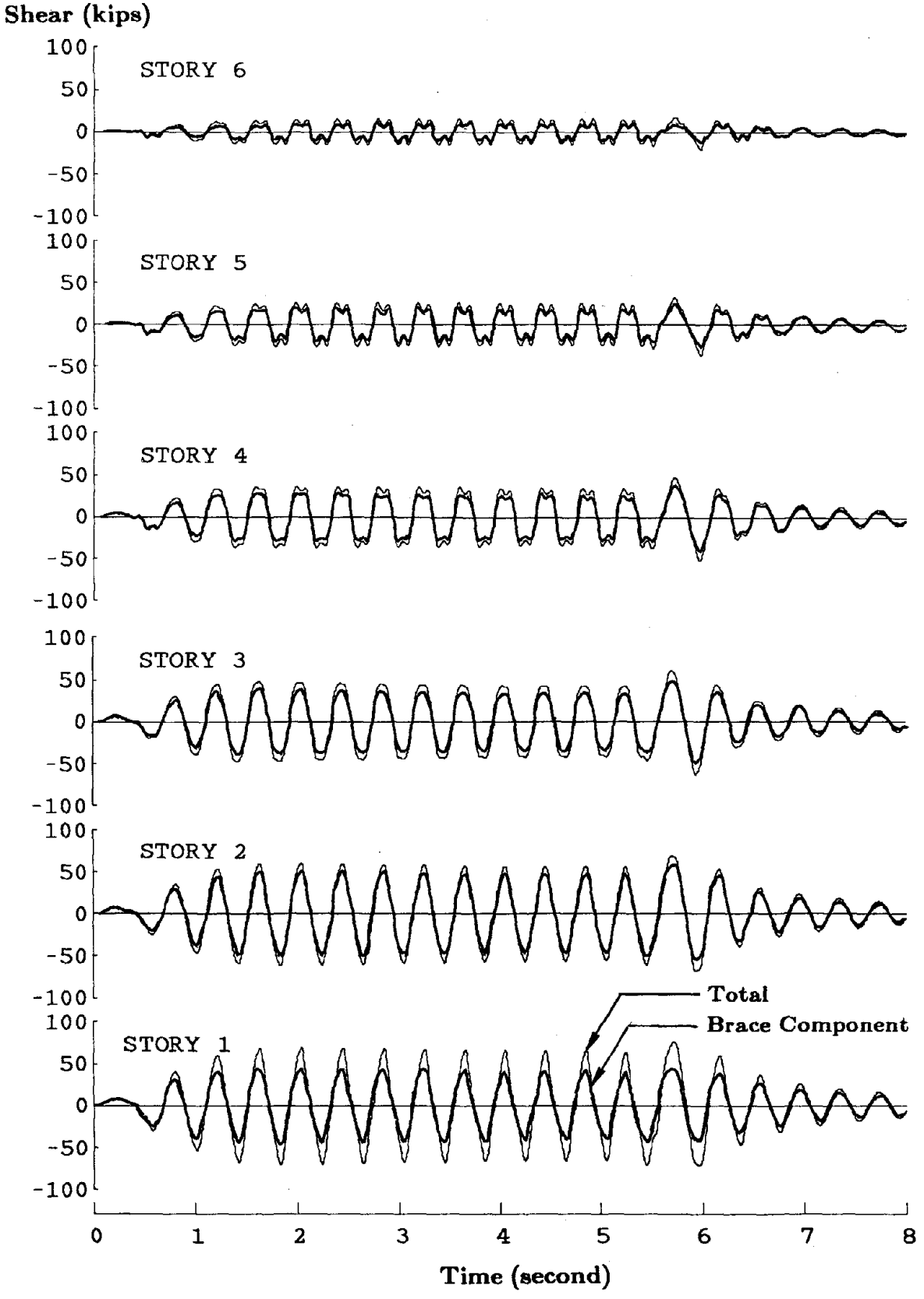


**FIGURE 8.75 SINE-70 STORY SHEAR TIME HISTORY**

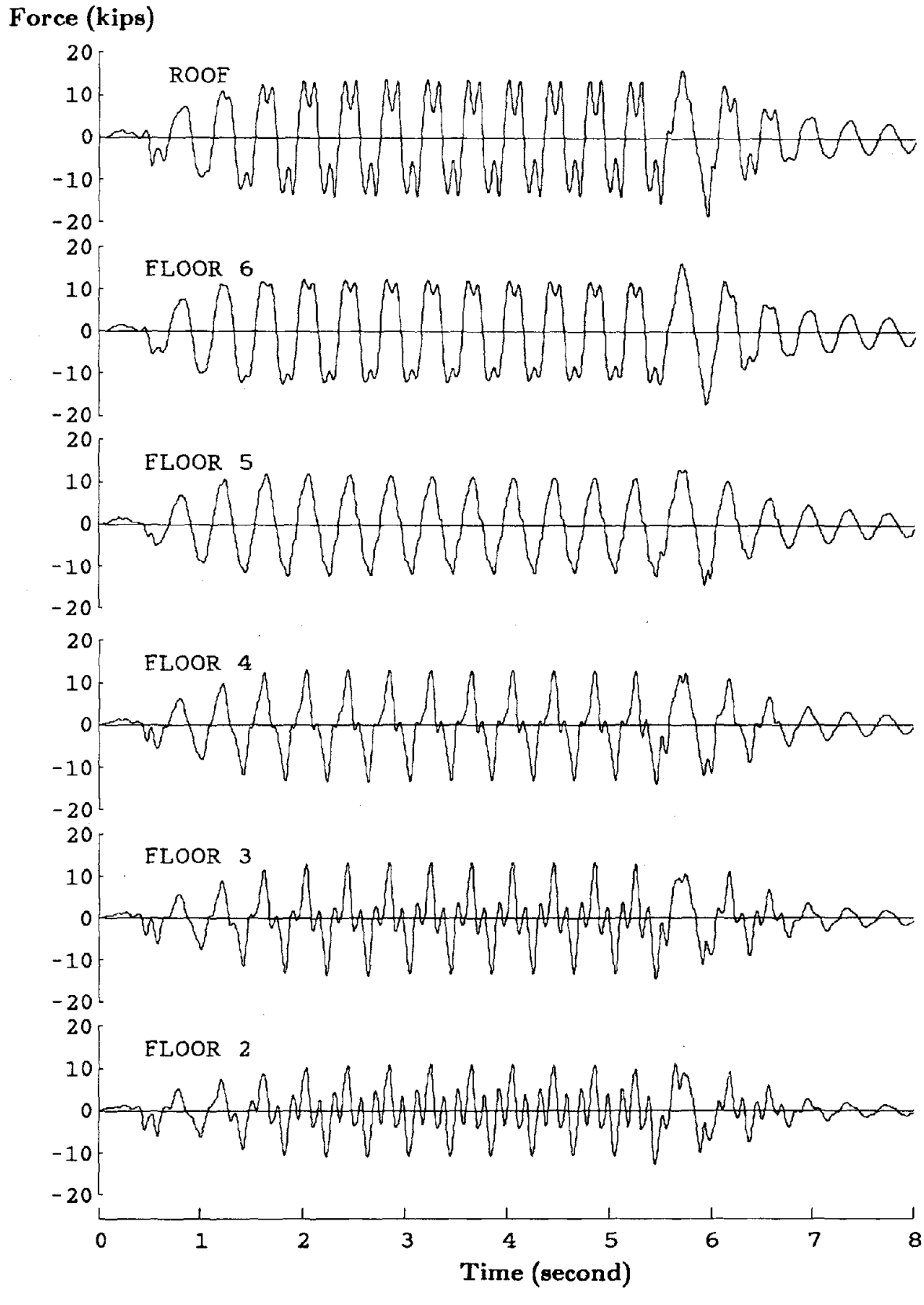


**FIGURE 8.76 SINE-70 INERTIA FORCE TIME HISTORY**

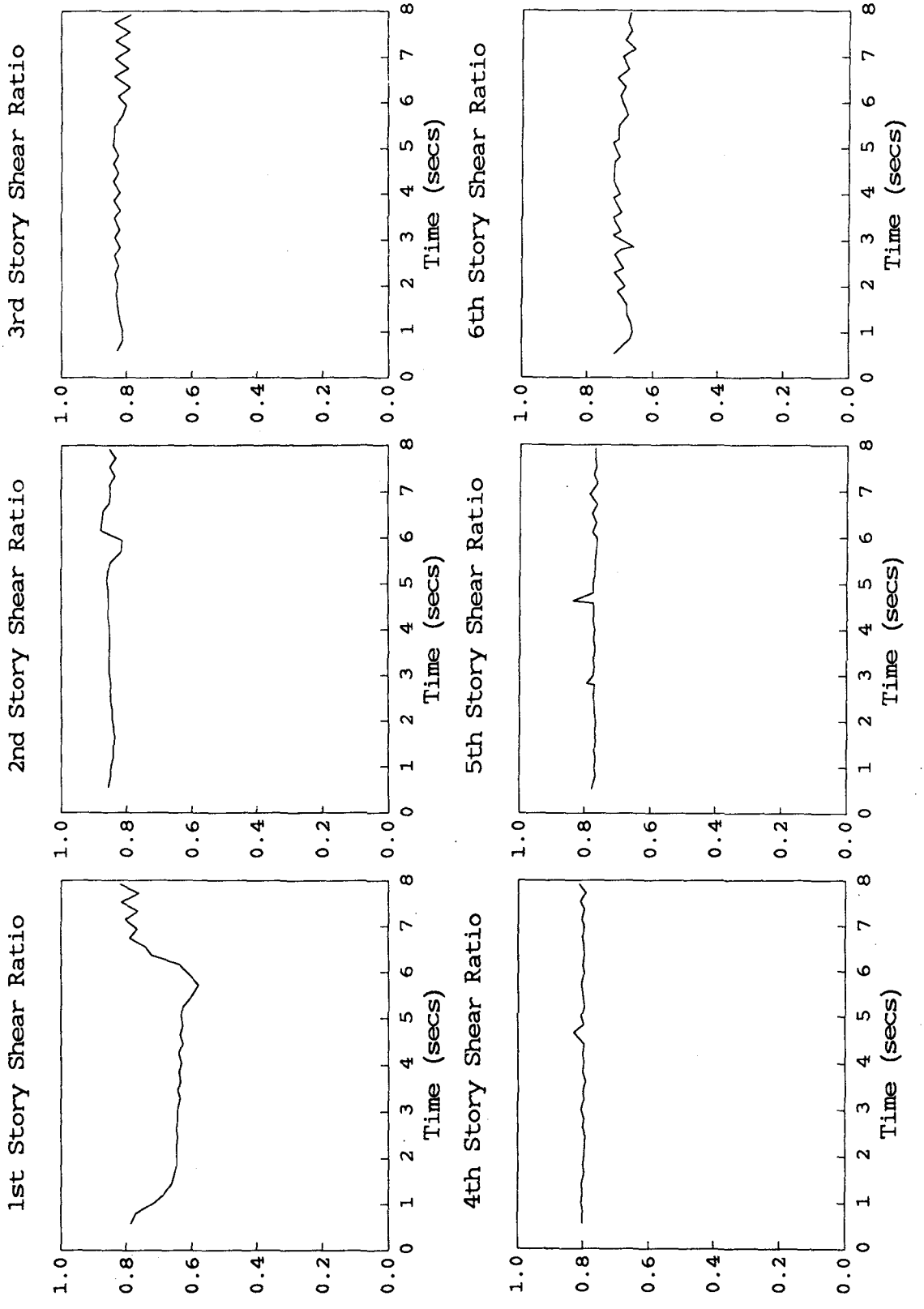


**FIGURE 8.77 SINE-70 STORY SHEAR RATIO**

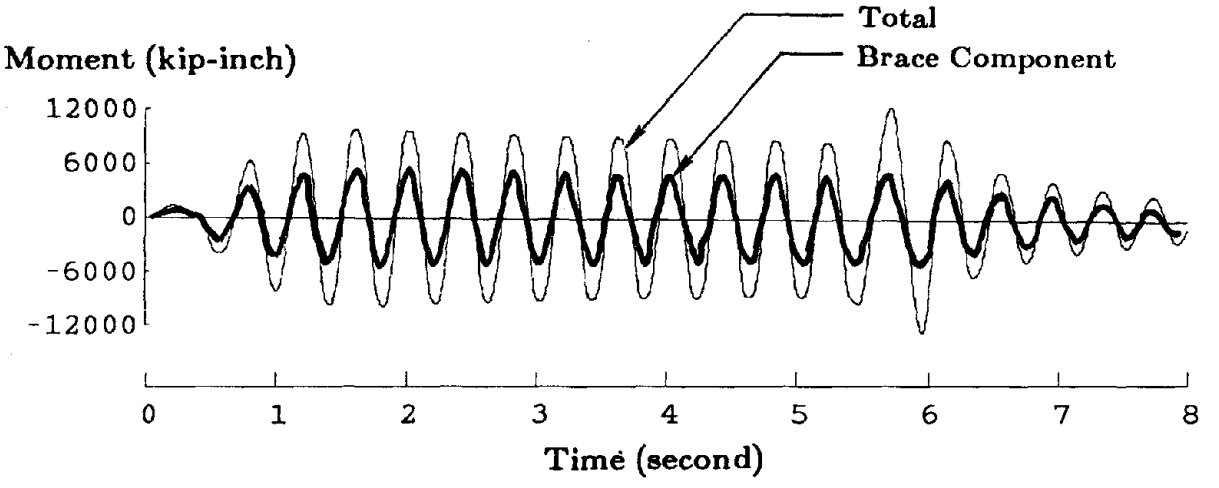


**FIGURE 8.78 SINE-70 BASE OVERTURNING MOMENT TIME HISTORY**

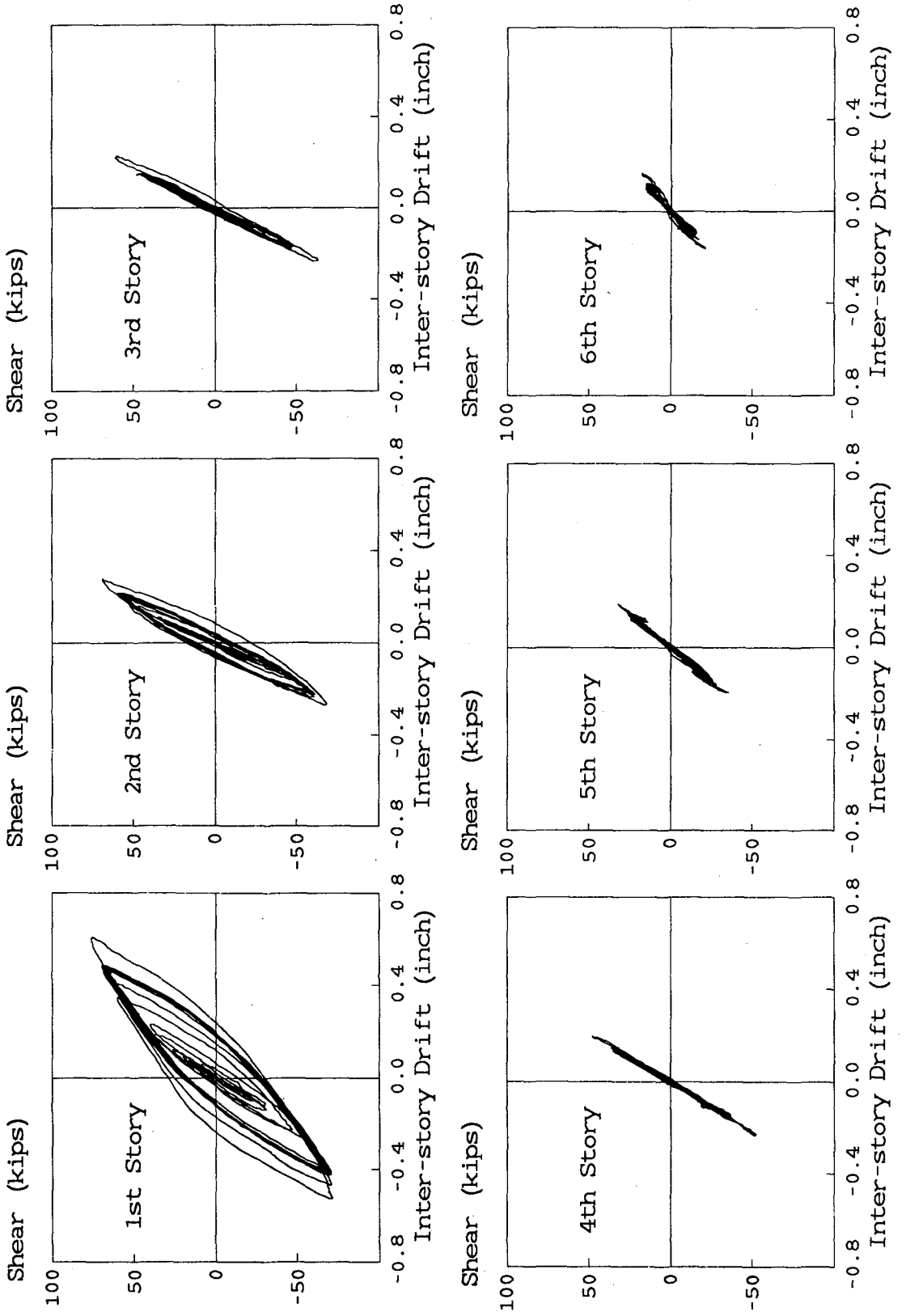


**FIGURE 8.79 SINE-70 TOTAL STORY SHEAR AND INTER-STORY DRIFT**

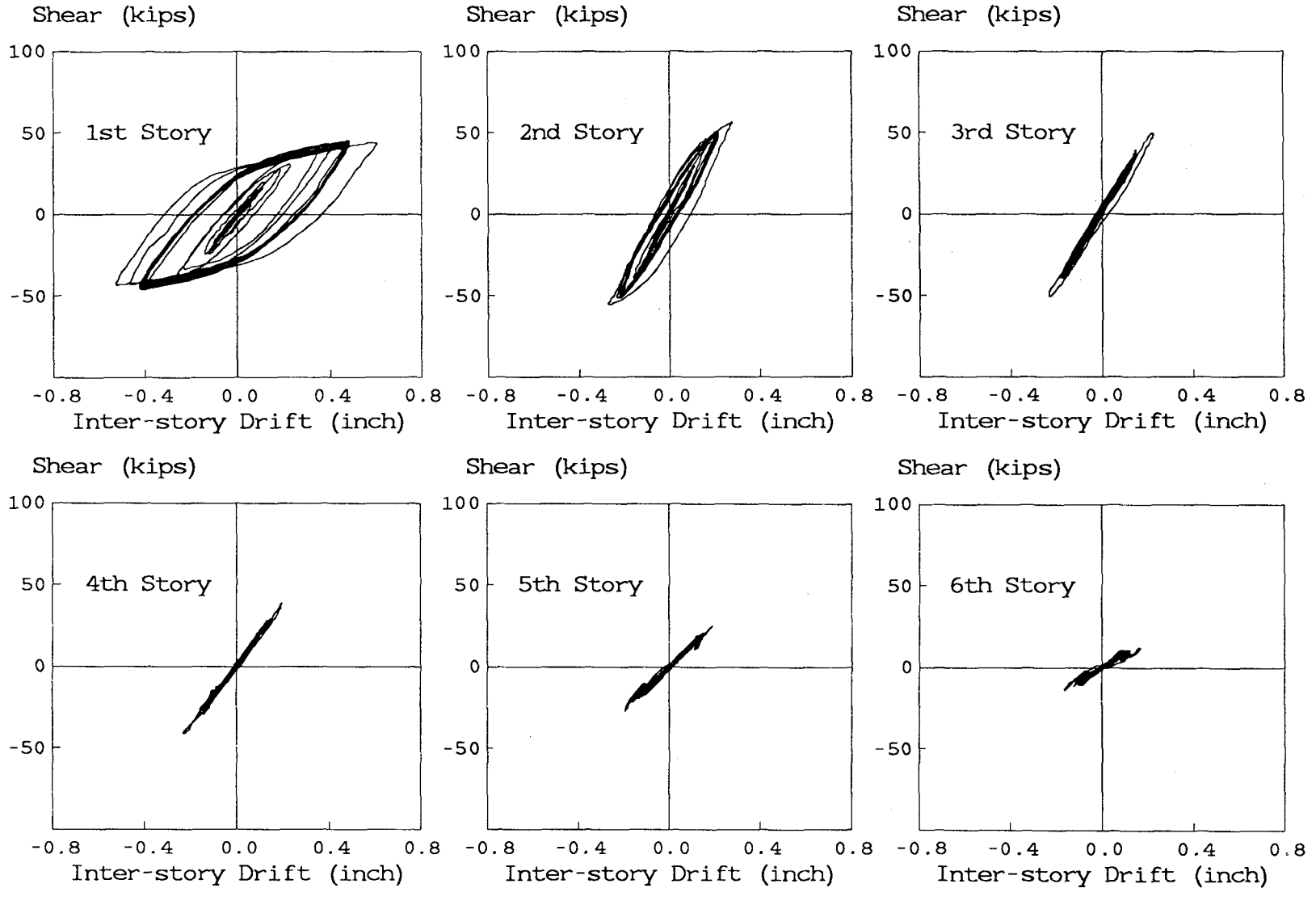


**FIGURE 8.80 SINE-70 BRACE STORY SHEAR AND INTER-STORY DRIFT**

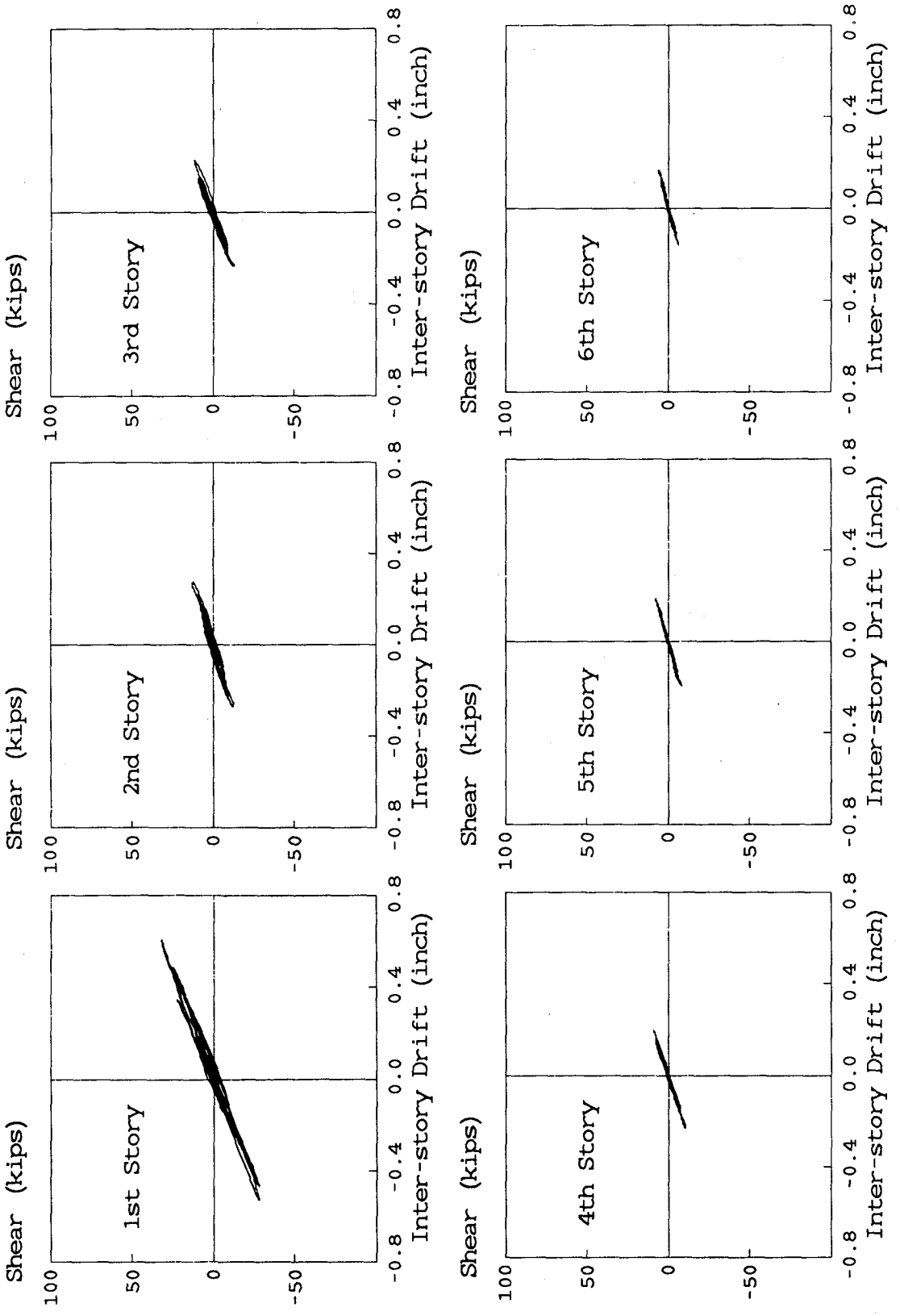


**FIGURE 8.81 SINE-70 DMRSF STORY SHEAR AND INTER-STORY DRIFT**

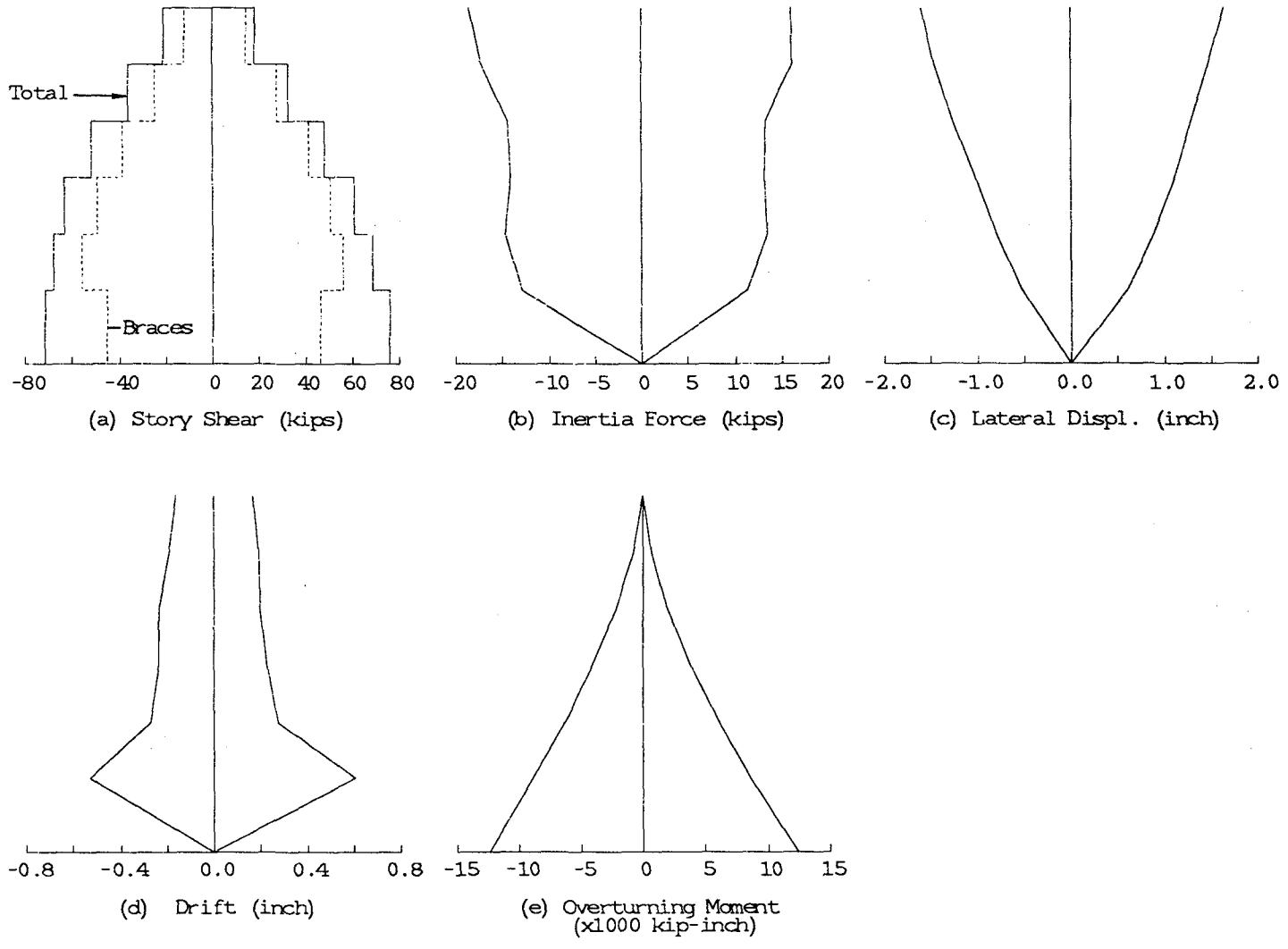


**FIGURE 8.82 SINE-70 RESPONSE ENVELOPES**

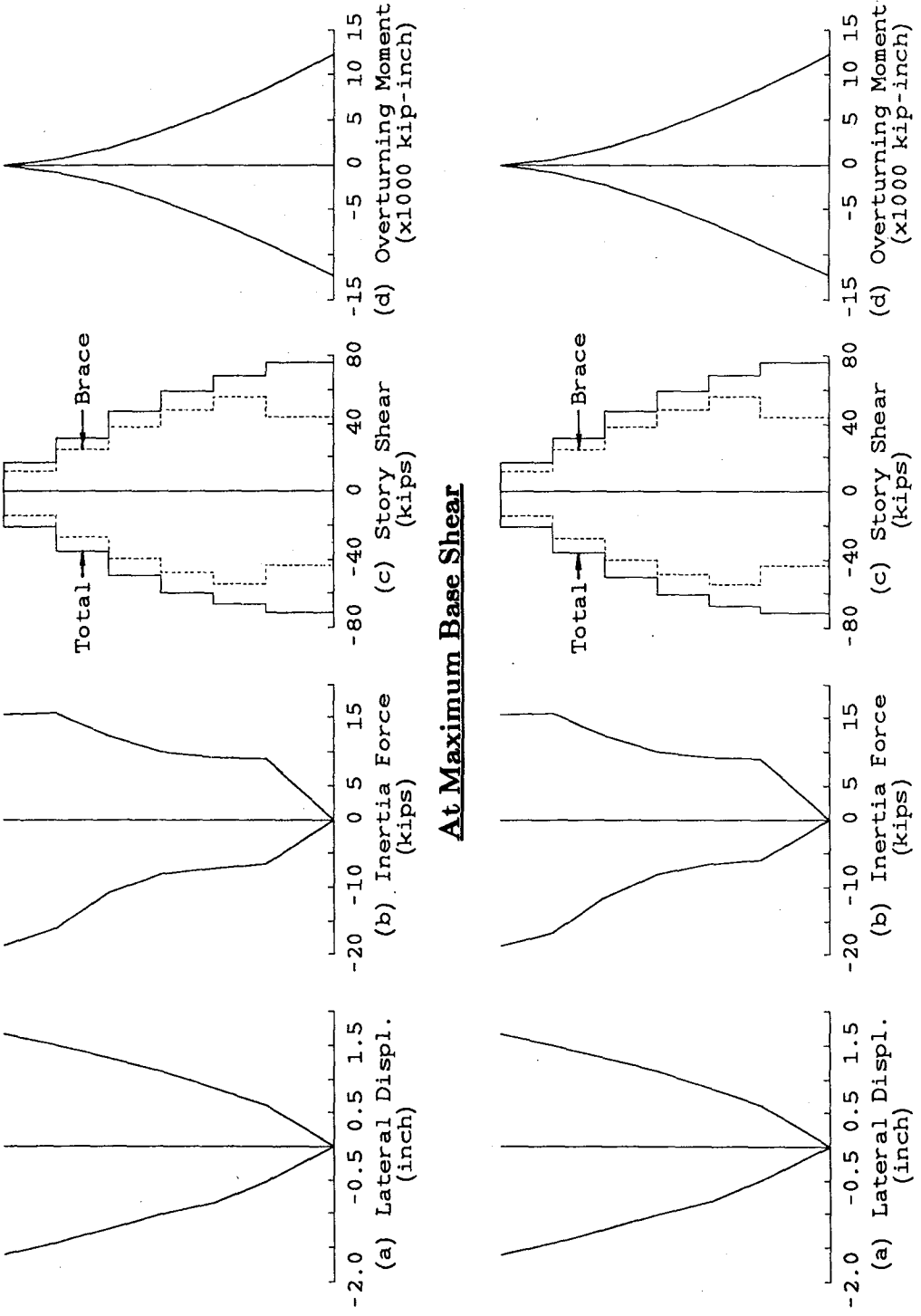


**FIGURE 8.83 SINE-70 RESPONSE PROFILES AT MAXIMUM RESPONSE**

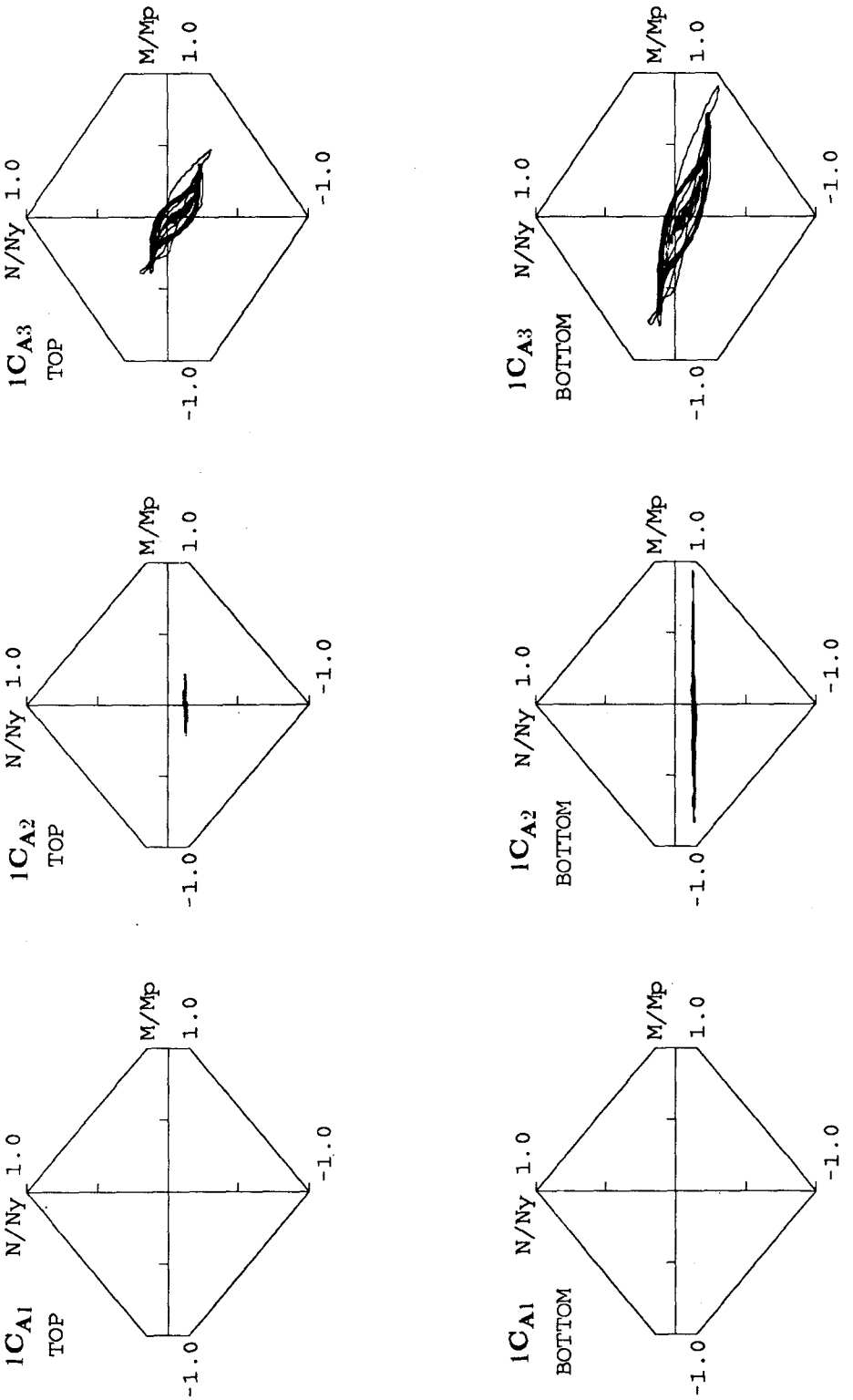


FIGURE 8.84 SINE-70 FIRST STORY COLUMN AXIAL FORCE AND END MOMENT INTERACTION CURVES (FRAME A)

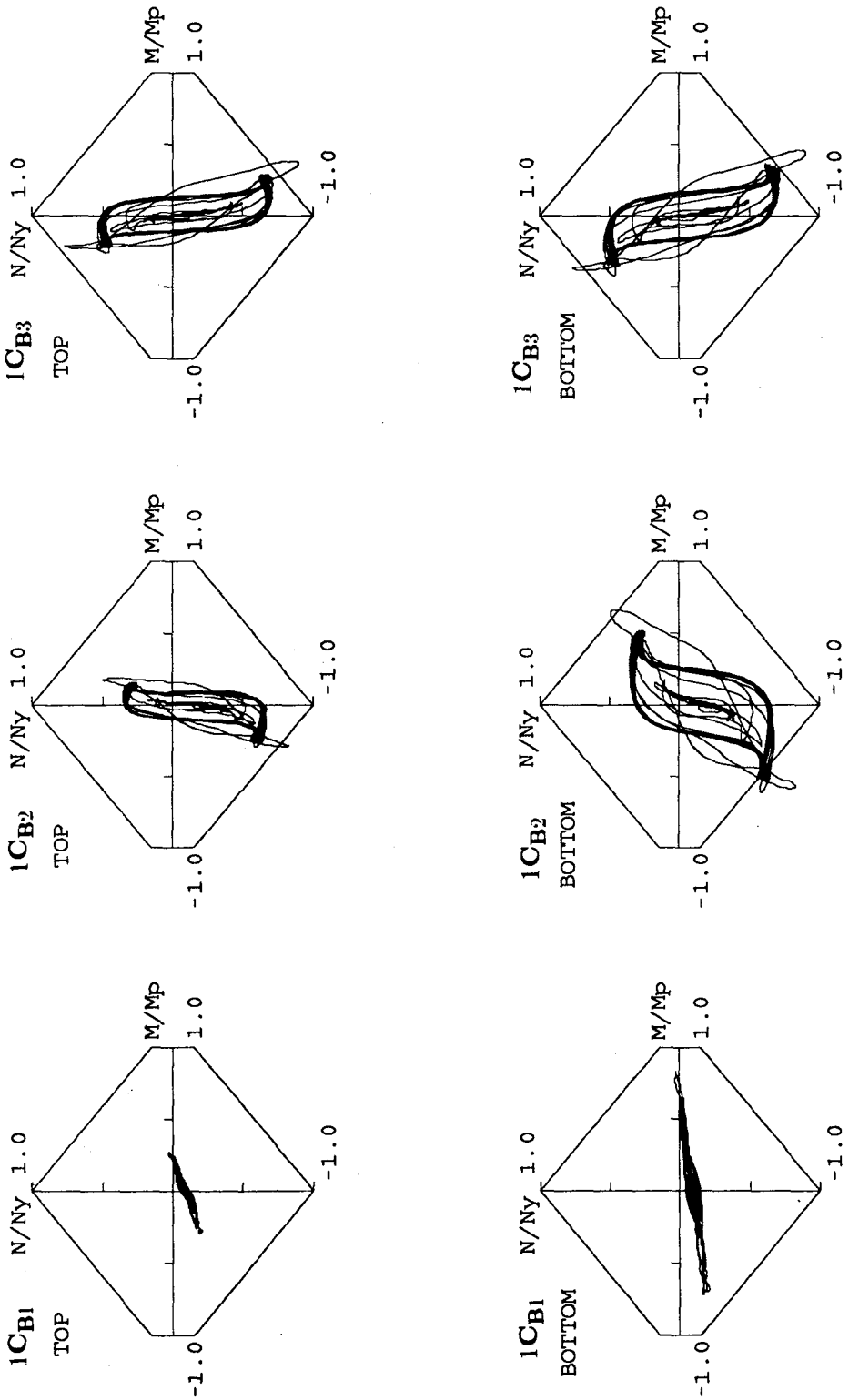


**FIGURE 8.85 SINE-70 FIRST STORY COLUMN AXIAL FORCE AND END MOMENT INTERACTION CURVES (FRAME B)**

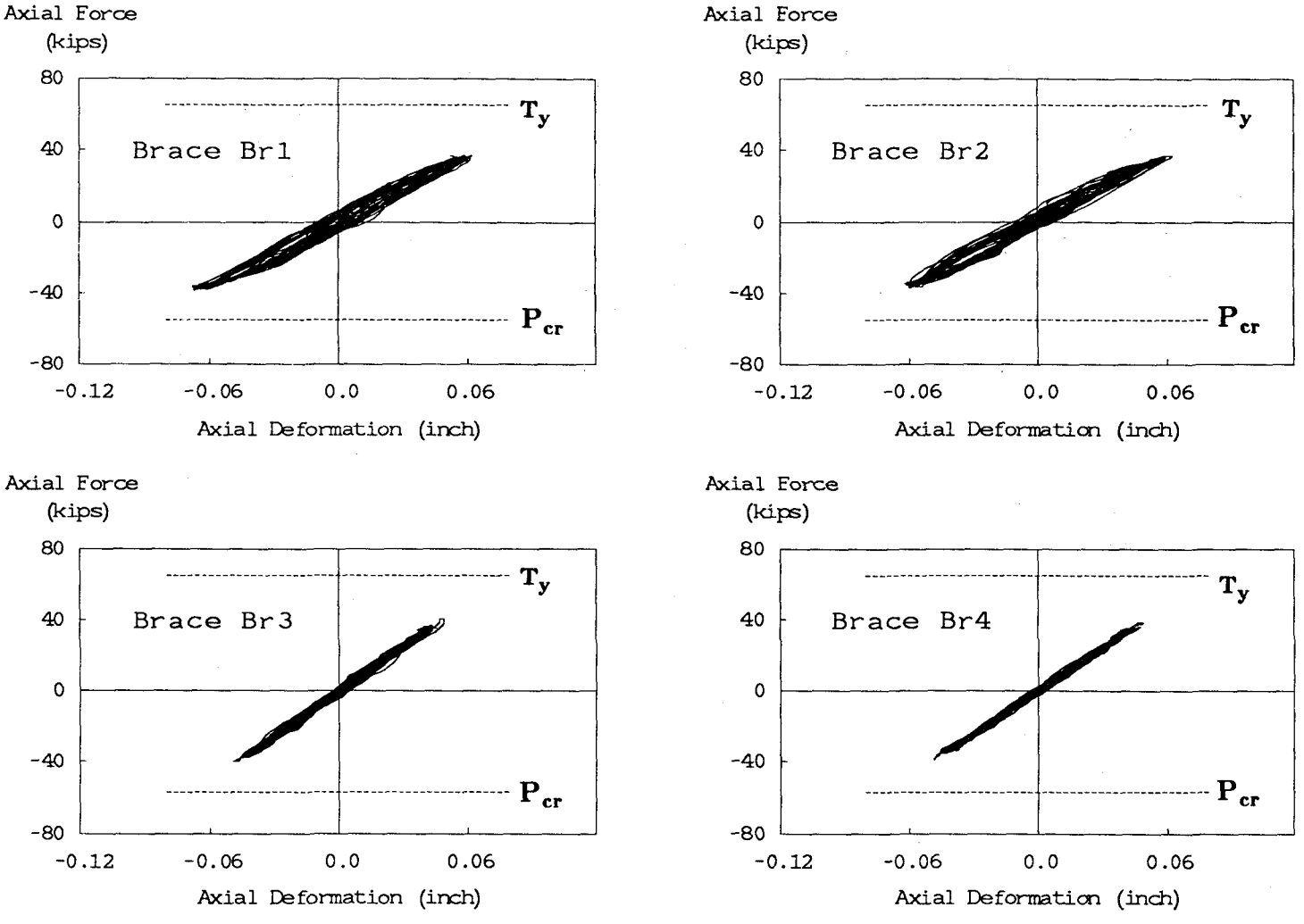


**FIGURE 8.86 SINE-70 BRACE AXIAL FORCE AND DEFORMATION RELATIONSHIP**

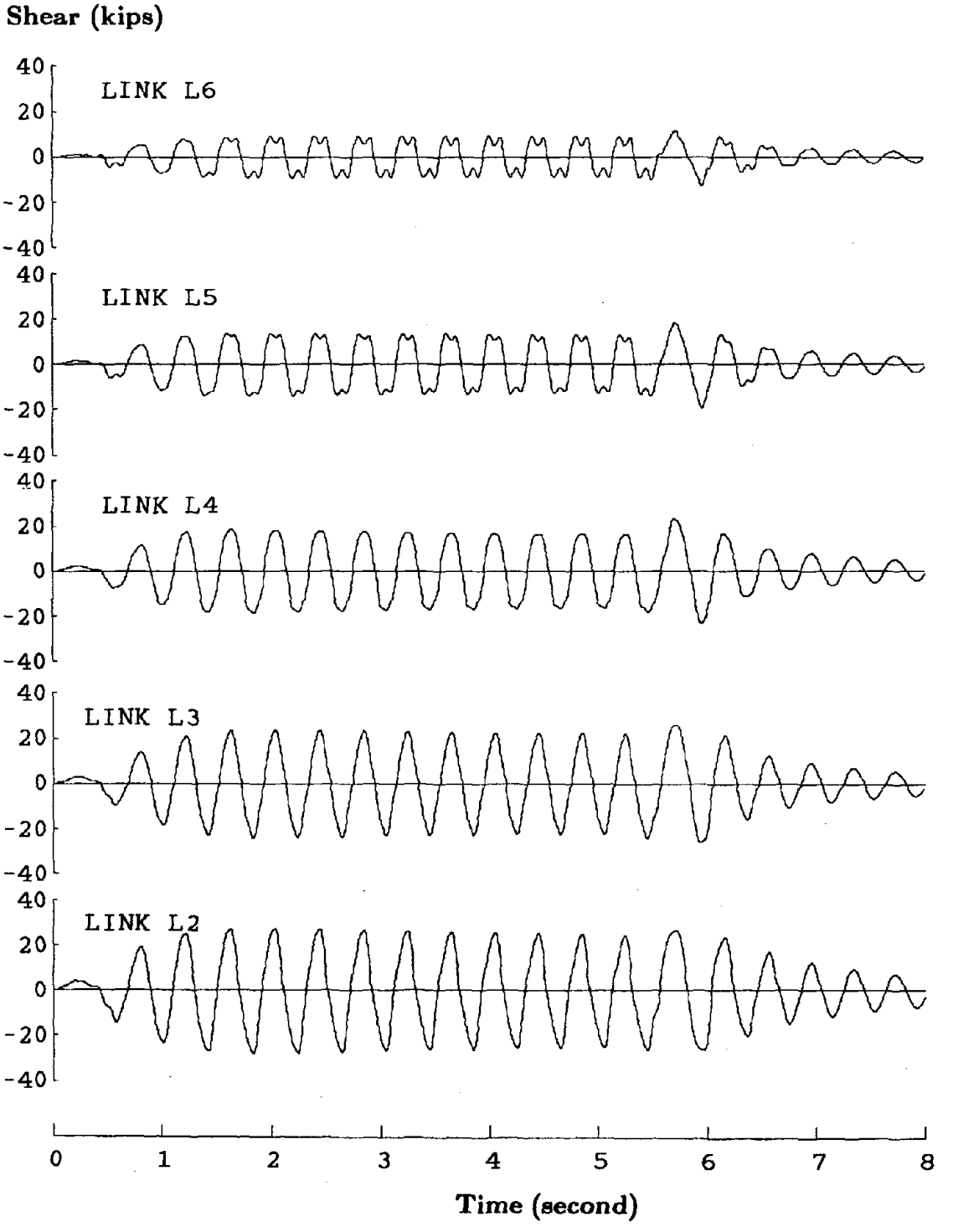


**FIGURE 8.87 SINE-70 LINK SHEAR FORCE TIME HISTORY**

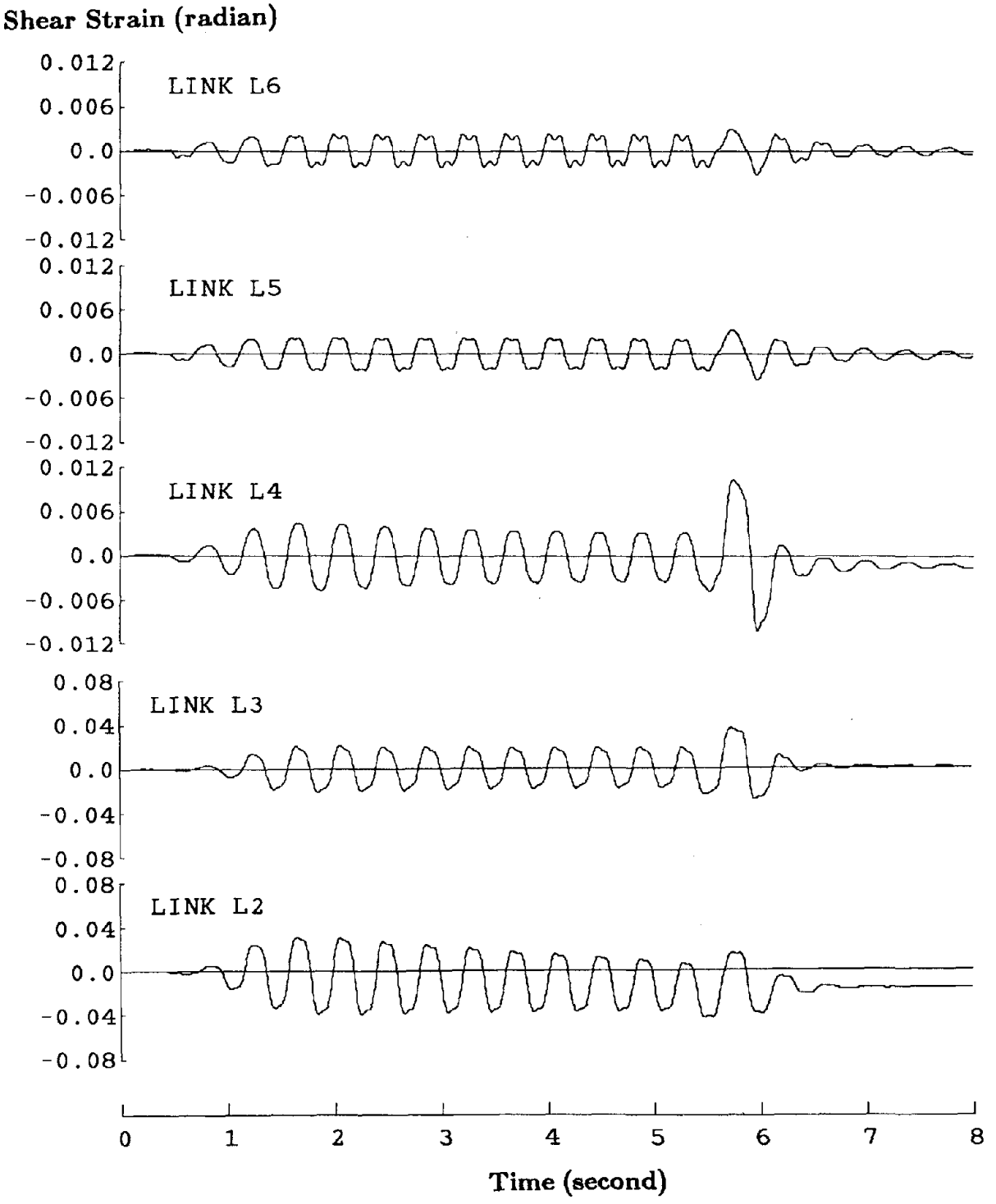


**FIGURE 8.88 SINE-70 LINK SHEAR STRAIN TIME HISTORY**

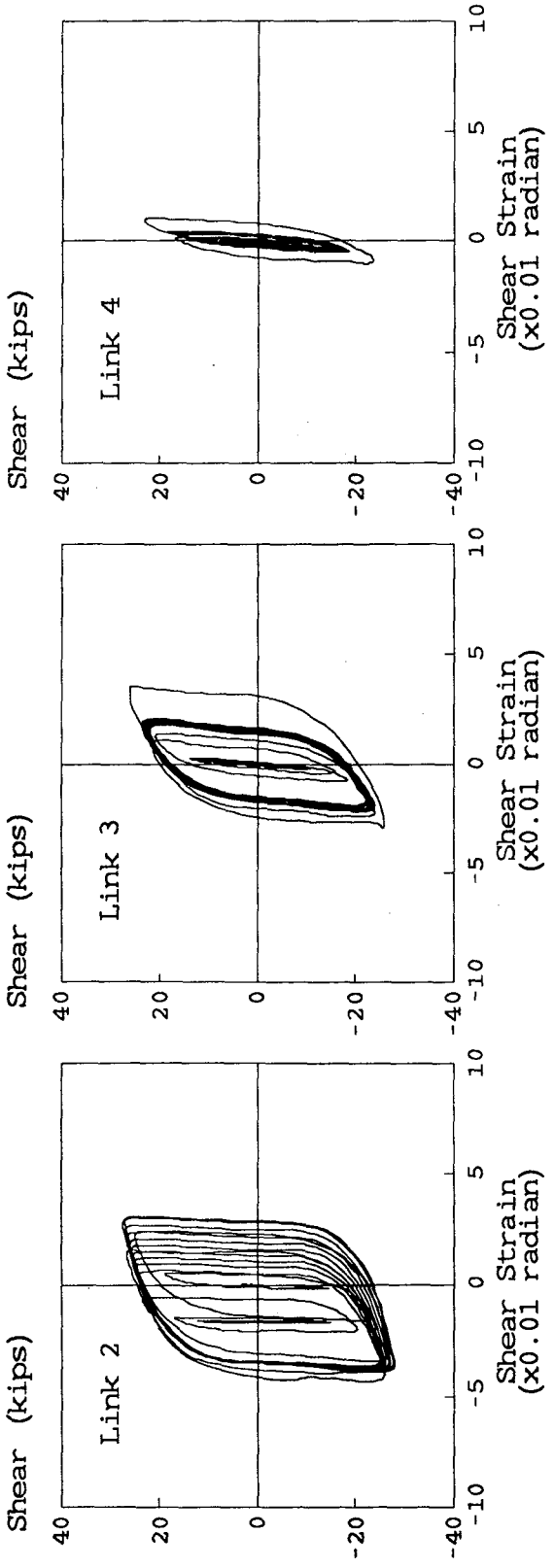


**FIGURE 8.89 SINE-70 LINK SHEAR FORCE AND SHEAR STRAIN RELATIONSHIPS**

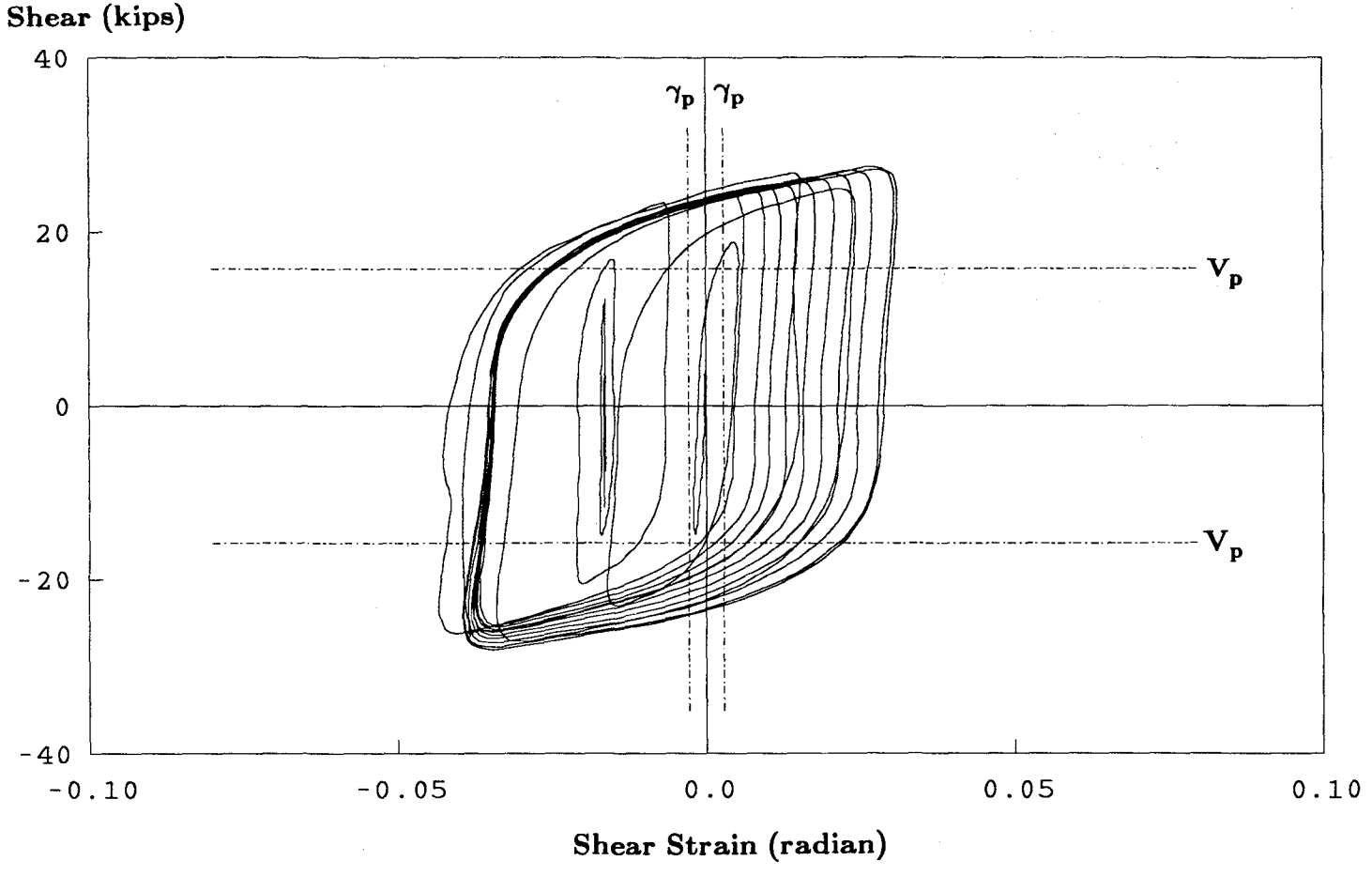


**FIGURE 8.90 SINE-70 LINK L2 SHEAR FORCE AND SHEAR STRAIN RELATIONSHIP**

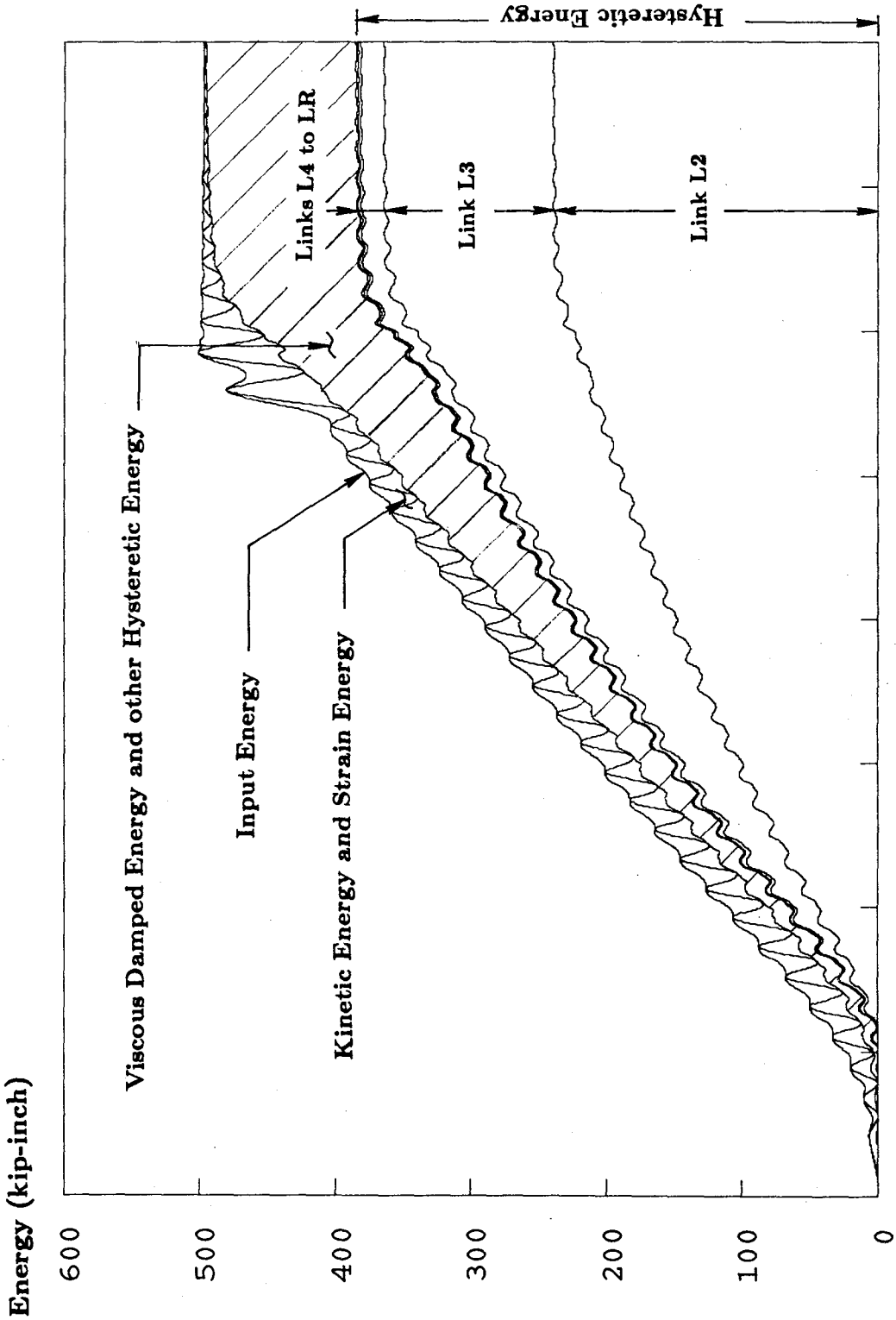


FIGURE 8.91 SINE-70 ENERGY TIME HISTORY

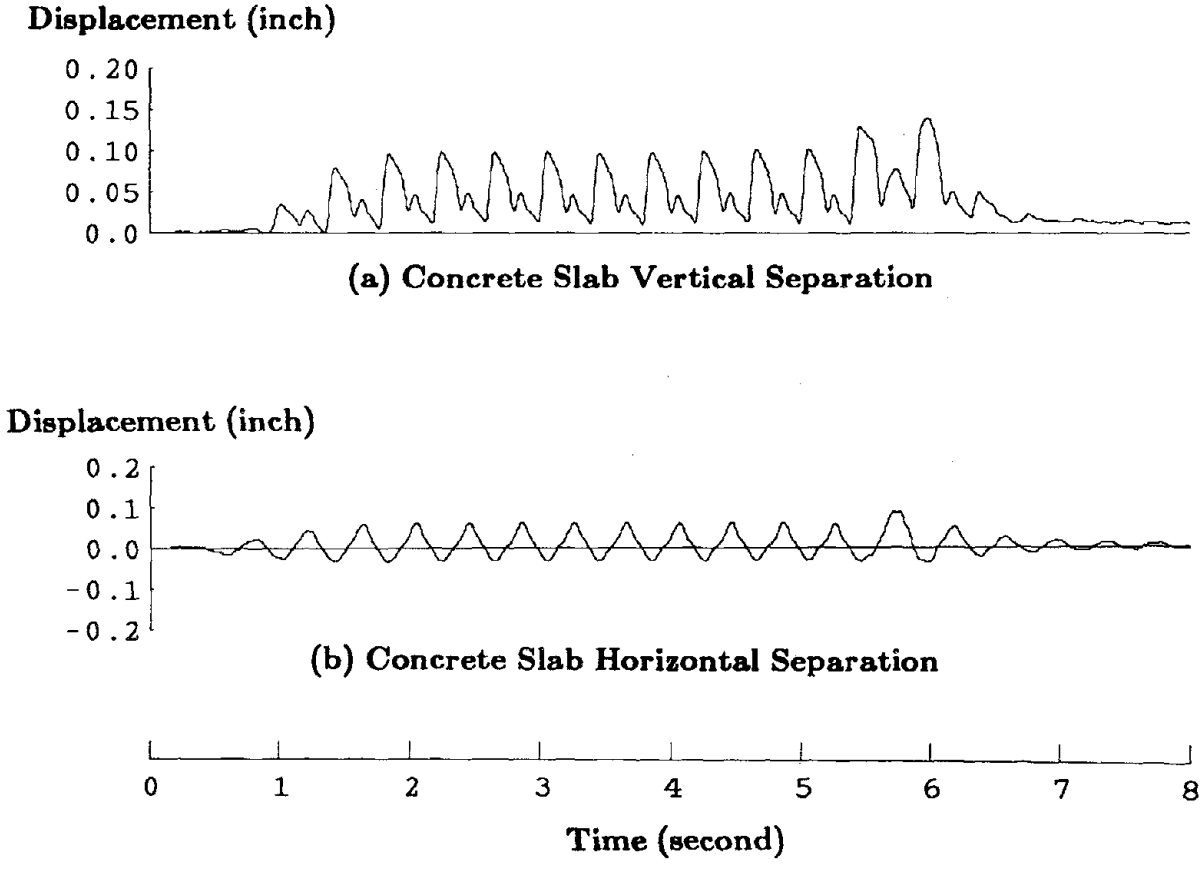


**FIGURE 8.92 SINE-70 L2 COMPOSITE SLAB SEPARATION TIME HISTORY**

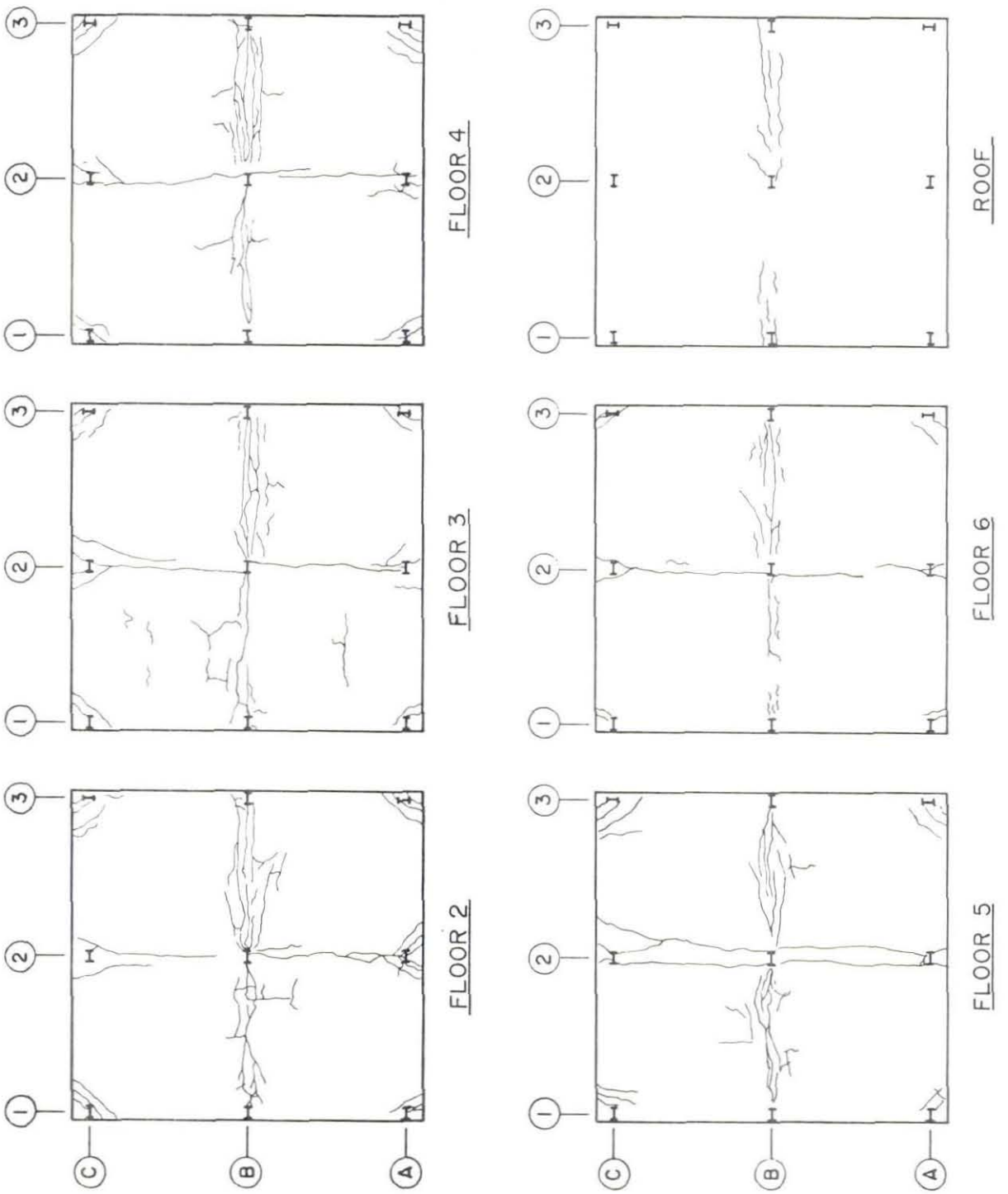


**FIGURE 8.93 CONCRETE SLAB CRACKING PATTERN - POST SINE-70 TEST**

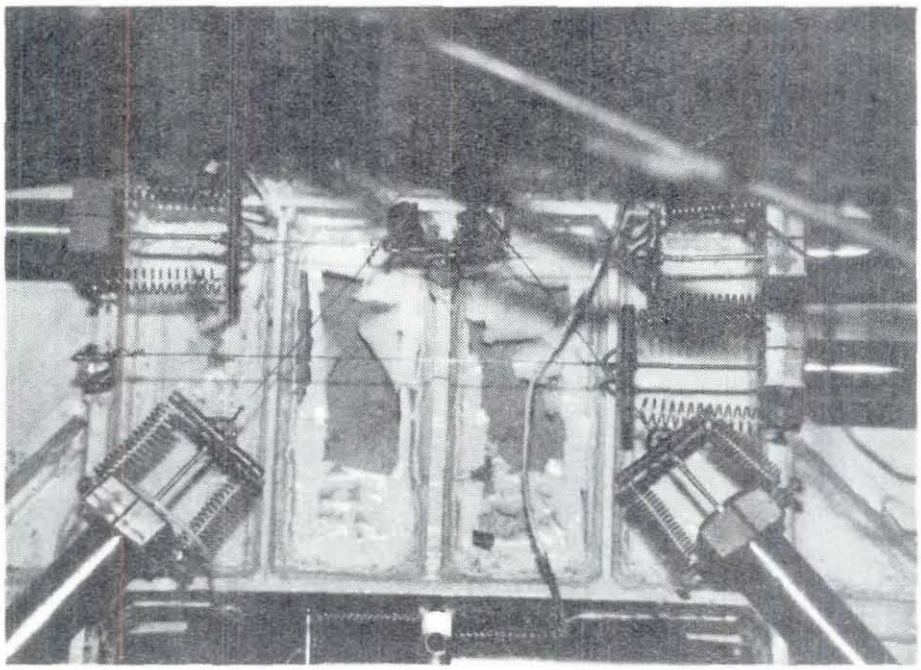

FIGURE 8.94 L2 SHEAR LINK - POST TAFT-57 TEST

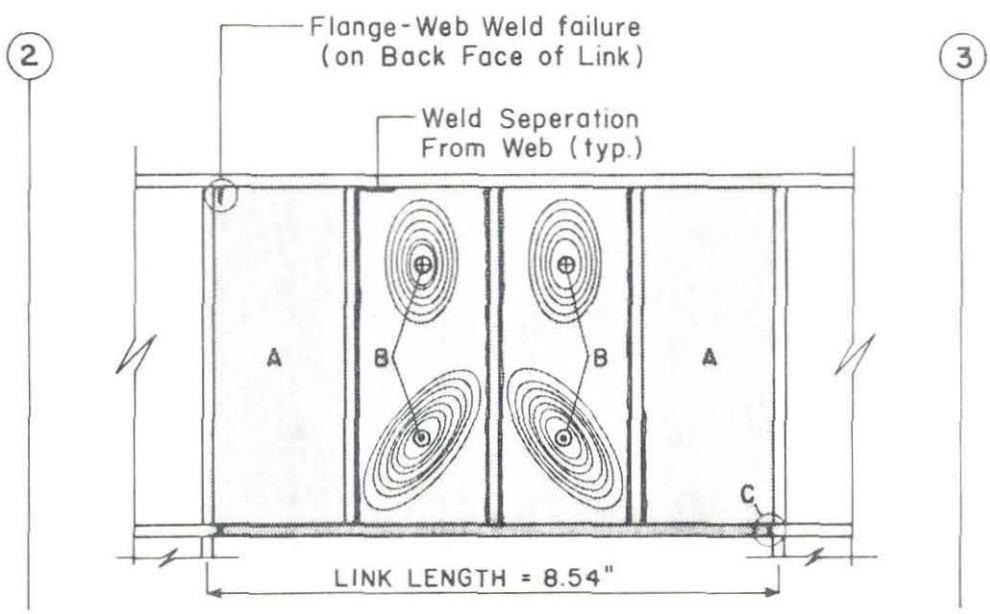


A – *Minor Web Buckling in End Panels.*

B – Symmetric & Anti-Symmetric Web Buckles.

C – *Weld & Flange Fracture: Propagation* Over Width of Flange.

FIGURE 8.95 L2 SHEAR LINK WEB DEFORMATION FIELD

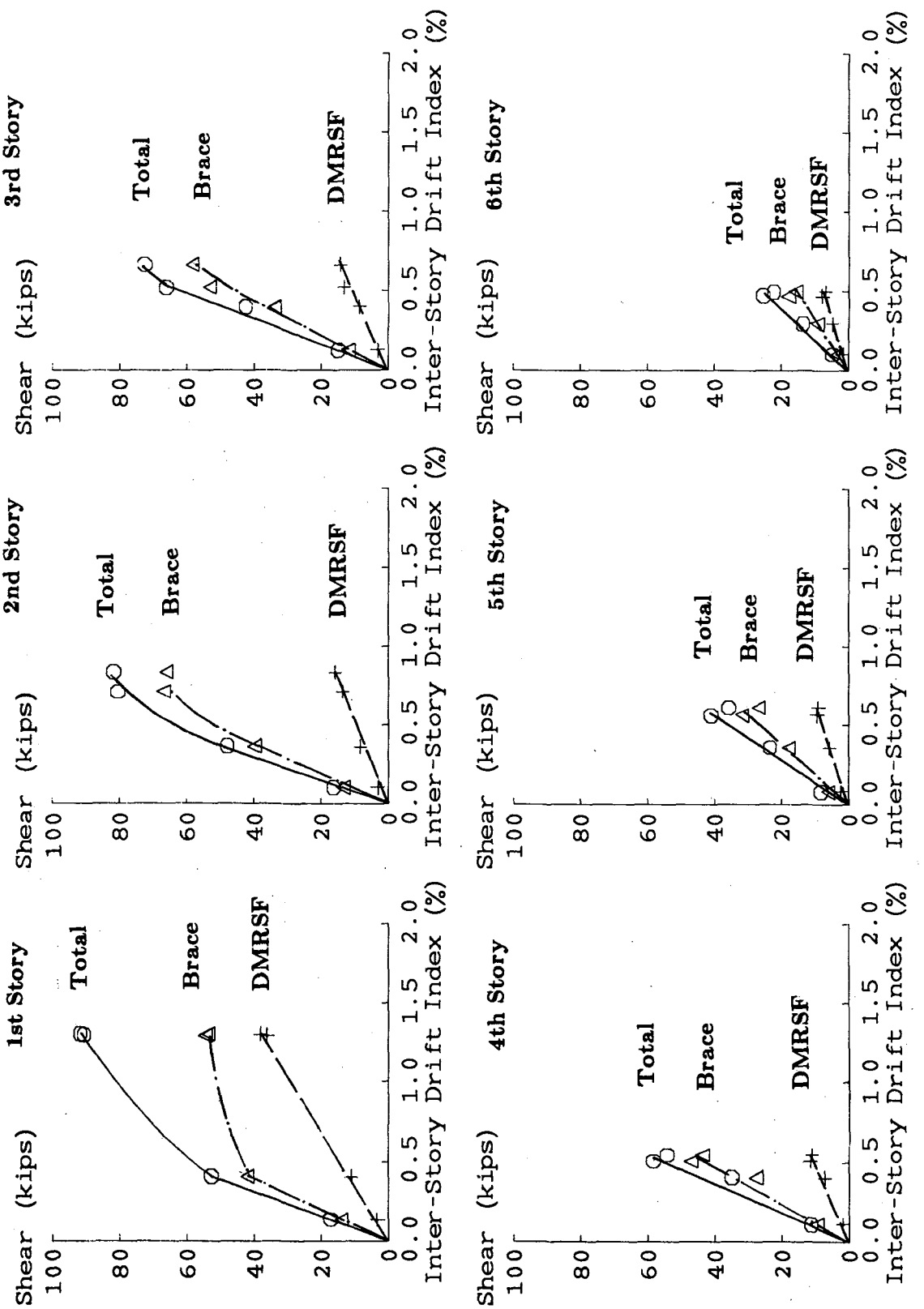


**FIGURE 9.1 STORY SHEAR AND INTER-STORY DRIFT ENVELOPES**

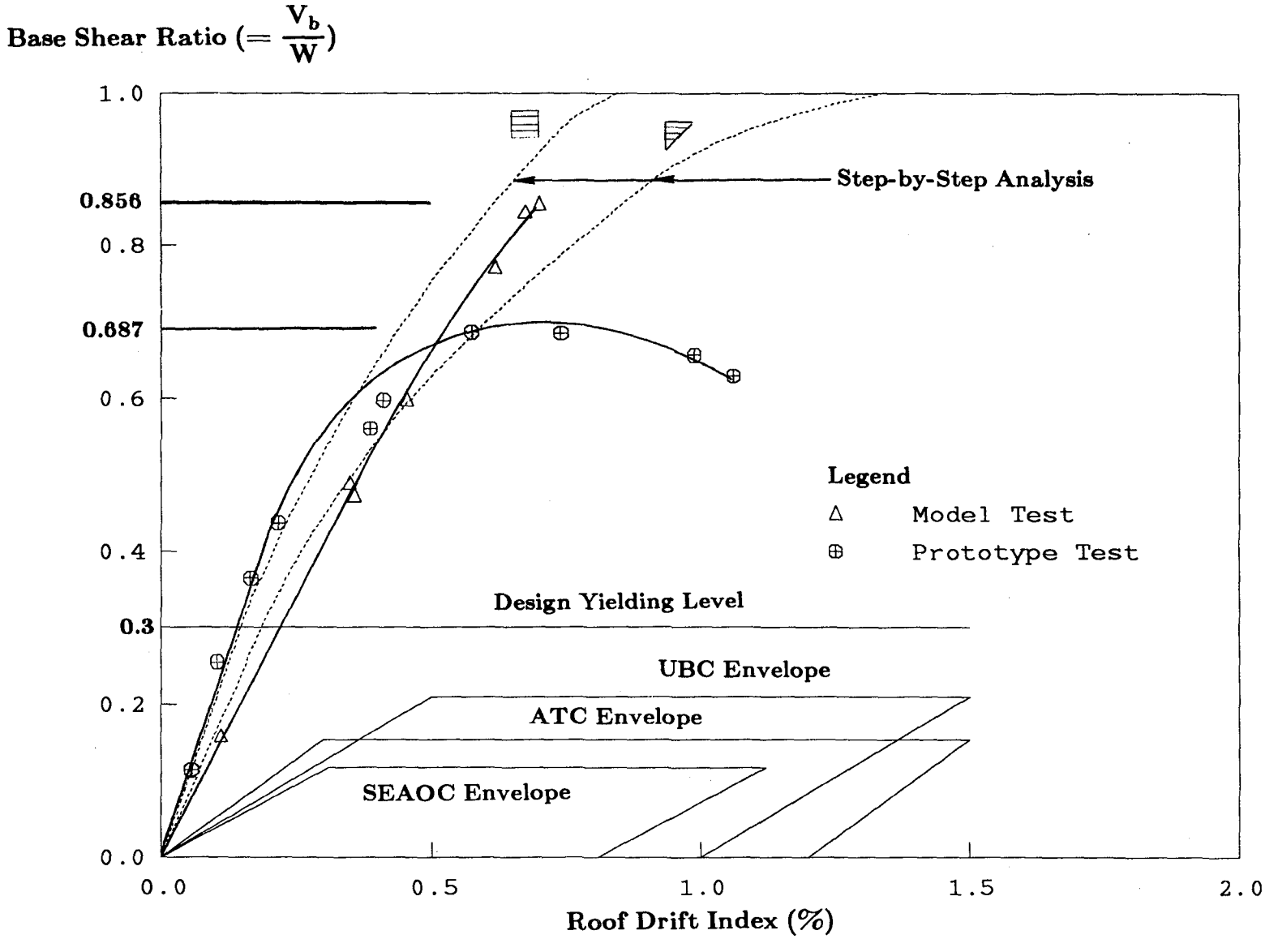


FIGURE 9.2 BASE SHEAR RATIO AND ROOF DRIFT INDEX RELATIONSHIP

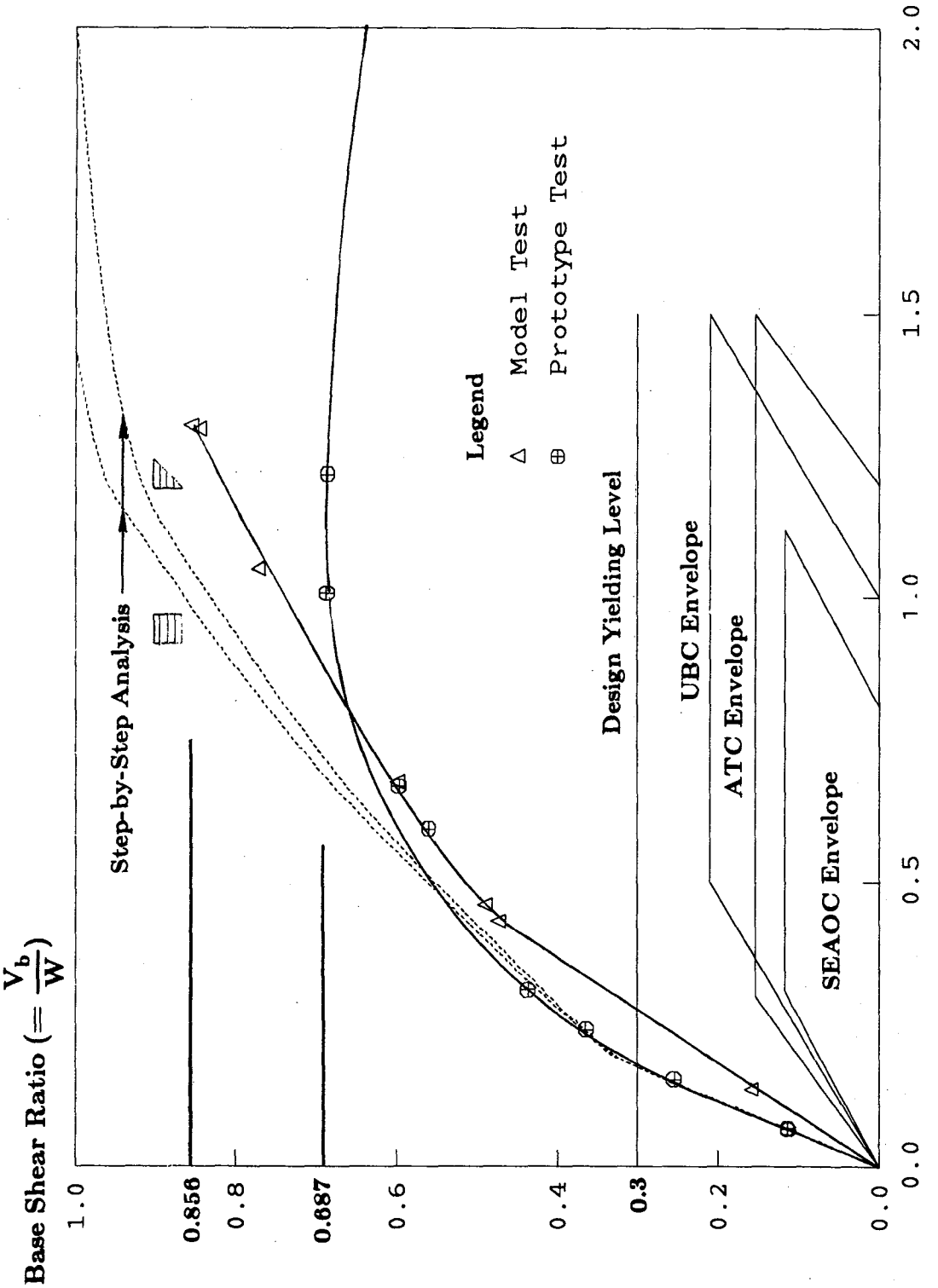


FIGURE 9.3 BASE SHEAR RATIO AND FIRST IDI RELATIONSHIP

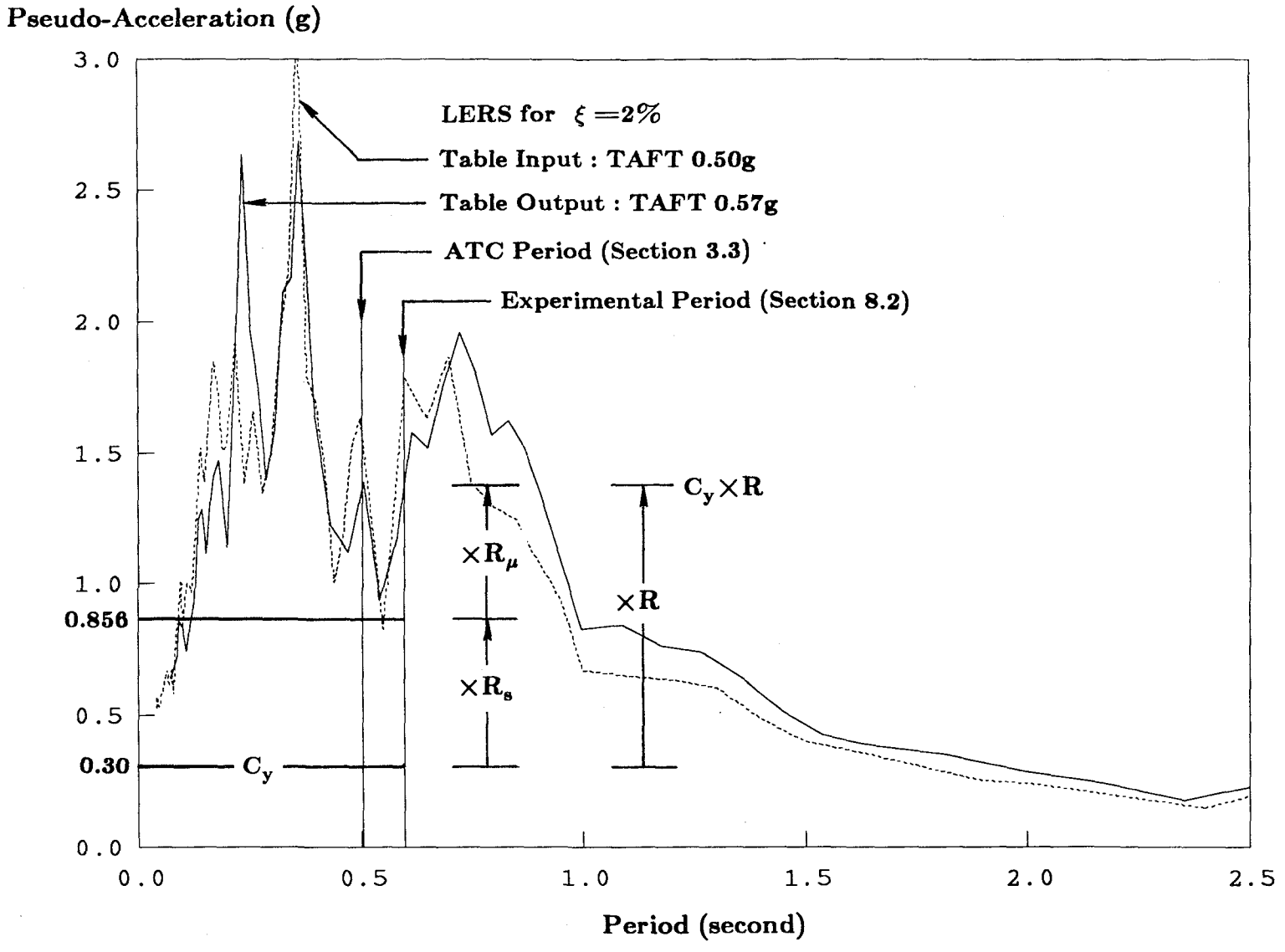


**FIGURE 9.4 COMPARISON OF THE TAFT LERS AND THE STRENGTH OF THE MODEL**

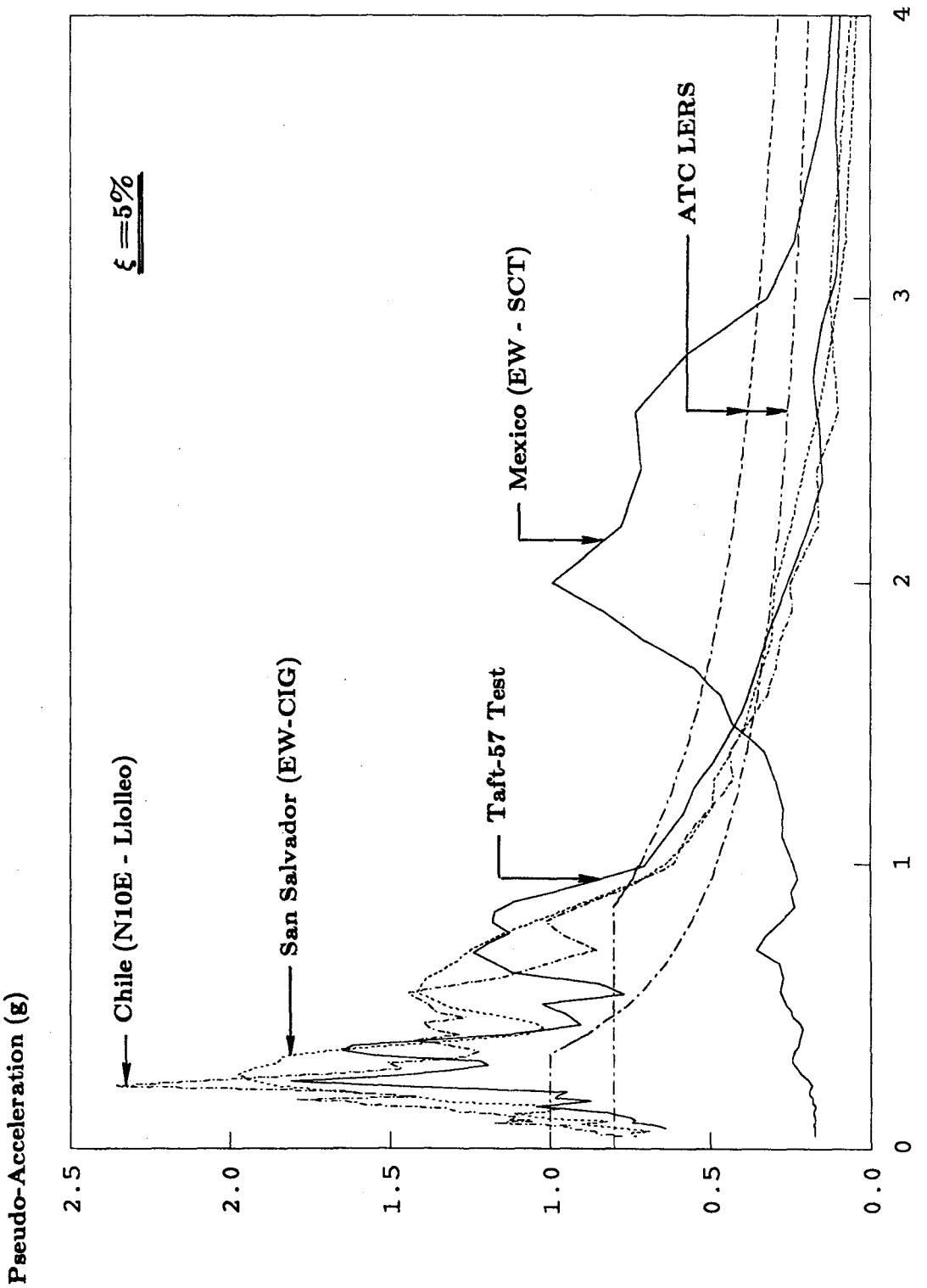


FIGURE 9.5 GROUND MOTION LERS AND ATC LEDRS

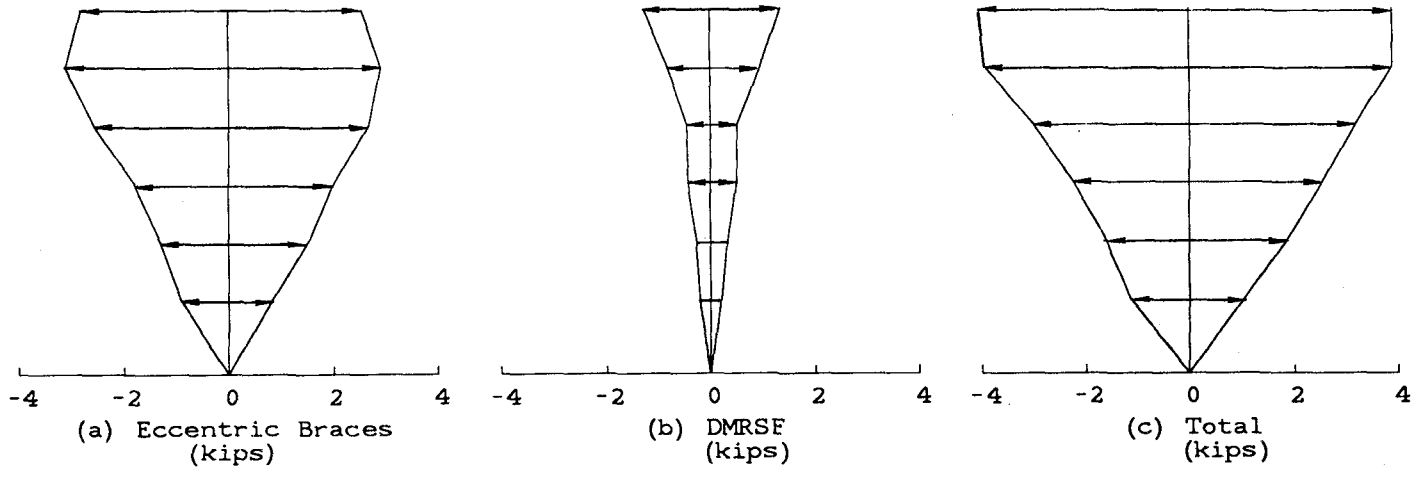


**TAFT-08 TEST**

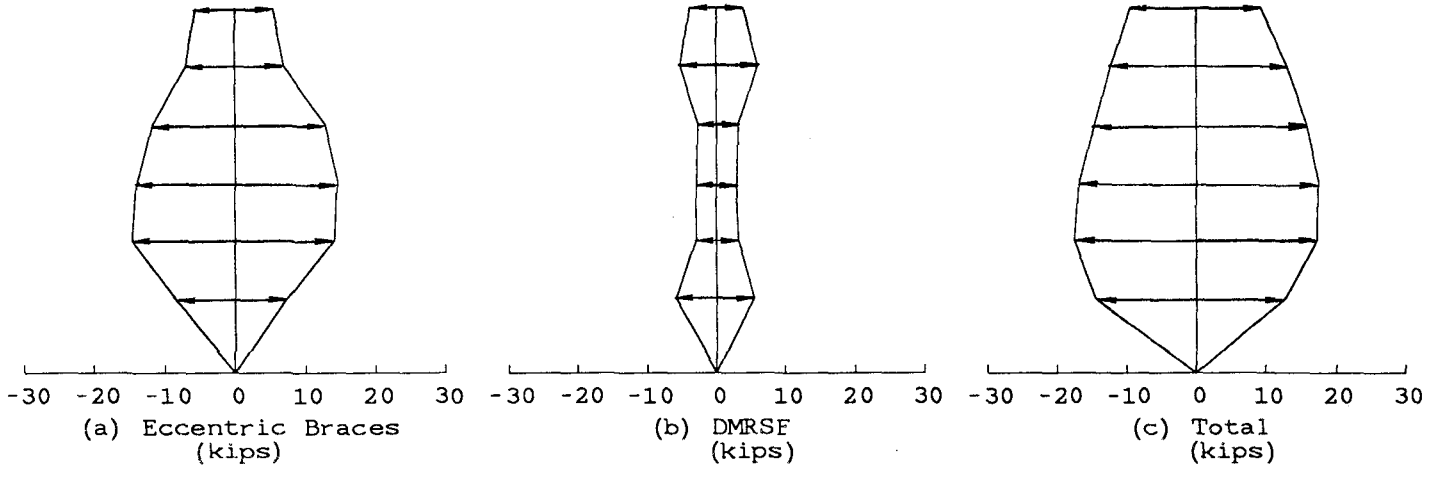


**TAFT-66 TEST**

**FIGURE 9.6 LATERAL FORCE DISTRIBUTIONS AT MAXIMUM BASE SHEAR**

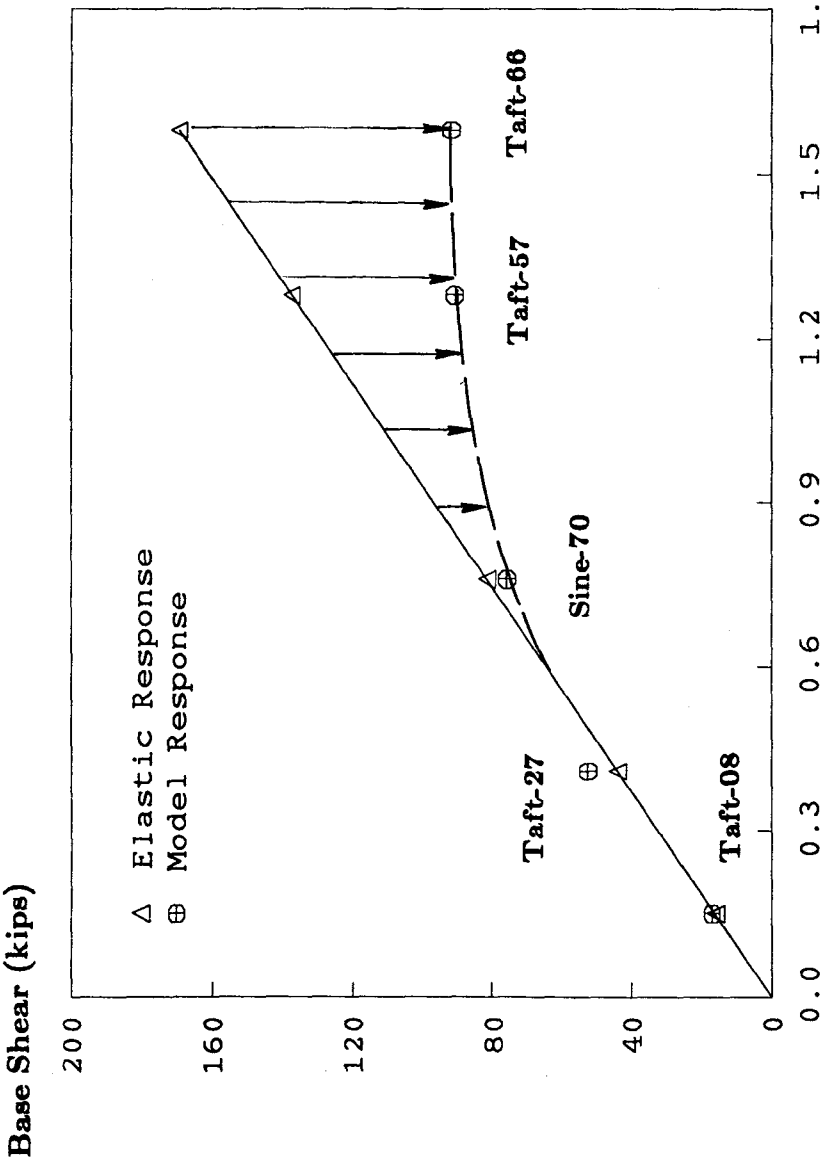


FIGURE 9.7 ENVELOPE OF MAXIMUM BASE SHEAR AND PSA/G

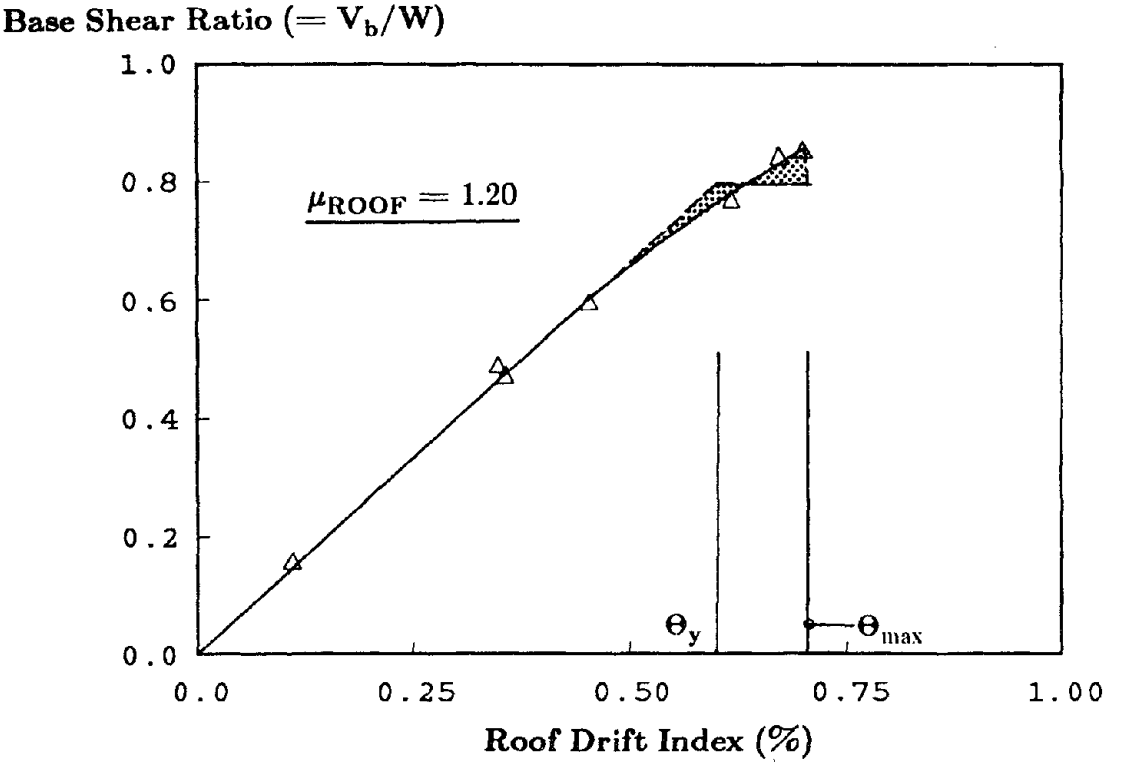


(a) Global Displacement Ductility

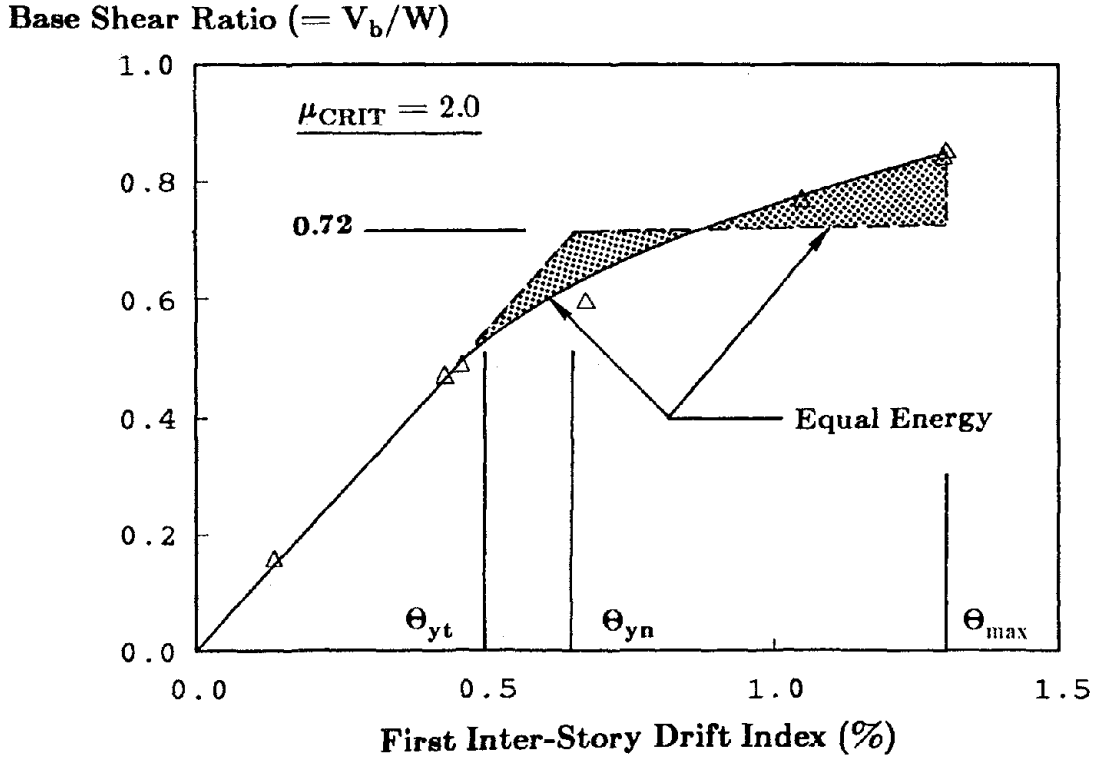


(b) Critical Displacement Ductility

FIGURE 9.8 DUCTILITY OF THE MODEL

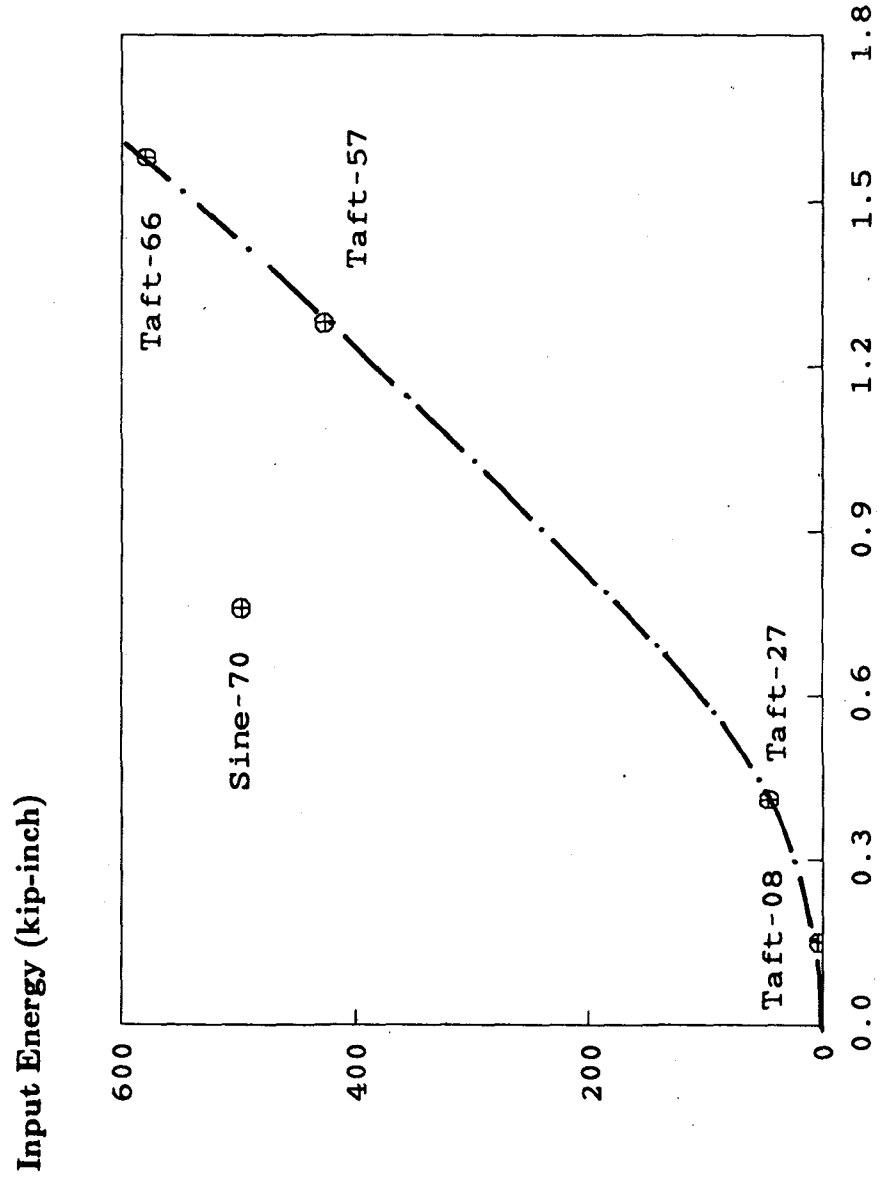


FIGURE 9.9 ENVELOPE OF INPUT ENERGY AND PSA/G

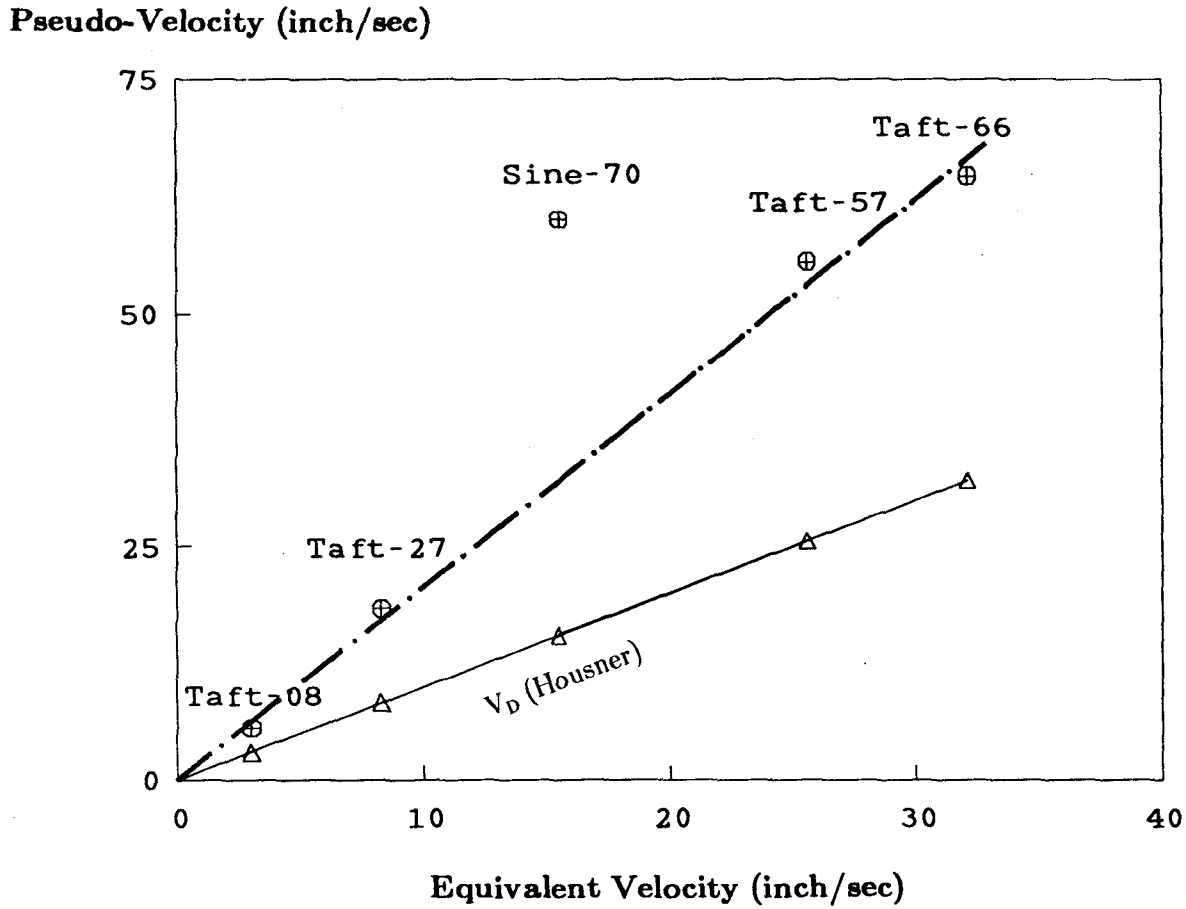


**FIGURE 9.10 ENVELOPE OF EQUIVALENT VELOCITY AND PSV**

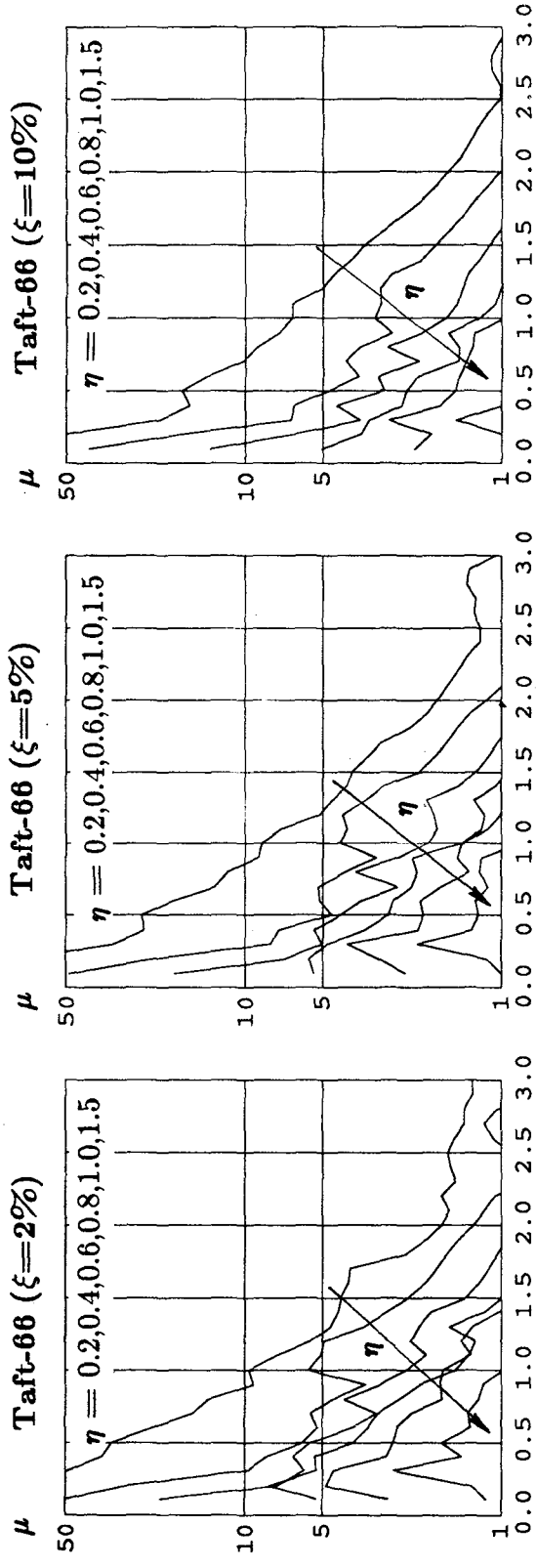


FIGURE 9.11 TAFT-66 DISPLACEMENT DUCTILITY SPECTRA

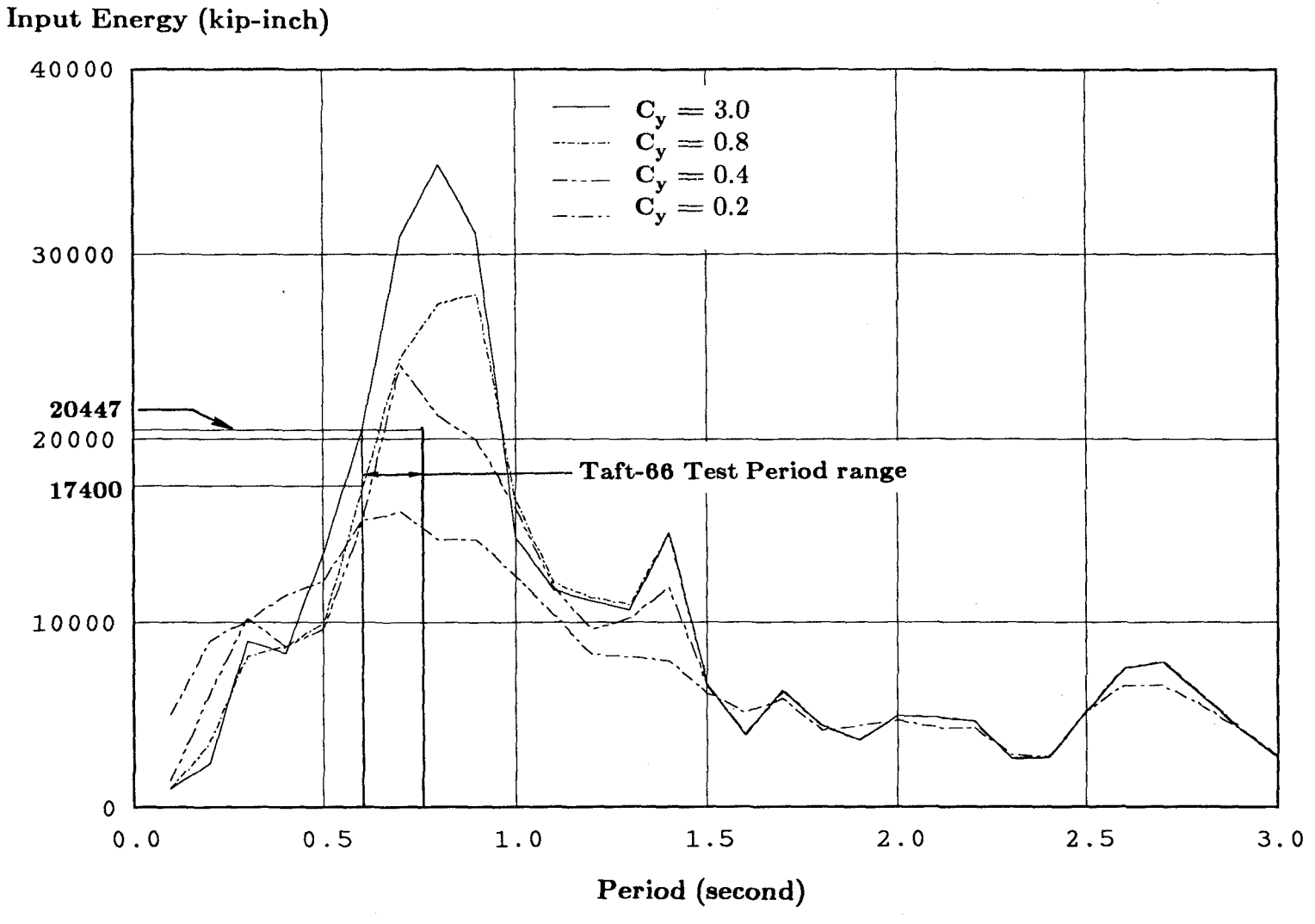


**FIGURE 9.12 TAFT-66 ENERGY SPECTRA FOR 2% DAMPING**

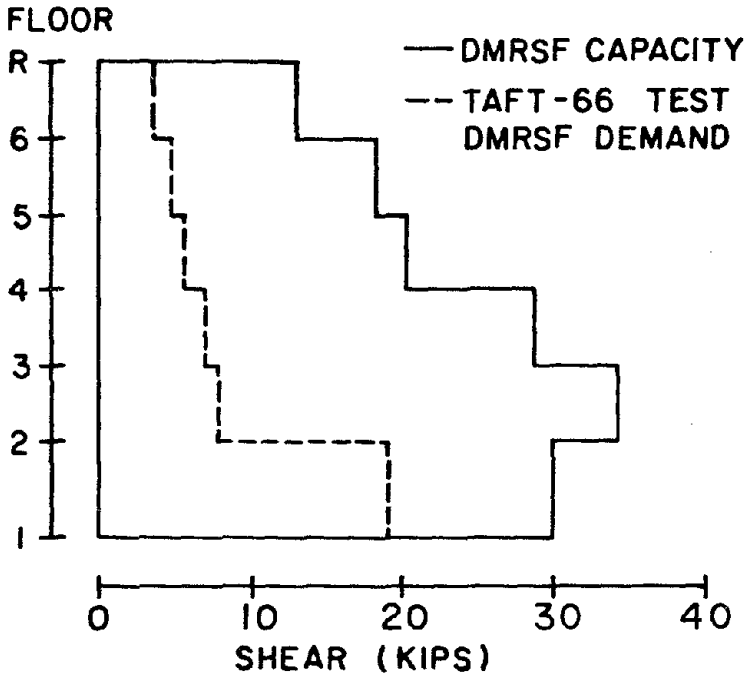


FIGURE 9.13 DMRSF STRENGTH DEMAND

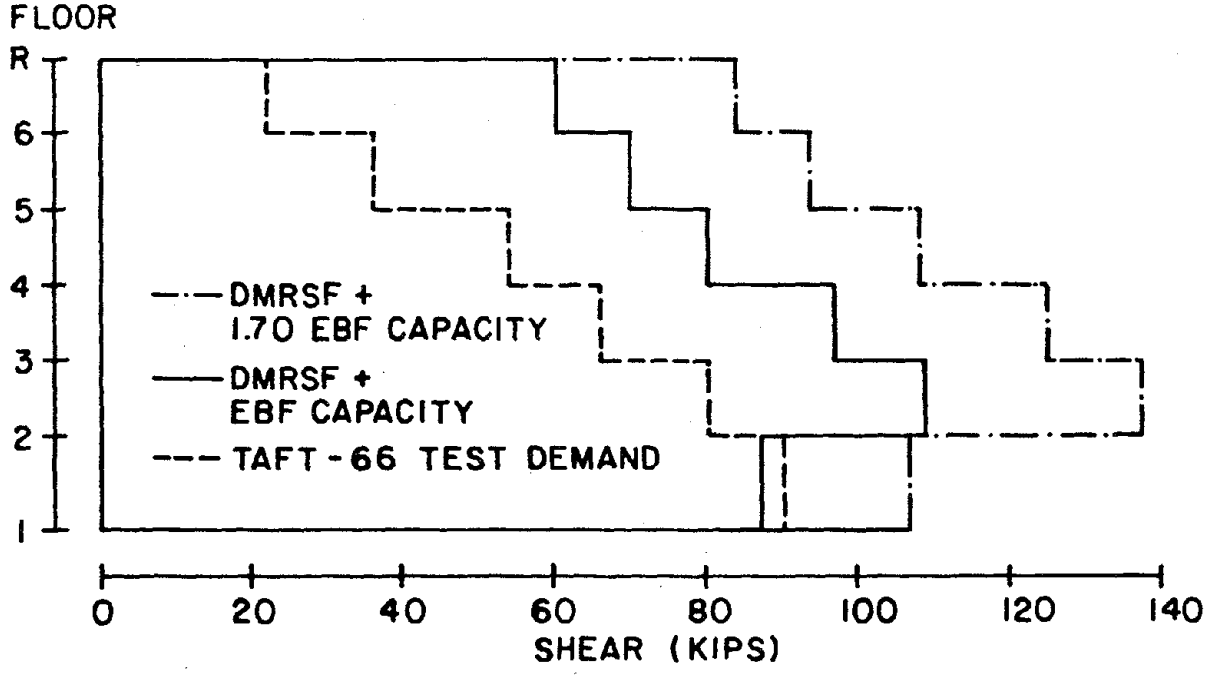


FIGURE 9.15 DUAL SYSTEM STRENGTH DEMAND

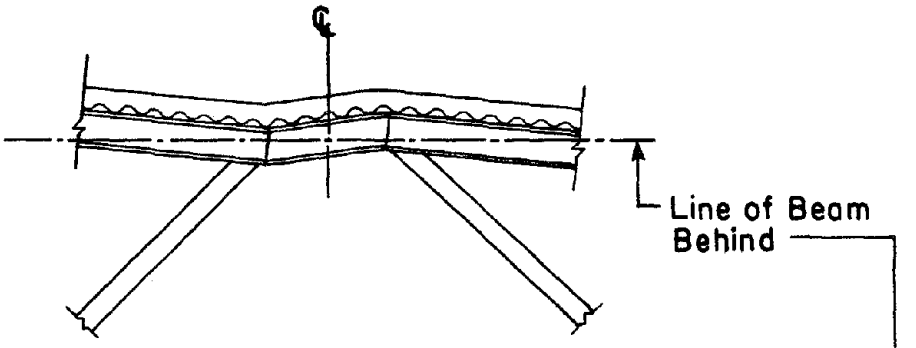


(a) Section A : Frame B Inelastic Deformation Field

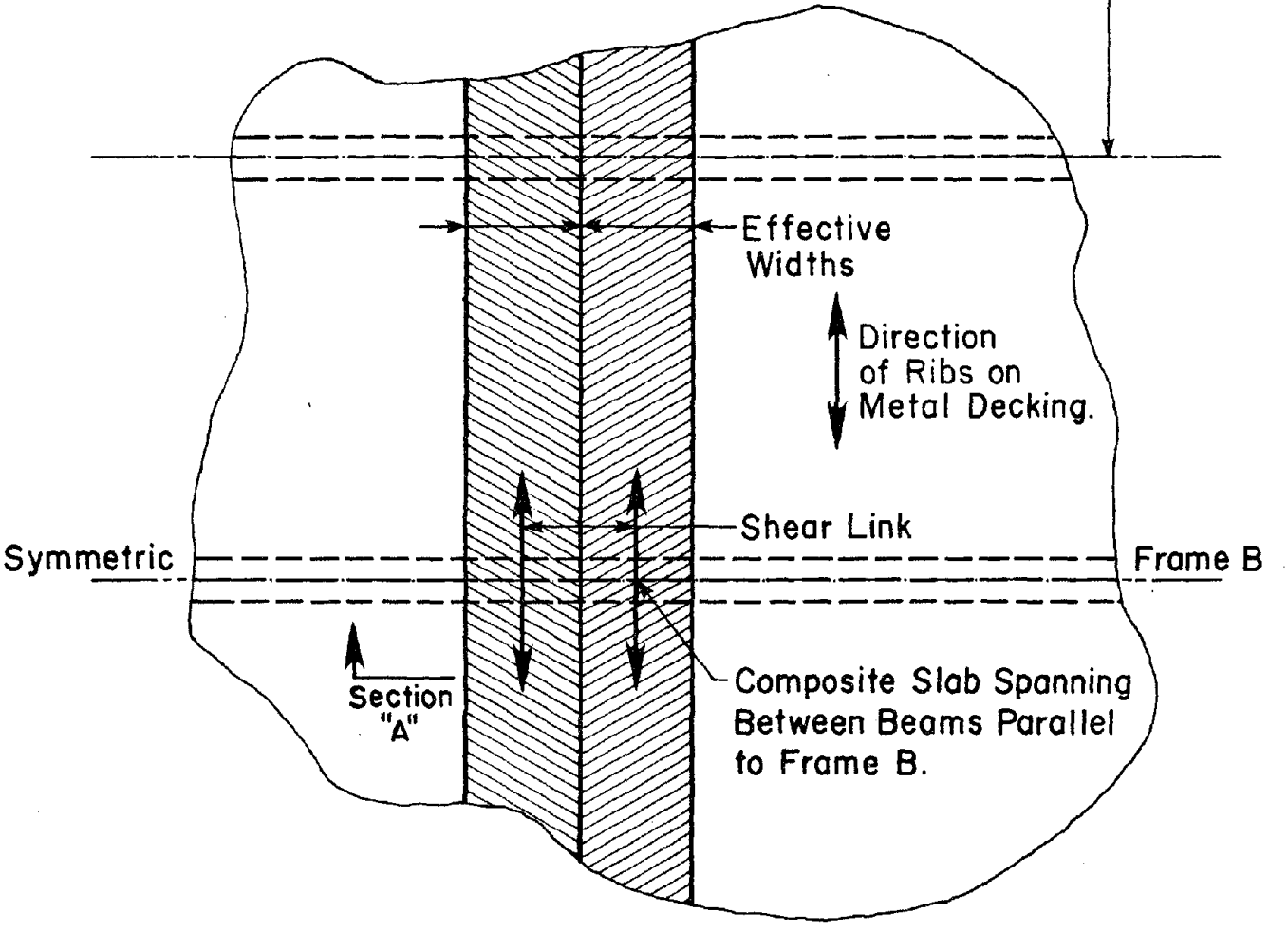


(b) Plan View

**FIGURE 9.14 THREE-DIMENSIONAL COUPLING EFFECT**

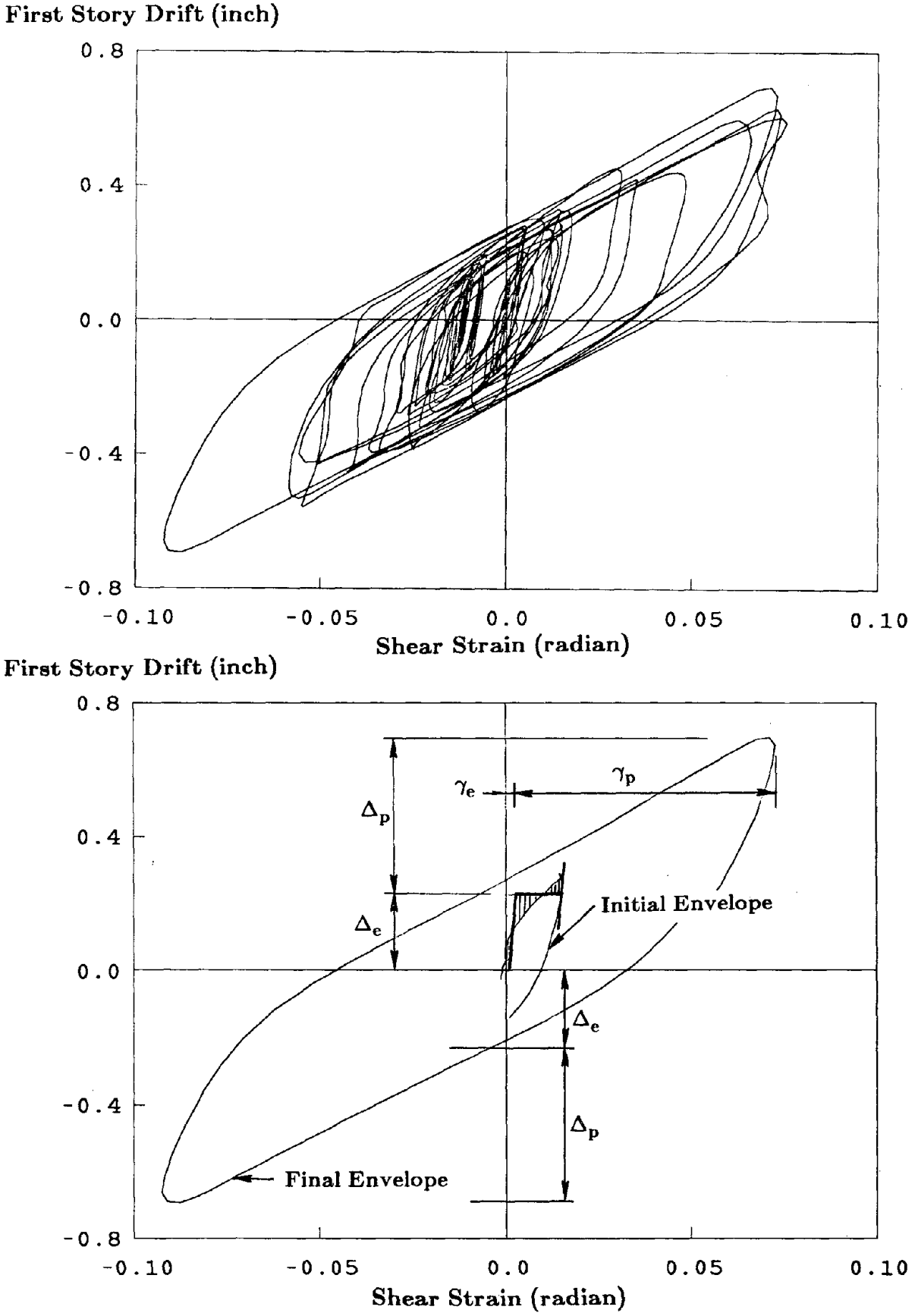


**FIGURE 9.16 TAFT-66 FIRST IDI AND L2 SHEAR STRAIN RELATIONSHIP**

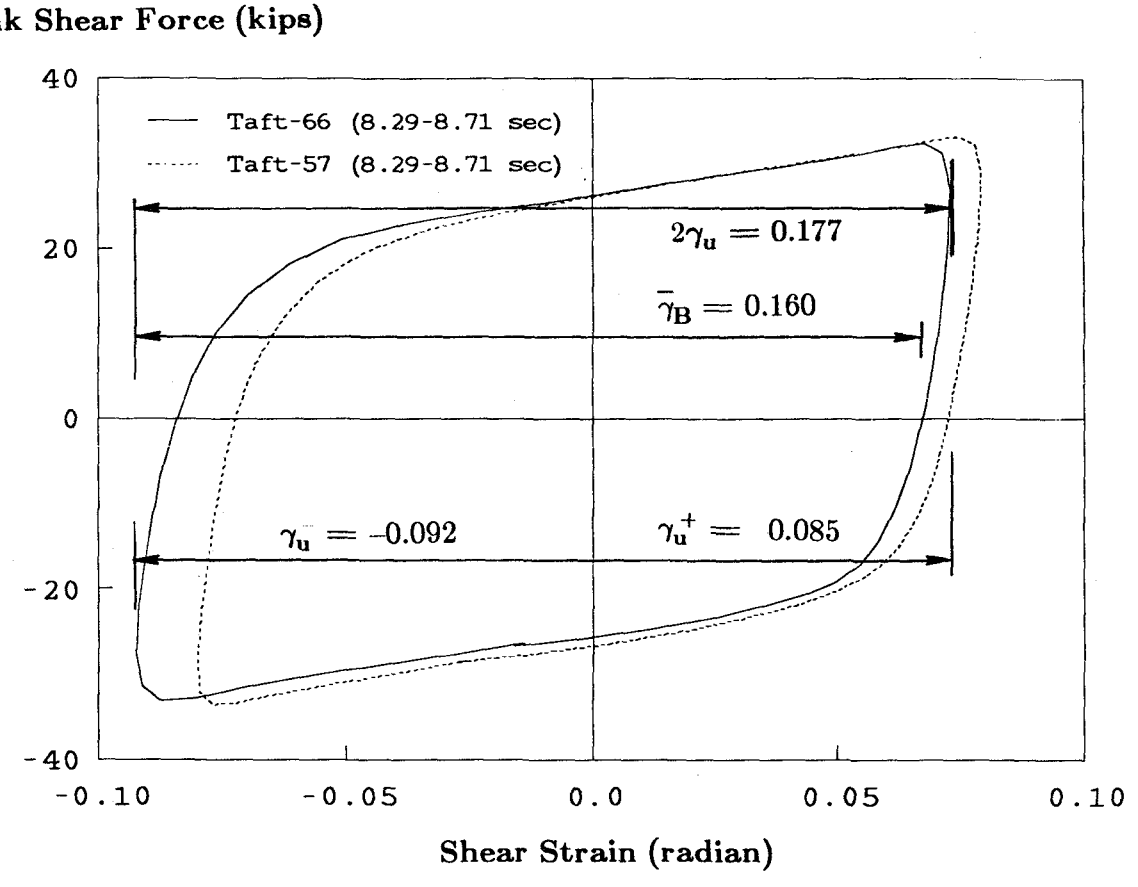


**FIGURE 9.17 MAJOR CYCLES OF LINK L2 SHEAR FORCE AND SHEAR STRAIN**

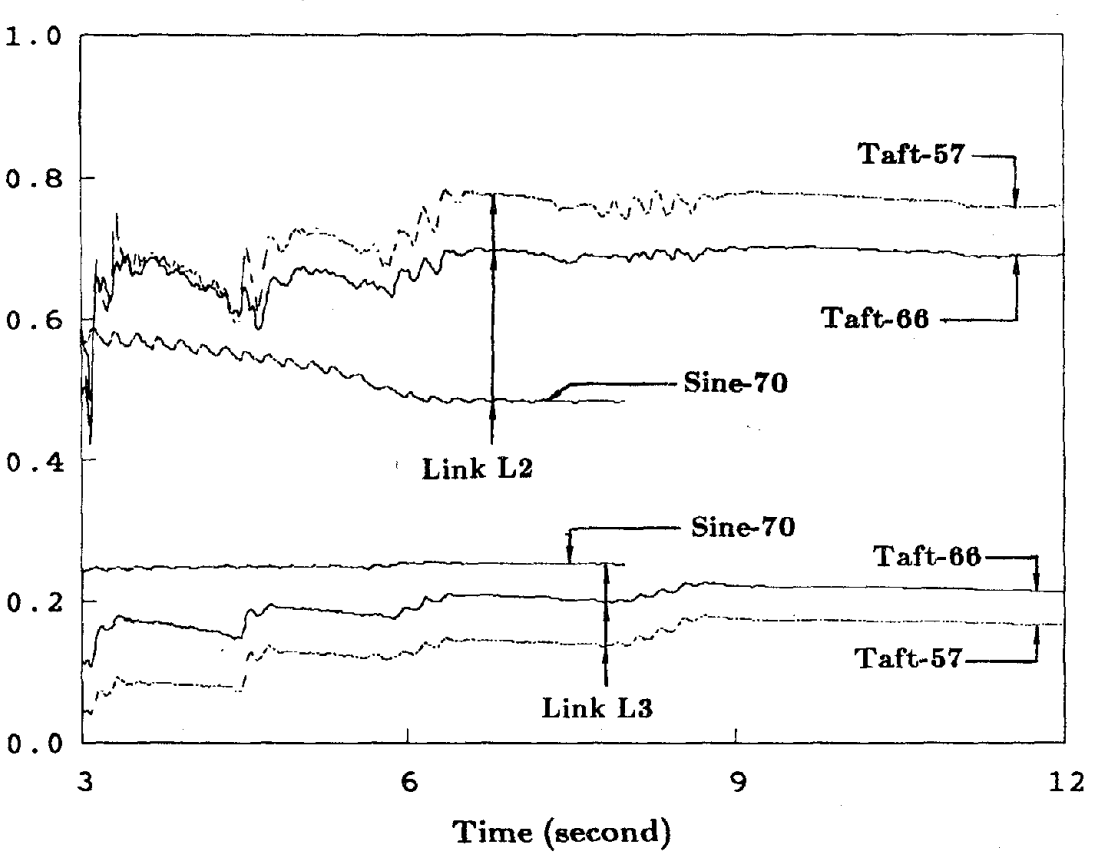


**FIGURE 9.18 SHEAR LINK ENERGY DISSIPATION**

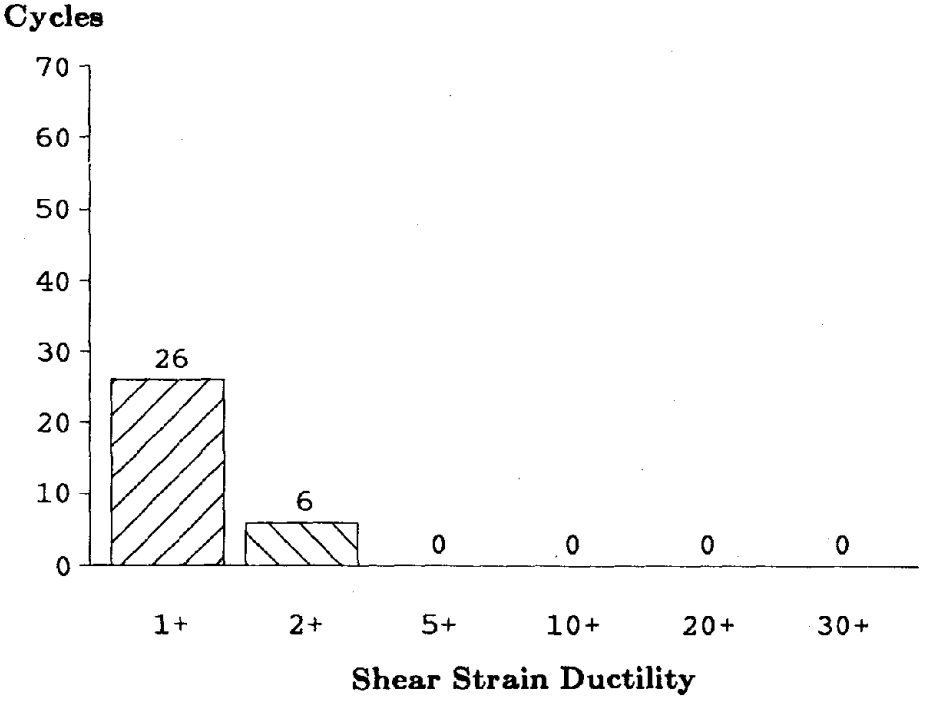


**FIGURE 9.19 TAFT-27 SHEAR STRAIN DUCTILITY**

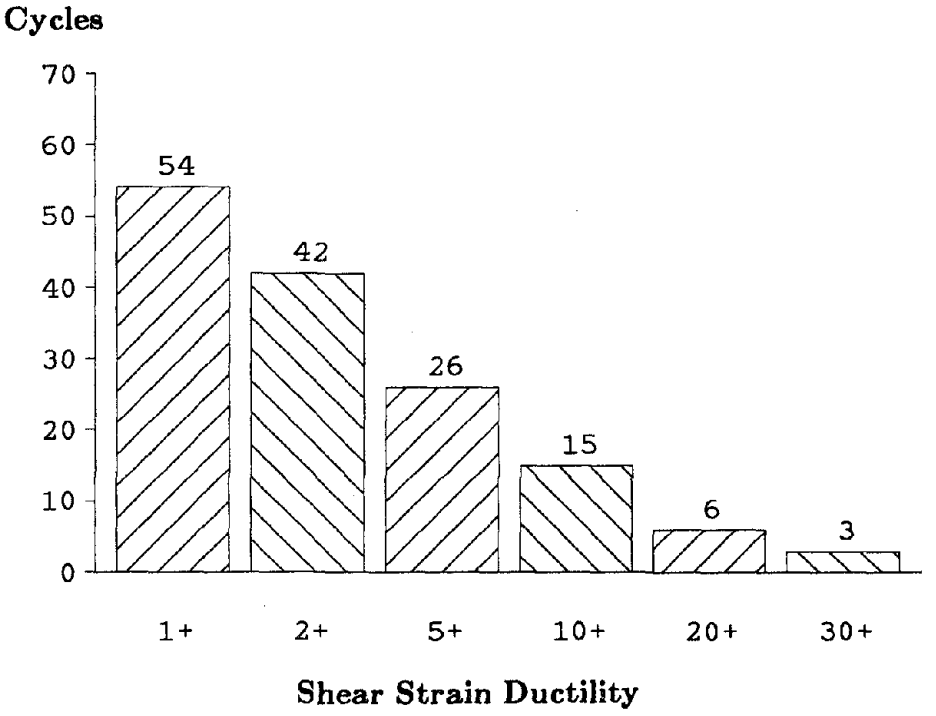


**FIGURE 9.20 TAFT-57 SHEAR STRAIN DUCTILITY**

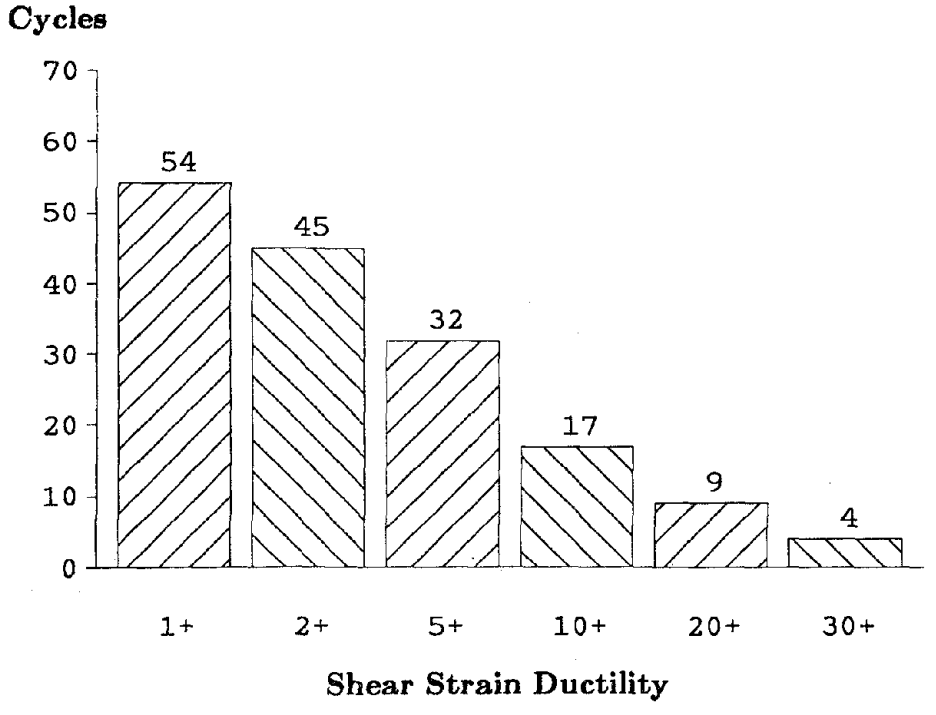


**FIGURE 9.21 TAFT-66 SHEAR STRAIN DUCTILITY**

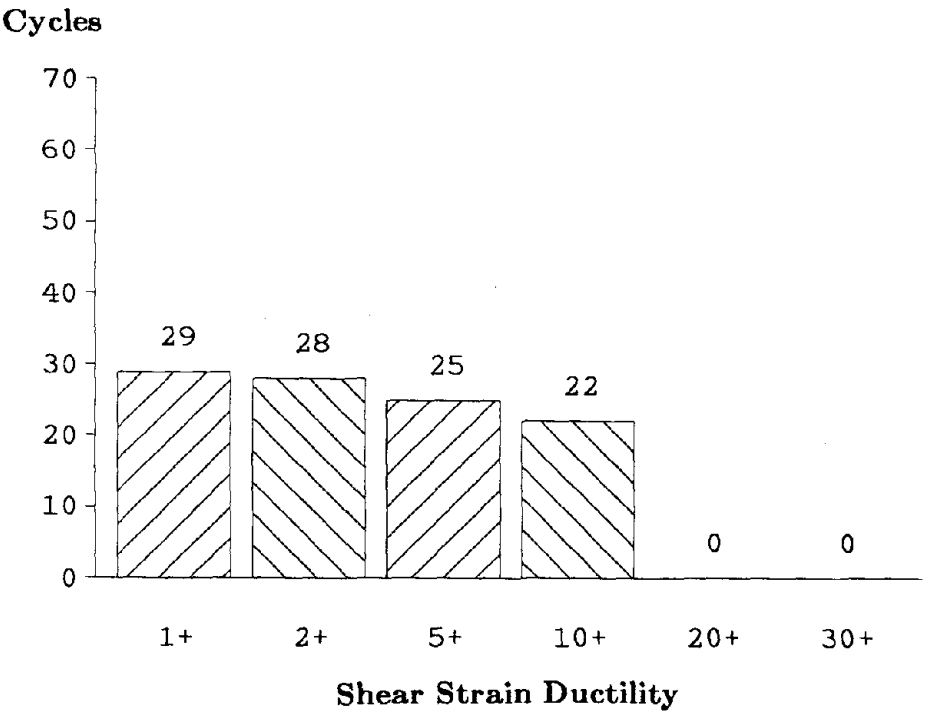


**FIGURE 9.22 SINE-66 SHEAR STRAIN DUCTILITY**

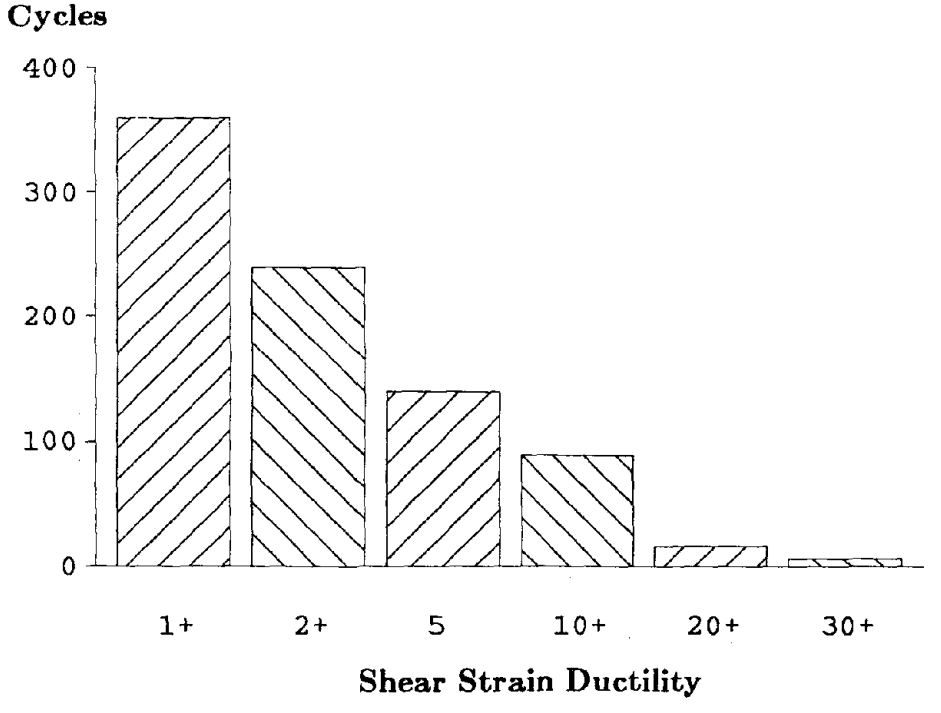


**FIGURE 9.23 LINK L2 SHEAR STRAIN DUCTILITY**

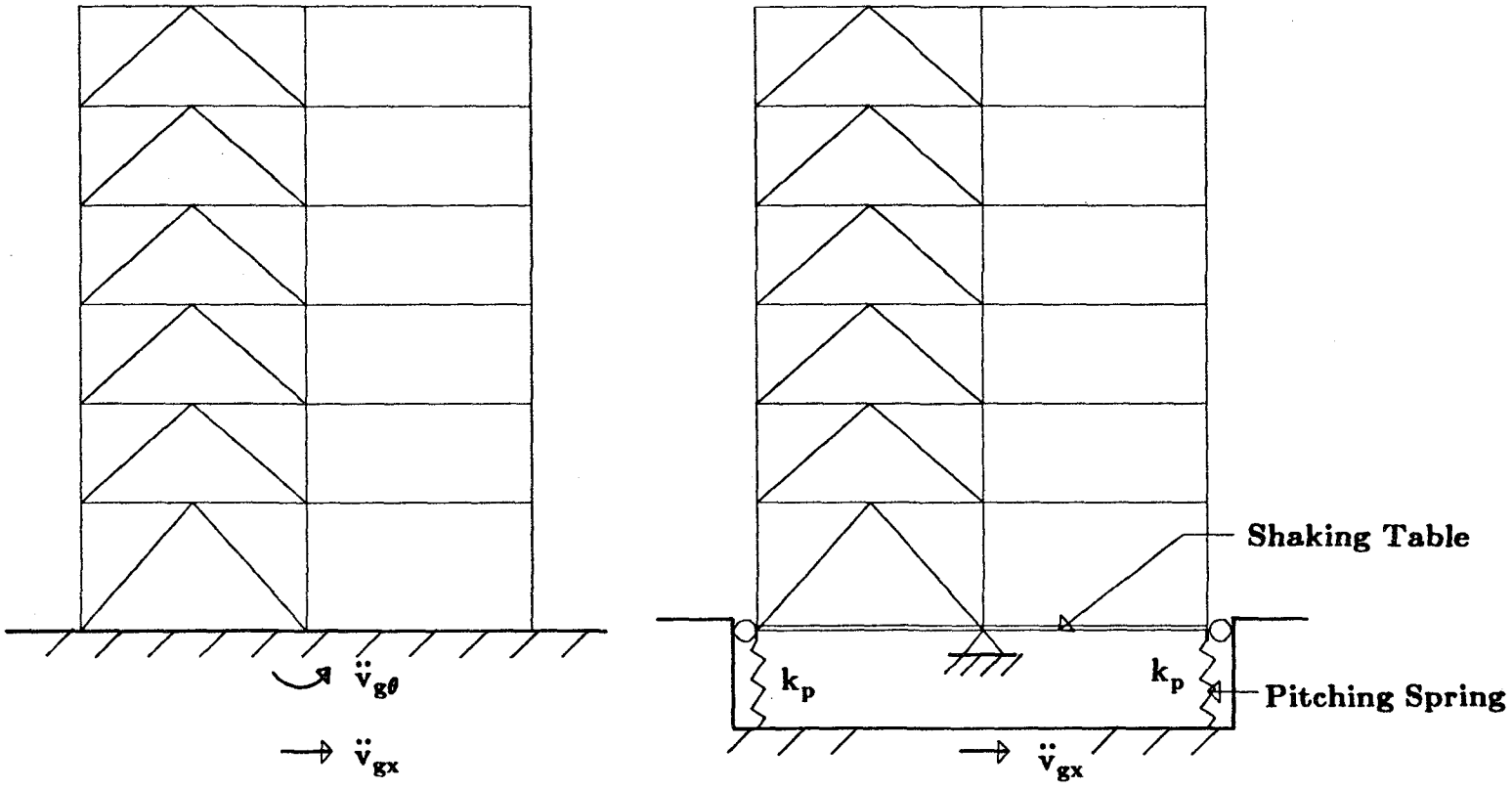


(a) Model 1

(b) Model 2

FIGURE 10.1 MATHEMATICAL MODEL OF THE TEST STRUCTURE

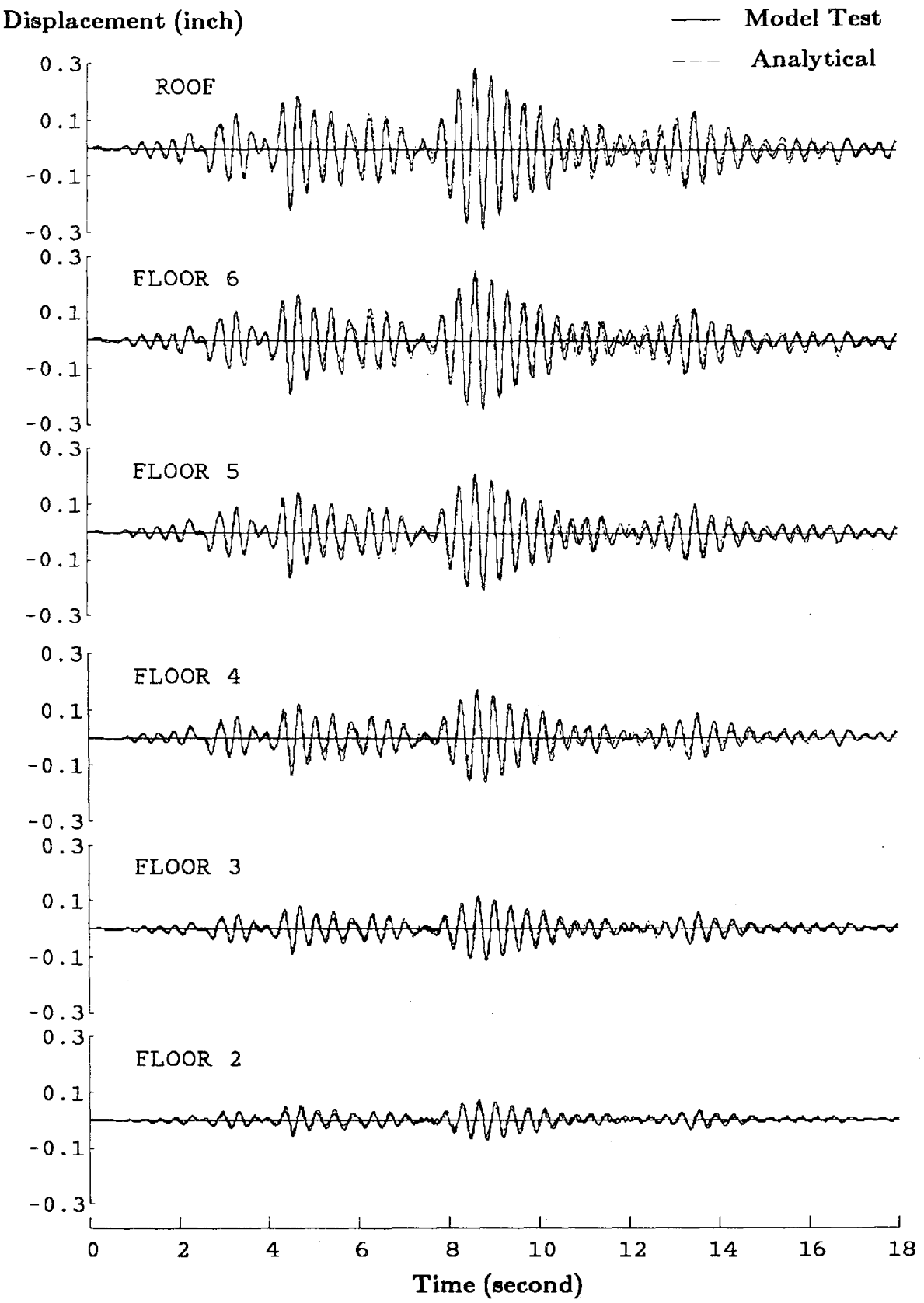


**FIGURE 10.2 TAFT-08 LATERAL DISPLACEMENT CORRELATION**

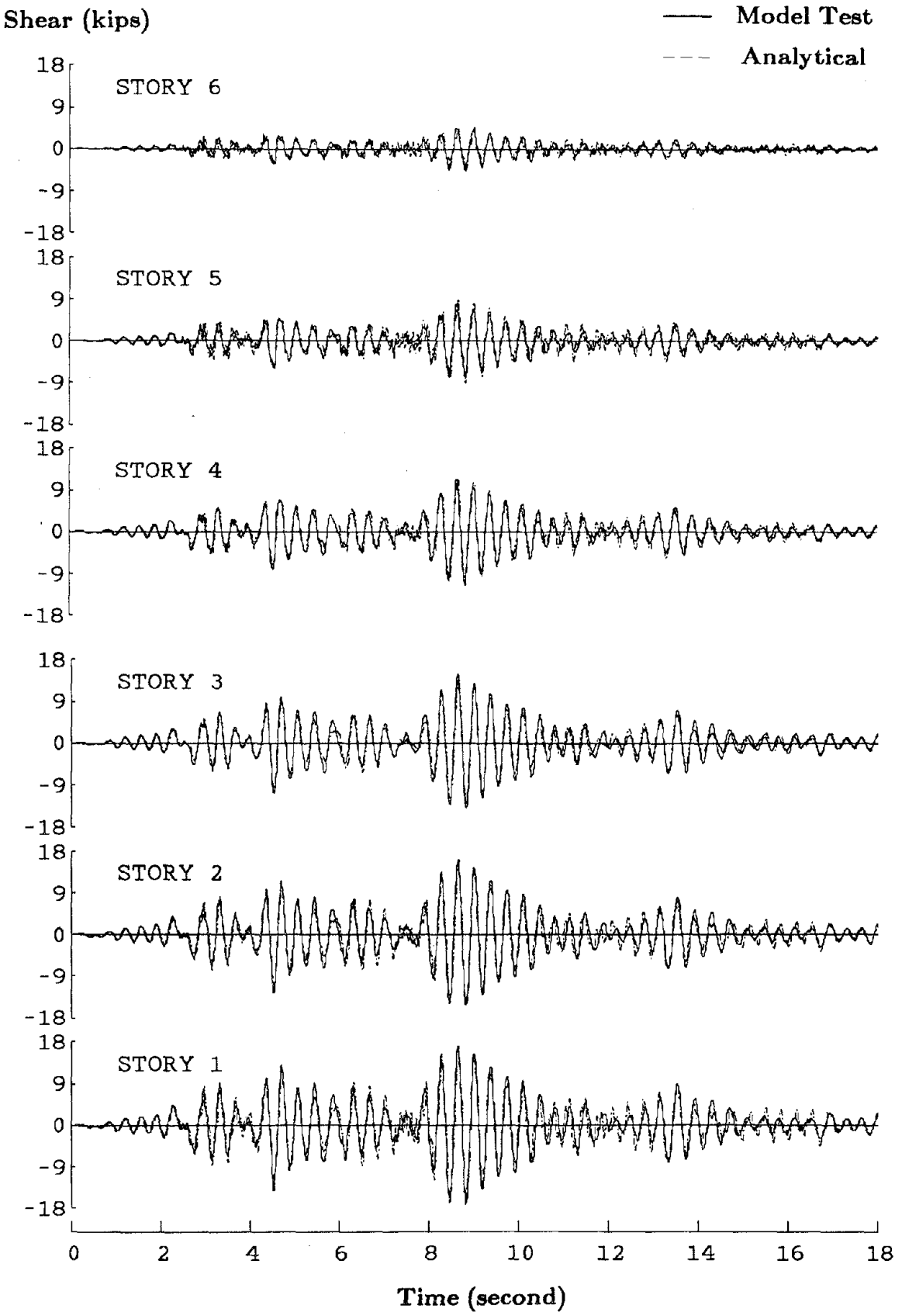


**FIGURE 10.3 TAFT-08 STORY SHEAR CORRELATION**

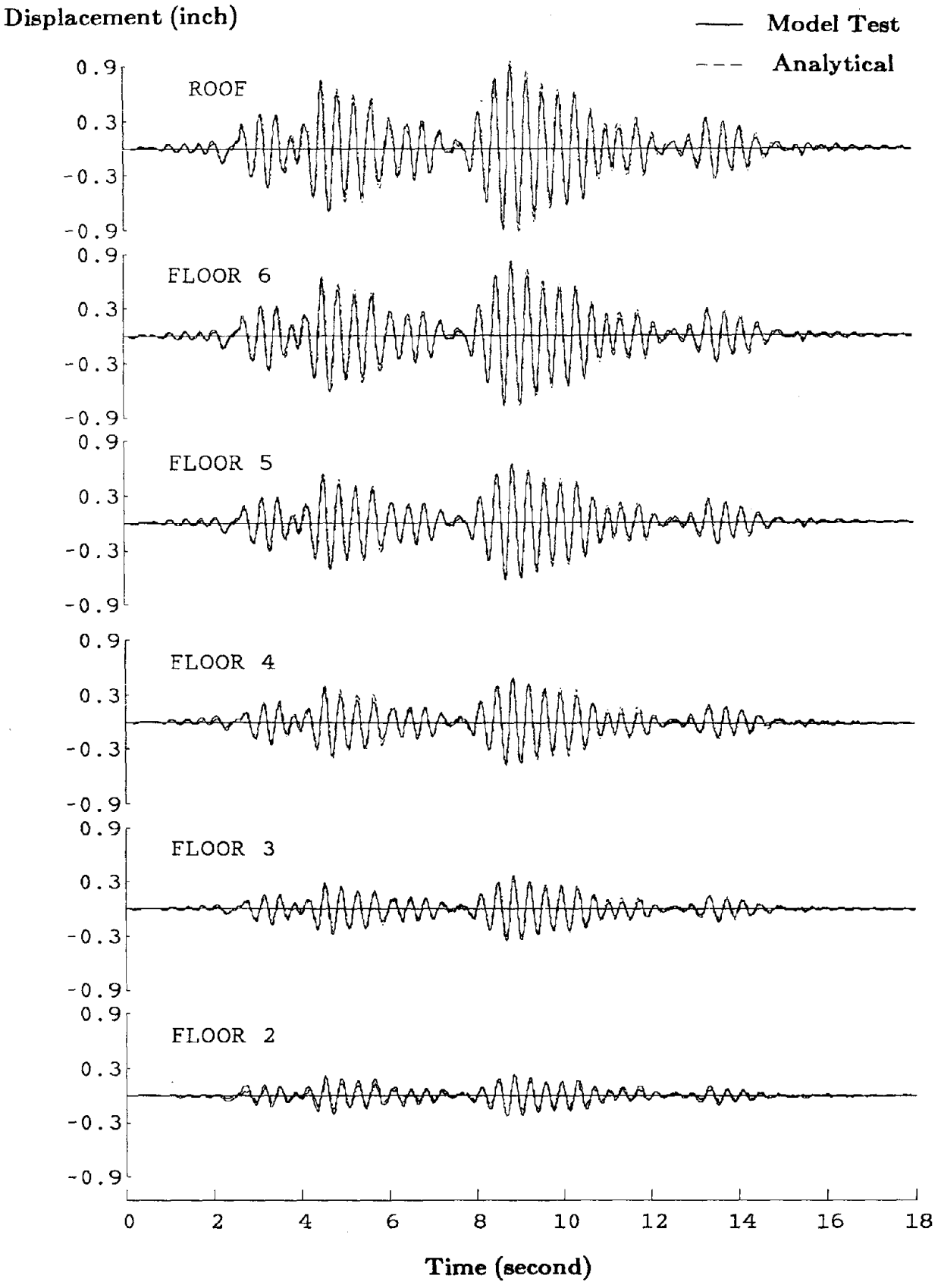


**FIGURE 10.4 TAFT-27 LATERAL DISPLACEMENT CORRELATION**

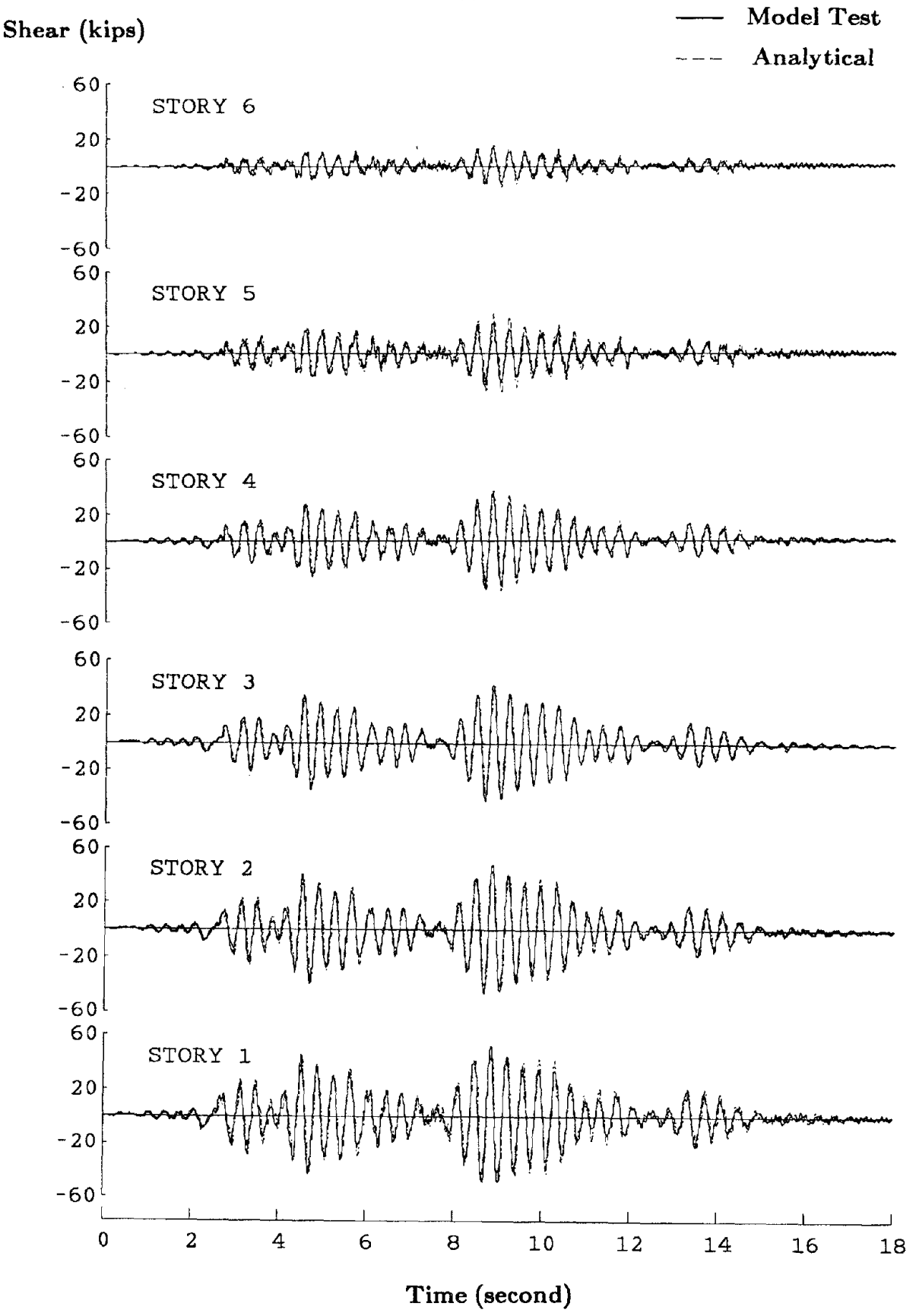


**FIGURE 10.5 TAFT-27 STORY SHEAR CORRELATION**

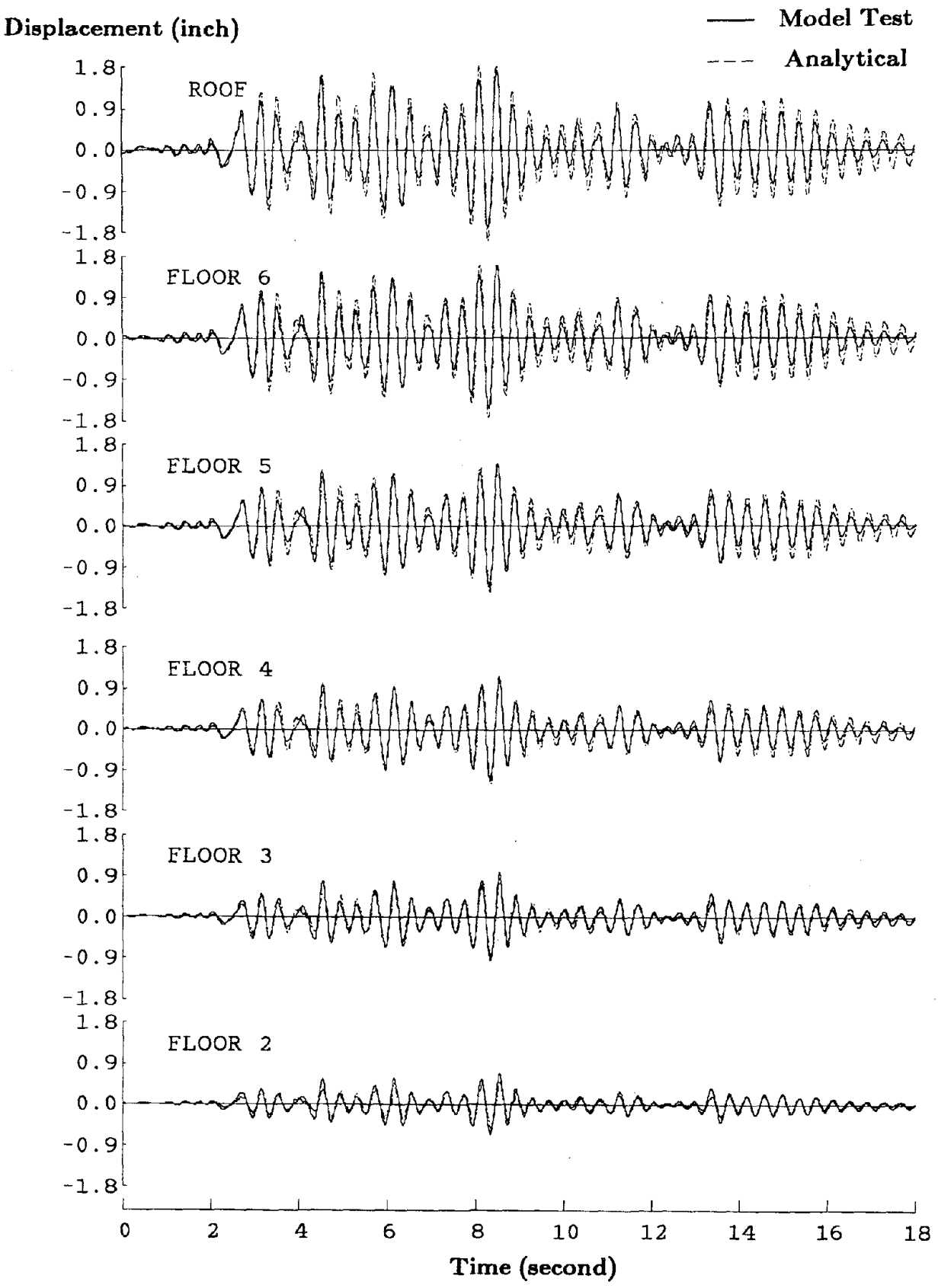


**FIGURE 10.6 TAFT-57 LATERAL DISPLACEMENT CORRELATION**

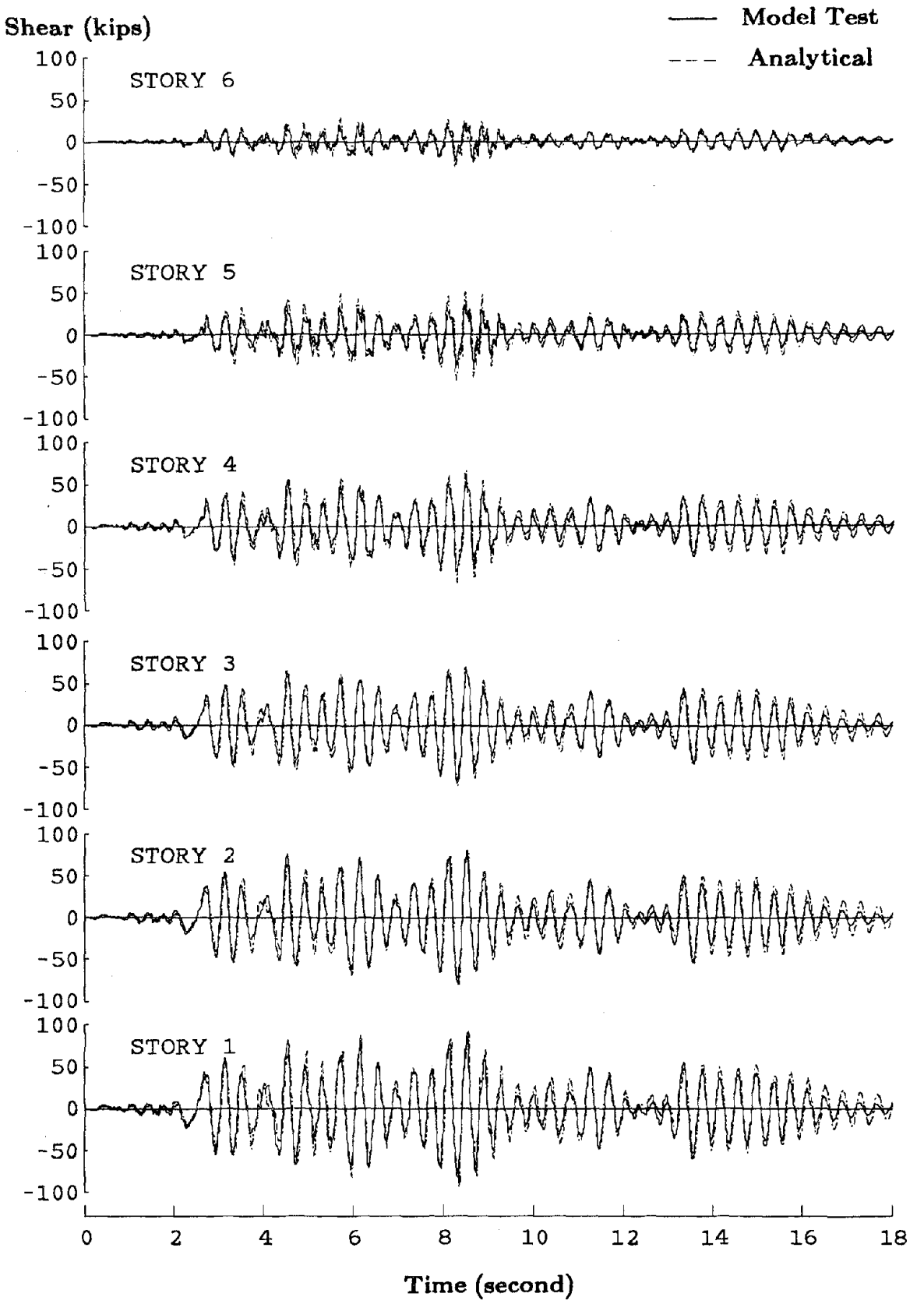


**FIGURE 10.7 TAFT-57 STORY SHEAR CORRELATION**

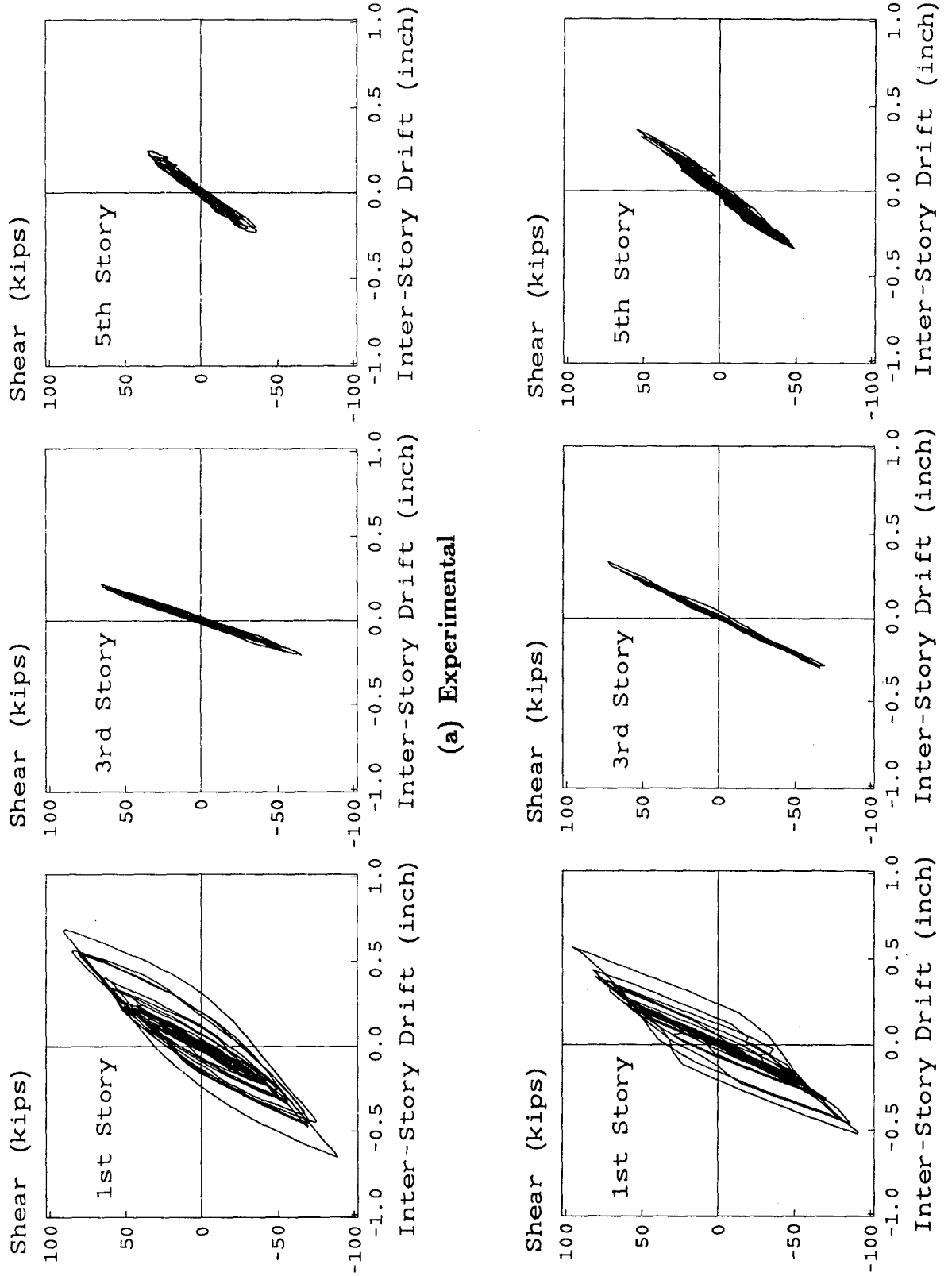


(a) Experimental

(b) Analytical

**FIGURE 10.8 TAFT-57 STORY SHEAR AND STORY DRIFT CORRELATION**

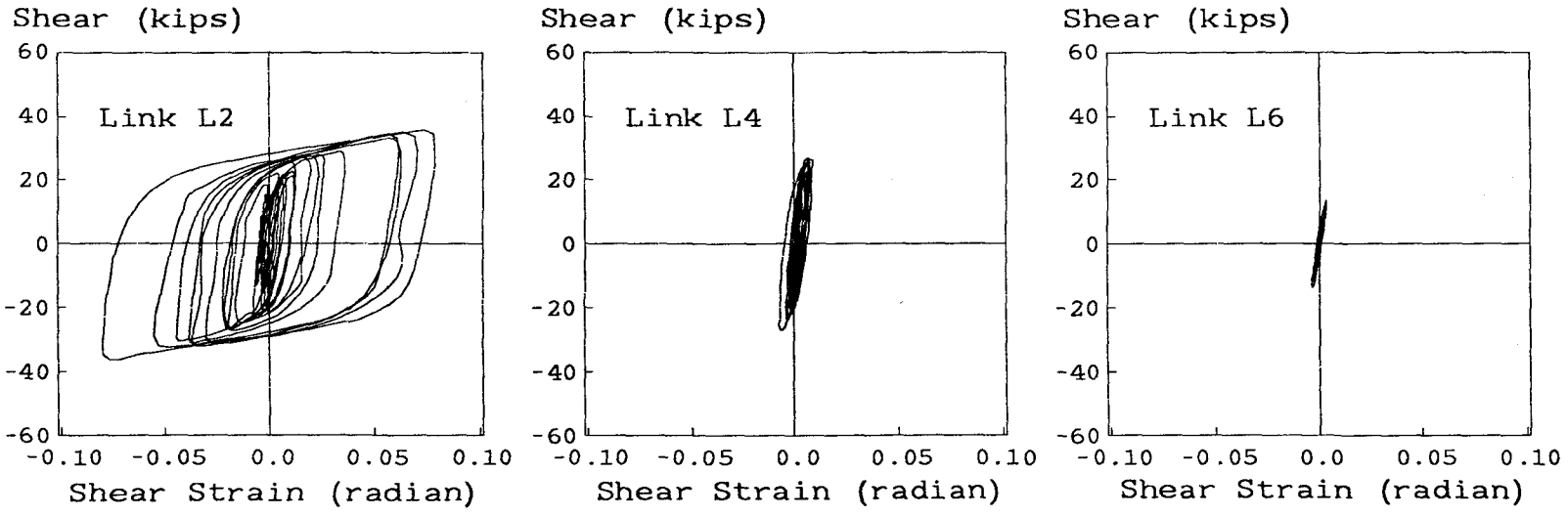


**(a) Experimental**

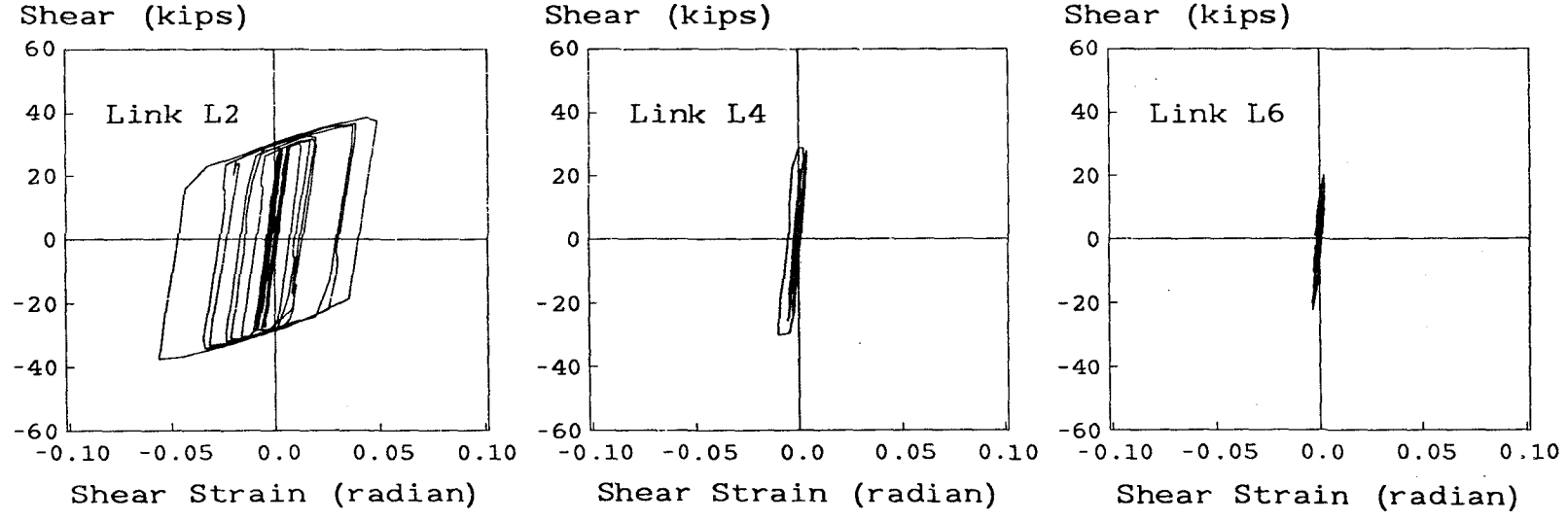


**(b) Analytical**

**FIGURE 10.9 TAFT-57 LINK SHEAR FORCE AND SHEAR STRAIN CORRELATION**

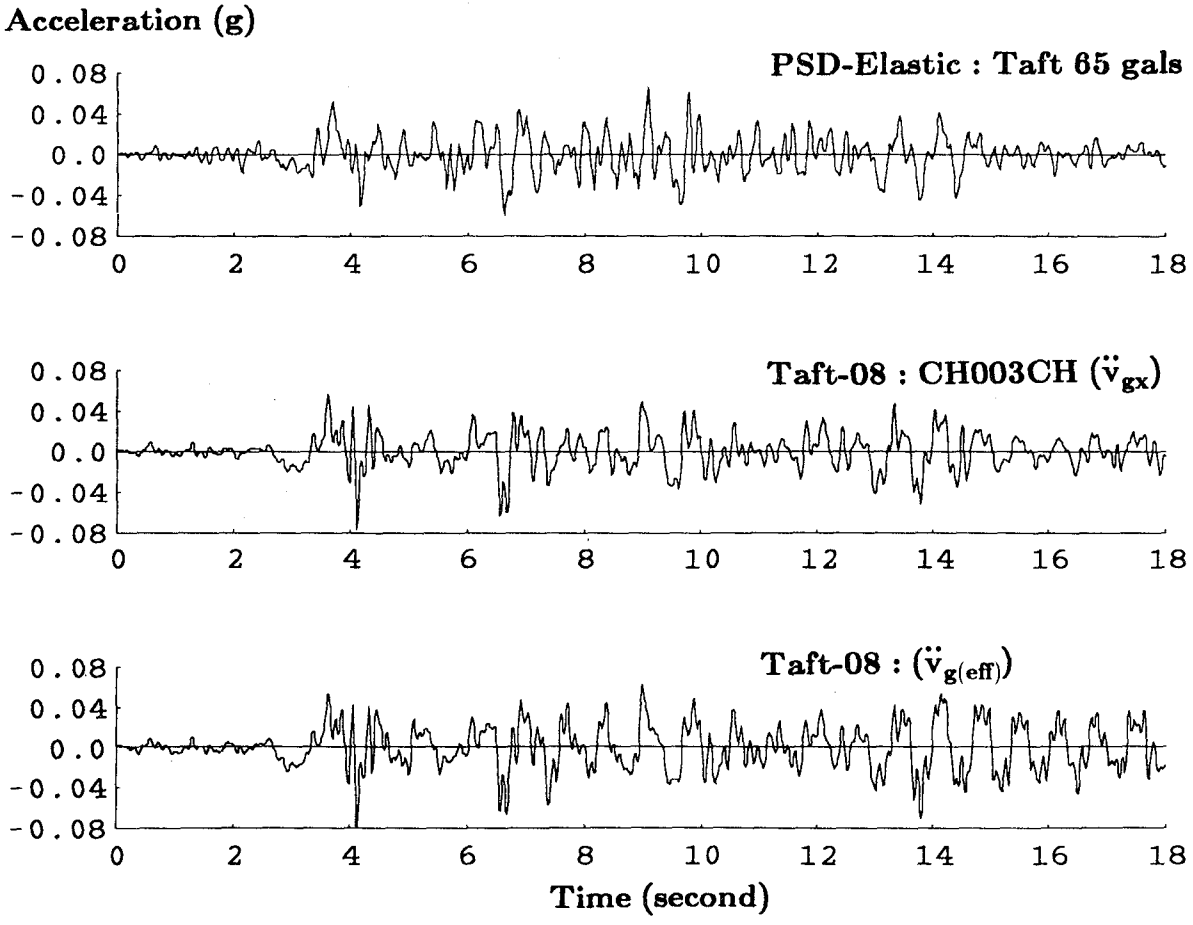


(a) Acceleration

**FIGURE 10.10 PSD-ELASTIC AND TAFT-08 TEST INPUT MOTIONS**

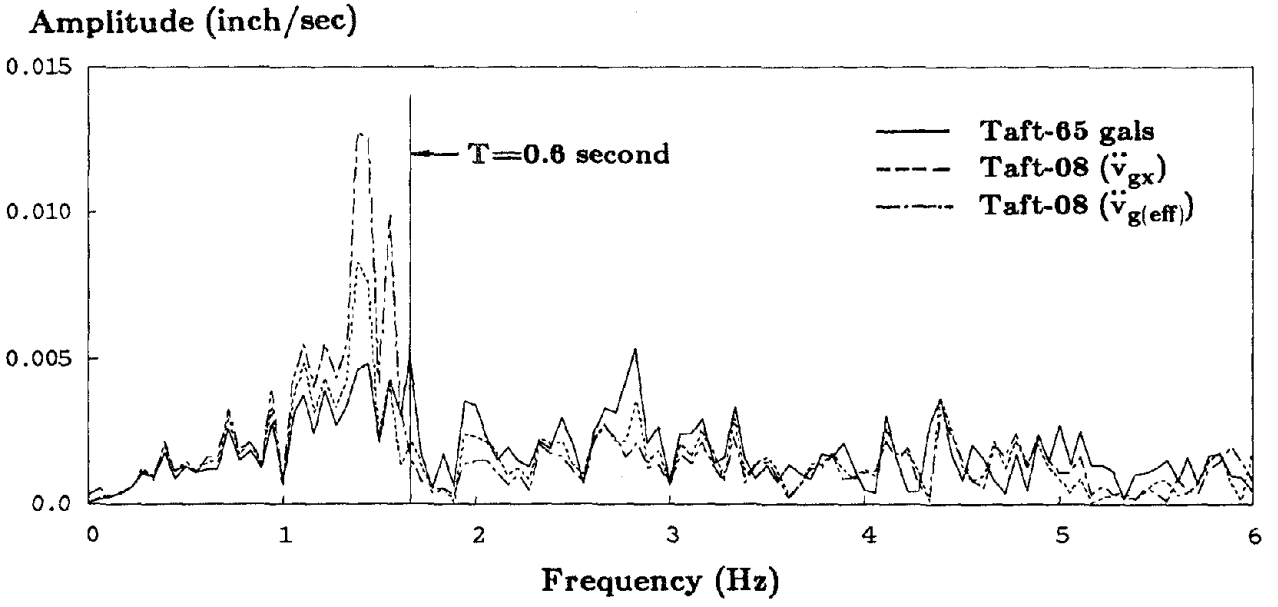


(b) Fourier Amplitude Spectrum

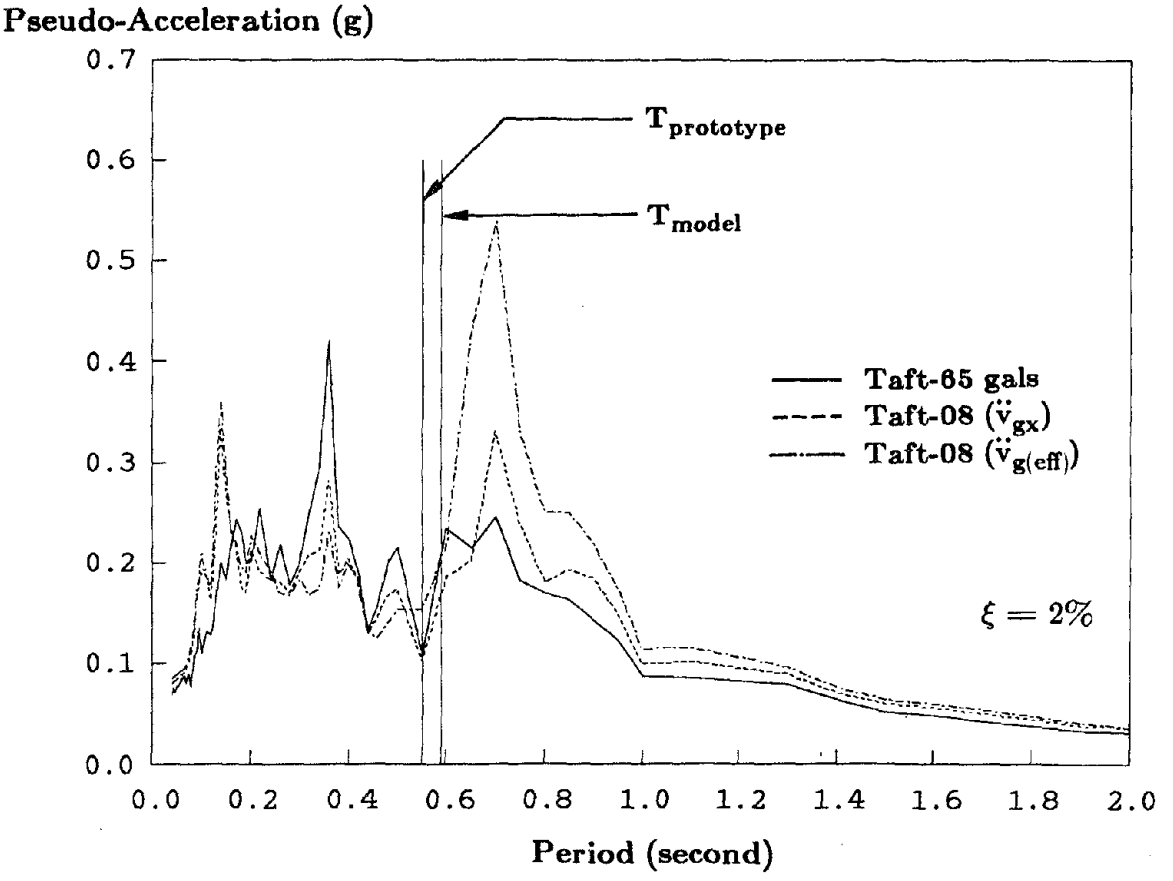


(c) Linear Elastic Response Spectra

FIGURE 10.10 PSD-ELASTIC AND TAFT-08 TEST INPUT MOTIONS

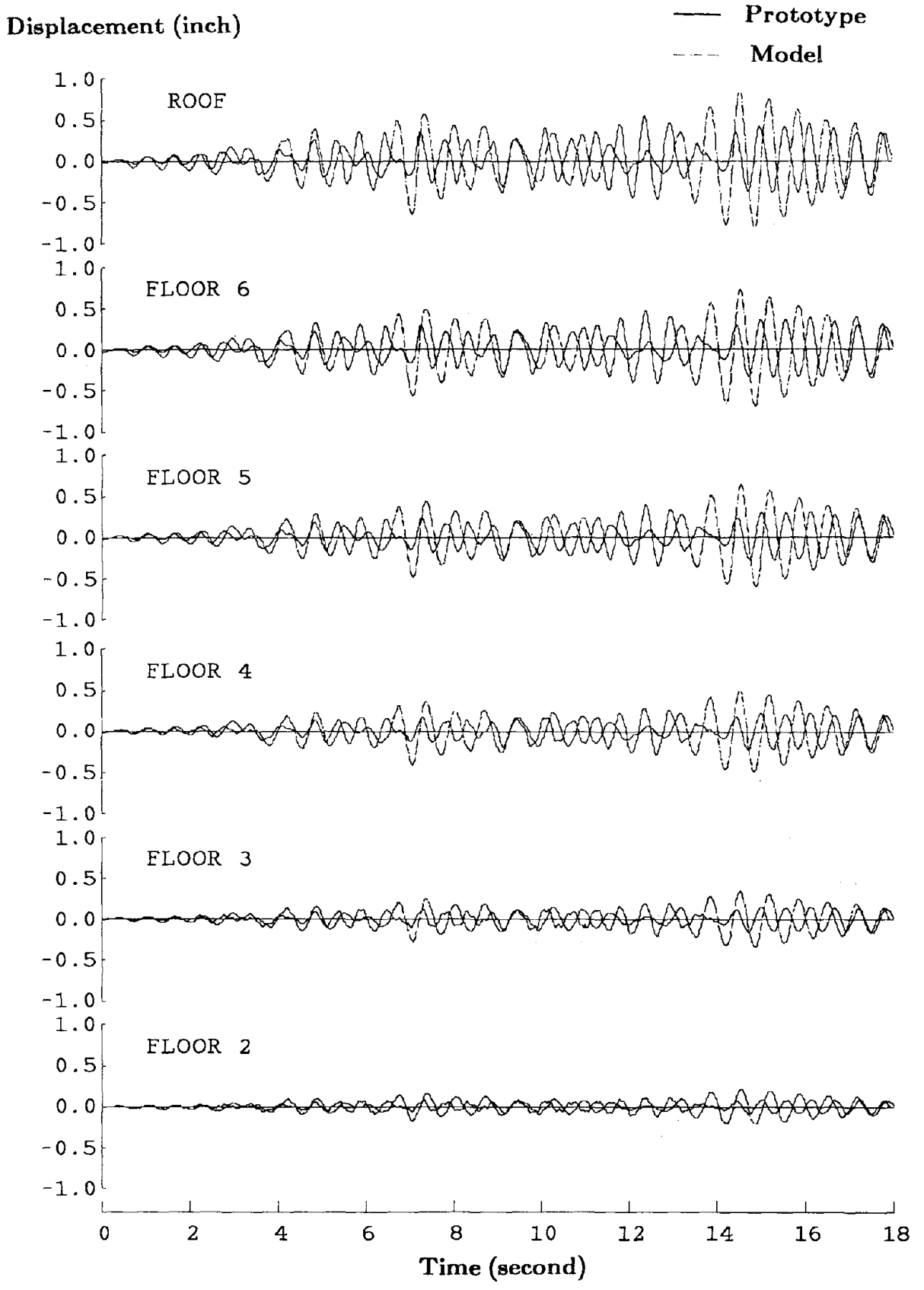


**FIGURE 10.11 PSD-ELASTIC AND TAFT-08 LATERAL DISPLACEMENT CORRELATION**

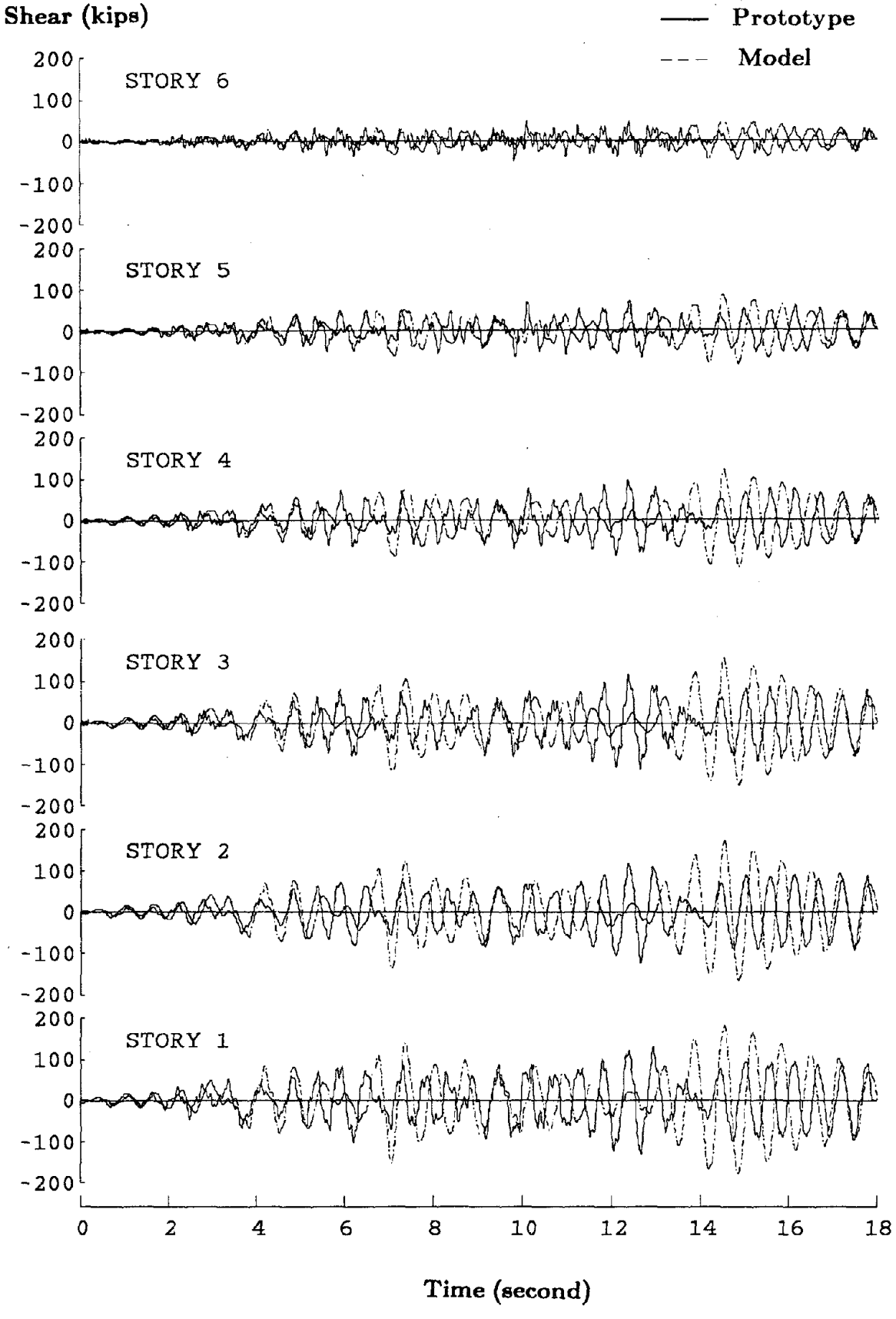


**FIGURE 10.12 PSD-ELASTIC AND TAFT-08 STORY SHEAR CORRELATION**

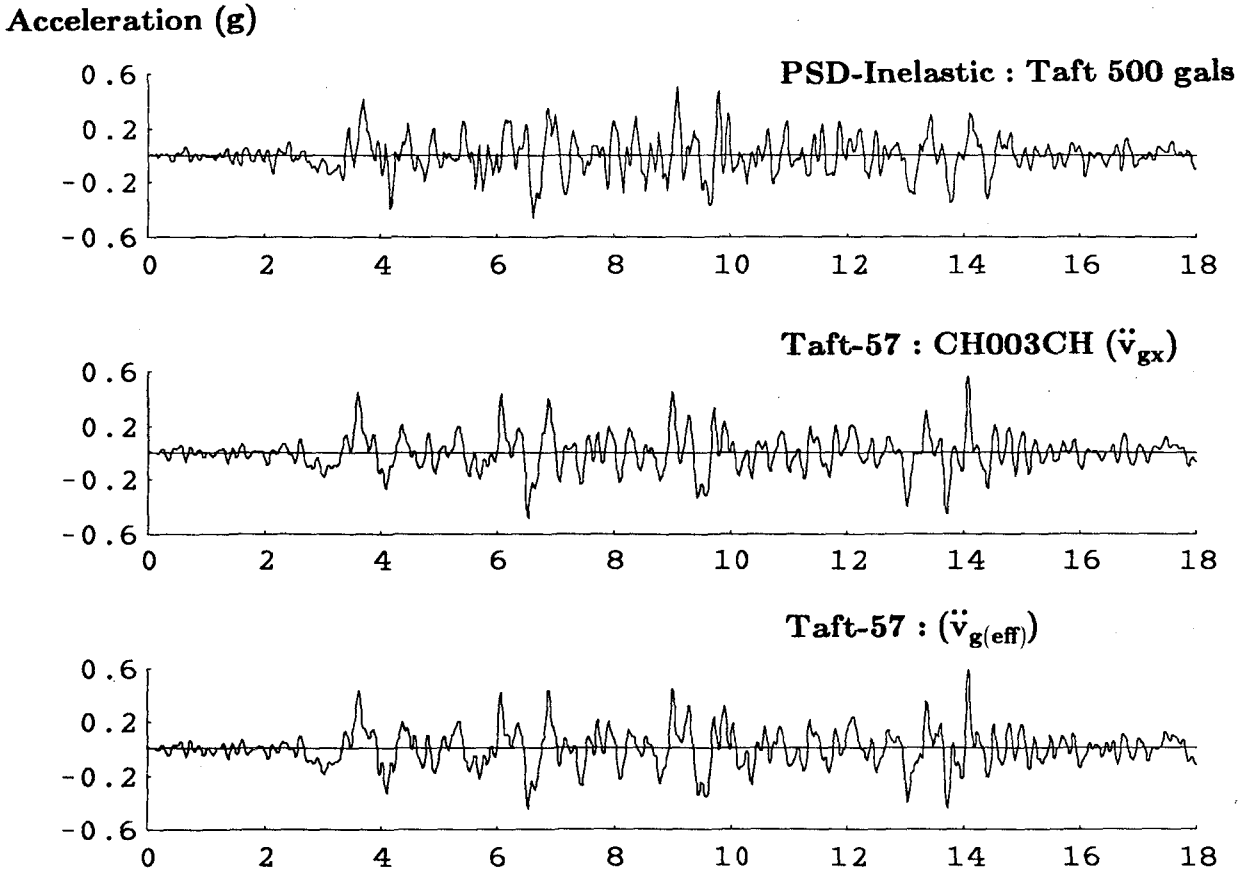


(a) Acceleration

FIGURE 10.13 PSD-INELASTIC AND TAFT-57 TEST INPUT MOTIONS

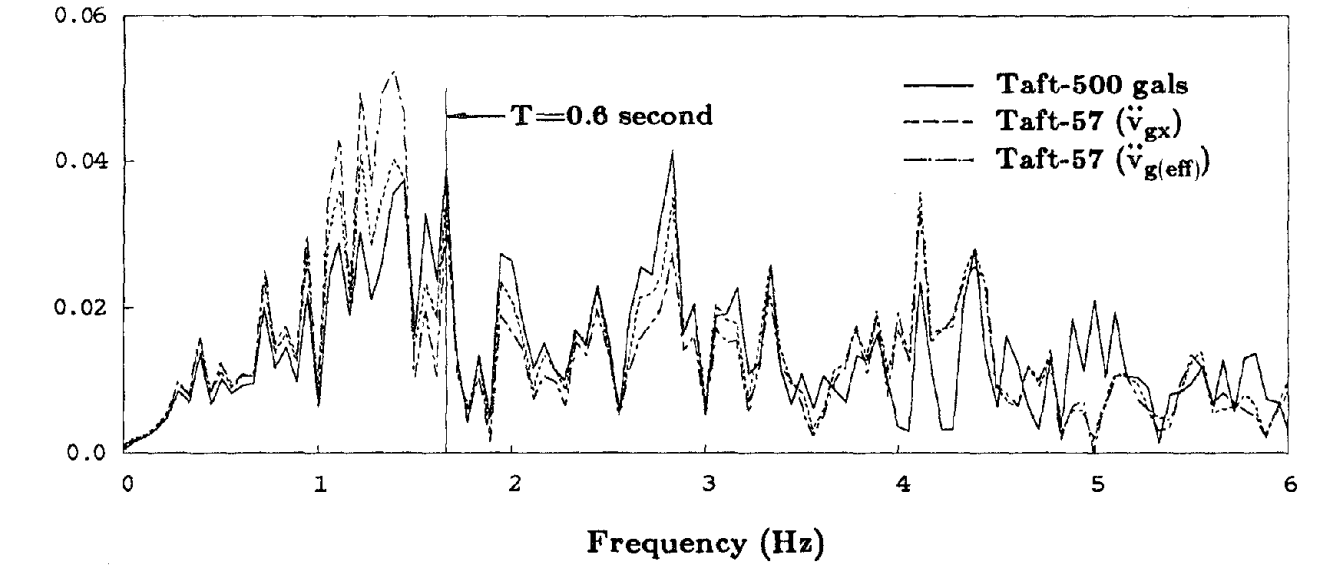


(b) Fourier Amplitude Spectrum

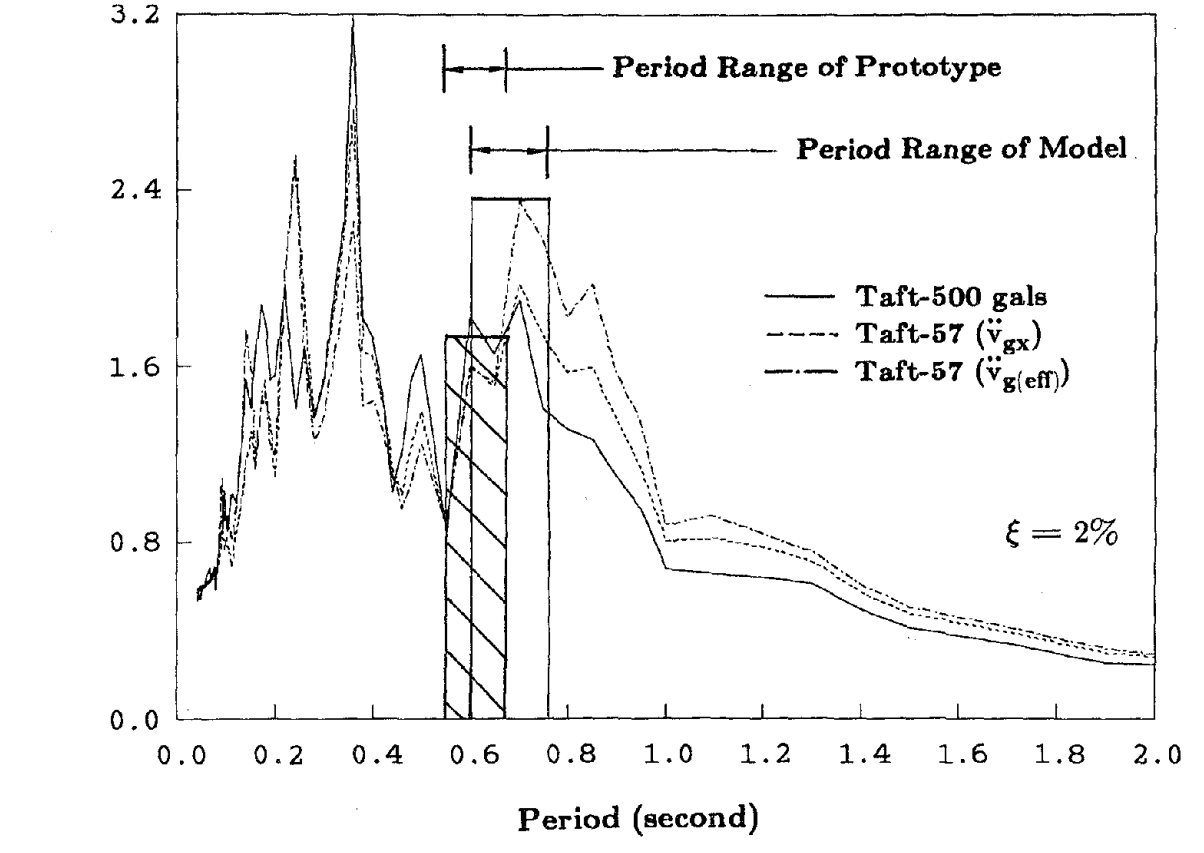


(c) Linear Elastic Response Spectra

FIGURE 10.13 PSD-INELASTIC AND TAFT-57 TEST INPUT MOTIONS

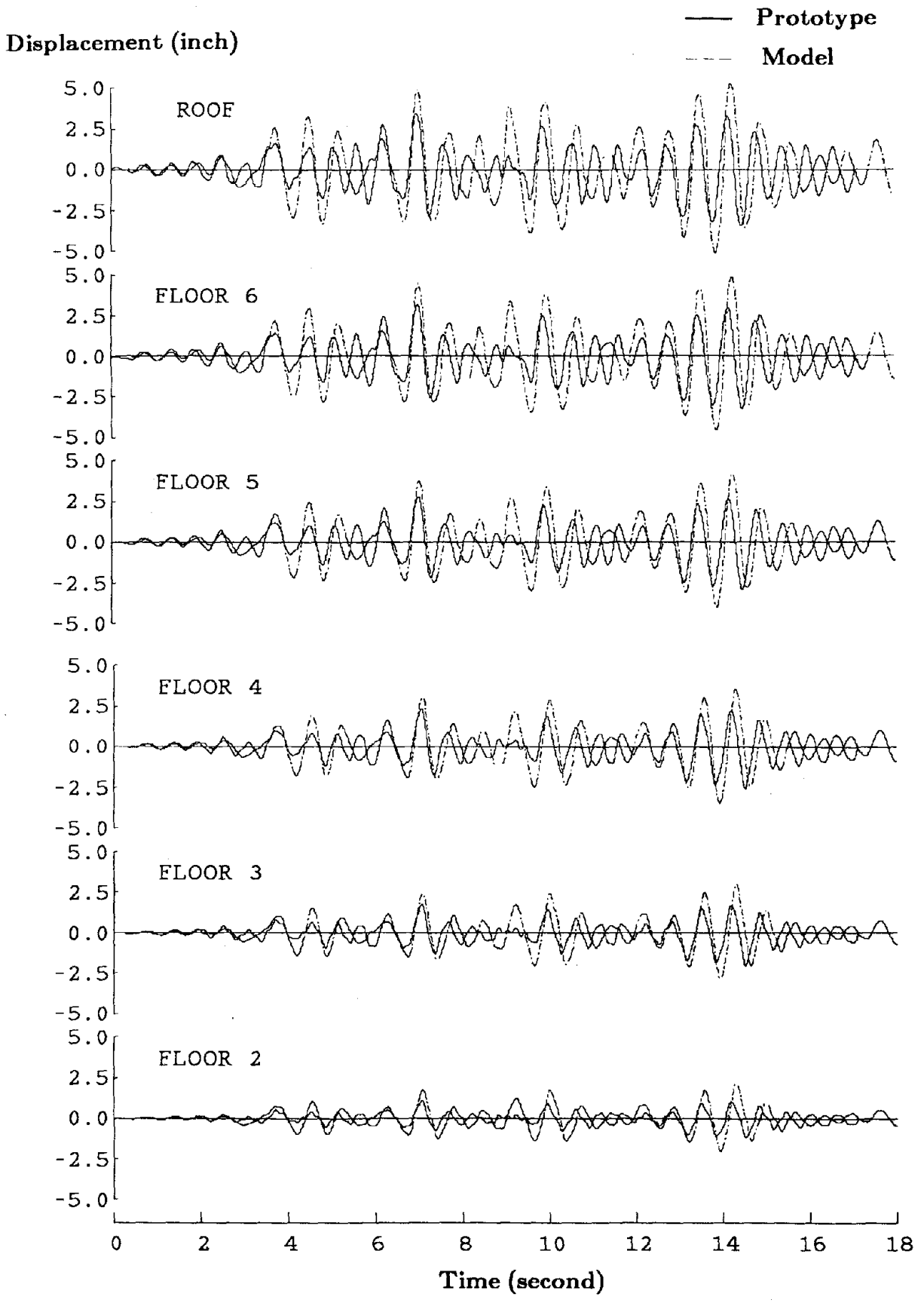


**FIGURE 10.14 PSD-INELASTIC AND TAFT-57 LATERAL DISPLACEMENT CORRELATION**

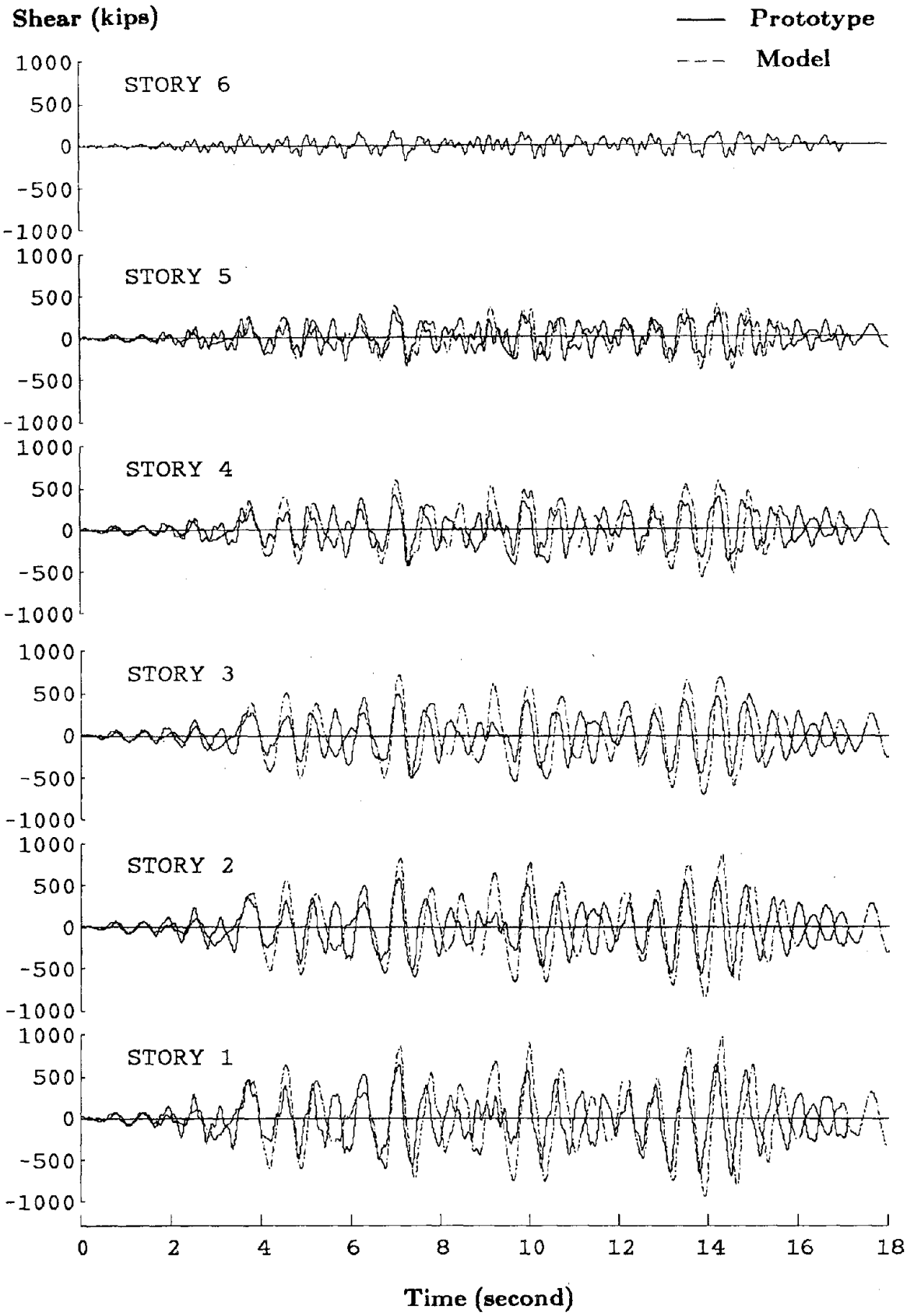


**FIGURE 10.15 PSD-INELASTIC AND TAFT-57 STORY SHEAR CORRELATION**

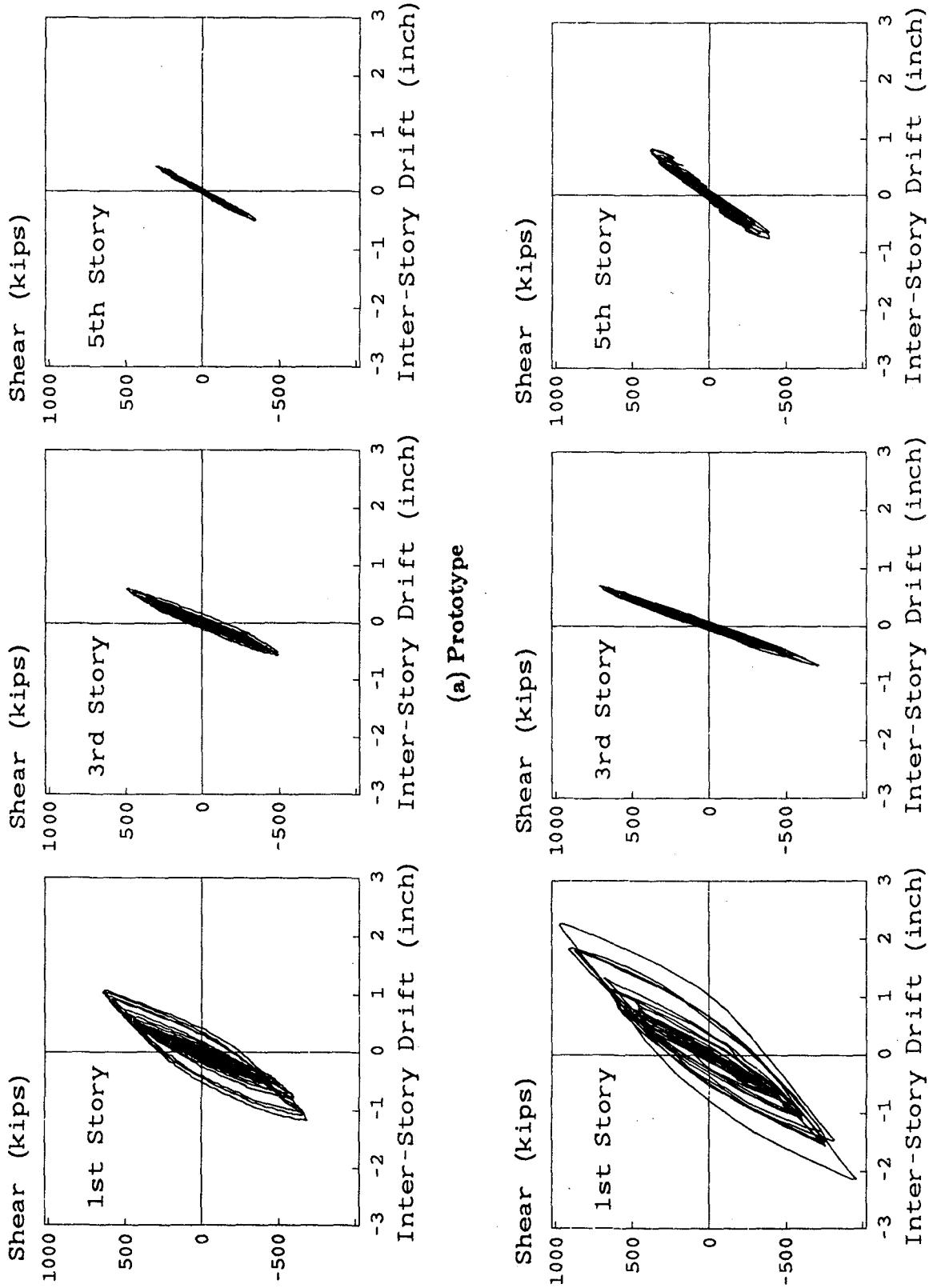


(a) Prototype

(b) Model

**FIGURE 10.16 PSD-INELASTIC AND TAFT-57 STORY SHEAR AND DRIFT CORRELATION**

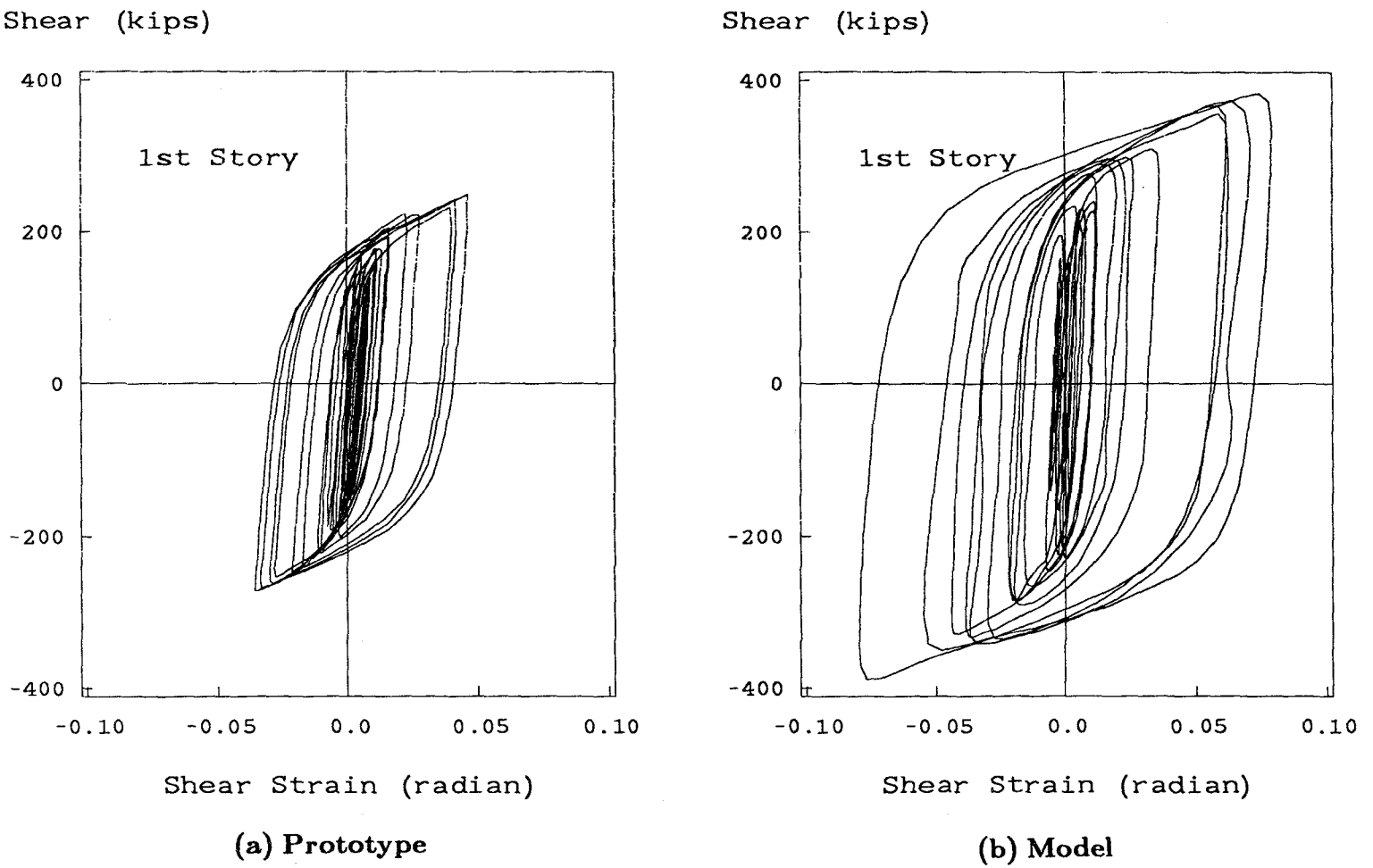


**(a) Prototype** **(b) Model**

**FIGURE 10.17 PSD-INELASTIC AND TAFT-57 HYSTERETIC BEHAVIOR OF THE SHEAR LINKS AT LEVEL L2**

## EARTHQUAKE ENGINEERING RESEARCH CENTER REPORT SERIES

EERC reports are available from the National Information Service for Earthquake Engineering(NISEE) and from the National Technical Information Service(NTIS). Numbers in parentheses are Accession Numbers assigned by the National Technical Information Service; these are followed by a price code. Contact NTIS, 5285 Port Royal Road, Springfield Virginia, 22161 for more information. Reports without Accession Numbers were not available from NTIS at the time of printing. For a current complete list of EERC reports (from EERC 67-1) and availablity information, please contact University of California, EERC, NISEE, 1301 South 46th Street, Richmond, California 94804.

UCB/EERC-80/01 "Earthquake Response of Concrete Gravity Dams Including Hydrodynamic and Foundation Interaction Effects," by Chopra, A.K., Chakrabarti, P. and Gupta, S., January 1980, (AD-A087297)A10.

UCB/EERC-80/02 "Rocking Response of Rigid Blocks to Earthquakes," by Yim, C.S., Chopra, A.K. and Penzien, J., January 1980, (PB80 166 002)A04.

UCB/EERC-80/03 "Optimum Inelastic Design of Seismic-Resistant Reinforced Concrete Frame Structures," by Zagajeski, S.W. and Bertero, V.V., January 1980, (PB80 164 635)A06.

UCB/EERC-80/04 "Effects of Amount and Arrangement of Wall-Panel Reinforcement on Hysteretic Behavior of Reinforced Concrete Walls," by Iliya, R. and Bertero, V.V., February 1980, (PB81 122 525)A09.

UCB/EERC-80/05 "Shaking Table Research on Concrete Dam Models," by Niwa, A. and Clough, R.W., September 1980, (PB81 122 368)A06.

UCB/EERC-80/06 "The Design of Steel Energy-Absorbing Restrainers and their Incorporation into Nuclear Power Plants for Enhanced Safety (Vol 1a): Piping with Energy Absorbing Restrainers: Parameter Study on Small Systems," by Powell, G.H., Oughourlian, C. and Simons, J., June 1980.

UCB/EERC-80/07 "Inelastic Torsional Response of Structures Subjected to Earthquake Ground Motions," by Yamazaki, Y., April 1980, (PB81 122 327)A08.

UCB/EERC-80/08 "Study of X-Braced Steel Frame Structures under Earthquake Simulation," by Ghanaat, Y., April 1980, (PB81 122 335)A11.

UCB/EERC-80/09 "Hybrid Modelling of Soil-Structure Interaction," by Gupta, S., Lin, T.W. and Penzien, J., May 1980, (PB81 122 319)A07.

UCB/EERC-80/10 "General Applicability of a Nonlinear Model of a One Story Steel Frame," by Sveinsson, B.I. and McNiven, H.D., May 1980, (PB81 124 877)A06.

UCB/EERC-80/11 "A Green-Function Method for Wave Interaction with a Submerged Body," by Kioka, W., April 1980, (PB81 122 269)A07.

UCB/EERC-80/12 "Hydrodynamic Pressure and Added Mass for Axisymmetric Bodies.," by Nilrat, F., May 1980, (PB81 122 343)A08.

UCB/EERC-80/13 "Treatment of Non-Linear Drag Forces Acting on Offshore Platforms," by Dao, B.V. and Penzien, J., May 1980, (PB81 153 413)A07.

UCB/EERC-80/14 "2D Plane/Axisymmetric Solid Element (Type 3-Elastic or Elastic-Perfectly Plastic) for the ANSR-II Program," by Mondkar, D.P. and Powell, G.H., July 1980, (PB81 122 350)A03.

UCB/EERC-80/15 "A Response Spectrum Method for Random Vibrations," by Der Kiureghian, A., June 1981, (PB81 122 301)A03.

UCB/EERC-80/16 "Cyclic Inelastic Buckling of Tubular Steel Braces," by Zayas, V.A., Popov, E.P. and Martin, S.A., June 1981, (PB81 124 885)A10.

UCB/EERC-80/17 "Dynamic Response of Simple Arch Dams Including Hydrodynamic Interaction," by Porter, C.S. and Chopra, A.K., July 1981, (PB81 124 000)A13.

UCB/EERC-80/18 "Experimental Testing of a Friction Damped Aseismic Base Isolation System with Fail-Safe Characteristics," by Kelly, J.M., Beucke, K.E. and Skinner, M.S., July 1980, (PB81 148 595)A04.

UCB/EERC-80/19 "The Design of Steel Emergy-Absorbing Restrainers and their Incorporation into Nuclear Power Plants for Enhanced Safety (Vol.1B): Stochastic Seismic Analyses of Nuclear Power Plant Structures and Piping Systems Subjected to Multiple Supported Excitations," by Lee, M.C. and Penzien, J., June 1980, (PB82 201 872)A08.

UCB/EERC-80/20 "The Design of Steel Energy-Absorbing Restrainers and their Incorporation into Nuclear Power Plants for Enhanced Safety (Vol 1C): Numerical Method for Dynamic Substructure Analysis," by Dickens, J.M. and Wilson, E.L., June 1980.

UCB/EERC-80/21 "The Design of Steel Energy-Absorbing Restrainers and their Incorporation into Nuclear Power Plants for Enhanced Safety (Vol 2): Development and Testing of Restraints for Nuclear Piping Systems," by Kelly, J.M. and Skinner, M.S., June 1980.

UCB/EERC-80/22 "3D Solid Element (Type 4-Elastic or Elastic-Perfectly-Plastic) for the ANSR-II Program," by Mondkar, D.P. and Powell, G.H., July 1980, (PB81 123 242)A03.

UCB/EERC-80/23 "Gap-Friction Element (Type 5) for the Ansr-II Program," by Mondkar, D.P. and Powell, G.H., July 1980, (PB81 122 285)A03.

UCB/EERC-80/24 "U-Bar Restraint Element (Type 11) for the ANSR-II Program," by Oughourlian, C. and Powell, G.H., July 1980, (PB81 122 293)A03.

UCB/EERC-80/25 "Testing of a Natural Rubber Base Isolation System by an Explosively Simulated Earthquake," by Kelly, J.M., August 1980, (PB81 201 360)A04.

UCB/EERC-80/26 "Input Identification from Structural Vibrational Response," by Hu, Y., August 1980, (PB81 152 308)A05.

UCB/EERC-80/27 "Cyclic Inelastic Behavior of Steel Offshore Structures," by Zayas, V.A., Mahin, S.A. and Popov, E.P., August 1980, (PB81 196 180)A15.

UCB/EERC-80/28 "Shaking Table Testing of a Reinforced Concrete Frame with Biaxial Response," by Oliva, M.G., October 1980, (PB81 154 304)A10.

UCB/EERC-80/29 "Dynamic Properties of a Twelve-Story Prefabricated Panel Building," by Bouwkamp, J.G., Kollegger, J.P. and Stephen, R.M., October 1980, (PB82 138 777)A07.

UCB/EERC-80/30 "Dynamic Properties of an Eight-Story Prefabricated Panel Building," by Bouwkamp, J.G., Kollegger, J.P. and Stephen, R.M., October 1980, (PB81 200 313)A05.

UCB/EERC-80/31 "Predictive Dynamic Response of Panel Type Structures under Earthquakes," by Kollegger, J.P. and Bouwkamp, J.G., October 1980, (PB81 152 316)A04.

UCB/EERC-80/32 "The Design of Steel Energy-Absorbing Restrainers and their Incorporation into Nuclear Power Plants for Enhanced Safety (Vol 3): Testing of Commercial Steels in Low-Cycle Torsional Fatique," by Spanner, P., Parker, E.R., Jongewaard, E. and Dory, M., 1980.

UCB/EERC-80/33 "The Design of Steel Energy-Absorbing Restrainers and their Incorporation into Nuclear Power Plants for Enhanced Safety (Vol 4): Shaking Table Tests of Piping Systems with Energy-Absorbing Restrainers," by Stiemer, S.F. and Godden, W.G., September 1980, (PB82 201 880)A05.

UCB/EERC-80/34 "The Design of Steel Energy-Absorbing Restrainers and their Incorporation into Nuclear Power Plants for Enhanced Safety (Vol 5): Summary Report," by Spencer, P., 1980.

UCB/EERC-80/35 "Experimental Testing of an Energy-Absorbing Base Isolation System," by Kelly, J.M., Skinner, M.S. and Beucke, K.E., October 1980, (PB81 154 072)A04.

UCB/EERC-80/36 "Simulating and Analyzing Artificial Non-Stationary Earth Ground Motions," by Nau, R.F., Oliver, R.M. and Pister, K.S., October 1980, (PB81 153 397)A04.

UCB/EERC-80/37 "Earthquake Engineering at Berkeley - 1980," by , September 1980, (PB81 205 674)A09.

UCB/EERC-80/38 "Inelastic Seismic Analysis of Large Panel Buildings," by Schricker, V. and Powell, G.H., September 1980, (PB81 154 338)A13.

UCB/EERC-80/39 "Dynamic Response of Embankment, Concrete-Gavity and Arch Dams Including Hydrodynamic Interation," by Hall, J.F. and Chopra, A.K., October 1980, (PB81 152 324)A11.

UCB/EERC-80/40 "Inelastic Buckling of Steel Struts under Cyclic Load Reversal.," by Black, R.G. , Wenger, W.A. and Popov, E.P., October 1980, (PB81 154 312)A08.

UCB/EERC-80/41 "Influence of Site Characteristics on Buildings Damage during the October 3,1974 Lima Earthquake," by Repetto, P., Arango, I. and Seed, H.B., September 1980, (PB81 161 739)A05.

UCB/EERC-80/42 "Evaluation of a Shaking Table Test Program on Response Behavior of a Two Story Reinforced Concrete Frame," by Blondet, J.M., Clough, R.W. and Mahin, S.A., December 1980, (PB82 196 544)A11.

UCB/EERC-80/43 "Modelling of Soil-Structure Interaction by Finite and Infinite Elements," by Medina, F., December 1980, (PB81 229 270)A04.

UCB/EERC-81/01 "Control of Seismic Response of Piping Systems and Other Structures by Base Isolation," by Kelly, J.M., January 1981, (PB81 200 735)A05.

UCB/EERC-81/02 "OPTNSR- An Interactive Software System for Optimal Design of Statically and Dynamically Loaded Structures with Nonlinear Response," by Bhatti, M.A., Ciampi, V. and Pister, K.S., January 1981, (PB81 218 851)A09.

UCB/EERC-81/03 "Analysis of Local Variations in Free Field Seismic Ground Motions," by Chen, J.-C., Lysmer, J. and Seed, H.B., January 1981, (AD-A099508)A13.

UCB/EERC-81/04 "Inelastic Structural Modeling of Braced Offshore Platforms for Seismic Loading. ," by Zayas, V.A., Shing, P.-S.B., Mahin, S.A. and Popov, E.P., January 1981, (PB82 138 777)A07.

UCB/EERC-81/05 "Dynamic Response of Light Equipment in Structures," by Der Kiureghian, A., Sackman, J.L. and Nour-Omid, B., April 1981, (PB81 218 497)A04.

UCB/EERC-81/06 "Preliminary Experimental Investigation of a Broad Base Liquid Storage Tank," by Bouwkamp, J.G., Kollegger, J.P. and Stephen, R.M., May 1981, (PB82 140 385)A03.

UCB/EERC-81/07 "The Seismic Resistant Design of Reinforced Concrete Coupled Structural Walls," by Aktan, A.E. and Bertero, V.V., June 1981, (PB82 113 358)A11.

UCB/EERC-81/08 "Unassigned," by Unassigned, 1981.

UCB/EERC-81/09 "Experimental Behavior of a Spatial Piping System with Steel Energy Absorbers Subjected to a Simulated Differential Seismic Input," by Stiemer, S.F., Godden, W.G. and Kelly, J.M., July 1981, (PB82 201 898)A04.

UCB/EERC-81/10 "Evaluation of Seismic Design Provisions for Masonry in the United States," by Sveinsson, B.I., Mayes, R.L. and McNiven, H.D., August 1981, (PB82 166 075)A08.

UCB/EERC-81/11 "Two-Dimensional Hybrid Modelling of Soil-Structure Interaction," by Tzong, T.-J., Gupta, S. and Penzien, J., August 1981, (PB82 142 118)A04.

UCB/EERC-81/12 "Studies on Effects of Infills in Seismic Resistant R/C Construction," by Brokken, S. and Bertero, V.V., October 1981, (PB82 166 190)A09.

UCB/EERC-81/13 "Linear Models to Predict the Nonlinear Seismic Behavior of a One-Story Steel Frame," by Valdimarsson, H., Shah, A.H. and McNiven, H.D., September 1981, (PB82 138 793)A07.

UCB/EERC-81/14 "TLUSH: A Computer Program for the Three-Dimensional Dynamic Analysis of Earth Dams," by Kagawa, T., Mejia, L.H., Seed, H.B. and Lysmer, J., September 1981, (PB82 139 940)A06.

UCB/EERC-81/15 "Three Dimensional Dynamic Response Analysis of Earth Dams," by Mejia, L.H. and Seed, H.B., September 1981, (PB82 137 274)A12.

UCB/EERC-81/16 "Experimental Study of Lead and Elastomeric Dampers for Base Isolation Systems," by Kelly, J.M. and Hodder, S.B., October 1981, (PB82 166 182)A05.

UCB/EERC-81/17 "The Influence of Base Isolation on the Seismic Response of Light Secondary Equipment," by Kelly, J.M., April 1981, (PB82 255 266)A04.

UCB/EERC-81/18 "Studies on Evaluation of Shaking Table Response Analysis Procedures," by Blondet, J. Marcial, November 1981, (PB82 197 278)A10.

UCB/EERC-81/19 "DELIGHT.STRUCT: A Computer-Aided Design Environment for Structural Engineering. ," by Balling, R.J., Pister, K.S. and Polak, E., December 1981, (PB82 218 496)A07.

UCB/EERC-81/20 "Optimal Design of Seismic-Resistant Planar Steel Frames," by Balling, R.J., Ciampi, V. and Pister, K.S., December 1981, (PB82 220 179)A07.

UCB/EERC-82/01 "Dynamic Behavior of Ground for Seismic Analysis of Lifeline Systems," by Sato, T. and Der Kiureghian, A., January 1982, (PB82 218 926)A05.

UCB/EERC-82/02 "Shaking Table Tests of a Tubular Steel Frame Model," by Ghanaat, Y. and Clough, R.W., January 1982, (PB82 220 161)A07.

UCB/EERC-82/03 "Behavior of a Piping System under Seismic Excitation: Experimental Investigations of a Spatial Piping System supported by Mechanical Shock Arrestors," by Schneider, S., Lee, H.-M. and Godden, W. G., May 1982, (PB83 172 544)A09.

UCB/EERC-82/04 "New Approaches for the Dynamic Analysis of Large Structural Systems," by Wilson, E.L., June 1982, (PB83 148 080)A05.

UCB/EERC-82/05 "Model Study of Effects of Damage on the Vibration Properties of Steel Offshore Platforms," by Shahrivar, F. and Bouwkamp, J.G., June 1982, (PB83 148 742)A10.

UCB/EERC-82/06 "States of the Art and Pratice in the Optimum Seismic Design and Analytical Response Prediction of R/C Frame Wall Structures," by Aktan, A.E. and Bertero, V.V., July 1982, (PB83 147 736)A05.

UCB/EERC-82/07 "Further Study of the Earthquake Response of a Broad Cylindrical Liquid-Storage Tank Model," by Manos, G.C. and Clough, R.W., July 1982, (PB83 147 744)A11.

UCB/EERC-82/08 "An Evaluation of the Design and Analytical Seismic Response of a Seven Story Reinforced Concrete Frame," by Charney, F.A. and Bertero, V.V., July 1982, (PB83 157 628)A09.

UCB/EERC-82/09 "Fluid-Structure Interactions: Added Mass Computations for Incompressible Fluid. ," by Kuo, J.S.-H., August 1982, (PB83 156 281)A07.

UCB/EERC-82/10 "Joint-Opening Nonlinear Mechanism: Interface Smeared Crack Model," by Kuo, J.S.-H., August 1982, (PB83 149 195)A05.

UCB/EERC-82/11 "Dynamic Response Analysis of Techi Dam," by Clough, R.W., Stephen, R.M. and Kuo, J.S.-H., August 1982, (PB83 147 496)A06.

UCB/EERC-82/12 "Prediction of the Seismic Response of R/C Frame-Coupled Wall Structures," by Aktan, A.E., Bertero, V.V. and Piazzo, M., August 1982, (PB83 149 203)A09.

UCB/EERC-82/13 "Preliminary Report on the Smart 1 Strong Motion Array in Taiwan," by Bolt, B.A. , Loh, C.H., Penzien, J. and Tsai, Y.B., August 1982, (PB83 159 400)A10.

UCB/EERC-82/14 "Shaking-Table Studies of an Eccentrically X-Braced Steel Structure," by Yang, M.S., September 1982, (PB83 260 778)A12.

UCB/EERC-82/15 "The Performance of Stairways in Earthquakes," by Roha, C., Axley, J.W. and Bertero, V.V., September 1982, (PB83 157 693)A07.

UCB/EERC-82/16 "The Behavior of Submerged Multiple Bodies in Earthquakes," by Liao, W.-G., September 1982, (PB83 158 709)A07.

UCB/EERC-82/17 "Effects of Concrete Types and Loading Conditions on Local Bond-Slip Relationships," by Cowell, A.D., Popov, E.P. and Bertero, V.V., September 1982, (PB83 153 577)A04.

UCB/EERC-82/18 "Mechanical Behavior of Shear Wall Vertical Boundary Members: An Experimental Investigation," by Wagner, M.T. and Bertero, V.V., October 1982, (PB83 159 764)A05.

UCB/EERC-82/19 "Experimental Studies of Multi-support Seismic Loading on Piping Systems," by Kelly, J.M. and Cowell, A.D., November 1982.

UCB/EERC-82/20 "Generalized Plastic Hinge Concepts for 3D Beam-Column Elements," by Chen, P. F.-S. and Powell, G.H., November 1982, (PB83 247 981)A13.

UCB/EERC-82/21 "ANSR-II: General Computer Program for Nonlinear Structural Analysis," by Oughourlian, C.V. and Powell, G.H., November 1982, (PB83 251 330)A12.

UCB/EERC-82/22 "Solution Strategies for Statically Loaded Nonlinear Structures," by Simons, J.W. and Powell, G.H., November 1982, (PB83 197 970)A06.

UCB/EERC-82/23 "Analytical Model of Deformed Bar Anchorages under Generalized Excitations," by Ciampi, V., Eligehausen, R., Bertero, V.V. and Popov, E.P., November 1982, (PB83 169 532)A06.

UCB/EERC-82/24 "A Mathematical Model for the Response of Masonry Walls to Dynamic Excitations," by Sucuoglu, H., Mengi, Y. and McNiven, H.D., November 1982, (PB83 169 011)A07.

UCB/EERC-82/25 "Earthquake Response Considerations of Broad Liquid Storage Tanks," by Cambra, F.J., November 1982, (PB83 251 215)A09.

UCB/EERC-82/26 "Computational Models for Cyclic Plasticity, Rate Dependence and Creep," by Mosaddad, B. and Powell, G.H., November 1982, (PB83 245 829)A08.

UCB/EERC-82/27 "Inelastic Analysis of Piping and Tubular Structures," by Mahasuverachai, M. and Powell, G.H., November 1982, (PB83 249 987)A07.

UCB/EERC-83/01 "The Economic Feasibility of Seismic Rehabilitation of Buildings by Base Isolation," by Kelly, J.M., January 1983, (PB83 197 988)A05.

UCB/EERC-83/02 "Seismic Moment Connections for Moment-Resisting Steel Frames.," by Popov, E.P., January 1983, (PB83 195 412)A04.

UCB/EERC-83/03 "Design of Links and Beam-to-Column Connections for Eccentrically Braced Steel Frames," by Popov, E.P. and Malley, J.O., January 1983, (PB83 194 811)A04.

UCB/EERC-83/04 "Numerical Techniques for the Evaluation of Soil-Structure Interaction Effects in the Time Domain," by Bayo, E. and Wilson, E.L., February 1983, (PB83 245 605)A09.

UCB/EERC-83/05 "A Transducer for Measuring the Internal Forces in the Columns of a Frame-Wall Reinforced Concrete Structure," by Sause, R. and Bertero, V.V., May 1983, (PB84 119 494)A06.

UCB/EERC-83/06 "Dynamic Interactions Between Floating Ice and Offshore Structures," by Croteau, P., May 1983, (PB84 119 486)A16.

UCB/EERC-83/07 "Dynamic Analysis of Multiply Tuned and Arbitrarily Supported Secondary Systems. ," by Igusa, T. and Der Kiureghian, A., July 1983, (PB84 118 272)A11.

UCB/EERC-83/08 "A Laboratory Study of Submerged Multi-body Systems in Earthquakes," by Ansari, G.R., June 1983, (PB83 261 842)A17.

UCB/EERC-83/09 "Effects of Transient Foundation Uplift on Earthquake Response of Structures," by Yim, C.-S. and Chopra, A.K., June 1983, (PB83 261 396)A07.

UCB/EERC-83/10 "Optimal Design of Friction-Braced Frames under Seismic Loading," by Austin, M.A. and Pister, K.S., June 1983, (PB84 119 288)A06.

UCB/EERC-83/11 "Shaking Table Study of Single-Story Masonry Houses: Dynamic Performance under Three Component Seismic Input and Recommendations," by Manos, G.C., Clough, R.W. and Mayes, R.L., July 1983, (UCB/EERC-83/11)A08.

UCB/EERC-83/12 "Experimental Error Propagation in Pseudodynamic Testing," by Shiing, P.B. and Mahin, S.A., June 1983, (PB84 119 270)A09.

UCB/EERC-83/13 "Experimental and Analytical Predictions of the Mechanical Characteristics of a 1/5-scale Model of a 7-story R/C Frame-Wall Building Structure," by Aktan, A.E., Bertero, V.V., Chowdhury, A.A. and Nagashima, T., June 1983, (PB84 119 213)A07.

UCB/EERC-83/14 "Shaking Table Tests of Large-Panel Precast Concrete Building System Assemblages," by Oliva, M.G. and Clough, R.W., June 1983, (PB86 110 210/AS)A11.

UCB/EERC-83/15 "Seismic Behavior of Active Beam Links in Eccentrically Braced Frames," by Hjelmstad, K.D. and Popov, E.P., July 1983, (PB84 119 676)A09.

UCB/EERC-83/16 "System Identification of Structures with Joint Rotation," by Dimsdale, J.S., July 1983, (PB84 192 210)A06.

UCB/EERC-83/17 "Construction of Inelastic Response Spectra for Single-Degree-of-Freedom Systems," by Mahin, S. and Lin, J., June 1983, (PB84 208 834)A05.

UCB/EERC-83/18 "Interactive Computer Analysis Methods for Predicting the Inelastic Cyclic Behaviour of Structural Sections," by Kaba, S. and Mahin, S., July 1983, (PB84 192 012)A06.

UCB/EERC-83/19 "Effects of Bond Deterioration on Hysteretic Behavior of Reinforced Concrete Joints," by Filippou, F.C., Popov, E.P. and Bertero, V.V., August 1983, (PB84 192 020)A10.

UCB/EERC-83/20 "Analytical and Experimental Correlation of Large-Panel Precast Building System Performance," by Oliva, M.G., Clough, R.W., Velkov, M. and Gavrilovic, P., November 1983.

UCB/EERC-83/21 "Mechanical Characteristics of Materials Used in a 1/5 Scale Model of a 7-Story Reinforced Concrete Test Structure," by Bertero, V.V., Aktan, A.E., Harris, H.G. and Chowdhury, A.A., October 1983, (PB84 193 697)A05.

UCB/EERC-83/22 "Hybrid Modelling of Soil-Structure Interaction in Layered Media," by Tzong, T.-J. and Penzien, J., October 1983, (PB84 192 178)A08.

UCB/EERC-83/23 "Local Bond Stress-Slip Relationships of Deformed Bars under Generalized Excitations," by Eligehausen, R., Popov, E.P. and Bertero, V.V., October 1983, (PB84 192 848)A09.

UCB/EERC-83/24 "Design Considerations for Shear Links in Eccentrically Braced Frames," by Malley, J.O. and Popov, E.P., November 1983, (PB84 192 186)A07.

UCB/EERC-84/01 "Pseudodynamic Test Method for Seismic Performance Evaluation: Theory and Implementation," by Shing, P.-S. B. and Mahin, S.A., January 1984, (PB84 190 644)A08.

UCB/EERC-84/02 "Dynamic Response Behavior of Kiang Hong Dian Dam," by Clough, R.W., Chang, K.-T., Chen, H.-Q. and Stephen, R.M., April 1984, (PB84 209 402)A08.

UCB/EERC-84/03 "Refined Modelling of Reinforced Concrete Columns for Seismic Analysis," by Kaba, S.A. and Mahin, S.A., April 1984, (PB84 234 384)A06.

UCB/EERC-84/04 "A New Floor Response Spectrum Method for Seismic Analysis of Multiply Supported Secondary Systems," by Asfura, A. and Der Kiureghian, A., June 1984, (PB84 239 417)A06.

UCB/EERC-84/05 "Earthquake Simulation Tests and Associated Studies of a 1/5th-scale Model of a 7-Story R/C Frame-Wall Test Structure," by Bertero, V.V., Aktan, A.E., Charney, F.A. and Sause, R., June 1984, (PB84 239 409)A09.

UCB/EERC-84/06 "R/C Structural Walls: Seismic Design for Shear," by Aktan, A.E. and Bertero, V.V., 1984.

UCB/EERC-84/07 "Behavior of Interior and Exterior Flat-Plate Connections subjected to Inelastic Load Reversals," by Zee, H.L. and Moehle, J.P., August 1984, (PB86 117 629/AS)A07.

UCB/EERC-84/08 "Experimental Study of the Seismic Behavior of a Two-Story Flat-Plate Structure. ," by Moehle, J.P. and Diebold, J.W., August 1984, (PB86 122 553/AS)A12.

UCB/EERC-84/09 "Phenomenological Modeling of Steel Braces under Cyclic Loading," by Ikeda, K., Mahin, S.A. and Dermitzakis, S.N., May 1984, (PB86 132 198/AS)A08.

UCB/EERC-84/10 "Earthquake Analysis and Response of Concrete Gravity Dams," by Fenves, G. and Chopra, A.K., August 1984, (PB85 193 902/AS)A11.

UCB/EERC-84/11 "EAGD-84: A Computer Program for Earthquake Analysis of Concrete Gravity Dams," by Fenves, G. and Chopra, A.K., August 1984, (PB85 193 613/AS)A05.

UCB/EERC-84/12 "A Refined Physical Theory Model for Predicting the Seismic Behavior of Braced Steel Frames," by Ikeda, K. and Mahin, S.A., July 1984, (PB85 191 450/AS)A09.

UCB/EERC-84/13 "Earthquake Engineering Research at Berkeley - 1984," by , August 1984, (PB85 197 341/AS)A10.

UCB/EERC-84/14 "Moduli and Damping Factors for Dynamic Analyses of Cohesionless Soils," by Seed, H.B., Wong, R.T., Idriss, I.M. and Tokimatsu, K., September 1984, (PB85 191 468/AS)A04.

UCB/EERC-84/15 "The Influence of SPT Procedures in Soil Liquefaction Resistance Evaluations," by Seed, H.B., Tokimatsu, K., Harder, L.F. and Chung, R.M., October 1984, (PB85 191 732/AS)A04.

UCB/EERC-84/16 "Simplified Procedures for the Evaluation of Settlements in Sands Due to Earthquake Shaking," by Tokimatsu, K. and Seed, H.B., October 1984, (PB85 197 887/AS)A03.

UCB/EERC-84/17 "Evaluation of Energy Absorption Characteristics of Bridges under Seismic Conditions," by Imbsen, R.A. and Penzien, J., November 1984.

UCB/EERC-84/18 "Structure-Foundation Interactions under Dynamic Loads," by Liu, W.D. and Penzien, J., November 1984, (PB87 124 889/AS)A11.

UCB/EERC-84/19 "Seismic Modelling of Deep Foundations," by Chen, C.-H. and Penzien, J., November 1984, (PB87 124 798/AS)A07.

UCB/EERC-84/20 "Dynamic Response Behavior of Quan Shui Dam," by Clough, R.W., Chang, K.-T., Chen, H.-Q., Stephen, R.M., Ghanaat, Y. and Qi, J.-H., November 1984, (PB86 115177/AS)A07.

UCB/EERC-85/01 "Simplified Methods of Analysis for Earthquake Resistant Design of Buildings," by Cruz, E.F. and Chopra, A.K., February 1985, (PB86 112299/AS)A12.

UCB/EERC-85/02 "Estimation of Seismic Wave Coherency and Rupture Velocity using the SMART 1 Strong-Motion Array Recordings," by Abrahamson, N.A., March 1985, (PB86 214 343)A07.

UCB/EERC-85/03 "Dynamic Properties of a Thirty Story Condominium Tower Building," by Stephen, R.M., Wilson, E.L. and Stander, N., April 1985, (PB86 118965/AS)A06.

UCB/EERC-85/04 "Development of Substructuring Techniques for On-Line Computer Controlled Seismic Performance Testing," by Dermitzakis, S. and Mahin, S., February 1985, (PB86 132941/AS)A08.

UCB/EERC-85/05 "A Simple Model for Reinforcing Bar Anchorages under Cyclic Excitations," by Filippou, F.C., March 1985, (PB86 112 919/AS)A05.

UCB/EERC-85/06 "Racking Behavior of Wood-framed Gypsum Panels under Dynamic Load," by Oliva, M.G., June 1985.

UCB/EERC-85/07 "Earthquake Analysis and Response of Concrete Arch Dams," by Fok, K.-L. and Chopra, A.K., June 1985, (PB86 139672/AS)A10.

UCB/EERC-85/08 "Effect of Inelastic Behavior on the Analysis and Design of Earthquake Resistant Structures," by Lin, J.P. and Mahin, S.A., June 1985, (PB86 135340/AS)A08.

UCB/EERC-85/09 "Earthquake Simulator Testing of a Base-Isolated Bridge Deck," by Kelly, J.M., Buckle, I.G. and Tsai, H.-C., January 1986, (PB87 124 152/AS)A06.

UCB/EERC-85/10 "Simplified Analysis for Earthquake Resistant Design of Concrete Gravity Dams," by Fenves, G. and Chopra, A.K., June 1986, (PB87 124 160/AS)A08.

UCB/EERC-85/11 "Dynamic Interaction Effects in Arch Dams," by Clough, R.W., Chang, K.-T., Chen, H.-Q. and Ghanaat, Y., October 1985, (PB86 135027/AS)A05.

UCB/EERC-85/12 "Dynamic Response of Long Valley Dam in the Mammoth Lake Earthquake Series of May 25-27, 1980," by Lai, S. and Seed, H.B., November 1985, (PB86 142304/AS)A05.

UCB/EERC-85/13 "A Methodology for Computer-Aided Design of Earthquake-Resistant Steel Structures," by Austin, M.A., Pister, K.S. and Mahin, S.A., December 1985, (PB86 159480/AS)A10 .

UCB/EERC-85/14 "Response of Tension-Leg Platforms to Vertical Seismic Excitations," by Liou, G.-S., Penzien, J. and Yeung, R.W., December 1985, (PB87 124 871/AS)A08.

UCB/EERC-85/15 "Cyclic Loading Tests of Masonry Single Piers: Volume 4 - Additional Tests with Height to Width Ratio of 1," by Sveinsson, B., McNiven, H.D. and Sucuoglu, H., December 1985.

UCB/EERC-85/16 "An Experimental Program for Studying the Dynamic Response of a Steel Frame with a Variety of Infill Partitions," by Yanev, B. and McNiven, H.D., December 1985.

UCB/EERC-86/01 "A Study of Seismically Resistant Eccentrically Braced Steel Frame Systems," by Kasai, K. and Popov, E.P., January 1986, (PB87 124 178/AS)A14.

UCB/EERC-86/02 "Design Problems in Soil Liquefaction," by Seed, H.B., February 1986, (PB87 124 186/AS)A03.

UCB/EERC-86/03 "Implications of Recent Earthquakes and Research on Earthquake-Resistant Design and Construction of Buildings," by Bertero, V.V., March 1986, (PB87 124 194/AS)A05.

UCB/EERC-86/04 "The Use of Load Dependent Vectors for Dynamic and Earthquake Analyses," by Leger, P., Wilson, E.L. and Clough, R.W., March 1986, (PB87 124 202/AS)A12.

UCB/EERC-86/05 "Two Beam-To-Column Web Connections," by Tsai, K.-C. and Popov, E.P., April 1986 , (PB87 124 301/AS)A04.

UCB/EERC-86/06 "Determination of Penetration Resistance for Coarse-Grained Soils using the Becker Hammer Drill," by Harder, L.F. and Seed, H.B., May 1986, (PB87 124 210/AS)A07.

UCB/EERC-86/07 "A Mathematical Model for Predicting the Nonlinear Response of Unreinforced Masonry Walls to In-Plane Earthquake Excitations," by Mengi, Y. and McNiven, H.D., May 1986, (PB87 124 780/AS)A06.

UCB/EERC-86/08 "The 19 September 1985 Mexico Earthquake: Building Behavior," by Bertero, V.V., July 1986.

UCB/EERC-86/09 "EACD-3D: A Computer Program for Three-Dimensional Earthquake Analysis of Concrete Dams," by Fok, K.-L., Hall, J.F. and Chopra, A.K., July 1986, (PB87 124 228/AS)A08.

UCB/EERC-86/10 "Earthquake Simulation Tests and Associated Studies of a 0.3-Scale Model of a Six-Story Concentrically Braced Steel Structure," by Uang, C.-M. and Bertero, V.V., December 1986.

UCB/EERC-86/11 "Mechanical Characteristics of Base Isolation Bearings for a Bridge Deck Model Test," by Kelly, J.M., Buckle, I.G. and Koh, C.-G., 1987.

UCB/EERC-86/12 "Modelling of Dynamic Response of Elastomeric Isolation Bearings," by Koh, C.-G. and Kelly, J.M., 1987.

UCB/EERC-87/01 "FPS Earthquake Resisting System: Experimental Report," by Zayas, V.A., Low, S.S. and Mahin, S.A., June 1987.

UCB/EERC-87/02 "Earthquake Simulator Tests and Associated Studies of a 0.3-Scale Model of a Six-Story Eccentrically Braced Steel Structure," by Whittaker, A., Uang, C.-M. and Bertero, V.V., July 1987.